Physics of the Solid State, Vol. 47, No. 5, 2005, pp. 797–800. Translated from Fizika Tverdogo Tela, Vol. 47, No. 5, 2005, pp. 771–776.

Serafim Nikolaevich Zhurkov (May 29, 1905–September 18, 1997)

S.N. Zhurkov belongs to the league of scientists who have devoted their academic careers to a single main problem. For Zhurkov, the physical nature of the mechanical properties of solids and, above all, of their strength was such a problem. When investigating this line of research, Zhurkov obtained new efficient results that envisaged the possibilities of future successful developments of the science of strength of materials.

Zhurkov began his scientific career in Leningrad in 1930 at the Ioffe Physicotechnical Institute of the USSR Academy of Sciences after graduating from the physicochemical faculty of Voronezh State University. By then, the theoretical mechanical strength of solids had already been calculated using data on the interatomic bonding forces for perfect, defect-free structures (M. Born, F. Zwicky, and others). It became obvious that there was a large (hundred times or larger) discrepancy between the intrinsic capacities of solids provided by nature and their low real strength. It was necessary to establish the reasons for so large a discrepancy and to determine how to bring the real strength closer to the theoretical value. The classical studies carried out by A.F. Ioffe on rock salt (in 1924) showed that the removal of defects from the sample surface causes the strength to increase by several times. Zhurkov, together with A.P. Aleksandrov, continued these experiments using glass and quartz filaments. Surface cracks were eliminated by etching filaments in hydrofluoric acid, which resulted in the achievement of an outstandingly high tensile strength of up to 6 GPa for glass and 13 GPa for quartz. These values were comparable to the theoretical strength of the materials studied. The results were summarized in the widely recognized monograph by Zhurkov and Aleksandrov "The Phenomenon of Brittle Fracture" (1933).

In his first serious study, Zhurkov solved a fundamental problem: he demonstrated the possibility of achieving the theoretical strength. This extremely important result encouraged and still encourages studies aimed at searching for ways to enhance technical strength.

In the mid-1930s, the fabrication of synthetic polymers, whose mechanical properties are of considerable scientific and practical interest, began to intensely develop. Unusually great reversible deformations, a strong temperature dependence of the elastic properties, the ability to strengthen through orientation, and a gradual transition from a solid to a liquidlike state all necessitated profound systematic studies. A team consisting of outstanding scientists from the Physicotechnical Institute (PTI), including P.P. Kobeko, A.P. Aleksandrov, E.V. Kuvshinskiĭ, S.E. Bresler, and Yu.S. Lazurkin applied themselves to studying these very interesting objects. Zhurkov also belonged to this group. The pioneering contribution made by these PTI scientists to the physics of polymers is widely recognized.

Zhurkov began to study the role that intermolecular interactions play in determining the mechanical properties of polymers. This problem is important for the physics of polymers. When studying the softening effect that is produced by the introduction of low-molecular compounds into polymers on the hardness and the softening temperature of polymers, he came to explain polymer solidification as being controlled by the formation of local binding "bridges" between the side groups of chain molecules. The Great Patriotic War suspended these studies.

After being evacuated to Kazan, Zhurkov successfully used his discovery of the softening-agent effect to solve the important defense problem of increasing the resistance of oil lubricants to cold. In 1942, Zhurkov founded and took charge of the Laboratory of Physicomechanical Properties of Polymers (which was transformed later into the Department of the Physics of Strength of the PTI). When he returned from Kazan, Zhurkov carried out concluding studies on the solidification and devitrification of polymers, and in 1948 he submitted his doctoral dissertation on "Studies of the Mechanism of Polymer Transition from the Solid to Rubberlike State." In this work, Zhurkov established a rule of equivalence according to which the shift of the interval where softening and a decrease in the relaxation time occur is the same for equimolecular amounts of various low-molecular substances added to a polymer. In addition to its theoretical significance, this rule is of practical importance, because it enables one to reasonably choose a softening agent and to forecast its effect.

However, Zhurkov did not restrict himself to phenomenological studies. Having already presented his dissertation and being inclined to prove directly his conclusion on the role of intermolecular bonds in the solidification of polymers, Zhurkov made fine and elegant measurements of the temperature dependence of specific heat and, particularly, of the infrared absorption spectra of polymers. This allowed him to directly

1063-7834/05/4705-0797$26.00

detect and determine the concentration of intermolecular bridges.

Thus, the second large period of Zhurkov's scientific activities, focused on the fundamental problem of the physics of polymers (the molecular mechanism of solidification) was also successful and led to excellent results and a widely recognized theory.

The most important period of Zhurkov's academic activities started from the end of the 1940s; he began to study the atomic–molecular mechanism of fracture of solids. At that time, it went without saying that an external tensile load applied to a solid is shared between atomic bonds and, if it is sufficiently large, the load causes atoms to separate, which results in fracture of the solid. Thereof, the idea of the breaking point appeared according to which there is a critical external stress above which a solid abruptly loses its integrity.

Zhurkov doubted the existence of the critical strength as a real physical characteristic. His doubts arose due to the fact that solids can fracture under stresses below the critical strength, not at once, however, but after a certain amount of time. Before Zhurkov's studies, data on this were few and disembodied. Such observations were not considered to be serious. It was presumed that various factors (like corrosion, aging, fatigue, etc.) had side effects on the ultimate strength and caused it to decrease with time. Zhurkov believed that these facts were evidence of a common physical feature of fracture.

A new approach to the analysis of the tensile strength and the time under stress proved essential and to play a decisive role. Before Zhurkov's studies, the ultimate strength was mostly regarded as a function of the duration of loading. Along this line (where time is an argument and the breaking stress is a function), no physical explanation has been offered for the features of fracture. Zhurkov suggested "inversion": he treated the time it takes for fracture to occur as a function of the applied load, which reached a breaking point. This approach (in which the load is an argument and the expectation time of fracture is a function) opened the way to understanding the physics of fracture as a kinetic phenomenon.

In his laboratory, Zhurkov carried out comprehensive systematic studies of the durability of solids under tension (the elapsed time between loading and fracture) as a function of the applied stress and temperature. The setups devised made it possible to carry out the experiments within a wide range of durability (ranging over ten orders of magnitude, from thousandths of one second to months). More than 100 materials representing basic types of solids, such as metals, alloys, crystals with various types of atomic bonds, glasses, polymers, and composite and heterogeneous materials, were studied. The dependence of durability (τ) on stress (σ) and temperature (T) was found to be surprisingly uniform (except for the range of very low and very high stresses and temperatures):

$$\tau(\sigma, T) = \tau_0 \exp\left(\frac{U_0 - \gamma\sigma}{kT}\right).$$

Here, k is the Boltzmann constant, $\tau_0 \sim 10^{-13}$ s is a time constant that is on the order of the period of atomic oscillations in solids (corresponding to the maximum frequency in the Debye spectrum), U_0 is an energy that is close to the dissociation energy of a substance, and $\gamma = qV_a$, where V_a is the activation volume for an elementary event of dissociation and the coefficient q characterizes local overstresses (due to defects in actual solids, this coefficient can be 10 to 100 or even higher and accounts for the difference between the experimental and the theoretical strength). The fundamental temperature dependence of durability in the form of the Boltzmann–Frenkel factor, together with the identification of the parameters involved in the $\tau(\sigma, T)$ function, brought Zhurkov to the very important conclusion that the fracture of solids is related to thermal fluctuations. Macroscopic fracture of a solid is a process of successive elementary breaks of strained interatomic bonds caused by fluctuations in the thermal energy of atoms.

The $\tau(\sigma, T)$ dependence indicated above is known as the Zhurkov formula in strength (fracture) science.

As mentioned above, Zhurkov did not restrict himself to phenomenological studies. In his laboratory, many physical techniques were developed for direct and detailed studies of fracture kinetics, which was unprecedented in the laboratories concerned with strength problems at that time (1950s–1960s). Mass spectrometry, electron paramagnetic resonance, infrared and Raman spectroscopy, chromatography, radioactive analysis, nuclear magnetic resonance, small- and large-angle x-ray diffraction, electron microscopy, and precision dilatometry were applied. Later on, some other methods were also employed, including acoustic emission, ultrasonic sounding, electron emission, luminescence, plasmon spectroscopy, Auger spectroscopy, high-and low-energy electron diffraction, polariton spectroscopy, electron–nuclear double resonance, tunneling electron microscopy, and computer simulation.

A distinctive feature of Zhurkov's experimental approach was the use of all of these techniques for studying specimens under mechanical loads. This approach makes it possible to obtain detailed information on the processes of nucleation and propagation of fracture in loaded solids.

The places of overstress localization were determined, and the overstresses imposed on interatomic bonds were estimated. It was established that successive interatomic breaks are caused by thermal fluctuations (for solids with covalent bonds). The generation of microscopic nucleating cracks was detected, and the kinetics of their growth leading to the formation of through cracks was traced. Thus, along with the funda-

mental results following from phenomenological studies of durability, the concept of microscopic fracture kinetics was founded, which continues to be developed.

In 1958, Zhurkov was elected a Corresponding Member of the USSR Academy of Sciences (physics of polymers), and in 1968 he was elected a Full Member (Academician) of the USSR Academy of Sciences (physics).

Since the 1970s–1980s, fracture physics has been actively studied in the directions created by Zhurkov and his followers.

Based on extensive experience from around the world and his own results obtained in the 1930s (strengthening of samples by surface treatment), Zhurkov pointed out the importance of detailed study of the processes that occur in the surface layer of a loaded solid. For crystals and other objects under load, active specific variations in the state of surface and near-surface layers were established, including the formation of a nanostructure up to amorphization, intense dislocation processes, and crack formation.

At the first stage of these studies, the fracture kinetics was treated at the atomic–molecular level Later on, it became progressively clearer that not only the atomic–molecular subsystem but also the electronic subsystem of solids under stress had to be analyzed. Indeed, the binding between atoms is actually due to electron interaction; the mechanical loading causes disturbances in the electron subsystem, and the breakage of interatomic bonds results in abrupt excitation of the electronic states. Therefore, it was natural to consider "electronic problems," and the possibility of performing such studies was aided by the complex of techniques developed. New data were obtained concerning the electronic processes in solids under stress. Based on phenomenological studies of the effect of electric fields on the kinetics of mechanical fracture, parallel studies of the kinetics of mechanical and electrical breakdown (measurements of the expectation time of electrical breakdown of dielectrics), the discovery of the effect of mechanical stress on the kinetics of electrical breakdown, and the results of detailed physical studies, it was concluded that there is a close connection between the mechanical and the electrical processes.

Since the fracture mechanism is related to thermal fluctuations, Zhurkov attached importance to studies of local fluctuations in atomic energy in solids. This significant problem required special consideration and was also raised by Ya.I. Frenkel, but it was not actually elaborated until recently. Computer simulations and experimental studies performed by Zhurkov and his school of scientists, have greatly advanced our understanding of the nature and characteristics of these phenomena, which are most important for solid-state physics on the whole and for fracture physics in particular.

The study of the transition from the microscopic to macroscopic level is very important in understanding the fracture kinetics. Zhurkov and his followers have developed a two-stage fracture concept for heterogeneous solids. At the first stage, numerous scattered small-scale cracks are accumulated, and, at the second stage, large-scale fracture nuclei are formed as a result of coalescence of the primary cracks. This two-stage fracture model can be successively applied to larger and larger scale fracture processes. It was directly confirmed by the results of acoustic emission studies of heterogeneous objects under stress.

Since the thermal-fluctuation mechanism of fracture was established for the classical temperature range (above the Debye temperature), it was of interest to study low-temperature fracture. Studies carried out on solids with a high Debye temperature (boron, polymers) have shown that the fracture kinetics is observed down to very low temperatures (measurements have been performed down to liquid-helium temperature). However, the mechanism of elementary events changed from over-barrier transfer (at elevated temperatures) to under-barrier tunneling transfer. Therefore, at elevated temperatures, the corresponding atomic–molecular and electron transitions are driven by atomic energy fluctuations, whereas at low temperatures they are due to fluctuations in coordinates in accordance with the wave properties of particles. Thus, the concepts of the kinetics and thermal-fluctuation mechanism of fracture can be extended to the entire temperature range, including very low temperatures.

The results of fundamental studies also stimulate the solution of important practical problems.

The kinetic approach to fracture makes it possible to make long- a short-term fracture forecasts.

The Zhurkov formula determines the durability of a loaded solid and can be used to solve the problem of long-term (*a priori*) fracture forecasting. This forecasting under real operational conditions (where loads, temperature, the structure and imperfection of materials, the effect of environment, etc., are temperature-dependent) is certainly a complicated problem. However, the fracture kinetics laws established by Zhurkov provide a physical grounds for its solution. A few successful practical techniques for long-term forecasting of fracture have already been developed.

The acoustic emission method can be very efficiently used for short-term forecasting of fracture. This method has been used for a long time in forecasting practice, but the empirical correlations, which were previously commonly used in the analysis of acoustic signals, reduced the efficiency of this method. The staged model of fracture kinetics developed by Zhurkov and his followers, along with improvements made in the interpretation of the acoustic-emission spectrum, made it possible to develop a new system of analysis and make far more reliable forecasts of catastrophic fractures.

Computerized systems of acoustic testing of the state of objects, which enable one to detect an impending catastrophe and to estimate the time before its out-

break, have been created and are currently in operation. Such systems are used to forecast fracture of large structures (main pipelines, boilers, reservoirs, etc.), rock bumps in mines, and earthquakes.

In practical applications of strength physics, the main problem is, naturally, improvement of the strength properties of materials. Here, the kinetic approach also leads to considerable advances.

For example, the well–known technique for strengthening polymers, namely, orientation stretching, is based on applying a tensile stress to an initially nonoriented polymer. In this case, the polymer structure is ordered, which results in its strengthening and, simultaneously, in its decay (because of breakage of the chain molecules). Therefore, two processes, which differ in terms of their kinetic characteristics, occur in parallel. Kinetic analysis of these processes, in combination with a special structural preparation of samples, has made it possible to find the optimum regimes of orientation and to obtain the highest breaking strength of polymers in the world, up to 10 GPa or higher. These values are only 2 to 3 times lower than the theoretical strength of polymers. In addition to the record "laboratory" strength achieved, a significant (by several times) increase in the technical strength of polymers has been attained using the kinetic approach and relevant recommendations were given for large-scale manufacturing.

The problem of extending the operational life also relates to the problems of strength and reliability of materials. The results of studies of the mechanisms of fracture (in most cases, nucleation and growth of cracks) have made it possible to raise a question regarding enhancement of the durability using purposeful elimination or "treatment" of the cracks generated or accumulated during the operational time. Studies into the kinetics of regenerating the continuity of a solid (this process is the reciprocal of fracture) showed that the durability can be increased by tens of times. A computerized system for thermal and pressure treatment of failed objects was developed, which significantly increased the duration of their operational life.

The methods developed for eliminating microcracks and pores can be used to improve the electrical and optical properties of materials.

Serafim Nikolaevich Zhurkov lived a long fruitful academic life full of research work and outstanding scientific findings. He is acknowledged as the founder of both the concept and the school of the kinetic nature of strength. Discussions pertaining to fracture kinetics are still going on, which is quite natural for living science. The basis for the kinetic theory of strength has already been established, and the discussions only concern details, practical implementation, and paths of future development. Zhurkov had the honored name of leader of the domestic school of strength physics. of Zhurkov's contribution to strength science was acknowledged with his election to the International Fracture Congress as vice-chairman (1968–1976). His seventieth anniversary (1975) was marked by an event rare for the scientific community, namely, the dedication of a special anniversary edition of the international journal *Fracture*.

Zhurkov worked for 67 years at the Ioffe Physicotechnical Institute and was one of the most revered and beloved leaders of the institute.

To the end of his days, Zhurkov vigorously continued to do research work with the intention of finding answers to the problems concerning fluctuation processes in fracture that he was interested in.

Zhurkov played an important part in the establishment and assertion of the authority of the journal *Physics of the Solid State* founded by Ioffe in 1959. Zhurkov was head of the Editorial Board from 1961 to 1988 and helped achieve world-wide recognition for the journal.

In honor of Serafim Nikolaevich Zhurkov's centenary, we would like to once again emphasize his outstanding contribution to solid-state physics and to the development of the theory of strength of solids and to wish his scientific school successful development of his ideas on the physics of strength.

The Editorial Board
of the journal *Physics of the Solid State*

Translated by E. Borisenko

Physics of the Solid State, Vol. 47, No. 5, 2005, pp. 801–811. Translated from Fizika Tverdogo Tela, Vol. 47, No. 5, 2005, pp. 777–787.

Atomic-Level Fluctuation Mechanism of the Fracture of Solids (Computer Simulation Studies)

A. I. Slutsker

Ioffe Physicotechnical Institute, Russian Academy of Sciences, Politekhnicheskaya ul. 26, St. Petersburg, 194021 Russia

e-mail: Alexander.Slutsker@mail.ioffe.ru

Abstract—Experimental studies of the fracture kinetics of solids have shown that the process culminating in fracture of a stressed solid comprises a sequence of elementary events in which stressed atomic bonds are ruptured by local energy fluctuations. This recognition sparked investigations into elementary fracture events and into the fluctuations themselves that are responsible for bond rupture. Currently, only computer simulation of the dynamics of atoms offers the possibility of tracing, in considerable detail, the evolution of fluctuation events characterized by very short duration ($\sim 10^{-13}$–10^{-12} s). An analysis is made of the results obtained in computer simulation experiments on the temporal and spatial localization of atomic-energy fluctuations and atomic-bond strains, fluctuation migration, the mechanism of fluctuation formation, the role of anharmonicity in atomic interactions, and the magnitude of the volume activated in an elementary fracture event. *© 2005 Pleiades Publishing, Inc.*

1. INTRODUCTION

The kinetic theory of the nature of the strength of solids developed by S.N. Zhurkov rests on the concept that elementary events in the processes culminating in the fracture of a solid in the classical temperature region (above the Debye temperature) are ruptures of stressed atomic bonds caused by local energy fluctuations. This conclusion has been drawn from an analysis of the dependence of the lifetime of solids on temperature and stress under applied load [1, 2] and corroborated by a variety of direct physical studies [2].

The conclusion that fracture occurs through the fluctuation mechanism has naturally spurred a desire to obtain more detailed information on the elementary fluctuation events and resulted in the formulation of a number of problems to be solved, among them the extent of energy fluctuation localization in space and time, the mechanism of formation of energy fluctuations, detailed analysis of the action of the rupturing fluctuation, the role played by atomic interaction anharmonicity in fluctuation-induced fracture events, and the activated volume in which an elementary fracture event occurs.

Modern methods employed in physical experiments are not capable of providing direct answers to the above questions. While these methods can successfully determine the average characteristics of atomic dynamics and detect the products forming in fluctuation dynamics, local energy fluctuations themselves still cannot be detected and the evolution of a fluctuation event in time cannot be followed.

It appeared therefore only natural to invoke computer simulation of atomic dynamics, which can, to a certain extent, assist in finding answers to the above questions and to other similar questions. Effective use of this method was aided by recent progress in computer technology and software, which allow analysis of the behavior of each atom in many-atomic systems (in models operating with hundreds and thousands of atoms) in considerable detail.

The present paper presents several results that are relevant to the above problems of fluctuation dynamics and were obtained by computer simulation.

The results of studies performed by the present author in collaboration with his colleagues [3–6] and by other researchers are also discussed.

2. BRIEF OUTLINE OF THE METHOD OF COMPUTER SIMULATION OF ATOMIC DYNAMICS

The method itself and its applications have been described in numerous publications starting with the pioneering papers of E. Fermi in 1952 [7] and continued, in particular, in reviews [8, 9].

A basic description of the method can be given as follows. A model of atomic arrangement (atomic coordinates r_i) and interatomic potential $U(r)$ are prescribed. An energy (temperature) is introduced by assigning momenta or displacements to the atoms. Next, the equations of motion are numerically solved for each atom at a given integration step. This step is a small fraction (as a rule, 0.01 to 0.10) of the calculated atomic vibration period τ_0. The integration yields instantaneous (to within the integration step) values of

1063-7834/05/4705-0801$26.00

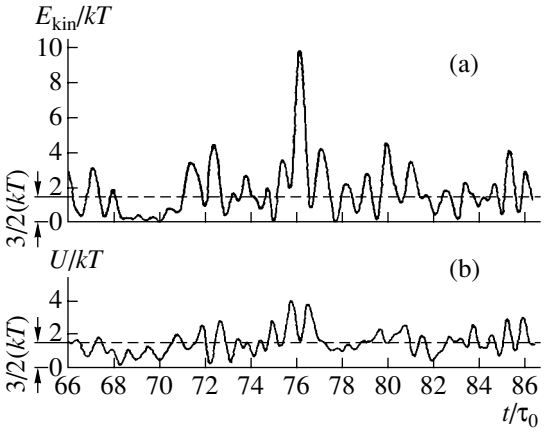

Fig. 1. Fragment of the thermal life of an atom. Three-dimensional model with 864 atoms and the Stillinger–Weber potential with nickel parameters; $T = 500$ K, integration step, $0.05\tau_0$. (a) Kinetic energy of an atom and (b) potential energy per atom.

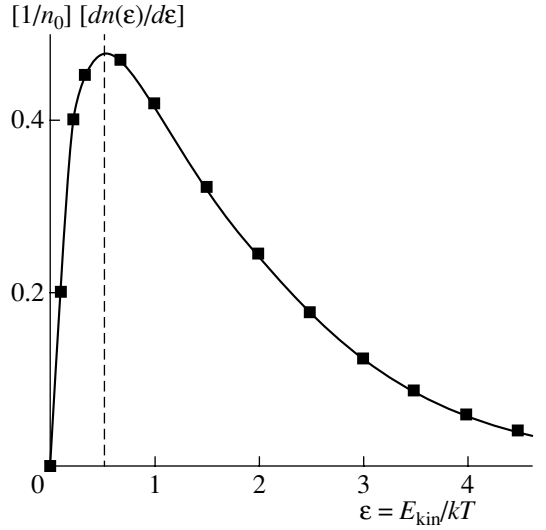

Fig. 2. Differential distribution of instantaneous values of the kinetic energy of atoms. Three-dimensional model with 864 atoms and the Stillinger–Weber potential with nickel parameters; $T = 500$ K, integration step, $0.05\tau_0$. Points are computer simulation data, and the line is a theoretical distribution [11].

the coordinates of each atom $r_i(t)$ and of the velocity of each atom $\dot{r}_i(t)$.

These data are used to derive the instantaneous values of the kinetic energy of each atom $E_k(t) = \frac{1}{2}m \times \dot{r}_i^2(t)$ (m is the mass of an atom), the strain of each atomic bond $\Delta r_i(t) = r_{i+1}(t) - r_i(t)$, and the potential energy of each atomic bond $U[\Delta r_i(t)]$.

In the course of calculation, one has to monitor preservation of the integrals of motions, thermalization of the system (i.e., to check that the system reached thermodynamic equilibrium after it acquired energy), and the stability of the phase trajectory of the system. Thus, one can follow, with a high resolution, the evolution of the main dynamic parameters (the atom energy and compressive or tensile bond strains) for each atom and each atomic bond.

Figure 1 presents, by way of illustration, a typical scan of the thermal life of an atom. One readily sees periods of time where the kinetic energy of the atom oscillates in the vicinity of the average energy ($\langle E_k \rangle = \frac{3}{2}kT$) and a period where a fairly large kinetic energy fluctuation occurs (Fig. 1a). Oscillations in the potential energy for the same atom are shown in Fig. 1b. Note that dynamics simulation offers extremely broad possibilities for varying the characteristics of a model and the conditions under which it functions. One can vary the structure, interaction potentials, initial and boundary conditions, loading of the model by external forces, etc. This was used to advantage in obtaining the results presented below, which helped answer a number of questions.

3. TESTING THE VALIDITY OF THE SIMULATION METHOD WITH RESPECT TO FLUCTUATIONS

The ability of the model to describe the mean values of dynamic characteristics of a real solid was tested by computing the values and temperature dependences of the thermal expansion coefficient, the bulk compression modulus, the Debye–Waller factor, and the temperature dependence of heat capacity.

Dynamics simulation of a system with an fcc lattice, the interatomic potential, and atomic mass corresponding to nickel yielded satisfactory agreement between calculations and the experimental data on nickel for all the above characteristics [10].

Consider now testing of the fluctuation aspect of the adequacy of the model. To do this, the model of a crystal was used to find the distribution of instantaneous values of the kinetic energy of atoms. This distribution was determined at 300 instants of time, and the results thus obtained were averaged over 300 sets of data. The resultant differential distribution $(1/n_0)dn(\varepsilon)/d\varepsilon$ (where $n_0 = 864$ is the number of atoms in the model, $\varepsilon = E_k/kT$, E_k is the kinetic energy of the atom) is shown with points in Fig. 2. The solid line in Fig. 2 plots

the theoretical relation of the probability density of an atom having an energy in the vicinity of $\varepsilon = E_k/kT$ [11]:

$$\frac{dW}{d\varepsilon} = \frac{2}{\sqrt{\pi}}\varepsilon^{1/2}\exp(-\varepsilon). \quad (1)$$

We witness a practically perfect matching between the computer simulation and the theoretical data. This coincidence permits the following two conclusions. First, it lends support to the idea that computer simulation provides reasonable results not only for the mean characteristics of atomic dynamics (which is corroborated by a comparison with the experimentally measured characteristics) but also for the energy partitioning among atoms (i.e., for energy fluctuations).

The second conclusion is as follows. After Maxwell had derived the relation for the energy distribution of atoms in a gas (1859), direct experimental confirmation of this distribution was demonstrated only 60 years later (by O. Stern in 1920). Direct experimental evidence of the validity of distribution (1) for solids is still lacking because of the limited possibilities for measuring atomic energy fluctuations in solids. Therefore, the results displayed graphically in Fig. 2 can also be treated, in a certain sense, as experimental evidence in support of theoretical distribution (1).

Now that arguments for the validity of the computer simulation technique have been presented, let us turn to some aspects of the fluctuation dynamics phenomena that are studied by computer simulation of atomic dynamics.

4. EXTENT OF THE FLUCTUATION LOCALIZATION IN SPACE AND TIME

The extent of fluctuation localization in time, i.e., the duration of a fluctuation in kinetic energy, can be estimated from Fig. 1a. We readily see that the duration of a fluctuation (which we define here as the time an atom resides in a state with an energy in excess of the average energy level) is about one vibration period τ_0. Similar data were also obtained for many kinetic-energy fluctuations of atoms in one-, two-, and three-dimensional models. In all cases, the fluctuations in the kinetic energy of the atoms are highly localized in time (within about one vibration period). This appears only natural for periodic (or quasi-periodic) vibrations of an atom residing among like vibrating neighboring atoms.

The potential energy is determined by the state of the interatomic bond (elastic tension or compression). The concept of the potential energy of an atom can be conventionally introduced and expressed by a half-sum of potential energies of the bonds connecting the given atom with its nearest neighbors. Figure 1b displays a time scan of the potential energy defined in this way for the same atom and at the same instants of time as in Fig. 1a, which shows a scan of the kinetic energy. We readily see potential-energy fluctuations of various amplitude. The duration of such fluctuations is also close to the atomic vibration period. This warrants the conclusion that potential-energy fluctuations are likewise narrowly localized in time.

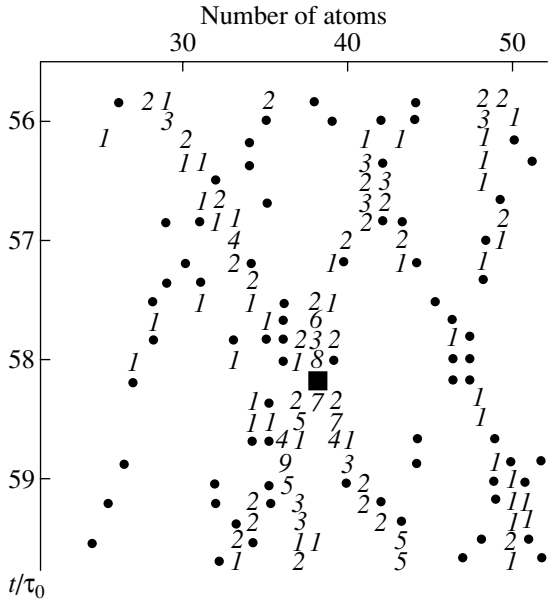

Fig. 3. Space–time scan of the total energy of atoms. One-dimensional model with 100 atoms and harmonic potential. E_{fl} is a fluctuation of the total atom energy. Space corresponds to $E_{fl} < 1.5\ kT$; points correspond to $E_{fl} = 1.5$–$2.0\ kT$; (*1*) 2.0–2.5 *kT*; (*2*) 2.5–3.0 *kT*; (*3*) 3.0–3.5 *kT*; (*4*) 3.5–4.0 *kT*; (*5*) 4.0–4.5 *kT*; (*6*) 4.5–5.0 *kT*; (*7*) 5.0–5.5 *kT*; (*8*) 5.5–6.0 *kT*; (*9*) 6.0–6.5 *kT*; and the square corresponds to $E_{fl} > 7.0\ kT$.

The problem of spatial localization of fluctuations, (which is characterized by the number of atoms or bonds involved at the same instant of time in a fluctuation) can be conveniently considered using a spatial–temporal scan. This scan would also reflect localization of fluctuations in time, thus providing new information on the behavior of fluctuations.

This scan looks the simplest for a one-dimensional model, which is a chain of atoms vibrating along the axis of the chain. Figure 3 shows a scan of the total energy of atoms (the sum of the kinetic and potential energy of each atom) in a chain with harmonic bonds (the application of this interaction potential will be analyzed below), and Fig. 4 shows a scan of interatomic bond strains (tensile and compressive strains are given separately), i.e., of strain fluctuations, which characterize fluctuations in the potential energy of the bonds.

The arrangement of fluctuations along the vertical (time) axis for each individual atom (numbered accordingly on the horizontal axis) exhibits narrow localization of fluctuations of all types in time, which was already pointed out above (see Figs. 3, 4). Indeed, the duration of a fluctuation lies within one vibration period in all cases.

An idea of the extent of spatial localization can be gained from the distribution of fluctuations over atoms

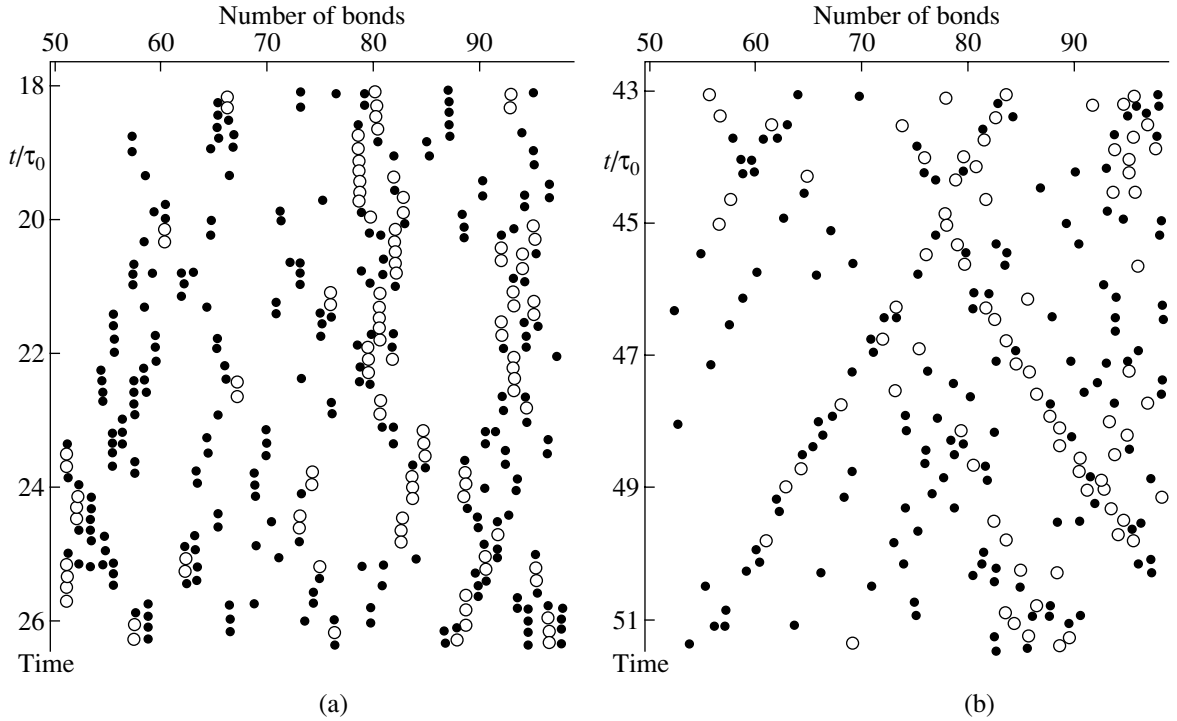

Fig. 4. Space–time scans of atomic bond strains. One-dimensional model with 100 atoms and Morse potential; λ is the relative bond strain. (a) Tensile strain; space corresponds to $\lambda < 10\%$, filled circles are $\lambda = 10$–16%, and open circles are $\lambda > 16\%$. (b) Compressive strain; space corresponds to $\lambda < 4\%$, filled circles are $\lambda = 4$–7%, and open circles are $\lambda > 7\%$.

or bonds (along the abscissa axis) for each instant of time. We readily see that, at any instant of time, fluctuations encompass only a small number of atoms (Fig. 3) or of neighboring bonds of the same strain sign (Fig. 4). Most often, a fluctuation encompasses one or two neighboring elements (atoms or bonds) and, less frequently, three or four of them or more. One may thus conclude that fluctuation localization in space is very narrow.

A significant result, strongly revealed in Figs. 3 and 4, is the migration of fluctuations, i.e., hopping of a high-energy atomic state (Fig. 3) and of a strained bond state (Fig. 4) from one element to another. Note that the magnitude of a fluctuation, rather than remaining constant, varies along the line of migration (i.e., this motion is not soliton-like). Nevertheless, the migration lines can be reliably traced over a fairly long path.

The migration of fluctuations implies the possibility of their collision, i.e., encounter at one atom or one bond. As is evident from Fig. 3, collision of total-energy fluctuations can give rise to an enhanced energy fluctuation. In Fig. 3, the largest energy fluctuation resulted from a crossing of two lines of fluctuation migration.

This capacity of fluctuations to migrate and thus collide with one another brings about a whole range of consequences of such encounters.

Fluctuations in the kinetic energy of atoms imply fluctuations in atomic velocity. Being vector quantities, velocities also have a sign. Therefore, when velocity fluctuations migrating from two sides meet at the same atom, the result will depend on the actual signs of the velocities. If the velocities point in the same direction (i.e., have the same sign), the final result will be an increased velocity of the atom and, hence, an increased kinetic energy. Conversely, if the velocities have opposite signs, the velocity of the atom will be damped to some extent and its kinetic energy will decrease.

A similar situation holds for interatomic bonds with respect to the sign of elastic bond strain (tensile or compressive). If migrating fluctuations of the same sign meet at a bond, the bond strain will be amplified, as will the potential energy of the bond. Encounter of strain fluctuations of opposite sign will bring about a decrease in the strain and a drop in potential energy. Figure 5 displays such situations as revealed by computer simulation. We directly see the dependence of the final result on the signs of colliding bond-strain fluctuations. From Fig. 5b (bottom panel), it can also be seen that damping of the potential energy of two bonds dramatically enhances the kinetic energy of the atom located between these bonds. In other words, the potential energy transforms into kinetic energy in the event of fluctuation encounter.

This example illustrates the rich potential offered by computer simulation for detailing dynamic processes occurring at the atomic level. This potential has still not

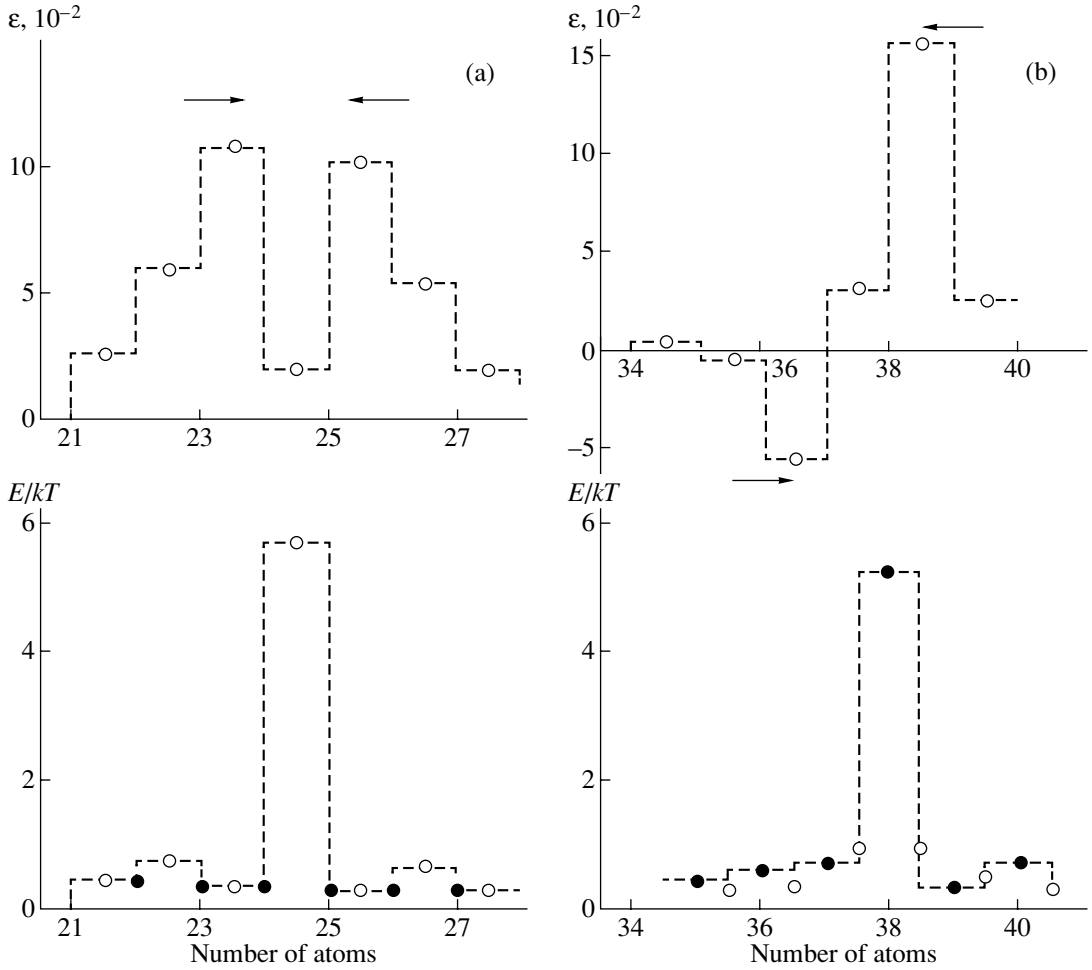

Fig. 5. Collision of fluctuations. One-dimensional model with 100 atoms and Morse potential. (a) Top panel shows head-on moving tensile strain fluctuations $0.5\tau_0$ before collision at a bond. Bottom panel shows collision. The case of a strong bond potential energy fluctuation (open circles) and low kinetic energy of atoms (filled circles). (b) Top panel shows head-on moving strain fluctuations opposite in sign at the instant $0.5\tau_0$ before collision at a bond. Bottom panel shows collision. The case of strong atom kinetic energy fluctuation (filled circles) and low bond potential energy (open circles).

been exhausted by far, and the paths toward this are clear.

The one-, two-, and three-dimensional models reveal narrow temporal and spatial localization of fluctuations. Two- and three-dimensional systems also exhibit fluctuation migration. In a three-dimensional system, such migration occurs primarily over close-packed atomic planes [10].

5. MECHANISM OF FLUCTUATION FORMATION

The question is formulated as follows: how or at the expense of what does an energy fluctuation, i.e., an energy in excess of its average level, form for a short time (about one vibration period) at an individual atom or an interatomic bond?

The problem regarding the mechanism of formation of energy fluctuations in a gas can be solved by considering the conditions of successive interaction of a gas atom (molecule) with a large number of other atoms, with each transferring small portions of energy to the given atom [5].

In a solid, where an atom interacts directly with a small number of neighboring atoms (forming the coordination shell), no such conditions for pumping energy to an atom (or bond) exist.

Two possible mechanisms for the formation of energy fluctuation can be conceived *a priori* for a solid: (a) energy repartitioning among different vibration modes, which is possible for a system with anharmonic atomic interaction, and (b) interference of elastic waves (normal vibrations), for which anharmonicity is not a necessary condition.

The possibilities inherent in computer simulation allow one to pinpoint the dominant mechanism. For this purpose, computer simulation experiments were performed in which harmonic potentials were tried in addition to the realistic anharmonic interaction potential.

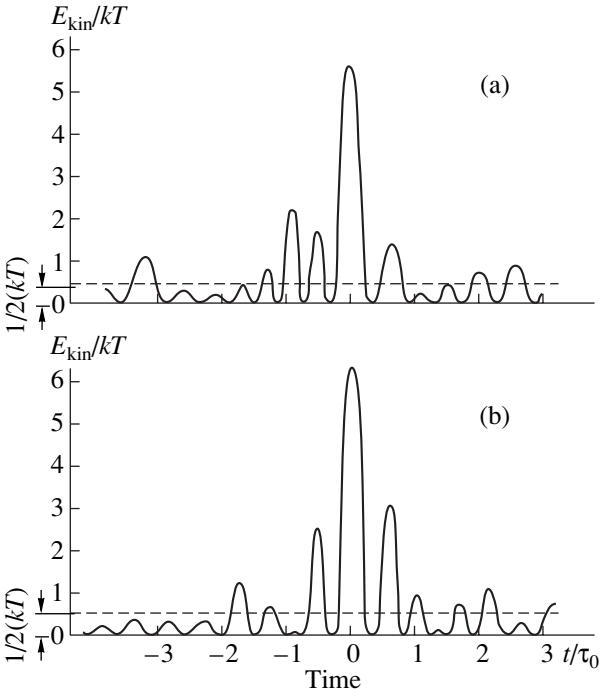

Fig. 6. Fragments of the thermal life of an atom. One-dimensional models with 100 atoms. Periods of time with strong kinetic energy fluctuations. Integration step, $0.1\tau_0$. (a) Morse potential and (b) harmonic potential.

The linear elasticity coefficient at the equilibrium position of an atom was assumed to be the same in both cases.

Figure 6 shows scans in time of the kinetic energy of an atom for the anharmonic (Fig. 6a) and harmonic (Fig. 6b) potentials. We readily see that the atomic energy fluctuations generally follow the same pattern. Significantly, pronounced energy fluctuations are also observed in the harmonic model. Analogous results demonstrating a noticeable similarity in the fluctuation dynamics between the anharmonic and harmonic systems have also been obtained for the two- and three-dimensional models [10].

This similarity suggests that fluctuations form in the interference of elastic waves (phonons). This conclusion is borne out by the abovementioned fairly strong variation in the fluctuation amplitude in the course of its migration (Figs. 3, 4). This variation should obviously be assigned to atoms vibrating with different phases along the fluctuation migration trajectory, which is essential for interference. The idea of fluctuations being of phonon origin was put forward before by Fabelinskiĭ [12]: "…fluctuations are actually the result of interference among Debye waves." The results of relevant computer simulation provide a firm basis for this statement. The conclusions drawn from an analytical consideration of atomic energy fluctuations as many-particle beats in a harmonic system [3] agree well with the results of computer simulation experiments.

The migration of fluctuations and their interaction are additional factors conducive to the formation of large fluctuations.

6. RUPTURING FLUCTUATIONS

Since the fluctuation mechanism of fracture of stressed solids is dominant, which has been shown by experimental studies of fracture kinetics, it is of primary interest to consider rupturing fluctuations, i.e., fluctuations causing breaking of stressed atomic bonds.

It appears natural to consider bond rupture to be a strong enough elongation (stretching) of the bond for the atoms to be moved apart to the extent where they no longer attract each other. Thus, bond rupture can be considered a strong fluctuation of (tensile) bond strain paralleled by a corresponding fluctuation in the potential bond energy. A detailed analysis of fluctuation-induced bond rupture requires following the evolution of various quantities: the tension (i.e., potential energy) of a given bond, the strain (with its sign) and the energy of a number of nearest neighbor bonds, and the velocity (with its sign) and kinetic energy of atoms (primarily those at the ends of this bond, as well as a few of the nearest neighbor atoms). Computer simulation is capable of providing all these characteristics. The pioneering results containing this information can be found in [13, 14], where one-dimensional dynamics of an anharmonic chain of atoms under application of tensile stress along the chain axis was modeled. Fluctuation-induced bond ruptures were recorded. The behavior of atoms and bonds in the vicinity of the breaking bond with time was established, both before and after the rupture. Significantly, a certain correlation in the motion of atoms near the breaking bond was detected, which demonstrates that there is a certain collective pattern governing the fluctuation-induced rupture of one bond and raises interesting questions concerning the relationship between the energy barrier to an elementary rupture event and the bond dissociation energy. The entropy factor is also of interest. The realization of the rich potential of computer simulation both for one-dimensional systems with inclusion of "transverse" dynamics and of a still larger set of dynamic characteristics and for two- and three-dimensional systems appears an indispensable step in developing a deeper understanding of elementary events in the fracture of solids.

7. THE ROLE PLAYED BY INTERATOMIC-INTERACTION ANHARMONICITY IN THE FLUCTUATION DYNAMICS AND KINETICS OF FRACTURE

The effect of anharmonicity (nonlinearity) of atomic interactions is known to be different in dynamic processes and effects in solids.

For instance, anharmonicity is essential for thermal expansion of low-molecular solids, thermoelasticity, and the Grüneisen effect. By contrast, such characteris-

tics as heat capacity and elasticity are fundamentally related to the linear component of atomic interaction, while anharmonicity makes them dependent on temperature. The existence of phonons is likewise not connected with anharmonicity in any way, but nonlinearity governs, for instance, the phonon mean free path (lifetime).

Let us consider in more detail the part played by anharmonicity in atomic interactions in elementary fracture events and fluctuation dynamics.

Anharmonicity certainly plays a dominant role in the strength of solids, because it is the specific nonlinearity of the atomic interaction potential and of the bond elasticity that accounts for the finite bond dissociation energy and finite ultimate force of atomic bonding (theoretical bond strength).

In the case where the anharmonic atomic interaction potential is a cubic trinomial,

$$U(x) = -D + \frac{1}{2}fx^2 - \frac{1}{3}gx^3$$

we obtain approximate expressions for the dissociation energy

$$D = \frac{1}{6}\frac{f^3}{g^2},$$

and ultimate force

$$F_m = \frac{1}{4}\frac{f^2}{g}.$$

We see that it is the nonzero anharmonicity coefficient g (we deal here only with first-order anharmonicity) that provides finite values of D and F_m. It is this fact that justifies the concept of the energy fluctuation E_{fl} required to rupture an unstressed bond, $E_{\text{fl}} \geq D$.

Another effect of anharmonicity of the potential is that the tensile force F lowers the bond rupture barrier to zero at $F = F_m$ [15].

For small values of F, we have

$$U(F) \cong D - \frac{f}{g}F.$$

Hence, tensile loading of a bond reduces the energy fluctuation needed to break the bond.

Thus, anharmonicity plays a dominant part in the strength of a solid and in the conditions determining the fracture of a solid in terms of energy and force.

The role played by anharmonicity in fluctuations is somewhat different. As demonstrated by computer simulation, anharmonicity is not a dominant factor in the onset of fluctuations themselves (created by phonon interference), as it also is not in the generation of phonons. The tendency of fluctuations to migration is likewise not related to anharmonicity (see Fig. 3).

Lifetimes of migrating fluctuations with dilatations opposite in sign

Potential	Tensile fluctuations	Compressive fluctuations
Morse	$(25 \pm 10)\tau_0$	$(90 \pm 10)\tau_0$
Harmonic	$(46 \pm 3)\tau_0$	$(46 \pm 3)\tau_0$

However, computer simulation revealed the influence of anharmonicity on the characteristics of fluctuations and on their mobility.

Space–time scans of atomic bond strain (Fig. 4) reveal a noticeable difference in the lifetime of fluctuations (i.e., the time a bond resides in a stressed state); more specifically, fluctuations of bond tension last, on the average, longer than those of bond compression. Indeed, statistical treatment showed that, for the same fluctuation energy ($4kT$), the duration of a fluctuation Δt_{fl} is found to be $\cong 1.7\tau_0$ and $\cong 0.8\tau_0$ for tensile and compressive fluctuations, respectively.

Bond anharmonicity naturally results in the tensile strain being noticeably larger than the compressive strain for equal potential energy. This is possibly what brings about a difference in the fluctuation duration.

The same scan (Fig. 4) also reveals that the migration lines of fluctuations look different; indeed, these lines are more pronounced for compressive fluctuations.

Space–time scans (like those in Figs. 3, 4) can be used to estimate the mean free path and the lifetime of fluctuations from the length of the fluctuation migration line measured from the fluctuation formation point (more or less clearly defined) to its dissipation. Typical averaged results calculated for a chain of 100 atoms are presented in the table.

As is evident from the table, fluctuations with dilatations opposite in sign (for the Morse potential) differ noticeably. There is also a difference in the migration velocity of bond strain fluctuations. Figures 3 and 4 show that, while the fluctuation migration velocity is of the order of the sonic velocity, this velocity for compressive fluctuations is noticeably higher (by a factor of approximately 1.5) than for tensile fluctuations.

In order to check that it is the anharmonicity of interaction potentials that accounts for the observed differences in the fluctuation characteristics, we also calculated the lifetime of fluctuations, their mean free path, and the migration velocity for harmonic systems. It turned out that these characteristics are the same for dilatations opposite in sign. This is also evident from the table, which presents, for comparison, the corresponding data for a harmonic chain.

To sum up, computer simulation of atomic dynamics made it possible to establish the part played by the atomic potential anharmonicity in the fluctuation dynamics. This result could not be obtained either analytically or in experiments.

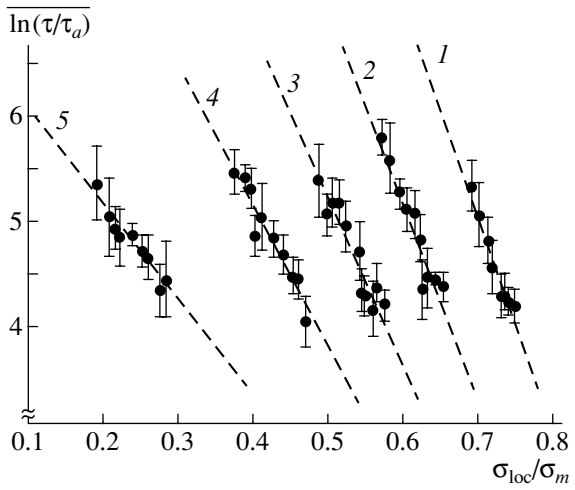

Fig. 7. Lifetime (time to rupture) plotted as a function of tensile stress and temperature [25]. One-dimensional model with 40 atoms and Morse potential. *D* is the atomic bond dissociation energy. The values of *kT*/*D* are (*1*) 0.02, (*2*) 0.03, (*3*) 0.04, (*4*) 0.06, and (*5*) 0.09.

8. ACTIVATED VOLUME OF ELEMENTARY EVENTS OF STRESSED BOND RUPTURE

The significance of this issue is stressed by the difficulties encountered in analyzing experimental data on fracture kinetics, i.e., on the lifetimes of solids as a function of temperature and stress parameters. The dependence of the lifetime τ on tensile stress σ and temperature T over a broad range (excluding very small and very large values of σ and T) can be generally written in the following form (the Zhurkov relation) [1, 2]:

$$\tau \cong \tau_0 \exp\left(\frac{U_0 - \gamma\sigma}{kT}\right), \qquad (2)$$

where $\tau_0 \cong 10^{-13}$–10^{-12} s is the average period of atomic vibrations or the period corresponding to the maximum vibration frequency in the Debye spectrum and U_0 is the initial fracture activation energy, which is reduced by the applied stress σ.

If the process preceding the fracture of a stressed solid is considered to be a sequence of elementary and random events, then the lifetime τ of this solid can be shown to coincide logarithmically with the average expectation time of the elementary events governing the process of fracture [2]. The activation energy U_0 in Eq. (2) in this case has the meaning of the initial potential barrier in an elementary event of fracture. It is the closeness of the values of U_0 to the energies of dissociation of atomic bonds [1, 2] that gives one grounds to treat elementary events of fracture as ruptures of atomic bonds. For molecularly one-dimensional systems (polymers), this conclusion has been substantiated by direct experiments [2].

The coefficient γ in Eq. (2) is a measure of the lowering of the initial barrier U_0 by the applied stress σ. From Eq. (2), we find that

$$\gamma \cong -kT\frac{\Delta \ln \tau}{\Delta \sigma}.$$

The coefficient γ has the dimensions of volume, and its characteristic values as extracted from real experiments on solids range from 0.5 to 5 nm^3 [2]. We immediately see that the barrier height U_0 is of the atomic scale, while the coefficient γ is several orders of magnitude greater than the atomic volume (~0.01 nm^3). Nevertheless, the coefficient γ is frequently called the activated volume and is referred to as the volume of a "particle" hopping over the barrier U_0 in an elementary event. We may add that the derivative $\Delta \ln V/\Delta P$ encountered in other activated processes that are characterized by their rate V under application of a stress or pressure P is also called the activated volume [16–19].

By the accepted definition, the activated volume in an elementary bond rupture event is the increment of volume for which the work done by the applied stress acting on the bond together with the work done by the fluctuation makes it possible to overcome the bond dissociation barrier [20].

We introduce the following notation: V_A is the activated volume, σ_{loc} is the stress acting directly on the bond (as distinct from the average stress σ in a loaded solid, which was employed above), $A(\sigma_{loc}) = V_A\sigma_{loc}$ is the work done by the applied stress to rupture the bond, D is the original bond dissociation energy (initial bond rupture barrier), and $U(\sigma_{loc})$ is the rupture barrier lowered by the local stress and surmounted through the occurrence of an energy fluctuation $E_{fl} = U(\sigma_{loc})$. With this notation, the condition imposed on the fluctuation-induced bond rupture can be written (in terms of energy) as

$$D = E_{fl} + A(\sigma_{loc}) = U(\sigma_{loc}) + V_A\sigma_{loc},$$

whence

$$V_A = -\frac{dU(\sigma_{loc})}{d\sigma_{loc}}. \qquad (3)$$

As follows from Eq. (3), in order to find V_A, we need to know the function $U(\sigma_{loc})$, i.e., the dependence of the bond rupture barrier height on the stress acting on the bond.

In [15, 21–23], the dependence of the bond rupture barrier height on stress in a diatomic molecule was found with a Morse potential. This relation is nonlinear and fairly cumbersome. However, there is the following quite satisfactory approximation valid within the interval ~$(0.2–1.0)\sigma_m$, where σ_m is the limiting stress in a bond subjected to an elastic tensile stress:

$$U(\sigma_{loc}) \cong D(1 - \sigma_m^{-1/2}\sigma_{loc}^{1/2}). \qquad (4)$$

Using Eqs. (3) and (4), the activated volume is found to be

$$V_A \cong \frac{1}{2} D \sigma_m^{-1/2} \sigma_{\mathrm{loc}}^{-1/2}. \quad (5)$$

We readily see that V_A is not a constant but the dependence of V_A on σ_{loc} in the specified interval is fairly weak.

Equations (4) and (5) were derived for a single bond and characterize the activated volume under fluctuation-induced rupture of a single stressed bond in a diatomic molecule. However, we are interested in calculating the activated volume of an elementary event of fracture in a many-atomic solid. Computer simulation was also found to be effective for answering this question. In [24, 25], fluctuation-induced rupture of a stressed atomic chain was simulated. The lifetime (time to rupture) of such a chain and the dependence of the lifetime on stretching force and temperature were found. The results of those numerical experiments are presented graphically in Fig. 7.

For comparison, Fig. 8 shows experimental data on the dependence of the lifetime of a sample of an oriented polymer (polyethylene) on temperature and stress.

We readily see that the results obtained in the simulation and real experiments follow practically the same functional pattern. The only difference is that the simulation deals with a true stress (force) acting on chains, whereas the quantity featured in the experimental data is the average stress undergone by the sample.

Based on the fundamental relation for the mean expectation time τ_{fl} for an energy fluctuation E_{fl} [27], $\tau_{\mathrm{fl}} \cong \tau_0 \exp(E_{\mathrm{fl}}/kT)$ (this relation was directly derived from statistical treatment of computer simulation data [3–6]), and on the condition of rupture, $U(\sigma_{\mathrm{loc}}) = E_{\mathrm{fl}}$, we use the following expression for the simulation data on the lifetime:

$$\tau \cong \tau_0 \exp \frac{U(\sigma_{\mathrm{loc}})}{kT},$$

whence

$$U(\sigma_{\mathrm{loc}}) = kT \ln \frac{\tau}{\tau_0}.$$

This relation permits one to reduce the data on the dependence of $\ln(\tau/\tau_0)$ on $\sigma_{\mathrm{loc}}/\sigma_m$ (Fig. 7) to a $U(\sigma_{\mathrm{loc}})$ relation. The results of this transformation are shown graphically in Fig. 9, which plots the values of $U(\sigma_{\mathrm{loc}})/D$ (normalized against the bond dissociation energy D) corresponding to the extreme points on each of the linear sections of the stress relation $\ln(\tau/\tau_0)$ plotted for different temperatures in Fig. 8. All the sections are seen to join to form one weakly nonlinear relation $U(\sigma_{\mathrm{loc}})/D$.

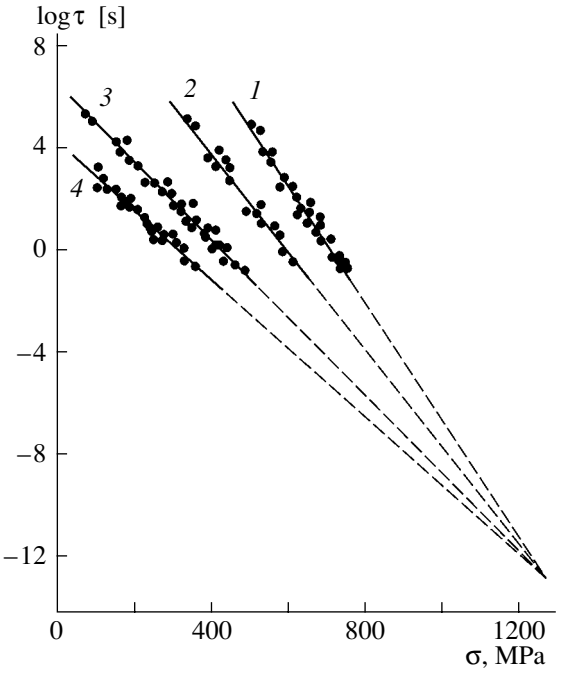

Fig. 8. Lifetime of oriented polyethylene fibers plotted as a function of tensile stress and temperature [26]. The temperature T is (*1*) 203, (*2*) 233, (*3*) 291, and (*4*) 323 K.

Figure 9 also presents, for comparison, the $U(\sigma_{\mathrm{loc}})/D$ relation that corresponds to a single bond and is given by Eq. (4). The model and analytical "diatomic" relations are seen to be similar. This clearly shows that inclusion of more than one atom in the model does not radically change the energetics of fluctuation-induced bond rupture as compared to the diatomic case. Therefore, the activated volume of an elementary event of atom chain rupture can be estimated using Eq. (3) for a single bond.

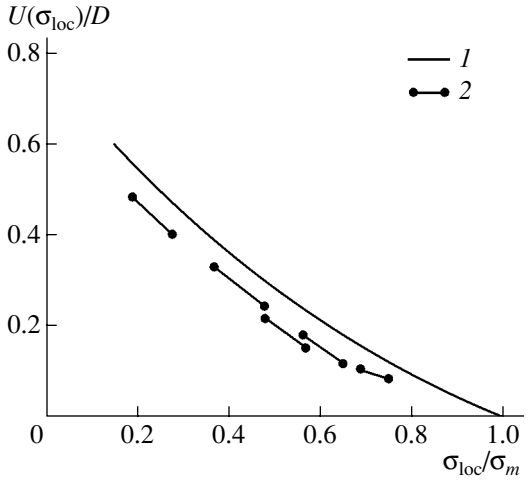

Fig. 9. Stress dependence of the potential barrier to rupture. (*1*) Theoretical dependence given by Eq. (4) for a single bond and (*2*) the results derived from computer simulation data given in Fig. 7.

By cutting out a quasi-linear section in the central part of the plot in Fig. 9, we estimate the activated volume from its slope as

$$V_A \cong -\frac{\Delta U}{\Delta \sigma_{\text{loc}}} \cong 0.87\frac{D}{\sigma_m}.$$

For the Morse potential, we have $\sigma_m = \frac{1}{2}\frac{D\alpha}{S_M}$, where α is a parameter of the potential (taken to be 2×10^{10} m^{-1}) and S_M is the cross-sectional area of the molecule. Thus, we obtain

$$V_A \cong 0.87 \times 10^{-10} S_M.$$

For the polyethylene molecule, $S_M = 1.8 \times 10^{-19}$ m^2 [28]; hence, for polyethylene, $V_A \cong 1.6 \times 10^{-29}$ m^3 $\cong$ 0.016 nm^3.

Thus, the activated volume for rupture of an atomic chain with parameters of the polyethylene molecule has an atomic-scale value (this volume is close to 0.023 nm^3, which is the volume of the CH_2 building block of the chain molecule of polyethylene).

Experimental data for polyethylene (Fig. 8) fitted by the expression $\tau \cong \tau_0 \exp\frac{U_0 - \gamma\sigma}{kT}$ yield $\gamma \cong 0.14$ nm^3. In other words, the coefficient γ exceeds the activated volume for rupture of the polyethylene molecule by about one order of magnitude.

The reason for this discrepancy consists obviously in that, in computer simulation, the activated volume was calculated from true (local) stresses in a chain molecule, whereas the coefficient γ was extracted from specimen-averaged stresses.

The idea that various structural defects in a real stressed specimen bring about local overstresses was put forward a long time ago [29, 30], after which these overstresses were detected directly in polymer molecules [31] and shown to exist in crystalline solids [32–35]. This implies that elementary events of the processes accounting for the fracture of real solids occur predominantly (because of the strong exponential dependence of the event probability on stress) at stress concentration points, i.e., at $\sigma_{\text{loc}} \cong q\sigma$ (q is the stress concentration coefficient, σ is the stress averaged over the specimen cross section) [2]. Therefore, we can write

$$\gamma \cong -\frac{dU(\sigma)}{d\sigma} \cong -\frac{dU(\sigma)}{d\sigma_{\text{loc}}}q \cong V_A q.$$

It appears that the data amassed in computer simulation experiments, which have made it possible to determine the activated volume in elementary rupture events (thus far in one-dimensional systems only), have shown convincingly that the results based on taking into account solely averaged stresses can in no case be identified with the activated volume. This conclusion is also supported by analytical estimation of the activated volume in elementary events of rupture of three-dimensional systems (metals), which shows the activated volume to have an atomic scale in this case [36]. It should be stressed that treating the coefficient γ as the activated volume is essentially equivalent to ignoring local overstresses, an approach which cannot be considered correct.

9. CONCLUSIONS

The results presented here were obtained as a result of a detailed description of both the fluctuation-induced elementary events in the fracture kinetics of solids and the local fluctuations themselves. This description remains accessible only through computer simulation of atomic dynamics.

The method of computer simulation may be called, in a certain sense, an "ultrachronomicroscope," and the results obtained reveal the rich potential of this peculiar microscopy to follow the behavior of individual atoms with a resolution of a fraction of the atomic vibration period.

The above results are the first step in the development of the microscopy of fluctuation phenomena. Many areas to which this approach could be applied to advantage are immediately evident. Among them are attempts to provide an even more detailed description of fluctuations of all kinds (atom velocities and bond stresses, including their sign), as well as fluctuation migration in two- and, particularly, three-dimensional models, and a detailed description of elementary fracture events in three-dimensional models (this description has thus far been done within the framework of the one-dimensional model only). Investigation of the energetics of an elementary fracture event in models should promote a deeper understanding of the values of the activation energy of fracture extracted from real experiments, where many questions invariably arise. A very important step would be a transfer from model results to a deeper insight into the so-called compensation effect (the relation between the prefactors and exponents of the exponential functions in Boltzmann-type expressions for the experimentally studied rates of activated processes).

The potential of computer simulation is rich enough to permit solution of this and other similar problems, thus providing a firm basis for further development of the fluctuation kinetics approach in the theory of the strength of solids.

ACKNOWLEDGMENTS

The author feels a sense of deep gratitude toward Serafim Nikolaevich Zhurkov, who introduced him to the hard but fascinating realm of the physics of fluctuations and aided his progress along this road in warm, helpful, and rewarding contacts over many years of joint work.

REFERENCES

1. S. N. Zhurkov, Vestn. Akad. Nauk SSSR **11**, 78 (1957).

2. V. R. Regel', A. I. Slutsker, and É. E. Tomashevskiĭ, *Kinetic Nature of the Strength of Solids* (Nauka, Moscow, 1974) [in Russian].
3. Yu. V. Rakitskiĭ, E. D. Shchukin, V. S. Yushchenko, I. A. Tsukerman, Yu. B. Suris, and A. I. Slutsker, Dokl. Akad. Nauk SSSR **265** (4), 941 (1985).
4. A. I. Slutsker, A. I. Mikhaĭlin, and I. A. Slutsker, Usp. Fiz. Nauk **164** (4), 357 (1994) [Phys. Usp. **37**, 335 (1994)].
5. A. I. Slutsker, A. I. Mikhaĭlin, and I. A. Slutsker, in *Problems in Theoretical Physics* (Peterb. Inst. Yad. Fiz., St. Petersburg, 1994), p. 42 [in Russian].
6. A. I. Mikhaĭlin, L. V. Zhigileĭ, and A. I. Slutsker, Fiz. Tverd. Tela (St. Petersburg) **37** (6), 1784 (1995) [Phys. Solid State **37**, 972 (1995)].
7. E. Fermi, *Scientific Works* (Nauka, Moscow, 1972), Vol. 2.
8. *Computer Simulation in Studying Materials*, Ed. by D. B. Pozdeev (Mir, Moscow, 1974).
9. D. W. Heermann, *Computer Simulation Methods in Theoretical Physics* (Springer, New York, 1986; Nauka, Moscow, 1990).
10. I. A. Slutsker, Candidate's Dissertation (Leningrad State Technical Univ., Leningrad, 1990).
11. L. D. Landau and E. M. Lifshitz, *Course of Theoretical Physics*, Vol. 5: *Statistical Physics*, 3rd ed. (Nauka, Moscow, 1976; Pergamon, Oxford, 1980), Part 1.
12. I. L. Fabelinskiĭ, *Molecular Scattering of Light* (Nauka, Moscow, 1965; Plenum, New York, 1968).
13. A. I. Mel'ker, A. I. Mikhaĭlin, and N. Yu. Zolotarevskiĭ, Fiz. Tverd. Tela (Leningrad) **21** (5), 1545 (1979) [Sov. Phys. Solid State **21**, 890 (1979)].
14. A. I. Mel'ker and A. I. Mikhaĭlin, Fiz. Tverd. Tela (Leningrad) **23** (6), 1746 (1981) [Sov. Phys. Solid State **23**, 1016 (1981)].
15. E. Poncelet, Colloid. Chem. **6**, 77 (1946).
16. Ya. S. Umanskiĭ, B. N. Finkel'shteĭn, M. E. Blanter, S. T. Kishkin, N. S. Fastov, and S. S. Gorelik, *Physical Metallurgy* (Metallurgiya, Moscow, 1955) [in Russian].
17. A. H. Cottrell, *Dislocations and Plastic Flow in Crystals* (Clarendon, Oxford, 1953; Mir, Moscow, 1958).
18. R. Berner and H. Kronmüller, *Plastische Verformung von Einkristallen* (Springer, Berlin, 1965; Mir, Moscow, 1968).
19. G. M. Bartenev and Yu. S. Zuev, *Strength and Fracture of Hyperelastic Materials* (Khimiya, Moscow, 1964) [in Russian].
20. H. Eyring, S. H. Lin, and S. M. Lin, *Basic Chemical Kinetics* (Wiley, New York, 1980; Mir, Moscow, 1983).
21. W. Kauzmann and H. Eyring, J. Am. Chem. Soc. **62**, 7 (1940); **62**, 3113 (1940).
22. A. I. Gubanov and A. D. Chevychelov, Fiz. Tverd. Tela (Leningrad) **4** (5), 928 (1962) [Sov. Phys. Solid State **4**, 681 (1962)].
23. É. E. Tomashevskiĭ, Fiz. Tverd. Tela (Leningrad) **12** (12), 3202 (1970) [Sov. Phys. Solid State **12**, 2588 (1970)].
24. M. G. Zaĭtsev and I. V. Razumovskaya, Vysokomol. Soedin., Ser. B **21** (6), 461 (1979).
25. A. I. Mel'ker and A. I. Mikhaĭlin, Fiz. Tverd. Tela (Leningrad) **26** (4), 1236 (1984) [Sov. Phys. Solid State **26**, 753 (1984)].
26. A. V. Amelin, O. F. Pozdnyakov, V. R. Regel', and T. P. Sanfirova, Fiz. Tverd. Tela (Leningrad) **12** (10), 2528 (1970) [Sov. Phys. Solid State **12**, 2034 (1970)].
27. Ya. I. Frenkel', *Kinetic Theory of Liquids* (Nauka, Moscow, 1975) [in Russian].
28. K. Bunn, Trans. Faraday Soc. **35**, 482 (1939).
29. A. A. Griffith, Philos. Trans. R. Soc. London, Ser. A **221**, 163 (1921).
30. A. F. Ioffe, M. V. Kirpicheva, and M. A. Levitskaya, Zh. Russ. Fiz.–Khim. O-va, Chast Fiz. **56**, 489 (1924).
31. S. N. Zhurkov, V. I. Vettegren, V. E. Korsukov, and I. I. Novak, Fiz. Tverd. Tela (Leningrad) **11** (2), 290 (1969) [Sov. Phys. Solid State **11**, 233 (1969)].
32. V. A. Zakrevskii and A. V. Shuldiner, Philos. Mag. B **71** (2), 127 (1995).
33. A. V. Shuldiner and V. A. Zakrevskii, J. Phys.: Condens. Matter **14**, 9555 (2002).
34. I. I. Afanas'ev, O. L. Volkova, K. V. Naumov, and B. I. Smirnov, Fiz. Tverd. Tela (Leningrad) **27** (10), 2826 (1985) [Sov. Phys. Solid State **27**, 1704 (1985)].
35. F. Appel, H. Bethge, and U. Messercshmidt, Phys. Status Solidi A **38**, 103 (1976).
36. A. I. Slutsker, Fiz. Tverd. Tela (St. Petersburg) **46** (9), 1606 (2004) [Phys. Solid State **46**, 1658 (2004)].

Translated by G. Skrebtsov

Physics of the Solid State, Vol. 47, No. 5, 2005, pp. 812–816. Translated from Fizika Tverdogo Tela, Vol. 47, No. 5, 2005, pp. 788–792.

Diagnostics and Forecasting of Breakage of Large-Scale Objects

V. S. Kuksenko

Ioffe Physicotechnical Institute, Russian Academy of Sciences, Politekhnicheskaya ul. 26, St. Petersburg, 194021 Russia
e-mail: victor.kuksenko@mail.ioffe.ru

Abstract—Using a kinetic approach to the breakage of solids, a two-stage model of breakage is constructed. The model is invariant for objects of various scale. A physical approach to forecasting the final stage of macroscopic breakage is developed. The applicability of the methods devised is tested on laboratory samples, industrial constructions, and large-scale objects. © *2005 Pleiades Publishing, Inc.*

1. INTRODUCTION

The kinetic approach to the theory of the strength of solids proposed by Zhurkov assumes that breakage is a thermally activated process. This approach has made it possible to forecast macroscopic breakage. According to [1, 2], the durability τ of a sample under uniaxial tensile stress is given by

$$\tau = \tau_0 \exp(U_0 - \gamma\sigma/kT), \quad (1)$$

where σ is the applied tensile stress; T is the temperature of the sample; U_0 is the activation energy for breakage, which is close to the heat of sublimation; γ is a parameter characterizing the properties of the material and the local stresses; k is the Boltzmann constant; and τ_0 is the period of vibration of atoms.

Given the instant of time at which the load is applied and the parameters involved in Eq. (1), we can predict the instant of fracture of a sample, though only with logarithmic accuracy. In actual practice, however, this accuracy is often insufficient. A significant advance in this direction has been made by studying the kinetics of fracture on the atomic and microscopic levels, especially by experimentally studying the kinetics of accumulation and development of initial submicroscopic cracks [3–6].

2. MICROMECHANICS OF FRACTURE OF SOLIDS

Considerable advances in developing the micromechanics of fracture of solids were made in the 1960s by studying the formation and development of initial submicroscopic cracks using small-angle x-ray scattering (SAXS). According to [7], the size and concentration of cracks can be determined by measuring SAXS from cracks. Such studies were performed in [3–6] on various materials: polymers, metals, and composites. It has been found that the size of initial microcracks depends on the structure of a material, which determines local overstresses and limits their growth at the heterointerfaces. More interesting results have been obtained in studies into the kinetics of accumulation of submicroscopic cracks. As an example, Fig. 1 shows the crack accumulation with time in an oriented kapron film under various loading conditions. The following two results are of great interest. First, the rate of crack accumulation $\dot{C}$ is described by an expression similar to Eq. (1) for the durability:

$$\dot{C} = \dot{C}_0 \exp(U_0 - \gamma\sigma/kT). \quad (2)$$

This fact indicates that the kinetics of crack accumulation determines the durability of a loaded material.

Second, the microcrack concentration immediately before fracture is independent of the loading conditions and depends only on the size of the microcracks that form during loading.

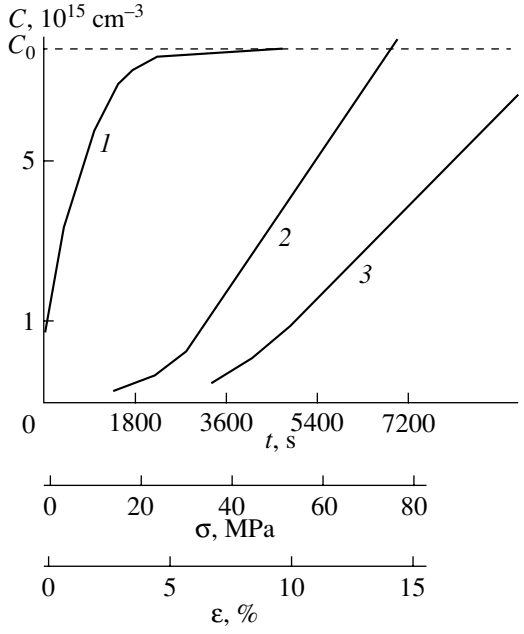

Fig. 1. Accumulation of submicrocracks in a kapron film under uniaxial tensile stress. (*1*) Under static stress (t scale), (*2*) under increasing tensile stress (σ scale), and (*3*) at a constant strain rate (ε scale).

1063-7834/05/4705-0812$26.00 © 2005 Pleiades Publishing, Inc.

As seen from Fig. 1, the microcrack concentration can be very high. Therefore, in order to gain an understanding of the transition from microscopic to macroscopic fracture of a solid, large ensembles should be considered and statistical relations should be used when qualitatively analyzing the interaction and development of microcracks. In this way, a two-stage model of fracture was constructed in [5, 6]. This model is illustrated schematically in Fig. 2. At the first stage (Fig. 2a), single stable microcracks accumulate in the entire solid and then, due to fluctuations in their density, ensembles of closely spaced cracks form. These ensembles interact with one another, coalesce, and finally form a fracture nucleus. At the second stage (Fig. 2b), the fracture nucleus increases and a through crack arises, causing the solid to fracture. The transition from the first stage of crack accumulation to the formation of ensembles or clusters was analyzed quantitatively in [8, 9]. The concentration parameter that controls this transition is the ratio

$$K = r_i/L,$$

where L is the size of cracks that form in a solid and r_i is the average spacing between cracks. The intensive formation of clusters begins at $K \simeq 3$.

In [3–6], the formation of cracks was studied by measuring the number of cracks that form during a fixed period of time. In this case, information on the discrete generation of individual cracks is lost. The acoustic-emission method does not suffer this disadvantage. This method enables one to determine the instant of time t_i at which the ith microcrack forms in a loaded solid and the parameters of the acoustic signal caused by the formation of this crack, such as the amplitude and duration, which are related to the size of the crack [10, 11]. A sequence of acoustic signals that are generated in a solid under an applied static load is shown schematically in Fig. 2c. In the first stage of the local nucleation of microcracks, the distribution of signals on a time axis is close to a Poisson distribution. In this case, the instants of time t_i at which acoustic signals are generated and the spacing R_i between these signals, as well as their variances, were shown to be important statistical parameters. The acoustic-emission method made it possible to study a wider range of materials and, what is very important, a wider size range of the objects under study. As an example, let us consider an experiment that supported the main assumptions of the two-stage model of fracture and revealed important details of the transition from the first stage to the second [12].

Figure 3 shows a schematic diagram of the experiment. A uniaxial compressive stress was applied to a cylindrical fine-grained granite sample 190-mm high and 75 mm in diameter by a controllable press in a high-pressure chamber (50 MPa in this experiment). The sample was encased in a protective polymer jacket into which acoustic-signal detectors were embedded. Moreover, acoustic transducers were used to determine

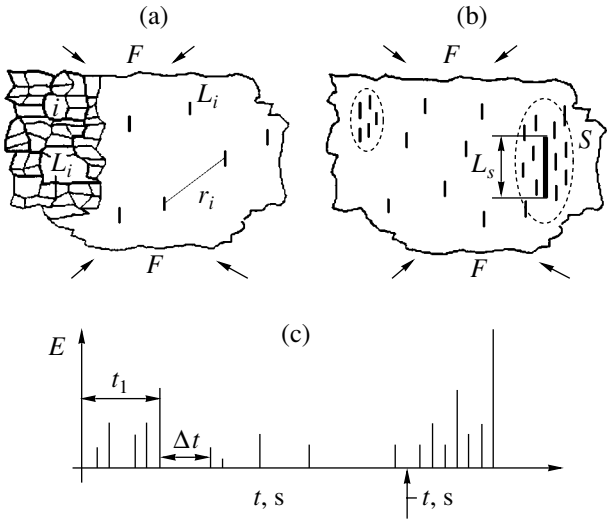

Fig. 2. (a, b) Schematic diagrams illustrating two stages of fracture: (a) the steady-state and (b) fracture nucleation stages; and (c) acoustic signals generated during crack formation. E is the energy of an acoustic signal, t is time, F is the applied load, L_i is the size of initial cracks, L_s is the size of second-level crack clusters, and S is the region of a fracture nucleus.

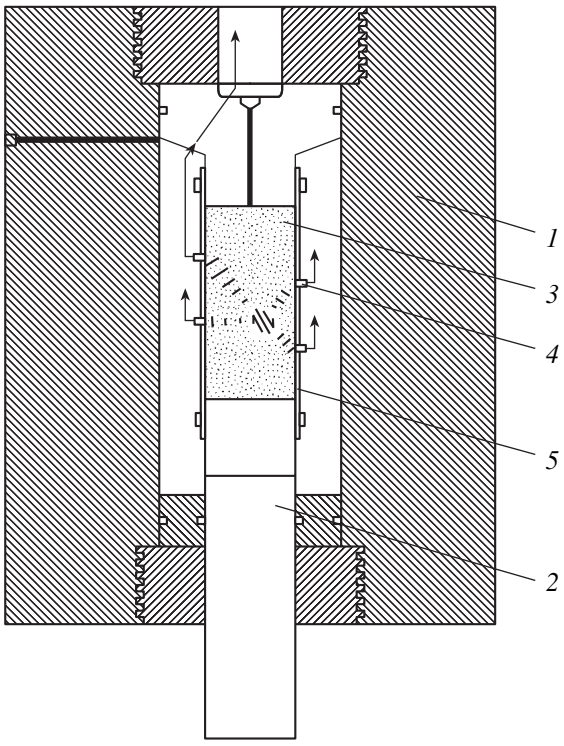

Fig. 3. Experimental setup for a compression test: (*1*) high-pressure chamber, (*2*) loading piston, (*3*) granite sample, and (*4, 5*) piezoelectric transducers for the generation of acoustic waves and detection of acoustic pulses associated with crack formation.

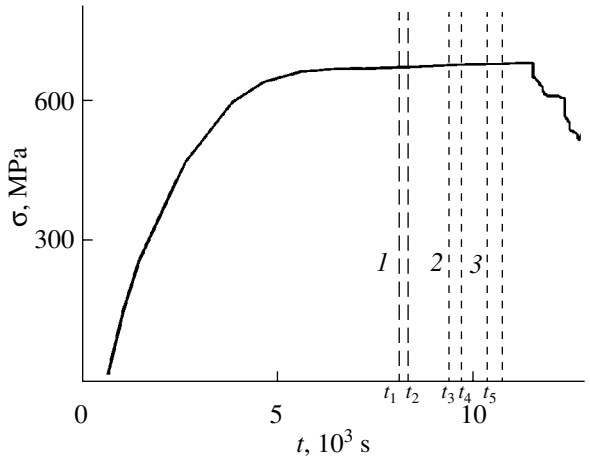

Fig. 4. Time dependence of the compressive stress.

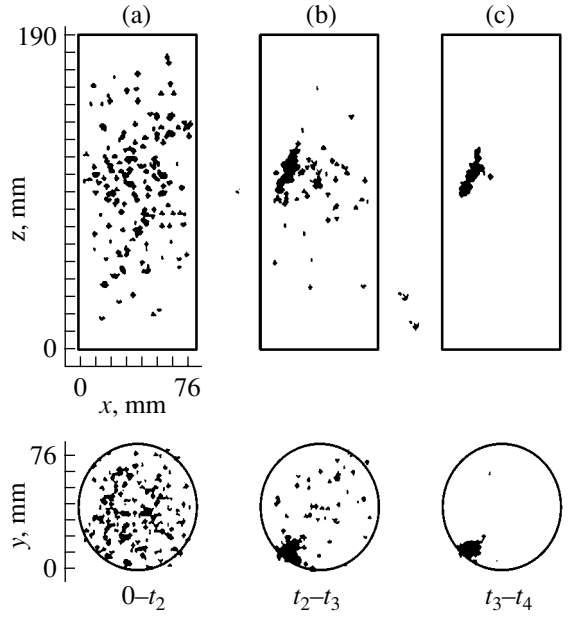

Fig. 5. Distribution of microcracks over a sample (a) at the first stage, in the time interval between t_1 and t_2, and (b, c) at the fracture nucleus stage, between the times t_2 and t_4, as indicated in Fig. 4.

the velocity of acoustic waves (which was used to calculate the variations in the sample dilatation in the course of deformation and more accurately determine the site at which cracks form). In order to examine the details of the transition from the first stage to the second, computer-controlled loading was used for which the acoustic-emission intensity did not exceed a certain value. The applied uniaxial compressive stress was varied in time as shown in Fig. 4. At the beginning of loading (i.e., at small loads), the acoustic-emission intensity is low and the load increases at a constant rate. As the acoustic-emission intensity increases, the loading rate decreases, so the sample is under a fairly constant load (i.e., under creep conditions) for the greater part of the duration of the experiment. At the final stage, the load decreases due to the requirement that the acoustic-emission intensity be constant. The acoustic-emission pattern can be studied over various periods of time.

Before the instant t_1 (Fig. 5a), the pattern corresponds to the first stage of nucleation of microcracks in the entire sample (Fig. 2a). Then, a fracture nucleus arises at the instant t_2, and its growth results in fracture of the sample.

3. THE PHYSICAL APPROACH TO FORECASTING MACROSCOPIC BREAKAGE

As mentioned above, the Zhurkov equation can be used to estimate, with logarithmic accuracy, the time until a loaded solid fractures if the parameters entering this equation are known. The two-stage model enables one to develop a physical approach to forecasting macroscopic breakage of a loaded solid and make significantly more accurate estimates of the time at which breakage will occur. In general, the durability of a loaded solid τ can be written as a sum [13]:

$$\tau = t_1 + \Delta t,$$

where t_1 is the time it takes for stable microcracks to accumulate. This time accounts for the greater part of the overall durability of a loaded solid. In order to forecast the onset of fracture, one has to be able to monitor the process of damage accumulation and determine the instant of time at which the transition from the first stage to the second begins. It is also important to keep in mind that the accumulation of damages is a stochastic process. Therefore, various statistical parameters can be used to predict the transition of this process from the stage of quasistatic accumulation of damages to the stage of local growth of a fracture nucleus. Figure 6 shows the expected variations in the crack formation parameters in a solid under an applied static load. Curve *1* in Fig. 6a describes the accumulation of defects (cracks). This curve first rises and then becomes flat (creep). When a fracture nucleus arises and begins to grow, the defect nucleation intensity increases again until fracture occurs. The concentration parameter K decreases accordingly (Fig. 6b), which indicates that the average spacing between defects decreases as their concentration increases. Whereas the increase in crack concentration cannot be characterized by a critical value, the concentration parameter has a threshold value (indicated by the dashed line in Fig. 6b) below which clusters of defects are intensively created and a fracture nucleus develops.

When defects arise chaotically over the entire solid at the first stage, the average spacing between them remains constant and then decreases sharply after the appearance of a fracture nucleus. Accordingly, the variance increases after the formation of this nucleus.

The parameter that characterizes the time intervals between successive events of defect formation is especially informative; it carries information on the nucleation rate of defects and can describe the kinetics of their accumulation [12]. This parameter remains unchanged at the steady-state stage, where the accumulation rate of defects is constant, and begins to decrease when a fracture nucleus develops intensively. It is important that the variance of this parameter is equal to unity in the case where the events of defect nucleation are characterized by a Poisson distribution in time (at the first stage) and begins to increase when the process becomes nonsteady. All these parameters can be reliably measured using acoustic emission and enable one to determine the instant of time at which the transition occurs from the steady-state stage of defect nucleation to the fracture nucleus stage and predict the onset of the final breakage.

It should be noted that there is a relation between the final stage of fracture nucleus development and the overall durability of a loaded solid. Figure 7 shows these relations for steel subjected to tensile stresses and granite samples subjected to uniaxial compressive stresses. These findings are of considerable practical importance. After the onset of the final stage is revealed, the remaining durability can be estimated and appropriate steps can be taken.

4. DISCUSSION OF THE RESULTS

In this paper, we outlined the physical approach to forecasting macroscopic breakage. This approach has been used to develop practical methods for checking the integrity of various mechanical structures and predicting their macroscopic breakage.

It should be noted that the problem of forecasting the onset of breakage has been virtually solved for laboratory samples. An understanding has been gained of both the kinetics of accumulation of microcracks and the features of their formation, in particular, the trigger effect that occurs under weak influences [14]. As for large-scale constructions, underground structures, mines, and earthquake sources, there are certain difficulties associated with the complexity of these objects, the inefficiency of the methods used to detect the defect nucleation, and the absence of a prehistory of the development of breakage processes.

In order to develop more reliable methods for checking serviceable constructions, extensive bench tests have been performed at production plants (Central Boiler–Turbine Institute NPO, Izhora plants, Neva plant). Comprehensive tests have been carried out on large-scale samples and construction members in highly stressed states that are similar to actual objects. Based on the results of those tests, efficient techniques for checking the integrity of real objects have been devised. A wealth of experience has been accumulated in checking various operative objects in the oil and gas

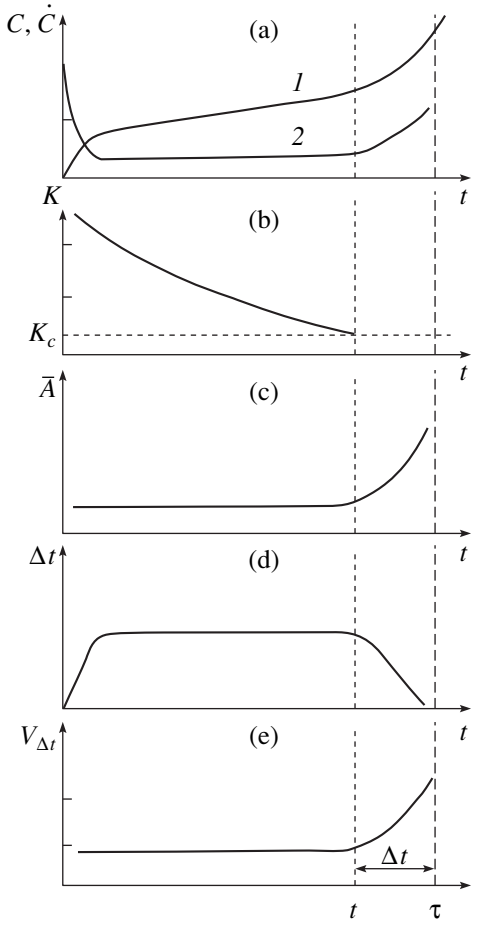

Fig. 6. Time dependence of the statistical parameters characterizing crack accumulation (schematic): (a) crack accumulation C and accumulation rate $\dot{C}$; (b) concentration parameter K (the dashed line indicates the threshold value K_c); (c) average amplitude of acoustic signals $\bar{A}$; (d) average time interval Δt between successive events of defect formation; and (e) the variance $V_{\Delta t}$ of the time intervals.

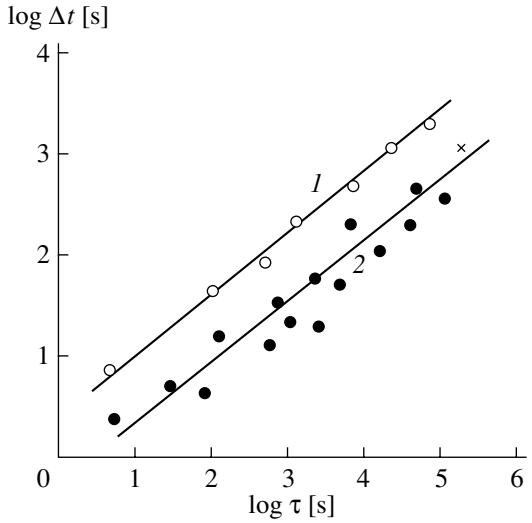

Fig. 7. Relation between the time it takes for a fracture nucleus to develop and the durability of loaded samples for (*1*) granite and (*2*) steel samples.

industry and at nuclear power plants and other large-scale objects.

In order to develop a method for forecasting rock bumps in a deep bauxite mine, a preliminary analysis of microseismic impulses prior to rock bumps was performed. Based on this analysis, a technique for forecasting rock bumps was devised and has been applied in practice for the past several years [15]. A detailed analysis of microseismic patterns in terms of the two-stage model and the concentration criterion for breakage was performed in [16].

Based on this model, forecasting of earthquakes was considered in [17, 18]. For complex objects such as mines and earthquake sources, forecasting is probabilistic in character and is hampered by the fact that the microseismic events prior to a rock bump or an earthquake are small in number, which makes it difficult to use statistical analysis techniques, as indicated above.

Nevertheless, in principle, forecasting is possible for various objects. The fact that forecasting techniques can be based on the same physical concepts of kinetic theory of strength and the two-stage model of breakage indicates that these techniques are universal in character.

In closing, it should be noted that S.N. Zhurkov was an active proponent of this approach and that the author's studies in this field were published in collaboration with him.

ACKNOWLEDGMENTS

This study was supported by the Russian Foundation for Basic Research (project nos. 02-05-39017, 04-05-65287) and ISTC (project no. 1745).

REFERENCES

1. S. N. Zhurkov, Vestn. Akad. Nauk SSSR **11**, 78 (1957).
2. V. R. Regel, A. I. Slutsker, and É. E. Tomashevskiĭ, *Kinetic Nature of the Strength of Solids* (Nauka, Moscow, 1974) [in Russian].
3. V. S. Kuksenko, A. I. Slutsker, and A. A. Yastrebinskiĭ, Fiz. Tverd. Tela (Leningrad) **9**, 2390 (1967) [Sov. Phys. Solid State **9**, 1869 (1967)].
4. S. N. Zhurkov, V. S. Kuksenko, and A. I. Slutsker, Probl. Prochn., No. 2, 45 (1971).
5. S. N. Zhurkov and V. S. Kuksenko, Mekh. Polim. **10** (5), 792 (1974).
6. V. P. Tamuzh and V. S. Kuksenko, *Micromechanics of Fracture of Polymer Materials* (Zinatne, Riga, 1978) [in Russian].
7. A. Guanier and A. Fournet, *Small-Angle Scattering of X-rays* (Wiley, New York, 1955).
8. S. N. Zhurkov, V. S. Kuksenko, V. N. Savel'ev, and U. Sultonov, Izv. Akad. Nauk SSSR, Fiz. Zemli, No. 6, 11 (1977).
9. V. A. Petrov, Fiz. Tverd. Tela (Leningrad) **21**, 3681 (1979) [Sov. Phys. Solid State **21**, 2123 (1979)].
10. V. S. Kuksenko, S. A. Stanchits, and N. G. Tomilin, Mekh. Kompoz. Mater., No. 3, 536 (1983).
11. V. S. Kuksenko, A. I. Lyashkov, *et al.*, Defektoskopiya, No. 6, 53 (1980).
12. D. A. Lockner, J. D. Byerly, V. S. Kuksenko, and A. V. Ponomarev, Nature **350**, 39 (1991).
13. V. S. Kuksenko and V. A. Petrov, Mekh. Kompoz. Mater., No. 1, 31 (1988).
14. V. S. Kuksenko, B. Ts. Manzhikov, K. Tiligenov, Zh. K. Shatemirov, and B. É. Émil'bekov, Fiz. Tverd. Tela (St. Petersburg) **45** (12), 2182 (2003) [Phys. Solid State **45**, 2287 (2003)].
15. A. Yu. Gor, V. S. Kuksenko, N. G. Tomilin, and D. I. Frolov, FTPRPI, No. 3, 54 (1989).
16. V. S. Kuksenko and B. Ts. Manzhikov, Fiz. Tverd. Tela (St. Petersburg) **47** (2005) (in press).
17. A. V. Zav'yalov, Fiz. Tverd. Tela (St. Petersburg) **47** (6) (2005) (in press).
18. N. G. Tomilin, E. E. Damaskinskaya, and P. I. Pavlov, Fiz. Tverd. Tela (St. Petersburg) **47** (5), 955 (2005) [Phys. Solid State **47**, 989 (2005)].

Translated by Yu. Epifanov

Physics of the Solid State, Vol. 47, No. 5, 2005, pp. 817–824. Translated from Fizika Tverdogo Tela, Vol. 47, No. 5, 2005, pp. 793–800.

Structural Mechanisms of Fracture of Nanocrystalline Materials

V. A. Pozdnyakov and A. M. Glezer

Bardin Central Research Institute for the Iron and Steel Industry, Vtoraya Baumanskaya ul. 9/23, Moscow, 105005 Russia
e-mail: Glezer@imph.msk.ru

Abstract—Structural mechanisms and features of brittle and quasi-brittle fracture of nanocrystalline materials are theoretically analyzed. The role of size effects and internal stresses caused by a nonequilibrium structure during brittle trans- and intercrystallite fracture is studied. The dependence of the nanocrystalline material durability on the working stress and grain size is calculated. The conditions for certain mechanisms of plastic deformation to be operative in nanocrystalline materials are analyzed. The influence of the grain-boundary and dislocation mechanisms of plastic deformation on the conditions of nanocrack formation is studied. The dependence of the fracture toughness of nanomaterials on structure parameters is calculated. © *2005 Pleiades Publishing, Inc.*

1. INTRODUCTION

The main distinctive features of the structure of nanocrystalline material (NM) are an extremely small grain size; the resulting large area of grain boundaries and their long junction length per unit volume; hampering or suppression of dislocation mechanisms of plastic deformation at grain sizes smaller than a certain limiting value; and nonequilibrium states of grain boundaries (GBs) [1–4].

The most important structural elements of NMs, which control their macroscopic properties in many respects, are GBs. It is known that GBs can have a significant effect on polycrystal fracture. Crack nucleation and growth can be facilitated at GBs, which are regions of stress concentration and decreased strength. In NMs featuring a very high density of GBs and their junctions, the influence of GBs on crack propagation should be much stronger than in conventional materials. Depending on the methods of producing a NM, such as nanopowder compaction, mechanical alloying, nanocrystallization of amorphous alloys, and severe plastic deformation, various grain structures can arise that differ in terms of the degree of structure nonequilibrium, misorientation spectrum, degree of imperfection, and chemical composition of GBs. In this case, the NM structure can contain uncompensated GB junctions.

Fractographic studies of brittle-fracture surfaces of NMs have shown the intercrystallite fracture mechanism to play a dominant role [1, 4]. In [5], the indentation method was applied to measure the fracture toughness of an *n*-FeMoSiB alloy with an α-Fe grain size from 11 to 35 nm, produced from an amorphous state. It was shown that the dominant fracture mechanism is intercrystallite crack propagation. The average size of fracture pits on the fracture surface for samples with grain sizes d = 11, 25, and 35 nm is 0.5, 2, and 5 μm, respectively. For samples with grain sizes from 11 to 35 nm, the crack resistance increases from 2.7 to 4.6 MPa $m^{1/2}$. The variation in the fracture strength with grain size is independent of NM plastic strain [5].

The NM tensile strength is higher than that of the corresponding coarse-grained materials by a factor of q, where q = 1.5–8.0 depending on the NM material and grain size [2, 3]. In NMs produced by crystallization of amorphous Ni–P alloys, the ultimate strain before fracture decreases with increasing grain size [6]. On the fracture surface of such materials, plastic flow traces were observed [6]; it was assumed that plastic deformation can have a significant effect on NM fracture conditions.

The study of cracking features in NMs seems to be important in developing methods for increasing the fracture toughness (crack resistance) of brittle materials with a disperse structure. There are experimental data on increased values of the fracture toughness of multiphase brittle materials in a nanostructured state (see, e.g., [1]). At the same time, some data [1] show that NMs do not exhibit higher plasticity. Theoretical studies on the size effects in the NM strength and the cracking features in NMs are only beginning to be published [7, 8].

Our current notion of the structural mechanisms of NM fracture is rather schematic and qualitative in character. There are no experimental data on the dependence of the fracture stress and toughness on the NM grain size.

In this paper, we consider the problem of purely brittle fracture of NMs. The dependence of the NM durability on the working stress and grain size is calculated. We determine the dependence of the fracture stress on the GB energy and grain size, as well as the role of size effects in fracture. Possible mechanisms of plastic deformation and their role in microcracking are analyzed. The influence of the grain-boundary mechanism of plastic deformation on the fracture toughness of NMs is studied.

1063-7834/05/4705-0817$26.00 © 2005 Pleiades Publishing, Inc.

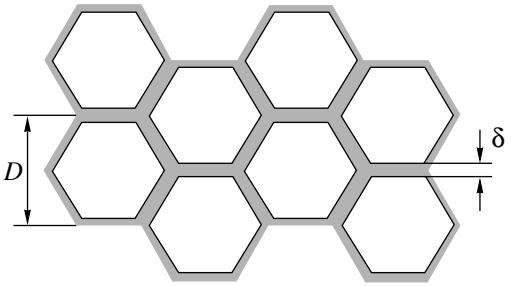

Fig. 1. Grains and grain boundaries in a nanomaterial (schematic).

2. BRITTLE FRACTURE OF NANOCRYSTALLINE MATERIALS

The cracking mechanism in polycrystals and the corresponding conditions of the initiation of trans- or intercrystallite fracture are controlled by the relation between the cohesion (γ_0) and grain-boundary (γ_e) fracture energies. The specific energies of trans- and intercrystallite fracture are given by

$$\gamma_0 = 2\gamma, \quad \gamma_e = \eta(2\gamma + 2\gamma_s - \gamma_b), \tag{1}$$

where γ and γ_b are the specific energies of the free surface and GB, respectively; γ_s is the cleavage step energy; and η is the roughness factor of the fracture surface.

In ordinary polycrystalline materials, the contribution of GB junctions to the fracture energy is negligible and is disregarded in the fracture analysis [9]. The volume fraction of the material involved in GBs and triple junctions increases as the grain size decreases. For NMs, the volume fraction of triple junctions becomes comparable to the volume fractions of GBs and intragrain material and their contribution to the fracture energy should be taken into account. For a crack propagating in a material, the effective fracture energy is

$$\gamma_0^* = f_0\gamma_0 + f_b\gamma_e + f_j\gamma_j, \tag{2}$$

where f_0, f_b, and f_j are the crack area fractions in the internal volume of grains, GBs, and GB junctions, respectively, which depend on the crack propagation trajectory, and γ_0, γ_b, and γ_j are the contributions of the corresponding structural components to the specific energy of NM fracture.

If the crack propagation plane is perpendicular to the axis of the applied external stress σ and the crack tip deflects from its trajectory, then, for a kink crack oriented at an angle θ to the plane of the basic crack, the local stress coefficients k_1 and k_2 [10] are given by

$$k_1 = \cos^3(\theta/2)K_1, \quad k_2 = \sin(\theta/2)\cos^2(\theta/2)K_1, \quad K_1 = \zeta\sigma\sqrt{L}, \tag{3}$$

where ζ is a numerical coefficient and L is the length of the basic crack.

The condition of crack propagation along the grain face at an angle θ to the basal plane is [9]

$$k_1^2 + k_2^2 \geq [2E\gamma_e/(1-\nu^2)], \tag{4}$$

where $E = 2\mu(1 + \nu)$ is the Young's modulus, ν is the Poisson ratio, and μ is the shear modulus. In the case where

$$K_1 \geq K_{1c} = [2E\gamma_0^*/(1-\nu^2)]^{1/2} \tag{5}$$

the crack will develop into the grain bulk, which will result in transcrystallite fracture.

In the case of intercrystallite fracture of NMs, the contribution of linear tension of the crack surface to the fracture energy becomes significant. As the crack front is bent between grains or is curved with a small curvature radius r, the fracture energy is [8]

$$\gamma_e^* = \gamma_e + T/r, \tag{6}$$

where T is the linear tension of the crack front and $2r \approx D$ is the grain size.

By comparing Eqs. (4) and (5), we find the condition of intercrystallite fracture to be

$$(\gamma_e^*/\gamma_0^*) \leq \cos^4(\theta_{max}/2). \tag{7}$$

With typical values of the parameters, we find from Eqs. (2) and (6) that the specific fracture energy increases by 15–20% due to GB junctions and the surface tension of an intercrystallite crack for NMs with grain sizes of 10–20 nm.

The Griffiths crack size [9] in a homogeneous continuum material is $L_G = 4E\gamma_0^*/\pi(1-\nu^2)\sigma_f^2$. At $\gamma_0^* = \mu b/20$ (where b is the interatomic distance) and $\sigma_f = \mu/50$, we have $L_G \approx 500b \gg D$ (~10 nm); i.e., the Griffiths crack size can greatly exceed the NM grain size.

Due to the high density of GBs and their junctions, purely transcrystallite fracture cannot take place in NMs. The crack front periodically passes through the internal volume of grains, GBs, and their junctions even for a straight crack. Hence, the fracture energy periodically varies. In the case of intercrystallite fracture of NMs, the fracture energy on a scale much larger than the grain size is also a periodic function of the crack length. The specific fracture energy γ^* (fracture toughness G_c) is a periodic (quasiperiodic) function of the crack propagation path with a period approximately equal to the grain size D. In this case, a number of thermodynamically steady metastable states of nanocracks arise [7, 8].

A nanocrystalline material can be considered to consist of two phases, namely, grain boundaries and intragrain regions (Fig. 1). In order to determine the fracture toughness of a nanomaterial, we need to generalize Eq. (2). If the volume fractions of grain volumes,

boundaries, and junctions are f_V, f_B, and f_J, respectively, the fracture toughness can be written as

$$G_c = G_V f_V + G_B f_B + G_J f_J, \quad (8)$$

where G_V, G_B, and G_J are the critical rates of energy release during the crack motion in the grain volume, boundaries, and junctions, respectively.

The volume fractions of grain and grain-boundary phases are

$$f_V \approx 1 - \delta/D, \quad f_B \approx \delta/D, \quad (9)$$

where δ is the GB thickness. The dependence of the fracture toughness on the grain size is given by

$$G_c = G_V + \delta(G_B - G_V)D^{-1}. \quad (10)$$

In the case of intercrystallite fracture, we should also take into account that the effective crack length increases by a factor of $(1 + \psi f_V)^{1/2}$, where the numerical coefficient $\psi \approx 2$ accounts for the grain configuration.

Taking into account the increase in the intercrystallite fracture toughness by K_{II}/K_I due to friction between crack faces [11], we obtain

$$G_c^* = G_c[1 + \psi f_V]^{1/2}[1 - f_V^{1/2}]^{-1}. \quad (11)$$

Using relations (10) and (11), one can also estimate the fracture toughness of heterophase NMs. By varying the sizes and properties of the phase components in heterophase NMs or nanocomposites, the crack resistance parameters can be improved using the fact that the fracture energy increases with the trajectory length of an intercrystallite crack or a crack propagating over an interlayer of a more brittle phase.

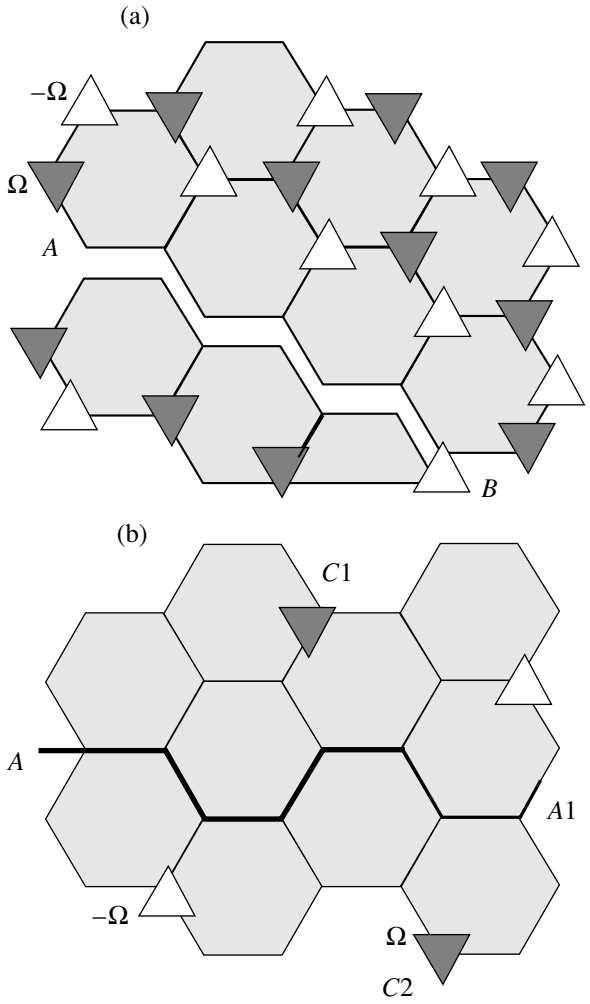

Fig. 2. (a) Intergrain crack motion through a system of uncompensated triple junctions of grain boundaries and (b) crack propagation between uncompensated junctions of grain boundaries.

3. FRACTURE CRITERION FOR NANOMATERIALS WITH NONEQUILIBRIUM BOUNDARIES AND UNCOMPENSATED GRAIN JUNCTIONS

A GB junction with an uncompensated rotation angle Ω of nearby grains induces a long-range elastic stress field similar to a disclination stress field of strength Ω [12]. An additional stress concentration in GB junctions can be caused by uncompensated dislocation densities in GBs. The equilibrium size of cracks formed at disclinations was analyzed in [12–14]. Such nonequilibrium GBs and their junctions can have a significant effect not only on the crack formation but also on the propagation of a crack in a material.

Let us consider the condition of passage of a crack of length L through alternating tension and compression regions caused by junction disclinations. The stress intensity factor of a crack in an inhomogeneous stress field is given by [9]

$$K_{\text{eff}} = K_0 + \sqrt{\frac{2}{\pi}} \int_{a-d}^{a} \frac{\sigma(x)dx}{\sqrt{a-x}}, \quad K_0 = \sigma_a[\pi L/2]. \quad (12)$$

If all GB junctions are uncompensated (Fig. 2a) and the GB strength is low to the extent that intercrystallite fracture takes place, the crack will move through a system of alternating positive and negative disclinations. The grain-boundary (interphase) crack will pass through alternating tension and compression regions associated with junction disclinations if the stress intensity factor exceeds a critical value, which can be determined from Eq. (12) with substituted disclination stress fields [12]:

$$K_c = K_{cb} + \Delta K, \quad (13)$$

$$\Delta K = \zeta[\mu\Omega/2\pi^{3/2}(1-\nu)]D^{1/2}, \quad \zeta = 6.738, \quad (14)$$

where K_{cb} is the critical value of the stress intensity factor for crack propagation over GBs in a material with compensated GB junctions. If only a fraction of the GB junctions is uncompensated (Fig. 2b), it is more favorable for the crack to move between them. The condition of crack propagation between two uncompensated triple junctions spaced by $Q_n = nD$ is given by

$$\Delta K = \zeta_1\sigma^*(Q_n)^{1/2}; \quad \sigma^* = 2[\mu\Omega/2\pi(1-\nu)][\ln(2R/Q_n) - 2]. \quad (15)$$

Let us consider the fracture condition for NMs with uncompensated triple junctions and nonequilibrium GBs. The free surface formation due to crack opening in a material with long-range internal stresses results in stress relaxation in the neighborhood of the crack.

The crack tip propagation will cause relaxation of stress fields of junction disclinations arranged along the front motion line. Moreover, the energy of uncompensated junctions arranged at a certain distance from the crack (rather than immediately along the line of crack front motion) will decrease. The energies of a disclination at the center of a crystal of size R and of a disclination near the crystal free surface at a distance ξ from it are [12]

$$E_{d(0)} = \frac{\mu\Omega^2}{4\pi(1-\nu)}R^2; \quad E_{d(1)} = \frac{\mu\Omega^2}{4\pi(1-\nu)}\xi^2; \quad (16)$$

respectively. Hence, as the crack tip moves by dL, the energy of junction disclinations arranged at a distance less than L_e from the crack surface, i.e., in a region of area $L_e dL$, will significantly decrease (L_e is the screening length of the disclination field in a disclination ensemble). An analysis of L_e shows [15] that $L_e \approx 3L^*$, where L^* is the average distance between disclinations in the ensemble. As the crack propagates by dL, the disclination system energy decreases on the average by $\Delta E = \varphi[\mu\Omega^2/4\pi(1-\nu)]L_e dL$, where φ is a numerical coefficient of order unity. The stress field relaxation decreases the effective fracture energy by the quantity

$$\Delta\gamma_d = \varphi[\mu\Omega^2/4\pi(1-\nu)]L_e. \quad (17)$$

The energy of nonequilibrium GBs [16] is given by

$$\gamma_B = \gamma_{B0} + \Delta\gamma, \quad \Delta\gamma = \mu b^2\rho\ln(R/2b)/4\pi(1-\nu). \quad (18)$$

The Griffiths criterion for the appearance of a crack of length L in such a material is written as

$$\sigma_f = [4\mu(\gamma_e - \Delta\gamma_d)/\pi(1-\nu)L]^{1/2} + \zeta[\mu\Omega/2\pi^2(1-\nu)](D/L)^{1/2}. \quad (19)$$

Let us estimate characteristic values of the material parameters. The energy of a perfect large-angle GB is approximately three times lower than the free-surface energy, $\gamma_b \approx \gamma/3$ [13]. The energy of nonequilibrium boundaries with excess dislocation density ρ is $\gamma_{bn} \approx (4/3)\gamma$, so we have $\gamma_e \approx \mu b/30$. The average value $\langle\Omega\rangle = 0.02$–$0.04$. At $L = (5$–$10)D$, we obtain $\sigma_f \approx \mu/40$.

4. STRUCTURAL MECHANISMS OF PLASTIC DEFORMATION OF NANOMATERIALS

Fracture of even rather brittle materials, as a rule, is preceded by local plastic deformation. Plastic flow can play an important role during the crack formation and propagation in NMs. Currently, several different approaches to the description of plastic flow in NMs have been developed [17, 18].

A model of low-temperature plastic deformation in NMs was proposed in [19]. It is assumed that, at low temperatures, GB structural elements are restructured under strong shear stresses, which causes low-temperature grain-boundary slip over individual GB regions. This process, referred to as grain-boundary microslip (GBMS), occurs through the formation of microscopic regions of shear in GBs. Accommodation processes are grain rotation and dislocation generation in GBs. The deformation behavior of NMs is described by the relations [19]

$$\sigma_a(\varepsilon) = \sigma_s + A\mu(D/L)\varepsilon/qhm^2, \quad \varepsilon < \varepsilon^* = mqh(\delta/D)\gamma^*, \quad \sigma_a(\varepsilon) = \sigma_a(\varepsilon^*) + \alpha\mu[kb\varepsilon/m\zeta D]^{1/2}, \quad \varepsilon > \varepsilon^*, \quad (20)$$

where α, h, k, q, and ζ are numerical parameters [19]; m is the average orientation factor; $(\sigma_a - \sigma_s)m = \tau_a - \tau_s$; τ_a is the external shear stress; τ_s is the shear stress of resistance to free (not constrained) slip over a plane GB; and L is the average size of the GBMS region. The yield stress σ_y is determined from Eqs. (20) as a stress corresponding to a given plastic strain ε_y, which is accepted, e.g., as equal to 0.2%.

The critical grain size D_1^* for a change in the deformation mechanism was determined in [19]. For nanosized grains with $D < D_1^*$, plastic deformation of NMs is controlled by GBMS and the main accommodation mechanism is grain rotation. At $D \geq D_1^*$, dislocation generation in GBs becomes the main accommodation mechanism.

The NM yield stress can be written as

$$\sigma_y = \sigma_0 + k_y D^{-1/2}F(D) \equiv \sigma_0 + D^{-1/2+\chi}, \quad (21)$$

where $\chi = 0$ at $D \geq D_1^*$ and $\chi \geq 1/2$ at $D < D_1^*$.

If the dislocation generation stress in GBs is smaller than the stress required for a dislocation to penetrate into a grain of a sub critical size by bending, then there will exist a grain size range in which dislocations will remain in GBs. In NMs with larger grains, dislocation emission from GBs will take place.

In [20], molecular-dynamics simulation was used to study the mechanisms of plastic deformation of *n*-Ni with grain sizes from 3 to 12 nm; deformed was performed with uniaxial loading at finite temperatures. At small grain sizes in the range under study, plastic deformation of NMs was controlled by grain-boundary slip. In the upper region of the nanograin size range under study, two competing mechanisms of plastic deformation were operative: grain-boundary slip and dislocation emission from GBs.

At least four critical grain sizes of NMs may be distinguished: D_1^*, D_2^*, D_3^*, and D_4^* (and/or the corresponding intermediate grain size ranges), which control the conditions for changing the structural mechanisms of NM plastic deformation (Fig. 3). Depending on the grain size and the ratio between the GB shear stress and the resistance stress to dislocation motion, the following patterns of the development of plastic flow are possible in the lattice.

(i) If the NM grain size is smaller than the minimum critical size D_1^*, then the main mechanism of plastic deformation is GBMS and the accommodation process of GB deformation of NMs is plastic rotation of grains.

(ii) In the range $D_2^* \geq D \geq D_1^*$, accommodation processes of dislocation generation in GBs become energetically more favorable than plastic rotation of grains under the GBMS conditions. The working stress is larger than the dislocation formation stress in GBs but is smaller than the stress of dislocation emergence from the boundary [18].

(iii) In the NM grain size range $D_3^* \geq D \geq D_2^*$, where D_2^* is the second critical grain size below which dislocation clusters cannot arise in nanograins [18], single lattice or partial dislocations become capable of escaping from GBs into the grain volume.

(iv) At $D > D_3^*$, deformation of an NM (or a submicrocrystalline material, depending on the value of D_2^*) will develop due to the generation of dislocation trains at GBs and the development of slip bands.

(v) At $D > D_4^*$, all conventional intragrain dislocation processes take place, e.g., multiplication and annihilation of dislocations [21]. The quantity χ in Eq. (21) can take on various values in all the nanograin size ranges under consideration. Depending on the NM properties, some of these ranges can be not covered. The critical grain size D^* beginning from which the classical Hall–Petch relation is satisfied can fall within one of ranges (i)–(v) of nano- and submicrograin sizes.

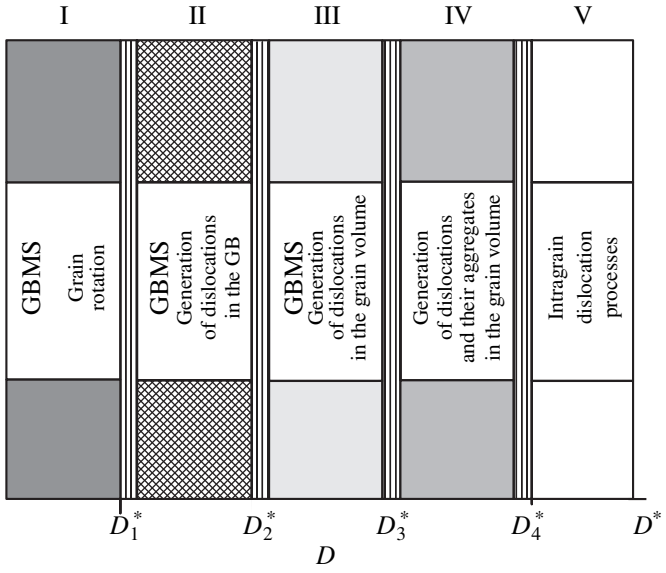

Fig. 3. Map of structural mechanisms of plastic deformation of nanomaterials in relation to grain size.

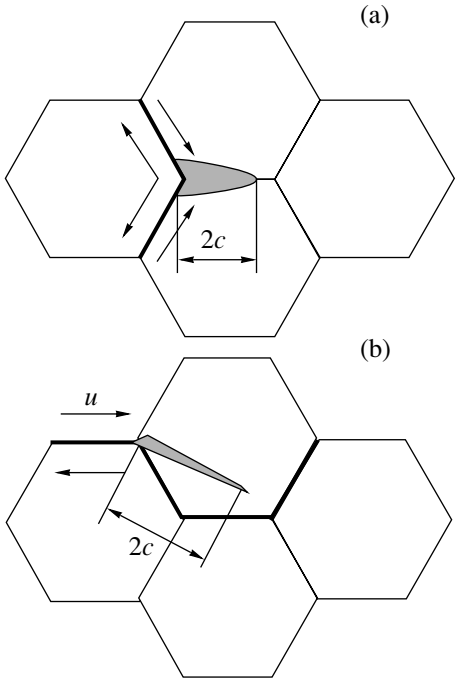

Fig. 4. Illustration of nanocracking mechanisms that are operative (a) in the region of crossed GBMS regions and (b) at a vertex of an individual GBMS region.

5. INFLUENCE OF PLASTIC DEFORMATION ON CRACK NUCLEATION AND FRACTURE STRESS OF NANOMATERIALS

GBMS regions are modeled by plane inclusions with shear deformation or continual aggregates of loops of effective dislocations. In both cases, the average shear displacement is

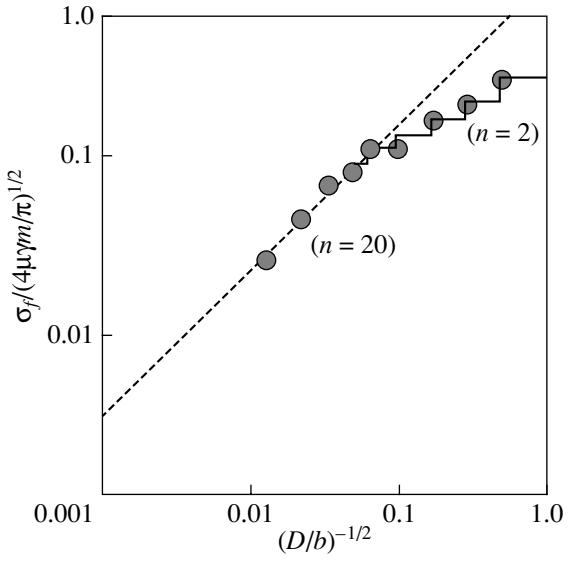

Fig. 5. Grain-size dependence of the reduced cracking stress at a vertex of a dislocation cluster in a nanomaterial.

$$u = A(\tau_a - \tau_s)L/\mu. \quad (22)$$

The coefficient A is close to unity in both cases.

In a vertex of a GBMS region, stresses are concentrated and promote microcracking. The most probable microcracking mechanisms (Fig. 4) are similar to the Cottrell and Stroh mechanisms [9].

The energy of a $2c$-long microcrack formed at the vertex of crossing GBMS regions (Fig. 4a), where the shear displacements are u, is given by

$$W = \frac{u^2\mu}{4\pi(1-\nu)}\ln\left(\frac{2R}{c}\right) + 4\gamma c - \frac{\pi(1-\nu)(\sigma_a^2+\tau_a^2)}{2\mu}c^2 - \theta u\sigma_a c. \quad (23)$$

Here, the first to fourth terms are the deformation energy of a dislocation-type wedge crack, the surface energy, the energy of elastic deformation of a solid with a crack, and the work done by the external forces in creating a microcrack, respectively, and θ is a numerical parameter dependent on the orientation of the crack opening plane [9].

The equilibrium crack length is determined from the condition $\partial W/\partial c = 0$, which yields a quadratic equation for c. Therefore, there exist two stable crack lengths or the equation roots are both imaginary, which corresponds to a spontaneous decrease in energy. At the intermediate point, we have

$$u[(\sigma_a^2 + \tau_a^2)^{1/2} + \theta\sigma_a] = 4\gamma_0. \quad (24)$$

If a crack is nucleated in one GBMS region (Fig. 4b), Eq. (24) becomes similar to the Stroh fracture condition $\sigma = 2\gamma/u$. Substituting Eqs. (21) and (22) into this condition, we obtain the following dependence of the fracture stress on the grain size:

$$\sigma_f \geq (2\mu\gamma_0/k_y)D^{-1/2}F(D). \quad (25)$$

At $D > D^*$, Eq. (25) gives the known dependence of the fracture stress on the grain size [9].

In range (iv) of nanoscopic grain sizes, dislocation clusters form and microcracks can arise at a vertex of clusters pinned at a GB. To calculate the cracking stress, we use the following dependence of the number n of dislocations on the length L of a cluster of a small number of screw dislocations locked at a dislocation with Burgers vector mb [22]:

$$L^{-1/2} = (A/2\sigma)^{1/2}[2(n+m-1)^{1/2} - \Lambda 4(n+m-1)^{-1/6}], \quad (26)$$

where $\Lambda = 1.85575$ and $A = \mu b/\pi$.

The nanocracking stress at a vertex of the locked cluster is found to be

$$\sigma_f = \sqrt{\frac{4\mu m\gamma_0}{\pi}}D^{-1/2}\Phi(D) \equiv KD^{-1/2}\Phi(D). \quad (27)$$

Figure 5 shows the classical dependence of the reduced fracture stress on the grain size at $\Phi = 1$ (dashed line), an approximate solution for a small number of dislocations (solid line), and the exact solution (circles).

At $D \leq D^*$, the form of functions F and Φ, which determine the deviation of the dependence of the fracture stress on the NM grain size from the classical dependence, is dictated by the operative mechanism of plastic deformation of an NM.

6. DURABILITY OF NANOCRYSTALLINE MATERIALS

Zhurkov and his coworkers experimentally established the following expression for the durability τ of a loaded solid at a working stress σ and absolute temperature T:

$$\tau = \tau_0\exp\left[\frac{U_0 - \gamma\sigma}{kT}\right], \quad (28)$$

where U_0 is an energy constant of a material, τ_0 is the period of thermal atomic vibrations, and γ is the structure-sensitive parameter. The form of formula (28) and extensive experimental data on changes in the structure of solids under load suggest that the mechanism of atomic rearrangements resulting in fracture is thermal activation due to temperature fluctuations [23, 24]. Several models explaining the Zhurkov formula have been proposed (see, e.g., [25, 26]). The time it takes for fracture of a solid under load to occur, $\tau(\sigma)$, can be written as [26]

$$\tau = \tau_{cf} + \tau_{cg}, \quad (29)$$

where τ_{cf} is the time of formation of a macroscopic crack in an ensemble of microcracks and τ_{cg} is the time of crack growth up to the critical size for the loss of stability. In [26], it was shown that the times τ_{cf} and τ_{cg} can be expressed in terms of the average microcracking time τ_m

$$\tau_m = \tau_0 \exp[U(\sigma)/kT] \quad (30)$$

(U the microcracking activation energy, τ_0 is the period of thermal atomic vibrations) as follows:

$$\tau_{cf} = k_1\tau_m, \quad \tau_{cg} = k_2\tau_m, \quad (31)$$

where k_1 and k_2 are known structure parameters [26].

In other durability models, the material fracture time can also be expressed in terms of the microcracking time.

In an NM, the kinetic conditions of cracking in GBs and in the bulk become similar, which can result in a strong dependence of the NM durability on the grain size. A nanomaterial can be considered to consist of two phases: GBs and the intragrain material (Fig. 4).

Assuming that the microcracking processes occurring in grains and in grain boundaries are independent, the probability of microcracking in an NM can be written as

$$W = W_V f_V + W_B f_B, \quad (32)$$

where $W_V = \tau_V^{-1} = \nu_0 \exp[-U_V/kT]$ and $W_B = \tau_B^{-1} = \nu_0 \exp[-U_B/kT]$ are the probabilities of microcracking in grains and grain boundaries, respectively; f_V and f_B are the volume fractions of grains and grain boundaries, respectively; and $\nu_0 = \tau_0^{-1}$ is the atomic vibration frequency.

To a first approximation, we can write $U_V(\sigma) = U(0) - \gamma_V\sigma$ and $U_B(\sigma) = U(0) - \gamma_B\sigma$, where $U(0)$ is the energy fraction of the microcracking activation energy that is independent of the applied stress σ. The structure parameters γ_i also account for the stress concentration factors. The NM durability is given by

$$\tau = (k_1 + k_2)\frac{\tau_V}{f_V + f_B(\tau_V/\tau_B)}, \quad (33)$$

where $f_B \approx \delta/D$ and $f_V \approx 1 - \delta D$. At $f_B \longrightarrow 0$ and $f_V \longrightarrow 1$, Eq. (33) reduces to the Zhurkov formula (28).

7. INFLUENCE OF GRAIN-BOUNDARY DEFORMATION ON THE FRACTURE TOUGHNESS OF NANOMATERIALS

In the case of quasi-brittle fracture of NMs, it is important to know the influence of grain-boundary deformation on the fracture toughness. The plastic zone at the crack tip is defined as the region in which shear stresses initiated by a crack exceed the stress of resistance to GBMS.

Using the model proposed in [27] for the crack stress field in a hardening material characterized by a strain-hardening exponent n, the following asymptotic distribution of stresses in the crack line (the x axis) within the plastic zone can be derived:

$$\sigma_{yy} = S\sigma_y[r_p/r]^{n/n+1}, \quad (34)$$

where r_p is the distance from the crack tip to the interface between the elastic- and plastic-strain regions along the x axis ($y = 0$) and S is a function of the NM strain-hardening exponent. Assuming that the basic crack propagates via nanocracks nucleating at a distance r^* from its tip under a critical local stress σ_c [28], the fracture toughness can be found to be

$$K_{1c} = S^{(1+n)/2n}(K_{c0})[\sigma_c/\sigma_y]^{(1-n)/2n}, \quad (35)$$

where K_{c0} is a model parameter independent of the yield and fracture stresses [28]. Using Eqs. (21) and (27), we find the following dependence of the NM fracture toughness (crack resistance) on the grain size:

$$K_{1c} = S^{(1+n)/2n}(K_{c0}) \times [KD^{-1/2}\Phi(D)/\{\sigma_0 + k_yD^{-1/2}F(D)\}]^{(1-n)/2n}. \quad (36)$$

For $n = 1/2$ and typical values of the parameters, we find from Eq. (36) that, at D = 10–15 nm, K_{1c} can be 7–10 MPa m$^{1/2}$, which is at least two times larger than the fracture toughnesses of conventional ceramic materials.

8. CONCLUSIONS

It is convenient to introduce the notion of an "ideal NM," which means a homogeneous one-phase polycrystal without dislocations with grains ~10 nm in size and with GBs corresponding to coarse-grained materials. An analysis of the influence of the grain size on the mechanisms and conditions of fracture of the ideal NM makes it possible to separate size effects on strength. For NMs with $D < 10$ nm, the volume fraction of triple junctions becomes comparable to the volume fractions of GBs and intragrain material; hence, their contribution to the fracture energy should be take into account. In the case of intercrystallite fracture of NMs, the contribution of the linear tension of the crack surface to the fracture energy becomes significant. The increase in the specific fracture energy for NMs with grains 10–20 nm in size caused by triple junctions and crack surface tension can be estimated to be 20%.

In NMs produced using nanopowder compaction, mechanical alloying, or severe plastic deformation, the grain structure can be far from equilibrium. In this case, the NM structure can feature uncompensated GB junctions. An analysis has been performed of the influence of relaxation of uncompensated GB junction fields and external grain-boundary defects on the crack propagation conditions. It has been found that the crack tip

propagation results in relaxation of stress fields of junction disclinations that are located in the front motion line and at a small distance from it. The Griffiths criterion changes in two respects due to internal stresses: on the one hand, the effective fracture energy decreases, but on the other hand there appears an additional contribution to the stress of the loss of crack stability.

An important mechanism for increasing the fracture toughness of materials is the development of structures that facilitate bridging in the crack mouth. As applied to ceramic nanocomposites, this mechanism was analyzed in [29]. Since the nanostructured components of composite materials cannot be plastically deformed, it was concluded that internal stresses could be a source of increase in the fracture toughness, which enhance friction when nanograins of another phase are pulled during bridging.

An analysis of NM fracture mechanisms has shown that the most significant source of an increase in viscosity is grain-boundary plastic deformation. If the stress of resistance to grain-boundary microslip in an NM fabricated using a certain technology is less than the stress of the crack formation and/or propagation, such materials can exhibit plastic flow before fracture and show significant viscosity.

REFERENCES

1. R. A. Andrievskiĭ and A. M. Glezer, Fiz. Met. Metalloved. **88**, 50 (1999) [Phys. Met. Metallogr. **88**, 45 (1999)]; Fiz. Met. Metalloved. **89**, 91 (2000) [Phys. Met. Metallogr. **89**, 83 (2001)].
2. H. Hahn and K. A. Radmanabhan, Nanostruct. Mater. **6**, 191 (1995).
3. R. W. Siegel and G. E. Fougere, Nanostruct. Mater. **6**, 205 (1995).
4. Z. Li, S. Ramasamy, H. Hahn, and R. W. Siegel, Mater. Lett. **6**, 195 (1998).
5. Y. Gan and B. Zhou, Scr. Mater. **45**, 625 (2001).
6. M. L. Sui, S. Patu, and Y. Z. He, Scr. Metall. Mater. **25**, 1537 (1991).
7. V. A. Pozdnyakov, Pis'ma Zh. Tekh. Fiz. **29** (4), 46 (2003) [Tech. Phys. Lett. **29**, 151 (2003)].
8. V. A. Pozdnyakov, Izv. Ross. Akad. Nauk, Ser. Fiz. **67**, 867 (2003).
9. I. I. Novikov and V. A. Ermishkin, *Micromechanisms of Metal Fracture* (Nauka, Moscow, 1991) [in Russian].
10. B. Cottrell and J. R. Rice, Int. J. Fract. **16**, 155 (1980).
11. M. F. Ashby, Acta Metall. Mater. **41**, 1313 (1993).
12. V. I. Vladimirov and A. E. Romanov, *Disclinations in Crystals* (Nauka, Leningrad, 1986) [in Russian].
13. I. M. Zhukovskiĭ and V. V. Rybin, Fiz. Tverd. Tela (Leningrad) **33**, 1286 (1991) [Sov. Phys. Solid State **33**, 728 (1991)].
14. M. Yu. Gutkin and I. A. Ovid'ko, Philos. Mag. A **70**, 561 (1994).
15. A. Richter, A. E. Romanov, W. Pompe, and V. I. Vladimirov, Phys. Status Solidi B **143**, 43 (1987).
16. A. A. Nazarov, A. E. Romanov, and R. Z. Valiev, Nanostruct. Mater. **6**, 775 (1995).
17. M. Yu. Gutkin and I. A. Ovid'ko, *Physical Mechanics of Deformed Nanostructures*, Vol. 1: *Nanocrystalline Materials* (Yanus, St. Petersburg, 2003) [in Russian].
18. V. A. Pozdnyakov, Fiz. Met. Metalloved. **96**, 114 (2003).
19. V. A. Pozdnyakov and A. M. Glezer, Fiz. Tverd. Tela (St. Petersburg) **44**, 705 (2002) [Phys. Solid State **44**, 732 (2002)].
20. H. van Swygenhoven, M. Spaczer, A. Caro, and D. Farkas, Phys. Rev. B **60**, 22 (1999).
21. G. A. Malygin, Fiz. Tverd. Tela (St. Petersburg) **37** (8), 2281 (1995) [Phys. Solid State **37**, 1248 (1995)].
22. C. S. Pande, R. A. Masumura, and R. W. Armstrong, Nanostruct. Mater. **2**, 323 (1993).
23. S. N. Zhurkov, Vestn. Akad. Nauk SSSR, No. 3, 46 (1968).
24. V. R. Regel', A. I. Slutsker, and É. E. Tomashevskiĭ, *Kinetic Nature of the Strength of Solids* (Nauka, Moscow, 1974) [in Russian].
25. V. A. Petrov, Fiz. Tverd. Tela (Leningrad) **18**, 1290 (1976) [Sov. Phys. Solid State **18**, 741 (1976)].
26. A. N. Orlov, V. A. Petrov, and V. I. Vladimirov, Phys. Status Solidi B **47**, 292 (1971).
27. J. R. Rice, J. Appl. Mech. **35**, 379 (1968).
28. A. Ya. Krasovskiĭ, *Brittleness of Metals at Low Temperatures* (Naukova Dumka, Kiev, 1980) [in Russian].
29. T. Ohji, Y. K. Jeong, Y. H. Choa, and K. Niihara, J. Am. Ceram. Soc. **81**, 1453 (1998).

Translated by A. Kazantsev

Physics of the Solid State, Vol. 47, No. 5, 2005, pp. 825–831. Translated from Fizika Tverdogo Tela, Vol. 47, No. 5, 2005, pp. 801–807.

Evolution of Microscopic Cracks and Pores in Solids under Loading

V. I. Betekhtin and A. G. Kadomtsev

Ioffe Physicotechnical Institute, Russian Academy of Sciences, Politekhnicheskaya ul. 26, St. Petersburg, 194021 Russia
e-mail: Vladimir.Betekhtin@mail.ioffe.ru

Abstract—Experimental data on the development and partial healing of microscopic cracks and pores in loaded crystalline materials are considered. An analysis of the data indicates that fracture development has a number of specific features depending on the state of the materials and the testing conditions and is a kinetic thermal fluctuation process occurring virtually throughout the entire time of loading. © *2005 Pleiades Publishing, Inc.*

1. INTRODUCTION

According to a concept formulated by Zhurkov, the fracture of solids begins from the instant they are loaded and is a kinetic thermal fluctuation process [1, 2]. This approach to the problem of fracture is generally consistent with the hypothesis of distributed damages, which has been developed mainly by scientists in the field of mechanics. According to this hypothesis, plastic loosening is caused by purely force-induced crack and pore nucleation [3–6] and is accumulated in solids under a load throughout the entire time of loading. The role of thermal fluctuations is neglected in this process.

Therefore, to understand the physical nature of fracture, it is important to determine the laws of formation and development of microscopic cracks and pores and the possibility of the reverse process, healing of pores and cracks. It is generally accepted that microscopic cracks and pores (hereafter, microdiscontinuities) are typical defects in solids (like dislocations and vacancies in crystals) [7]. We distinguish two types of microdiscontinuities: acquired discontinuities and self-discontinuities. The first type includes microdiscontinuities that form during plastic deformation under loading, radiation, high-energy lasers, etc. Self-discontinuities are induced by the technological features of the production of a material (ceramics, amorphous and powder alloys, electrodeposited and sputtered films, etc.). As a rule, the formation of microdiscontinuities deteriorates the physicomechanical properties of materials, but a decrease in their size (e.g., via healing) improves these properties.

In this work, we consider some general features of the development and healing of deformation-induced microdiscontinuities.

2. EXPERIMENTAL

To study the evolution of microdiscontinuities, we used Al (99.96%) single crystals and polycrystals; Zn (99.97%), Ni (99.9%), and Cu (99.92%) polycrystals; some steels and alloys; and NaCl and KCl synthetic single crystals.

To study the development of microdiscontinuities, tensile loads were applied to samples under creep conditions or at a constant rate at moderate (less than $0.5T_m$) or elevated temperatures. Under the loading conditions, the samples were in the plastic state (strain to failure $\varepsilon_r \approx 20$–50%). We also studied fracture in the quasi-brittle state ($\varepsilon_r \approx 1\%$).

Microdiscontinuity parameters were studied using a set of complementary methods. Nucleating microdiscontinuities were revealed with a modified method of small-angle x-ray scattering (SAXS) on an apparatus with Kratky collimation and a primary beam (MoK_α radiation) with a width varying from four to several tens of microns. It is important that, when the incident beam was the thinnest, scattering from a metal during deformation was observed only at ultrasmall angles (from ≈0.7 to 2.5′). Because of this, we could, first, virtually eliminate double Bragg reflections (which are characteristic of metals) and, second, obtain information on depth profiles of microdiscontinuities by scanning a beam from the surface of a deformed sample toward its bulk. The total volume of microdiscontinuities was determined by measuring a decrease in the density or using a flotation method with an accuracy of $5 \times 10^{-4}\%$ (Al, NaCl), as well as by triple hydrostatic weighing with an accuracy of $\approx 10^{-3}\%$. Usually, we determined the relative change in the density (density defect $\Delta\rho/\rho$) of a deformed sample as compared to its initial annealed state. Some deformed samples were also polished to find depth profiles of their loosening. Using scanning and transmission electron microscopy, microdiscontinuities forming upon deformation were detected and their parameters were determined.

1063-7834/05/4705-0825$26.00 © 2005 Pleiades Publishing, Inc.

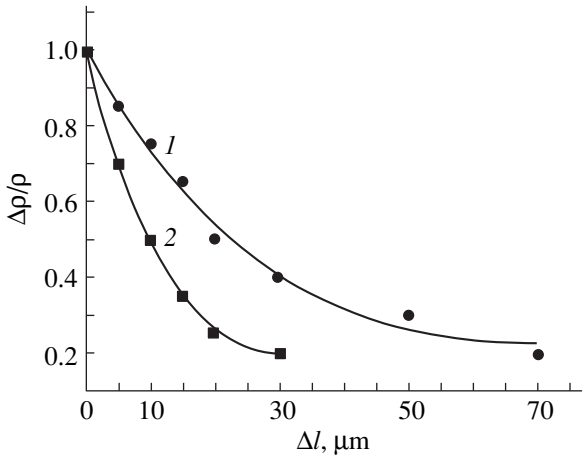

Fig. 1. Dependence of the loosening Δρ/ρ on the distance from the surface Δ*l* of (*1*) 7- and (*2*) 1-mm-thick aluminum samples.

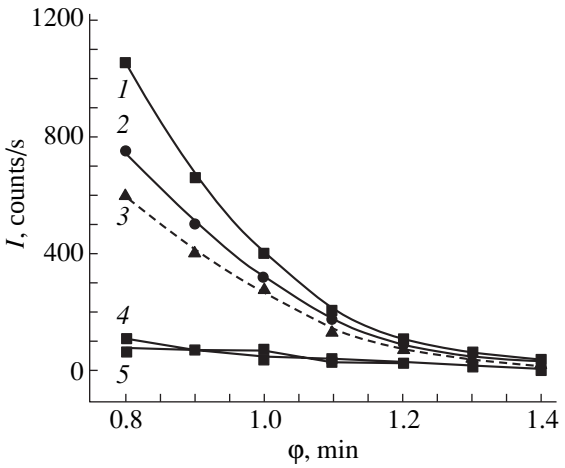

Fig. 2. Dependence of the scattering intensity *I* on the scattering angle φ at various distances Δ*l* from the surface of deformed Al samples: (*1*) 4 ± 2, (*2*) 10 ± 2, (*3*) 20 ± 2, and (*4*) 300 ± 2 μm. (*5*) Initial annealed aluminum sample.

3. EXPERIMENTAL RESULTS

Microdiscontinuities are often studied by measuring deformation-induced loosening (see, e.g., [3, 4]). However, a decrease in material density can be caused not only by microdiscontinuities but also by other defects that form during plastic deformation. To take into account the contribution of these defects, we studied polycrystalline Al (99.96%) samples. After preliminary annealing, they were tensioned under conditions of creep or active loading at moderate temperatures. The quantity Δρ/ρ of these samples after fracture was found to be 4×10^{-5} [8]. The contribution from dislocations (whose density was determined with an electron microscope) to Δρ/ρ was estimated to be less than 3×10^{-6}, and the contributions from oriented microstresses and equilibrium vacancies were estimated to be $\approx(2–4) \times 10^{-6}$ and $\approx 10^{-13}$, respectively. Quantitative data on Δρ/ρ obtained upon annealing indicate that the loosening is independent of nonequilibrium vacancies. Additional arguments for the absence of a relation between Δρ/ρ and these vacancies were obtained when we studied the depth profile of Δρ/ρ for deformed Al. Deformation-induced loosening is found to concentrate predominantly in thin surface layers (several tens of microns thick for a sample thickness of 1–2 mm; Fig. 1). Note that the thickness of the layer with a low density increases with sample thickness. Similar data were obtained for all the metals and ionic crystals under study. Estimates show that the loosening in these layers is one to two orders of magnitude higher than that averaged over volume (Table 1). These data allow us to conclude that the deformation-induced loosening (especially with allowance for its near-surface value) can only be related to defects such as microdiscontinuities. (Other factors, in particular, microstresses, can contribute to Δρ/ρ during severe plastic deformation, e.g., during equal-channel angular pressing.) The parameters of these microdiscontinuities were determined by SAXS at ultrasmall angles. When scanning a sample from its surface toward the bulk with a thin x-ray beam, we found that the scattering intensity (and, hence, the concentration of scattering heterogeneities [9]) decreases sharply with distance from the surface and, beyond the low-density layer, virtually coincides with the scattering intensity from an annealed, undeformed sample (Fig. 2). The latter finding is an additional argument for the scattering intensity being independent of the effect of double Bragg reflections in the range of ultrasmall angles under study, which is known to cause a substantial increase in the scattering intensity after deformation [10–12]. The average sizes and concentrations of heterogeneities as calculated (assuming them to be of void nature) from the data in Fig. 2 [9] allowed us to estimate the related decrease in density (loosening) at various distances from the sample surface. As follows from Table 1, this loosening coincides well with directly measured values of Δρ/ρ, which supports the assumption regarding the void nature of the scattering heterogeneities.

Table 1. Loosening Δρ/ρ depending on the distance from the surface Δ*l* for deformed aluminum

Δ*l*, μm	Δρ/ρ	
	flotation method	x-ray diffraction method
5	6.5×10^{-3}	4×10^{-3}
10	4×10^{-3}	3.5×10^{-3}
20	6×10^{-4}	5×10^{-4}
30	3×10^{-4}	10^{-4}

Table 2 gives the sizes and limiting (near-surface) concentrations of microdiscontinuities for all metals

under study and the microdiscontinuity parameters determined by electron-microscopic examination. The sizes of the smallest wedge and porelike discontinuities were measured using transmission and scanning electron microscopy, and their concentrations were estimated by studying fracture surfaces or lateral surfaces with scanning electron microscopy [7].

Now, we consider the development of microdiscontinuities during creep or active deformation of materials at moderate temperatures. Note that the microdiscontinuity-induced loosening appears at the early stage of plastic deformation, at strains of about 5% of ε_r (Fig. 3). During creep tests, loosening develops throughout the entire time interval until fracture and the variations in $\Delta\rho/\rho$ are similar in character to the creep curve (Fig. 4). As a typical example, Fig. 5 shows the dependence of the accumulation rate of loosening $V = \Delta(\Delta\rho/\rho)/\Delta l$ at the stage of steady-state creep on the stress σ at various temperatures T for a zinc sample. (A similar dependence was obtained for aluminum samples tested under creep conditions in the temperature range from 18 to 350°C at stresses from 5 to 70 GPa [13].) Processing of these data showed that these dependences can be described well by the equation

$$V = V_0 \exp\left(-\frac{Q - \alpha\sigma}{kT}\right), \quad (1)$$

where V_0, Q, and α are the coefficients characteristic of a metal.

Earlier, it was shown that both the loosening and concentration of nucleating microdiscontinuities are very nonuniformly distributed over the thickness of deformed samples. For Zn samples, we plotted the dependence of V on σ and T separately for the surface layer with a high loosening and for the bulk (Fig. 5). It is seen that the accumulation of $\Delta\rho/\rho$ described by Eq. (1) occurs in both the surface layer and the bulk of a sample. However, the rate of accumulation of $\Delta\rho/\rho$ in the surface layer is one to two orders of magnitude higher than that in the bulk. For aluminum samples, we also studied the accumulation kinetics of near-surface nucleating microdiscontinuities during creep (Fig. 4). At the stage of steady-state creep, this rate also increases exponentially with T (at a constant value of σ) or with σ (at a fixed value of T).

Table 2. Size L and maximum concentration N of nucleating microdiscontinuities in deformed metals

Material	L, μm		L, m^{-3}	
	x-ray diffraction method	electron-microscopic method	x-ray diffraction method	electron-microscopic method
Aluminum	0.14	0.2	10^{17}	–
Nickel	0.08	0.1	10^{18}	2×10^{18}
Platinum, gold, silver	–	0.2	–	2×10^{17}
Copper, zinc	–	0.25	–	5×10^{17}
Beryllium	0.12	–	5×10^{18}	–
Steel	–	0.1	–	–
Molybdenum	–	0.08	–	–

The relations considered above for microfracture are observed at moderate test temperatures. At elevated temperatures (where the experimental life increases as compared to the life calculated from the life formula derived in [1, 2]), the microfracture kinetics exhibit certain peculiar features. In this temperature range, at the first stage of creep, loosening is actively accumulated and microdiscontinuities are actively formed only in the surface layer; however, long before fracture, the microfracture accumulation rates in the surface layer and in the bulk of a sample become equal (Fig. 6).

Quasi-brittle fracture of well-annealed NaCl single crystals was studied *in situ* under tension at a constant

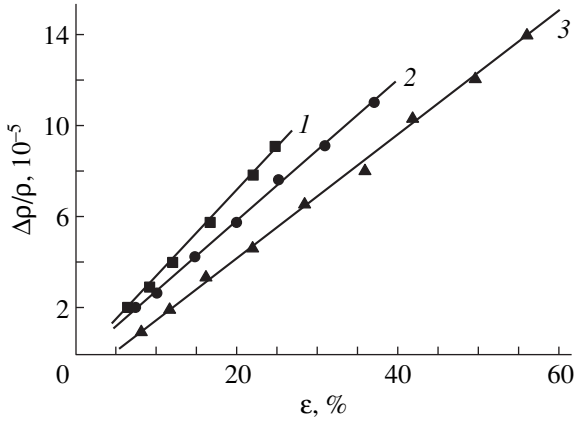

Fig. 3. Accumulation of loosening $\Delta\rho/\rho$ during active deformation ε at 18°C under (*1*) compression or (*2*, *3*) tension for (*1*) KCl, (*2*) Al, and (*3*) Zn.

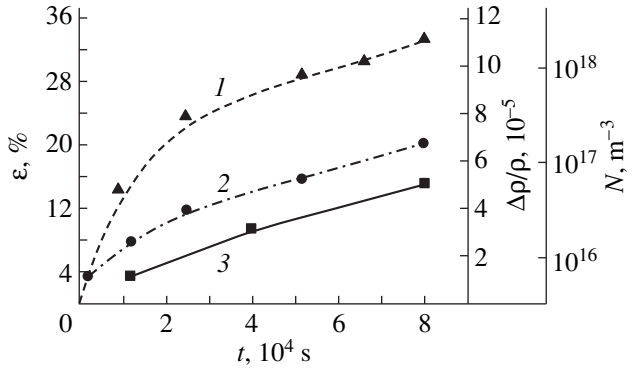

Fig. 4. (*1*) Creep curve and the evolution of (*2*) the loosening $\Delta\rho/\rho$ and (*3*) the concentration of near-surface microdiscontinuities N for Al at T = 100°C and σ = 35 MPa.

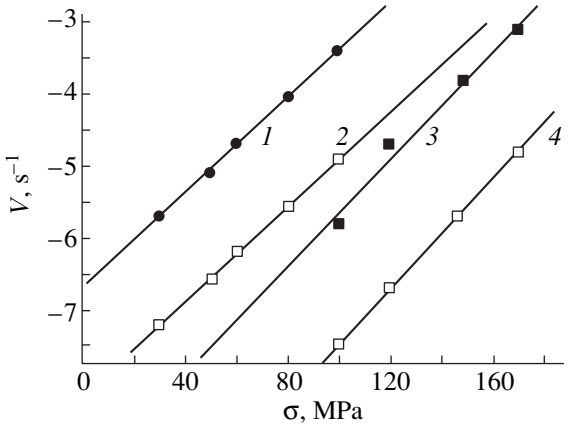

Fig. 5. Dependence of the loosening accumulation rate V on the stress σ at a temperature of (*1*, *3*) 150 and (*2*, *4*) 18°C for (*1*, *2*) the surface layer and (*3*, *4*) the bulk of a zinc sample.

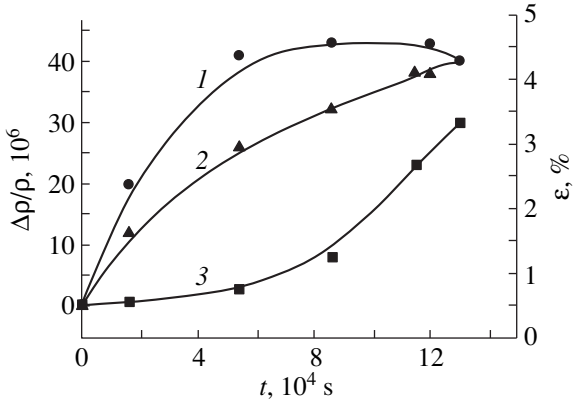

Fig. 6. Loosening $\Delta\rho/\rho$ in (*1*) the surface layer and (*3*) the bulk of Cu samples and (*2*) the creep curve at $T = 500$°C and $\sigma = 20$ MPa.

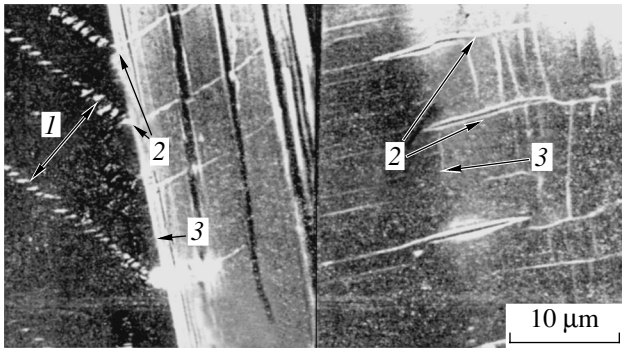

Fig. 7. (*1*) Breaks in a carbon film and (*2*) true microcracks on the surface of deformed NaCl single crystals. (*3*) Sample edges.

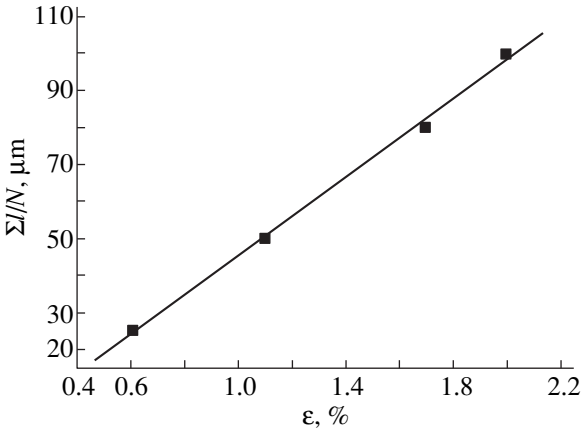

Fig. 8. Dependence of the average microcrack length $\Sigma l/N$ on the plastic strain, where Σl is the total length and N is the number of microcracks.

rate (10^{-3} mm/min) in the chamber of a scanning electron microscope at 18°C. We examined the kinetics of development of microcracks on the crystal surfaces. This examination is very important, since virtually all microcracks in the case of quasi-brittle fracture form only at the surface (as shown by transmission and scanning electron microscopy [14, 15]); their concentration in the bulk is four to five orders of magnitude lower than at the surface. Before tests, a 2-nm-thick carbon film was deposited on the surfaces of 30-mm-long samples having a cross section of 3×3 mm. Such a film is necessary to eliminate charge effects and also to detect traces of local plastic deformation. A carbon film is very brittle as compared to NaCl; therefore, it breaks during the appearance of slip traces. During tension of NaCl, the film was found to break in a characteristic direction along ⟨110⟩ slip bands and ⟨100⟩ slip steps (Fig. 7). When slip bands intersect the edge of a sample, sharp cracks form along the edge in the (100) plane (i.e., in the direction normal to the load direction). Their multiple formation begins at a strain $\varepsilon \approx 0.1\%$. Since the total strain at the instant of fracture is $\varepsilon \approx 2\%$, microcracks begin to form at a strain of 5% of ε_r, as in the case of ductile fracture. Examination of regions containing about one hundred microcracks showed that, unlike ductile fracture, the number of microcracks remains virtually unchanged with increasing strain and their lengths increase. Microcracks grow jumpwise and chaotically, and the average microcrack length increases in proportion to the strain (Fig. 8). Fracture begins when one of the growing microcracks reaches a critical size.

4. DISCUSSION OF THE RESULTS

Let us first analyze the data on nucleating microdiscontinuities. As is seen from Table 2, the SAXS and electron-microscopic data agree well with each other, which allows us to conclude that the smallest (nucleating) microdiscontinuities that form during deformation of metals and alloys are about 10^{-4} mm in size and that

their maximum concentration is $\approx 10^{17}$–10^{18} m^{-3}. These values are consistent with the results of electron-microscopic studies obtained by other researchers. For example, microcracks 0.1–0.3 μm in size have been detected during *in situ* deformation of Ag, Zn, Fe, and Al in the chamber of a transmission or scanning electron microscope [16–18]. The smallest deformation cracks were found to be ≈0.2 μm in length in deformed W, Mo, and Nb [19–21] and ≈0.1 μm in a ferritic steel [22]. In 12MKh and 15MKh steels, porelike microcracks having a size of 0.05–0.3 μm and a concentration of $\approx 10^{15}$ m^{-3} in the bulk of the steels were observed to form during creep [23, 24]. (Note that this concentration is two to three orders of magnitude lower than that detected in the surface layers (see Table 2).)

The experimentally observed sizes of nucleating microdiscontinuities agree well with theoretical estimates. For example, the authors of [25] took into account thermal fluctuations to analyze the mechanisms of microdiscontinuity nucleation via collective effects in a system of dislocations (e.g., the Zener–Stroh or the Cottrell mechanism) and could calculate the sizes of nucleating microdiscontinuities as $L \approx (1/2)n^2b$, where b is the Burgers vector and n is the number of dislocations in pileups. At $n = 20$–40 (which is experimentally observed in pileups in, at least, fcc metals), $L \approx 0.1$–0.25 μm. The appearance of microdiscontinuities as a result of one thermal fluctuation makes it possible to explain the explosive character of their appearance (which is observed in *in situ* experiments [17]), when stress relaxation after coalescence of the leading dislocations of a pileup causes avalanche coalescence of the other dislocations and an increase in the microdiscontinuity size to L. The duration of the avalanche-like microdiscontinuity growth is estimated to be $\approx 10^{-6}$ s [25, 26]. Note that the value of L estimated for the disclination mechanism of formation of a nucleating microcrack is about 0.1 μm [27].

As noted above, microdiscontinuities forming during plastic deformation at moderate temperatures are mainly concentrated in thin surface layers, where their maximum concentration is $N \approx 10^{17}$–10^{18} m^{-3}. A substantially lower value of N in the bulk of a metal makes it difficult to make a strict estimate using a x-ray diffraction method.

Nevertheless, based on a number of comparative estimates (in particular, by measuring $\Delta\rho/\rho$), it may be presumed that the value of N in the bulk is more than two orders of magnitude lower than that in the surface layers. This difference is likely to be one of the reasons for the difficulty in observing nucleating microdiscontinuities in electron-microscopic studies. The formation of microdiscontinuities is known to be related to localization of shear and rotational plastic deformation. Therefore, the formation of dislocation and disclination structures in the surface layers is an important factor causing high defect concentration in these layers. It is well known that surface layers play a specific role in the development of deformation and fracture. Indeed, it was shown in [28] for the aluminum under study here that loosened surface layers have a high density of chaotic dislocations, a low density of dislocations forming low-angle block boundaries, and a high degree of fragment misorientation (which, according to [29], characterizes the intensity of rotational processes).

The original cause of the change in the defect structure of a surface layer seems to be a high density of chaotic dislocations in it, which was earlier detected by many researchers. This factor obviously results from the operation of surface sources of dislocations, the increased mobility of dislocations in the surface layers, image forces, and a change in the stressed state of the surface layer due to the accumulation of dislocation charges ($\Delta N_D = \Delta N_{D+} - \Delta N_{D-}$). More intense accumulation of N_D in the surface layers leads to the fact that the critical dislocation density for rotational instability [30] is also reached faster near the surface than in the bulk. The more intensive development of rotational processes near the surface is also related to the fact that disclinations have a substantially lower energy near a surface [28].

It should be noted that, although the formation of nucleating microdiscontinuities $\approx 10^{-4}$ mm in size can be explained well in terms of dislocation–disclination mechanisms, other, more general mechanisms (related, e.g., to the energetics of the stability of microdiscontinuity nuclei) could also exist. Indeed, similar sizes of nucleating microdiscontinuities have been revealed in polymers and other materials [2, 7].

Let us analyze the accumulation kinetics of loosening induced by the formation and development of nucleating microdiscontinuities. We should note that the loosening appears at the early stage of plastic deformation and that the process of microfracture occurs throughout the entire time of loading of materials. The dependences of the $\Delta\rho/\rho$ accumulation rate on σ and T during creep is described by an equation typical of thermally activated processes.

The data obtained indicate that, at moderate temperatures, fracture is controlled by the continuous, thermally activated formation of nucleating microdiscontinuities, whose rate in thin surface layers is one to three orders of magnitude higher than that in the bulk of a material. During accumulation, microdiscontinuities grow and coalesce.

Indeed, a study of Al samples shows that the distribution of the microdiscontinuity concentration in size has two maxima: one is in the range of nucleus sizes, and the other (which is two to three orders of magnitude lower) corresponds to the block sizes in deformed aluminum (≈2 μm). Electron-microscopic data also indicate that discontinuities that are comparable to the blocks in size consist of almost merged nucleating microdiscontinuities [7, 26]. It is obvious that the high concentration of nucleating microdiscontinuities is caused by its continuous increase during deformation

and that structural heterogeneity is a factor that retards the coalescence of microdiscontinuities.

It should be noted that, at moderate temperatures, the formation and coalescence of microdiscontinuities develop mainly in thin surface layers, in which a critical loosening of ≈1% (which causes the formation of a macroscopic crack [7, 26] followed by crack growth deep into the material) forms a short time before the life has been exhausted.

As noted above, at elevated temperatures, microfracture rapidly propagates deep into the material. This is caused by the intensification of healing of near-surface microdiscontinuities through their vacancy dissolution followed by vacancy migration over dislocation cores to the surface (which is a natural sink) [31]. The activation energy for this process is substantially lower than the self-diffusion energy of metals; therefore, near-surface microdiscontinuities can easily be annealed at $T \approx (0.4–0.5)T_m$ (in kelvins). When nucleating microdiscontinuities forming in the bulk of a material are healed, coarser discontinuities act as vacancy sinks [32]. Therefore, loosening is continuously accumulated in the bulk, and its critical value required for the formation of a macroscopic crack can also be reached in the bulk.

The favored conditions of annealing of near-surface microdiscontinuities made it possible to use this effect to extend the life of metals tested under creep conditions at moderate temperatures. At these temperatures, as noted above, the life is mainly controlled by the accumulation and coalescence of near-surface microdiscontinuities. It has been shown that, for polycrystalline Al, Zn, Ti, and Ag samples that have exhausted about 50–70% of their life, intermediate healing annealing makes it possible to increase the time to failure twofold or more [31]. For creep tests at high temperatures (where grain-boundary microporosity develops throughout the entire volume of a metal or alloy), processing using a 1.5-GPa hydrostatic pressure has been found to be an effective intermediate healing treatment. This processing decreased the deformation-induced microporosity and increased the life [33–35]. The healing effect of hydrostatic pressure allows one to effectively decrease the self-microporosity in amorphous alloys [33–37], cement and concrete [38], and polymers [39] and thus substantially improve their mechanical properties, in particular, their strength, microhardness, and Young's modulus.

5. CONCLUSIONS

(1) Nucleating microdiscontinuities $\approx 10^{-4}$ mm in size are typical defects forming at the sites of localization of shear and rotational deformation. The process of fracture, which is related to their formation and development, occurs virtually throughout the entire time of loading of materials and is a thermal fluctuation process.

(2) In a physical approach to fracture as a kinetic phenomenon, this process is considered to consist of several stages. The initial stage is related to deformation localization and accounts for about 5% of the total deformation to fracture. The basic stage consists in the explosive appearance of nucleating microdiscontinuities and their accumulation and coalescence (ductile fracture) or development (quasi-brittle fracture). The final stage in ductile materials (in which a large number of blunt porelike discontinuities form) follows the coalescence of microdiscontinuities and the appearance of a critical (≈1%) local loosening, which causes the formation of macroscopic cracks. In quasi-brittle solids, a large number of sharp microcracks form throughout the entire time of deformation and one of them reaches a critical nonequilibrium size in the final stage.

(3) The scale of fracture, which is related to defect hierarchy, should be taken into account.

(4) When the physics of the development of microdiscontinuities (just as other defects) is analyzed, one has to take into account the specific properties of the surface and the surface layer, where the rate of development and, hence, the concentration of microdiscontinuities are a few orders of magnitude higher than those in the bulk of the material. At moderate temperatures, the basic stage of microfracture development, which results in the formation of a macroscopic crack, occurs in the thin surface layer.

(5) At elevated temperatures and low stresses, it is necessary to take into account the healing of microdiscontinuities, which is also most intense in the surface layer. The healing of deformation-induced micropores and self-micropores is a promising method for improving the properties of materials.

REFERENCES

1. S. N. Zhurkov, Izv. Akad. Nauk SSSR, Neorg. Mater. **3** (10), 1767 (1967).
2. V. R. Regel, A. I. Slutsker, and É. E. Tomashevskiĭ, *Kinetic Nature of the Strength of Solids* (Nauka, Moscow, 1979) [in Russian].
3. V. V. Novozhilov, Prikl. Mat. Mekh. **29** (4), 681 (1965).
4. V. V. Novozhilov, Yu. I. Kadashevin, and O. G. Rybakina, Dokl. Akad. Nauk SSSR **270** (4), 831 (1983) [Sov. Phys. Dokl. **28**, 514 (1983)].
5. Yu. I. Rabotnov, *Creep of Construction Elements* (Nauka, Moscow, 1996) [in Russian].
6. L. M. Kachanov, *Fundamentals of Fracture Mechanics* (Nauka, Moscow, 1974) [in Russian].
7. P. G. Cheremskiĭ, V. V. Slezov, and V. I. Betekhtin, *Pores in Solids* (Énergoatomizdat, Moscow, 1990) [in Russian].
8. B. Ya. Levin, V. I. Betekhtin, V. I. Vladimirov, A. N. Orlov, and A. I. Petrov, Fiz. Tverd. Tela (Leningrad) **12** (9), 2660 (1970) [Sov. Phys. Solid State **12**, 2130 (1970)].
9. A. Guinier and G. Fournet, *Small Angle Scattering of X-rays* (Wiley, New York, 1955).

10. W. T. Ogier, R. L. Wild, and I. C. Nickel, J. Appl. Phys. **30** (3), 408 (1959).
11. B. E. Warren, Aust. J. Phys. **13** (2A), 376 (1960).
12. V. I. Betekhtin and A. I. Slutsker, Fiz. Tverd. Tela (Leningrad) **8**, 767 (1966) [Sov. Phys. Solid State **8**, 614 (1966)].
13. V. I. Betekhtin, V. N. Savel'ev, and A. I. Petrov, Fiz. Met. Metalloved. **38** (4), 834 (1974).
14. V. I. Betekhtin and F. Shmidt, Fiz. Tverd. Tela (Leningrad) **15** (4), 1234 (1973) [Sov. Phys. Solid State **15**, 830 (1973)].
15. V. Shmidt, V. I. Betekhtin, and R. Albrecht, Phys. Status Solidi A **39**, 631 (1997).
16. I. A. Alic and R. M. Asimov, Eng. Fract. Mech. **6**, 223 (1974).
17. R. L. Lyles and H. G. F. Wilsdorf, Acta Metall. **23**, 269 (1975).
18. A. M. Leksovskiĭ, S. N. Sakiev, and F. Shmidt, Fiz. Met. Metalloved. **41** (3), 637 (1976).
19. V. V. Rybin and A. N. Vergazov, Fiz. Met. Metalloved. **41** (3), 371 (1976).
20. V. V. Rybin, A. N. Vergazov, and Yu. V. Solomko, Fiz. Met. Metalloved. **46** (3), 582 (1978).
21. V. V. Rybin and A. N. Vergazov, Fiz. Met. Metalloved. **43** (4), 858 (1977).
22. D. A. Miller and R. Pilkington, J. Mater. Sci. **13**, 2291 (1978).
23. I. I. Mints, T. G. Berezina, and L. E. Khodykina, Fiz. Met. Metalloved. **37** (4), 822 (1974).
24. I. I. Mints, T. G. Berezina, and L. E. Khodykina, Probl. Prochn., No. 6, 35 (1978).
25. V. V. Vladimirov, *Physical Nature of Metal Fracture* (Metallurgiya, Moscow, 1984) [in Russian].
26. V. I. Betekhtin, V. I. Vladimirov, A. G. Kadomtsev, and A. I. Petrov, Probl. Prochn., No. 7, 38 (1979); Probl. Prochn., No. 8, 51 (1979).
27. V. V. Rybin, A. A. Zisman, and K. M. Zhukovskiĭ, Probl. Prochn., No. 12, 10 (1982).
28. V. I. Betekhtin and A. G. Kadomtsev, Vopr. Materialoved., No. 1, 181 (2002).
29. V. I. Vladimirov and A. E. Romanov, *Disclinations in Crystals* (Nauka, Leningrad, 1986) [in Russian].
30. N. A. Koneva, D. V. Lychagin, and L. A. Teplyakova, *Theoretical and Experimental Studies of Disclination* (Fiz.–Tekh. Inst., Leningrad, 1986) [in Russian].
31. V. I. Betekhtin, V. I. Vladimirov, A. G. Kadomtsev, and A. I. Petrov, Poverkhnost, No. 7, 144 (1984).
32. I. M. Lifshitz and V. V. Slezov, Fiz. Tverd. Tela (Leningrad) **1** (9), 1479 (1959) [Sov. Phys. Solid State **1**, 1357 (1959)].
33. V. I. Betekhtin, A. I. Petrov, A. G. Kadomtsev, and V. Sklenicka, Fiz. Met. Metalloved., No. 5, 176 (1990).
34. V. Sklenicka, V. I. Betekhtin, K. Kucharova, A. G. Kadomtsev, and A. I. Petrov, Scr. Met. **25**, 2159 (1991).
35. V. I. Betekhtin, S. Yu. Veselkov, Yu. M. Dal', A. G. Kadomtsev, and O. V. Amosova, Fiz. Tverd. Tela (St. Petersburg) **45** (4), 618 (2003) [Phys. Solid State **45**, 649 (2003)].
36. V. I. Betekhtin, A. G. Kadomtsev, A. Yu. Kipyatkova, and A. M. Glezer, Fiz. Tverd. Tela (St. Petersburg) **40** (1), 85 (1998) [Phys. Solid State **40**, 74 (1998)].
37. V. I. Betekhtin, A. G. Kadomtsev, and O. V. Amosova, Izv. Ross. Akad. Nauk, Ser. Fiz. **67** (6), 818 (2003).
38. V. I. Betekhtin and A. G. Kadomtsev, Tsement, Nos. 5–6, 16 (1991).
39. A. I. Petrov, A. B. Sinani, M. V. Razuvaeva, and V. I. Betekhtin, Mekh. Kompoz. Mater., No. 6, 1121 (1989).

Translated by K. Shakhlevich

Physics of the Solid State, Vol. 47, No. 5, 2005, pp. 832–835. Translated from Fizika Tverdogo Tela, Vol. 47, No. 5, 2005, pp. 808–811.

Kinetic Theory of Strength and a Self-Organized Critical State in the Process of Fracture of Materials

V. L. Hilarov

Ioffe Physicotechnical Institute, Russian Academy of Sciences, Politekhnicheskaya ul. 26, St. Petersburg, 194021 Russia

e-mail: Vladimir.Hilarov@mail.ioffe.ru

Abstract—The basic principles of the Zhurkov kinetic approach are analyzed in light of the modern idea of self-organization of nonlinear systems under nonequilibrium conditions. It is indicated that the final state before fracture can be described in terms of the model of a self-organized critical state. © *2005 Pleiades Publishing, Inc.*

The basic principle of the Zhurkov kinetic approach [1, 2] is the idea that the fracture of solids is not a critical event that occurs when external factors (various combinations of the stress tensor components, as a rule) reach critical values. On the contrary, fracture is a kinetic process proceeding in space and time. The experimental basis for this approach is very broad and includes materials that differ in terms of their chemical nature and physical structure: polymers, metals, alkali halide crystals, etc. For these materials, the process can be described, over a wide range of values of external factors (temperature, load), by a universal relation (the well-known Zhurkov formula) for the material durability τ,

$$\tau = \tau_0 e^{\frac{U_0 - \gamma\sigma}{kT}},$$

where U_0 is the activation energy for the process, τ_0 is the preexponential factor (equal, in order of magnitude, to the period of thermal vibrations of atoms), γ is a structure-sensitive coefficient (activation volume), and σ is an externally applied stress (uniaxial load).

The Zhurkov formula has been given different physical interpretations. On the one hand, the universality of this formula indicates that there is a universal mechanism of fracture irrespective of the structure and properties of a material, which are taken into account by the parameters (activation energy, activation volume) in the Zhurkov formula. On the other hand, in the course of deformation and fracture of a material, its structure varies significantly and the system exhibits different kinetic behavior in different stages of this process following a dominant kinetic law [3].

In all cases, a solid subjected to a mechanical load that exceeds the elastic limit is a nonequilibrium system in which the defect structure varies in such a way as to minimize the influence of loading. Numerous attempts have been made to describe the deformation and fracture of materials in terms of the thermodynamics of irreversible processes. In such a description, the structure is rearranged and a kinetic phase transition occurs once an external factor (temperature or load) reaches a certain critical value (bifurcation point). Over the range between bifurcation points, the dissipative structures that have thus arisen remain stable. Therefore, the critical point at which the structure is rearranged corresponds to a special combination of external factors.

Another type of self-organization of dissipative structures was described theoretically by Bak, Tang, and Wiesenfeld [4, 5] and was called self-organized criticality (SOC). As an illustration, the case is often considered where sand is poured slowly over a sand hill. If the hill has a sufficiently gentle slope, the steepness of its slope increases due to the sand grain clusters sliding down it. When the difference in height between neighbor plateaus z_n becomes larger than a critical value, the system loses its stability and an avalanche occurs. The process goes on until all z_n become equal to the critical values. The pattern of the process changes qualitatively when the steepness of the hill reaches a critical value. The amount of avalanching sand can be arbitrary; i.e., the system becomes scale-invariant. Once the hill steepness reaches the critical value, it remains unchanged. The distribution of avalanches over their scales and the power density spectrum are power-law functions; i.e., the system exhibits scale invariance in both space and time. Note that the sand hill model is purely illustrative; the real dynamics of the systems under study can exhibit various patterns.

The following basic properties of a self-organized critical state can be indicated [6]: (i) the system being in a nonequilibrium state; (ii) the existence of a large number of metastable states that increases exponentially with the size of the system; (iii) nonlinear intrinsic dynamics of the system; (iv) space scaling invariance, which results in spatial fractal self-similarity; (v) time scale invariance, due to which the frequency spectrum of the system is flicker noise; (vi) the independence of the effect in question from the initial conditions, which is typical of nonlinear dynamics; and

1063-7834/05/4705-0832$26.00 © 2005 Pleiades Publishing, Inc.

(vii) the occurrence of the effect in question over a wide range of external control parameters.

The last property qualitatively differentiates the SOC from other analogous phenomena. There are four basic types of self-organization that occur in nonlinear systems. One type is self-organization during phase transitions. Indeed, phase transitions are characterized by space–time scale invariance; however, a transition occurs at a critical point where the external parameter (e.g., the temperature) reaches its critical value. In a similar way, self-organization occurs during geometrical (percolation-type) phase transitions, where the critical value of the probability of a cell being filled (percolation threshold) is reached. A third type of self-organization (the formation of a dissipative structure) occurs at a bifurcation point, where an external parameter (the temperature gradient in the classical Benard problem) also reaches a critical value. In the case of the SOC, on the contrary, there is no need to adjust an external parameter.

The SOC model has been applied to describe the fracture of solids and, especially, earthquakes. According to the Guttenberg–Richter law

$$\log N = a - bM \tag{1}$$

(where N is the number of earthquakes with a magnitude higher than M; a, b are constants), the magnitude distribution of earthquakes exhibits scaling invariance over a wide range of magnitudes, which suggests that earthquakes possess SOC properties. The corresponding geophysical models are based on dynamic stick-slip models, which are exemplified in Fig. 1.

In Figs. 1a and 1b, massive blocks of mass m (rectangles) connected by harmonic springs are shown to move along a rough surface with velocity-dependent friction. In models of the Frenkel–Kontorova type, point masses m moving along the sinusoidal surface of a substrate are considered instead of the blocks (Figs. 1c, 1d). The blocks are attached by torsion springs to a mobile surface located above them (Figs. 1a, 1d). The system is disturbed from an equilibrium state by imparting an infinitesimal velocity v to the upper surface or directly to the first block (point mass).

The nonlinear dynamics of these models reduces to the following [6]. Due to the motion of the upper surface (or the first block), a force is applied to each of the other blocks. If this force exceeds the static frictional force, the block begins to move in an accelerated fashion, because the kinetic friction force is much less than the static frictional force. Further, due to the interaction with its neighbors, the block stops moving, because the static friction force is usually stronger than the resultant interaction force. The nearest neighbor blocks can also begin to move due to the interaction. This motion can cause an "earthquake," which is defined (in terms of the model) as motion of the chain as a whole. The strength

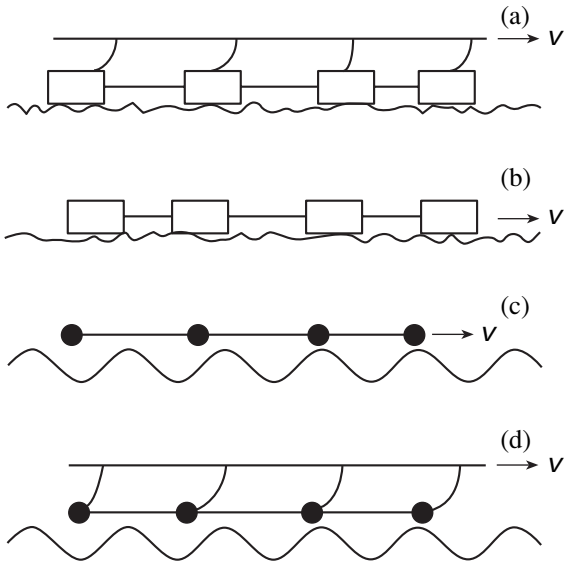

Fig. 1. Four dynamic stick-slip models of earthquakes: (a) the model considered in [7, 8], (b) the model proposed in [8], (c) the Frenkel–Kontorova model [6], and (d) a modified Frenkel–Kontorova model [6]. The SOC state arises in models (b, c) and does not arise in (a, d).

of this earthquake is defined as the sum of displacements:

$$S = \sum_{j=1}^{N} \left| x_j^{\text{after}} - x_j^{\text{before}} \right|. \tag{2}$$

The chain slippage length L is defined as the number of blocks involved in the slippage. To describe an earthquake, the space and time distributions of these parameters are plotted in logarithmic coordinates. If the bend of the rectilinear (scaling-invariant) portion of these plots shifts to larger dimensions as the size of the system increases, there is an indication that the model exhibits the SOC effect.

It is well known that fracture surfaces of solids are not plain but rather are fractal in nature. Studies into the fractal dimension of fracture surfaces have been performed for a wide range of materials subjected to either brittle or plastic fracture. The scaling-invariant state of fracture surfaces indicates that a universal mechanism of fracture is operative; this mechanism is associated with the nonlinear dynamics and the occurrence of SOC.

In order to verify this hypothesis, the available data on acoustic emission that arises during breakage of laboratory granite samples and industrial steel structures exposed to mechanical loads were analyzed in [9, 10]. The data contained the instants of time and amplitudes of emission and sometimes the coordinates of cracks that formed during breakage. Spatial and time correlations were studied to reveal nontrivial scaling-invariant dependences, which manifest themselves as power-law dependences of the correlators, and the corresponding scaling exponents were determined.

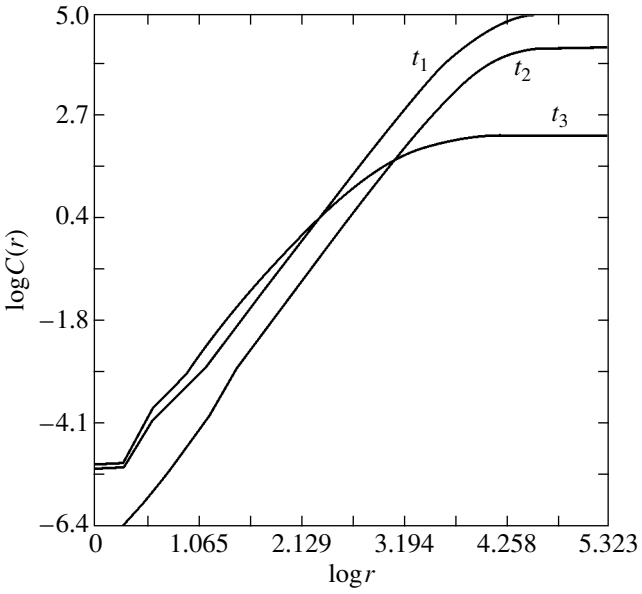

Fig. 2. Grassberger–Prokacci space correlator of acoustic noise caused by crack formation at various stages of breakage of a material ($t_1 < t_2 < t_3$).

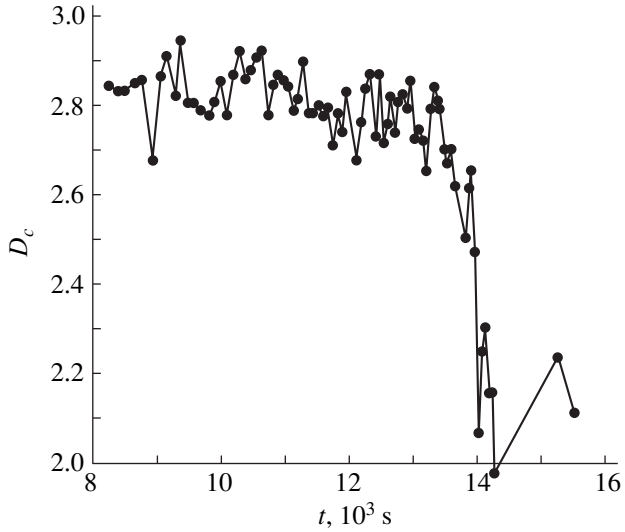

Fig. 3. Time dependence of the correlation fractal dimension D_c for acoustic noise caused by crack formation in a Westerly granite sample.

Spatial correlations were described by Grassberger–Prokacci spatial correlation functions,

$$C(r) = \frac{2}{N(N-1)}\sum_{j=1}^{N}\sum_{i=j+1}^{N} H(r - r_{ij}). \qquad (3)$$

These functions are defined as the number of pairs of cracks with the distance r_{ij} between them not exceeding r. In Eq. (3), $H(x)$ is the Heaviside step function and N is the number of events. The correlators were found to exhibit clearly defined scaling-invariant properties (which manifest themselves in the linearity of these correlators when plotted in logarithmic coordinates) at various stages of breakage (Fig. 2).

The fractal dimension D_c was determined from the slope of the straight line. Its time dependence is shown in Fig. 3.

At the initial stages of breakage, the fractal dimension is close to the dimensionality of 3D space. As the fracture is approached, the fractal dimension becomes close to the dimensionality of the fracture surface.

To study the temporal scaling properties of a system at the steady-state stages of breakage, the power density spectra of signals were calculated using various methods:

$$K(t_1, t_2) = \langle x(t_1)x(t_2)\rangle,$$
$$S(\omega) = \int_{-\infty}^{\infty} K(\Delta t)\exp(i\omega\Delta t)d\Delta t, \quad \Delta t = t_2 - t_1, \qquad (4)$$

where the random variable x was taken to be either the signal amplitude or the time interval between successive signals. It was found that the calculated power density spectrum at the final stages of breakage is of the $1/f$ type, namely, $S(\omega) \propto \omega^{-\beta}$ with $\beta \approx 1$, as is the case in a self-organized critical state.

Thus, both space and time correlators show clearly defined scaling-invariant dependences at the final stages of breakage, which indicates that, at least for the materials studied, the state of a material prior to fracture satisfies the SOC conditions. This finding is illustrated in Fig. 4, which shows the time dependences of both space- and time-scaling exponents measured in two different experiments. It is clearly seen that, as the instant of sample fracture is approached, the space- and time-scaling exponents vary synchronously. The enhancement of the low-frequency component of acoustic noise observed as the fracture of a material is approached indicates an increase in large-scale fluctuations in the final stage of breakage. Zhurkov was concerned with this problem in his final years.

The situation with regard to the occurrence of SOC during breakage of a material is similar to the situation regarding the Zhurkov kinetic approach. Does fracture of materials occur through a universal mechanism? The fact that the state of a material immediately prior to its fracture can be the SOC state (in which the statistical properties are dictated by fundamental space–time relations rather than by the microstructure of the material) counts in favor of this hypothesis. In the course of breakage, the defect structure of a material varies at a progressively coarser scale level until the material loses its ability to resist fracture. Thereafter, the specific features of the defect structure at all space and time scale levels lose their importance and the SOC state occurs. However, the question as to whether the SOC state occurs in the same way in all materials remains open.

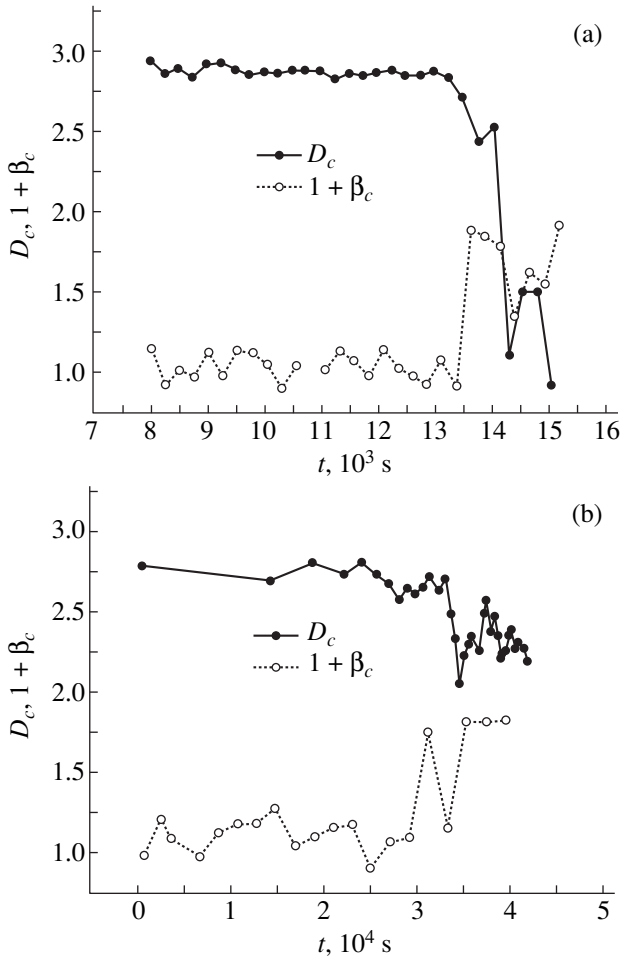

Fig. 4. Time dependences of the space- and time-scaling exponents for two different granite samples.

In particular, it is unclear whether the scaling exponents, which determine the scaling-invariant properties (such as the fractal dimension of the fracture surface), are universal constants or depend on the specific properties of a material. The scatter in the experimentally measured fractal dimensions of fracture surfaces is too wide to make it possible to reveal the existence of a universal mechanism characterized by material-independent scaling exponents. Further investigations are required to resolve these issues, especially in relation to physical substantiation of the Zhurkov kinetic approach.

ACKNOWLEDGMENTS

This study was supported by the Russian Foundation for Basic Research, project no. 03-05-64831.

REFERENCES

1. S. N. Zhurkov, Vestn. Akad. Nauk SSSR, No. 3, 46 (1968).
2. V. R. Regel', A. I. Slutsker, and É. E. Tomashevskiĭ, *Kinetic Nature of the Strength of Solids* (Nauka, Moscow, 1974) [in Russian].
3. V. L. Indenbom and A. N. Orlov, Fiz. Met. Metalloved. **43**, 469 (1977).
4. P. Bak, C. Tang, and K. Wiesenfeld, Phys. Rev. Lett. **59** (4), 381 (1987).
5. P. Bak, C. Tang, and K. Wiesenfeld, Phys. Rev. A **38**, 364 (1988).
6. F. J. Elmer, in *Physics of Sliding Friction*, Ed. by B. N. J. Persson and E. Tosatti (Kluwer Academic, Dordrecht, 1996).
7. J. M. Carlson and J. S. Langer, Phys. Rev. A **40**, 6470 (1989).
8. R. Burridge and L. Knopoff, Bull. Seismol. Soc. Am. **57**, 341 (1967).
9. V. L. Galyarov, Fiz. Tverd. Tela (St. Petersburg) **36** (8), 2247 (1994) [Phys. Solid State **36**, 1224 (1994)].
10. V. L. Hilarov, Modell. Simul. Mater. Sci. Eng. **6**, 337 (1998).

Translated by Yu. Epifanov

Physics of the Solid State, Vol. 47, No. 5, 2005, pp. 836–839. Translated from Fizika Tverdogo Tela, Vol. 47, No. 5, 2005, pp. 812–815.

Loading Velocity and Brittleness of Solids

A. A. Kozhushko and A. B. Sinani

Ioffe Physicotechnical Institute, Russian Academy of Sciences, Politekhnicheskaya ul. 26, St. Petersburg, 194021 Russia
e-mail: alex@mdlab.ioffe.ru

Abstract—The ductile–brittle transition observed in many solids due to either a decrease in temperature or an increase in the loading velocity can be supplemented with a reversible brittle–ductile transition under loading at a hypervelocity exceeding the velocity of propagation of fracture cracks. This phenomenon occurs in the course of high-velocity penetration of solids into organic and inorganic glasses, as well as into ceramic materials. © *2005 Pleiades Publishing, Inc.*

1. INTRODUCTION

The possibility of attaining a high-strength state in brittle solids was demonstrated in the monograph by Aleksandrov and Zhurkov [1]. This state can be achieved by eliminating the effect of surface microdefects that, under loading conditions, play the role of fracture nuclei. For fibers fabricated from quartz and silicate glasses, it has been shown that the strengths of these materials approach the theoretical values.

The idea developed in [1] appeared very fruitful for studying high-velocity penetration of solids into brittle materials. Reasoning from the conclusions drawn in [1], Vitman and Zlatin [2] were the first to establish a correlation between the high indentation resistance of brittle solids and their high-strength state, which can be achieved by the elimination of brittle fracture propagating in front of an indenting solid.

In the general case, the resistance of a target to indentation has the form

$$P = \frac{1}{2}\rho_T U^2 + R \qquad (1)$$

and involves inertial ($1/2\rho_T U^2$) and strength (R) components. Here, ρ_T is the density of the material of the target and U is the penetration velocity.

The indentation resistance of plastic solids has been extensively investigated, and its nature is well understood [3–6]. Numerous experimental studies have demonstrated that the strength component R of the indentation resistance correlates best with the Meyer dynamic hardness, which is measured upon penetration of a solid conic indenter at velocities in the range 1–10 m/s.

The problem concerning the strength resistance to indentation of solids into brittle materials is significantly more complicated. As was shown in our previous works [7, 8], progressively increasing fracture in front of an indenting solid leads to a transformation of the material of the target into a fragmented discontinuous medium with a negligible strength. In this situation, it makes sense to consider only a strength resistance which is averaged over time and over the penetration depth and which, according to the estimates made by Sternberg [9], can amount to 0.2–0.4 of the strength of the target material.

By extrapolating the strength component R of the indentation resistance to the initial instant of penetration, it was found that the strength resistance is very high and close to the hardness of brittle targets [10]. The same strength was obtained upon penetration of solids into inorganic glasses and ceramic materials at velocities higher than the velocity of propagation of the fracture front [11–13]. It is assumed that, under these conditions, the penetrating solid continuously interacts with the intact medium and the dominant contribution to the strength component of the indentation resistance is made by the plastic deformation rather than by the kinetics of fracture of the target material. In other words, an increase in the penetration velocity in brittle solids should result in an anomalous brittle–ductile transition and the formation of a crater should occur in much the same manner as in plastic materials.

The conclusions drawn in earlier investigations [11–13] are based on the results of experiments performed at impact velocities V = 4–8 km/s, which ensure penetration velocities that are higher than the velocity of propagation of the fracture front in glasses and ceramics. The question arises as to whether the observed behavior of brittle materials under a high-velocity impact has a general character, i.e., whether this behavior is typical of any solid in the brittle state over a wide range of velocities. However, performing indentation experiments with ceramic materials distinguished by high velocities of propagation of fracture cracks requires impact velocities of approximately 10 km/s or higher. At present, such experiments are difficult to execute. From this viewpoint, it is interesting to perform investigations with polymer glasses in which the velocity of propagation of fracture cracks is one order of magnitude lower than that in ceramic materials [14].

In the present work, we investigated the strength resistance of polymer glasses to indentation over a wide

1063-7834/05/4705-0836$26.00 © 2005 Pleiades Publishing, Inc.

range of loading (impact) velocities and compared the behavior of the polymer glasses with the behavior of high-strength ceramic materials. The main objective of this work was to elucidate the general behavior of brittle materials under a high-velocity impact and to establish a criterion for crossover to a hypervelocity impact for brittle materials.

2. SPECIMENS AND EXPERIMENTAL TECHNIQUE

The experiments were performed with a polymer glass, namely, poly(methyl methacrylate) (*PMMA*). The physicomechanical characteristics of this material are presented in the table.

Physicomechanical characteristics of poly(methyl methacrylate)

Characteristic	Temperature, K		Measurement conditions
	300	77	
Density ρ, g/cm^3	1.18	1.20	
Longitudinal wave velocity C_L, m/s	2700	3100	ν = 5 MHz
Shear wave velocity C_S, m/s	1300	1600	ν = 1.67 MHz
Poisson ratio μ	0.34	0.32	
Hardness H, MPa	250	900	$U = 2 \times 10^{-4}$ m/s

It should be noted that penetration of solids into polymer materials does not necessarily lead to a ductile–brittle transition even at high loading velocities. To overcome this impediment, the experiments were performed at liquid-nitrogen temperature (77 K).

Rigid indenters (HRC hardness ~60) with a 90° conical head were introduced into specimens of poly(methyl methacrylate) at indentation (or impact) velocities ranging from 10^{-4} to 10^3 m/s.

The penetration depth h and the load P applied to the indenter were measured at velocities in the range from 10^{-4} to 1.0 m/s. The hardness of the material under investigation was determined from a smooth portion of the curve $P(h)$ (Fig. 1) according to the formula [15]

$$H = \frac{P_2}{\pi \Delta h^2}\left(1 - \sqrt{\frac{P_1}{P_2}}\right), \quad (2)$$

where Δh is the increment of the depth of the indentation due to an increase in the applied load from P_1 to P_2.

The indentation resistance R was determined from the maximum of the mean load P (as shown by dashed line *2* in Fig. 1) according to the expression

$$R = P/\pi r_0^2, \quad (3)$$

where r_0 is the radius of the indentation on the initial surface of the specimen.

The impact load in the velocity range 10^2–10^3 m/s was applied using rigid projectiles 7.62 mm in diameter and 60 mm in length with a 90° conical head. In the experiments, the positions of the rear part of the slowed projectile were recorded with a multiframe high-frequency photographic camera. By this means, we obtained a "projectile position–time" curve. This curve was used to determine the instantaneous values of the indentation resistance [3, 6].

3. RESULTS AND DISCUSSION

The indentation resistance thus determined can be identified with the strength resistance R. This identification is fully justified, because, under experimental conditions (i.e., at a relatively low impact velocity and at a low density of the target material), the inertial resistance forces play a very minor role in the total resistance and, to a first approximation, these forces can be ignored.

In hardness measurements, the radius r_0 of an indentation produced by a 90° conical indenter is equal to the penetration depth h. Therefore, relationship (3) can be rewritten in the form

$$R = P/\pi r_0^2 = P/\pi h^2. \quad (4)$$

Judging from the smooth curve $P(h)$ (Fig. 1, curve *1*), the hardness H coincides with the indentation resistance R. This coincidence holds for soft loading at a velocity of 0.06 mm/s. For a higher velocity (8 mm/s), the curve $P(h)$ has a saw-tooth shape (Fig. 1, curve *2*). This shape is associated both with the nucleation and growth of cracks around the indentation and with partial unloading of the material. The averaged curve $P(h)$ (Fig. 1, dashed line *2*) passes significantly below smooth curve *1*. This discrepancy between these curves clearly demonstrates that, at higher velocities of load-

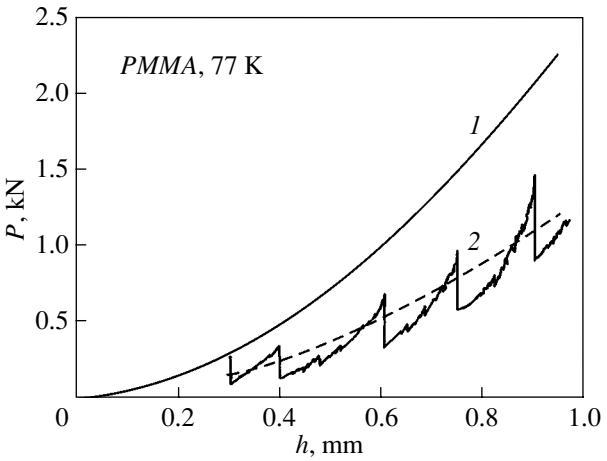

Fig. 1. Load–penetration depth (P–h) diagram for *PMMA* at penetration velocities of (*1*) 0.06 and (*2*) 8.00 mm/s.

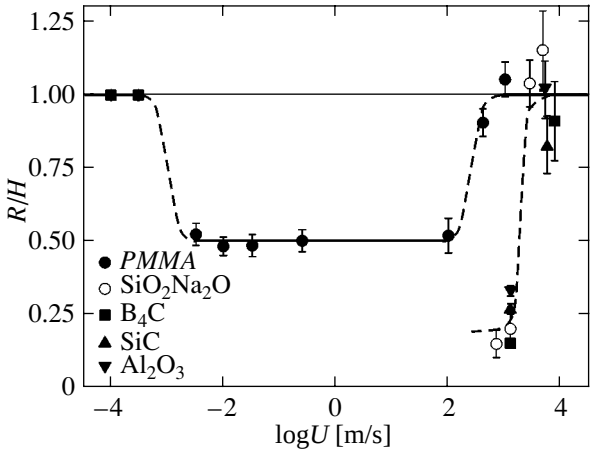

Fig. 2. Ratio of the indentation resistance R to the hardness H of the material of the target as a function of the penetration velocity.

ing, the indentation resistance R becomes less than the hardness H.

The ratio of the indentation resistance R to the hardness H of the target material as a function of the penetration velocity is presented in Fig. 2. In contrast to plastic materials with a nearly constant ratio R/H, poly(methyl methacrylate) is characterized by a ratio R/H that is dependent on the penetration velocity. Analysis of this dependence revealed two transitions. The first transition can be treated as a ductile–brittle transition. The penetration velocity corresponding to this transition (~10^{-3} m/s) can be referred to as the embrittlement velocity by analogy with the brittle temperature characteristic of polymer glasses. Beginning with this velocity, the indentation resistance is predominantly determined by the fracture kinetics, because the nucleation and growth of fracture cracks around the indentation (crater) are responsible for the decrease in the indentation resistance as compared to the hardness of the target material. A further increase in the penetration velocity very weakly affects the indentation resistance, which remains approximately constant and amounts to 0.5 of the hardness.

The ratio $R/H = 0.5$ observed for poly(methyl methacrylate) is considerably larger than the mean ratio R/H obtained for ceramics in [9] (Fig. 2). This finding implies that, unlike ceramics, poly(methyl methacrylate) even in the brittle state does not transform into a strength-free medium. This suggests that, in the velocity range under consideration, the penetration of solids into polymer glasses occurs through a mixed (plastic flow and fracture) mechanism.

For impact velocities higher than 400 m/s, the indentation resistance increases drastically and the ratio R/H tends to unity ($R/H \longrightarrow 1$). This indicates that, in poly(methyl methacrylate), the crater formation occurs through the mechanism of plastic flow and the projectile–target interface moves ahead of the fracture front. Under these conditions, the indentation resistance is governed by the fundamental properties of the target material and the brittle material attains a high-strength state. It can be assumed that an impact velocity of approximately 400 m/s is close to the limiting velocity of propagation of the fracture front V_f in poly(methyl methacrylate). This is in agreement with the results obtained in direct measurements of the velocity of propagation of fracture cracks [16].

Figure 2 also presents the data obtained for the silicate glass and ceramic materials in our previous works [11, 12]. The behavior of these materials is similar to that of poly(methyl methacrylate): the silicate glass and ceramics also undergo a brittle–ductile transition. However, in the ceramic materials, this transition occurs at velocities higher than those in poly(methyl methacrylate) by one order of magnitude. This is in complete agreement with the difference in the elastic properties of poly(methyl methacrylate) and ceramics, specifically in the velocity of sound, which determines the highest velocity of fracture propagation.

Thus, the experiments performed over a wide range of indentation (impact) velocities (from 10^{-4} to 10^3 m/s) demonstrated that the velocity has a twofold effect on the indentation resistance of brittle solids.

First, at low indentation (impact) velocities, an increase in the loading velocity brings about embrittlement of the material, i.e., the nucleation and growth of cracks around the indentation area (indentation or crater). The velocity at which there occurs a ductile–brittle transition can be referred to as the embrittlement velocity (V_b). For velocities $V > V_b$, the indentation resistance is governed by the kinetics of fracture of the target material. The embrittlement leads to an abrupt decrease in the indentation resistance as compared to the hardness of the target.

Second, at penetration velocities higher than the velocity V_f (V_f is the velocity of propagation of the fracture front), there occurs a reverse brittle–ductile transition. Under these conditions, the material once again acquires a high strength resistance to indentation at the level of its hardness. The crater formation at penetration velocities higher than the velocity of propagation of the fracture front $V > V_f$ and the indentation at velocities $V < V_b$ are essentially identical phenomena, because, in both cases, the effect of cracks is excluded. This implies that the indentation resistance is governed primarily by the fundamental properties of the target material.

The second (brittle–ductile) transition can be used to define, in physical terms, the hypervelocity impact as applied to brittle solids.

There are grounds to believe that the impact velocity ensuring a brittle–ductile transition can be considered a criterion for hypervelocity impact for brittle targets. It is obvious that the criterion for hypervelocity is greatly affected by the velocity of fracture propagation and,

consequently, by the velocity of sound in brittle materials.

It should be emphasized that there is a fundamental difference in the character of the crossover to hypervelocities for plastic and brittle targets. In the case of plastic targets, the crossover is determined by the velocity at which the strength properties of the target material can be ignored as compared to the inertial indentation resistance forces. In the case of brittle targets, the crossover is governed by the velocity at which the brittle–ductile transition occurs and the strength resistance of the material to indentation drastically increases to a value comparable, in some cases, to the inertial resistance.

REFERENCES

1. A. P. Aleksandrov and S. N. Zhurkov, *Phenomenon of Brittle Fracture (*GTTI, Leningrad, 1993), p. 51 [in Russian].
2. F. F. Vitman and N. A. Zlatin, in *Behavior of Materials at Artillery and Superartillery Impact Velocities* (Kiev, 1958), part 2, p. 134 [in Russian].
3. F. F. Vitman and V. A. Stepanov, in *Problems of the Strength of Solid* (Akad. Nauk SSSR, 1959), p. 207 [in Russian].
4. V. P. Alekseevskiĭ, Fiz. Goreniya Vzryva, No. 2, 99 (1966).
5. A. Tate, J. Mech. Phys. Solids **15**, 387 (1967).
6. N. A. Zlatin, in *Ballistic Installations and Their Application in Experimental Research* (Nauka, Moscow, 1974), p. 344 [in Russian].
7. A. S. Vlasov, Yu. A. Emel'yanov, E. L. Zel'berbrand, A. A. Kozhushko, A. I. Kozachuk, G. S. Pugachev, and A. B. Sinani, Pis'ma Zh. Tekh. Fiz. **23** (3), 68 (1997) [Tech. Phys. Lett. **23**, 117 (1997)].
8. A. S. Vlasov, Yu. A. Emel'yanov, E. L. Zel'berbrand, A. A. Kozhushko, A. I. Kozachuk, G. S. Pugachev, and A. B. Sinani, Fiz. Tverd. Tela (St. Petersburg) **41**, 1785 (1999) [Phys. Solid State **41**, 1638 (1999)].
9. J. Sternberg, J. Appl. Phys. **65** (9), 3417 (1989).
10. G. Hauver, W. Gooch, P. Netherwood, R. Bench, W. Perciballi, and M. Burkins, in *Proceedings of 13th International Symposium on Ballistics* (1992), Vol. 3, p. 257.
11. A. A. Kozhushko, I. I. Rykova, and A. B. Sinani, Fiz. Goreniya Vzryva, No. 1, 89 (1992).
12. V. B. Lazarev, A. S. Balankin, A. D. Izotov, and A. A. Kozhushko, *Structural Stability and Dynamic Strength of Inorganic Materials* (Nauka, Moscow, 1993), p. 175 [in Russian].
13. E. L. Zilberbrand, A. S. Vlasov, J. U. Cazamias, S. J. Bless, and A. A. Kozhushko, Int. J. Impact Eng. **23** (1), 995 (1999).
14. V. R. Regel, A. I. Slutsker, and É. E. Tomashevskiĭ, *Kinetic Theory of the Strength of Solids* (Nauka, Moscow, 1974), p. 560 [in Russian].
15. A. B. Sinani and V. A. Stepanov, in *Research in Materials in the Course of Measurement of Strength* (Standartizdat, Moscow, 1967), p. 180 [in Russian].
16. O. F. Kireenko, A. M. Leksovskiĭ, and V. R. Regel, Mekh. Polim., No. 5, 842 (1970).

Translated by I. Volkov

Physics of the Solid State, Vol. 47, No. 5, 2005, pp. 840–844. Translated from Fizika Tverdogo Tela, Vol. 47, No. 5, 2005, pp. 816–819.

High Strength and Superplasticity of Nanocrystalline Materials

B. I. Smirnov, V. V. Shpeĭzman, and V. I. Nikolaev

Ioffe Physicotechnical Institute, Russian Academy of Sciences, Politekhnicheskaya ul. 26, St. Petersburg, 194021 Russia
e-mail: shpeizm.v@mail.ioffe.ru

Abstract—The part played by grain boundaries in nanocrystalline materials produced by equal-channel angular pressing is considered. The tensile strength and tensile and compressive yield stresses of various materials and alloys were studied over a broad low-temperature range. It was found that, at close-to-liquid helium temperatures, the strength is the highest possible for the given material and that strain localization is better pronounced than in conventional materials. The results obtained are interpreted in terms of the influence of boundaries, which act as the dominant hardening factor increasing the resistance to dislocation motion. By contrast, experiments conducted at elevated temperatures showed the boundaries to become mobile, thus imparting superplasticity to materials in some cases. The actual maximum tensile and torsional shears are compared. It is demonstrated that, despite the closeness between the tensile- and torsional-deformation activation energies, the stress–strain curves and the shears differ strongly, which implies that these characteristics are affected by the actual type of deformation involved. © *2005 Pleiades Publishing, Inc.*

1. INTRODUCTION

Nanocrystalline (submicrocrystalline) materials have recently been attracting considerable interest in connection with studies on how the mechanical properties of solids are related to their structure [1, 2]. The main structural elements in these materials are grain boundaries. On the one hand, they are efficient obstacles for moving dislocations (at low and moderate temperatures) and favor hardening, while on the other, mobile boundaries (at high temperatures) can provide high strains unattainable for processes operating inside grains. The fabrication of bulk specimens of metals and alloys with an average grain size ranging from 100 nm to a few micrometers by multiple equal-channel angular pressing (ECAP) [3] offers the possibility of loading fairly large volumes of a material and, in contrast to local loading (for instance, in the case of indentation in microhardness measurements), of investigating the strain-averaged characteristics.

The present paper reports on some results obtained in a study of low-temperature high strength and high-temperature superplasticity of ECAP materials.

2. EXPERIMENTAL TECHNIQUES

Experiments were carried out on various metals (aluminum, copper, and nickel with the fcc structure; bcc niobium) and aluminum- and copper-based compounds (an Al–5.5 wt % Mg–2.1 wt % Li alloy, Cu : ZrO_2 composite). The last composite was prepared from a Cu–0.15 wt % Zr solid solution through internal oxidation [4] and contained 0.3 vol % ZrO_2 in the form of nanoparticles about 10 nm in size. The ultrafine granular structure was produced through multiple ECAP (up to 16 times) by rotating the bar through 90° after each cycle [3]. X-ray structural data, which made it possible to separate the contributions from the finite size of coherent-scattering regions and lattice distortions (the relative change in the lattice parameter $\Delta a/a$) to line broadening, and the grain sizes are listed in Table 1. As follows from Table 1, the coherent-scattering regions in copper, niobium, and the two alloys are small, while in nickel and aluminum these regions are larger. The relative change in the unit cell parameter $\Delta a/a$ caused by internal stresses is large for both alloys and aluminum; in the latter case, an increase in the number of ECAP runs brings about a decrease in the size of grains and coherent-scattering regions and an increase in $\Delta a/a$.

The ECAP procedure produced bars about 50-mm long and ~14×14 mm in cross section. The specimens intended for mechanical tests at low and moderate temperatures were cut along the longer side of the bars and had the following dimensions: a height of 6 mm for compressive tests, a 10- or 15-mm-long working part for tension, and a diameter of 3 mm in both cases. The

Table 1. Structural characteristics of materials after ECAP

Material	Grain size, nm	Size of coherent-scattering regions, nm	Relative lattice parameter change, $10^3\,\Delta a/a$
Cu	≤200	50	≤0.5
Cu : ZrO_2	≤200	55	2.5
Ni	≤200	130	5
Nb	≤200	30	1.1
Al	≤500	87	2.7
	≤1000	210	1.3
Al–Mg–Li	≤2000	65	2.75

1063-7834/05/4705-0840$26.00

specimens were deformed on an Instron 1342 universal testing machine in the temperature range 4.2–300 K. Low-temperature measurements were conducted in an Oxford liquid-helium cryostat. Cooling of specimens to temperatures $T \geq 77$ K, as well as precooling for tests in the range 4.2–77 K, was achieved using liquid nitrogen. Liquid helium was supplied to the cryostat by means of two pumps producing weak rarefaction in the cryostat. Tension and compression were performed at a rate of 0.15–1 mm/min.

Tests at elevated temperatures were conducted on cylindrical specimens 3 mm in diameter, as well as on plane specimens about 1-mm thick and 2-mm wide. The working part of both types of specimens was 5- or 10-mm long. The tension rate varied from 0.5 to 50 mm/min, and the temperature ranged from 523 to 673 K. Cylindrical specimens with square heads were also subjected to torsional tests at rates of 18 and 180 rad/min using a specially designed attachment to the Instron 1342 machine, in which the rotation rate of the crosshead was set by an electric motor with a reducing gear. The torque was measured with a 10-N load standard Instron cell, whose output signal was processed by the Instron controller and entered into a PC.

The measurement error of the strain and of the strain rate (which is axial for tensile or compressive tests and shear for torsional tests) was 2.5%, and that of the axial force and torque was 1%. During measurements, the temperature was maintained constant to within ±3 K.

3. EXPERIMENTAL RESULTS AND DISCUSSION

3.1. Low-Temperature Strength of Nanocrystalline Materials

The mechanical properties of microcrystalline materials, including those obtained by ECAP, have recently become a subject of considerable interest [1–3]. While the low-temperature region is potentially interesting both for gaining a better understanding of the mechanism of deformation and, hopefully, for obtaining the highest possible levels of material strength, this region still remains the least studied. We carried out studies of the low-temperature deformation of various fcc and bcc metals and alloys. The fcc metals are known to retain high plasticity down to very low temperatures. The same applies to pure niobium loaded at low rates. Generally speaking, this behavior is not typical of bcc metals, which become brittle when the temperature is lowered [5]. Another reason accounting for the interest in the low-temperature deformation of niobium is its transition to the superconducting state at $T_c = 8.7$ K [6], which affects its deformation characteristics [7, 8]. Furthermore, analyzing the dependence of strength on grain size offers the possibility of testing the validity of the Hall–Petch relation, which has been repeatedly discussed in connection with the problem of nanocrystallinity [9–11].

Table 2. Compressive yield stress of nanostructural Nb, Cu, and Ni, and a Cu : ZrO_2 composite

Material	Nb	Cu			Cu : ZrO_2		Ni	
T, K	4.2	4.2	77	290	4.2	290	4.2	290
σ_y, MPa	1810	578	570	403	680	412	1450	1002

Studies of the tension and compression diagrams have shown plastic deformation to be unstable at liquid-helium temperature; serrations were observed to accompany low-temperature deformation of metals with larger grains (see, e.g., [12, 13]). It was found that serrations appear immediately beyond the yield stress; their amplitude is initially small and then increases with strain. The nanocrystalline structure apparently favors broadening of the region where serrated yielding persists. Indeed, in our case, serrations in nickel were observed to occur at temperatures of 4.2–17 K, whereas annealed nickel did not exhibit serrated flow in this temperature interval [14]. Deformation of niobium is accompanied by large stress jumps, which demonstrate a strong localization of the strain. The serration amplitude $\Delta\sigma$ increases with strain, as reported, for instance, in [8, 14–16], and at a strain level $\varepsilon \approx 10\%$ the ratio of the serration amplitude to the applied stress can reach $\Delta\sigma/\sigma \approx 40\%$. Such deep stress serrations are accompanied by axial displacements of 0.5–0.6 mm, which can be identified with the giant localized strain associated with macroscopic shear bands [17–19] or cracks [17]. The data obtained in this work suggest that localized strains (serrations in the tension or compression diagrams) appear immediately after the yield stress σ_y is reached and that the deformation between the serrations is either fully elastic or elastic with a certain uniform plastic component. Serrations in compression diagrams for nanocrystalline niobium were also observed to occur at 10 K but were not detected at 20 K.[1]

A separate study was devoted to thermal effects occurring in serrated deformation of niobium at 4.2 K at its transition from the superconducting to normal state. Estimates of the temperature of a specimen of volume ~20 mm^3 undergoing a localized shear $\gamma \sim 800\%$ showed that it can reach as high as 70 K. At a serration, evaporated helium would form a ball up to 1.5 cm in radius with the specimen at its center.

Figure 1 depicts the temperature dependences of the yield stress of the metals studied, and Tables 2 and 3 separately list the yield stress σ_y, the ultimate strength σ_u, and maximum elongation δ at 4.2 K, 77 K, and room temperature. The yield stress was derived either directly from the stress–strain curve obtained for a given temperature or by repeatedly measuring σ_y on the

[1] Niobium undergoes tensile fracture, as a rule, already at the first serration. Tensile stress diagrams with more than one serration can be obtained only for very pure niobium, which does not exhibit high strength.

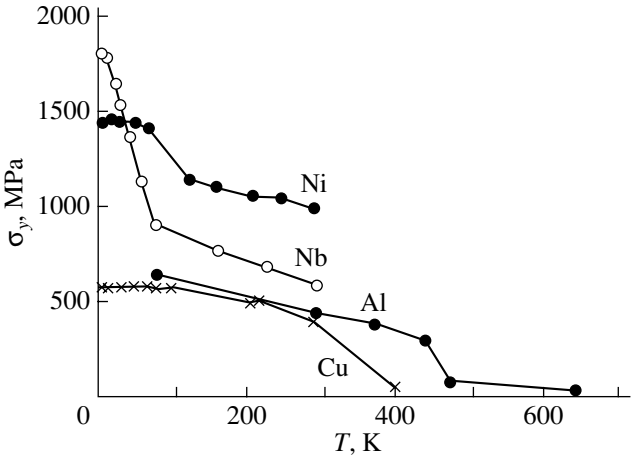

Fig. 1. Temperature dependence of the yield stress for nanostructural nickel, niobium, aluminum, and copper.

same specimen [20]. The first method was employed to determine the yield stress in tests conducted in liquid helium, liquid nitrogen, and at room temperature, and the second method was used at intermediate temperatures. In the latter case, the change in the flow stress at the serration temperature was found and then, by using known yield stresses as references, the value of the hardening at the given strain was reduced to the change in the yield stress $\Delta\sigma_y$ and σ_y was found. This method is indirect but has nevertheless a number of advantages. First, it does not involve the error associated with testing different specimens. Second, the change in the flow stress (its magnitude and sign) is determined very accurately; therefore, any possible small deviations from the basic $\sigma_y(T)$ relation, rather than being experimental errors, should be considered a specific feature of the deformation, as was pointed out in [20].

As follows from Fig. 1, three regions in the temperature dependence of the yield stress can be isolated for nanocrystalline materials, namely, a weak dependence (or athermic behavior in some cases) at low temperatures followed by a stronger dependence, which again becomes weak at higher temperatures.

These regions have different extents for different metals. Note that this type of pattern of the $\sigma_y(T)$ relation is typical of many polycrystalline materials; indeed, coarser grained niobium [8] exhibits an analogous three regions, but the critical points at which the $\sigma_y(T)$ relation changes pattern are shifted toward higher temperatures and the stress level is less than one-half those shown in Fig. 1.

Table 3. Tensile mechanical properties of nanostructural Al, Ni, Cu, and Cu : ZrO_2

Material	Cu		Cu : ZrO_2		Ni	Al	
T, K	4.2	290	4.2	290	4.2	77	290
σ_y, MPa	448	382	637	398	1220	607	391
σ_u, MPa	550	435	698	431	1292	650	445
δ, %	15	10	18	10	12	10	8

The strength and deformation characteristics of the Cu : ZrO_2 composite were measured over the temperature range 4.2–300 K [15]. A comparison of the temperature dependences of the yield stresses of copper and the composite revealed that, below ~200 K and above ~300 K, the yield stress of the composite is higher than that of copper, while in the intermediate domain, 200–300 K, the yield stresses of copper and of the composite practically coincide. In the high-temperature region, ZrO_2 particles hinder crystallization while favoring stabilization of the microcrystalline state; at low temperatures, the yield stress can increase because of the dislocations being damped by these particles in the initial stage of deformation of the material.

3.2. High-Temperature Superplasticity of Nanocrystalline Materials

Superplasticity of various materials, including that following ECAP, has recently become a topic of considerable interest [21–27]. A study of the high-temperature tensile deformation of an aluminum–lithium alloy [25, 26] has revealed that, at temperatures $T = 590$–670 K and strain rates $\dot{\varepsilon} = 10^{-2}$–$10^{-3}$ s^{-1}, the alloy is superplastic and the axial strain at rupture may be in excess of 1800%. It was established that the dependence of the true stress σ_t on the true strain ε_t under tension with $\dot{\varepsilon} =$ const exhibits, in place of a softening stage, an extended stationary region described by the expression $\dot{\varepsilon}_t \sim (\sigma_t/\sigma_0)^n \exp(-U/kT)$ with coefficients $n \approx 2$ and $U \approx 1$ eV characteristic of aluminum and its alloys; the strain rate $\dot{\varepsilon}_t$ turns out to be close to the creep rate under comparable strains and stresses. The pattern of the $\dot{\varepsilon}_t(\sigma_t, T)$ relation, the values of the coefficients, and the structural features observed suggest that, in this stage, deformation is mediated by intergrain sliding. At the hardening stage (preceding the stationary region), the activation energy is $U \approx 1.4$ eV, which indicates that self-diffusion in the grain bulk is responsible for deformation at this stage.

A similar result has been obtained under torsion on specimens of the same alloy with a cylindrical working part [27]. The shear strain rate $\dot{\gamma}$ was found to be related to tangential stress τ as $\dot{\gamma} = A(\tau/\tau_0)^n \exp(-U/kT)$, where, as in the above expression for $\dot{\varepsilon}_t$, the parameter τ_0 is introduced for dimension considerations and is $\tau_0 = 1$ MPa if τ is measured in megapascals; k is the Boltzmann constant; U is the activation energy for plastic deformation; T is the temperature; and $A \sim T^{-1}$ is a coefficient. The activation energy U and exponent n for the initial deformation stage and the superplasticity

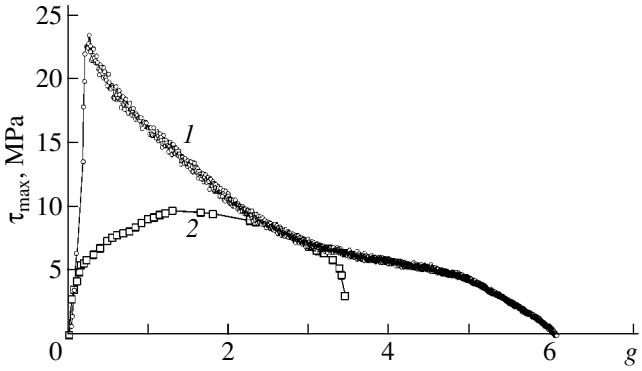

Fig. 2. Comparison of (*1*) torsional and (*2*) tensile diagrams constructed in the coordinates of maximum shear tress τ_{max} versus true logarithmic shear g for an aluminum alloy. T = 673 K. The torsional shear strain rate and initial tensile shear rate are ~10^{-2} s^{-1}.

region were found to be close to their values obtained under tension. However, there were also significant differences in the characteristics of the material obtained under tension and torsion. The torsional shear strain was several times larger than that under tension, and the superplasticity region itself was broader and shifted toward lower temperatures. The stress–strain diagrams were likewise different. Figure 2 compares stress–strain curves measured under tension and torsion for similar testing conditions and plotted in the coordinates of maximum shear stress τ_{max} versus true logarithmic shear g, which was calculated as $g = 1.5\varepsilon_t$ for tension and $g = \ln(1 + \gamma^2/2 + \gamma\sqrt{1 + \gamma^2/4})$ for torsion [28]. We readily see that the initial region of hardening under tension is more extended along the strain axis and corresponds to substantially lower stresses than that under torsion. In the region $g \approx 2$–3, the stress–strain curves approach one another, after which tension terminates in rupture of the specimen. Another distinctive feature of torsion diagrams in the low-temperature region is the presence of a second region of hardening at large strains [27].

4. CONCLUSIONS

We have shown that the low-temperature strength and yield stress of ECAP materials can be 1.5–2 times higher than the values observed previously. This suggests that the nanocrystalline state has a structure with the highest resistance to plastic deformation and fracture. In addition to a record-high strength for this material, nanostructural materials reveal a number of low-temperature deformation features; indeed, the serrated character of deformation is more clearly pronounced and manifests itself over a broader temperature and stress range, the flow stress is sensitive to the load sign, impurities have a different effect on the strength and yield stress in different temperature regions, etc. At elevated temperatures, the ECAP materials become superplastic, which should be attributed to the high mobility of grain boundaries.

ACKNOWLEDGMENTS

This study was supported in part by the Ministry of Education and Science of the Russian Federation (program “Solid-State Nanostructures”).

REFERENCES

1. A. I. Gusev, Usp. Fiz. Nauk **168** (1), 55 (1998) [Phys. Usp. **41**, 49 (1998)].
2. S. X. McFadden, R. S. Mishra, R. Z. Valiev, A. P. Zhilyaev, and A. K. Mukherjee, Nature **398**, 684 (1999).
3. V. M. Segal, V. I. Reznikov, A. E. Drobyshevskiĭ, and V. I. Kopylov, Izv. Akad. Nauk SSSR, Met., No. 1, 115 (1981).
4. I.-W. Chen and Y.-H. Chiao, Acta Metall. **31**, 1627 (1983).
5. V. I. Trefilov, Yu. V. Mil’man, and S. A. Firstov, *Physical Fundamentals of Strength of Refractory Metals* (Naukova Dumka, Kiev, 1975) [in Russian].
6. *Low-Temperature Physics*, Ed. by A. I. Shal’nikov (Inostrannaya Literatura, Moscow, 1959).
7. L. P. Kubin and B. Jouffrey, Philos. Mag. **24** (188), 437 (1971).
8. V. I. Startsev, V. Ya. Il’ichev, and V. V. Pustovalov, *Plasticity and Strength of Metals and Alloys at Low Temperatures* (Metallurgiya, Moscow, 1975) [in Russian].
9. G. A. Malygin, Fiz. Tverd. Tela (St. Petersburg) **37** (8), 2281 (1995) [Phys. Solid State **37**, 1248 (1995)].
10. D. A. Konstantinidis and E. C. Aifantis, Nanostruct. Mater. **10** (7), 1111 (1998).
11. M. Yu. Gutkin, Doctoral Dissertation (IPME, Russian Academy of Sciences, 1997).
12. G. A. Malygin, Fiz. Met. Metalloved. **81**, 3 (1996); **81**, 5 (1996) [Phys. Met. Metallogr. **81**, 235 (1996)].
13. V. I. Nikolaev and V. V. Shpeĭzman, Fiz. Tverd. Tela (St. Petersburg) **39** (4), 647 (1997) [Phys. Solid State **39**, 565 (1997)].
14. O. V. Klyavin, *Physics of Crystal Plasticity at Liquid-Helium Temperatures* (Nauka, Moscow, 1975) [in Russian].
15. V. V. Shpeĭzman, V. I. Nikolaev, B. I. Smirnov, A. B. Lebedev, and V. I. Kopylov, Fiz. Tverd. Tela (St. Petersburg) **42** (6), 1034 (2000) [Phys. Solid State **42**, 1066 (2000)].
16. O. V. Klyavin and A. V. Stepanov, Fiz. Tverd. Tela (Leningrad) **1** (6), 959 (1959) [Sov. Phys. Solid State **1**, 873 (1959)].
17. V. V. Shpeĭzman, V. I. Nikolaev, B. I. Smirnov, A. B. Lebedev, V. V. Vetrov, S. A. Pul’nev, and V. I. Kopylov, Fiz. Tverd. Tela (St. Petersburg) **40** (9), 1639 (1998) [Phys. Solid State **40**, 1489 (1998)].
18. A. R. Baraz and B. V. Molotilov, Fiz. Nizk. Temp. **3** (4), 514 (1977) [Sov. J. Low Temp. Phys. **3**, 249 (1977)].
19. M. Dolgin and V. Z. Benguz, Phys. Status Solidi A **94** (2), 529 (1968).

20. V. V. Shpeĭzman, V. I. Nikolaev, B. I. Smirnov, V. V. Vetrov, S. A. Pul'nev, and V. I. Kopylov, Fiz. Tverd. Tela (St. Petersburg) **40** (7), 1264 (1998) [Phys. Solid State **40**, 1151 (1998)].

21. A. V. Sergeeva, V. V. Stolyarov, R. Z. Valiev, and A. K. Mukherjee, Scr. Mater. **43** (9), 819 (2000).

22. A. M. Shammazov, N. K. Tsenev, R. Z. Valiev, M. M. Myshlyaev, M. M. Bikbulatov, and S. P. Lebedich, Fiz. Met. Metalloved. **89** (3), 107 (2000) [Phys. Met. Metallogr. **89**, 314 (2000)].

23. Z. Horita, M. Furukawa, M. Nemoto, A. J. Barnes, and T. G. Langdon, Acta Mater. **48** (14), 3633 (2000).

24. K. Neishi, Z. Horita, and T. G. Langdon, Scr. Mater. **45** (8), 965 (2001).

25. M. M. Myshlyaev, M. A. Prokunin, and V. V. Shpeĭzman, Fiz. Tverd. Tela (St. Petersburg) **43** (5), 833 (2001) [Phys. Solid State **43**, 865 (2001)].

26. M. M. Myshlyaev, V. V. Shpeĭzman, and M. M. Kamalov, Fiz. Tverd. Tela (St. Petersburg) **43** (11), 2015 (2001) [Phys. Solid State **43**, 2099 (2001)].

27. V. V. Shpeĭzman, M. M. Myshlyaev, M. M. Kamalov, and M. M. Myshlyaeva, Fiz. Tverd. Tela (St. Petersburg) **45** (11), 2008 (2003) [Phys. Solid State **45**, 2110 (2003)].

28. A. Nadai, *Theory of Flow and Fracture of Solids* (McGraw-Hill, New York, 1950; Inostrannaya Literatura, Moscow, 1954).

Translated by G. Skrebtsov

Physics of the Solid State, Vol. 47, No. 5, 2005, pp. 845–851. Translated from Fizika Tverdogo Tela, Vol. 47, No. 5, 2005, pp. 820–826.

Grain Size Refinement due to Relaxation of Disclination Junction Configurations in the Course of Plastic Deformation of Polycrystals

T. S. Orlova,* A. A. Nazarov, N. A. Enikeev,****
I. V. Alexandrov, R. Z. Valiev,** and A. E. Romanov***

**Ioffe Physicotechnical Institute, Russian Academy of Sciences, Politekhnicheskaya ul. 26, St. Petersburg, 194021 Russia*

***Institute of Physics of Advanced Materials, Ufa State Aviation Technical University, Ufa, 450000 Bashkortostan, Russia*

Abstract—A model is proposed for the formation of the substructure in polycrystals during plastic deformation. According to this model, fragmentation of a grain occurs through the formation of a system of diagonal low-angle boundaries, which originate at the edges of a rectangular grain. Misorientation boundaries form through relaxation of a nonsymmetric junction quadrupole disclination configuration accumulated at the grain corners under severe deformation when the disclination strength reaches a certain critical value. The energetics of this process is analyzed. A general case is considered where the disclinations at the junctions of the chosen grain differ in strength. The energetic approach used makes it possible to determine the misorientation angle ω_x of the resulting boundaries corresponding to the maximum energy gain and to find the dependence of this angle on the degree of asymmetry of the quadrupole configuration of junction disclinations. According to the proposed model, the splitting of a grain with a short edge greater than 0.5 μm is energetically favorable and decreases the latent energy of the grain for any ratio between the junction disclination strengths if the grain length-to-width ratio is less than 30. It is shown that the minimum possible grain size in the proposed model does not exceed 0.1 μm. © *2005 Pleiades Publishing, Inc.*

1. INTRODUCTION

A common feature of the evolution of the dislocation substructure of various crystals subjected to severe plastic deformation is the fragmentation and refinement of grains [1–4]. Studying the mechanisms of this process and its theoretical description is currently of considerable importance because of the need to develop methods for producing ultrafine-grained materials based on severe plastic deformation (twisting under pressure, equal-channel angular pressing (ECAP), forging, etc. [5]).

The experimental and theoretical studies carried out by Rybin and coworkers have shown that fragmentation occurs through the generation of pairs of broken dislocation boundaries at junctions and sharp bends of grain boundaries, which is equivalent to the formation of partial-disclination dipoles and their motion through a grain [2–4]. The appearance and growth of broken boundaries in a grain are accompanied by complicated rearrangement of the dislocations located near the ends of these boundaries, which can be treated as disclination dipoles. This rearrangement includes the generation of dislocations (under the combined action of the applied stress and the disclination dipole stress) and the motion and accumulation of dislocations with the formation of misorientation boundaries. In the course of this process, slip systems in which the shear stress exceeds the critical value become operative. A two-dimensional model of this process was proposed and investigated in [6–8]. The kinetics of accumulation of dislocations and disclinations was also analyzed in [9] in studying the plastic-strain hardening of polycrystals. However, quantitative models capable of predicting the evolution of the substructure of a polycrystal subjected to severe plastic deformation have not yet been proposed.

A comprehensive three-dimensional analysis of the structure formation in terms of the theory of dislocations and disclinations should take into account the grain strain distribution over slip systems, which makes this analysis extremely difficult. However, plastic deformation of polycrystals can be adequately described in terms of a micromechanical model based on an approximate continuum description of slip on a few systems, such as the viscoplastic self-consistent (VPSC) model [10]. In this model, a deformed grain is assumed to be embedded into an effective homogeneous medium that is equivalent to the neighbor grains surrounding the grain in question.

It is important that this model makes it possible to calculate the accumulated strain incompatibility between grains, which is the reason for the occurrence of disclinations in junctions and, in the final analysis, for the fragmentation of grains. Therefore, in order to describe the evolution of the substructure of a polycrystal, it may be advantageous to combine the concept of disclinations with the micromechanical model. In this case, the VPSC model can be used to perform a three-dimen-

1063-7834/05/4705-0845$26.00 © 2005 Pleiades Publishing, Inc.

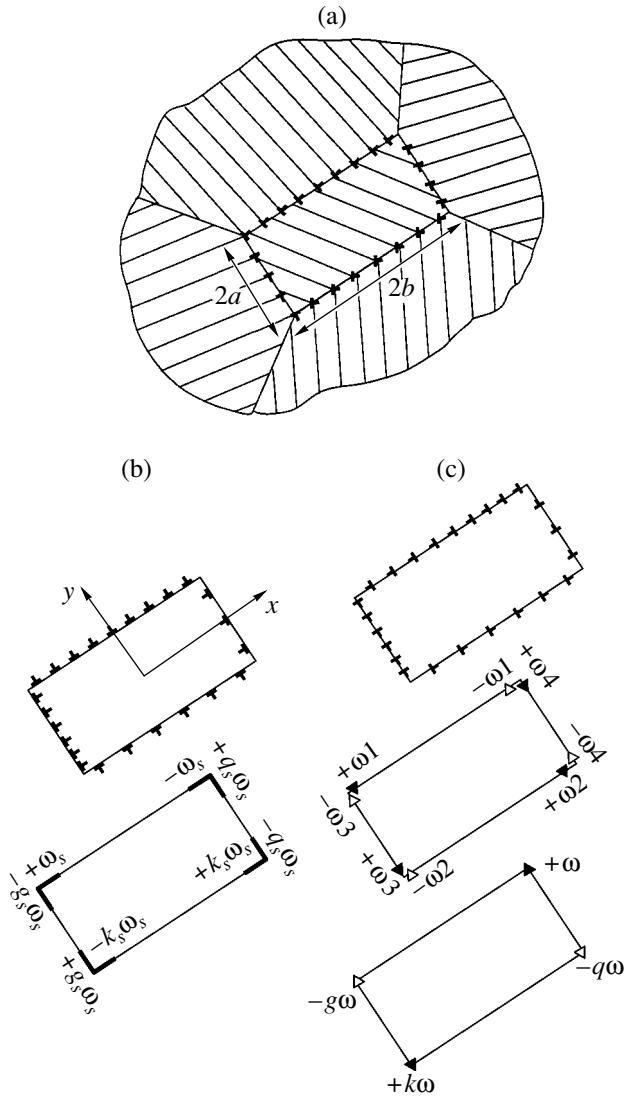

Fig. 1. Mesoscopic defects forming at a grain boundary due to a difference in plastic strain between the grain and the surrounding medium (schematic). (a) Misorientation of the slip systems that are operative in the grain and the surrounding medium and difference dislocations captured by the grain boundary as a result of this misorientation. (b, c) Decomposition of the defect structure of the grain boundary into (b) homogeneous distributions of tangential dislocations (which can be approximated by four SD dipoles) and (c) normal-dislocation walls forming disclination dipoles; the resultant configuration of difference disclination dipoles is shown.

sional computer simulation of the plastic deformation of a polycrystal and determine the misfit between the strain tensors of grains, while the disclination model can be applied to find the conditions for the fragmentation of grains through the formation of low-angle boundaries and determine the character of this fragmentation. A decisive role is played here by the criterion for fragmentation, which should be derived from an analysis of possible disclination configurations and will make it possible to determine the instant at which fragmentation will occur and to predict the geometric characteristics (low-angle boundary planes and misorientations, the shape and orientation of subgrains, etc.) of the substructure that will arise.

Grain fragmentation models based on the energetic criterion also show promise [11]. According to this criterion, as the strength of mesoscopic defects accumulated at grain boundaries and their junctions due to deformation reaches a certain value, these defects are replaced by an energetically more favorable system, which arises through the formation of new misorientation boundaries bringing about the fragmentation of grains into subgrains.

The objective of this work is to formulate a grain fragmentation criterion, which can subsequently be combined with the VPSC model.

2. MODEL

In a polycrystal subjected to deformation, grains are deformed depending on their crystallographic orientation relative to the neighbor grains and on the applied load. For simplicity, let us consider a grain in the form of a $2b \times 2a$ rectangle (two-dimensional approximation). Since the grain and its neighbors are deformed differently, a dislocation structure arises at its boundary (Fig. 1a), thereby adjusting the strained grain to its environment. This dislocation structure can be approximated by a disclination quadrupole and Somigliana dislocations. In general, due to nonhomogeneous deformation of the neighbor grains, there occur four dipoles of Somigliana dislocations (Fig. 1b) and four disclination dipoles at the edges of the chosen grain. As a result, at the corners of the grain, there appear four difference disclinations with strengths ω, $-q\omega$, $-g\omega$, and $k\omega$ (Fig. 1c), where q, g, and k are positive constants. In what follows, the system formed by these disclinations is referred to as the asymmetric disclination quadrupole. Thus, in the grain junctions, two types of mesoscopic defects are accumulated: Somigliana dislocations (which produce internal stresses but do not cause misorientations) and junction difference disclinations, which cause both stresses and misorientations. A detailed analysis of the formation of mesoscopic defects on the planar facets of grain boundaries was made by Zisman [12].

Experimental studies and theoretical estimates made by Rybin and coworkers [2–4] have shown that, as the strength of a disclination produced in a grain boundary junction through plastic deformation reaches a critical value $\Omega_c \approx 1°–3°$, the disclination can relax through the formation of a low-angle boundary growing from this junction. This boundary crosses the grain and causes it to split.

Let us consider a model in which stress relaxation of the asymmetric disclination quadrupole located at the corners of the chosen grain occurs through the forma-

tion of low-angle boundaries along the diagonals of the grain (Fig. 2). Once the geometric criterion $\Omega_c \approx 1°–3°$ is met, four boundaries with a misorientation ω_x begin to grow from the grain corners and the grain splits into subgrains as shown in Fig. 2b. In Fig. 2, the large ellipse and the four small ellipses denote the initial grain and subgrains, respectively, described in terms of the VPSC model, in which grains are assumed to be ellipsoidal in shape. In this way, the descriptions of grains in terms of the VPSC and disclination models are reconciled.

We consider two extreme cases: (1) the case where $0 < (q, g, k) \le 1$ and, therefore, ω is the highest of the strengths of the four disclinations and (2) the case where q, g, and k are greater than unity and, hence, ω is the lowest of the strengths of the four disclinations. In both cases, we assume that relaxation begins to occur at $\omega = \Omega_c$. Therefore, in the former case, the strengths of the other three disclinations are less than the critical value and, in the latter case, the strengths of all four disclinations exceed Ω_c.

Fragmentation of the chosen grain through relaxation of the disclination quadrupole will occur only if the disclination stresses, in combination with the applied stress, are favorable for additional grain strain associated with the formation of low-angle boundaries. This condition is met if the strain of the chosen grain is less than that of the surrounding medium.

3. ENERGETIC CRITERION FOR GRAIN FRAGMENTATION

Relaxation of the disclination configuration bringing about grain fragmentation through the formation of diagonal misorientation boundaries has to be accompanied by a decrease in the energy of the system. Let us analyze the energy conditions for such grain fragmentation.

The energy difference ΔE between the split and unsplit configurations consists of the following components: (i) the energy of the four misorientation boundaries with misorientation ω_x, (ii) the interaction energy between these boundaries and the disclinations at the corners of the chosen grain, (iii) the interaction energy between these boundaries and the four dipoles of Somigliana dislocations (SDs) located at the edges of the chosen grain, and (iv) the total surface energy of the resultant misorientation boundaries.

Each of the four resultant misorientation boundaries (semidiagonals of the chosen grain) is a broken dislocation wall, which can be approximated by a disclination dipole with arm $\sqrt{a^2 + b^2}$ and strength ω_x. The energy of the four misorientation boundaries with misorientation ω_x is equal to the energy of a quadrupole with arms $2b$ and $2a$ and strength $\pm\omega_x$ [13]:

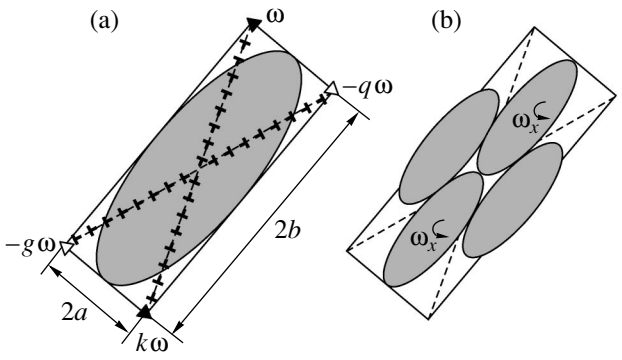

Fig. 2. Grain splitting due to low-angle boundaries growing from the grain junctions. (a) Low-angle tilt boundaries (dislocation walls) growing from junction disclinations with strengths ω, $-q\omega$, $-g\omega$, and $k\omega$. (b) The formation of four new grains, two of which are misoriented relative to the initial grain orientation through an angle ω_x.

$$E^{qx} = 2D\omega_x^2\left[a^2\ln\frac{b^2+a^2}{a^2} + b^2\ln\frac{b^2+a^2}{b^2}\right], \qquad (1)$$

where $2a$ and $2b$ are the dimensions of the chosen grain (Fig. 2), $D = G/2\pi(1-\nu)$, G is the shear modulus, and ν is Poisson's ratio.

The interaction energy ($E_{\text{int}}^{qz/qx}$) between the newly formed boundaries and the disclinations at the corners of the chosen grain can be found as the energy necessary for a quadrupole with arms $2b$ and $2a$ and strength $\pm\omega_x$ to form in the resultant elastic field of the four disclinations located at the corners of the grain:

$$E_{\text{int}}^{qz/qx} = D\omega\omega_x(1+q+g+k) \times\left[a^2\ln\frac{a^2}{a^2+b^2} + b^2\ln\frac{b^2}{a^2+b^2}\right]. \qquad (2)$$

Let us find the contribution from the interaction of SDs with the newly formed misorientation boundaries to the difference energy. The SD dipoles located at the grain edges differ in terms of strength. Indeed, at the $2b$-long edges, the strengths of the SD dipoles are equal to $\pm\omega_s$ and $\pm q_s\omega_s$, whereas at the $2a$-long edges they are equal to $\pm g_s\omega_s$ and $\pm k_s\omega_s$, where the coefficients q_s, g_s, and k_s are determined by the geometry of plastic deformation (Fig. 1b). A contribution to the difference energy is made by the interaction of all SDs with boundaries that have arisen with misorientation ω_x. This contribution is equal to the interaction energy $E_{\text{int}}^{\text{SD}/qx}$ of all SD dipoles with a newly formed quadrupole with strength $\pm\omega_x$.

This interaction energy can be found as the work done when a disclination quadrupole with arms $2b$ and $2a$ and strength $\pm\omega_x$ forms in the elastic field of all the

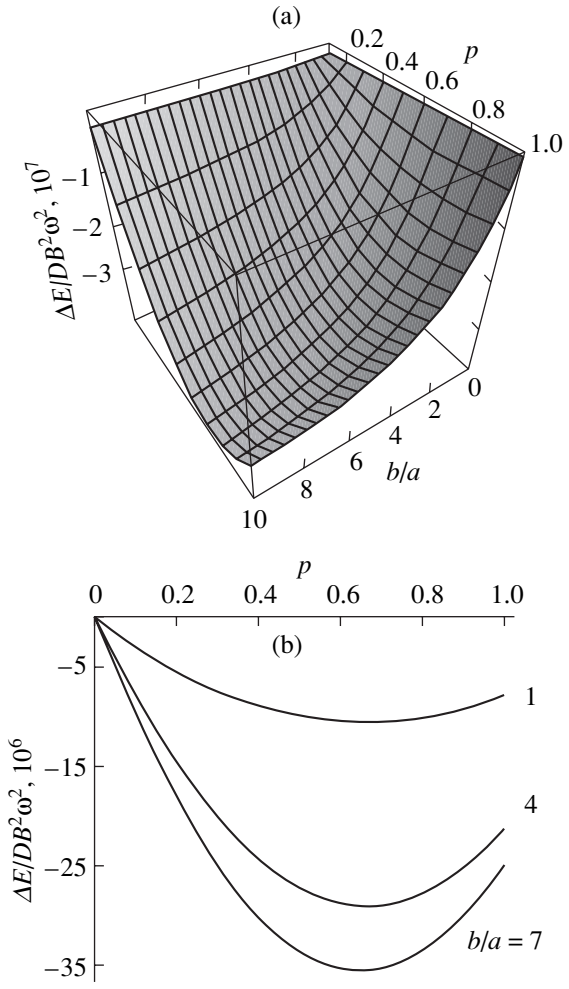

Fig. 3. Change in the energy of a grain due to its splitting along low-angle boundaries. (a) Dependence of ΔE on the grain length-to-width ratio b/a and the parameter $p = \omega_x/\omega$ varying within the range from 0 to 1 for $\nu = 2.8$ and $a = 1$ μm. (b) Dependence of ΔE on the parameter $p = \omega_x/\omega$ for b/a = 1, 4, and 7; $\nu = 2.8$ and $a = 1$ μm.

SDs. The formation of the disclination quadrupole involves only the stress components σ_{xy} of the four dipoles of SDs located at the four edges of the chosen grain (Fig. 1b).

The total stress due to the SDs forming one of these dipoles (e.g., the SDs located at the upper $2b$-long edge of the grain) can be found as

$$\sigma_{xy}^{\mathrm{SD}} = \int_{-b}^{b} \sigma_{xy}(x - x', y - a)\frac{dx'}{L_1}, \tag{3}$$

where $\rho_1 = 1/L_1$ is the dislocation density associated with the strength ω_s of this dipole of SDs with Burgers vector $B = \omega_s L_1$ (the origin of the coordinate frame is located at the center of the grain; Fig. 1b).

In this way, we can find the stresses due to each of the four SD dipoles and the sum of these stresses $\sigma_{xy}^{\Sigma\mathrm{SD}}$. The interaction energy $E_{\mathrm{int}}^{\mathrm{SD}/qx}$ can be written as

$$E_{\mathrm{int}}^{\mathrm{SD}/qx} = \omega_x \int_{-b}^{b} dx \int_{-a}^{a} \sigma_{xy}^{\Sigma\mathrm{SD}}(x, y)dy, \tag{4}$$

where $2a$ and $2b$ are the arms of the newly formed quadrupole and ω_x is its strength.

Calculations show that this interaction energy is zero. Therefore, only the disclinations make a contribution to the difference in energy between the split and unsplit configurations of the grain.

With inclusion of the effective surface energy of the four misorientation boundaries, the difference energy ΔE can be written as

$$\Delta E = E^{qx} + 4\gamma d + E_{\mathrm{int}}^{qz/qx}, \tag{5}$$

where d is the length of each of the misorientation boundaries ($d = \sqrt{a^2 + b^2}$ in our case) and γ is the effective surface energy per unit length of low-angle boundaries. The energy γ can be calculated using the Read–Shockley formula [14]

$$\gamma = \frac{D}{2}\omega_x B \ln\frac{e\alpha}{2\pi\omega_x}, \tag{6}$$

where the coefficient $\alpha = 2$–4 allows for the energy of the dislocation cores and B is the Burgers vector of low-angle boundary dislocations.

Introducing the notation $p = \omega_x/\omega$ and using Eqs. (1), (2), and (6), we write Eq. (5) in the final form

$$\begin{aligned}\Delta E = D\omega^2\Bigg[&-p^2(1 + q + g + k)\\ &\times\left(a^2\ln\frac{b^2 + a^2}{a^2} + b^2\ln\frac{b^2 + a^2}{b^2}\right)\\ &+ 2p^2\left(a^2\ln\frac{b^2 + a^2}{a^2} + b^2\ln\frac{b^2 + a^2}{b^2}\right)\\ &+ \frac{2pB}{\omega}\sqrt{a^2 + b^2}\ln\frac{e\alpha}{2\pi p\omega}\Bigg].\end{aligned} \tag{7}$$

4. ANALYSIS OF THE RESULTS

By analyzing the difference in energy between the split and unsplit grains, we can find physically reasonable values of ω_x.

First, we consider the case of $0 < (q, g, k) \le 1$. The dependence of ΔE on the ratio b/a and the parameter $p = \omega_x/\omega$ (varying in the range from 0 to 1) for the chosen grain is shown in Fig. 3. It can be seen that the formation of misorientation boundaries along the diago-

nals of the grain is energetically favorable everywhere over the range $0 < p \le 1$ for sufficiently large values of the ratio b/a (Fig. 3a). The greater the ratio b/a, the greater the energy gained in splitting the grain with the given initial disclination configuration (Fig. 3b).

For given values of a, b, q, g, and k, there is a value of the misorientation of newly formed boundaries ($\omega_{x,\,eq}$ or p_{eq}) at which ΔE reaches a negative minimum and, hence, the gain in energy is maximum. It can be seen that, when the grain splits along its diagonals, the strength of the accumulated disclinations relaxes only partially. According to Fig. 3b, the value of p_{eq} is almost independent of the ratio b/a but varies with q, g, and k.

It is noteworthy that the asymmetry coefficients q, g, and k enter into Eq. (7) only through the combination $\nu = 1 + q + g + k$, which characterizes the degree of asymmetry of the disclination distribution over the grain edges. In the case, where $0 < (q, g, k) \le 1$, ν decreases as the degree of asymmetry increases, whereas in the case where q, g, and k are greater than unity, on the contrary, a more symmetric quadrupole configuration corresponds to a smaller value of the parameter ν. Calculations show that, as the parameters q, g, and k vary at a fixed value of ν, the parameter p_{eq} remains unchanged. The dependence of p_{eq} on ν is linear (Fig. 4a). The higher the general asymmetry (i.e., the smaller the value of ν), the greater the difference between ω_x and ω. Note that in the particular case where the initial disclination configuration consists of two disclination dipoles ($g = 1$, $k = q$) or is a symmetric quadrupole ($q = g = k = 1$), the most probable splitting (corresponding to the negative minimum value of ΔE) also takes place at a value of ω_x that is different from ω (more specifically, it is slightly smaller than ω). The $p_{eq}(\nu)$ dependence varies with the dimension $2a$ of the initial grain but remains linear (Fig. 4b).

From this fact, it follows that the relaxation of the energy accumulated in the disclination configuration that occurs after a single act of grain splitting through the formation of misorientation boundaries is incomplete; the higher the general asymmetry of the disclination configuration, the greater the difference between ω_x and ω.

In the model considered, the disclination strength in some junctions can increase as a result of the grain splitting along the diagonals. In this case, the relaxation of the accumulated energy can cause an additional concentration of internal stresses in these junctions, which, in turn, can initiate fragmentation of a neighbor grain.

Note that the size of the initial grain is also of considerable importance. We analyzed the energetics of grain fragmentation for the grain size range from 0.05 μm to 0.5 mm. It is found that the grain splitting through the formation of misorientation boundaries along the grain diagonals remains energetically favorable only for grain sizes down to a certain critical size $2a_c$ dependent on the parameter ν. Further grain size refinement becomes energetically unfavorable in the model considered.

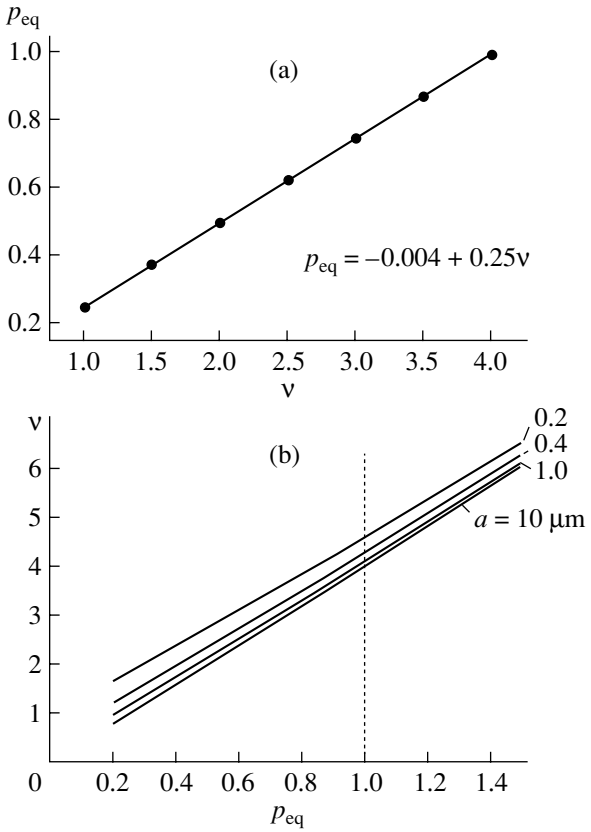

Fig. 4. (a) Parameter p_{eq} corresponding to the formation of equilibrium misorientation boundaries as a function of the parameter ν characterizing the asymmetry of the disclination configuration located at the corners of a grain; $a = b = 1$ μm. (b) Relation between p_{eq} and the asymmetry parameter ν for various values of the initial grain dimensions: $a = b = 0.2$, 0.4, 1.0, and 10 μm.

Figure 5a shows the dependence of the energy difference ΔE on the parameter p and the ratio b/a for the initial grain dimension $2a = 0.4$ μm. It can be seen that there are values of the ratio b/a and the parameter p (and, therefore, of the asymmetry parameter ν) for which the energy difference is positive, i.e., for which the grain fragmentation is energetically unfavorable. Figure 5b shows the dependence of the energy difference on the ratio b/a for grains with various values of the initial dimension a and the parameter $\nu = 3$. It is seen that the range of b/a values for which the grain fragmentation is energetically favorable narrows as the grain dimension becomes smaller. For example, for $\Omega_c = 1°$ and $\nu = 3$, grain fragmentation becomes unfavorable for $b/a > 7$ if $2a \approx 400$ nm and for $b/a > 4$–5 if $2a \approx 300$ nm. Estimates show that, for $\Omega_c = 1°$, grain fragmentation is favorable for any value of ν if the smaller dimension $2a$ exceeds 0.8–1.0 μm and $b/a \le 30$. In the case of $\Omega_c = 3°$, the restriction on the values of

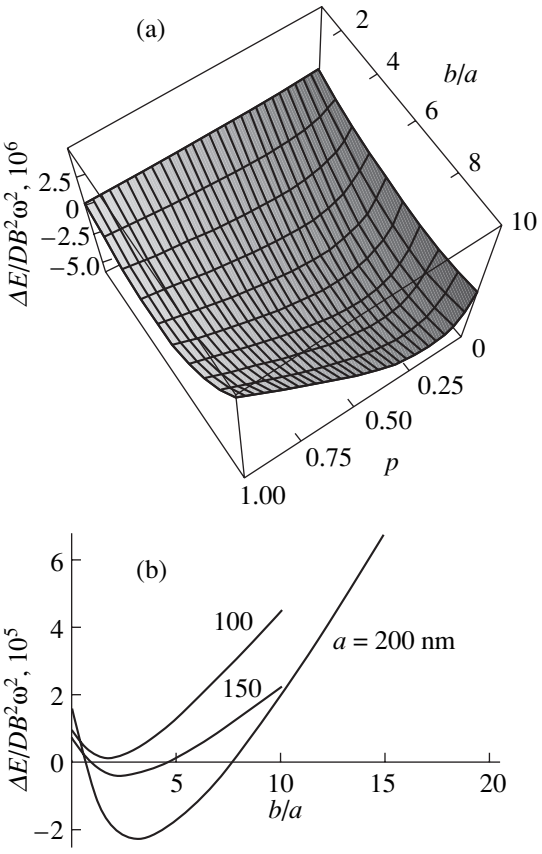

Fig. 5. (a) Change in energy due to grain splitting ΔE as a function of the grain length-to-width ratio b/a and the parameter $p = \omega_x/\omega$ for $\nu = 3$ and $a = 200$ nm. (b) Dependence of the energy change ΔE on the ratio b/a for the initial grain width $a = 200$, 150, and 100 nm and $\nu = 2.1$.

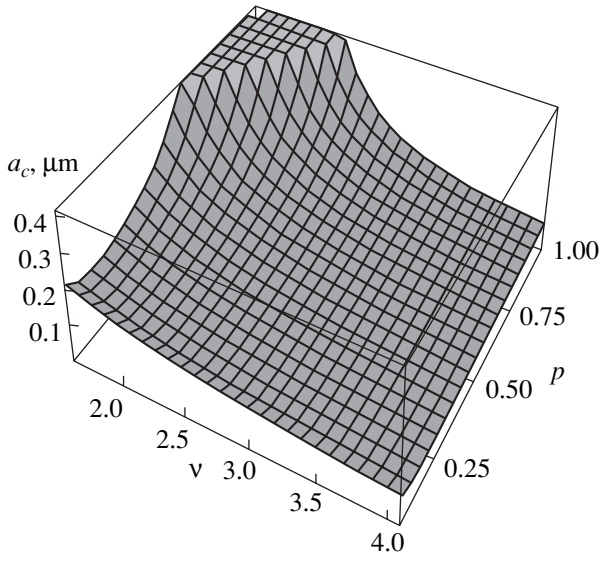

Fig. 6. Critical grain dimension a_c as a function of p and ν for $\Omega_c = 1°$ and $a = b$.

b/a is even less strong: grains can split at $b/a \le 30$ if the dimension $2a$ exceeds 0.5 μm.

We calculated the critical value $2a_c$ of the smaller grain dimension. The dependence of a_c on the asymmetry parameter ν and the parameter p for $\Omega_c = 1°$ is shown in Fig. 6. Taking into account the dependence of p_{eq} on ν (Fig. 4), we find that the critical value of the grain dimension for grain fragmentation in the model considered is $2a_c \approx 300$ nm for $\Omega_c = 1°$ and $2a_c \approx 100$ nm for $\Omega_c = 3°$.

Now, we consider the case where q, g, and k are greater than unity (case 2). In this case, the relaxation of the asymmetric disclination quadrupole begins after the minimum disclination strength reaches the critical value Ω_c.

An analysis of the energy difference shows that the grain fragmentation through the formation of low-angle boundaries is also energetically favorable in this case, with the gain in energy being almost one order of magnitude greater than that in the case considered above (case 1) for equivalent values of the initial parameters. Figure 7 shows the dependence of ΔE on the parameter $p = \omega_x/\omega$ for various values of the ratio b/a. In this case, the equilibrium misorientation $\omega_{x,\,eq}$ of the boundaries that have arisen along the grain diagonals is always higher than the minimum strength ω of the initial disclinations.

Figure 8 shows the dependence of a_c on the asymmetry parameter ν and the parameter p for $\Omega_c = 1°$. It can be seen that the restrictions on the initial grain dimension under which grain fragmentation occurs in the model considered in case 2 are significantly weaker than those in case 1. The critical grain size for fragmentation is $2a_c \approx 100$ nm for $\Omega_c = 1°$ and $2a_c \approx 50$ nm for $\Omega_c = 3°$. Therefore, in case 2, our model covers almost any experimentally attainable degree of grain size refinement.

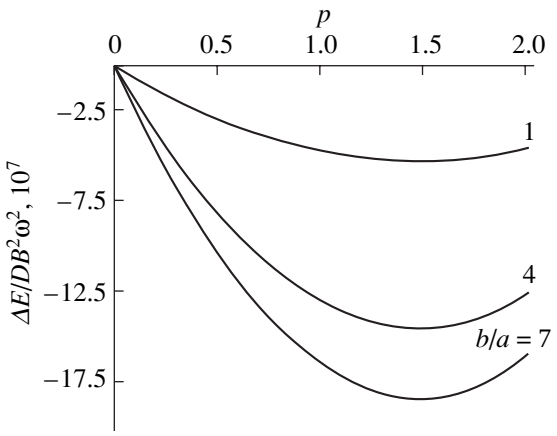

Fig. 7. Energy change ΔE as a function of the parameter $p = \omega_x/\omega$ for the grain length-to-width ratio $b/a = 1$, 4, and 7; $\nu = 6$ and $a = 1$ μm.

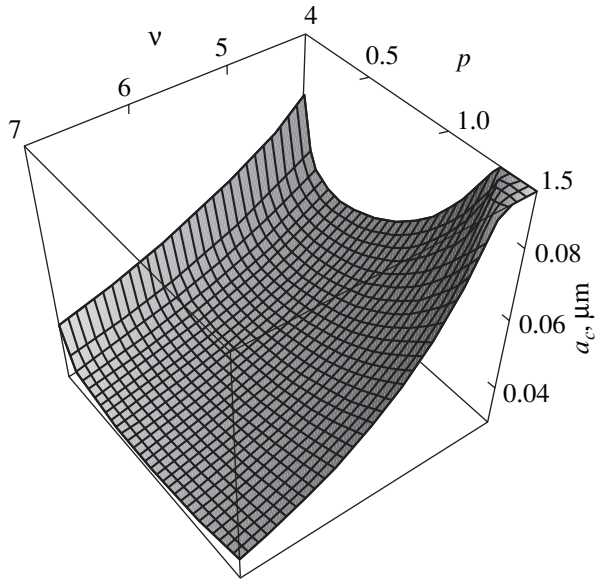

Fig. 8. Critical grain dimension a_c as a function of the asymmetry parameter ν and the parameter p for $\Omega_c = 1°$.

5. CONCLUSIONS

We have considered a model for the relaxation of an asymmetric disclination configuration forming in grain junctions under inhomogeneous plastic deformation. In this model, relaxation occurs through the formation of low-angle boundaries along the grain diagonals. It has been shown that the grain fragmentation is energetically favorable for any value of the grain length-to-width ratio and any misorientation of the newly formed boundaries (in the range from 0 to ω) if the grain width is not less than approximately 0.5 μm. The larger the ratio b/a, the greater the elastic energy $|\Delta E|$ released in the grain splitting along the diagonals. The equilibrium misorientation of low-angle boundaries $\omega_{x,\,eq}$ is not equal to ω and is almost independent of the grain length-to-width ratio but depends on the asymmetry parameter ν of the initial disclination configuration. We have found an analytical expression for this dependence in terms of the equilibrium misorientation $\omega_{x,\,eq}$. The conditions for fragmentation of grains with widths from 50 nm to 0.5 μm, dependent on the asymmetry parameter ν and the grain geometric parameters, have been analyzed. It has been shown that there is a critical value of the grain width (equal to approximately 100 nm) below which grains cannot split according to the energetic criterion of our model.

It should be noted that in [15] computer simulation of the evolution of the texture and fragmentation of grains in the course of ECAP was performed using the VPSC model. The simulation was based on a fairly simple, physically ill-founded criterion for grain splitting, according to which a grain undergoes fragmentation if the grain length-to-width ratio is greater than 5. In this study, we have proposed a physically well-founded criterion for grain splitting, which can be used in simulations of the ECAP process based on our combined model. This will be the subject of a future publication.

ACKNOWLEDGMENTS

This study was supported by CRDF (project no. REO-10505-SR-02) and the Ministry of Education and Science of the Russian Federation (program "Solid-State Nanostructures").

REFERENCES

1. V. I. Trefilov, V. Yu. Mil'man, and S. A. Firstov, *Physical Foundations of Strength of Refractory Metals* (Naukova Dumka, Kiev, 1975) [in Russian].
2. V. V. Rybin, *Large Plastic Strains and Fracture of Metals* (Metallurgiya, Moscow, 1986) [in Russian].
3. V. V. Rybin, Izv. Vyssh. Uchebn. Zaved., Fiz. **34** (3), 7 (1991).
4. V. V. Rybin, Vopr. Materialoved. **29** (1), 11 (2002).
5. R. Z. Valiev and I. V. Alexandrov, *Nanostructural Materials Obtained as a Result of Intense Plastic Deformation* (Lotos, Moscow, 2000) [in Russian].
6. V. I. Vladimirov and A. E. Romanov, Fiz. Tverd. Tela (Leningrad) **20** (10), 3114 (1978) [Sov. Phys. Solid State **20**, 1795 (1978)].
7. A. A. Zisman, Solid State Phenom. **87**, 147 (2002).
8. K. N. Mikaelyan, M. Seefeldt, M. Yu. Gutkin, and A. E. Romanov, Fiz. Tverd. Tela (St. Petersburg) **45**, 2002 (2003) [Phys. Solid State **45**, 2104 (2003)].
9. M. Seefeldt, L. Delannay, B. Peeters, E. Aernoudt, and P. van Houtte, Acta Mater. **49**, 2129 (2001).
10. R. A. Lebensohn and C. N. Tome, Acta Metall. Mater. **41**, 2611 (1993).
11. A. E. Romanov, T. S. Orlova, N. A. Enikeev, A. A. Nazarov, I. V. Alexandrov, and R. Z. Valiev, in *Ultrafine Grain Materials III: Proceedings of Symposium*, Ed. by Y. T. Zhu, T. G. Langdon, R. Z. Valiev, S. L. Semiatin, D. H. Shin, and T. C. Lowe (TMS, Warrendale, Pa., 2004), p. 211.
12. A. A. Zisman, Doctoral Dissertation (St. Petersburg, 2003).
13. V. I. Vladimirov and A. E. Romanov, *Disclinations in Crystals* (Nauka, Leningrad, 1986) [in Russian].
14. J. P. Hirth and J. Lothe, *Theory of Dislocations*, 2nd ed. (McGraw-Hill, New York, 1982; Atomizdat, Moscow, 1972).
15. I. J. Beyerlein, R. A. Lebensohn, and C. N. Tome, Mater. Sci. Eng. A **345**, 122 (2003).

Translated by Yu. Epifanov

Physics of the Solid State, Vol. 47, No. 5, 2005, pp. 852–855. Translated from Fizika Tverdogo Tela, Vol. 47, No. 5, 2005, pp. 827–829.

Fracture of Solids in Aggressive Gases

Yu. M. Dal'

St. Petersburg State University, Universitetskaya nab. 7/9, St. Petersburg, 199034 Russia
e-mail: dahl@apmath.spb.ru

Abstract—An interrelation between the surface energy of a material and the work of plastic deformation at a crack tip is analyzed. Theoretical relationships for the limiting stress intensity factors of a crack tip in a medium of aggressive gases and in vacuum are derived. The results of the calculations are compared with the experimental data. © *2005 Pleiades Publishing, Inc.*

1. GENERAL STATEMENTS

Fracture of materials is associated with the emergence of a new surface. The main characteristic of the surface of a deformed solid is the surface energy γ_c. When the surface energy γ_c at a solid–gas interface decreases (as compared to the surface energy in vacuum), the work expended on forming a new surface can appear to be significantly reduced as a result of the absorption and diffusion of active substances on the surface and in the bulk of the solid. These statements have been confirmed by the results of numerous theoretical and experimental investigations [1–4].

Since plastic deformation always precedes the appearance of discontinuities [5], the problem regarding the influence of the surface of a deformed solid on its plastic properties is of considerable research interest (the case in point is the manifestations of plasticity, such as the yield strength, hardening, and the ultimate strain). When the interatomic bonds in surface regions of a solid undergo a transformation under the action of a medium, the plastic deformation of this solid due to the motion of dislocations can either proceed readily or become hindered. In particular, the hardening of surface layers hinders the emergence of dislocations on the surface of the sample. In this case, the surface and near-surface defects (such as grooves, microcracks, pores, and vacancies [6]) can heal up. Conversely, the softening of these layers facilitates not only the motion of existing dislocations but also the generation of new dislocation sources. Therefore, if the surface and near-surface regions of a solid make a substantial contribution to the total resistance to residual deformations, then, however, paradoxically enough, the plasticity can be considered (of course, only to a certain extent) a surface property.

A characteristic feature of the fracture of polycrystalline materials in an adsorption-active medium is that the generation and propagation of microcracks in these solids predominantly occur along the grain boundaries. This intercrystalline mechanism of fracture is associated with both the excess energy of the boundaries and the fast motion of the adsorbate atoms along the grain contour (as compared to the diffusion into the grain). In this case, unlike the conventional brittle fracture characterized by a high velocity of propagation of a macrocrack (which is comparable to the velocity of sound in a solid), the cracks of adsorption fracture propagate relatively slowly. As a rule, the velocity of their propagation does not exceed several centimeters per second.

It is known that the theoretical strength of a material σ_c is related to the surface energy γ_c through the expression $\sigma_c = A\gamma_c^{1/2}$ (A = const). As can be seen from this fundamental relationship, the surface energy γ_c is of the utmost importance in elaborating mechanical theories of strength that would be consistent with modern concepts of solid-state physics. Unfortunately, the majority of these theories are constructed without regard for the surface energy. Partly, this can be explained by the fact that structural materials, as a rule, exhibit pronounced plastic properties. Upon fracture of these materials, the energy is expended first of all for plastic deformation, then for elastic deformation, then for heating, and finally, for the surface energy itself. The surface energy as if steps back, in contrast to the case of brittle fracture, in which the role of the surface energy is decisive. It is not self-evident from the aforesaid that one can disregard the surface energy γ_c as compared to the work a_p expended for plastic deformation in the vicinity of the crack tip (as is the case with all quasi-brittle strength criteria of the Irwin type). Of course, such disregard would be correct if the work a_p were to be independent of the surface energy γ_c. Actually, these two characteristics are interrelated through a functional expression. This circumstance has been repeatedly emphasized by many authors [7–10].

Since the fact is unquestionable that the work a_p depends on the surface energy γ_c, we can write this dependence in the form

$$a_p = A\gamma_c^n, \quad A, n = \text{const}. \tag{1}$$

1063-7834/05/4705-0852$26.00 © 2005 Pleiades Publishing, Inc.

Here, A and n are the parameters determined by the mechanical properties of the material, its physical structure, and the character of the stressed state.

Let us consider the situation where a deformed solid is placed in an active gaseous medium. In this case, molecules of the medium will continuously interact with atoms of the solid on its surface. This interaction results in physicochemical reactions, which, in turn, lead to a change in the functional γ_c. Such change is particularly significant for samples with cracks, because, according to the Griffith–Orowan energy criterion for fracture, we have $dW/ds = a_p + 2\gamma_c$. Here, dW is the increment of the strain energy when the area of the crack increases by ds.

2. THE INFLUENCE OF PHYSICAL ADSORPTION OF GASES

In the case of physical adsorption, the gas molecules are confined to the surface of the crack by relatively weak van der Waals attractive forces. Physical adsorption is a reversible exothermal high-rate process occurring at low pressures and at temperatures $T < 50°C$.

Relationship (1) can be represented in the equivalent form

$$a_p^* = a_p^0(\gamma_c^*/\gamma_c^0)^n, \tag{2}$$

where the superscripts * and 0 refer to the gaseous medium and vacuum, respectively. According to [11], we can write the expression $d\gamma_c = -\Gamma kTd\ln a$. Here, Γ is the number of gas molecules adsorbed on a unit area in a crack mouth, k is the Boltzmann constant, T is the absolute temperature, and a is the gas activity. If the gas pressure p is low in comparison with the saturation vapor pressure p_0, we have $d\gamma_c = -\Gamma kTd\ln p$. Upon integrating the last equality, we find

$$\gamma_c^* = \gamma_c^0 - k\int_0^p \Gamma d\ln p.$$

After substituting this expression into relationship (2), we obtain

$$a_p^* = a_p^0\left[1 - \frac{kT\int_0^p \Gamma d\ln p}{\gamma_c^0}\right]^n. \tag{3}$$

Following Langmuir (see the monograph by Adamson [12]), we can write

$$\Gamma = \Gamma_m\frac{b_1 p}{1 + b_1 p}, \quad b_1 = \text{const}.$$

Here, Γ_m is the limiting adsorption at saturation (the number of adsorbed gas molecules necessary for a dense monolayer to cover one square centimeter of the crack surface).

After substituting the last relationship into formula (3), we obtain the expression

$$a_p^* = a_p^0\left[1 - \frac{kT\Gamma_m\ln(1 + b_1 p)}{\gamma_c^0}\right]^n. \tag{4}$$

The Langmuir isotherm describes monomolecular gas adsorption on a homogeneous surface of the crack in the absence of dissociation of gas molecules. As a rule, biatomic gas molecules that are physically adsorbed on solids dissociate into atoms. The monolayer isotherm of these gases has the form

$$\Gamma = \frac{\Gamma_m\sqrt{b_2 p}}{1 + \sqrt{b_2 p}}, \quad b_2 = \text{const}. \tag{5}$$

If the crack surface is covered with several monolayers of adsorbed gas molecules [13, 14], we can write the relationship

$$\Gamma = \frac{\Gamma_m cp/p_0}{(1 - p/p_0)[1 + (c-1)p/p_0]}, \quad c = \text{const}, \tag{6}$$

where p_0 is the saturation gas pressure. After substituting relationships (5) and (6) into formula (3), we obtain the following expressions:

for monolayer adsorption with dissociation of gas molecules,

$$a_p^* = a_p^0\left[1 - \frac{2kT\Gamma_m\ln(1 + \sqrt{b_2 p})}{\gamma_c^0}\right]^n; \tag{7}$$

for multilayer adsorption (without dissociation) of gas molecules,

$$a_p^* = a_p^0\left[1 - \frac{2kT\Gamma_m\ln\left(1 + \dfrac{cp/p_0}{1 - p/p_0}\right)}{\gamma_c^0}\right]^n. \tag{8}$$

The work a_p is related to the critical stress intensity factor K_c through the expression $a_p = BK_c^2$ (B = const). Hence, from expressions (4), (7), and (8), we obtain the following relationships:

for monolayer adsorption of gas molecules in a crack mouth (without dissociation),

$$K_c^* = K_c^0\left[1 - \frac{kT\Gamma_m\ln(1 + b_1 p)}{\gamma_c^0}\right]^{n/2}; \tag{9}$$

for monolayer adsorption (with dissociation into atoms),

$$K_c^* = K_c^0\left[1 - \frac{2kT\Gamma_m\ln(1 + \sqrt{b_2 p})}{\gamma_c^0}\right]^{n/2}; \tag{10}$$

for multilayer adsorption (without dissociation),

$$K_p^* = K_p^0\left[1 - \frac{2kT\Gamma_m \ln\left(1 + \frac{cp/p_0}{1 - p/p_0}\right)}{\gamma_c^0}\right]^{n/2}. \quad (11)$$

Let us now numerically estimate the effect of the physical hydrogen adsorption on the work a_p for structural steels. The surface energy for a structural steel in vacuum is taken to be $\gamma_c^0 = 1000$ erg cm^{-2}. By assuming that $n = 1$, $b_1 = 3.7 \times 10^2$ Pa^{-1}, and $\Gamma_m = 12 \times 10^{14}$ cm^{-2} in relationship (4) [15], we find that the H_2 pressure of the order of 133 Pa at temperature $T = 293$ K decreases the work of plastic deformation by ≈40% (as compared to this quantity in vacuum). This result is in good agreement with the experimental data obtained by Fedchenko *et al.* [16].

3. THE INFLUENCE OF CHEMICAL ADSORPTION OF GASES

Chemical adsorption (chemisorption) is associated with the transformation of the electron shells due to the interaction of the atoms of the medium with the atoms of the deformed solid. A chemisorbed compound involves a stable monolayer [17], in which molecules of the medium are bonded to the atoms of the material through strong covalent forces. In the case of chemisorption, unlike physical adsorption, not all molecules of the medium, but only those with the necessary activation energy, can be bonded to the atoms of the surface. This reaction is an exothermal heterogeneous process occurring at temperatures $T \geq 200$°C. According to Roberts and McKee [18], the gas molecules impinging on the surface of the solid transform into a presorption state. From the presorption state, these molecules are either chemisorbed at a rate $V_+ = \alpha C f(\theta) e^{-E_+/kT}$ (α = const) or desorbed at a rate $V_- = \beta C e^{-E_-/kT}$. Here, C is the surface concentration of gas molecules in the presorption state, E_+ is the activation energy of chemisorption, E_- is the activation energy of desorption, and $f(\theta)$ is the relative fraction of free centers of chemisorption.

Following Trapnell [17], we can write the following expressions:

$$V_+ - V_- = \frac{q}{\sqrt{2\pi mkT}[1 + \varphi t]},$$

$$\varphi = e^{(E_+ - E_-)/kT}, \quad q = \text{const}.$$

Here, m is the mass of a gas molecule.

The decrease in the surface energy of the material $d\gamma_c$ for time dt is determined from the equality $d\gamma_c = -\alpha(V_+ - V_-)dt$. Upon substituting the above expression for $V_+ - V_-$ into the right-hand part of this equality and integrating, we find

$$\gamma_c^* = \gamma_c^0\left[1 - \frac{\alpha q \ln(1 + \varphi t_*)}{\varphi\gamma_c^0\sqrt{2\pi mkT}}\right].$$

From this expression, we obtain the critical stress intensity factor

$$K_c^* = K_c^0\left[1 - \frac{\alpha q \ln(1 + \varphi t_*)}{\varphi\gamma_c^0\sqrt{2\pi mkT}}\right]^{n/2}. \quad (12)$$

When the time required for the onset of the fracture t_* is very short, the condition $\ln(1 + \varphi t_*) = \varphi t_* \ll 1$ is satisfied; consequently, we have

$$K_c^* \approx K_c^0\left[1 - \frac{\alpha q n t_*}{2\gamma_c^0\sqrt{2\pi mkT}}\right]^{n/2}.$$

Conversely, if the condition $\varphi t_* \gg 1$ is satisfied, we obtain $\ln(1 + \varphi t_*) \approx \ln(\varphi t_*)$. Taking this circumstance into account, from formula (12), we derive the following relationship:

$$t_* \approx \frac{1}{\varphi}\exp\left[\frac{\varphi\gamma_c\sqrt{2\pi mkT}}{\alpha q}\left(1 - \frac{K_c^*}{K_c^0}\right)^{2/n}\right].$$

This relationship is similar to the known formula proposed by S.N. Zhurkov (see the monograph by Regel *et al.* [19]).

ACKNOWLEDGMENTS

This work was supported by the Russian Foundation for Basic Research, project no. 03-01-00601.

REFERENCES

1. V. I. Likhtman, P. A. Rebinder, and G. V. Karpenko, *The Influence of a Surface-Active Medium on Processes of Metal Deformation* (Nauka, Moscow, 1974) [in Russian].
2. G. V. Karpenko, *The Influence of a Medium on the Strength and Durability of Metals* (Naukova Dumka, Kiev, 1976) [in Russian].
3. J. D. Fast, *Interaction of Metals and Gases* (Centrex, Eindhoven, 1965 and 1971; Metallurgiya, Moscow, 1975), Vols. 1 and 2.
4. B. D. Kolachev, *Hydrogen Brittleness of Metals* (Metallurgiya, Moscow, 1985) [in Russian].
5. A. V. Stepanov, *Fundamentals of Practical Strength of Crystals* (Nauka, Leningrad, 1974) [in Russian].
6. V. I. Betekhtin, S. Yu. Veselkov, Yu. M. Dal', A. G. Kadomtsev, and O. V. Amosova, Fiz. Tverd. Tela (St. Petersburg) **45** (4), 618 (2003) [Phys. Solid State **45**, 649 (2003)].
7. P. A. Rebinder and E. D. Shchukin, Usp. Fiz. Nauk **108** (1), 3 (1972) [Sov. Phys. Usp. **15**, 533 (1973)].

8. D. McLean, *Mechanical Properties of Metals* (Clarendon, Oxford, 1961; Metallurgiya, Moscow, 1965).
9. D. H. Kaelbly, J. Appl. Polym. Sci. **18** (6), 1869 (1974).
10. V. M. Finkel', *Physics of Fracture* (Metallurgiya, Moscow, 1970) [in Russian].
11. *Interphase Gas–Solid Boundary* (Mir, Moscow, 1970).
12. A. W. Adamson, *The Physical Chemistry of Surfaces*, 4th ed. (Wiley, New York, 1982; Mir, Moscow, 1979).
13. A. Zangwill, *Physics at Surfaces* (Cambridge Univ. Press, Cambridge, 1988; Mir, Moscow, 1990).
14. I. O. Protod'yakonov and S. V. Siparov, *Mechanics of Adsorption Process in the Gas–Solid Systems* (Nauka, Leningrad, 1985) [in Russian].
15. G. W. C. Kaye and T. H. Laby, *Tables of Physical and Chemical Constants and Some Mathematical Functions*, 16th ed. (Longman, New York, 1995; Fizmatgiz, Moscow, 1962).
16. V. S. Fedchenko, A. I. Radkevich, and L. M. Korvatskiĭ, Fiz.-Khim. Mekh. Mater. **12** (4), 96 (1976).
17. B. M. W. Trapnell, *Chemisorption* (Butterworths, London, 1955; Inostrannaya Literatura, Moscow, 1958).
18. M. W. Roberts and C. S. McKee, *Chemistry of the Metal–Gas Interface* (Clarendon, Oxford, 1978; Mir, Moscow, 1981).
19. V. R. Regel, A. I. Slutsker, and É. E. Tomashevskiĭ, *Kinetic Nature of the Strength of Solids* (Nauka, Moscow, 1974) [in Russian].

Translated by O. Moskalev

Physics of the Solid State, Vol. 47, No. 5, 2005, pp. 856–862. Translated from Fizika Tverdogo Tela, Vol. 47, No. 5, 2005, pp. 830–836.

The Kinetics and Energy Balance of Mechanochemical Transformations

P. Yu. Butyagin and A. N. Streletskiĭ

Semenov Institute of Chemical Physics, Russian Academy of Sciences, ul. Kosygina 4, Moscow, 119991 Russia
e-mail: str@center.chph.ras.ru

Abstract—The kinetic theory of strength formulated by Zhurkov is expanded to include an energy consumption analysis of the processes of deformation and fracture of solids and their compounds. The dependence of the kinetics of the structure defect formation and of chemical reactions in the processes of deformation and fracture of solids on the energy expended is found. Experiments and calculations concerning energy yields of the defect formation, deformational mixing, and mechanochemical reactions are discussed. © *2005 Pleiades Publishing, Inc.*

1. INTRODUCTION

The Zhurkov equation [see Eq. (1) below] is the foundation of both the kinetic theory of strength and mechanochemistry, the study of the reactivity of solids during their deformation and fracture. This paper presents an analysis of the kinetics and energy consumption in the processes of the formation of crystal structure defects, deformational mixing, and chemical synthesis in solids under mechanical load.

2. THE ZHURKOV MODEL

The kinetics of the interatomic-bond rupture caused or assisted by elastic deformation of solids is usually analyzed in terms of classical chemical kinetics. This approach was developed by Zhurkov [1] and his coworkers from a hypothesis to an elegant theory in numerous papers. A summary can be found in the now classic work [2].

According to the Zhurkov theory, the exact moment at which a solid is destroyed by a mechanical load depends on the lifetime before rupture of deformed interatomic bonds:

$$\tau = \tau_0 \exp(U_0 - \gamma\sigma)/RT, \qquad (1)$$

where τ is the lifetime before rupture, τ_0 is the period of atomic oscillations, $(U_0 - \gamma\sigma)$ is the reaction activation energy, U_0 is the bond energy, and the product $\gamma\sigma$ is an equivalent of the deformation energy.

3. ENERGY RELATIONS IN THE ZHURKOV MODEL

Kinetic equation (1) used in the Zhurkov model implies that there is an ensemble of deformed interatomic bonds and that the process ends with fracture. However, the fracture is accompanied by the relaxation of residual stresses in the entire bond ensemble after the moment of fracture. Hence, according to Zhurkov, the thermally activated rupture of deformed bonds is supplemented by a subsequent relaxation of energy accumulated before the rupture. The rupture and subsequent energy relaxation differ in terms of calorific effect, its sign, and characteristic times. Thermally activated rupture is an endothermic reaction, while relaxation is an exothermic process. Therefore, the equation of energy balance is (Fig. 1a)

$$A = Q_{\text{rel}} + \sum N_i H_i'. \qquad (2)$$

The ensemble of interatomic bonds is deformed and broken by applied work A; free radicals and atoms with low coordination numbers created at the point of rupture have a net excess energy $\sum N_i H_i'$ (where H_i' is the partial molar enthalpy of one of the products of the rup-

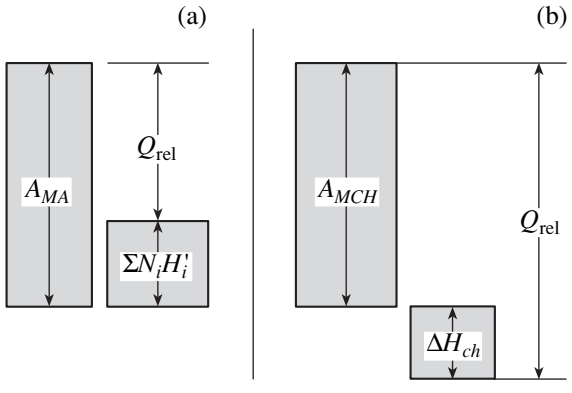

Fig. 1. Relations (a) between the work done in creating structural defects A_{MA} and the defect enthalpy $\sum N_i H_i'$ and (b) between the work done during mechanochemical synthesis A_{MCH} and the mechanochemical reaction enthalpy ΔH_{ch}.

1063-7834/05/4705-0856$26.00 © 2005 Pleiades Publishing, Inc.

ture and N_i is the fraction of defects of this kind). After the rupture, the deformation energy of bonds in the parts released from stress is transformed into heat Q_{rel} over the time span τ_{rel}. The release of Q_{rel} is often accompanied by secondary dissociation reactions which produce low molecular–weight products [3–5].

4. ENERGY YIELDS OF MECHANOCHEMICAL PROCESSES

The energy yield G of a mechanochemical process is the ratio of the amount of the product ΔN (in moles) to the expended energy, that is, to the dose D:

$$G = \Delta N/D \text{ [mol/J]}. \quad (3)$$

The inverse of the yield $A = 1/G$ [J/mol], the formation energy, characterizes the work done to create products of the mechanochemical process.

The concept of the energy yield [6, 7] is valid for the process of formation of point defects, dislocations, grain boundaries, and phase boundaries, as well as for structural and chemical transformations that occur during the deformation and fracture of crystals and their mixtures.

The diagrams in Fig. 1 qualitatively show the energy balance of structural defect creation and mechanochemical transformation. A mechanical load, which is applied in order to create structural defects and/or active centers, always leads to an exothermic process of energy relaxation, i.e., a release of heat (Fig. 1a) $Q_{rel} = A_{MA} - \sum N_i H_i'$.

During a mechanochemical reaction, the work A_{MCH} is spent on grinding and deformational mixing of the components. Finally, a synthesis takes place ($X_S + Y_S \longrightarrow XY_S$) and the system transfers to the energy level ΔH_{ch}. Additional heat from the synthesis reaction ΔH_{ch} is produced in the process. Therefore, in this case, Q_{rel} consists of the expended energy A_{MCH} and the reaction heat ΔH_{ch} (Fig. 1b): $Q_{rel} = A_{MCH} + \Delta H_{ch}$. The quantities A and G characterize the way the elastic energy is converted into the energy of crystal defects or products of chemical reactions.

The most popular equipment for mechanical activation of powder materials and carrying out mechanochemical processes is energy-intensive mills of various types. Systematic measurements [8] and calculations [9, 10] of the energy intensity (specific power) I [W/g] of mechanochemical reactors of different types were performed in order to determine the work A_{MA} or A_{MCH} done during mechanical processing of powders. Various methods of measuring the energy intensity (calorimetric method, test-object method, etc.) are described in [10, 11]. The energy intensity of mechanochemical reactors is 10^{-1}–10^2 W/g, and the mechanical energy dose D transferred to the powder material can be as high as $D = It \sim 10^2$–10^3 kJ/g.

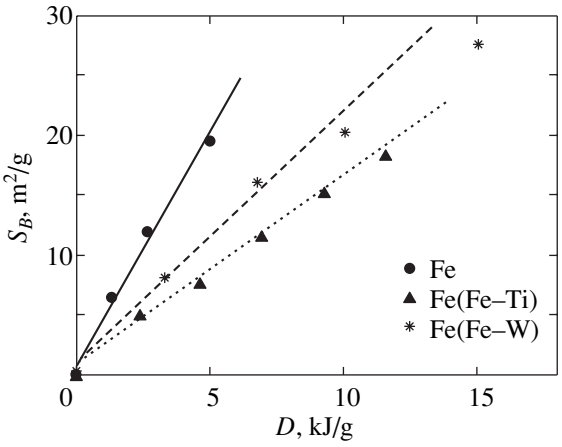

Fig. 2. Growth of the surface area S_B of iron grain boundaries during mechanical processing of Fe and powder mixtures Fe/X = 80/20 (data taken from [21]).

5. DEFECT FORMATION ENERGY

5.1. Dislocation Processes

Dislocation-assisted plastic deformation can be described by a model in which an advance of atomic configuration by one step (the lattice parameter) results from the regrouping of atomic bonds under a shear stress σ_T. The work done at each step is $\sigma_T V_0$ (where V_0 is the atomic volume), and the strain ε depends directly on the absorbed energy (dose) D: $\varepsilon = f(D)$. If the concentration of dislocations is low, the interaction between them can be neglected and all steps are equivalent (σ_T = const). In this case, the energy characteristic of a regrouping event is the energy yield G, given by $G = 1/\sigma V_0$.

All the main dislocation processes—multiplication of dislocations, their annihilation and merging into grain boundaries, capture of impurities by dislocations, etc.—also depend on the dose D.

5.1.1. Multiplication of dislocations. The expected energy yield of dislocation multiplication can be estimated using the Frank–Read model. According to this model, before an atom is inserted into a dislocation line, the dislocation bows out and is stretched between two pinning points. The tension of a dislocation segment favors inserting lattice atoms into the dislocation line, and its flexure sweeps a section of the slip plane under the dislocation loop.

If a dislocation segment is displaced from position A to position A' by a distance dR, its length l grows by dl (see, e.g., [12, Figs. 3–16]). In this case, dl/b atoms (where b is the lattice parameter) are inserted into the dislocation and the dislocation loop in the slip plane sweeps over an area containing $n_S = ldR/b^2$ lattice sites. Atoms inserted into the dislocation line increase its energy by $W_b dl/b$ (where W_b is the dislocation energy per length b), and the work done is $n_S \sigma_T V_0$.

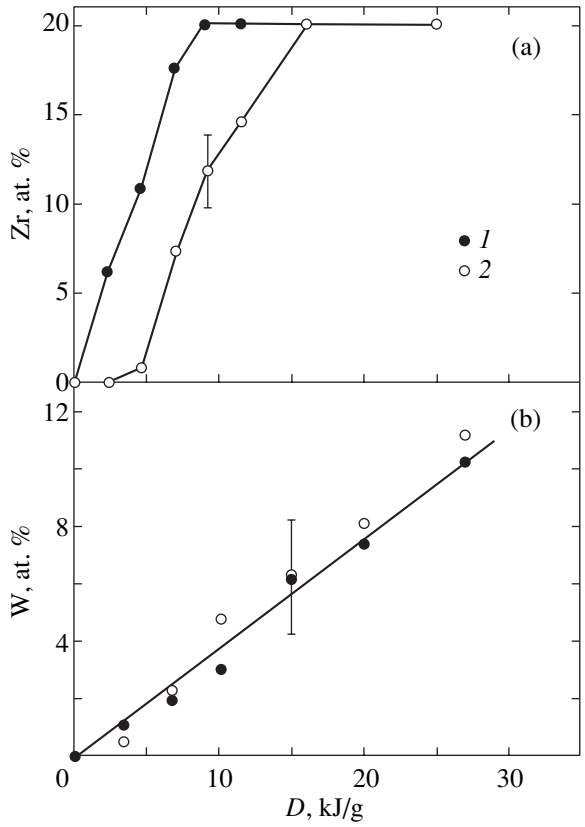

Fig. 3. (*1*) Consumption of the component *X* and (*2*) appearance of *X* in the products during deformational mixing of the Fe/*X* mixtures for (a) *X* = Zr and (b) *X* = W (data taken from [21]).

The energy yield of the dislocation multiplication G_D is given by the ratio of the number of atoms inserted into the dislocation to the work done in this process:

$$G_D = 1/\{W_b + \sigma V_0(R/b)\}. \quad (4)$$

The maximum energy yield $G_D^{\max}$ is achieved when both terms in the denominator of Eq. (4) are equal. In this case, $G_D^{\max} \sim 1$ mol/MJ. The actual yield G_D is much lower than $G_D^{\max}$ and is estimated below by using the results obtained by Gilman [13]. According to [13], the dislocation generation rate dN_D/dt during plastic flow, as well as the strain rate $d\varepsilon/dt$, is proportional to the dislocation concentration N_D:

$$dN_D/dt \approx M v_D N_D, \quad (5a)$$

$$d\varepsilon/dt \approx b v_D N_D. \quad (5b)$$

Here, v_D is the gliding velocity of dislocations [m/s] and M is the dislocation multiplication factor [m^{-2}]. The values of M for a number of crystals are listed in Table 1.

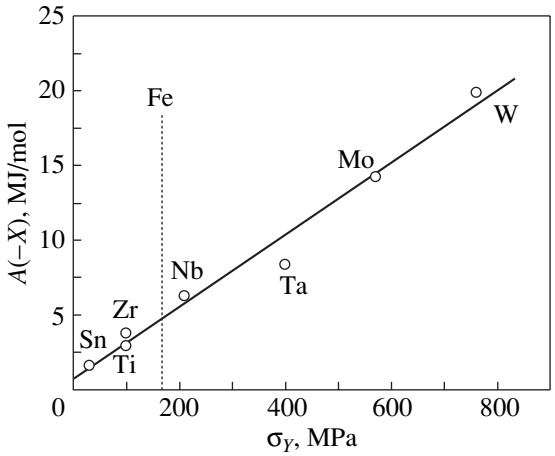

Fig. 4. Work $A(-X)$ done during the deformational mixing of a Fe/*X* mixture as a function of the yield stress σ_Y of the component *X* (data taken from [22]).

It follows from Eqs. (5a) and (5b) that the energy yield of the dislocation multiplication G_D is given by

$$G_D = (dN_D/dt)/\sigma_T(d\varepsilon/dt) \quad \text{or} \quad G_D = M/(b\sigma_T). \quad (6)$$

Estimations made using Eq. (6) and the available M data (Table 1) show that the G_D values for a number of metals (Al, Cu, Fe, Ni) fall in the range 0.005–0.1 mol/MJ. According to the Gilman model, the main contribution to the work done in the generation of dislocations A_D is due to internal friction, which is inevitable during dislocation formation.

5.1.2. Grain boundary formation. Grain boundaries in ductile metals are usually formed by polygonization. In this process, the mean free path of dislocations before merging into grain boundaries is

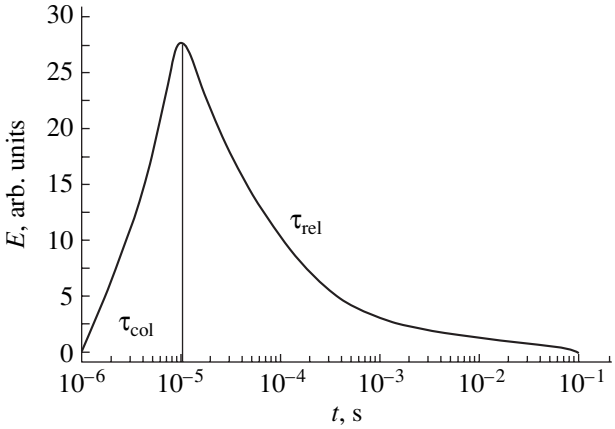

Fig. 5. Energy transformations for impact of a ball and a powder material: the inelastic interaction between the ball and the powder lasts for $\tau_{col} \sim 10^{-5}$ s followed by a relaxation of stresses for τ_{rel} ($\tau_{rel} \gg \tau_{col}$). The stresses are characterized by a wide range of relaxation times.

comparable to the size L of the crystallites being created (for example, to the size L_{RCS} of the coherent scattering regions). In this case, the work done to create grain boundaries A_B can be estimated as $A_B = L_{RCS}N_S\sigma_T V_0$, where N_S is the surface density of atoms on the grain boundaries. According to estimations based on this model, the work done in the formation of grain boundaries is about $10–10^2$ J/m^2 [14]; that is, A_B is tens or hundreds of times larger than the boundary energy.

The work A_B was measured for various metals (Fig. 2, Table 2) by mechanical processing of powder materials. The area of the boundaries created was estimated by analyzing the shape of x-ray diffraction lines and calculating the size of coherent scattering regions ($S_B \sim 1/L_{RCS}$). The work A_B in metals (corresponding to the slope of the lines in Fig. 2) remains constant as the crystallite size decreases to tens of nanometers. For the majority of metals, A_B is in the range $10^2–10^3$ J/m^2; i.e., there is agreement, in order of magnitude, with the expected values.

Usually, the energy yield of dislocation processes G_0 depends only slightly on the parameters of mechanical processing, such as the temperature and intensity (dose rate).

Table 1. Dislocation multiplication factor M according to Gilman [13]

Crystal	M, 10^{-2} m^{-2}
Ta	1000
Ag	230
Fe	30–250
Al	80
Cu	50
Ni	8
Ge	1
KCl	0.5

Table 2. Work done in forming grain boundaries during mechanical processing of metal powders

Metal	A_B, J/m^2
Al	120
Fe	230
Ni	220
Cu	310
Ag	530
W	710

5.2. Surface Formation

5.2.1. Crystal cleavage. The growth of a crack during cleaving of a brittle crystal can be taken as a model of the formation of a new surface with a relatively small amount of energy required.

For example, it is common to assume that, in the Griffiths relation, the work δA_S done to increase the surface area during the expansion of a cavity in the bulk of a crystal is equal, in a first approximation, to the increase in the surface energy:

$$\delta A_S = \gamma \delta S. \quad (7)$$

Here, S is the surface area of the cavity and γ is the surface energy.

However, Eq. (7) is valid only at thermodynamic equilibrium. In actual conditions, when a crack grows during a destruction process, the energy is lost to collateral processes: plastic deformation of the surface layer (A_{SL}) and electrization of the crack walls (A_E). In addition, the separating parts of the crystal acquire kinetic energy (A_K) and, in practice, it is difficult to avoid friction between them (A_F). Therefore, the actual value of A_S significantly exceeds the surface energy γ: $A_S = \gamma + A_K + A_{SL} + A_E + A_F$.

These terms can be calculated using different models. The kinetic energy of the separating parts of the crystal is calculated using equations of theoretical mechanics based on measurements of the crack growth rate and geometry of the sample. In order to estimate the plastic deformation, the following model of interaction between the growing crack and dislocations is used: the compression region in front of the propagating crack tip does not cut the transverse dislocation as a knife cuts a thread but rather drags it and stretches the dislocation along the crack edges at a small depth [15]. Afterward, the elastic stresses of deformed parts of the cleaved crystal push the dislocations out to the surface. The number of dislocations can be measured by counting the atomic steps on the mirror-smooth cleavage surface.

Dislocations in crystals are electrically charged. They take this charge outside when they come to the surface from the surface layer. The cleavage is rarely exactly symmetric; the thinner part is more bent than the broader part. Therefore, in the thinner part, there are more dislocations, which take their charge to the surface [16]. The difference in charge density between the opposite sides of the crack can reach tens of CGSE/cm^2 (up to 10^{10} elementary charges per square centimeter). Growth of such a crack can be stopped by an electric field [17].

The work A_E done to separate the charged walls of the crack can be calculated using formulas for a capacitor [18]. If the cleavage takes place in vacuum, the charge is preserved at its maximum all along the crack and the electrostatic component A_E of the destruction energy is maximum. The charge is so large that electrons are torn off the surface and accelerated up to doz-

Table 3. Main channels of energy absorption during crack growth in LiF crystal, in units of A_i/γ [7]

γ	A_K	A_{SL}	A_E
1	3–5	>10	2

Table 4. Work done in forming the surface during milling measured by the Brunauer–Emmet–Teller method

Compound	A_S, J/m^2
BN	6
Graphite	30–60
Nb_2O_5	30
SiO_2	100
Si	900

ens of kiloelectronvolts in the electric field of the crack (the Deryagin effect [18]).

Contributions from different channels of energy absorption in the process of crack growth in LiF crystals are compared in Table 3, which is compiled from review [7]. Energy losses in each channel are normalized to the surface energy of the LiF crystal. It is clear that the work done in forming a surface is 10–20 times larger than the surface energy even neglecting the friction term. The quantity A_S depends on the crack growth rate and the defect concentration in the crystal. There are numerous papers devoted to the nature of collateral processes (see, e.g., review [16]).

5.2.2. Milling. A high specific surface area of tens and hundreds of square meters per gram, to which formally correspond particle sizes of 10^{-8}–10^{-7} m, is obtained by milling layered and brittle materials.

The specific surface of graphite increases in proportion to the dose up to ~ 350–400 m^2/g. The surface formation energy of graphite remains constant in the range of mill power (energy intensity) from 0.35 to 80 W/g [10, Fig. 2]. Therefore, A_S is an energy parameter of the surface formation of the material.

Values of A_S for several layered and brittle materials are compared in Table 4. It is clear that A_S of different materials varies within more than two orders of magnitude. A new surface is most easily created in layered materials (boron nitride, graphite). A_S of silicone oxide reaches 100 J/m^2. Surface formation is most difficult for silicon [19].

Thus, in all the examples considered above, the work done to create structural defects through the mechanical processing of crystals is several orders of magnitude higher than the partial molar enthalpy of the defects themselves and the main contribution to G and A comes from external or internal friction.

6. DEFORMATIONAL MIXING AND MECHANOCHEMICAL SYNTHESIS

The deformational mixing and mechanochemical synthesis are achieved by mechanically processing several components of a reaction mixture, alloy, or composite together. The components are ground and mixed, and the accumulated energy is released in the formation of the crystal structure of the products.

To model deformational mixing and/or synthesis in a ball mill, where the material is subjected to multiple pulsed loads (~10^{-5} s), a method based on the energy balance is used. During an inelastic impact, the ball transfers an energy dose D^* to the powder material. As a result, synthesis products form in the powder mixture and the energy of chemical reaction $GS\Delta HD^*$ is released. Here, G is the energy yield of the reaction per unit contact area [(mol/MJ)/(m^2/g)], S is the specific surface of the contact [m^2/g], and ΔH is the transformation enthalpy [J/mol]. Therefore, the relaxation energy Q_{rel} is given by

$$Q_{\text{rel}} \approx (1 + GS\Delta H)D^*. \quad (8)$$

Equation (8) establishes the relation between the relaxation energy Q_{rel} and the intensity of milling (the surface formation energy is $S \sim 1/A$), the intensity of mixing (G), the reaction enthalpy ΔH, and the impact energy D^*. The relaxation energy Q_{rel} affects the kinetics of product formation, its type, and the chemical composition. A prominent example is explosive deformational processes [20]. In order to achieve self-propagating high-temperature synthesis, the adiabatic temperature during relaxation has to be higher than the melting temperature of one of the mixture components.

As an example of cold mechanical fusion, we consider the atomic mixing of two-component combinations of bcc metals 80Fe + 20X, where X is Sn, Ti, Zr, Nb, Ta, Mo, or W [21, 22]. For all the compositions, the Fe grain boundary area was observed to grow as a result of milling, the X component was consumed, and X atoms appeared in the Fe phase as a result of mixing. For a conversion fraction of up to 0.5–0.75, the energy characteristics of milling A_S(Fe) and mixing $A(-X)$ and $A(+X)$ are constant (Figs. 2, 3) and the work $A(-X)$ that characterizes solving the X phase in α-Fe is proportional to the yield stress of the metal X. This rule holds for all metals from Sn to W (Fig. 4).

The behavior of the atoms of the dissolved component depends on its nature. Atoms of Nb, Ta, Mo, and W appear in the solid solution simultaneously with their disappearance from the initial phase X (Fig. 3b); they form crystalline (Mo, W) or amorphous (Nb, Ta) solutions in α-Fe. The yield stress (σ_Y) of Nb, Ta, Mo, and W is higher than σ_Y of Fe, and we can presume that the deformational mixing in this group of metals occurs through the substitution of Fe atoms by X in the lattice.

Atoms of Sn, Ti, and Zr leave their phases as fragments (clusters), which cannot be detected using x-ray

analysis (i.e., L_{RCS} < 1–2 nm), and appear significantly later with respect to the dose in the structure of crystalline or amorphous solutions (Fig. 3a). Thus, in the succession of Fe + *X* mixtures, the mechanism of deformational mixing—the atomic solution for refractory metals and fragmentation for softer metals (Sn, Ti, Zr)—depends on the relation between the yield stress values of the components.

Similarly, the products of mechanochemical reactions of the type $X_S + Y_S \longrightarrow XY_S$ form either immediately at the contact of reagents (in this case, $G(XY) \sim \delta S_{XY}/\delta D$; for example, the reaction $Nb_2O_5 + PbO \longrightarrow Pb_2Nb_2O_7$ [23]) or during the mass-transfer processes in the contact zone. The latter case is prevalent, and the energy yield of the products $G(XY) = \delta\alpha/\delta D$ (where α is the conversion fraction) is proportional to the interphase boundary area $S_{X/Y}$:

$$\delta\alpha/\delta D \sim S_{X/Y}. \quad (9)$$

7. RELAXATION EFFECTS

The diagram in Fig. 5 shows the kinetics of energy transformations for the case when reagents or their mixtures are subjected to a pulsed load. For example, the inelastic impact of a ball is only $\tau_{col} \approx 10^{-5}$-s long and during this period the kinetic energy of the ball is transferred to the powder of reagents. The powder absorbs the energy dose D^* and turns to a nonequilibrium state where external stresses no longer act and internal residual stresses relax, causing the material to transfer to the equilibrium state. From experience, it is known that the relaxation time τ_{rel} is usually much longer than the duration of the impact of a ball and material and also that there is a wide range of relaxation times.

Short relaxation times are measured by analyzing the reactivity of solids with gases during the destruction process. It turns out that the yields of heterogeneous reactions of hydrogen and oxygen with silicon oxide [24], of oxygen with silicon [25], and of carbon oxide with zirconium [26] during mechanical processing are tens times greater than those after the processing is terminated. In order to determine the relaxation times from the decrease in the chemical activity, we can use the dependence of the yield of the heterogeneous reaction $X_S + Y_G$ on the gas pressure. When the pressure is high, the yield is maximum, because molecules hit the surface at a high rate and all of them become involved in the reaction. When the pressure is low, the reaction yield is low, because the fresh surface loses its reactivity due to relaxation before it is hit by a gas molecule. A drawback of this method is that the relaxation times remain uncertain because the adhesion factor is unknown.

Slow relaxation and a gradual accumulation of residual stresses were discovered using the method of intermittent mechanical processing. The mechanical processing was periodically terminated for a given time and resumed after a pause. For the quasi-explosive mechanochemical synthesis [20], periodic breaks of 10–30 min caused a significant increase in the induction period. Similar experiments with "resting" breaks of several hours [27] confirmed the long relaxation time in the Fe + C system. Quenching and subsequent thermal relaxation of phases with an excess energy of molecular interaction were studied in experiments on polymers in [28].

Thus, the wide range of the relaxation times is established experimentally but information about the limits and mechanisms of the relaxation is still lacking.

8. CONCLUSIONS

In the studies we have discussed, a method of energy balance analysis of structural and mechanochemical transformations during plastic deformation and fracture of solids was developed and quantitatively substantiated.

There are several fields concerned with the effects of deformation and fracture. The values of deformations and stresses and the state of the crystal structure immediately prior to the point of failure, which itself is defined by Eq. (1), are important for the kinetic theory of strength created by Zhurkov and his co-workers. The chemical structure and reactivity of deformed materials, low-coordinated atoms and free radicals, fragments of molecules and ions, and excited states carrying an excess energy Q_{rel} released after fracture are important for mechanochemistry.

The moment of rupture of atomic bonds is both the critical point in the diagram of the mechanical properties and the staring point for the release of accumulated energy and a drastic increase in reactivity. Zhurkov and his coworkers considered processes separated by the breaking point together, but the tradition has not always been followed in recent years; strength theory and mechanochemistry are drifting apart in the flux of practical applications.

In the present paper, we tried to return to the complex consideration of destruction and reactivity based on analysis of the energy properties of these processes.

ACKNOWLEDGMENTS

This work was supported by the Russian Foundation for Basic Research (project no. 04-03-32215), the program of the Russian Academy of Sciences "Controlled Synthesis of Compounds with Given Properties and Creation of Novel Functional Materials" (grant no. 12/04, dated May 11, 2004), and the program of the Chemical Sciences and Medicine Division of the Russian Academy of Sciences "Creation of Novel Metallic, Ceramic, Glass, Polymer, and Composite Materials."

REFERENCES

1. S. N. Zhurkov and B. N. Narzulaev, Zh. Tekh. Fiz. **23**, 1677 (1953).
2. V. R. Regel', A. I. Slutsker, and É. E. Tomashevskiĭ, *Kinetic Nature of the Strength of Solids* (Nauka, Moscow, 1974) [in Russian].
3. V. R. Regel', T. M. Muinov, and O. F. Pozdnyakov, Fiz. Tverd. Tela (Leningrad) **4**, 2468 (1962) [Sov. Phys. Solid State **4**, 1809 (1962)].
4. V. A. Radtsig, V. S. Pudov, and P. Yu. Butyagin, Vysokomol. Soedin., Ser. B **9** (6), 414 (1967).
5. N. S. Enikolopjan, L. S. Zarxin, and E. V. Prut, J. Appl. Polym. Sci. **30**, 2291 (1985).
6. P. Yu. Butyagin and I. K. Pavlychev, React. Solids **1**, 361 (1986).
7. P. Yu. Butyagin, Chem. Rev. **23** (2), 89 (1998).
8. A. B. Borunova, Yu. V. Zhernovenkova, A. N. Streletskiĭ, and V. K. Portnoĭ, *Treatment of Dispersed Materials and Media* (Odessa, 1999), No. 9, p. 158.
9. N. Burgio, A. Iasonna, M. Magini, S. Martelli, and F. Padella, Nuovo Cimento D **13**, 459 (1991).
10. A. N. Streletskii, in *Proceedings of 2nd International Conference on Structural Applications of Mechanical Alloying*, Ed. by J. J. de Barbadillo, F. H. Froes, and R. Swartz (Vancouver, 1993), p. 51.
11. P. Yu. Butyagin, A. R. Kuznetsov, and I. K. Pavlychev, Prib. Tekh. Éksp., No. 6, 771 (1986).
12. P. Yu. Butyagin, *Chemical Physics of Solid State: Diffusion and Reactivity* (Mosk. Fiz.–Tekh. Inst., Moscow, 1991), p. 95 [in Russian].
13. J. J. Gilman, J. Appl. Phys. **31**, 2208 (1960).
14. P. Yu. Butyagin, Yu. V. Zhernovenkova, and I. V. Povstugar, Kolloidn. Zh. **65** (2), 163 (2003) [Colloid. J. **65**, 141 (2003)].
15. S. I. Burns and W. W. Webb, J. Appl. Phys. **41**, 2078 (1970).
16. M. I. Molotskii, Sov. Sci. Rev., Sect. B **13**, 1 (1989).
17. V. M. Finkel', Yu. I. Tyalin, Yu. I. Golovin, L. N. Muratora, and M. V. Gorsheneva, Fiz. Tverd. Tela (Leningrad) **21**, 1943 (1979) [Sov. Phys. Solid State **21**, 1116 (1979)].
18. B. V. Deryagin, N. A. Krotova, and V. P. Smilga, *Adhesion of Solids* (Nauka, Moscow, 1973) [in Russian].
19. A. N. Streletskiĭ, A. V. Leonov, and P. Yu. Butyagin, Kolloidn. Zh. **63** (5), 690 (2001) [Colloid. J. **63**, 630 (2001)].
20. P. Yu. Butyagin and K. B. Shelimov, Dokl. Akad. Nauk SSSR **316** (6), 1439 (1991).
21. I. V. Povstugar and P. Yu. Butyagin, J. Mater. Sci. **39**, 5461 (2004).
22. P. Yu. Butyagin and I. V. Povstugar, Dokl. Akad. Nauk **398** (5), 1 (2004).
23. A. N. Streletskiĭ, A. B. Borunova, P. A. Shiryaev, and D. P. Shashkin, Zh. Fiz. Khim. **69** (5), 980 (1995).
24. A. V. Bystrikov, I. V. Berestetskaya, A. N. Streletskiĭ, and P. Yu. Butyagin, Kinet. Katal. **21** (3), 765 (1980).
25. P. Yu. Butyagin, A. N. Streletskiĭ, I. V. Berestetskaya, and A. V. Borunova, Kolloidn. Zh. **63** (5), 699 (2001).
26. A. N. Streletskiĭ, P. Yu. Butyagin, and A. V. Leonov, Kolloidn. Zh. **58** (2), 248 (1996).
27. P. Matteazzi, F. Miani, and G. LeGaer, J. Hard Mater. **2** (3–4), 171 (1991).
28. P. Butyagin, Sov. Sci. Rev., Sect. B **14**, 1 (1989).

Translated by G. Tsydynzhapov

Physics of the Solid State, Vol. 47, No. 5, 2005, pp. 863–868. Translated from Fizika Tverdogo Tela, Vol. 47, No. 5, 2005, pp. 837–842.

Dynamic Diffusion of Helium into Various Types of Solids during Their Deformation and Dispersion

O. V. Klyavin, B. A. Mamyrin, L. V. Khabarin, and Yu. M. Chernov

Ioffe Physicotechnical Institute, Russian Academy of Sciences, Politekhnicheskaya ul. 26, St. Petersburg, 194021 Russia
e-mail: klyavin@mail.ioffe.ru

Abstract—Quantitative relations governing the penetration of helium atoms into various types of solids in the course of their plastic deformation in liquid ^{3}He (T = 0.6–1.8 K) and ^{4}He (T = 4.2 K) and dispersion in gaseous helium at 300 K were obtained and analyzed. Experiments were carried out on metals with different lattice types, ionic single crystals, amorphous alloys, and barite and titanium dioxide powders dispersed in helium. Curves illustrating helium extraction from deformed specimens under dynamic annealing were obtained. The temperature range of helium extraction was found to correlate with the melting temperature and the initial and deformed structures of a material, which determine the number and character of helium traps present in the material. The dependence of helium penetration intensity on the type of defects forming under plastic deformation for various materials, as well as the formation of chemical bonds of helium atoms to the defected structure of these materials, is discussed. © *2005 Pleiades Publishing, Inc.*

1. INTRODUCTION

Studies of the mechanochemical penetration of particles of an ambient medium into various types of solids are based on the experimentally observed phenomenon of dislocation-mediated dynamic diffusion (DMDD), i.e., the penetration of atoms and molecules of the ambient medium into crystalline materials over nucleating and moving dislocations in the course of plastic deformation [1, 2]. The gradient of chemical potential at the ambient-medium–solid interface, as well as the large amplitudes of atomic vibrations in moving dislocations due to which dynamic lowering of potential barriers occurs in the dislocation cores, accounts for the efficient penetration of particles of the ambient medium into the surface layer of materials subjected to deformation. The surface layer can become either stronger or softer depending on the actual type of atoms or molecules of the medium (their size and chemical affinity), the atomic parameters of the material structure, the dislocation types, and the structure and dimensions of the impurity centers present in the surface layer. The atomic particles contained in the cores of moving dislocations give rise to a change in the energy parameters of the interaction between the dislocations and impurity centers (stoppers) due to which they multiply in the surface layer of the deformed material.

In this study, we obtain and analyze helium extraction curves from crystalline materials and amorphous eutectic alloys having different initial structure and deformed to different extents in liquid ^{3}He and ^{4}He (T = 0.6–4.2 K) or dispersed in gaseous helium at 300 K.

2. MATERIALS STUDIED AND EXPERIMENTAL TECHNIQUES

The materials used in the study were as follows: metals with the fcc (Al, Cu, Pb), hcp (Cd, Ti), bcc tetragonal (Sn), tetragonal ($BaSO_4$), and rhombic (TiO_2) structures; ionic single crystals (NaCl, LiF); films of amorphous eutectic alloys Ni_{78}–Si_8–B_{14} (10 × 60 × 0.125 mm) and $Pd_{84.5}$–$Si_{15.5}$ (2 × 60 × 0.06 mm); and powders of barite ($BaSO_4$, d = 100 μm) and rutile (TiO_2, d = 150 μm). The purity, original structure, and test conditions of the materials used are as follows: for Al(99.9%), polycrystals, grain size d = 0.15–0.17 mm, tension, strain rate $\dot{\varepsilon} = 10^{-4}$ s^{-1}, and T = 0.6 K; for Cu(99.998%), single crystals, tension, $\dot{\varepsilon} = 10^{-4}$ s^{-1}, and T = 4.2 K; for Cu(99.996%), nanocrystalline (d = 100 nm), compression, $\dot{\varepsilon} = 10^{-4}$ s^{-1}, and T = 4.2 K; for Sn(99.998%), single crystals, tension, $\dot{\varepsilon} = 10^{-3}$ s^{-1}, and T = 3.0 K; for Cd(99.8%), a polycrystal, tension, $\dot{\varepsilon} = 10^{-4}$ s^{-1}, and T = 3 K; for Pb (technical grade), compression, $\dot{\varepsilon} = 10^{-4}$ s^{-1}, and T = 3 K; for α-Ti(99.94%), a 0.1-mm-thick polycrystalline foil, tension, $\dot{\varepsilon} = 10^{-4}$ s^{-1}, and T = 4.2 K; for ionic single crystals of NaCl and LiF (LOMO grade), compression, $\dot{\varepsilon} = 10^{-4}$ s^{-1}, and T = 3 K; and for amorphous eutectic films of $Pd_{84.5}$–$Si_{15.5}$ at T = 0.6 K and Ni_{78}–Si_8–B_{14} at T = 4.2 K, tension at a rate of 0.02 mm/min. $BaSO_4$ and TiO_2 powders were ground in a ball mill in standard mode (over 5 h). Tests in liquid ^{3}He were conducted in a setup designed at UPTI (Kharkov) [3], and in ^{4}He, in a setup designed at the Ioffe Institute (St. Petersburg) [4].

1063-7834/05/4705-0863$26.00

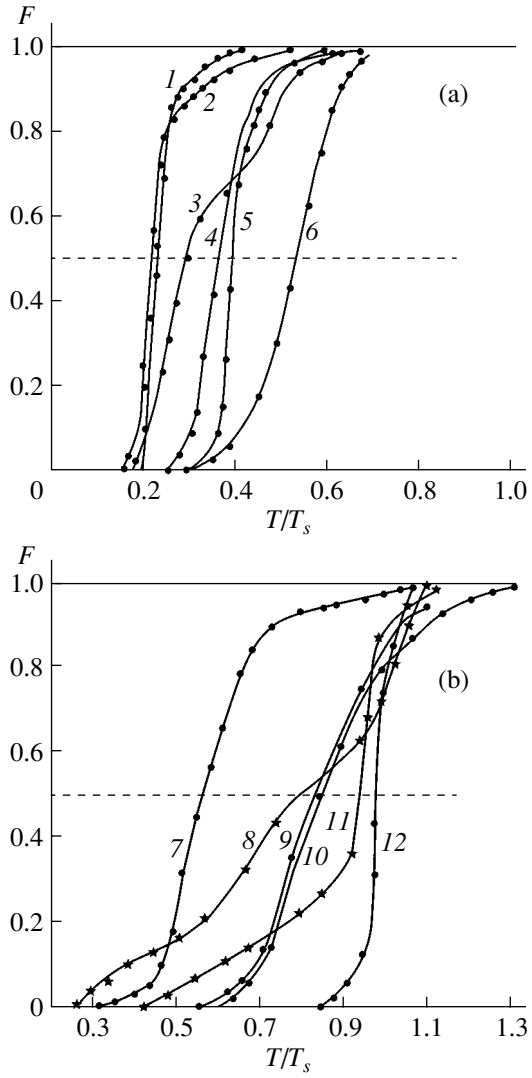

Fig. 1. Fraction F of helium released from materials with different melting points plotted vs. reduced temperature T/T_s of annealing: (a) (*1*) $BaSO_4$, (*2*) TiO_2, (*3*) Ti, (*4*) NaCl, (*5*) Cu, and (*6*) LiF; (b) (*7*) Al, (*8*) Ni_{78}–Si_8–B_{14}, (*9*) Pb, (*10*) Cd, (*11*) $Pd_{84.5}$–$Si_{15.5}$, and (*12*) Sn.

The helium content in deformed specimens was determined with a high-resolution resonance mass spectrometer [5] with a sensitivity of ~10^5 atoms for ^{3}He and ~10^9 atoms for ^{4}He. Helium extraction curves were recorded for deformed specimens of various materials under dynamic annealing at rates of 5–10 K/min. The curves were reduced to graphs of the fraction F of liberated helium plotted versus the temperature T and the reduced temperature T/T_s, where T_s is the melting point of the material.

3. EXPERIMENTAL RESULTS AND DISCUSSION

The curves obtained by dynamic annealing of materials deformed in liquid helium were used to construct

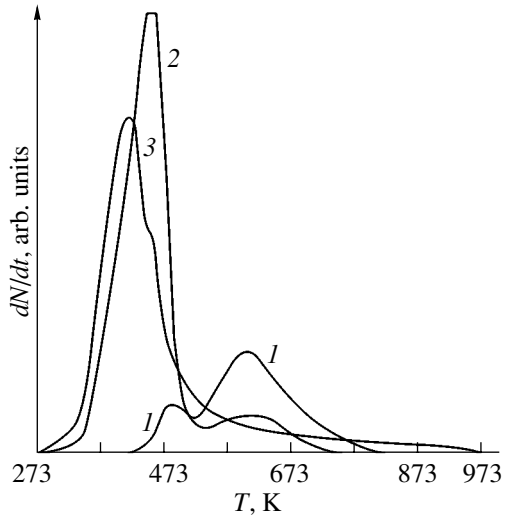

Fig. 2. Helium extraction curves from (*1*, *2*) $BaSO_4$ and (*3*) TiO_2 powders dispersed with a ball mill at 300 K: (*1*) original powder and (*2*, *3*) after dispersion in helium.

$F(T/T_s)$ graphs. The graphs were obtained for all specimens containing approximately equal amounts of helium per unit surface area (N, atoms/cm^2). The curves are S shaped (Fig. 1), which implies the existence of three helium extraction stages of different extent, depending on the type of material, its original and deformed structures, and melting point. These are a low-temperature stage with $T = (0.2–0.3)T_s$; a stage close to and at the recrystallization temperature, $T = (0.4–0.6)T_s$; and a high-temperature stage in the vicinity of T_s (below, above, and at this point). The existence of different stages and the number of peaks in the helium extraction curves are determined by various parameters. Among them are the type and melting point of the material, its original defect structure, and its deformed structure (which determines the types of helium traps forming in the course of plastic deformation). Let us consider the experimental relations in more detail. Curves *1–6* in Fig. 1a relate to $BaSO_4$ (T_s = 1853 K), TiO_2 (T_s = 1833 K), Ti (T_s = 1933 K), NaCl (T_s = 1073 K), Cu (T_s = 1356 K), and LiF (T_s = 1113 K), respectively. These materials feature high melting points, and all curves relating to them are confined to the interval T/T_s = 0.15–0.65.

$BaSO_4$ and TiO_2 powders (macroscopically brittle, crystalline, but not metallic materials) exhibited the presence of noticeable amounts of helium after they were dispersed with a ball mill in helium ambient. The corresponding helium extraction curves are given in Fig. 2. These curves are confined to the region $T = (0.15–0.33)T_s$ for these materials. A $BaSO_4$ powder studied in the initial state (before dispersion) revealed two peaks of the amount of released helium, at T = 480 K ($0.25T_s$) and T = 600 K ($0.33T_s$). After dispersion of the powder, the peak at T = 600 K decreases noticeably,

while the peak at T = 480 K, by contrast, increases sharply (compare curves *1*, *2*). This implies helium transfer from deep to shallower traps forming in the course of dispersion. The amount of helium in the powder increases by nine times (from 3×10^{13} to 28×10^{13} atoms/g). A dispersed TiO_2 powder exhibits two closely lying peaks at T = 420–460 K (0.22–0.25)T_s, and the amount of helium increases by 13 times (from 0.1×10^{13} to 1.3×10^{13} atoms/g). For both powder types, the grain diameter after dispersion in helium decreases by 40% (as compared to 20% in the air ambient). This means that helium penetrates efficiently into TiO_2 and $BaSO_4$ powders. The microcracks forming in the powder grains in the course of dispersion bring about microplastic deformation through the formation of short dislocation loops near the microcrack propagation front. By penetrating into dislocations, helium pins them, which gives rise to additional embrittlement of the powder grains and, hence, facilitates their dispersion. Dislocation pinning by helium atoms has been demonstrated for the specific case of a screw dislocation in bcc iron by computer modeling [6]. The data obtained suggest that the efficiency of this process can be substantially increased in a specially chosen gas medium, which may be of practical significance in industrial technologies involving dispersion of various types of materials.

Polycrystalline titanium with a high temperature T_s = 1933 K likewise reveals a narrow helium extraction interval of T = (0.2–0.6)T_s (curve *3*, Fig. 1a) with three low-temperature peaks (at T = 520, 700, 870 K; Fig. 3). The increase in the amount of helium from 1.5×10^{11} to 3×10^{11} atoms/cm^2 in specimens deformed at 4.2 K (ε = 5%) results in a growth of these peaks and the appearance of a new peak at T = 1000 K (compare curves *1*, *2* in Fig. 3) associated with the formation of deeper helium traps. The range of helium extraction from NaCl (T_s = 1073 K), LiF (T_s = 1113 K), and Cu (T_s = 1356 K) single crystals shifts slightly toward higher temperatures (0.25–0.65)T_s (curves *4*–*6* in Fig. 1a). For Cu and NaCl, the helium extraction curves have two broad maxima located at T = 570 and 670 K for Cu and at T = 420 and 570 K for NaCl [7]. LiF single crystals are characterized by three maxima of helium release at T = 420, 480, and 620 K [1]. These peaks can be identified with helium release from interstices [8] and divacancies [9] (at T = 420 K), monovacancies (T = 480 K) [10], and edge dislocations (T = 620 K) and are characterized by activation energies E_1 = 0.32 eV, E_2 = 0.63 eV, and E_3 = 0.42 eV, respectively. The energy E_3 coincides with the helium binding energy with LiF lattice cations, which was also found experimentally in [11] using helium spectroscopy. Therefore, chemical bonding takes place for helium interacting with the lattice and, hence, with moving dislocations, into which helium penetrates in the course of plastic deformation of these crystals. The bonding energy was found to be 30 times higher than the van der Waals interaction characteristic of inert gases.

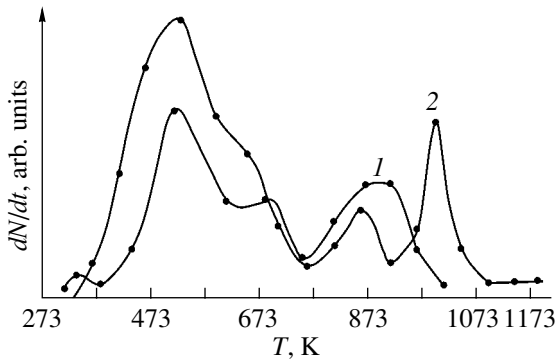

Fig. 3. Helium extraction curves from titanium samples that were deformed at T = 4.2 K to ε = 5% and contain different amounts of helium: (*1*) 1.5×10^{11} and (*2*) 3×10^{11} atoms/cm^2.

For metals with lower melting points, namely, for Al (T_s = 932 K), Pb (T_s = 601 K), Cd (T_s = 594 K), and Sn (T_s = 505 K), the $F(T/T_s)$ curves spread over a very broad temperature interval, (0.25–1.3)T/T_s (curves *7*, *9*, *10*, *12* in Fig. 1b). Significantly, the $F(T/T_s)$ relation for tin (curve *12*) differs strongly from that for Al, Cd, and Pb. This curve lies within a substantially narrower temperature interval, $T/T_s \sim$ 0.8–1.1, which may be associated with the fact that tin specimens are single crystals, whereas Al, Pb, and Cd are polycrystals. The number of helium traps of different depth in polycrystalline specimens was considerably higher than that in tin because of the polycrystals being of granular structure and of the existence of an additional grain boundary mechanism of deformation in them. Cadmium and lead are the most remarkable in this respect, as they have practically equal melting temperatures. About 20% of the helium present in these metals continues to evolve at temperatures exceeding their T_s by 100–200 K (curves *9*, *10*). The intensity of recrystallization taking place in the deformed structure of cadmium is so high that, after maximum predeformation at 4.2 K (7%), the tensile strain curve practically coincides with that obtained at 300 K for this metal [12]. This means that warming a specimen from 4.2 to 300 K and subsequent dynamic annealing activate intense internal stress relief and recrystallization of the deformed cadmium structure through dislocation annihilation and growth of the grains in size because of a high density of thermal and strain-induced vacancies. The vacancies merge to form pores, in which helium atoms build up. Dynamic annealing of deformed specimens initiates pore growth, with the result that, at $T > T_s$, they leave the melt, culminating in large and broad helium extraction maxima [12].

Let us consider curves of helium extraction from Ni_{78}–Si_8–B_{14} (T_s = 1223 K) and $Pd_{84.5}$–$Si_{15.5}$ (T_s = 1073 K) amorphous eutectic films (curves *8*, *11* in Fig. 1b), which have high melting points T_s. These curves spread

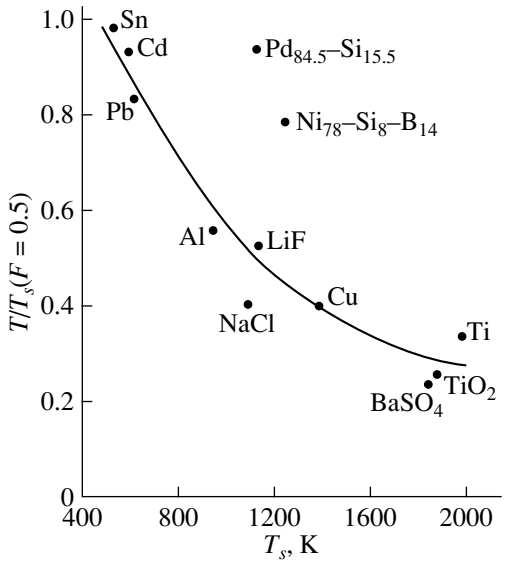

Fig. 4. T/T_s at a fraction $F = 0.5$ of helium extracted from materials with different melting temperatures plotted as a function of T_s.

over a very broad temperature region, $T/T_s \sim 0.25$–1.15, which practically coincides with that characteristic of materials with a low T_s (cf. Figs. 1a, 1b). The reason for this strange coincidence can be traced to the specific features of the atomic structure of amorphous films consisting of metal–metalloid clusters. The clusters are separated by buffer layers with a very loose atomic structure containing various disclination–dislocation defects, as well as various vacancy and atomic configurations due to the presence of a large number of nanosized pores in the amorphous films, particularly in the surface layers of the films [13]. This distinctive feature of the amorphous film microstructure gives rise to a radical change in the mechanism of their plastic deformation. This mechanism operates not through the generation of dislocations but rather through viscous plastic flow of the material down to liquid-helium temperatures [14]. This mechanism is characterized, unlike in crystalline materials, by the absence of strengthening in deformed films. Plastic deformation in amorphous films takes place over cluster interfaces (buffer layers). Plastic shear over cluster boundaries may occur, for instance, through homogeneous nucleation of Somigliana quasi-dislocations with a variable Burgers vector, which are free of long-range stresses [15]. Apart from this, plastic deformation of amorphous films in liquid helium is accompanied by local heating of plastic-shear regions up to the melting point of the material, a phenomenon that has been both observed experimentally and described theoretically [14]. All this gives rise to a sharp intensification of helium penetration into amorphous films through the formation of various nanosized helium traps in the course of their plastic deformation and, hence, to the existence of a very broad temperature region of helium release, which practically coincides with that for metals with a low T_s (Fig. 1b).

The above anomaly in the $F(T/T_s)$ curves is particularly clearly seen when one constructs the plot of the parameter T/T_s for $F = 0.5$ as a function of T_s for all materials with different T_s (Fig. 4). We readily see that the crystalline materials fit to this (exponential) curve with a small scatter, except for the amorphous alloys, which fall far from this curve. For metals with a low T_s (Pb, Cd, Sn), the fraction of released helium $F = 0.5$ is reached at temperatures close to their T_s, $T/T_s = 0.8$–0.95, while for materials with a high T_s ($BaSO_4$, TiO_2, Ti, Cu, NaCl, LiF) this fraction is attained even at $T/T_s = 0.20$–0.55. This difference may be accounted for by the fact that high bond strengths in the rigid lattices of Ti, TiO_2, and $BaSO_4$ favor the formation of shallow helium traps only and helium is extracted from them at $T \ll T_s$. By contrast, in metals with the metallic (soft) bonding type and low T_s, deep helium traps form more easily, so these traps manifest themselves at temperatures close to T_s. Aluminum occupies an intermediate position in T_s between these two groups of materials (cf. Figs. 1a, 1b). One should also take into account the effect of the polycrystalline structure of aluminum on the formation of deep helium traps. Both these factors combine to extend the region of helium extraction from aluminum to its melting point.

A question may also arise as to the effect that the various types of defects forming in the course of plastic deformation exert on the intensity of helium penetration. It was experimentally revealed in [16] that nanocrystalline copper deforms at $T = 4.2$ K and $\varepsilon < 5\%$ through the motion and multiplication of dislocations. As the strain increases to $\varepsilon \sim 14\%$, intragrain sliding is replaced by twinning, and for $\varepsilon > 14\%$, the grain boundary (rotation) deformation mechanism becomes operative. The amount of released helium N depends on ε in a nontrivial way. For small values of ε, N increases threefold as compared to an undeformed specimen. After the dislocation-mediated deformation has transformed into the twinning mechanism, helium no longer penetrates into the specimen under deformation, because the process of twinning is accompanied by very small atomic displacements, which (unlike dislocations) do not favor helium penetration into the material under deformation. For $\varepsilon > 14\%$, twinning in nanocrystalline copper is replaced by a jumplike grain boundary mechanism of deformation, through which helium penetration into deformed specimens becomes intensified. Rotation plastic shear forming in these conditions gives rise to a strong localization of deformation, which is about one order of magnitude stronger than that in dislocation-assisted plastic shear. The values of N increase sevenfold as compared to those for an undeformed specimen and are about three times larger than those in the initial stage of their compression $\sigma(\varepsilon)$ curves, where the dislocation-assisted mechanism of deformation is realized (218×10^9 and

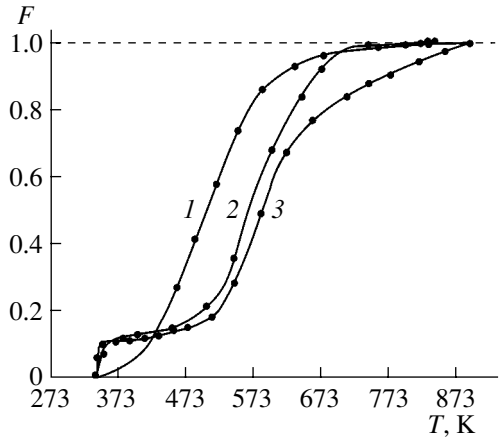

Fig. 5. Fraction F of helium extracted from (*1*) single crystal and (*2*, *3*) nanocrystalline copper plotted as a function of temperature for various values of ε: (*1*, *2*) 14 and (*3*) 19%.

69×10^9 atoms/cm^2, respectively). At T = 4.2 K, the grain boundary mechanism of jumplike deformation is accompanied by appreciable specimen heating, which can reach tens of kelvins [17]. This heating intensifies the localization of deformation in grain boundary plastic shear and, hence, helium penetration into the material.

Thus, the change of the type of defects favoring plastic deformation of nanocrystalline copper from dislocations to twins followed by grain boundary sliding has a significant effect on the rate of helium penetration into this material. Amorphization of the original structure of crystalline materials also radically changes the character of helium traps and, hence, the temperature region and the intensity of helium penetration into amorphous films under deformation, the points discussed above.

The original defected structure of copper specimens also strongly influences the character of helium evolution. For single crystals, the $F(T)$ curves have a symmetric shape (curve *1* in Fig. 5), while nanocrystalline copper deformed to the same extent (ε = 14%) exhibits a plateau at T = (350–500) K (curve *2* in Fig. 5). As ε increases to 19%, the pattern of the $F(T)$ graph in its initial stage does not change (curve *3*) but the curve becomes less steep and helium continues to evolve up to T = 900 K ($T = 0.6\ T_s$). The plateaus in curves *2* and *3* for nanocrystalline copper can be caused, as shown in [18], by grain boundary dislocations being pinned by point defects (unlike the case with single crystals, where there are no such defects). The flattening and stretching of curve *3* is associated with activation of the grain boundary mechanism of deformation for ε > 14%, which accounts for the formation of deeper helium traps at grain boundaries (this mechanism does not yet operate in curve *2*).

4. CONCLUSIONS

Our studies of helium penetration into materials of various types have shown that the intensity of this process depends both on their original defected structure and on the type of deformation-induced nanosized defects forming in them. These data, as well as the results obtained with LiF single crystals [1], suggest that helium atoms are capable of chemical bonding to various deformation-induced defects in the crystalline and amorphous materials studied. This is indicated by the fact that the temperature region of helium penetration and the amount of helium released from specimens undergoing deformation depend strongly on the melting point of the material and on the actual type of its atomic and defect structure. More comprehensive information concerning the energy parameters and types of helium traps in the materials studied by us may be gained by invoking dynamic (at different rates) and isothermal annealings of specimens deformed in liquid helium. This problem would require further coordinated studies.

Thus, the carriers providing penetration of particles (helium atoms) of an ambient medium into solids of various types (crystalline and amorphous) are mobile, chemically activated nanosized defects (localized states of groups of atoms or molecules) undergoing a rearrangement of electronic structure due to plastic deformation or other dynamic processes in which mechanical fields acting on a solid change the energy parameters of the interaction between the solid and particles of the external medium. These processes can also be affected by physical fields that are not mechanical (for instance, magnetic fields) [19].

REFERENCES

1. O. V. Klyavin, N. P. Likhodedov, and A. N. Orlov, Prog. Surf. Sci. **33** (4), 259 (1990).
2. O. V. Klyavin, Fiz. Tverd. Tela (St. Petersburg) **35** (3), 513 (1993) [Phys. Solid State **35**, 261 (1993)].
3. V. I. Dotsenko, A. I. Landau, and V. V. Pustovalov, *Modern Problems of Low-Temperature Plasticity of Materials* (Naukova Dumka, Kiev, 1987) [in Russian].
4. O. V. Klyavin, Zavod. Lab., No. 4, 461 (1963).
5. B. A. Mamyrin, B. N. Shustrov, and G. S. Anufriev, Zh. Tekh. Fiz. **42** (12), 2577 (1972) [Sov. Phys. Tech. Phys. **17**, 2001 (1972)].
6. O. V. Klyavin, N. V. Likhodedov, and A. N. Orlov, Fiz. Tverd. Tela (Leningrad) **27** (11), 3388 (1985) [Sov. Phys. Solid State **27**, 2039 (1985)].
7. O. V. Klyavin, B. A. Mamyrin, L. V. Khabarin, Yu. M. Chernov, and V. S. Yudenich, Fiz. Tverd. Tela (Leningrad) **24** (7), 2001 (1982) [Sov. Phys. Solid State **24**, 1143 (1982)].
8. S. Kalbitzer and J. Kiko, Z. Naturforsch. A **24** (12), 1996 (1969).
9. Kh. I. Amirkhanov, S. B. Brand, and E. P. Bartnitskiĭ, *Radiogenic Argon in Minerals and Rocks* (Makhachkala, 1960) [in Russian].

10. P. Subtitz and J. Teltov, Phys. Status Solidi **23** (1), 9 (1967).

11. A. I. Kupriyanov and A. Yu. Kurkin, Fiz. Tverd. Tela (St. Petersburg) **35** (11), 3003 (1993) [Phys. Solid State **35**, 1475 (1993)].

12. O. V. Klyavin, B. A. Mamyrin, L. V. Khabarin, Yu. M. Chernov, and V. S. Yudenich, Fiz. Tverd. Tela (St. Petersburg) **44** (2), 291 (2002) [Phys. Solid State **44**, 302 (2002)].

13. A. M. Glezer and B. V. Molotilov, *Structure and Mechanical Properties of Amorphous Alloys* (Metallurgiya, Moscow, 1992) [in Russian].

14. E. D. Tabachnikova, V. Z. Bengus, É. S. Shumilin, L. I. Voronova, and Yu. F. Efimov, Metallofizika (Kiev) **13** (4), 47 (1997).

15. A. K. Emaletdinov and R. L. Nurullaev, in *Abstracts of XIV Petersburg Reading on Problems of Strength* (St. Petersburg, 2003), p. 146.

16. O. V. Klyavin, V. I. Nikolaev, L. V. Khabarin, Yu. M. Chernov, and V. V. Shpeĭzman, Fiz. Tverd. Tela (St. Petersburg) **45** (12), 2187 (2003) [Phys. Solid State **45**, 2292 (2003)].

17. G. A. Malygin, Fiz. Tverd. Tela (St. Petersburg) **39** (11), 2019 (1997) [Phys. Solid State **39**, 1806 (1997)].

18. Yu. A. Burenkov, S. P. Nikanorov, B. I. Smirnov, and V. I. Kopylov, Fiz. Tverd. Tela (St. Petersburg) **45** (11), 2017 (2003) [Phys. Solid State **45**, 2119 (2003)].

19. V. I. Al'shits, E. V. Darinskaya, M. V. Koldaeva, and E. A. Petrzhik, Kristallografiya **48** (5), 826 (2003) [Crystallogr. Rep. **48**, 768 (2003)].

Translated by G. Skrebtsov

Physics of the Solid State, Vol. 47, No. 5, 2005, pp. 869–875. Translated from Fizika Tverdogo Tela, Vol. 47, No. 5, 2005, pp. 843–849.

Kinetics of Failure of Polycrystalline Ferroelectric Ceramics in Mechanical and Electric Fields

V. V. Shpeĭzman* and L. V. Zhoga**

** Ioffe Physicotechnical Institute, Russian Academy of Sciences, Politekhnicheskaya ul. 26, St. Petersburg, 194021 Russia*
e-mail: shpeizm.v@mail.ioffe.ru

*** Volgograd State Architecture and Building Academy, Akademicheskaya ul. 1, Volgograd, 400074 Russia*
e-mail: postmaster@vgasa.ru

Abstract—The kinetics of mechanical failure and electrical breakdown in polycrystalline ferroelectric ceramics was studied under the simultaneous action of an electric field and a mechanical load. A kinetic approach is shown to be preferable as compared to the concepts that treat the failure and breakdown as critical phenomena. The mechanical failure and electrical breakdown are shown to be interrelated. It is found that a weak action of one of the fields retards failure caused by the other field and that the simultaneous action of these strong fields accelerates both the mechanical failure and electrical breakdown. Methods for determining the activation characteristics of both processes only from the failure kinetics in one of these processes are developed. © *2005 Pleiades Publishing, Inc.*

1. INTRODUCTION

During operation, ferroelectric (FE) materials are subject to electrical and mechanical loads. The characteristic of failure of such materials in an electric field is the breakdown voltage or the breakdown electric field, i.e., the value of a uniform electric field E_{br} at which breakdown occurs. The analogous characteristic for a mechanic field is the strength upon tension or bending [1, 2].

Mechanical stresses σ that appear inside solid ferroelectrics placed in an electric field E are known to be an important factor affecting the development of breakdown and the electric strength E_{br} of materials [2]. Owing to strong electrostriction or the piezoelectric effect (e.g., in ferroelectrics and related materials), electric fields can cause high stresses that are sufficient for failure or microcracking of samples in some cases [3, 4]. The development of such processes is also favored by the reorientation of FE domains (mechanical twins) under the action of the field E (e.g., during the polarization of polycrystalline ferroelectric ceramics (FCs) [5]). Under resonance conditions in FC samples (acoustic transducers [6]), the stresses σ can reach ultimate tensile strength even in a relatively low field $E < E_{br}$, whereas in constant or low-frequency electric fields microscopic failure processes develop at higher values of E.

The role of mechanical stresses in the development of electrical breakdown in FE crystals and FCs has been analyzed qualitatively in the literature. In particular, the authors of [7] were the first to take into account the role of mechanical distortions in the structure of $BaTiO_3$ FC when a pulse field E is applied at temperatures below the Curie temperature T_C. It was also found experimentally [8] that electrical breakdown in an imperfect FE crystal is preceded by mechanical failure. It was also shown that thermal breakdown occurs in the paraelectric phase. The strong effect of polarization on E_{br} of a highly dense FC based on $Pb(Zr,Ti)O_3$ (PZT) can also be explained by mechanical stresses appearing in a sample during the magnetization reversal of non-180° domains [9]. These facts indicate the importance of electromechanical interactions for the development of electrical breakdown in ferroelectric materials.

To solve the problem of failure of ferroelectric ceramics in an electric field (electrical breakdown), it is important to analyze the effect of mechanical stresses in ferroelectric ceramics on the development of breakdown in time under application of an electric field E. Experimental studies dealing with delayed failure of ferroelectric ceramics in an electric field (breakdown kinetics) are rather scarce. The kinetic characteristics of these materials were studied in [9–12]. The effect of the mechanical stresses appearing as a result of the converse piezoelectric effect in $BaTiO_3$ piezoelectric ceramics was theoretically considered in [13, 14]. However, in those studies, failure was considered to be a critical phenomenon; that is, it was assumed to occur only when the electric field reaches a certain value.

In [15], we showed that the processes of failure of FCs in electric and mechanic fields are interrelated. The breakdown-voltage and mechanical-strength distributions were shown to be similar; we detected hardening and softening regions when an electric field affected the mechanical strength and analogous regions for the case where the breakdown voltage was influenced by a mechanical load. The failure kinetics in electric or mechanic fields were found to be similar.

1063-7834/05/4705-0869$26.00 © 2005 Pleiades Publishing, Inc.

In this work, we are the first to study the failure kinetics under the simultaneous action of electric and mechanic fields and to try to describe both types of failure using the same approach.

2. ANALYSIS OF FAILURE IN ELECTRIC AND MECHANIC FIELDS AFTER GRIFFITH

Interest in the failure of insulators in an electric field (breakdown) and in the relation between various types of breakdown and failure under a mechanical load appeared a long time ago. Almost a hundred years ago, Griffith [16] proposed a concept of failure based on a comparison of the elastic energy released during crack growth and the energy required to increase the crack surface. When analyzing electrical failure, the authors of [1, 17, 18] proposed to replace the elastic energy by an electric energy, i.e., by the energy of charges generated on the crack surface.

Let us consider a plate of unit thickness with a thin, through edge crack of length l. The energy associated with the crack in the case of mechanical loading is

$$U_M = 2l\gamma - \frac{\pi l^2 \sigma^2}{2E_M}, \quad (1)$$

where γ is the specific surface energy, σ is the stress, and E_M is the elastic modulus. For the same plate placed in an electric field E, the energy associated with the crack is

$$U_E = 2l\gamma - \frac{\varepsilon l^2 E^2}{16}, \quad (2)$$

where ε is the permittivity.[1]

From the condition $dU/dl = 0$, we can find the critical stress σ_{cr} (electric field E_{cr}) above which the crack growth becomes energetically favorable:

$$\sigma_{cr} = \sqrt{\frac{2\gamma E_M}{\pi l}}, \quad (3)$$

$$E_{cr} = 4\sqrt{\frac{\gamma}{\varepsilon l}}. \quad (4)$$

It is interesting that, by dividing Eq. (3) by Eq. (4), we can eliminate γ and l (if they have the same meaning for both cases of failure). Thus, we can bypass many difficulties associated with verifying Eq. (3) experimentally and interpreting γ. The calculated and experimental estimates of the σ_{cr}/E_{cr} ratio given in [1, 2] are similar only in order of magnitude and raise doubts on the validity of this approach to the relation between electrical and mechanical failure. The data from [15], where strength and breakdown were studied under the simultaneous action of an electric field and a mechanic load, only partly support the possibility of using a "modified" energy Griffith criterion.

Indeed, in this case, instead of Eq. (1) or (2), we have

$$2\gamma = \frac{\pi l \sigma^2}{E_M} + \frac{\varepsilon l E^2}{8}. \quad (5)$$

In the σ–E coordinates, a curve corresponding to failure is part of an ellipse ($\sigma, E \geq 0$) with semiaxes σ_{cr} and E_{cr}. We restrict ourselves only to the description of the shape of the curves given in [15] and note that only the middle portions of the curves (at σ and E close to half their critical values) are somewhat similar to Eq. (5). In the ranges close to the coordinate axes, both the value of the effect and its sign are different.

Although the idea of using the Griffith energy criterion to describe dielectric breakdown appeared long ago, it has not gained acceptance. One of the reasons for this was likely the recognition that failure is not a critical event but rather a kinetic phenomenon that cannot be described by critical characteristics.

3. KINETIC APPROACH TO FAILURE IN ELECTRIC AND MECHANIC FIELDS

It was shown in [19] that, although brittle bodies subjected to a constant load often exhibit a large scatter of experimental values of the strength and lifetime, the time to failure (the lifetime τ) for them can be described by the Zhurkov formula

$$\tau = \tau_0 \exp\frac{U_0 - V_{eff}\sigma}{kT}. \quad (6)$$

Here, $V_{eff} = nV$ is the effective activation volume; n is an overstress coefficient, which depends only on the structure of a material in a steady-state state (which takes place only at either very short or very long loading times) and, in an intermediate range, also depends on the relaxation rate; σ is the applied stress ($\sigma_l = n\sigma$ is the local stress); V is the true failure activation volume; U_0 is the effective activation energy; T is the temperature of the experiment; k is the Boltzmann constant; and τ_0 = const. For a constant temperature, Eq. (6) reduces to $\tau = Ae^{-B\sigma}$, where A determines the effective failure activation energy and B determines the effective failure activation volume. In [19], expressions were also derived for calculating A and B from the average strength $\bar{\sigma}$ and from the probability W of failure occurring under constant σ in a time interval from τ_{min} to τ_{max}:

$$\log\frac{A}{\tau_{min}} = \frac{\bar{\sigma}\log\tau_{max}/\tau_{min}}{\int_{-\infty}^{\infty} W d\sigma}, \quad B = \frac{\log A/\tau_{min}}{\bar{\sigma}}. \quad (7)$$

[1] Note that Eqs. (1) and (2) can contain various coefficients depending on the crack shape and the state of stress near the crack. However, this is insignificant for the purposes of this work.

For example, the coefficients A and B can be calculated for steplike loading at a step height $\Delta\sigma$ that satisfies certain conditions [20].

In [15], the analysis of failure kinetics described above was applied for studying breakdown upon a steplike increase in the electric field. It was assumed that, when an electric field is applied to ferroelectric ceramics, the defect sites at which local stresses appear are the same as those in the case of mechanical loading. The electromechanical characteristics of defect sites differ from those of the surrounding material; therefore, local tensile stresses can appear in them [4, 5]. In particular, if breaking stresses in ferroelectric ceramics have an electrostrictive nature, we can write

$$\sigma_l = \delta_e E^2; \tag{8}$$

and, if they have a piezoelectric nature, then

$$\sigma_l = \delta_p E. \tag{9}$$

Here, the coefficient δ_e depends on the elastic and electrostrictive constants of a material and the coefficient δ_p depends on the elastic constants, the piezoelectric modulus, and the relative orientation of the polarization vector **P** of the defect volume of the material and the external electric field **E**. Therefore, the dependence of the electric lifetime τ on E can be written as $\log\tau = \log A_e - B_e E^2$ if the local mechanical breaking stresses have an electrostrictive nature and as $\log\tau = \log A_p - B_p E$ if the local stresses have a piezoelectric nature. It is obvious that all considerations regarding the experimental determination of the coefficients A and B involved in the equation for mechanical failure given above are also valid for analogous equations for breakdown; i.e., we can use Eqs. (7) by substituting E for σ.

We now consider the general case of failure of a material subjected simultaneously to electric and mechanic fields. We will use the designations for the failure activation energy and the preexponential factor (U_0 and τ_0, respectively) for any type of failure (electrical failure at a constant σ and mechanical failure at a constant E). As will be shown below, the coefficients A and B, as estimated from Eqs. (7) and experimental data, are independent of whether these coefficients are constant or depend on the type of loading involved. For definiteness, we consider the case where Eq. (9) holds true. Then, we can write

$$\tau = \tau_0 \exp\frac{U_0 - V^{\sigma}_{\text{eff}}\sigma - V^{E}_{\text{eff}} bE}{kT}, \tag{10}$$

where, according to [14], $\sigma_l = bqE$ (where q is the overstress coefficient; i.e., the local field strength is $E_l = qE$). Thus, we assume that $V^{E}_{\text{eff}} = qV^{E}$ and that the coefficient b, which has the dimensions C/m^2, is the polarization charge per unit area. As in the case of mechanical loading (for which $V^{\sigma}_{\text{eff}} = nV^{\sigma}$), the effective and true activation volumes for electrical failure are connected by the relation $V^{E}_{\text{eff}} = qV^{E}$. Then, for electrical failure in the presence of mechanical stresses, we can use Eq. (10) and obtain $\log\tau = A_{\text{EM}} - B_{\text{EM}}E$, where

$$A_{\text{EM}} = \tau_0 \exp\frac{U_0 - V^{\sigma}_{\text{eff}}\sigma}{kT} = \tau_0 \exp\frac{U^{E}_{\text{eff}}}{kT},$$
$$B_{\text{EM}} = \frac{V^{E}_{\text{eff}} b}{kT}. \tag{11}$$

Here, U^{E}_{eff} is the σ-dependent effective activation energy for electrical failure. Thus, in semilogarithmic coordinates, $\log A_{\text{EM}}$ depends linearly on σ, and the slope of this straight line can be used to determine V^{σ}_{eff} by a method that is not related to mechanical failure. A similar method can be used to determine V^{E}_{eff} from experiments with mechanical failure in the presence of an electric field and to compare this value with that calculated from experimental data on the breakdown kinetics:

$$A_{\text{ME}} = \tau_0 \exp\frac{U_0 - V^{E}_{\text{eff}} bE}{kT} = \tau_0 \exp\frac{U^{\sigma}_{\text{eff}}}{kT},$$
$$B_{\text{ME}} = \frac{V^{\sigma}_{\text{eff}}}{kT}. \tag{12}$$

To check this approach to failure, we performed experiments on the steplike mechanical loading of PZT-19 disks at room temperature and various values of the applied electric field and experiments on a steplike increase in the electric field under a constant mechanical load. The average grain size in samples was 4 μm, and the pore content varied from 17 to 20%. Mechanical loading was carried out by axisymmetric bending. The maximum tensile stresses were calculated from the following formula for bent round plates in which the neutral plane is not deformed [21]:

$$\sigma = \frac{3(1+\nu)}{2\pi h^2}\left(\ln\frac{b}{a} + \frac{(1+\nu)(b^2 - a^2)}{2(1-\nu)c^2}\right)Q. \tag{13}$$

Here, $c = 10$ mm and $h = 0.7$ mm are the radius and thickness of an FC disk, respectively; $b = 6.5$ mm is the support radius; $a = 3.5$ mm is the radius of the loading ring punch; Q is the load; and ν is the Poisson ratio of the piezoelectric ceramics. The load step was $\Delta\sigma = 1.7$ MPa, and the time of storing under a constant load was 900 s.

An electric field in a sample was created with silver electrodes deposited on its flat surfaces. To eliminate surface breakdown, one of the electrodes was located at the center of the plate and had the same dimensions as the circular area under the loading punch. The sample was placed in liquid ethyl siloxane, and a voltage U was applied stepwise to its electrodes. The rate of increasing

Table 1. Electrical failure of polarized ferroelectric ceramics under a mechanical load $\sigma = 2$ MPa and $\mathbf{E} \uparrow\uparrow \mathbf{P}$

	E, MV/m											
	3.5	4.0	4.5	5.0	5.5	6.0	6.5	7.0	7.5	8.0	8.5	9.0
$n\downarrow$	–	4	9	13	19	24	29	34	39	40	43	45
n_i	1	4	3	5	5	3	3	1	1	0	–	–
$n\uparrow$	44	37	33	27	21	18	13	10	5	5	2	–
n_i/n	0.022	0.088	0.066	0.11	0.11	0.066	0.066	0.022	0.022	0	0	0

Note: $n\downarrow$ is the number of samples that failed upon increasing E; n_i is the number of samples that failed at E = const at the step of a given level; and $n\uparrow$ is the number of samples that did not suffer failure until reaching the next step.

the voltage was 1 kV/s, the step height was $\Delta U = 500$ V, and the storing time was $\Delta t = 4$ s. The electrical strength was taken to be the electric field $E = U/h$. For polarized samples, the field direction was coincident with or opposite to the polarization vector.

The breakdown kinetics was studied in detail under a constant mechanical stress and a steplike increase in the electric field. As an example, Table 1 and Fig. 1 give data for $\sigma = 2$ MPa ($\mathbf{E} \uparrow\uparrow \mathbf{P}$). Table 1 presents the statistics of failure when the stress increases step by step and the statistics of failure at E = const. Figure 1 shows the integral distribution of the breakdown field and the failure probability at E = const for each step. Based on these data, using Eq. (7) and analogous formulas in which E is substituted for σ, we can calculate the coefficients A and B in Eqs. (11) and (12) to determine the electrical and mechanical strengths under the simultaneous action of E and σ.

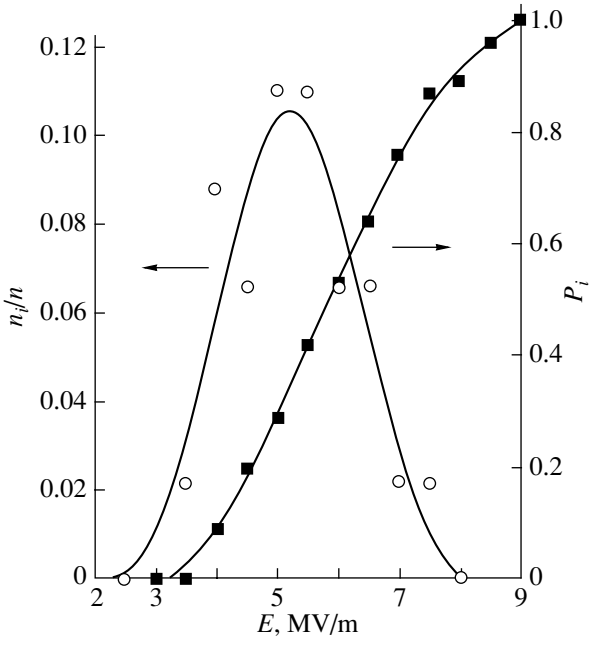

Fig. 1. Failure probability at E = const for the case of a steplike increase in E and the integral distribution of the breakdown field. $\sigma = 2$ MPa.

From the data in Fig. 1, we obtain $\int_{-\infty}^{\infty} W d\sigma = 0.33$ MV/m, $\bar{E} = 5.83$ MV/m, $\log A = 39$, and $B = 6.57 \times 10^{-6}$ C/N. The coefficients A and B and the value of $\bar{E}$ for other values of the stress σ and for the case of $\mathbf{E} \uparrow\downarrow \mathbf{P}$ are given in Table 2.

A similar processing of the results of studying the kinetics of mechanical failure in an electric field of various values was made in [22]. The final characteristics of the analysis of the probability of mechanical failure in an electric field, as well as coefficients (12) calculated from them, are listed in Table 3.

Figure 2 shows the $\log A_{EM}(\sigma)$ dependence, whose slope specifies V_{eff}^{σ}, and the dependence of the average electrical strength $\bar{E}(\sigma)$ on the mechanical stress. As follows from Eq. (10), the slope of the latter dependence is equal to the ratio B_{ME}/B_{EM}. In Fig. 2, the straight lines are plotted through points having high σ, since low stresses σ strengthen the FC (as follows from this work and from the data from [15, 22]) and, according to Eq. (10), this hardening can occur only in the case when variable coefficients are involved in Eq. (10). For the case of $\mathbf{E} \uparrow\uparrow \mathbf{P}$, we can use the data from Table 2 and Fig. 2a and find $V_{eff}^{\sigma} = 9.5 \times 10^{-27}$ m^3 and $V_{eff}^{E} b = 6.3 \times 10^{-26}$ C m. Using the data from Table 3, we find the average value $V_{eff}^{\sigma} = 12 \times 10^{-27}$ m^3, which is close to the experimental value obtained in the experiments on electrical failure under a mechanical load. The $V_{eff}^{\sigma}/V_{eff}^{E} b$ ratio is equal to 0.15 V m/N, which coincides with the slope of the straight line in Fig. 2b. We can also compare V_{eff}^{σ} with $V_{eff}^{\sigma} = 11 \times 10^{-27}$ m^3, which was obtained in [23] in mechanical tests of the same ceramics. These values are seen to be in good agreement, which suggests that electrical loading causes mechanical failure in defect sites due to electromechanical coupling in the FE ceramics and that this failure results in the breakdown of a sample [8]. After the mechanical failure of individual defect volumes, an electrical breakdown begins because the electric field in microcracks increases and, as a consequence, electron

transfer occurs from one crack edge to the other. This transition from mechanical to electrical failure is corroborated by experiments on electron emission in polycrystalline $Pb(Zr,Ti)O_3$ ferroelectric ceramics [3].

Note that the hardening effect of low mechanical stresses on the breakdown is stronger in the case where vectors **E** and **P** are directed opposite to one another.

Table 3 shows the characteristics obtained by processing the data on the kinetics of mechanical failure in an electric field of various values. The main tendencies, e.g., hardening in weak fields and softening in strong fields, are seen to remain the same. Using the slope of the $\log A_{ME}(\sigma)$ curve given in [22], we found $V_{eff}^{E} b = 5.2 \times 10^{-26}$ C m, which is close to the value calculated from the breakdown data obtained in the presence of mechanical stresses. Using the average value of the coefficient B_{ME} (Table 3), we can independently find $V_{eff}^{\sigma} = 12 \times 10^{-27}$ m^3, which also agrees with the estimates given above. Finally, according Eq. (10), the product of the slopes of the $E(\sigma)$ straight line in Fig. 2b and the $\sigma(E)$ straight line from [22], which were plotted using the results of different experiments, must be equal to unity. In our case, the former slope is equal to 0.15 V m/N and the latter is 6.4 N/V m, so their product is 0.96. These estimates support the validity of the approach to describing electrical and mechanical failures and the assumption that both processes are controlled by the same defect regions in a material. The relation between both cases of failure is seen in Fig. 3, which shows the $E(\sigma)$ and $\sigma(E)$ dependences; they are seen to coincide in the range $3 \le E \le 5$ MV/m and $6 \le \sigma \le 17$ MPa.

It should be noted that, when describing the electrical failure of the polarized ferroelectric ceramics in this work, we used the dependence $\tau = A_{EM}\exp(-B_{EM}E)$, which is valid for the piezoelectric effect. In [15], a better fit to the experimental data on mechanical failure was obtained by substituting the electrostrictive stresses into the exponent: $\tau = A_{EM}\exp(-B_{EM}E^2)$. In this case, the preexponential factor A_{EM} coincides with the value determined from the experiments on mechanical failure. The experiments on unpolarized ferroelectric ceramics performed in [15] differ from those carried out in this work in terms of the time of storing at a step with E = const: this time in [15] is more than two orders of magnitude longer. FE ceramics undergoes three types of deformation throughout the entire time an electric field is applied: the deformation of a crystallite due to the reorientation of non-180° domains is accompanied by the piezoelectric effect of orientated domains, and this effect is superimposed on true electrostriction [24]. These effects are likely to occur; however, depending on the experimental conditions (storing time, stress, temperature), one of them will be dominant. The fact that these effects can explain the time effects during electrical failure indicates the leading role of the mechanical failure of ferroelectric ceramics under application of an electric field.

Table 2. Characteristics of the breakdown kinetics of a polarized FC under the action of different mechanical stresses σ. The field and polarization vectors are codirectional (**E** ↑↑ **P**) or oppositely directed (**E** ↑↓ **P**)

	σ, MPa	A_{EM}, s	B_{EM}, 10^{-6} C/N	$\bar{E}$, MV/m
E ↑↑ **P**	0	10^{38}	6.95	5.65
	2	10^{39}	6.57	5.83
	6	10^{36}	6.78	5.35
	10	10^{33}	6.53	5.25
	14	10^{29}	6.59	4.46
	17	10^{27}	6.55	4.17
E ↑↓ **P**	2	10^{39}	6.06	6.65
	6	10^{36}	5.47	6.82

Table 3. Characteristics of the failure kinetics of a polarized FC under a mechanical load in the presence of an electric field of various values. **E** ↑↑ **P**

E, MV/m	A_{ME}, s	B_{ME}, MPa^{-1}	$\bar{\sigma}$, MPa
0	10^{28}	1.31	21.3
1	10^{30}	1.17	25.6
2	10^{29}	1.31	22.2
3	10^{25}	1.19	21.0
4	10^{20}	1.36	14.7
5	10^{13}	1.47	8.8

The value of V_{eff}^{E} can be estimated by taking b to be the piezoelectric constant e_{33} = 14.9 C/m^2 [24] (upon bending along the **P** direction, we have compressive deformation). In this case, we find $V_{eff}^{E} = 4 \times 10^{-27}$ m^3 (since $V_{eff}^{E} b = 6.3 \times 10^{-26}$ C m), which is fairly close to the value of V_{eff}^{σ} obtained in this work. This fact further supports the possibility of describing the processes of electrical and mechanical failure using the same approach.

4. CONCLUSIONS

Thus, physically, the failure of ferroelectric ceramics under the simultaneous action of electric and mechanic fields occurs as follows: after mechanical and electrical loads are applied, the processes of stress relaxation and failure begin in the defect regions in ferroelectric ceramics. If one of the fields is weak, its effect on the failure due to the other field consists mainly in relaxation; that is, the failure rate decreases and the strength increases. At high values of the fields, on the contrary, the failure

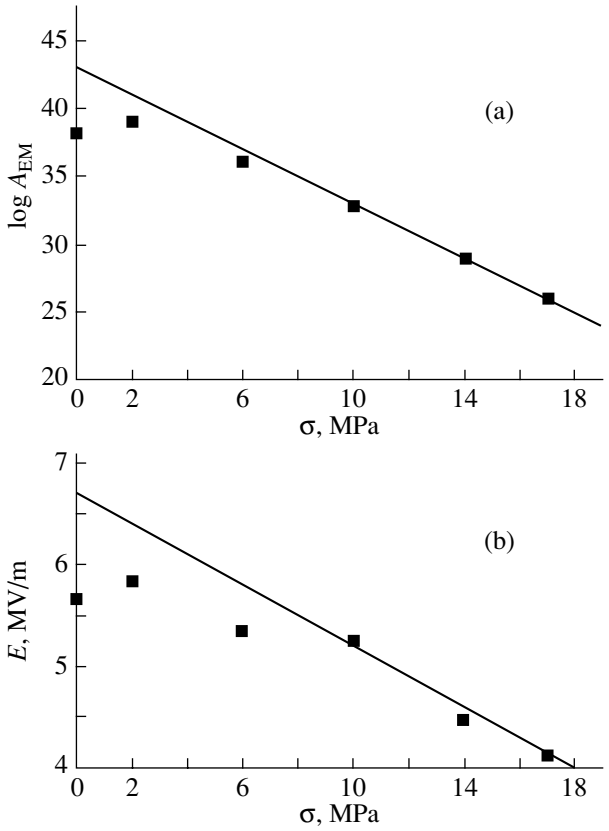

Fig. 2. Effect of mechanical stresses on (a) the parameter A_{EM} during electrical failure and (b) the average electrical breakdown field.

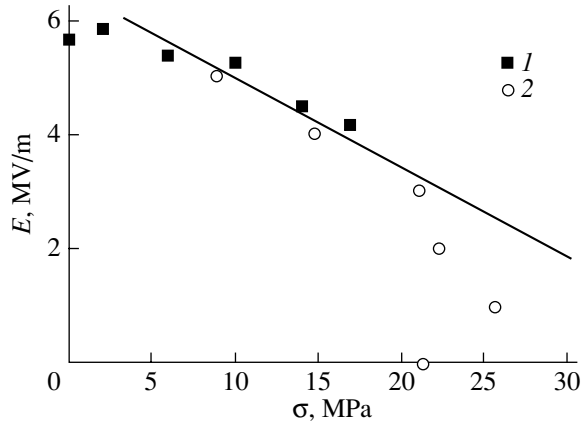

Fig. 3. Combined dependences of (*1*) the average electrical breakdown field on the mechanical stresses and (*2*) the average breaking mechanical stresses on the electric field.

accelerates and the strength decreases. Thus, under the simultaneous action of electric and mechanic fields, the failure can proceed faster or slower than under the action of one of the fields and the failure kinetics is described by one equation, Eq. (10).

When an electric field is applied, the deformations of the matrix and a crystallite are different due to the converse piezoelectric effect and electrostriction; therefore, internal mechanical stresses arise in the crystallite. These stresses favor either relaxation via domain-wall motion or the appearance of microcracks at 90° domain walls, resulting in breakdown [25]. Microcracks at 90° domain walls inside individual crystallites were observed when polycrystalline $BaTiO_3$ was polarized in fields that were about half the breakdown field [26, 27].

ACKNOWLEDGMENTS

This work was supported by the Russian Foundation for Basic Research (project no. 02-02-16232), the Competition Center of the Ministry of Education of the Russian Federation (project no. E02-3.4-424), and a grant from the Ministry of Education of the Russian Federation, "Ceramics and Ferroelectric Ceramics" (project no. 202-03-02-04).

REFERENCES

1. G. I. Skanavi, *Physics of Dielectrics (Strong Field Region)* (Fizmatgiz, Moscow, 1958) [in Russian].
2. A. A. Vorob'ev and G. A. Vorob'ev, *Electric Breakdown and Fracture of Solid Dielectrics* (Vysshaya Shkola, Moscow, 1966) [in Russian].
3. K. Okazaki, *Ceramic Engineering for Dielectrics* (Tokyo, 1969; Énergiya, Moscow, 1976).
4. E. I. Bondarenko, V. Yu. Topolov, and A. V. Turik, Kristallografiya **37** (6), 1572 (1992) [Sov. Phys. Crystallogr. **37**, 852 (1992)].
5. *Polarization of Piezoceramics*, Ed. by E. G. Fesenko (Rostov. Gos. Univ., Rostov-on-Don, 1968) [in Russian].
6. Val. A. Doroshenko, M. M. Pikalev, and V. A. Doroshenko, in *Strength of Materials and Construction Elements at Sonic and Ultrasonic Loading Frequencies* (Naukova Dumka, Kiev, 1983), p. 181 [in Russian].
7. I. Ueda, M. Takeuchi, S. Ikegami, and H. J. Sato, Phys. Soc. Jpn. **17** (10), 1679 (1962).
8. V. A. Dyatlov and E. V. Sinyakov, Ukr. Fiz. Zh. **19** (12), 2053 (1974).
9. A. D. Feronov and V. A. Servuli, *Physics of Dielectrics and Semiconductors* (Volgograd, 1981), p. 111 [in Russian].
10. S. N. Koĭkov and A. I. Tsikin, *Electrical Age Hardening of Solid Dielectrics* (Énergiya, Leningrad, 1968) [in Russian].
11. M. A. Bagirov, Ya. T. Razimov, T. F. Abbasov, and S. A. Abbasov, Fiz. Tverd. Tela (Leningrad) **15** (5), 1579 (1973) [Sov. Phys. Solid State **15**, 1055 (1973)].
12. M. S. Dakhiya, V. A. Zakrevskiĭ, and A. I. Slutsker, Fiz. Tverd. Tela (Leningrad) **26** (9), 2716 (1984) [Sov. Phys. Solid State **26**, 1645 (1984)].
13. E. I. Bondarenko, V. Yu. Topolov, and A. V. Turik, Zh. Tekh. Fiz. **57** (7), 1416 (1987) [Sov. Phys. Tech. Phys. **32**, 841 (1987)].

14. E. I. Bondarenko, V. Yu. Topolov, and A. V. Turik, Zh. Tekh. Fiz. **62** (12), 155 (1992) [Sov. Phys. Tech. Phys. **37**, 1206 (1992)].
15. L. V. Zhoga and V. V. Shpeĭzman, Fiz. Tverd. Tela (St. Petersburg) **34** (8), 2578 (1992) [Sov. Phys. Solid State **34**, 1382 (1992)].
16. A. A. Griffith, Philos. Trans. R. Soc. London, Ser. A **221**, 163 (1921).
17. G. E. Gorovits, Zh. Russ. Fiz.–Khim. O-va **59**, 369 (1927).
18. G. E. Gorovits, Zh. Russ. Fiz.–Khim. O-va **59**, 533 (1927).
19. V. A. Stepanov, N. N. Peschanskaya, and V. V. Shpeĭzman, *Strength and Relaxation Phenomena in Solids* (Nauka, Leningrad, 1984) [in Russian].
20. V. V. Shpeĭzman, Fiz. Tverd. Tela (St. Petersburg) **34** (7), 2261 (1992) [Sov. Phys. Solid State **34**, 1209 (1992)].
21. F. F. Vitman, Ya. S. Uflyand, and B. S. Ioffe, Prikl. Mekh. **5** (6), 122 (1970).
22. L. V. Zhoga, A. V. Shil'nikov, and V. V. Shpeĭzman, Fiz. Tverd. Tela (St. Petersburg) **47** (4), 628 (2005) [Phys. Solid State **47**, 652 (2005)].
23. L. V. Zhoga, A. V. Shil'nikov, and V. V. Shpeĭzman, Izv. Ross. Akad. Nauk, Ser. Fiz. **67** (8), 1207 (2003).
24. B. Jaffe, W. R. Cook, and H. Jaffe, *Piezoelectric Ceramics* (Academic, New York, 1971; Mir, Moscow, 1974).
25. J. T. Dickinson, L. C. Jensen, and W. D. Williams, J. Am. Ceram. Soc. **68** (5), 235 (1985).
26. B.-C. Shin and H.-G. Kim, Ferroelectrics **100** (1–4), 209 (1989).
27. B.-C. Shin and H.-G. Kim, in *Proceedings of 3rd International Conference on Conduction Breakdown in Solid Dielectrics* (Trondheim, 1989), p. 474.

Translated by K. Shakhlevich

Physics of the Solid State, Vol. 47, No. 5, 2005, pp. 876–881. Translated from Fizika Tverdogo Tela, Vol. 47, No. 5, 2005, pp. 850–855.

Atomic Structure and Strength of Inorganic Glasses

V. P. Pukh, L. G. Baĭkova, M. F. Kireenko, L. V. Tikhonova, T. P. Kazannikova, and A. B. Sinani

Ioffe Physicotechnical Institute, Russian Academy of Sciences, Politekhnicheskaya ul. 26, St. Petersburg, 194021 Russia
e-mail: pukh@sglass.ioffe.ru

Abstract—The role of the atomic structure in the fracture processes is considered using borate, silicate, and phosphate glasses as an example. Primary attention is focused on the degree of connectivity of the atomic structure. It is shown that the degree of connectivity is a major factor responsible for the structural strength of glasses under conditions excluding the influence of both accidental surface defects and the environment. The change in the Young's modulus as a measure of elastic deformation and the change in the hardness as a characteristic of irreversible deformation are analyzed. The ultimate elastic strain experienced by a glass at the instant of fracture is examined. It is found that the ultimate elastic strain is approximately equal to 10% for glasses with a three-dimensional atomic structure and 5% for glasses with a two-dimensional (layered) or chain structure. It is assumed that this behavior of the strength as a function of the degree of connectivity of the atomic structure is associated with the degree of uniformity of the external load distribution over atomic bonds. © *2005 Pleiades Publishing, Inc.*

1. INTRODUCTION

Physicists began to express particular interest in problems regarding the strength of inorganic glasses already in the early 1930s following the publication of the pioneering works by S.N. Zhurkov and A.P. Aleksandrov, who demonstrated that the strength of glass fibers is close to the theoretical limit [1, 2]. Subsequent investigations performed in this field of glass science at the laboratory headed by F.F. Vitman at the Ioffe Physicotechnical Institute revealed that a high natural strength is inherent not only in glass fibers but also in massive sheet glasses, i.e., in any material in the vitreous state [3–7]. This raised the question as to which role is played by the atomic structure of glasses in the fracture processes. In the present paper, we summarize the results of our investigations carried out in this direction over the last twenty five years [8–13]. Apart from the data on the tensile strength, we analyze the changes in other important strength characteristics, such as the elastic modulus E, the hardness H, and the ultimate elastic strain ε.

2. EXPERIMENTAL TECHNIQUE

The elastic moduli were determined from the velocities of longitudinal and shear waves. These velocities were measured by the pulsed technique. The hardness was measured on a PMT-3 tester using a standard Vickers diamond pyramid with an apex angle of 136°.

The strength of glasses should be measured under conditions excluding the influence of both accidental surface defects and the environment (moisture). In our experiments, we used three-point bending of glass fibers with diameters ranging from 100 to 150 μm [14]. In this case, the maximum tensile stress acts in a microregion approximately 10^{-3} mm^2 in area and, consequently, the effect of accidental surface defects is virtually ruled out. Moreover, the use of this method insures against contact damages of operating surfaces of samples during drawing of glass fibers and subsequent manipulations with the samples. However, the spread of strengths about a mean value indicates that microinhomogeneities of different types arise in the structure of glasses because of the disadvantages of the techniques and conditions used for the melting and drawing of glass fibers.

It should be noted that the surface crystallization occurring in the course of drawing of glass fibers can also bring about the formation of structural defects. In our case, these defects were removed by chemical etching [15]. In order to prevent the influence of water contained in the environment and adsorbed on the surface of samples, the structural strength was measured in liquid nitrogen [15].

Table 1 presents the data on the strength of commercial sheet sodium calcium silicate glasses.

It can be seen from Table 1 that the structural strength of the fibers drawn from the sheet glass is equal to 7.5 GPa, which is close to the theoretical strength of this glass [7]. It is interesting to note that, for the commercial sheet glass subjected to etching, the strength determined by the symmetric bending method (when the area of the operating surface is four orders of magnitude greater than the area used in the case of fiber bending) is only 30% less than the structural strength of glass fibers. Therefore, it can be said with assurance that the structure of sheet glasses is almost on a par in terms of strength with the structure of glass fibers approximately 100 μm in diameter.

1063-7834/05/4705-0876$26.00 © 2005 Pleiades Publishing, Inc.

Table 1. Strengths of sodium calcium silicate glasses for different types of samples, measurement techniques, and media of measurements

Sample type	Measurement technique	State of the sample	Strength σ, GPa		
			air	liquid nitrogen	vacuum (residual pressure, 10^{-4} Torr)
Fiber (diameter, 100–150 μm) drawn in the flame of a burner	Three-point lateral bending	Initial	1.20	2.40	–
		Etched	3.20	7.50	–
Sheet glass plates (thickness, 2.5 mm)	Central bending (ring in ring)	Initial	0.25	–	0.50
		Etched	2.50	–	5.00

The structural strength of glasses should be treated as a physical characteristic indicating the potential (theoretical) limit of their strength.

3. RESULTS AND DISCUSSION

Let us consider the deformation of silica glasses under loading. The main structural units of silicate glasses are silicon–oxygen tetrahedra. A silicon atom is located at the center of a silicon–oxygen tetrahedron. This silicon atom is bonded to four oxygen atoms due to the sp^3 hybridization. The adjacent tetrahedra are joined together via the bridging oxygen atom; i.e., the tetrahedra are shared by vertices (Fig. 1) [16]. It turns out that, in the strength field of two silicon atoms, the oxygen atom is bonded to these atoms owing to a complex *spd* hybridization and the bond involves a free Si *d* orbital, which is used by *p* electrons of the oxygen atom. This results in the formation of a partial donor–acceptor bond. The Si–O–Si angle between two adjacent tetrahedra can vary from 120° to 180°, whereas this angle in the structure of crystalline quartz modifications is fixed. The elastic deformation of silica and silicate glasses occurs predominantly through a change in the angles between tetrahedra, i.e., through their rotations [17]. By virtue of the density defect and the presence of discontinuities in the silicon–oxygen network, the structure of the silica glass is capable of orientating and hardening (as is the case with organic polymers) and the elastic modulus increases with an increase in the strain under tension (Fig. 2) [17].

The irreversible deformation of the silica glass at room temperature manifests itself only under local loading, for example, upon indentation of a diamond pyramid. It is worth noting that the deformation occurs only through the densification of the structure. Recall that the density defect of silica glass as compared to crystalline quartz amounts to ~18%. The hardness of silica glass with an ultimately cross-linked structure is approximately equal to 8.5 GPa and is maximum among the known inorganic glasses. The structural or ultimate strength of silica glass reaches ~12 GPa.

The introduction of sodium oxide Na_2O into silica glass leads to a loosening of the structure due to the breaking of a number of Si–O bonds formed by the bridging oxygen atoms through which the adjacent tetrahedra are joined together. This is accompanied by the formation of nonbridging oxygen atoms. The introduction of Na_2O (up to 33%) results in the formation of two-dimensional structures in which the planes (layers) involve chemically bonded SiO_4 tetrahedra. These layers are linked through a weak ionic interaction (Fig. 1). Such a decrease in the degree of connectivity of the atomic structure of the glass leads to a decrease in the strength to 3.5 GPa.

The formation of layers linked to each other through weak ionic interactions brings about the deformation of these structures due to mutual shears of the layers. This is accompanied by a more than twofold decrease in the hardness to 3.7 GPa. The elastic modulus *E* decreases by 18% and is equal to 60 GPa.

When the third component, namely, a divalent- or trivalent-metal oxide, for example, zinc oxide ZnO or aluminum oxide Al_2O_3, is introduced into the silicate glass modified with sodium oxide, there arise additional donor–acceptor bonds that are involved in formation of ZnO_4 or AlO_4 tetrahedra, which are isomorphically incorporated into the silicon–oxygen network (Fig. 1). This leads to a partial or complete compensation for the adverse effect exerted by sodium oxide, the recovery of broken Si–O bonds, and an increase in the degree of connectivity of the glass-forming network. The anionic network consists of tetrahedra of two types, namely, SiO_4 and MeO_4. The strength and hardness of the ternary glasses are higher than those of the binary glass. Sodium aluminosilicate glasses possess extremely high strengths close to the strength of silica glass, because the energy of the Al–O bond is only slightly less (by 15%) than that of the Si–O bond [18, 19]. Glasses of optimum compositions contain Na_2O and Al_2O_3 with identical molar concentrations. In these glasses, all oxygen atoms introduced with sodium oxide participate in the formation of AlO_4 tetrahedra, whereas the Na^+ cations compensate for the negative charge of the tetrahedra. The role of glass formers and donors can also be played by other oxides. For example, in magnesium aluminosilicate glasses, AlO_4 tetrahedral groups are formed by donor–acceptor bonds between aluminum atoms and oxygen atoms intro-

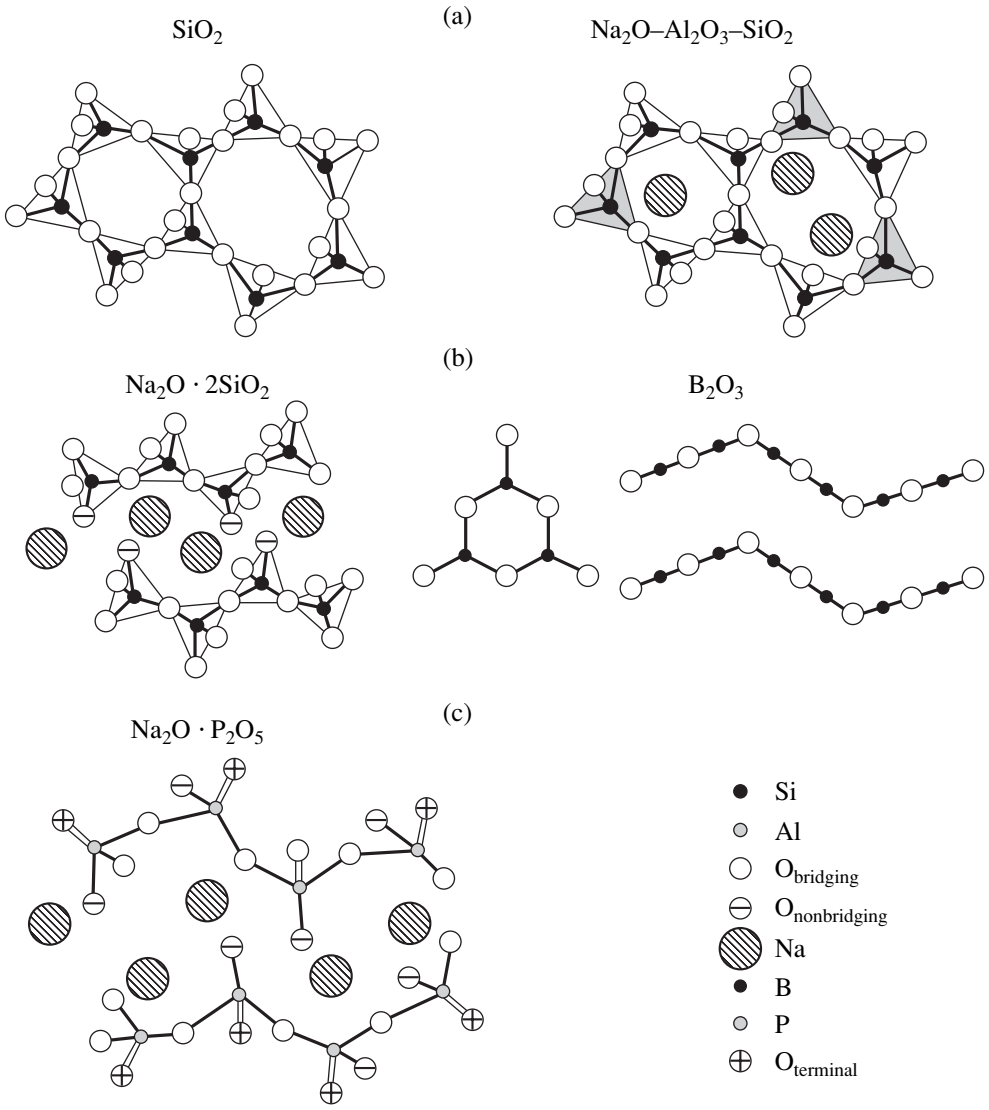

Fig. 1. Types of atomic structure of oxide glasses: (a) a three-dimensional glass-forming (anionic) network (SiO_2 silica glass, Na_2O–Al_2O_3–SiO_2 ternary glass), (b) a two-dimensional layered structure ($Na_2O \cdot 2SiO_2$ silicate glass, B_2O_3 borate glass), and (c) a chain structure ($Na_2O \cdot P_2O_5$ phosphate glass).

duced with magnesium oxide. In these glasses, the anionic network also forms a continuous three-dimensional structure. The strength and hardness of magnesium aluminosilicate glasses appear to be even higher than those of sodium aluminosilicate glasses (Table 2).

Let us now analyze the elastic moduli E of inorganic glasses. As can be seen from the data presented in Table 2, the elastic moduli of sodium aluminosilicate glasses are equal to the elastic modulus of the silica glass. The elastic modulus of the magnesium aluminosilicate glass (E = 95 GPa) is 30% greater than those of sodium aluminosilicate and silica glasses. This can be explained by the fact that, as was noted above, the elastic deformation of glasses occurs through mutual rotations of tetrahedra. Modifier cations interact with negatively charged tetrahedra and, thus, hinder their mutual rotations and displacements. In this case, the greater the cation charge, the stronger the interaction and the larger the elastic modulus.

It is of interest to elucidate how the degree of connectivity of the atomic structure affects the mechanical properties of borate glasses. Boron atoms are characterized by the sp^2 hybridization and, hence, have three valence electrons. As a consequence, the reaction of boron with oxygen gives boron oxide B_2O_3 with a structure consisting of BO_3 planar triangles joined into B_3O_6 planar boroxol rings. To put it differently, the valence chemical bonds in this glass are two-dimensional bonds. Such two-dimensional systems are bound by weaker van der Waals forces. Therefore, the B_2O_3 single-component glass has a graphite-like structure with strong chemical bonds inside the planes and weak bonds between the planes (layers). The strength, the

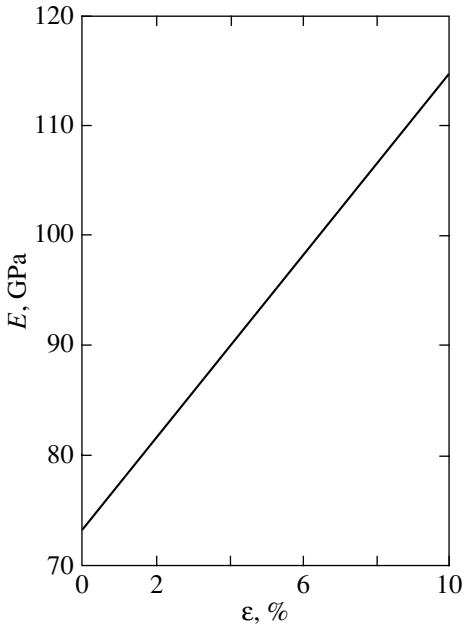

Fig. 2. Dependence of the Young's modulus E on the strain ε for the silica glass under tension [17].

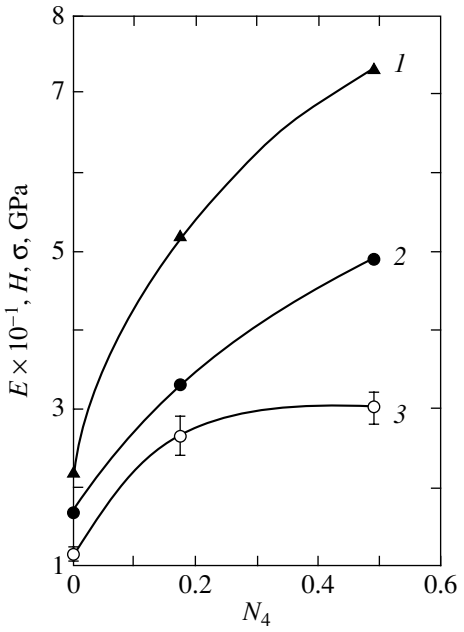

Fig. 3. Dependences of (*1*) the Young's modulus E, (*2*) the hardness H, and (*3*) the structural strength σ on the fraction of fourfold-coordinated boron atoms for borate glasses in the Na_2O–B_2O_3 system.

elastic modulus, and the hardness of this glass are approximately equal to 1.2, 22.0, and 1.7 GPa, respectively.

If sodium oxide is incorporated into boron oxide, the oxygen ions introduced with sodium oxide can play the role of donors. As a result, boron atoms having a

Table 2. Mechanical characteristics of inorganic glasses in three oxide systems

Glass no.	Chemical composition	Strength in liquid nitrogen σ, GPa	Hardness H, GPa	Young's modulus E, GPa	Ultimate elastic strain ε = σ/E, %
	Borate glasses				
1	B_2O_3	1.2	1.7	22	5.5
2	$15Na_2O \cdot 85B_2O_3$	2.7	3.9	52	5.2
3	$33Na_2O \cdot 67B_2O_3$	3.0	4.9	73	4.1
	Silicate glasses				
4	SiO_2	12.0	8.5	73(100*)	12.0*
5	$33Na_2O \cdot 67SiO_2$	3.5	3.7	60	5.8
6	$12.5Na_2O \cdot 12.5Al_2O_3 \cdot 75SiO_2$	8.3	5.4	72	11.5
7	$16.5Na_2O \cdot 16.5Al_2O_3 \cdot 67SiO_2$	8.4	5.5	73	11.6
8	$25Na_2O \cdot 25Al_2O_3 \cdot 50SiO_2$	8.5	6.0	74	11.4
9	$14.5MgO \cdot 14.5Al_2O_3 \cdot 71SiO_2$	10.4	6.4	95	10.9
10	$6TiO_2 \cdot 94SiO_2$	7.5	6.5	68	11.0
	Phosphate glasses				
11	$16.5Cs_2O \cdot 16.5Al_2O_3 \cdot 67P_2O_5$	1.6	3.5	50	3.2
12	$16.5Rb_2O \cdot 16.5Al_2O_3 \cdot 67P_2O_5$	2.4	3.8	55	4.4
13	$16.5K_2O \cdot 16.5Al_2O_3 \cdot 67P_2O_5$	2.5	4.1	59	4.2
14	$16.5Na_2O \cdot 16.5Al_2O_3 \cdot 67P_2O_5$	3.0	4.5	68	4.4
15	$16.5Li_2O \cdot 16.5Al_2O_3 \cdot 67P_2O_5$	3.4	4.9	74	4.6
16	$27.5Al_2O_3 \cdot 67.5P_2O_5$	4.0	5.7	89	4.5
17	$17.5Al_2O_3 \cdot 15ZnO \cdot 67.5P_2O_5$	5.7	5.5	81	7.0

* The parameter obtained with due regard for the increase in the Young's modulus with an increase in the strain [17].

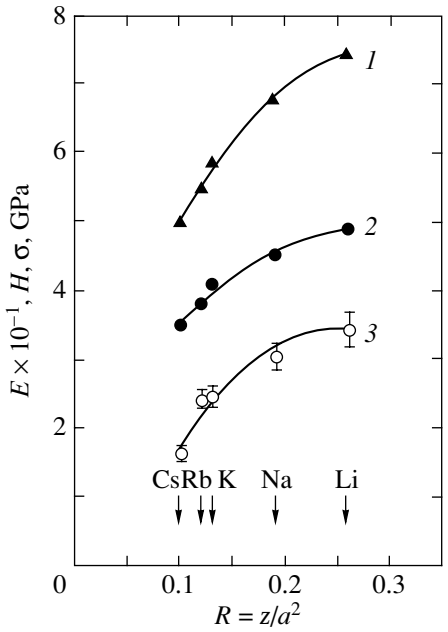

Fig. 4. Dependences of (*1*) the Young's modulus *E*, (*2*) the hardness *H*, and (*3*) the structural strength σ on the cation field strength *R* for phosphate glasses in the R_2O–Al_2O_3–P_2O_5 (R = Cs, Rb, K, Na, Li) systems. Notation: $R = z/a^2$, where *z* is the cation charge and *a* is the cation–anion distance with due regard for the coordination number.

free *p* orbital form additional donor–acceptor bonds with oxygen atoms. In Na_2O–B_2O_3 glasses, the sp^3 hybridization leads to the formation of BO_4 spatial (three-dimensional) tetrahedra. For each molecule of sodium oxide there is only one boron atom in a fourfold-coordinated state. This brings about the formation of a mixed structure in which BO_3 planar triangles alternate with BO_4 three-dimensional tetrahedra. In turn, this structure provides a partial chemical cross linking of planes and an increase in the degree of connectivity of the atomic structure. The higher the Na_2O content in the glass, the higher the degree of connectivity of the structure of glass. The dependences of the mechanical characteristics on the fraction of fourfold-coordinated boron atoms in borate glasses (Fig. 3) indicate that an increase in the degree of structural connectivity results in a considerable increase in the strength, the hardness, and the elastic modulus of the glass.

The understanding of the role played by the atomic structure of phosphate glasses in the fracture processes opens up new possibilities for purposefully changing the degree of polymerization of the anionic network in the structure of glasses. Unlike the SiO_4 tetrahedron, the PO_4 tetrahedron contains one terminal oxygen atom that is not involved in the formation of the anionic network. This circumstance *a priori* decreases the degree of connectivity of the anionic network in the structure of phosphate glasses. The introduction of alkali metal oxides R_2O into these glasses leads to the formation of chain structures. By varying the field strength of modifier ions, it is possible to control the interchain interaction and, thus, to change the mechanical characteristics of glasses.

The data presented in Table 2 and Fig. 4 demonstrate that, for glasses in the R_2O–Al_2O_3–P_2O_5 ternary systems, an increase in the field strength of modifier ions (in the series from Cs^+ to Li^+) results in an increase in the structural strength, the elastic modulus, and the hardness [12].

Aluminum ions in phosphate glasses can serve as modifiers and network formers. In the former case, aluminum ions participate in the formation of chain structures with strong ionic interaction between chains. In the latter case, aluminum ions favor the formation of three-dimensional network structures due to the transformation of terminal oxygen atoms (P=O) into bridging oxygen atoms [20].

Our earlier studies revealed [13] that, in phosphate glasses of the R_2O–Al_2O_3–P_2O_5 system, the aluminum ion has an octahedral coordination; i.e., it acts as a modifier. An increase in the aluminum oxide content in these glasses leads to an increase in the structural strength, the hardness, and the elastic modulus due to an enhancement of the ionic interaction between chain structures. The binary aluminophosphate glass with a composition similar to aluminum metaphosphate has the largest values of the elastic modulus and hardness (Table 2).

The maximum structural strength is observed for the zinc aluminophosphate glass, even though the elastic modulus of this glass is somewhat less than that for aluminum metaphosphate. We assume that, in the zinc aluminophosphate glass, the chain structures coexist with three-dimensional structures due to the incorporation of tetrahedrally coordinated zinc ions into the anionic network. An increase in the degree of connectivity of the anionic network results in an increase in the structural strength.

Therefore, the structural strength, the hardness, and the elastic modulus of phosphate glasses can be close and even exceed those of the known silicate glasses owing to the strong ionic interaction between chain structures and the formation of three-dimensional structures upon introduction of the second network former.

An important characteristic is the ultimate elastic strain, which, as can be seen from Table 2, also depends on the atomic structure of glass. In a structure with identical atomic bonds, the external load is uniformly distributed over individual bonds. Such a structure is optimum from the standpoint of high strength.

However, in a structure of glass in which the atomic and molecular bonds have different rigidities, the external load is distributed nonuniformly. The degree of uniformity of the external load distribution is determined

both by the difference between the rigidities of bonds and by their distribution over the bulk of the glass. In our opinion, it is this degree of uniformity of the external load distribution that is responsible for the highest structural strength and the maximum elastic strain (~10%) of three-dimensional structures. The ultimate elastic strain of layered and chain structures reaches only ~5%.

REFERENCES

1. S. N. Zhurkov, Zh. Éksp. Teor. Fiz. **1**, 189 (1931).
2. A. P. Aleksandrov and S. N. Zhurkov, *Phenomenon of Brittle Fracture* (GTTI, Moscow, 1933) [in Russian].
3. F. F. Vitman, G. S. Pugachev, and V. P. Pukh, Steklo Keram. **9**, 12 (1965).
4. L. G. Baĭkova, F. F. Vitman, G. S. Pugachev, and V. P. Pukh, Dokl. Akad. Nauk SSSR **163** (3), 617 (1965) [Sov. Phys. Dokl. **10**, 666 (1966)].
5. F. F. Vitman, G. S. Pugachev, N. N. Shenberg, and V. P. Pukh, Izv. Akad. Nauk SSSR, Neorg. Mater. **2**, 197 (1966).
6. L. G. Baĭkova, V. A. Bershteĭn, F. F. Vitman, L. D. Volovets, G. S. Pugachev, and V. P. Pukh, Fiz. Tverd. Tela (Leningrad) **10** (5), 1315 (1968) [Sov. Phys. Solid State **10**, 1046 (1968)].
7. V. P. Pukh, *Strength and Fracture of Glasses* (Nauka, Leningrad, 1973) [in Russian].
8. T. I. Pesina, L. V. Romanenko, V. P. Pukh, and I. I. Novak, Fiz. Khim. Stekla **7** (1), 68 (1981).
9. T. I. Pesina, V. A. Zakrevskiĭ, and V. P. Pukh, Fiz. Khim. Stekla **5** (4), 497 (1979).
10. M. S. Aslanova, L. G. Baĭkova, V. P. Pukh, L. A. Sapozhnikova, and M. I. Stepanov, Fiz. Khim. Stekla **8** (5), 560 (1982).
11. L. G. Baĭkova, Yu. K. Fedorov, M. N. Tolstoĭ, V. P. Pukh, L. V. Tikhonova, S. G. Lunter, and A. B. Sinani, Fiz. Khim. Stekla **16** (3), 384 (1990).
12. L. G. Baĭkova, Yu. K. Fedorov, V. P. Pukh, T. I. Pesina, T. P. Kazannikova, L. V. Tikhonova, and M. F. Kireenko, Fiz. Khim. Stekla **19** (5), 725 (1993).
13. L. G. Baĭkova, Yu. K. Fedorov, V. P. Pukh, T. I. Pesina, L. V. Tikhonova, and T. P. Kazannikova, Fiz. Khim. Stekla **21** (2), 177 (1995).
14. V. P. Pukh, T. I. Pesina, and M. I. Ivanov, Fiz. Khim. Stekla **7** (3), 328 (1981).
15. L. G. Baĭkova, V. P. Pukh, and T. I. Pesina, Fiz. Khim. Stekla **9** (6), 654 (1983).
16. V. P. Pryanishnikov, *The Silica System* (Stroĭizdat, Leningrad, 1971) [in Russian].
17. F. P. Mallinder and B. A. Proctor, Phys. Chem. Glasses **5** (4), 91 (1964).
18. T. I. Pesina, L. G. Baĭkova, V. P. Pukh, I. I. Novak, and M. F. Kireenko, Fiz. Khim. Stekla **12** (1), 26 (1986).
19. H. K. Sun, J. Am. Ceram. Soc. **30** (9), 277 (1947).
20. S. Chakraborty and A. Paul, J. Mater. Sci. Lett. **8** (12), 1358 (1989).

Translated by O. Borovik-Romanova

Physics of the Solid State, Vol. 47, No. 5, 2005, pp. 882–885. Translated from Fizika Tverdogo Tela, Vol. 47, No. 5, 2005, pp. 856–859.

Electromagnetic Phenomena Entailed by Deformation and Fracture of Dielectric Solids

Kh. F. Makhmudov and V. S. Kuksenko

Ioffe Physicotechnical Institute, Russian Academy of Sciences, Politekhnicheskaya ul. 26, St. Petersburg, 194021 Russia
e-mail: victor.kuksenko@mail.ioffe.ru

Abstract—Mechanoelectric effects caused by elastic deformation of glasses and marbles are studied in a neutral environment and with weak electric polarization of samples. It is found that the electric potentials that are produced by bending a sample are opposite in sign in compressed and stretched regions. The mechanoelectric effects increase or decrease depending on the direction of the electric field applied to the sample. It is concluded that the electric polarization and the polarization induced by mechanical deformation are of a common nature. Electromagnetic precursors of earthquakes are discussed. © *2005 Pleiades Publishing, Inc.*

1. INTRODUCTION

Besides being of purely scientific interest, the electromechanical phenomena in naturally occurring insulators are of great practical importance because of the problem of interpreting electromagnetic precursors of earthquakes [1–3]. In addition, they facilitate understanding of the physical nature of powerful responses to weak causes (including electromagnetic responses to seismic events [4]) and a special state of solids [5, 6]. It is demonstrated in [7] that the phenomenon of an electric field arising in solid dielectric materials under load has a lot in common with the polarization of materials in a weak electric field. In the present paper, we study the influence of mechanical stress on the polarization of solid dielectric materials in weak electric fields. For the sake of brevity, we will call the electric potential arising under mechanical stress the mechanoelectric potential to distinguish it from the electric potential arising during usual polarization by an electric field. In this paper, we present the results of a study of quartz glass and marble samples. Marble is widely used in laboratory studies, because it has all the main features of solid dielectrics and does not exhibit the piezoelectric effect, a property important for our study.

2. EXPERIMENTAL SETUP

The experimental setup is presented in Fig. 1. Marble sample *1*, in the form of a $40 \times 40 \times 100$ mm prism, is loaded by a uniaxial compressive stress produced by a hydraulic press through glass ceramic insulators. Two electrodes *2* made of a silver powder mixed with epoxy are attached to opposite surface sides of the sample. The electric voltage between the electrodes is created by a dc power source. The electrodes can be grounded if required. The distribution of electric potentials in the sample is measured with a specially designed electrometer (EM) in a contactless mode. Electrometer probe *3* is attached to a micrometer feed system permitting scanning along the sample surface maintaining a 2-mm clearance between the probe and the surface.

Under uniaxial compressive loading, an induced electric field arises in a marble sample, with the side surface taking a positive potential. Without a mechanical load, the sample is polarized if a voltage is applied to the electrodes. In the latter case, the induced electric field is symmetric relative to the sample center and there are parts of the sample surface with positive and negative potentials. For brevity, we will call the phenomenon of an electric field arising under a mechanical load mechanical polarization and the phenomenon of an electric field appearing when an electric voltage is applied to the electrodes electric polarization.

A sequence of measurements of the induced electric field performed with the probe position fixed is presented in Fig. 2. The sample was subjected to a uniaxial compressive load P equal to 0.3 of the failure load at time t_1, and the load was immediately released. A positive induced potential F_e was detected. Next, at time t_2, a positive voltage (of the same polarity as under a mechanical load) was applied to the electrodes. When the electric potential reached the steady state in the

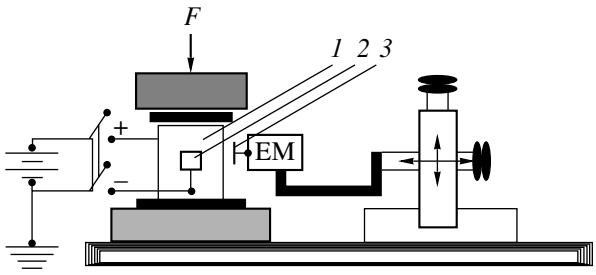

Fig. 1. Experimental setup including (*1*) sample, (*2*) electrodes, and (*3*) electrometer probe.

1063-7834/05/4705-0882$26.00 © 2005 Pleiades Publishing, Inc.

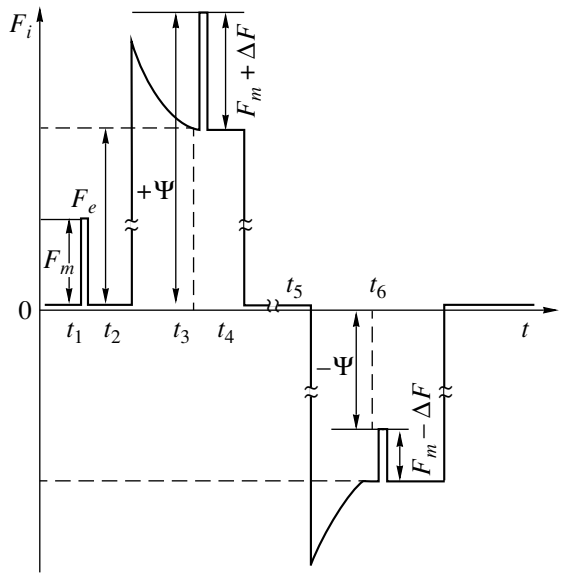

Fig. 2. Variations in the electric and mechanoelectric potentials under the action of a sequence of mechanical and electric fields applied to the sample.

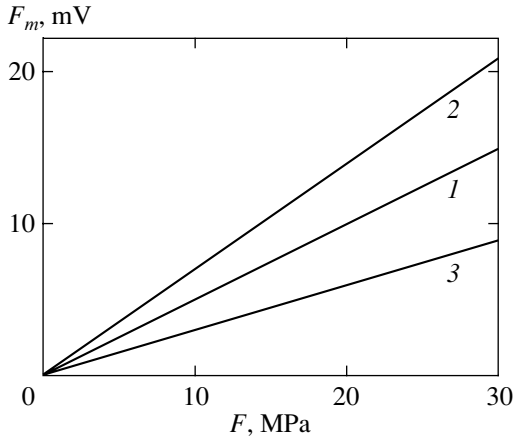

Fig. 3. Mechanoelectric potential as a function of the compressive mechanical load F measured (*1*) without electric polarization; (*2*) in the case where the polarities of the electric potentials coincide, that is, where F_m and F_e have the same sign; and (*3*) where the polarities of the induced electric field and the electric polarization are opposite.

period t_2–t_3, the sample was subjected to the same mechanical load again and then was again released. This time, the induced electric potential increased by ΔF. Let us denote the total potential at this moment as $+\Psi$. The induced potential returned to F_m when the mechanical load was removed. Then, at time t_4, the voltage on the electrodes was switched off and they were grounded. At time t_5, a voltage of the same magnitude but of opposite sign was applied to the electrodes again. The probe detected a negative potential, which soon reached a constant level F_m. Next, at time t_6, the sample was subjected to the same uniaxial load. The detected potential decreased by ΔF, and the total electric potential was equal to $-\Psi$. After the load was removed, the potential returned to F_m. Then, electrodes were grounded to ensure electric neutrality of the sample.

This sequence was repeated with the voltage between the electrodes kept constant and with the mechanical load changed in steps. In another case, the mechanical load was kept constant and the voltage was varied. The induced potential F_m increased or decreased depending on the direction of electric polarization of the sample.

Figure 3 shows the induced electric potential F_m as a function of the mechanical load. Line *1* corresponds to no electric polarization; line *2* corresponds to the case where the polarities of the induced electric field and electric polarization are the same, that is, where F_m and F_e have the same sign; and line *3* corresponds to the case where the polarities of the induced electric field and electric polarization are opposite. All the dependencies are linear in this range of loads, but they have different slopes.

Let us formally introduce the electromechanical modulus of a material by analogy with the piezoelectric modulus:

$$E = F_m \pm \Delta F.$$

In our experiment, it would make no sense to measure the absolute value for the modulus, because it depends on the probe design, its size, the gap between the probe and the sample, etc. However, the relative variation in A is characteristic for the effect of mechanical stress on an induced electric field in the presence of electric polarization. It was found that the electric modulus increases (decreases) when the polarities of the electric fields induced by the electric and mechanical polarizations are of the same sign (opposite in sign).

Figure 4 shows variations in the induced electric potential when the mechanical load is constant and the potential of electric polarization is varied. Three sections can be separated in the line shown in Fig. 4. The point on the vertical axis corresponds to the induced electric potential without any electric polarization, i.e., to $F_e = 0$.

Section *1* corresponds to the case where the electric and mechanical polarizations are of the same sign. Here, for the same load, the sample response is stronger, so the modulus is larger.

Sections *2* and *3* correspond to the case when the electric potential and induced electric field are opposite in sign.

In this case, the electromechanical modulus decreases and, at a certain point, the sample does not react to the mechanical load F^* at all. It is interesting that a further increase (in magnitude) of the negative polarizing electric field causes the potential to appear

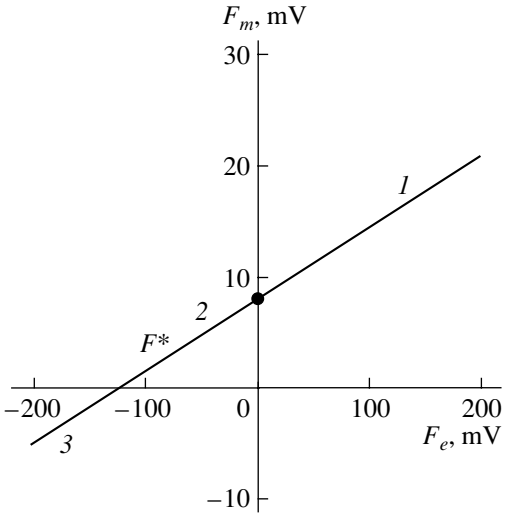

Fig. 4. Dependence of F_m on the electric potential F_e.

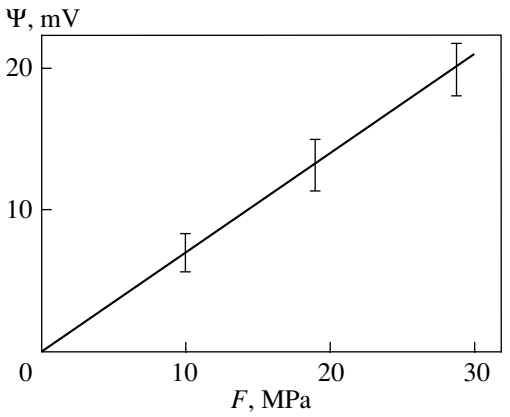

Fig. 5. Total potential Ψ of the induced electric field as a function of mechanical load for the case of opposite polarities of the electric fields.

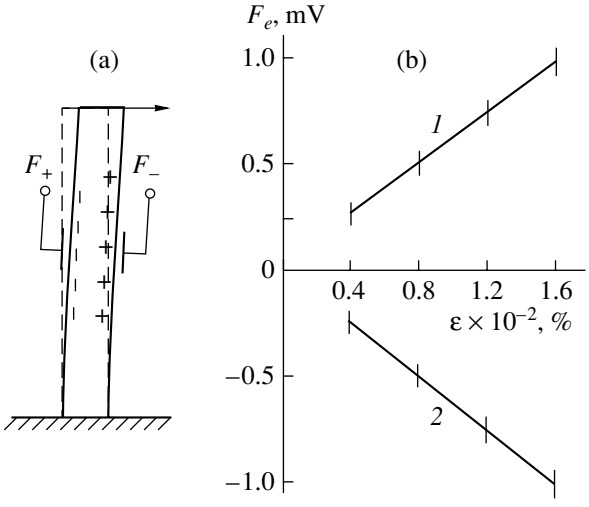

Fig. 6. Bending of a sample. (a) The field distribution and (b) the induced electric potential F_e as a function of deformation for the case of (*1*) compression and (*2*) tension.

again when the mechanical load is applied, but in this case the potential is negative. So, a rather complex interaction occurs between the electric and mechanical polarization fields.

There is another parameter of great interest, especially for practical applications. Let us consider Fig. 2.

The total potential Ψ increases under load if the polarities of the electric fields induced by the electric and mechanical fields coincide (section *1* in Fig. 4), and the total potential decreases under load if the polarities mentioned above are opposite (sections *2*, *3* in Fig. 4). Let us introduce a generalized parameter Ψ

$$\Psi = (+\Psi) + (-\Psi),$$

which is the sum of two electric potentials equal in magnitude that arise on the opposite-polarity electrodes when both the load and electric field are applied simultaneously. This parameter turns out to be the sum of the potentials measured under load (Fig. 5).

This dependence is linear because it is the sum of two linear functions, *2* and *3* in Fig. 3. It is almost independent of the electric polarizing field. As the field increases, the slope of line *2* grows but the slope of line *3* decreases. For this reason, this parameter is theoretically useful for measurements of unknown mechanical stresses (for example, in the bulk of rocks). Practical estimations of mechanical stresses by this method are complicated by the relaxation of the induced electric field [4]. Therefore, this technique can be suitable for measurements of variations in mechanical stresses, which are equally important for forecasting dynamical manifestations of macroscopic breakage (in particular, in an earthquake epicenter at the active stage).

3. DISCUSSION

Thus, our data provide compelling evidence in favor of interaction of the electric fields induced by mechanical and electric polarizations. This interaction is not limited to simple addition of the field potentials but rather is more complex in nature. The phenomenological studies presented in this paper are insufficient for a complete understanding of this phenomenon. Theoretical development of a microscopic model based, e.g., on materials with a simpler structure, is necessary. However, it is possible to outline the direction of development for this model by comparing the induced electric fields under compressive and tensile strains. This comparison can be made most simply through bending of a sample.

The corresponding experimental setup is shown in Fig. 6a. One end of a beam-shaped sample is fixed, and a bending moment is applied to the other end. The probe is fixed in one place, and the transition between compression and tension at this point is produced by changing the direction of the bending moment.

Figure 6b shows that the induced electric fields are opposite in sign for compression and tension. More-

over, the magnitude of the electric field is strongly affected by the gradient of the mechanical stress field.

In [8], an attempt was made to relate the induced electric field to the orientation of dipoles by the gradient of the mechanical stress field. It is noteworthy that the appearance of an induced electric field under the action of a mechanical stress field is a rather universal phenomenon. Manifestations of this effect for glass and marble are qualitatively similar despite the great difference in the physical properties of these materials. Therefore, electromagnetic phenomena that accompany deformations and destructions of dielectric solids (in particular, rocks) can be treated on common grounds.

In [2], the electromagnetic pulses that accompany the formation of cracks were explained in terms of the separation of charges on the walls of a crack. Without denying the possibility of this mode of generation of electromagnetic pulses, we can suggest that all dynamic processes, including the formation of cracks, must cause drastic changes in local mechanical fields and, therefore, in the induced electric fields that accompany electromagnetic pulse emission. This universal mechanism can explain the electromagnetic phenomena, both static and dynamic, that occur in epicenters of rock bumps and earthquakes.

It is our pleasure to stress that Zhurkov has supported this line of research and emphasized the importance of the interaction between various physical fields.

ACKNOWLEDGMENTS

This work was supported by the Russian Foundation for Basic Research (project nos. 02-05-39017, 04-05-65287) and the International Science and Technology Center (grant no. 1745).

REFERENCES

1. D. A. Lockner, J. D. Biyearly, V. S. Kuksenko, and A. V. Ponomarev, Pure Appl. Geophys. **123**, 601 (1986).
2. V. S. Kuksenko, R. Sh. Kil'keev, and M. I. Miroshnichenko, Dokl. Akad. Nauk SSSR **25** (4), 481 (1981).
3. G. A. Sobolev, *Fundamentals of the Earthquake Forecasts* (Nauka, Moscow, 1993) [in Russian].
4. N. T. Tarasov, Dokl. Akad. Nauk **353** (4), 542 (1997).
5. E. G. Fateev, Zh. Tekh. Fiz. **71** (1), 92 (2001) [Tech. Phys. **46**, 89 (2001)].
6. E. G. Fateev, in *Papers of 10th International Conference on the Physics and Chemistry of Leci* (St Johns, Newfoundland, Canada, 2002), p. 14.
7. V. S. Kuksenko, Kh. F. Makhmudov, and A. V. Ponomarev, Fiz. Tverd. Tela (St. Petersburg) **39** (7), 1202 (1997) [Phys. Solid State **39**, 1065 (1997)].
8. Kh. F. Makhmudov, Candidate's Dissertation (St. Petersburg, 1997), p. 11.

Translated by G. Tsydynzhapov

Physics of the Solid State, Vol. 47, No. 5, 2005, pp. 886–890. Translated from Fizika Tverdogo Tela, Vol. 47, No. 5, 2005, pp. 860–864.

Internal Friction and Young's Modulus of a Carbon Matrix for Biomorphic Silicon Carbide Ceramics

B. K. Kardashev*, Yu. A. Burenkov*†, B. I. Smirnov*,
A. R. de Arellano-Lopez, J. Martinez-Fernandez**, and F. M. Varela-Feria****

**Ioffe Physicotechnical Institute, Russian Academy of Sciences, Politekhnicheskaya ul. 26, St. Petersburg, 194021 Russia*
e-mail: smir.bi@mail.ioffe.ru
***Universidad de Sevilla, Sevilla, 41080 Spain*

Abstract—The amplitude, temperature, and time dependences of the Young's modulus and internal friction (ultrasonic attenuation) of a eucalyptus-based carbon biomatrix intended for preparing biomorphic silicon carbide ceramics were studied. Adsorption and desorption of molecules of the ambient medium (air) was shown to determine, to a considerable extent, the effective Young's modulus and acoustic vibration decrement of a specimen. A doublet maximum in the temperature dependence of ultrasonic attenuation was observed at a temperature close to the sublimation temperature of solid CO_2. The microplastic properties of the material were estimated from acoustic measurement data. © *2005 Pleiades Publishing, Inc.*

1. INTRODUCTION

This communication reports on the continuation of an investigation [1, 2] into the elastic and inelastic characteristics of biomorphic silicon carbide ceramics. Biomorphic SiC ceramics (bio-SiC) have attracted considerable interest over the past decade because they are distinguished from conventional high-strength ceramic-based composites in that, in addition to a high strength, they exhibit a high resistance to oxidation and corrosion, low density, high thermal conductivity, and heat shock resistance [3–7].

Our earlier publication [1] dealt with a study of the high-temperature (up to 1300 K) elastic properties of wood-based biomorphic SiC ceramics prepared by pyrolysis of eucalyptus and oak followed by silicon infiltration. It was shown that the decrease in the Young's modulus E with an increase in temperature is accompanied by the appearance of acoustic anomalies in the form of a number of jumps (splitting) in the resonance frequency.

In [2], the influence of vibrational strain amplitude on the Young's modulus and ultrasonic attenuation at moderate temperatures (116–296 K) was studied in bio-SiC specimens prepared from white eucalyptus. Vibrational loading of samples in air and in vacuum was also found to produce a number of unexpected effects. In particular, it was observed that adsorption and desorption of molecules of the ambient medium (air) can noticeably increase or decrease both the effective Young's modulus and the ultrasonic vibration decrement.

It was concluded in [1, 2] that the effects observed in SiC bioceramics are due to pores and residual carbon. In this connection, acoustic studies of preforms (carbon matrix) intended for preparing bio-SiC would present a certain interest. In this study, particular attention was focused on the behavior of acoustic characteristics (Young's modulus E, ultrasonic vibration decrement δ) of the white-eucalyptus carbon biomatrix. Acoustic measurements were carried out both in air and in vacuum over a broad strain amplitude range at temperatures ranging from ~100 to 296 K. The results obtained are compared with similar earlier measurements performed in [2] on SiC bioceramics also prepared from white eucalyptus.

2. SPECIMENS AND EXPERIMENTAL TECHNIQUES

We studied a carbon biomatrix of white eucalyptus (precursor). It was prepared by pyrolysis of a piece of wood (containing approximately 50% carbon) in argon at 1000°C [4, 7]. In the course of this procedure, the weight of the original material decreased by about 75%. The final product was a carbon biomatrix, which retained the main microstructural characteristics of the original natural material, namely, the cellular structure extended in the tree growth direction. Microstructural SEM studies of eucalyptus biomatrix specimens clearly reveal this pattern, as well as the presence of pores ranging up to 100 μm in size [1].

The specimens intended for acoustic studies were ~20-mm-long rods with a roughly square cross section ~16 mm^2 in area. The specimens were oriented either along or perpendicular to the original tree fibers. The density of the material was 0.68 g/cm^3.

As in the earlier work dealing with bio-SiC [2], the Young's modulus E and the ultrasonic vibration decre-

† Deceased.

1063-7834/05/4705-0886$26.00 © 2005 Pleiades Publishing, Inc.

ment δ were measured using the composite-oscillator technique. Longitudinal resonance vibrations at a frequency of about 100 kHz were excited in a rod-shaped specimen. The vibrational strain amplitudes ε varied from ~10^{-7} to 2×10^{-4}. A more detailed description of the method can be found in [8].

The studies were conducted in the following order. First, the strain amplitude dependences of $E(\varepsilon)$ and $\delta(\varepsilon)$ were measured on a specimen stored in normal conditions after preparation, i.e., in air under atmospheric pressure at room temperature. Next, the acoustic system (the specimen and the quartz oscillator) was placed into a vacuum chamber and subsequent measurements were carried out at a pressure of ~10^{-3} mm Hg. The measurements yielded data on the time, temperature, and strain amplitude dependences of the Young's modulus E and the decrement δ.

3. EXPERIMENTAL DATA AND DISCUSSION

Figure 1 depicts the measured $E(\varepsilon)$ and $\delta(\varepsilon)$ dependences for two carbon matrix specimens, one of which was cut along (*C* along), and the other across (*C* across), the original wood fibers. In these measurements, the as-prepared specimens were subjected to high strain amplitudes. We readily see that the first increase in acoustic stress applied to the specimens brings about a noticeable rise in the Young's modulus. The decrement δ of the specimen cut along the fibers decreases gently, while that of the specimen cut across the fibers exhibits a more complex behavior. Just as for SiC bioceramics [2], the changes in the modulus turn out to be irreversible to a considerable degree; indeed, after the measurements are terminated, the modulus increases to above its original value in the region of small ε. Contrary to the bio-SiC, the decrement measured on the *C*-along specimen remains practically unchanged, while the decrement of the *C*-across specimen even uncreases. The $E(\varepsilon)$ and $\delta(\varepsilon)$ curves obtained in repeated measurements under increasing and decreasing strain amplitude practically coincide with one another and with the original curve measured under decreasing ε. The principal difference between the carbon biomatrix and the SiC bioceramic is that the former has low values of the modulus and higher values of the decrement (by one order of magnitude or greater). Nevertheless, high strain amplitudes affect the modulus and the decrement in SiC more clearly than in the carbon matrix.

Vacuum turned out to affect the matrix considerably more strongly than the SiC ceramic. By way of illustration, Fig. 2 displays the time evolution of $E(t)$ and $\delta(t)$ of a carbon matrix specimen cut across the original wood fibers measured in a vacuum chamber under pumping. It can be seen that the Young's modulus increases noticeably and the decrement decreases with time when subjected to vacuum, thus implying an effect

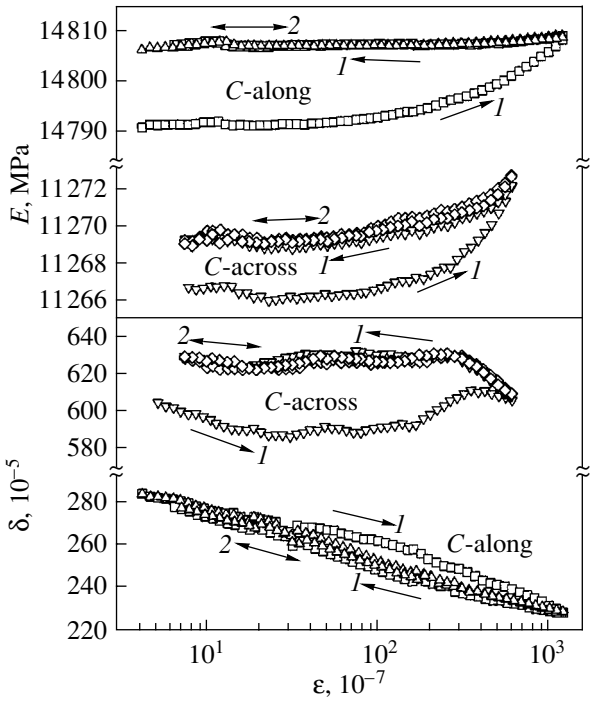

Fig. 1. Strain amplitude dependences of the Young's modulus E and of the decrement δ for two carbon matrix specimens cut along (*C* along) and across (*C* across) the original wood fibers. Two measurements were performed one after the other at an interval of about 1 min in air at atmospheric pressure on as-prepared specimens; (*1*) first measurement and (*2*) second measurement. The arrows identify the direction of ε variation. T = 296 K.

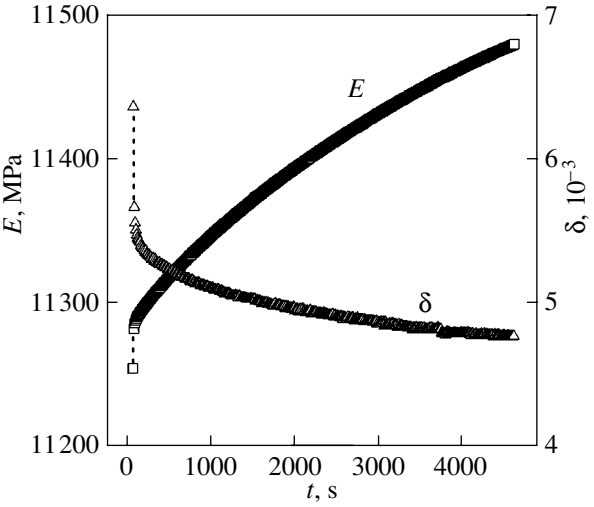

Fig. 2. Time evolution of the Young's modulus E and of the decrement δ for a carbon matrix specimen subjected to longitudinal vibrations across the original wood fibers. The measurements were conducted in a vacuum chamber in the course of evacuation for $\varepsilon = 5.0 \times 10^{-7}$ at T = 296 K.

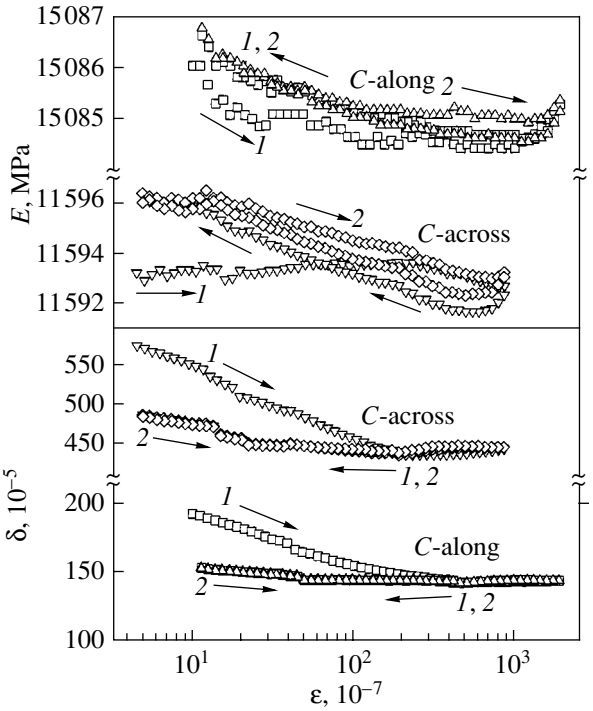

Fig. 3. Strain amplitude dependences of the Young's modulus E and decrement δ for two carbon matrix specimens cut along (C along) and across (C across) the original wood fibers. Two measurements were performed one after the other at an interval of about 1 min in vacuum on specimens subjected to high amplitude acoustic vibrations and low temperatures; (*1*) first measurement and (*2*) second measurement. The arrows identify the direction of ε variation. T = 296 K.

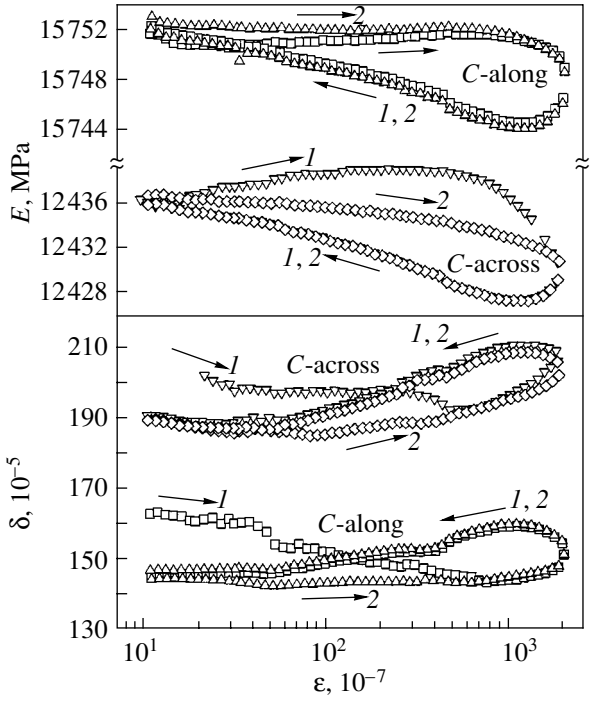

Fig. 4. Strain amplitude dependences of the Young's modulus E and of the decrement δ for two carbon matrix specimens cut along (C along) and across (C across) the original wood fibers. Two measurements were performed one after the other at an interval of about 1 min in vacuum on specimens subjected to high amplitude acoustic vibrations and low temperatures; (*1*) first measurement and (*2*) second measurement. The arrows identify the direction of ε variation. T = 106 K.

of adsorbed air molecules on the acoustic parameters of interest.

Figure 3 plots the $E(\varepsilon)$ and $\delta(\varepsilon)$ curves obtained in vacuum at room temperature. A comparison of Figs. 1 and 3 shows that the effect of high strain amplitudes in vacuum is clearly stronger for the decrement and is barely distinguishable for the Young's modulus. Measurements conducted in air revealed the reverse effect (Fig. 1). Notice also the higher values of the Young's modulus and the lower values of the decrement, a pattern typical of measurements performed in vacuum.

The $E(\varepsilon)$ and $\delta(\varepsilon)$ dependences measured at low temperatures (Fig. 4) differ in some respects from those measured at room temperature (Fig. 3). Here also, however, high-amplitude acoustic vibrations bring about only a small change in the decrement and have a barely discernible effect on the modulus at low values of ε.

Figure 5 shows the temperature dependences of $E(T)$ and $\delta(T)$ measured under cooling (Fig. 5a) and warming (Fig. 5b) of carbon biomatrix specimens. The most interesting feature appears to be the existence of two ultrasonic-attenuation peaks, one of which lies below, and the other above, the CO_2 ice sublimation temperature of 194.5 K [9]. The effect of the phase transition in the region of 273 K (the temperature of freezing of water and melting of ice) becomes pronounced in this material only under warming, when ice transforms into water.

As already pointed out, the irreversible changes in the modulus and decrement in specimens maintained in vacuum can be accounted for by the desorption of various molecules present in the air. Adsorption and desorption of gas molecules affect, to some degree, the level of ultrasonic attenuation and the effective elasticity modulus in both bio-SiC [2] and the carbon biomatrix, which is indicated by the strain amplitude, time, and temperature dependences of E and δ.

The most remarkable and certainly unexpected result of this work is the observation of a doublet maximum of ultrasonic attenuation (Fig. 5), which we believe to be caused by a change in the phase state of adsorbed carbon dioxide molecules. This maximum reveals some fine features of the phase transition and is most likely due to the difference in the bonding strength of the carbon matrix to the atoms of the complex CO_2 molecule. Obviously enough, the carbon–carbon and oxygen–carbon bond strengths should be different. It is this fact that apparently accounts for the doublet struc-

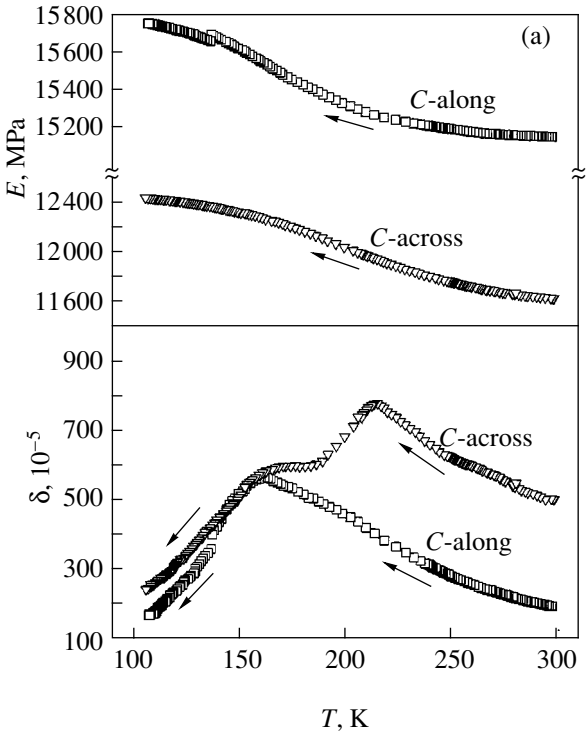

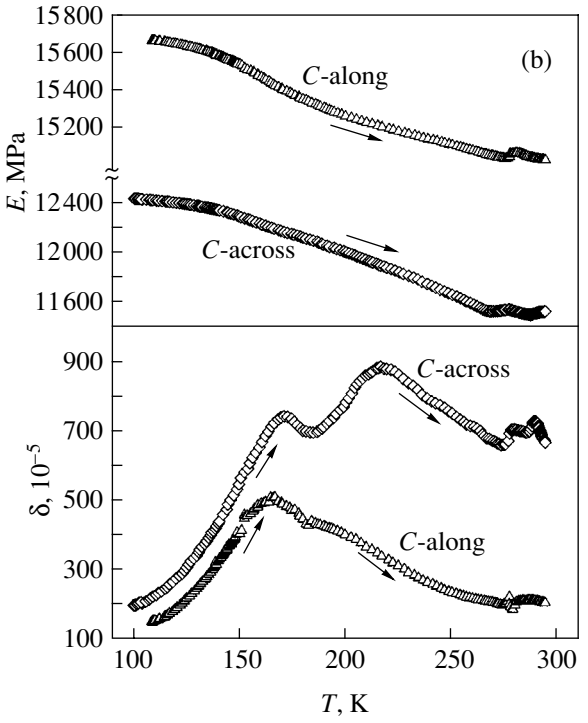

Fig. 5. Temperature dependences of the Young's modulus and of the decrement δ measured on two carbon matrix specimens cut along (*C* along) and across (*C* across) original wood fibers. The measurements were conducted in vacuum under (a) cooling and (b) warming on specimens subjected to high-amplitude acoustic vibrations at room temperature. The arrows identify the direction of *T* variation. $\varepsilon = 5.0 \times 10^{-7}$.

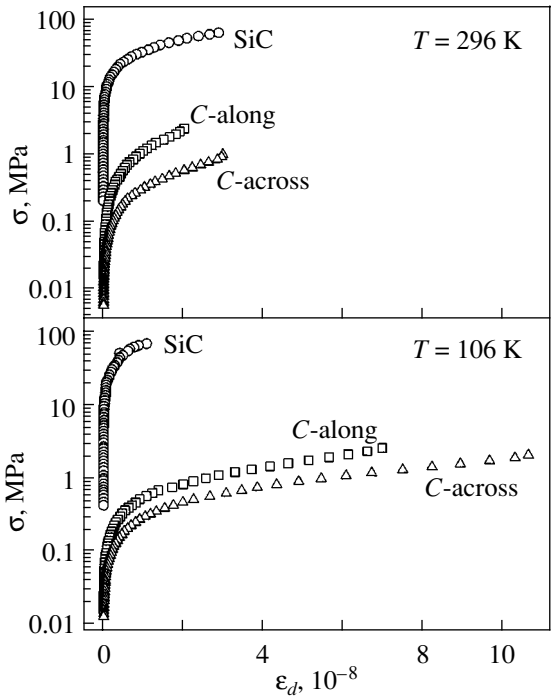

Fig. 6. Stress–microplastic strain curves derived at two temperatures from acoustic measurements on a SiC-along biomorphic ceramic specimen and on carbon matrix specimens cut along (*C* along) and across (*C* across) the original wood fibers.

ture; indeed, the breakage of bonds of one type requires a higher temperature than that of the other. As for the intensities of the two lines of the doublet, they are determined by the specimen prehistory and the actual character of the stressed state. This state is obviously different for specimens cut along and across the wood fibers (Fig. 5). Interestingly, there is no such maximum in silicon carbide ceramics [2]. This fact suggests that the bio-SiC contains almost no adsorbed CO_2 molecules.

Note that the carbon biomatrix studied in this work also exhibits microplastic properties. Figure 6 presents stress versus microplastic-strain curves derived from acoustic measurements. The graphs were constructed with the use of curves *2* for $E(\varepsilon)$ (Figs. 3, 4) measured under decreasing strain amplitude. The details pertaining to how such diagrams are constructed can be found in [10, 11]. The microplastic properties of the carbon biomatrix and bio-SiC ceramics studied are compared in Fig. 6 and the table. Comparison clearly shows that the behavior of the microplastic flow stress σ for the biomatrix differs from that observed in bio-SiC; indeed, the level of these stresses decreases with decreasing temperature. For a specimen cut along the wood fibers, this stress drops to less than one-half, while σ for the specimen cut across the fibers decreases only slightly.

Currently, it would be difficult to identify the microstructural elements responsible for the microplastic

Microplastic flow stress σ determined for a strain $\varepsilon_d = 1.0 \times 10^{-8}$ (conventional yield point)

Specimen	σ, MPa	
	T = 296 K	T = 106 K
SiC-along	33	67
C-along	1.2	0.55
C-across	0.32	0.29

deformation of both the carbon biomatrix and SiC bioceramics. Nevertheless, the microstrains revealed in the acoustic experiments show that these materials are not absolutely brittle, thus suggesting that they should contain plastic-deformation carriers analogous to dislocations in conventional crystals.

4. CONCLUSIONS

Our studies have shown that adsorption and desorption of molecules of the ambient medium (air) noticeably affect the effective elasticity modulus and internal friction in the carbon biomatrix employed in the fabrication of biomorphic SiC ceramics, i.e., that the carbon biomatrix exhibits effects typical of the bio-SiC itself [2]. A doublet ultrasonic-attenuation maximum has been observed at a temperature close to that of solid CO_2 sublimation. Acoustic measurements were also used to estimate the microplastic properties of the carbon biomatrix.

ACKNOWLEDGMENTS

This study was supported by the Russian Foundation for Basic Research (project no. 04-03-33183) and the Spanish Ministry of Science and Technology (project MAT 2003-05202-C02-01).

REFERENCES

1. B. I. Smirnov, Yu. A. Burenkov, B. K. Kardashev, F. M. Varela-Feria, J. Martinez-Fernandez, and A. R. de Arellano-Lopez, Fiz. Tverd. Tela (St. Petersburg) **45** (3), 456 (2003) [Phys. Solid State **45**, 482 (2003)].
2. B. K. Kardashev, Yu. A. Burenkov, B. I. Smirnov, A. R. de Arellano-Lopez, J. Martinez-Fernandez, and F. M. Varela-Feria, Fiz. Tverd. Tela (St. Petersburg) **46** (10), 1811 (2004) [Phys. Solid State **46**, 1873 (2004)].
3. D. Kovar, B. H. King, R. W. Trice, and J. W. Halloran, J. Am. Ceram. Soc. **80** (10), 2471 (1997).
4. M. Singh, Ceram. Eng. Sci. Proc. **21** (4), 39 (2000).
5. J. Martinez-Fernandez, F. Varela-Feria, S. Lopez-Pombero, A. R. de Arellano-Lopez, and M. Singh, Ceram. Eng. Sci. Proc. **22** (3), 135 (2001).
6. J. Martinez-Fernandez, A. Munoz, A. R. de Arellano-Lopez, F. M. Varela-Feria, A. Dominiguez-Rodriguez, and M. Singh, Acta Mater. **51**, 3259 (2003).
7. A. R. de Arellano-Lopez, J. Martinez-Fernandez, P. Gonzalez, C. Dominiguez, V. Fernandez-Quero, and M. Singh, Int. J. Appl. Ceram. Technol. **1**, 95 (2004).
8. S. P. Nikanorov and B. K. Kardashev, *Elasticity and Dislocation Inelasticity of Crystals* (Nauka, Moscow, 1985) [in Russian].
9. *Handbook of Chemistry and Physics*, 37th ed. (Chemical Rubber, Cleveland, Ohio, 1955).
10. V. M. Chernov, B. K. Kardashev, L. M. Krjukova, L. I. Mamaev, O. A. Plaksin, A. E. Rusanov, M. I. Solonin, V. A. Stepanov, S. N. Votinov, and L. P. Zavialsky, J. Nucl. Mater. **257**, 263 (1998).
11. B. I. Smirnov, Yu. A. Burenkov, B. K. Kardashev, D. Singh, K. C. Goretta, and A. R. de Arellano-Lopez, Fiz. Tverd. Tela (St. Petersburg) **43** (11), 2010 (2001) [Phys. Solid State **43**, 2094 (2001)].

Translated by G. Skrebtsov

Physics of the Solid State, Vol. 47, No. 5, 2005, pp. 891–895. Translated from Fizika Tverdogo Tela, Vol. 47, No. 5, 2005, pp. 865–869.

Cleavage of C_{60} Fullerite Crystals

S. V. Lubenets*, L. S. Fomenko*, A. N. Izotov, R. K. Nikolaev**, Yu. A. Osip'yan**, and N. S. Sidorov****

**Institute for Low Temperature Physics and Engineering, National Academy of Sciences of Ukraine, Kharkov, 61103 Ukraine*
e-mail: lubenets@ilt.kharkov.ua
*** Institute of Solid State Physics, Russian Academy of Sciences, Chernogolovka, Moscow oblast, 142432 Russia*

Abstract—It is found that, under certain conditions, C_{60} fullerite crystals can be cleaved along cleavage planes that are close-packed planes of the {111} type. Rigid gas-phase grown crystals exhibit good cleavage properties. In experiments with active compressive deformation, these crystals showed a high yield point τ_y = 2.65 MPa, a "parabolic" stress–strain curve, and brittle fracture after attaining a shear strain of about 8%. The fracture surface was clearly seen to have fragments parallel to the (111) plane. Typical microstructures observed in the cleavage plane are discussed: crystallographic cleavage steps, an indentation pattern, and a dislocation prick rosette. The fact that the activation volume $V \simeq 60b^3$ is small (b is the Burgers vector of a dislocation) and strain-independent indicates the Peierls character of fullerite deformation or dislocation drag in a dense network of local defects. © *2005 Pleiades Publishing, Inc.*

1. INTRODUCTION

The physical properties of C_{60} fullerite crystals depend on method of their growth and on the purity of the original raw material; they are sensitive to the presence of impurities and extended structural defects in the crystal and can change due to the effect of the ambient atmosphere and illumination. Crystals grown from a solution contain traces of solvent, C_{70} molecules, and a large number of stacking faults. In the as-grown state, the microhardness of such crystals is low ($H_V \lesssim$ 20 MPa); after prolonged exposure to air at room temperature, the microhardness increases by a factor of almost 10 [1, 2].

The gas-phase grown crystals have fcc structure and, as a rule, are distinguished by high purity and perfection. For such crystals, measurements on the (111) plane at room temperature have usually exhibited a well-reproduced value of the Vickers hardness, $H_V \simeq$ 150–200 MPa [3–5]. The possibility of preparing rather large C_{60} crystals has facilitated the beginning of studies into their mechanical properties using the methods of standard compression tests [1, 6–8]. In [7, 8], it was shown that, at T = 295 K, the stress–strain curve for a C_{60} single crystal has several stages, which is typical of fcc metals, and the yield point (i.e., critical shear stress τ_y in the [110](111) slip system) is approximately 0.7 MPa. The crystal was deformed without fracture to a shear strain of about 30% [8].

The ambient atmosphere has a significant effect on the mechanical properties of the C_{60} fullerite [1, 2, 9–11]. Exposure to an argon or oxygen atmosphere produces a strong hardening of the crystal [10] due to the introduction of gas impurities into the octahedral voids of the fcc lattice.

Illumination of C_{60} crystals increases their hardness [10, 11] and creates cracks on the surface [12–14]. The effect of hardening depends on the wavelength of the incident light, its intensity, and the duration of illumination [10, 15, 16]. The nature of fullerite photosensitivity is related to the formation of covalently bonded dimers or chains in the surface layer of the molecular lattice of the crystal [17]. Due to polymerization and oxidation, prolonged storage of fullerite in air under natural illumination conditions results in substantial surface degradation even at room temperature [18].

Thus, the mechanical properties of the C_{60} fullerite are affected by numerous factors, which most often lead to hardening of the crystal. Existing modifications of the gas-phase growth methods and the features of the growth process [12, 13, 19–21] allow one to fabricate crystals which, even in the original state, can substantially differ in terms of the degree of structural perfection in them and, therefore, of their strength characteristics.

When studying the mechanisms of crystal plasticity and strength, microhardness measurements are not sufficient, since this characteristic is weakly sensitive to the defect structure of the crystal as a whole. The method of recording the stress–strain curves in compression or tension experiments under a variation in the strain rate and temperature is more informative. In [7, 8], such curves were measured at room temperature for soft C_{60} fullerite single crystals. In this study, we attempt a comparative study of the plastic and strength properties of rigid C_{60} crystals at T = 293 K using methods of macro- and micromechanical tests: we determine the yield point τ_y, fracture stress τ_f, activation volume V, and microhardness H_V. The cleavage properties

1063-7834/05/4705-0891$26.00 © 2005 Pleiades Publishing, Inc.

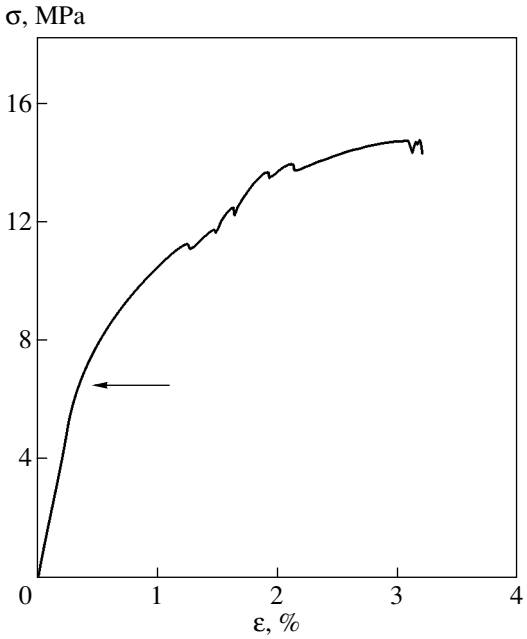

Fig. 1. Stress–strain curve of a C_{60} fullerite crystal at room temperature. The strain rate is 2.5×10^{-5} s^{-1}, the sample height is 3.98 mm, and the cross-sectional area is 5.73 mm^2.

of crystals are observed, and the cleavage plane is established.

2. EXPERIMENTAL

C_{60} crystals were grown from the gas phase. An original C_{60} fullerite powder of 99.95% purity was placed into a quartz cell and exposed to two-stage cleaning in a dynamic vacuum of ~10^{-3} Torr. At the first stage, the traces of organic solvents were cleaned at temperatures of 300–400°C for 2–3 h. At the second stage, the powder evaporated and condensed on the cold part of the cell at temperatures of 600–650°C. At this stage, other impurities, in particular, oxygen, were also removed.

After the procedure described above, an originally prepared powder with a mass of 1–2 g was placed inside a quartz cell 9–10 mm in diameter, which was pumped to a residual pressure of ~10^{-4} Torr and then soldered. The cell was placed in a horizontal resistance furnace heated to 650°C. In the furnace, a temperature gradient of 2–3°C was created over a distance of 100–120 mm (the cell length). The duration of the single crystal growth process was 5–7 days. After cooling to room temperature, the crystals were taken from the cell, visually sorted by quality and size, and then put into new glass cells, which were evacuated and in which the crystals were stored with protection from light before the beginning of experiments.

For compression experiments, we chose single crystals of up to 6 mm in length. The axis of the crystals was parallel to the ⟨110⟩ direction, and the lateral sides were formed by the {110} and {111} planes. The end faces of the samples were polished using fine emery paper with slight pressure; the lateral sides were not polished. To protect the samples against possible fracture at deformation, thin steel plates were glued to the end faces (using BF-2 glue). The prepared sample was glued to the lower support of the deformation device.

Compression of samples was performed at a rate of about 10^{-5} s^{-1} using an MRK-1 device designed and constructed at the Institute for Low Temperature Physics and Engineering, National Academy of Sciences of Ukraine [22]. For four ⟨110⟩{111} slip systems, the Schmid factor was equal to 0.408. To determine the activation volume, stress relaxation curves were recorded after the onset of plastic yield, before the first cracks appeared.

Hardness was measured with a PMT-3 microhardness meter, and the surface structure was studied using an MIM-7 optical microscope.

Except for the optical studies, all operations were performed under natural illumination conditions.

3. RESULTS AND DISCUSSION

From the measurements on the habitus (111) plane in the original state of one of our crystals under a load of 0.05 N, we determined values of the microhardness typical of C_{60} crystals grown from the gas phase; however, these values varied over a sufficiently wide range (from 150 up to 250 MPa), depending on the place of indentation.

The stress–strain curve is shown in Fig. 1, where the normal stress σ is plotted as a function of the compressive strain ε. By comparing this curve with that obtained in [8], we note the following differences in the behavior of the tested samples. We observe no stage structure in the σ–ε curve; this curve has a virtually parabolic shape characteristic of multiple slip. Indeed, optical studies showed that there are two active slip systems in the sample. The appearance of cracks after small plastic deformation and the low reserve of plasticity before fracture of the sample are possibly due to this fact. The edges of the slip bands are very clearly visible; there are no bifurcations of the slip bands. Such a pattern is typical of brittle crystals in the case where the cross slip of dislocations is difficult. Electron microscopic observations [23], theoretical analysis [24], and computer simulation [25] show that, in the C_{60} fullerite, dislocations are strongly split, which complicates their exit to the cross-slip planes.

In [8], the easy glide stage, the second hardening stage, and plastic flow up to 30% of shear strain without fracture were observed for one active slip system. In our case, the fracture of the sample occurred at a stress $\tau_f = 6.4$ MPa ($\tau_f/G = 1.2 \times 10^{-3}$, where $G = 5.28$ GPa is the shear modulus of the C_{60} fullerite [26]) and at a shear strain of about 8%. The yield point τ_y as defined

from the stress–strain curve as the stress corresponding to the beginning of the deviation of the curve from elastic behavior (in Fig. 1, this point is marked by an arrow) was equal to 2.65 MPa ($\tau_f/G = 5 \times 10^{-4}$), which is almost four times greater than that obtained in [8]. For the second tested sample of about the same size, a somewhat smaller value of the yield point was obtained but the fracture of the sample occurred almost immediately after the elastic-strain stage. For the first sample, the activation volume $V \simeq 60b^3$ (where $b = 10.02$ Å is the Burgers vector of the dislocation) did not depend on strain in a narrow strain interval of up to 2%.

Thus, during active deformation, the tested samples of the C_{60} fullerite behaved in the same way as do rigid and fragile crystals. Failure occurred gradually with increasing stress. At the final stage, a sample was split along the compression axis (along a surface almost parallel to the habitus {111} plane) into fragments of various sizes, for which optical studies were possible.

The reasons for the elevated rigidity and brittleness of our crystals are not clear. Probably, these properties are related to the growth method. Attention should be paid to the following fact. For one of the flat samples grown using the technique described above, a significant difference in the values of the hardness (135, 264 Pa) on the opposite (111) habitus surfaces of the crystal was observed [25]; this sample had a thickness of approximately 1 mm and covered an area of about 6 mm^2. As noted above, the values of hardness varied approximately in the same range, even for the same face of the tested crystal subjected to compression. This difference indicates a strong structural inhomogeneity of the crystals formed during growth. The significant internal stresses responsible for the high yield point can be related to this inhomogeneity.

Of course, the increase in the sample rigidity could, to a certain degree, be affected by illumination and interaction with the ambient atmosphere at the stage of preparation. However, in this case, hardening can take place in a thin surface layer, which has only a weak effect on the plastic properties of the sample as a whole [27, 28]. Illumination, as well as mechanical processing of the end faces, can most likely result in the formation of microcracks at the surface and, accordingly, in premature fracture of the sample. Finally, all these factors apparently determine the behavior of the sample during deformation.

Optical studies of fragments of the tested samples showed that fracture frequently occurs along crystallographic planes. This is somewhat unexpected, since attempts to cleave a sample using a blade or a scalpel appear to be unsuccessful, as also noted in [8, 21]. Indeed, taking into account the Van der Waals bonding type, we might expect the existence of cleavage in C_{60} crystals by analogy with graphite, which is easily cleaved along the basal plane. However, in the case of C_{60}, it seems to be difficult to realize this possibility in a standard way because of the weak anisotropy of the fcc lattice.

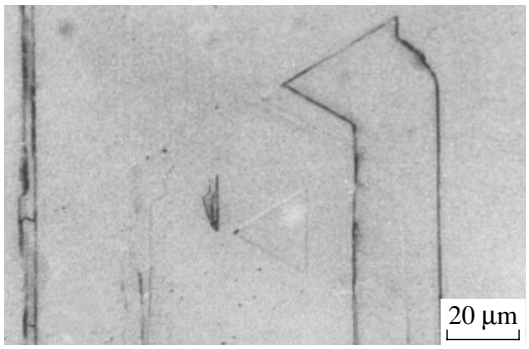

Fig. 2. Cleavage steps on the (111) cleavage plane for a C_{60} fullerite crystal.

A C_{60} crystal is easily cleaved along the cleavage planes if the sample glued by the {111} plane is separated from the substrate. In this case, the force applied is rather small, although it is known that the corresponding stress must be comparable to the theoretical fracture stress of ~(0.1–0.2)G [29]. Internal stress of this order of magnitude can appear at concentrators formed, for example, when the end faces of the sample are polished. However, easy cleavage is also possible in the absence of introduced surface defects, e.g., in the case of a crystal with a strongly inhomogeneous structure or for brittle materials, where the plastic relaxation is difficult or does not occur at all. Crystals are cleaved more easily after hardening because of the introduction of impurities and irradiation and also after lowering the temperature in the case of high Peierls barriers.

As expected, the cleavage planes of the C_{60} crystals are close-packed {111} planes; therefore, their surface energy can be smaller than that for other crystallographic planes.

The cleavage phenomenon can be used to study the character of fracture and plastic deformation. Some possible types of microstructures observed on the cleavage plane of the fullerite crystals under study are shown in Figs. 2–4.

In Fig. 2, we see cleavage steps that are located mainly along the ⟨011⟩ close-packed directions and form closed figures in some cases. Sometimes, they may have a curved shape. It is interesting to note that the position of the main slip plane parallel to the plane of Fig. 2 is practically the same, probably because of the strong anisotropy in the strength properties of the sample, which is related to the crystal growth conditions.

In the vicinity of the indenter imprint on the slip plane, we see the indentation pattern (typical of fcc crystals) formed by the traces of the {111} planes, along which strong plastic slips occur (Fig. 3). One of the triangles in the indentation pattern is formed by the traces of the planes along which the slip penetrates into

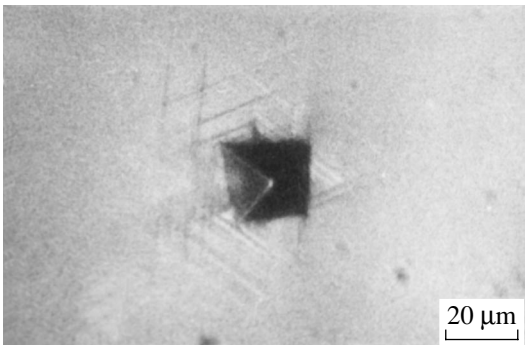

Fig. 3. Indentation pattern in the vicinity of the indenter imprint on the (111) cleavage plane for a C_{60} fullerite crystal. The indenter load is 5 g.

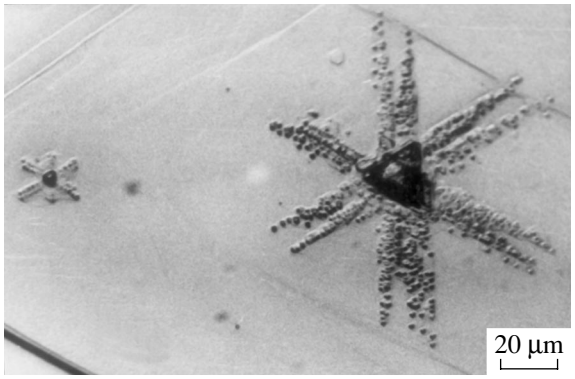

Fig. 4. Dislocation rosettes in the vicinity of the indenter imprint and of the internal defect observed on the (111) cleavage plane of C_{60} fullerite crystals after etching in toluene. The indenter load is 2 g.

the crystal, and the other triangle is formed by the traces coming to the surface. On exposure to air, the cleavage plane gradually changes its properties so that, near the indenter imprint, a local fracture is observed rather than a slip. We note that the microhardness of the crystal measured for slip planes does not depend on the exposure time (about a month) and preserves its initial value of ~135 MPa. This fact means that changes in the properties occur only in a rather thin surface layer.

Figure 4 shows a dislocation rosette near the indenter imprint, which was revealed on a cleavage plane of a C_{60} crystal by etching in toluene using the technique described in [14]. In Fig. 4, we also see a dislocation rosette formed, apparently, near an inclusion. The slip pattern in the region of local deformation is typical of fcc crystals. Fresh dislocations can also be observed when etching the surface polished in benzene. It is interesting that, for some reason, old (growth) dislocations and dislocations that can be present in the region of cleavage steps (as, e.g., in the case of soft alkali halide crystals) were not observed. It is possible that this fact is related to fast crack propagation, such that plastic relaxation has no time to occur during the transition of the crack to a parallel plane. This pattern is typical of fragile materials. After a certain period of time (several hours), because of the effect of the ambient atmosphere and illumination, the cleavage plane could not be etched any more.

4. CONCLUSIONS

Thus, we assert that, under certain conditions, it is possible to observe sufficiently good cleavage of almost isotropic fcc C_{60} fullerite crystals at room temperature. Obviously, this can be due to weak Van der Waals bonding between molecules, to the presence of close packed planes, and to a high shear strength of the sample excluding the possibility of stress relaxation at the top of the crack due to dislocation slip. Inhomogeneity of the sample structure, revealed by indentation, should also be taken into account in the analysis of the reasons for cleavage.

In summary, we note that, to date, the nature of braking forces acting on dislocations in fullerite crystals has not been established. In [8], when comparing the yield points (normalized by the shear modulus) for copper and fullerite, the assumption was made that their difference by a factor of 10 could indicate that the Peierls stress in C_{60} was greater than that in Cu. However, is plastic deformation in fullerite controlled by the mechanism of dislocation motion in the Peierls relief? To answer this question, special studies of the deformation kinetics are necessary. With caution, we may cite two facts giving evidence in favor of the Peierls mechanism: (i) a small activation volume $\simeq 60b^3$ and (ii) the absence of its dependence on strain. However, both of these facts require additional verification. As noted in [29], materials with a high Peierls barrier are characterized by elevated fragility at low temperatures. Our observations indicate that fullerite is a fragile rather than a plastic material. On the whole, one cannot deny that C_{60} crystals could be attributed to the Peierls class from analyzing their mechanical properties. Subsequent studies will make it possible to estimate the contributions of lattice and local barriers to dislocation braking.

ACKNOWLEDGMENTS

The authors thank V.D. Natsik, M.A. Strzhemechnyĭ, and A.I. Prokhvatilov for useful discussions and valuable remarks.

This study was supported by the Science and Technology Center in Ukraine (project no. 2669).

REFERENCES

1. Yu. A. Ossipyan, V. S. Bobrov, Y. S. Grushko, R. A. Dilanyan, O. V. Zharikov, M. A. Lebyodkin, and V. S. Sheckhtman, Appl. Phys. A **56**, 413 (1993).

2. V. S. Bobrov, R. A. Dilanyan, L. S. Fomenko, M. A. Lebyodkin, S. V. Lubenets, and V. I. Orlov, Solid State Phenom. **35–36**, 519 (1994).
3. M. Tachibana, M. Michiyama, K. Kikuchi, Y. Achiba, and K. Kojima, Phys. Rev. B **49**, 14945 (1994).
4. L. S. Fomenko, V. D. Natsik, S. V. Lubenets, V. G. Lirtsman, N. A. Aksenova, A. P. Isakina, A. I. Prokhvatilov, M. A. Strzhemechnyĭ, and R. S. Ruoff, Fiz. Nizk. Temp. **21**, 4665 (1995) [Low Temp. Phys. **21**, 364 (1995)].
5. S. V. Lubenets, V. D. Natsik, L. S. Fomenko, A. P. Isakina, A. I. Prokhvatilov, M. A. Strzhemechnyĭ, N. A. Aksenova, and R. S. Ruoff, Fiz. Nizk. Temp. **23**, 338 (1997) [Low Temp. Phys. **23**, 251 (1997)].
6. D. V. Dyachenko-Dekov, Yu. L. Iunin, A. N. Izotov, V. V. Kveder, R. K. Nikolaev, V. I. Orlov, Yu. A. Ossipyan, N. S. Sidorov, and E. A. Steinman, Phys. Status Solidi B **222**, 111 (2000).
7. M. Tachibana, K. Nishimura, T. Komatsu, T. Sunakava, and K. Kojima, Proc. SPIE **3142**, 229 (1997).
8. T. Komatsu, M. Tachibana, and K. Kojima, Philos. Mag. A **81**, 659 (2001).
9. V. S. Bobrov, R. A. Dilanyan, L. S. Fomenko, Yu. L. Iunin, M. A. Lebyodkin, S. V. Lubenets, V. I. Orlov, and Yu. A. Ossipyan, J. Supercond. **8**, 1 (1995).
10. M. Haluska, M. Zehetbauer, M. Hulman, and H. Kuzmany, Mater. Sci. Forum **210–213**, 267 (1996).
11. M. Tachibana, H. Sakuma, and K. Kojima, J. Appl. Phys. **82**, 4253 (1997).
12. J. Li, T. Mitsuki, M. Ozava, H. Horiuchi, K. Kitazava, K. Kikuchi, and Y. Achiba, J. Cryst. Growth **143**, 58 (1994).
13. M. Halushka, H. Kuzmany, M. Vybornov, P. Rogl, and P. Fejdi, Appl. Phys. A **56**, 161 (1993).
14. V. I. Orlov, V. I. Nikitenko, R. K. Nikolaev, I. N. Kremenskaya, and Yu. A. Osip'yan, Pis'ma Zh. Éksp. Teor. Fiz. **59** (10), 667 (1994) [JETP Lett. **59**, 704 (1994)].
15. M. Tachibana, K. Kojima, H. Sakuma, and K. Komatsu, J. Appl. Phys. **84**, 1944 (1998).
16. I. Manika, J. Maniks, R. Pokulis, and J. Kalnacs, Fiz. Tverd. Tela (St. Petersburg) **44**, 417 (2002) [Phys. Solid State **44**, 432 (2002)].
17. P. C. Eklund, A. M. Rao, P. Zhou, and Y. Wang, Thin Solid Films **257**, 185 (1995).
18. C. Sekar, A. Thamizhavel, and C. Subramanian, Physica C (Amsterdam) **275**, 193 (1997).
19. R. L. Meng, D. Ramirez, X. Jiang, P. C. Chou, C. Diaz, K. Matsuishi, S. C. Moss, P. H. Hor, and C. W. Chu, Appl. Phys. Lett. **59**, 3402 (1991).
20. J. Z. Liu, J. W. Dykes, M. D. Lan, P. Klavins, R. N. Shelton, and M. M. Olmstead, Appl. Phys. Lett. **62**, 531 (1993).
21. K. Kojima, M. Tachibana, Y. Maekawa, H. Sakuma, M. Michiyama, K. Kikuchi, and Y. Achiba, in *Conference Proceedings: Ser. Crystal Growth of Organic Materials*, Ed. by A. S. Myerson, D. A. Green, and P. Meenan (American Chemical Soc., 1996), p. 231.
22. M. V. Zinov'ev, G. S. Med'ko, and V. P. Podkuĭko, Probl. Prochn., No. 7, 95 (1997).
23. S. Muto, G. Van Tendeloo, and S. Amelinckx, Philos. Mag. B **67**, 443 (1993).
24. M. A. Stzhemechny and R. S. Ruoff, in *Recent Advances in Chemistry and Physics of Fullerenes*, Ed. by R. Kadish and R. Ruoff (Electrochemical Soc., Pennington, 1995), Vol. 2, p. 973.
25. Sh. Tamaki, N. Ide, I. Okada, and K. Kojima, Jpn. J. Appl. Phys. **37**, 6115 (1998).
26. D. Fioretto, G. Garlotti, G. Socino, S. Modesti, C. Cepec, L. Giovannini, O. Donezelli, and F. Nizzoli, Phys. Rev. B **52**, R8707 (1995).
27. S. V. Lubenets, L. S. Fomenko, A. N. Izotov, R. K. Nikolaev, N. S. Sidorov, and É. A. Shteĭnman, in *Proceedings of 6th International Conference on Physical Phenomena in Solids* (Kharkov, 2003), p. 41.
28. S. V. Lubenets and L. S. Fomenko, Fiz. Tverd. Tela (Leningrad) **32**, 3144 (1990) [Sov. Phys. Solid State **32**, 1825 (1990)].
29. J. Friedel, *Dislocations* (Pergamon, Oxford, 1964; Mir, Moscow, 1967).

Translated by I. Zvyagin

Physics of the Solid State, Vol. 47, No. 5, 2005, pp. 896–902. Translated from Fizika Tverdogo Tela, Vol. 47, No. 5, 2005, pp. 870–875.

Structure Factors That Influence the Stability of Plastic Strain of BCC Metals under Tensile Load

G. A. Malygin

Ioffe Physicotechnical Institute, Russian Academy of Sciences, Politekhnicheskaya ul. 26, St. Petersburg, 194021 Russia
e-mail: malygin.ga@mail.ioffe.ru

Abstract—The effect of the Peierls stress on the ultimate tensile stress and uniform strain prior to the formation of a neck during stretching of metals and alloys with bcc structure is theoretically analyzed. The analysis is based on the equation for the variation of the dislocation density with deformation; this equation determines the shape of the work-hardening curve for a bcc material and the effect of the Peierls stress on the parameters of this equation (the annihilation coefficient for screw dislocations). Using the Considére condition for plastic instability of the neck type, the ultimate tensile stress and the magnitude of uniform strain are found theoretically as a function of the Peierls stress at different temperatures below $0.15T_m$, where T_m is the melting temperature of the bcc metal. Theoretical results are illustrated with experimental data on the temperature dependences of the annihilation coefficients for screw dislocations and of the magnitude of uniform strain in molybdenum and Armco iron. © *2005 Pleiades Publishing, Inc.*

1. INTRODUCTION

The results of long (over half a century) experimental and theoretical studies of the microscopic (dislocation) mechanism of strength and plasticity of crystals now form a theoretical basis for analyzing the effect of structure on the strength and plastic properties of constructional materials, above all, metals. At temperatures below $0.5T_m$ (T_m is the melting temperature), the strength and plasticity of these materials are usually characterized by the yield point σ_y, as well as by the stress σ_u and the magnitude of uniform strain ε_u at which plastic instability (called neck type) appears in a stretched sample, and the localization of strain begins, terminating in plastic disintegration (fracture) of the sample. Not only the values of the cited characteristics but also the relations between them are of practical interest. It is known that an increase in material strength is accompanied, as a rule, by a decrease in its plasticity. The achievements made in understanding the effect of material structure on the work-hardening curve have opened the way for analysis of the effect of structural factors both on the characteristics of strength and plasticity and on the relation between them.

In [1], this relation was analyzed using the example of metals and alloys having an fcc lattice. In that study, the effect of the stacking fault energy, doping, and grain size on the ultimate tensile stress σ_u and strain ε_u was first theoretically considered for a number of copper and aluminum alloys. In this study, a similar analysis is performed for metals and alloys with bcc structure. Compared to fcc structures, bcc metals and alloys have two specific features. First, at temperatures below $0.15T_m$, the Peierls relief is present, which considerably complicates the motion of screw dislocations in the crystal [2], and, second, the low concentrations of interstitial (C, N) atoms affect the yield point and yield stress at temperatures above $0.15T_m$ [3].

In this study, we analyze the effect of these structural factors on the character of the work-hardening curves and on the magnitude of uniform strain before the appearance of a neck when stretching bcc metals. The theoretical results are illustrated using experimental data obtained by the author when stretching polycrystalline specimens of Armco iron and molybdenum of 99.98% purity, 1 mm in diameter, having a 20-mm gage length in the temperature interval 77–800 K.

2. BASIC RELATIONS

According to the well-known Considére criterion for the appearance of plastic instability of the bottleneck type under uniaxial stretching of a sample,

$$\frac{d\sigma}{d\varepsilon} \le \sigma, \tag{1}$$

the critical strain ε_u and the corresponding stress σ_u are fully determined by the character of the work-hardening curve $\sigma(\varepsilon)$ of the material of the sample and by the effect of structural factors on this curve. According to another well-known relation that determines the magnitude of (dislocation) work-hardening of a material,

$$\tau(\gamma) = \tau_c + \alpha\mu b\rho(\gamma)^{1/2}, \tag{2}$$

the increase in the flow stress $\tau(\gamma)$ with shear strain γ and, therefore, the character of the $\sigma(\varepsilon)$ stretching diagrams depend on the variation of the average disloca-

1063-7834/05/4705-0896$26.00 © 2005 Pleiades Publishing, Inc.

tion density ρ with deformation γ in a deforming material. In Eqs. (1) and (2), $\sigma = m\tau$, $\varepsilon = \gamma/m$, m is the Taylor factor for a polycrystal, α is the interaction constant of dislocations, μ is the shear modulus, b is the Burgers vector, and τ_c is the critical shear stress.

According to numerous studies [2–4], the work-hardening curves for bcc single crystals at temperatures above $0.15T_m$ have two or three work-hardening stages and differ only slightly from the work-hardening curves for fcc metals. Therefore, we may expect that, just as in the case of fcc metals, in a polycrystalline bcc metal under conditions of multiple slip, variation of the average dislocation density with strain at low and moderate temperatures obeys the equation [5–9]

$$\frac{d\rho}{d\gamma} = k_m + k_f\rho^{1/2} - k_a\rho. \tag{3}$$

On the right-hand side of Eq. (3), the first term describes the rate of multiplication and accumulation of dislocations interacting with obstacles of nondeformation origin; the second term corresponds to the multiplication of dislocations at forest dislocations, where $bk_f \approx 10^{-2}$ is a coefficient that determines the intensity of multiplication of dislocations interacting with forest dislocations; the third term is the rate of annihilation of the screw segments of dislocation loops; and k_a is the dislocation annihilation coefficient. The existence of the third stage (the stage of dynamic rest) in the work-hardening curves for fcc metals is related to the annihilation of screw dislocations.

For small values of the coefficient of dislocation multiplication at obstacles of nondeformation origin, $k_m \ll k_f^2/4k_a$, we integrate Eq. (3) and, substituting the result into Eq. (2), obtain the strain dependence of the stress,

$$\sigma(\varepsilon) = \sigma_c + \sigma_3\left[1 - \exp\left(-\frac{1}{2}mk_a\varepsilon\right)\right],$$
$$\sigma_3 = m\alpha\mu\left(\frac{bk_f}{k_a}\right). \tag{4}$$

Here, $\sigma_c = m\tau_c$, σ_3 is the yield stress corresponding to the end of the third stage in the work-hardening curve, where equilibrium between the processes of dislocation multiplication and annihilation is established. Substituting the stress $\sigma(\varepsilon)$ from Eq. (4) into condition (1), we find the strain and stress at the beginning of the necking as a function of the critical shear stress σ_c and of the coefficients in Eq. (3):

$$\varepsilon_u = \frac{2}{mk_a}\ln\frac{1 + \frac{1}{2}mk_a}{1 + \frac{\sigma_c}{\sigma_3}}, \tag{5a}$$

$$\sigma_u = \frac{\frac{1}{2}mk_a}{1 + \frac{1}{2}mk_a}(\sigma_c + \sigma_3). \tag{5b}$$

It follows from Eqs. (4) and (5) that the uniform strain ε_u, the ultimate tensile stress σ_u, and the general character of the work-hardening curve depend on two structure-sensitive parameters, namely, the critical shear stress and the annihilation coefficient of screw dislocations. It is seen from Eq. (5a) that the greater the dislocation annihilation factor and the critical shear stress, the smaller the magnitude of the uniform strain. In the following section, we consider this relation in more detail.

3. CRITICAL SHEAR STRESS AND THE ANNIHILATION FACTOR FOR SCREW DISLOCATIONS IN BCC METALS

In the case of bcc metals at low and moderate temperatures, we have [10–13]

$$\sigma_c(T, c) = m\tau_P(T) + m\tau_f(c). \tag{6}$$

Here, $\tau_P(T)$ is the Peierls stress, $\tau_f(c) = \beta_n\mu c^n$ is the frictional stress arising due to the interaction of dislocations with interstitial and substitutional impurities, β_n is a factor characterizing the strength of this interaction, and $n = 0.5$–1.0 [12, 13]. The temperature dependence of the Peierls stress is determined by the dependence of the energy H of formation of double kinks in screw dislocations on the stress τ. According to the model of steep kinks [14, 15], $H(\tau) = 2H_k(1 - \sqrt{\tau/\tau_*})$, where $2H_k$ is the energy of formation of a double kink in the absence of stress and τ_* is a stress at which dislocations move over the Peierls potential relief without activation. Since $H(\tau) = kT\ln(\dot\varepsilon_0/\dot\varepsilon)$, where k is the Boltzmann constant, $\dot\varepsilon$ is the strain rate, and $\dot\varepsilon_0$ is the preexponential factor, the temperature dependence of the Peierls stress for this model is given by

$$\tau_P(T) = \tau_*\left(1 - \frac{T}{T_P}\right)^2, \quad T_P = \frac{2H_k}{k\ln(\dot\varepsilon_0/\dot\varepsilon)}. \tag{7}$$

Figure 1 shows our data on the temperature dependence of the yield point $\sigma_{0.2}$ for polycrystalline Armco iron and molybdenum samples. The theoretical curves are plotted using formulas (6) and (7) with the following parameter values: $\tau_* = 500$ and 870 MPa [10], $T_P = 350$ and 450 K [10], and stress $\tau_f = 70$ and 37 MPa for α-Fe and Mo, respectively; the Taylor factor is $m = 3$.

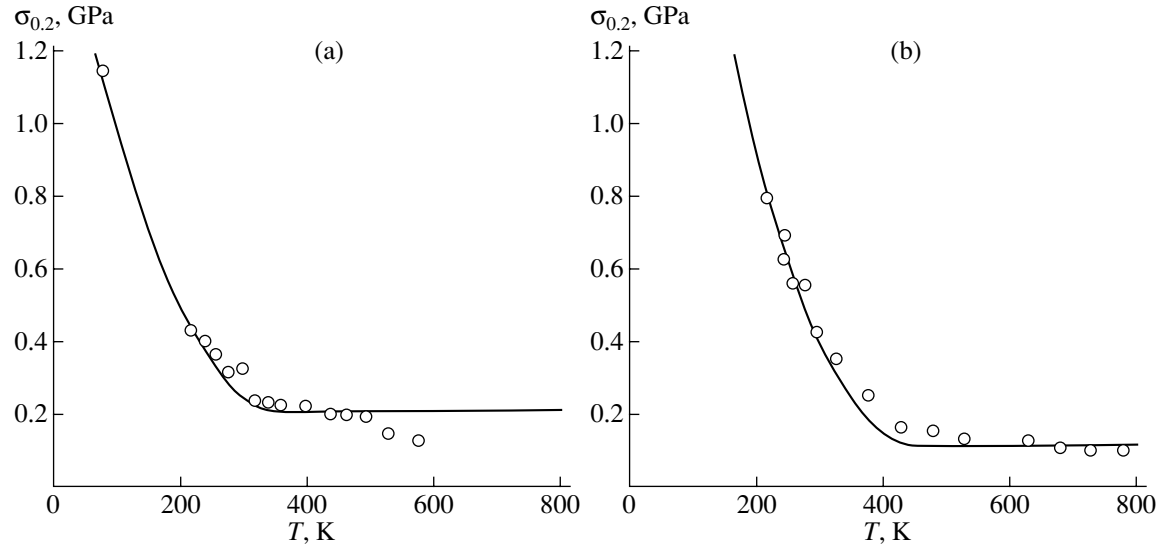

Fig. 1. Temperature dependence of the yield point for (a) Armco iron and (b) molybdenum.

The second structure-sensitive parameter in Eqs. (4) and (5) is the annihilation coefficient for screw dislocations k_a. According to [7, 16], this coefficient is given by

$$k_a = \frac{\omega_s^{5/2}}{2\pi^2 p\alpha}\left(\frac{\mu}{\tau_a}\right), \tag{8}$$

where ω_s is the fraction of screw segments in the expanding dislocation loops, p is the number of active glide systems, and τ_a is the frictional stress that determines the critical distance for spontaneous annihilation of screw dislocations of opposite sign. In the case of metals and alloys with fcc structure, we have $\tau_a = \tau_{III} + \tau_f$ [1, 16], where $\tau_{III}(T, \gamma_D)$ is the stress corresponding to the beginning of the third stage in the work-hardening curves for fcc metals; this stress depends on the temperature T and the stacking fault energy γ_D [17]:

$$\tau_{III}(T, \gamma_D) = \tau_{III}(0)\exp\left[-\left(1 + 180\frac{\gamma_D}{\mu b}\right)\frac{kT}{0.35\mu b^3}\ln\left(\frac{\dot\varepsilon_0}{\dot\varepsilon}\right)\right], \tag{9}$$

where $\tau_{III}(0)$ is the stress τ_{III} at $T = 0$. In the case of bcc metals, the Peierls stress τ_P must be added to the stresses τ_{III} and τ_f. As a result, we obtain $\tau_a = \tau_{III} + \tau_f + \tau_P$. Therefore, the temperature and concentration dependence of the annihilation coefficient for screw dislocations in bcc metals is

$$k_a(T, c, \gamma_D) = \frac{\omega_s^{5/2}}{2\pi^2\alpha p}\frac{\mu}{\tau_{III}(T, \gamma_D) + \tau_f(c) + \tau_P(T)}. \tag{10}$$

Experimentally, the dislocation annihilation coefficient is found by processing the $\sigma(\varepsilon)$ work-hardening curves at different temperatures and by plotting the dependence of the work-hardening coefficient $d\sigma/d\varepsilon$ on the stress σ [7, 8]. According to Eq. (4), at the stage of dynamic rest, this dependence is linear [5, 8]:

$$\frac{d\sigma}{d\varepsilon} = m^2\theta_2 - \frac{1}{2}mk_a(\sigma - \sigma_c). \tag{11}$$

Here, $\theta_2 = 1/2\alpha\mu b k_f \approx 2 \times 10^{-3}\mu$ is the work-hardening coefficient at the second stage in the work-hardening curves of fcc crystals. From formula (11), we see that the coefficient k_a determines the slope of these curves. The values of the coefficient k_a determined for α-Fe and Mo in the temperature range 77–800 K are shown in Fig. 2.

Figure 2a shows the dependence of the annihilation coefficient for these metals on the inverse of the yield stress $\sigma_{0.2}$ at different temperatures. We see that, according to expressions (8) and (10), the annihilation coefficient varies in inverse proportion to this stress. In Fig. 2a, the straight lines $k_a \sim \sigma_{0.2}^{-1}$ are not extrapolated to the origin at large values of $\sigma_{0.2}$; this implies that, in addition to $\sigma_P = m\tau_P$, the stress $\sigma_{0.2}$ includes deformation and impurity components, which are weakly temperature-dependent. Indeed, after replotting these curves in the k_a^{-1} versus $\sigma_{0.2}$ coordinates (Fig. 2b), we see that the values of these components of the yield stress are appreciable. From the slope of the straight lines in Fig. 2b, we can estimate the combination of parameters $\omega_s^{5/2}/2\pi^2\alpha p$ in formula (10). This quantity is equal to 2.4×10^{-3} and 3.5×10^{-3} for α-Fe and Mo, respectively. For $\alpha = 0.5$ and $p = 16$, these estimations give reasonable values of the parameter $\omega_s = 0.7$–0.8, which indicates that, at low temperatures, screw dislo-

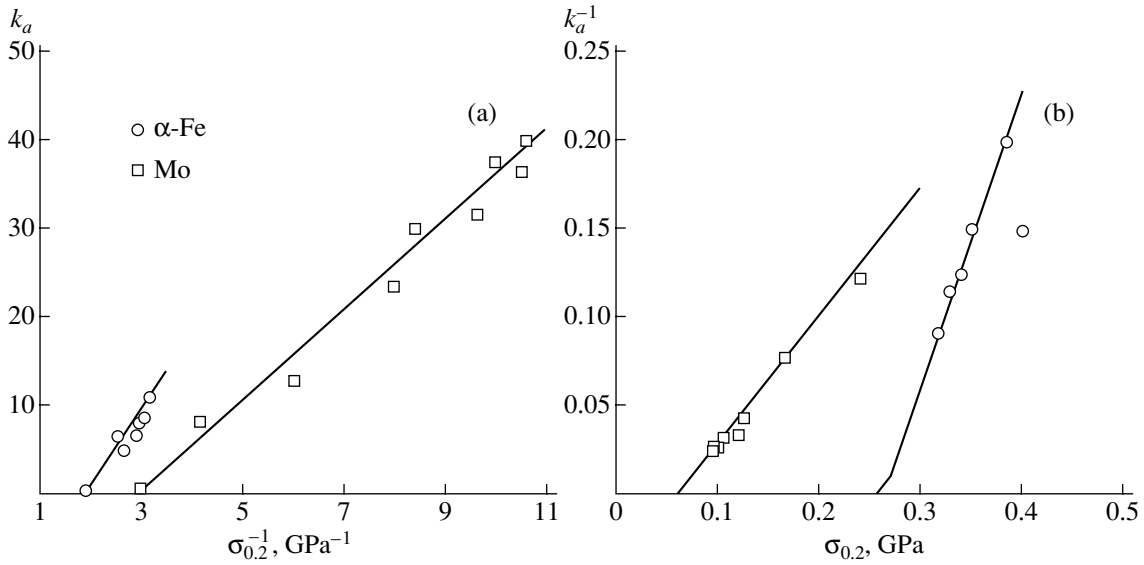

Fig. 2. Dependence (a) of the annihilation coefficient k_a for screw dislocations in α-Fe and Mo on the inverse yield stress and (b) of the inverse k_a coefficient on the yield point.

cations predominate in the dislocation structure of bcc metals [18].

Thus, due to a strong increase in the Peierls stress, at temperatures $T < T_P$, where $T_P \approx (0.15–0.20)T_m$, the dislocation annihilation coefficient in bcc metals is further reduced as compared to fcc metals. Figure 3 shows the dislocation annihilation coefficient calculated as a function of the homologous temperature from formulas (7)–(10) with the following values of the parameters characteristic of pure bcc metals: $\tau_*/\mu = 5 \times 10^{-3}$, $\tau_{III}(0)/\mu = 0.5 \times 10^{-3}$, $\tau_f/\mu = 0$, $kT_m/\mu b^3 = 1.2 \times 10^{-2}$, $\gamma_D/\mu b = 20 \times 10^{-3}$, $T_P/T_m = 0.16$, $\ln(\dot{\varepsilon}_0/\dot{\varepsilon}) = 35$, $\omega_s = 0.8$, $\alpha = 0.5$, and $p = 16$. In Fig. 3, the dashed curve illustrates the temperature dependence of k_a in the absence of the Peierls stress ($\tau_P = 0$ in Eq. (10)) and the solid curve corresponds to the presence of the Peierls stress ($\tau_P \neq 0$). We see that, at temperatures $T < 0.16T_m$, the annihilation rate of the screw segments of dislocation loops sharply falls because of the strong increase in the Peierls stress.

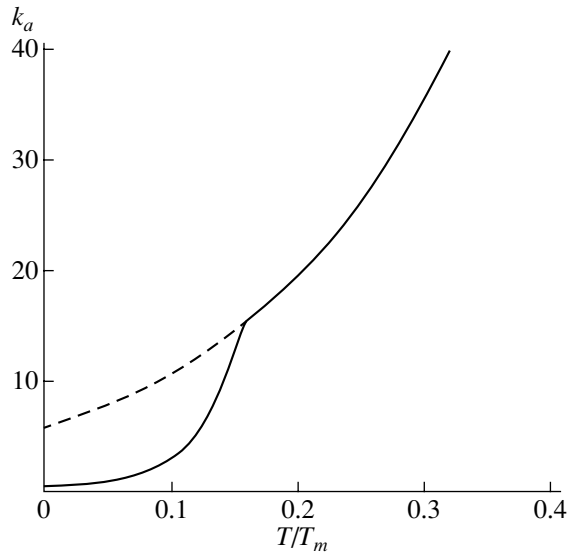

Fig. 3. Annihilation coefficient for screw dislocations in bcc (solid line) and fcc (dashed line) metals calculated as a function of the reduced temperature from Eq. (10).

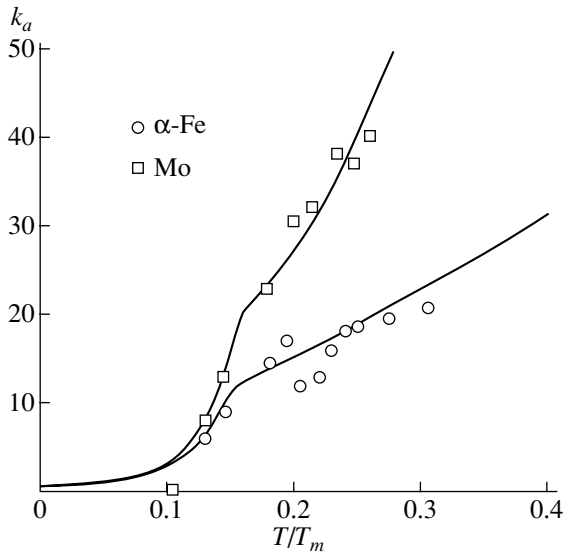

Fig. 4. Temperature dependence of the dislocation annihilation coefficient for Armco iron and molybdenum.

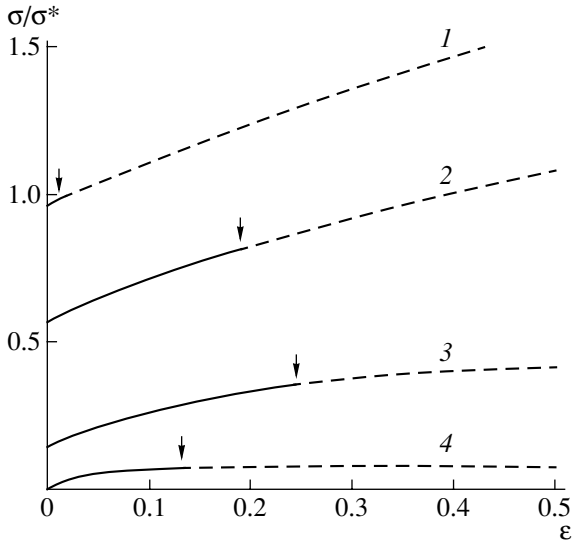

Fig. 5. Work-hardening curves for a typical bcc metal at low and intermediate temperatures calculated from Eq. (4). The values of T/T_m are (*1*) 5×10^{-3}, (*2*) 5×10^{-2}, (*3*) 0.1, and (*4*) 0.2. Arrows indicate the strains corresponding to the beginning of the neck formation.

In Fig. 4, the temperature dependences of the dislocation annihilation coefficient for Armco iron and molybdenum are shown. The theoretical curves are plotted using formulas (7)–(10) with the above values of the parameters. In the calculations, we assumed that the stacking fault energy in Mo is $\gamma_D/\mu b = 26 \times 10^{-3}$, which is higher than that in α-Fe. Calculations show that the annihilation coefficient is sensitive to the stress τ_f and, therefore, to the concentration of interstitial impurities in the material, such as carbon and nitrogen atoms in α-Fe. For example, according to [12, 19], in the case of carbon, $\tau_f = (1–5) \times 10^{-2}\mu c^{1/2}$, and for $c = 10^{-4}$ we find $\tau_f = (1–5) \times 10^{-4}\mu$. However, to the experimental data in Fig. 4 corresponds a lower stress of $\tau_f = 0.5 \times 10^{-4}\mu$.

Besides being present in the solid solution, carbon atoms can form atmospheres around dislocations and further reduce the dislocation annihilation coefficient in α-Fe. This is indicated by a dip in the experimental points for the temperature dependence of the dislocation annihilation coefficient in Armco iron in the temperature interval of T/T_m = 0.20–0.25 (350–470 K) (Fig. 4). It is precisely in this temperature interval that dynamic strain ageing is observed in Armco iron at strain rates of 10^{-4} s^{-1}; as a result, the σ–ε diagrams become tooth-like (the Portevin–Le Chatelier effect).

4. WORK-HARDENING CURVES AND THE CRITERION FOR PLASTIC INSTABILITY

In Fig. 5, dashed lines show the work-hardening curves calculated from Eqs. (4) for a typical bcc metal at different temperatures with regard to the temperature dependence of the critical shear stress σ_c and of the annihilation coefficient k_a for screw dislocations described by Eqs. (6)–(10). Along the ordinate axis, we plotted the flow stress normalized to $\sigma_* = m\tau_*$. We should pay attention to the fact that, at temperatures below $0.1T_m$, the third stage (the stage of dynamic rest) disappears because of the sharp decrease in the dislocation annihilation coefficient; as a result the hardening curves become single-stage.

In Fig. 5, the dashed curves are the work-hardening curves for steady plastic deformation of a sample in the absence of localization of the deformation in a neck. The initial solid segments of the dashed curves show the regions of stable deformation; the points corresponding to the beginning of the loss of stability and the formation of a neck are marked by arrows. The strain ε_u was calculated using formula (5a) with allowance for the temperature dependences of the critical shear stress and the dislocation annihilation coefficient according to formulas (6)–(10). In Fig. 5, we see that the effect of temperature on the uniform strain ε_u is not monotonic: at temperatures above $0.15T_m$, the strain is low but it increases rapidly with decreasing temperature and then sharply falls at temperatures below $0.10T_m$, producing quasi-embrittlement of the material at these temperatures.

Such a nonmonotonic effect of temperature on the uniform strain is related to the fact that, according to Eq. (5a), the temperature dependence of the strain ε_u is determined by the temperature dependences of the critical shear stress σ_c and the dislocation annihilation coefficient k_a, which vary with temperature in opposite directions. In order to calculate the temperature and concentration dependences of the strain ε_u, we write formula (5a), with regard to relations (4) and (6)–(10), in the form

$$\varepsilon_u = \frac{2}{mk_a(T, c)} \ln \frac{1 + \frac{1}{2}mk_a(T, c)}{1 + B\frac{\sigma_c(T, c, d)}{\sigma_*}k_a(T, c)}, \quad (12a)$$

$$\sigma_c = m\tau_P(T) + m\tau_f(c) + K_H d^{-1/2}, \quad (12b)$$

where $B = \tau_*/\alpha\mu b k_f$. Formula (12b) for the critical shear stress contains an additional term corresponding to the stress that takes into account the effect of the grain size d on the stress σ_c, in accordance with the Hall–Petch law; in this formula, K_H is the Hall–Petch constant.

In Fig. 6, circles show the temperature dependence of the uniform strain in Armco iron and curve *1* is the corresponding theoretical curve calculated from Eq. (12a) with the following parameter values: $B = 2$, $K_H = 0.21$ MPa $m^{1/2}$ [20], $d = 10$ μm, $c = 4 \times 10^{-4}$, and $T_P/T_m = 0.2$; the other parameters are indicated above.

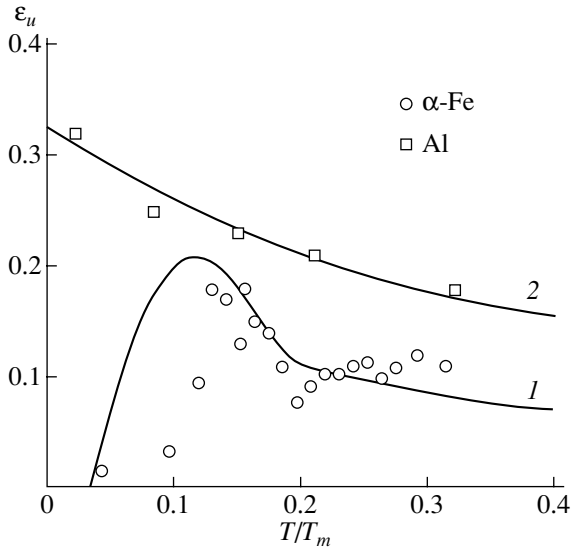

Fig. 6. Temperature dependence of the uniform strain in Armco iron and aluminum [21]. The theoretical curves correspond to the strain ε_u calculated from Eqs. (12a) and (13a) (*1*) in the presence and (*2*) in the absence of the Peierls stress, respectively.

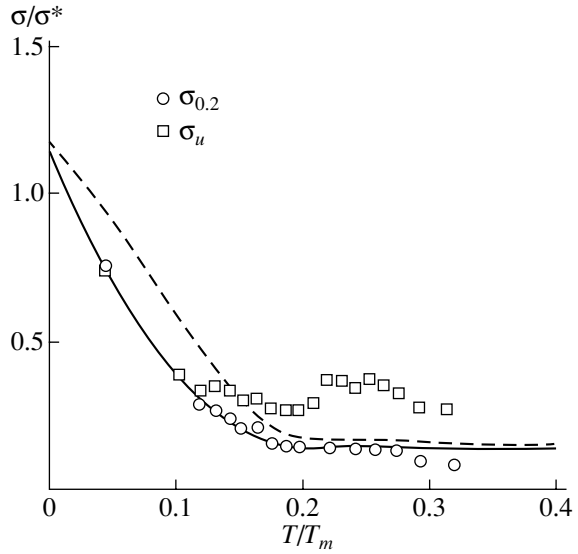

Fig. 7. Temperature dependence of the yield point and ultimate stress for Armco iron. The solid and dashed lines correspond to the stress calculated from Eqs. (12b) and (14), respectively.

We see that, at temperatures above $0.1T_m$, the uniform strain gradually decreases due to the increase in the dislocation annihilation coefficient with temperature. At temperatures below $0.1T_m$, the sharp decrease in ε_u is due to the fact that the increase in the critical shear stress with temperature has a stronger effect on the strain ε_u than does the decrease in the annihilation coefficient. For comparison, Fig. 6 also shows the temperature dependence of the uniform strain in pure aluminum [21], where the Peierls stress is virtually zero. Curve *2* in this figure shows the strain ε_u calculated from Eqs. (12) in the absence of the Peierls stress and Hall–Petch hardening:

$$\varepsilon_u = \frac{2}{mk_a(T, \gamma_D, \tau_f)} \ln\left(\frac{1 + \frac{1}{2}mk_a(T, \gamma_D, \tau_f)}{1 + B_f\frac{\tau_f}{\mu}k_a(T, \gamma_D, \tau_f)}\right), \quad (13a)$$

$$k_a = \frac{\omega_s^{5/2}}{2\pi^2\alpha p}\left(\frac{\mu}{\tau_{\text{III}}(T, \gamma_D) + \tau_f}\right), \quad B_f = \frac{1}{\alpha b k_f}. \quad (13b)$$

Agreement with experiment is achieved for the following parameter values: $\tau_f/\mu = 6.4 \times 10^{-4}$, $\gamma_D/\mu b = 20 \times 10^{-3}$, $\omega_s^{5/2}/2\pi^2\alpha p = 3 \times 10^{-3}$, and $B_f = 7.5 \times 10^2$.

Figure 7 shows (in the σ/σ_* versus T/T_m reduced coordinates) the experimentally determined ultimate stress σ_u for Armco iron and, for comparison, the temperature dependence of its yield point. The theoretical dependence of the stress σ_u is determined with Eq. (5b); for calculations, it is convenient to write Eq. (5b) (with allowance for Eq. (12)) in the explicit reduced form

$$\frac{\sigma_u}{\sigma_*} = \frac{\frac{1}{2}mk_a(T, c)}{1 + \frac{1}{2}mk_a(T, c)}\left(\frac{\sigma_c(T, c, d)}{\sigma_*} + \frac{1}{Bk_a(T, c)}\right). \quad (14)$$

The solid curve in Fig. 7 illustrates the critical shear stress calculated from Eq. (12b), and the dashed curve represents the stress σ_u calculated from Eq. (14) with the following parameter values: $c = 10^{-4}$, $d = 5$ μm, and $B = 1.25$. We see that there is only qualitative agreement between the theoretical and experimental values of σ_u. The peak in the temperature dependence of the stress in the temperature range $(0.20–0.25)T_m$ is related to dynamic strain ageing, i.e., to dislocation pinning by atmospheres of carbon atoms. In order to determine the reason for the quantitative disagreement between theory and experiment, special analysis is needed.

5. CONCLUSIONS

Thus, just as in the case of fcc metals [1], the approach to the work-hardening curves for bcc metals based on the equations of the dislocation kinetics allows us to reveal and physically substantiate the effect of structural factors (the Peierls stress in the case considered) on (i) the character of these curves, (ii) the corresponding strength and plasticity characteristics, such as the ultimate stress and uniform strain, and also (iii) on their variation with temperature. This approach opens the way for modeling the behavior of metals and

alloys with bcc structure under complicated varying operation conditions.

REFERENCES

1. G. A. Malygin, Fiz. Tverd. Tela (St. Petersburg) **47** (2), 236 (2005) [Phys. Solid State **47**, 246 (2005)].
2. V. Novak, S. Kadechkova, B. Sestak, and N. Zarubova, Cryst. Res. Technol. **19** (6), 781 (1989).
3. R. Lachenmann and H. Schultz, Scr. Metall. **7** (2), 155 (1973).
4. P. L. Pratt and F. Guin, Phys. Status Solidi **15** (2), 539 (1966).
5. H. Mecking and U. F. Kocks, Acta Metall. **29** (11), 1865 (1981).
6. Yu. Estrin and H. Mecking, Acta Metall. **32** (1), 57 (1984).
7. G. A. Malygin, Fiz. Tverd. Tela (Leningrad) **29** (7), 2067 (1987) [Sov. Phys. Solid State **29**, 1189 (1987)].
8. G. A. Malygin, Phys. Status Solidi A **119** (2), 423 (1990).
9. G. A. Malygin, Fiz. Tverd. Tela (St. Petersburg) **43** (10), 1832 (2001) [Phys. Solid State **43**, 1909 (2001)].
10. H. Conrad, in *Proceedings of Conference on the Relation between the Structure and Mechanical Properties of Metals* (Her Majestys Stationary Office, London, 1963; Metallurgiya, Moscow, 1967), p. 225.
11. Y. Nakada and A. S. Keh, Acta Metall. **16** (7), 903 (1968).
12. D. F. Stein and J. R. Low, Acta Metall. **14** (10), 1183 (1966).
13. P. Lewandowski, P. Chomel, and J. P. Cottu, Rev. Appl. Phys. **17** (1), 9 (1982).
14. A. P. Kazantsev and V. L. Pokrovskiĭ, Zh. Éksp. Teor. Fiz. **58** (2), 677 (1970) [Sov. Phys. JETP **31**, 362 (1970)].
15. G. A. Malygin, Fiz. Met. Metalloved. **58** (2), 360 (1984).
16. G. A. Malygin, Fiz. Tverd. Tela (St. Petersburg) **34** (9), 2882 (1992) [Sov. Phys. Solid State **34**, 1543 (1992)].
17. R. Berner and G. Kronmüller, *Plastische Verformung von Einkristallen* (Springer, Berlin, 1965; Mir, Moscow, 1969).
18. N. I. Noskova, A. I. Zhuravleva, N. F. Vil'dinova, and I. A. Pereturina, Fiz. Met. Metalloved. **64** (3), 554 (1987).
19. R. L. Fleischer and W. R. Hibbard, in *Proceedings of Conference on the Relation between the Structure and Mechanical Properties of Metals* (Her Majestys Stationary Office, London, 1963; Metallurgiya, Moscow, 1967), p. 85.
20. H. Conrad, in *Ultrafine Grain in Metals* (Syracuse Univ. Press, Syracuse, New York, 1970; Metallurgiya, Moscow, 1973).
21. R. P. Carreker and W. R. Hibbard, J. Met. **9** (10), 1157 (1957).

Translated by I. Zvyagin

Physics of the Solid State, Vol. 47, No. 5, 2005, pp. 903–906. Translated from Fizika Tverdogo Tela, Vol. 47, No. 5, 2005, pp. 876–879.

Structural Transformations on a Platinum Surface under Mechanical Tension

S. A. Knyazev and V. E. Korsukov

Ioffe Physicotechnical Institute, Russian Academy of Sciences, Politekhnicheskaya ul. 26, St. Petersburg, 194021 Russia

e-mail: knyazef@yandex.ru

Abstract—The effect of uniaxial tension on the structure of a recrystallized platinum surface is investigated using low-energy electron diffraction (LEED). The initial LEED patterns indicate that the (111) facet emerges on the surface of a platinum foil after a series of heating cycles under vacuum and in oxygen. After loading at ~80 MPa, the clean platinum surface is characterized by systems of regular and irregular atomic terraces. The regular terraces have a $(9(111) \times 100)$ structure. As the load increases to 90–100 MPa, the ordered arrangement of terraces transforms into a disordered arrangement. After the samples are held under these loads for ~2 h, the surface structure undergoes a transformation into the diffraction-disordered state. Under tensile deformation, the island structure of graphite molecules on the recrystallized platinum surface containing ~10 at. % C also undergoes a transformation. © *2005 Pleiades Publishing, Inc.*

1. INTRODUCTION

Griffith [1] was the first to consider the role played by the surface in the initiation of fracture. Later studies performed by Ioffe *et al.* [2], as well as more recent investigations carried out by Aleksandrov and Zhurkov [3], Vitman *et al.* [4], and Stepanov *et al.* [5], have demonstrated that surface treatment involving the removal of defects acting as concentrators of mechanical stresses makes it possible to increase the strength of ionic crystals, glasses, and semiconductors by a factor of several tens.

With the advent of the kinetic approach to solving the problem of mechanical failure, which was put forward by Zhurkov (see the paper by Zhurkov and Narzulaev [6]), a question arose as to the nucleation of defects of atomic, nanometric, and micrometric sizes under mechanical loading. It seemed to be especially important to reveal and investigate these defects on atomically clean surfaces.

The development of new techniques for analyzing surfaces enabled Zhurkov *et al.* [7] to begin research in this direction. Using electron-energy loss spectroscopy, Auger electron spectroscopy, low-energy electron diffraction, etc., it was established that the mechanical action on germanium and silicon single-crystal semiconductors, as well as on mica (muscovite), leads to a substantial transformation of the electronic and atomic structures of their surfaces [8–10].

In situ investigation of a loaded Ge(111) surface has revealed that the elastic and plastic strains arising in a 1-nm-thick layer are stronger than those observed in the bulk. As a result, the nucleation of defects (such as point defects, atomic steps, and nanocrystalline structures) occurs on the surface with subsequent propagation into the bulk of the crystals. The mechanical load and the related structural transformation of the surface lead to changes in the rates of chemical reactions [11].

This paper reports on the results of investigations into the structural transformations of a platinum surface under tensile deformation. It is well known that platinum serves as a catalyst for many chemical reactions. Investigations have revealed that the adsorption properties of platinum can be significantly different depending on its structure.

Therefore, study of the structural transformations of the platinum surface under mechanical actions is important both for determining the catalytic properties exhibited by platinum and for elucidating the mechanism responsible for the initiation of fracture.

2. SAMPLE PREPARATION AND EXPERIMENTAL TECHNIQUE

The experiments were performed using two methods: the surface structure of the samples was determined by low-energy electron diffraction (LEED), and the chemical composition of the samples was controlled using Auger electron spectroscopy. The objects of our investigation were thin strips of platinum (purity, 99.99%) that were recrystallized and purified in a series of heating cycles under vacuum and in oxygen.

The experimental setup for investigating the structural transformation of the platinum surface under mechanical loading is schematically shown in Fig. 1.

A 0.02-mm-thick platinum strip *2* was mounted on insulator *1*. The other end of the platinum strip was attached to insulator *5* through guide insulator *4*. Pusher *6* transferred the controlled tensile force to the

1063-7834/05/4705-0903$26.00 © 2005 Pleiades Publishing, Inc.

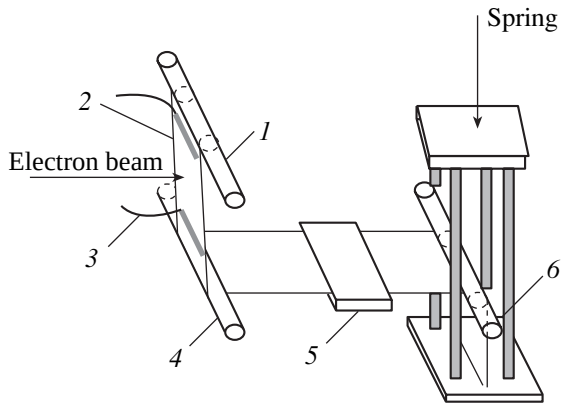

Fig. 1. Schematic diagram of the loading machine: (*1*, *4*, *5*) insulators, (*2*) platinum strip, (*3*) current leads, and (*6*) pusher.

sample through a spring. This loading machine was installed on the flange of a crystal holder of a standard low-voltage diffractometer. The platinum strip was heated by passing an electric current from a regulated ac voltage source through current leads *3*. The temperature of the sample was measured using a pyrometer. The diffraction chamber was filled with oxygen through a leak in a dynamic regime. This arrangement of the loading machine made it possible to retain the majority of the degrees of freedom of the sample manipulator and to record the diffraction patterns immediately during the controlled loading of the sample.

At the initial stage of sample preparation, no LEED pattern was observed, whereas the Auger spectra contained intense peaks attributed to oxygen. The sample was purified and recrystallized as follows. The platinum strip was heated first under vacuum at temperatures ranging from 700 to 800°C for 3 h and then in oxygen at a temperature of ~600°C and at an oxygen partial pressure of approximately 10^{-4} Pa for 1.5 h with subsequent heating under vacuum at a temperature of ~850°C for 20 min. After this treatment was repeated several times, there appeared diffraction patterns. These diffraction patterns exhibited reflections in the form of circles and circular arcs, because the surface contained carbon at a content of 5–25 at. %. The corresponding LEED patterns are shown in Figs. 2a and 2b. The last cycles of sample preparation were carried out at higher temperatures (~1200°C) under vacuum and at a lower oxygen partial pressure (~10^{-6} Pa). At the final stage of sample preparation, the Auger spectra did not exhibit peaks attributed to oxygen or carbon. The LEED patterns of the platinum surface recrystallized by the above method are displayed in Figs. 3a and 3b. As a rule, we managed to obtain LEED patterns that, for the most part, were uniform over the sample surface and whose quality was no lower than the quality of the LEED patterns of the single crystals. The LEED patterns thus obtained correspond to the (111) facet emerging on the surface with a (1×1) structure [12, 13]. Experiments with mechanical tension were performed for both the samples containing carbon impurities on the surface and the samples cleaned of carbon.

3. EXPERIMENTAL RESULTS AND DISCUSSION

The LEED patterns illustrating the influence of tensile deformation on the structure of the recrystallized platinum surface were compared with the data on the macroscopic deformation. For this purpose, we recorded the load–strain curves for samples prepared under vacuum according to the aforementioned procedure but not subjected to loading.

The results obtained are presented in Fig. 4. This figure also shows the ranges corresponding to the loads and strains (*A* and *B*) at which we recorded the diffraction patterns displayed in Figs. 2 and 3.

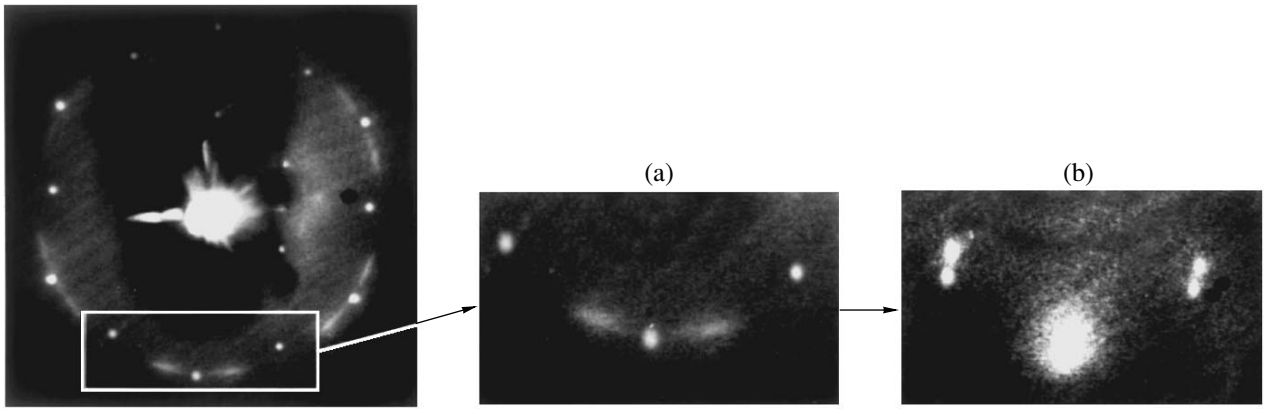

Fig. 2. Evolution of the LEED patterns of the recrystallized platinum surface containing ~10 at. % C: (a) the initial pattern and (b) the pattern recorded after loading at $\sigma = 80$ MPa.

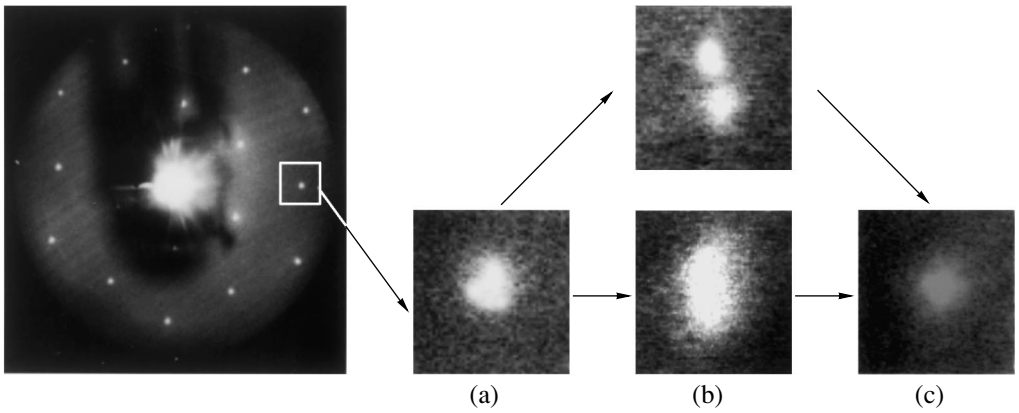

Fig. 3. Variation in the shape of the diffraction maxima in the LEED pattern of the recrystallized platinum surface: (a) the initial pattern and the patterns recorded after loading at σ = (b) 80 and (c) 90 MPa for 2 h.

We consider the evolution of the LEED patterns under loading of the samples with an atomically clean Pt(111) surface. Comparison of the LEED patterns displayed in Figs. 3a–3c shows that, under loading at $\sigma \sim$ 80 MPa, which amounts to ~3/4 of the breaking load, the structure of the recrystallized platinum surface undergoes a nonuniform transformation. Some regions of the surface are characterized by diffraction patterns with split reflections (see the upper part of Fig. 3b) that correspond to the formation of an ordered stepped structure of the Pt(9(111) $\times$ 100) type [14]. Other regions of the surface correspond to a disordered system of steps (the lower part of Fig. 3b). In both cases, the arrangement of the steps corresponds to the direction of the deformation. After unloading, the LEED pattern remains unchanged. Heat treatment of the plastically deformed sample under vacuum after unloading leads to a partial disappearance of the stepped structure and to reconstruction of the (111)-1 $\times$ 1 surface. Under loading up to breaking loads, the character of the diffraction pattern also remains unchanged. Upon holding the platinum strip under larger permanent prebreaking loads (~$0.9\sigma_{max}$), the surface undergoes a structural transformation with time (Fig. 3c). Under loading for 2 h, the ordered system of steps is transformed into a disordered system and the intensity of the diffraction maxima decreases. This suggests either the amorphization or the formation of a nanocrystalline surface under the load. The check experiments demonstrated that, over the same period of time, the LEED patterns of both the initial (not loaded) and unloaded samples change only slightly.

At the initial stages of plastic deformation (σ = 20–80 MPa), the diffraction maxima are characterized by an insignificant broadening. This indicates that only a small part of the surface is involved in the structural transformation. Portion *A* in the load–strain curve corresponds to the evolution of the LEED patterns due to the formation of steps in both the ordered and disordered systems. Portion *B* is associated with the disordering of the surface structure with time under a permanent load.

Let us now consider the evolution of the LEED patterns of the samples with a carbon-containing Pt(111) surface. It is known from the data available in the literature that carbon on the platinum surface is responsible for the appearance of arched reflections in the LEED patterns and forms a hexagonal mesh with a graphite structure [15]. The arched shape of the diffraction maxima in the LEED patterns shown in Fig. 2 implies that the platinum surface contains carbon species in the form of islands arranged in such a way that the *C* axis is perpendicular to the surface of the sample, whereas the islands themselves are misoriented in the surface plane by an angle of ±15° with respect to the platinum crystal lattice. Upon tensile deformation, the variation in the shape of the reflections attributed to platinum is similar to that of the sample cleaned of carbon. In this case, the arched reflections transform into large-sized circular reflections in accordance with the arrangement of platinum atoms (Fig. 2b). Thus, it is established that

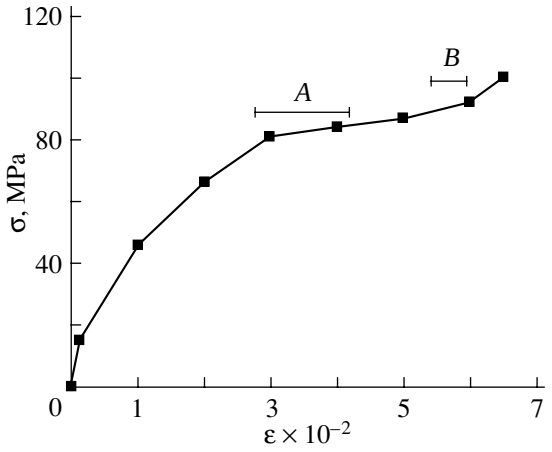

Fig. 4. Load–strain curve for a recrystallized platinum strip.

carbon islands are reoriented along the direction of mechanical deformation.

REFERENCES

1. A. A. Griffith, Philos. Trans. R. Soc. London, Ser. A **221**, 163 (1921).
2. A. F. Ioffe, M. V. Kirpicheva, and M. A. Levitinskaya, Zh. Russ. Fiz.–Khim. O-va **56**, 429 (1924).
3. A. P. Aleksandrov and S. N. Zhurkov, *Phenomenon of Brittle Fracture* (GTTI, Leningrad, 1993) [in Russian].
4. F. F. Vitman, V. A. Bershteĭn, and V. P. Pukh, in *Strength of Glass*, Ed. by V. A. Stepanov (Mir, Moscow, 1969), p. 7.
5. V. A. Stepanov, L. V. Zhoga, and V. V. Shpeu, Fiz. Met. Metalloved. **42** (5), 1068 (1976).
6. S. N. Zhurkov and B. N. Narzulaev, Zh. Tekh. Fiz. **23**, 1677 (1953).
7. S. N. Zhurkov, V. E. Korsukov, A. S. Luk'yanenko, B. A. Obidov, V. N. Svetlov, and A. P. Smirnov, Pis'ma Zh. Éksp. Teor. Fiz. **51** (6), 324 (1990) [JETP Lett. **51**, 370 (1990)].
8. S. A. Knyazev, V. E. Korsukov, and B. Obidov, Fiz. Tverd. Tela (St. Petersburg) **36** (5), 1315 (1994) [Phys. Solid State **36**, 718 (1994)].
9. V. E. Korsukov, S. A. Knyazev, and A. S. Luk'yanenko, Fiz. Tverd. Tela (St. Petersburg) **38** (1), 113 (1996) [Phys. Solid State **38**, 60 (1996)].
10. V. Korsukov, A. Lukyanenko, and B. Obidov, Surf. Rev. Lett. **5** (1), 1357 (1998).
11. Masanori Yata, Yuki Vesugi, and V. E. Korsukov, Phys. Rev. Lett. **91** (20), 206103 (2003).
12. H. B. Lyon and G. A. Somorgai, J. Chem. Phys. **46**, 2539 (1967).
13. V. P. Ivanov, V. I. Savchenko, G. K. Boreskov, and K. S. Teĭlor, Kinet. Katal. **19** (1), 210 (1978).
14. B. Lang, R. W. Joyner, and G. A. Somorjai, Surf. Sci. **30**, 440 (1972).
15. J. W. May, Surf. Sci. **17**, 267 (1969).

Translated by N. Korovin

Physics of the Solid State, Vol. 47, No. 5, 2005, pp. 907–912. Translated from Fizika Tverdogo Tela, Vol. 47, No. 5, 2005, pp. 880–885.

Initial Stage of Void and Crack Healing in Polycrystalline Metals under Uniform Compression

A. I. Petrov and M. V. Razuvaeva

Ioffe Physicotechnical Institute, Russian Academy of Sciences, Politekhnicheskaya ul. 26, St. Petersburg, 194021 Russia
e-mail: an.petrov@mail.ioffe.ru

Abstract—The effect of uniform pressure and temperature on voids and cracks located at grain boundaries in polycrystalline metals is studied. A high-sensitivity method for measuring density, scanning electron microscopy, and optical microscopy were used to analyze the healing of cavities. The results obtained are discussed on the basis of the existing notion of the kinetics of healing under pressure at various temperatures. © *2005 Pleiades Publishing, Inc.*

Microvoids and cracks, which are formed in the process of material compacting, processing, or operation under load, appreciably impair the physicomechanical characteristics of a material. It is known that healing of such defects makes it possible to improve the properties of a material and to restore its operational parameters [1–6]. It has been established that the application of uniform pressure is an effective way to perform healing[4–6]. Therefore, it is obviously important to establish the features and the mechanism of healing and to determine the physical parameters that control the process of healing of cavities under pressure.

The mechanism of healing under pressure depends substantially on temperature. At room temperature, the dislocation mechanism of healing is effective. According to [7–9], under pressure, shear stresses appear near voids, with the result that the pinned dislocation segments with edge orientation at the void surface become sources of new dislocations. Above a critical stress, a dislocation loop forms and the void boundary is displaced by the Burgers vector. The dislocation healing mechanism has been studied most completely for voids in alkali-halide crystals [7–10]. Theory and experiment have shown that the stabilized void size R as a function of pressure P is given by the equation [7]

$$1 - (R/R_0)^3 = CP^{1/4}\frac{(P - P^*)}{G} \sim P^{5/4}, \qquad (1)$$

where R_0 is the initial void size, C is a constant, P^* is a threshold pressure, and G is the shear modulus.

It is shown in [11–13] that Eq. (1) is also satisfied for metal single crystals; the size of spherical or pyramidal cavities on the surface of Pb, In, and Sn single crystals depends on pressure in the same way as in alkali-halide crystals. An analogous study has not been performed for polycrystalline metals.

With increasing temperature, the mechanism of void healing under pressure changes. In alkali-halide crystals, at the beginning, the healing process is due to the emission and slip of dislocations and then, after prolonged subjection of pressure, it is controlled by the creation of point defects responsible for the dissolution of dislocation loops [9]. For polycrystalline metals and alloys at temperatures $T \geq 0.5T_m$ (where T_m is the melting temperature), the healing of grain-boundary voids under pressure is due only to diffusive processes with an activation energy E_a, which is equal to the energy of grain-boundary diffusion [14]. In [14], estimations of E_a were made at the second stationary stage; the initial stage of the process of void healing under pressure at high temperatures was not analyzed.

We studied the kinetics of the healing of voids (including isolated voids) and cracks under pressure in polycrystalline metals over a wide temperature range (from room temperature to $0.77T_m$). The aim of the study was to establish the validity of expression (1) for polycrystals in the region of the dislocation mechanism of void healing. In the region where the diffusion mechanism is operative, we studied the features of healing on the initial (non-steady-state) segment of the curve of void healing. Conditions for transition from the dislocation to diffusion mechanism were also analyzed.

We investigated Al (99.4%), Zn (99.9%), Cu (99.8%), Ni (99.6%), and Fe (with carbon content below 0.01%). To create voids, samples were stretched in the regime of high-temperature creep or were hydrogenated (Fe). Creep tests were performed at temperatures of 460, 320, 500, and 800°C under a stress of 3.5, 2.5, 12.5, and 20 MPa for Al, Zn, Cu, and Ni, respectively. The active part of the samples was $5 \times 5 \times 40$ mm in size. Cylinder-shaped Fe samples 15 mm in diameter and 20-mm high were hydrogenated at 400°C under a pressure of 20 MPa over 20 h. Prior to the tests, the samples were exposed to recrystallization annealing. The degree of porosity of the samples W was assumed to be equal to the relative decrease in density $(\rho_0 - \rho)/\rho_0$

1063-7834/05/4705-0907$26.00

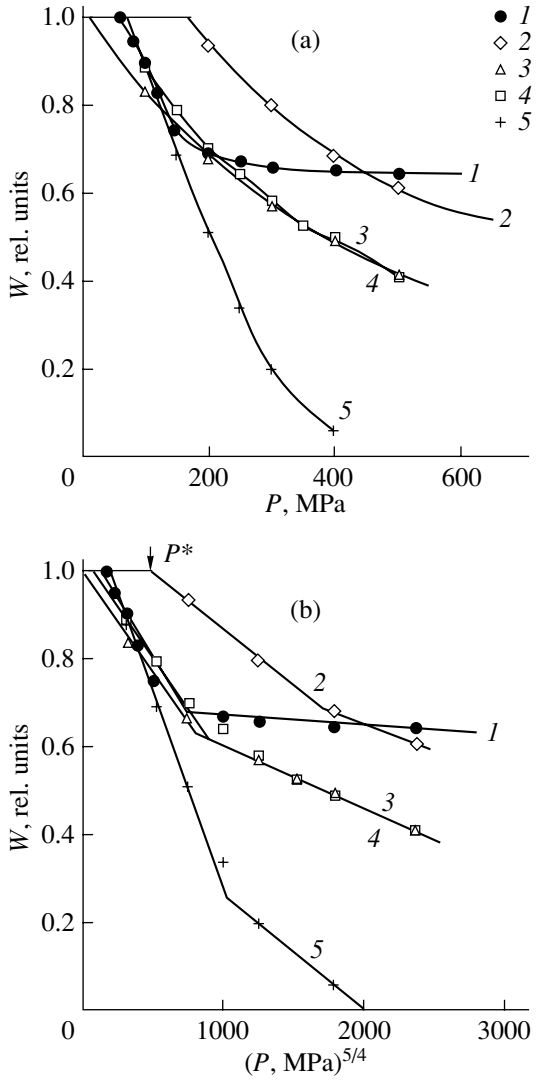

Fig. 1. Pressure dependence of the relative change in porosity for different polycrystalline metals plotted in the (a) W vs. P and (b) W vs. $P^{5/4}$ coordinates for (*1*) Zn, (*2*) Ni, (*3*) Fe, (*4*) Cu, and (*5*) Al.

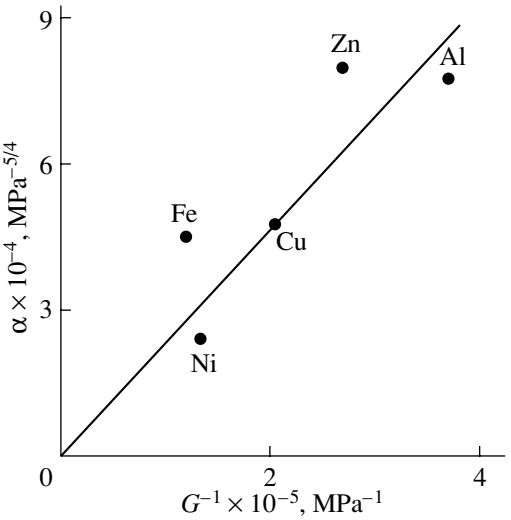

Fig. 2. Dependence of the slope of the initial segment of the W vs. $P^{5/4}$ curve on the inverse shear modulus.

(ρ_0 is the density of the original samples, ρ is the density of samples after tests) and was determined by the method of hydrostatic weighing with an accuracy of 5×10^{-4}. The size and shape of microcavities were determined using optical (Neophot-21) and scanning (JEM-35) microscopy. Microscopic studies showed that, during both creep tests and hydrogenation, microcavities were mainly localized in grain boundaries and their average size was about 10 μm. In Al, microcavities were spherical in shape; in Fe, flat microcracks were observed; and both voids and cracks were typically observed in other metals. The maximum degree of porosity was several percent.

Part of the experiments on healing at room temperature was performed with isolated "voids" 0.5 and 1 mm in diameter; in Al samples, such voids were created by drilling holes 1- and 2-mm deep, respectively. After annealing, an Al plate was soldered with tin to close the holes.

Void healing was performed in a high-pressure chamber with external heating up to 260°C. Silicone oil was used as a pressure-transmitting medium.

Let us consider the experimental data obtained for polycrystalline metals at room temperature, where the dislocation mechanism of void healing is operative [15]. Figure 1a shows the dependence of porosity (reduced to the porosity of original samples W_0) on the applied pressure. We see that, starting from a threshold pressure P^*, the degree of porosity decreases with increasing pressure: the healing curve becomes appreciably flatter with increasing pressure. Measurements also show that, for grain-boundary voids in Al, the pressure dependence of porosity practically coincides with the dependences obtained for isolated voids 0.5 and 1 mm in diameter (curve *5*).

As in [7], the time of exposure under pressure (ranging from several minutes to several hours) at 18°C has almost no effect on the porosity (for Zn, the data are given in Fig. 4, curve *4*).

Microscopic measurements showed that the decrease in porosity with increasing pressure is due to microplastic deformation near cavities, which decreases the cavity size. In Fe samples, the decrease in porosity is caused by the decrease in the transverse (normal to the grain boundaries) crack size, whereas the crack size along the boundaries remains virtually unchanged even at a pressure of $P = 1000$ MPa.

The curves of void healing under pressure shown in Fig. 1a are replotted in Fig. 1b in the W/W_0 versus $P^{5/4}$ coordinates, in accordance with Eq. (1). We note that,

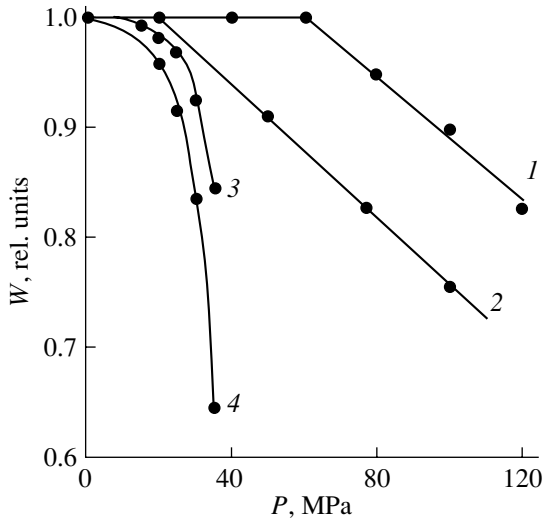

Fig. 3. Pressure dependence of zinc porosity at temperatures of (*1*) 18, (*2*) 93, (*3*) 210, and (*4*) 260°C. The annealing time is 0.5 h.

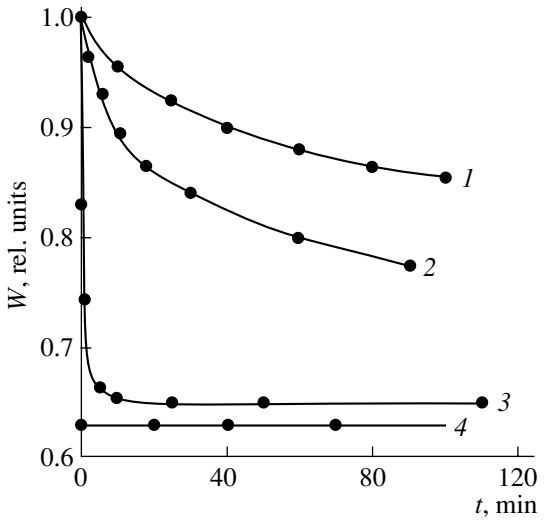

Fig. 4. Dependence of porosity on annealing time for zinc at various temperatures and pressures: (*1*) 210 and (*2*) 260°C at P = 30 MPa; (*3*) 93°C at P = 130 MPa; and (*4*) 18°C at P = 180 MPa.

since $W = N\bar{R}^3$ ($\bar{R}$ is the average void size, N is the void concentration), we have $W/W_0 = (\bar{R}/\bar{R}_0)^3$.

This procedure shows that, for polycrystals, the $(1 - W/W_0) \sim P^{5/4}$ law is satisfied only at the initial stage of healing in a relatively narrow pressure interval; this interval is, for example, 65–265 and 145–390 MPa for Al and Ni, respectively. At high pressures, there is a kink in the straight lines in Fig. 1b. The dependence of the slope $\alpha = \Delta W/\Delta P^{5/4}$ at the initial section of the healing curve on the inverse shear modulus G for the metals under study is shown in Fig. 2. The linearity of this dependence indicates that law (1) is also valid for polycrystalline metals. Just as for single crystals [9], a deviation from Eq. (1) at high pressures can be related to polygonization of the crystal regions adjoining the voids. It should also be noted that Eq. (1) is derived for an idealized case in which the healing process is controlled by the motion of dislocation loops in a matrix without defects; i.e., Eq. (1) does not take into account real defects of the material, such as dislocations, impurity atoms, inclusions, and block and grain boundaries. These defects can have a substantial effect the kinetics of healing under pressure.

Thus, the healing of cavities in polycrystalline metals under uniform pressure has a threshold character and is virtually independent of the duration of applied pressure. At the initial stage, at rather low pressures, the pressure dependence of the degree of healing corresponds to Eq. (1), whose validity has been established for different single crystals. The healing kinetics is virtually independent of the void size in the range 0.01–1 mm.

Let us consider the data on void healing under pressure at elevated temperatures. Figure 3 shows W as a function of P for Zn in the temperature range 18–260°C. We see that, for a fixed healing time t, the increase in temperature substantially accelerates the process of void healing. With increasing temperature, the kinetics of void healing (Fig. 4) also changes. As noted above, at 18°C, the quantity W is not affected by the duration of applied pressure. At 93°C, the porosity varies only slightly for durations of applied pressure of up to 5 min. Processing of the data obtained at 93°C showed that, in this case, the dependence of porosity is also described by Eq. (1) and that the slope α of the initial linear segment is the same as that at 18°C and is equal to 8×10^{-4} MPa$^{-5/4}$. The threshold pressure P^* decreases appreciably, from 64 MPa at 18°C to 15 MPa at 93°C.

At temperatures of 210 and 260°C, a time dependence of porosity is observed for any duration of applied pressure. The W versus t curves at these temperatures consist of an initial segment corresponding to the decay of W and a subsequent segment where W varies at a constant rate.

From the data in Figs. 3 and 4, it follows that, for temperatures in the range 100–260°C, the volume compressive plastic strain $\varepsilon_v = W_0 - W$ caused by void healing depends on the pressure, the duration of applied pressure, and the temperature. Processing of the data obtained (Figs. 5–7) showed that, at the initial stage of healing, the following relations are valid:

$$\varepsilon_v|_{T,\,P\,=\,\text{const}} = C_1 t^{1/2}, \tag{2}$$

$$\varepsilon_v|_{T,\,t\,=\,\text{const}} = C_2 P^n, \tag{3}$$

$$\varepsilon_v|_{P,\,t\,=\,\text{const}} = C_3 \exp\left(-\frac{E_a}{kT}\right), \tag{4}$$

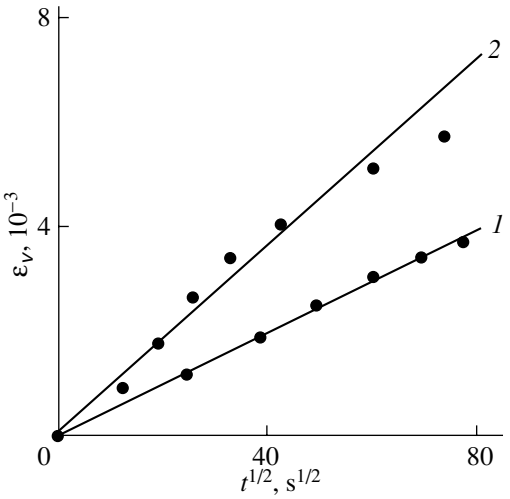

Fig. 5. Dependence of volume compressive strain on annealing time at a constant pressure P = 30 MPa and at temperatures of (*1*) 210 and (*2*) 260°C.

where C_1, C_2, C_3 are constants, n = 3.7, and the activation energy for the healing process E_a (according to the data from Figs. 4, 7) is 65 ± 5 kJ/mol, i.e., close to the energy of grain-boundary diffusion in Zn (E_b = 61.3 kJ/mol) [16].

Thus, in Zn at temperatures above 100°C, the process of healing of grain-boundary voids under pressure is controlled by vacancy diffusion from voids to drains at grain boundaries.

Using Eqs. (2)–(4), the dependence of the strain ε_v on T, t, and P in the general case can be found to be

$$\varepsilon_v(T, t, P) = AP^n(D_b t)^{1/2}, \quad (5)$$

where A is a constant and $D_b = 3 \times 10^{-5}\exp(-E_b/kT)$ is the grain-boundary diffusion factor (measured in m^2/s) [16].

To check the validity of Eq. (5), all experimental dependences obtained at temperatures of 100 to 260°C and various values of P and t were plotted in the $\varepsilon_v/(D_b t^{1/2})$ versus P coordinates. It is seen in Fig. 8a that all points fall on a common curve. Processing the data from Fig. 8a in logarithmic coordinates (Fig. 8b) showed that the slope of the straight line obtained does not depend on the test conditions and is equal to 3.66 ± 0.05, in accordance with the above estimation of this quantity.

Thus, the data obtained suggest that, in Zn, the dislocation mechanism of void healing under pressure is operative at temperatures 18–93°C and that the diffusion mechanism operates in the temperature range 100–260°C. Therefore, the change from the dislocation to diffusion mechanism of void healing occurs in Zn at about 100°C. This temperature virtually coincides with the temperature of the beginning of recrystallization in deformed zinc due to the migration of grain boundaries. Accordingly, we may assume that the absorption of vacancies emitted by voids under pressure occurs at the grain boundaries, which move during the process of recrystallization. For example, vacancies are absorbed by climbing edge-type segments of grain-boundary dis-

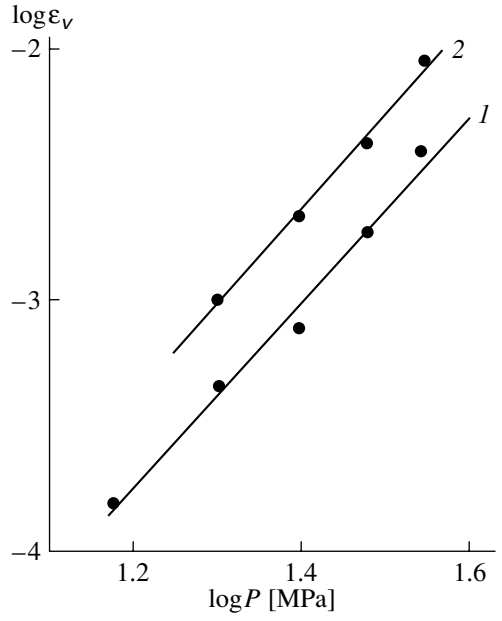

Fig. 6. Pressure dependence of volume compressive strain in zinc for a fixed annealing time of 0.5 h at temperatures of (*1*) 210 and (*2*) 260°C.

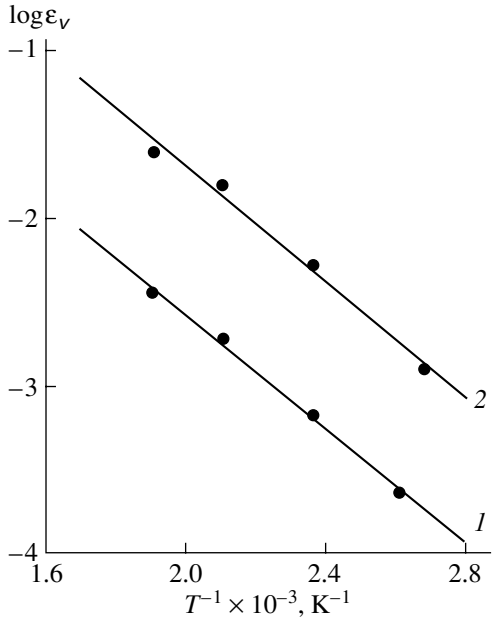

Fig. 7. Temperature dependence of volume compressive strain in zinc for a fixed annealing time of 0.5 h at pressures of (*1*) 30 and (*2*) 50 MPa.

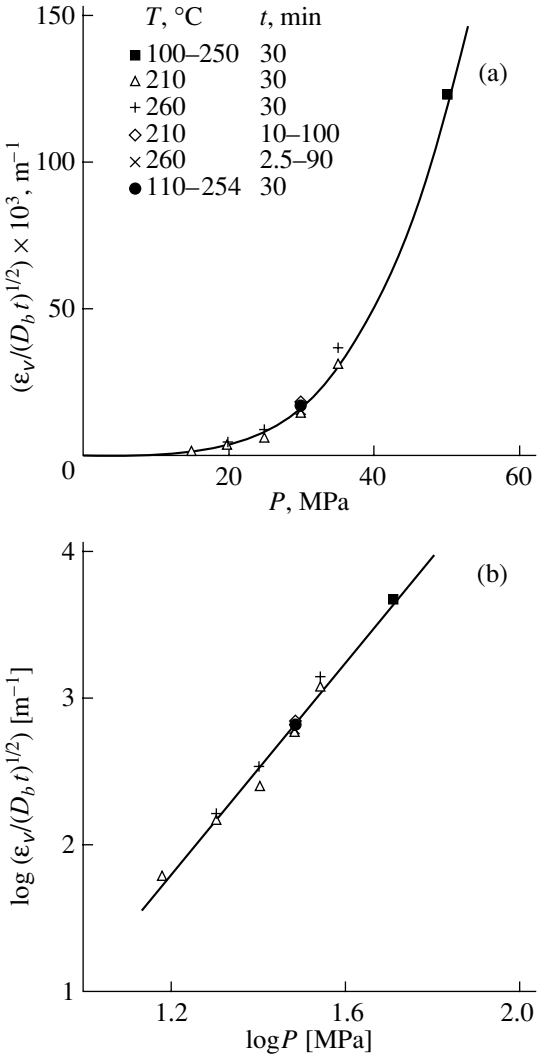

Fig. 8. (a) Pressure dependence of the reduced compressive strain of porous zinc in the temperature range 100–260°C for annealing times in the range 2.5–100 min. (b) The same dependence in logarithmic coordinates.

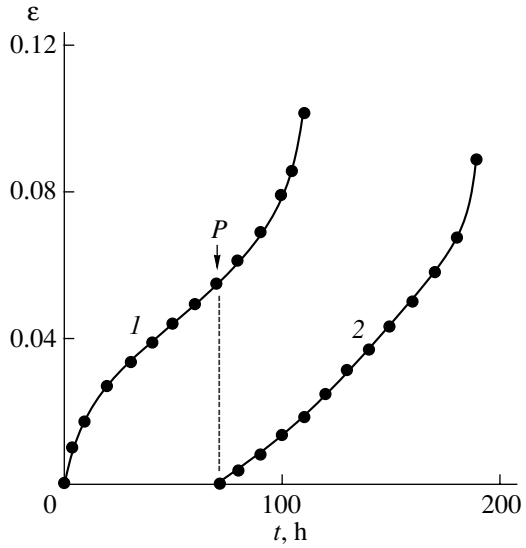

Fig. 9. Effect of pressure $P \cong 1250$ MPa applied at an intermediate stage of a creep test for nickel at $T = 800$°C and $\sigma = 20$ MPa.

locations. This mechanism of void healing operates until voids remain at the boundary. Voids penetrating into the grain bulk when the boundary is displaced from them are not healed. Metallographic data show that, for long times of exposure under pressure at 260°C, there occurs an appreciable increase in the grain size (by a factor of 2 to 3) and an increase in the number of voids in the grain bulk. This effect was earlier observed for a Ni + 2% Cr alloy [14].

The data obtained suggest that the transition from one healing mechanism to another in Zn occurs in a narrow temperature interval of $\Delta T \cong 7$ K at temperature $T = 0.54T_m$ (in kelvins). Just as for other metals studied earlier, the diffusive mechanism in Zn at the early healing stages is related to the grain-boundary diffusion of vacancies. The power-law pressure dependence of the degree of healing found in this study ($n = 3.7$), which is also observed under conditions of high-temperature creep [17], can be due to the effect of stresses (arising near the voids due to the applied pressure and the anisotropy of zinc compressibility) on the creep rate of grain-boundary dislocations.

The weak dependence of W on t observed at 93°C is probably a consequence of the cross slip of dislocations. Indeed, the activation volume ΔV as determined from $W(t)$ at 93°C at pressures of 130 and 100 MPa is $(8–10)b^3$. According to [18], the activation volume required for cross slip to occur is $l_a b^3 \geq db^3 = 7b^3$, where l_a is the activation length, i.e., the length by which a split screw dislocation is constricted before cross slip, and $d = 7b$ is the width of the split dislocation in the basal plane of zinc.

As noted above, void healing under pressure improves the strength and elastic characteristics of metals. Applying pressure is also an effective way to restore the lifetime of metals and alloys tested under conditions of high-temperature creep. As an example of this effect, we consider the data obtained for nickel. Figure 9 shows the original creep curve (curve *1*) and the creep curve after healing under pressure (curve *2*). Pressure was applied at the steady-creep stage after unloading and cooling of the samples to room temperature. The subsequent tests were performed at the same tensile stress. From these data, it is seen that the application of pressure results in a complete restoration of lifetime and appreciably affects the creep in nickel. After healing under pressure, the duration of the steady-creep stage increases and the time interval where the creep rate increases becomes shorter. Pressure has almost no effect on the steady-state creep rate. The observed effect of restoring the lifetime and creep

is probably related to the decrease in grain-boundary porosity rather than to the growth of the dislocation density near the boundaries, since excess dislocations must be annealed under the subsequent (after the application of pressure) slow heating of the unloaded sample to the test temperature.

The analysis of the data on the effect of uniform pressure and temperature on the healing of voids at grain boundaries in metals allows us to make the following conclusions.

(1) The dislocation mechanism of void healing is realized in polycrystalline metals under pressure at room temperature. The pressure dependence of porosity at the initial healing stage is described by an equation that was derived earlier for single crystals.

(2) The transition from the dislocation healing mechanism to the diffusion mechanism occurs at a temperature equal to $0.54T_m$ (in kelvins) for Zn.

(3) For the initial (nonstationary) stage of void healing in Zn at elevated temperatures, an empirical expression has been obtained relating the change in porosity to the grain-boundary diffusion factor, pressure, and the duration of applied pressure.

REFERENCES

1. A. I. Petrov, A. M. Kartashov, U. N. Azhimuratov, and V. I. Betekhtin, FKhMM, No. 3, 109 (1984).
2. H. Burt, J. P. Dennison, I. G. Elliot, and B. Wilshire, Mater. Sci. Eng. **63**, 245 (1982).
3. V. Sclenicka, K. Kucharova, J. Chadek, V. I. Betechtin, A. G. Kadomtsev, and A. I. Petrov, Kovove Mater. (Bratislava) **26** (4), 274 (1988).
4. V. I. Betekhtin, A. I. Petrov, Yu. A. Burenkov, A. M. Kartashov, U. N. Azhimuratov, A. G. Kadomtsev, and V. Sklenichka, Fiz. Met. Metalloved. **67** (3), 564 (1989).
5. V. I. Betekhtin, A. I. Petrov, N. K. Ormanov, V. Sklenichka, V. I. Monin, A. G. Kadomtsev, and V. V. Konovalenko, Fiz. Met. Metalloved. **67** (2), 318 (1989).
6. V. I. Betekhtin, A. I. Petrov, A. G. Kadomtsev, N. K. Ormanov, M. V. Razuvaeva, and V. Sklenichka, Fiz. Met. Metalloved. **68** (5), 175 (1990).
7. Ya. E. Geguzin and V. G. Kononenko, Fiz. Tverd. Tela (Leningrad) **15** (12), 3550 (1973) [Sov. Phys. Solid State **15**, 2370 (1973)].
8. H. E. Evans and G. K. Walker, Met. Sci. **4**, 210 (1970).
9. Ya. E. Geguzin and V. G. Kononenko, Fiz. Khim. Obrab. Mater., No. 2, 60 (1982).
10. R. A. Evans, A. S. Wronski, and B. A. Redjern, Philos. Mag. **29**, 1381 (1974).
11. G. P. Unit, Ya. E. Maniks, and I. P. Manika, Izv. Latv. SSR, Ser. Fiz.–Tekh. Nauk **5**, 15 (1980).
12. G. P. Unit, Ya. E. Maniks, and I. P. Manika, Izv. Latv. SSR, Ser. Fiz.–Tekh. Nauk **6**, 31 (1982).
13. G. P. Unit, Ya. E. Maniks, and I. P. Manika, Izv. Latv. SSR, Ser. Fiz.–Tekh. Nauk **6**, 36 (1982).
14. R. A. Stevans and P. E. J. Flewitt, Acta Met. **27** (1), 67 (1979).
15. A. I. Petrov and M. V. Razuvaeva, Zh. Tekh. Fiz. **72** (8), 130 (2002) [Tech. Phys. **47**, 1058 (2002)].
16. C. J. Smithells, *Metals: Reference Book*, 5th ed. (Butterworths, London, 1976; Metallurgiya, Moscow, 1980).
17. V. M. Rozenberg, *Fundamentals of High-Temperature Strength of Metallic Materials* (Metallurgiya, Moscow, 1973) [in Russian].
18. J. Friedel, *Dislocations* (Pergamon, Oxford, 1964; Mir, Moscow, 1967).

Translated by I. Zvyagin

Physics of the Solid State, Vol. 47, No. 5, 2005, pp. 913–919. Translated from Fizika Tverdogo Tela, Vol. 47, No. 5, 2005, pp. 886–892.

Structure and Mechanical Properties of Al–Si(Ge) Alloys upon Melt Centrifugation and Quenching

M. P. Volkov*, V. N. Gurin*, S. P. Nikanorov*, Yu. A. Burenkov*†, L. I. Derkachenko*, B. K. Kardashev*, L. L. Regel, and W. R. Wilcox****

** Ioffe Physicotechnical Institute, Russian Academy of Sciences, Politekhnicheskaya ul. 26, St. Petersburg, 194021 Russia*
e-mail: s.nikanorov@mail.ioffe.ru

*** International Center for Gravity Materials Science and Applications, Clarkson University, Potsdam, New York, 13699-5814 USA*

Abstract—The structures of eutectic binary Al–12.7 at. % Si and Al–29.7 at. % Ge alloys and a ternary Al–10 at. % Si–10 at. % Ge alloy produced by quenching levitated melts or through solidification either in the presence or in the absence of a centrifugal acceleration of 7*g* are studied. Centrifugation is found to cause an increase in the silicon content in the Al–Si alloy in the direction opposite to the direction of centrifugal acceleration and an increase in the germanium content in the Al–Ge alloy in the direction of centrifugal acceleration. These differences are explained by the fact that the densities of silicon and germanium clusters and solidification centers differ from the liquid-phase density at temperatures of solidification. The related changes in the values of the Young's modulus and in the stress–strain curves can be due to sedimentation-induced changes in the composition of samples cut from the middle part of an ingot. The processes of decomposition and recovery are shown to have a substantial effect on the elastic moduli of these alloys. © *2005 Pleiades Publishing, Inc.*

1. INTRODUCTION

Interest in the effect of centrifugation of melts on the structure and properties of solidifying alloys has recently intensified [1]. Centrifugation has been applied for studying the structure and composition of eutectics in multicomponent systems [2] and also for the development of new processes of solidification of aluminum-based alloys [3]. However, the effect of centrifugation on the structure and properties of aluminum alloys with silicon and germanium, on which many commercial alloys are based, has not been studied. Centrifugation has been used to estimate the heterogeneity of silumin melts. Sedimentation analysis of an Al–7.5% Si melt performed in [4] at a centrifugal acceleration of 600*g* revealed the formation of silicon-rich colonies with a slightly higher density than that of the liquid medium. Moreover, different parts of a sample solidified during centrifugation had different structures. The objective of [4] was to study structural inhomogeneities in a melt at high temperatures, so the change in the silicon concentration along the length of an ingot was determined as the difference in concentration between samples solidifying from a high temperature and from the temperature of solidification. It was noted in [4] that centrifugation could affect the structure of solidifying samples both through the sedimentation of alloy components at high homogenizing temperatures and through the effect of a force field during solidification.

The effect of centrifugation on the mechanical properties of aluminum alloys with silicon and germanium has not been studied. In this work, we study the effect of centrifugation on the structure, elasticity, and micro- and macroplasticity of eutectic Al–Si and Al–Ge alloys and a ternary Al–Si–Ge alloy. Since the physicomechanical properties of aluminum alloys are known to be sensitive to structural changes due to decomposition in the course of aging and recovery [5, 6], we also devote attention to the poorly known effect of decomposition and recovery on the structure and properties of alloys when studying the effect of centrifugation on them.

2. EXPERIMENTAL

Al–12.7 at. % Si, Al–29.7 at. % Ge, and Al–10 at. % Si–10 at. % Ge alloy samples were prepared by rapid cooling of levitated melts in a helium atmosphere at a pressure of 1×10^{-5} Pa under the action of an electromagnetic field (500 Hz, 10 kW). A liquid metal was poured into a copper mold. The cooling rate was about 10^4 K/s. The alloys produced by quenching of the levitated melts were vacuum-remelted in quartz crucibles in the furnace of an HIRB centrifuge [3]. The temperature in the central portion of the ampoules was increased to 980°C, maintained for 2.5 h, and then decreased (after the furnace was turned off) at a mean rate of about 10^{-2} K/s in the temperature range from 600°C to room temperature. The melts were homogenized and solidified at a centrifugal acceleration of 7*g*. Reference samples, which were used to reveal the effect of centrifugal forces on alloy structures, were melted in

† Deceased.

the centrifuge furnace without rotation. The geometry of these reference samples allowed us to perform hardness tests only. Therefore, Al–12.7 at. % Si samples were also prepared through directional solidification by the Bridgman–Stockbarger method in an Ar atmosphere. The melt was homogenized at about 950°C. The cooling rate from the eutectic temperature was about 10^{-2} K/s, which is close to the cooling rate of the samples during solidification on the centrifuge.

Microsection metallographic specimens were cut with a diamond saw, ground, and polished. Samples for density measurements and for studying mechanical properties were spark cut. The density was measured by hydrostatic weighing.

To determine the Young's modulus, the resonance frequency of longitudinal elastic vibration of rod-shaped samples 12.3- to 29.3-mm long was measured by a resonance method on a device with electrostatic excitation of vibrations at frequencies of 90–200 kHz. The Young's modulus was calculated from the formula $E = 4\rho l^2 f^2 n^{-2}/(1 + \Delta l/l)$, where ρ is the sample density at room temperature, l is the sample length, f is the resonance frequency of longitudinal vibration of the sample, n is the number of the excited harmonic ($n = 1$ in this work), and Δl is the reversible elongation of the sample due to thermal expansion. The thermal expansion coefficient of the Al–12.7 at. % Si alloy is about 0.88 of the thermal expansion coefficient of aluminum [4]. Therefore, the reversible elongation of a sample upon heating to 500°C changes the elastic modulus by only about 1%, which is negligibly small. However, when the temperature dependence of the Young's modulus was measured, the alloy density, sample length, and Young's modulus could change irreversibly because of changes in the residual stresses and the amount of silicon (germanium) in the α solid solution of Si (Ge) in Al. The heating and cooling rates were about 3×10^{-2} K/s. Each experimental point in the $E(T)$ dependences was recorded after holding to stabilize the temperature. During experiments, the densities and lengths of samples changed irreversibly at certain temperatures. These changes were taken into account by repeated measurements of the densities and lengths at room temperature after studying the temperature dependence of the Young's modulus.

The attenuation of elastic vibrations and the elastic modulus of the Al–Si samples at room temperature were also measured by a resonance method with a compound vibrator consisting of a sample and an electromechanical piezoelectric quartz transducer. A computer-assisted device was used to generate longitudinal vibrations in the sample at a resonance frequency of about 100 kHz and to measure the decrement $\delta$and Young's modulus of the sample. The measurements were conducted at a vibration strain amplitude varying in the range 10^{-6}–3×10^{-4}. The Vickers hardness was measured at a load of 5 kg. Deformation tests by three-point bending were carried out on an Instron 1341 machine at a bending-flexure speed of 0.5 μm/s, with the load being measured at 1-s intervals. The dimensions of the bending specimens were $1.6 \times 2.5 \times 20$ mm.

3. EXPERIMENTAL RESULTS

Figure 1 shows the microstructures of Al–12.7 at. % Si samples produced by rapid cooling of a levitated melt (Fig. 1a), solidification in the centrifuge furnace without rotation (Fig. 1b), and solidification in the centrifuge at a centrifugal acceleration of 7*g*. For the last case, Figs. 1c and 1d show the structures of the top part (which is closer to the centrifuge axis) and the bottom part (farther from the axis) of the ingot, respectively. It is seen that the ingot produced by rapid cooling of a levitated melt has a fine-grained structure (Fig. 1a). Solidification in the centrifuge furnace without rotation (Fig. 1b) causes the formation of an anomalous eutectic structure (dark regions correspond to silicon, and bright regions correspond to the α solid solution of silicon in aluminum) with primary crystals of the solid solution of silicon in aluminum (white oval zones). The structure of the top of the ingot solidified during centrifugation (Fig. 1c) is similar to the previous one except for the primary dendrites of the α solid solution. The bottom portion of the ingot (Fig. 1d) contains primary crystals of the α solid solution of silicon in aluminum (in the form of bright dendrites). Geometrical analysis of the polished sections shows that the silicon content at the bottom of the ingot is about 30% lower than that at the top, which is mainly due to the formation of primary crystals of the α solid solution.

Figures 1e–1h show the microstructures of Al–29.7 at. % Ge ingots. The alloy produced by casting a levitated melt (Fig. 1e) has a fine-grained structure containing fine dendrites of the α solid solution of germanium in aluminum (white regions). The grain size of the anomalous eutectic structure increases after solidification in the centrifuge furnace (Fig. 1f). The same character of the structure is observed at the bottom of the ingot solidified under the action of a centrifugal force at an acceleration of 7*g* (Fig. 1h). At the top of the ingot (Fig. 1g), the density of the germanium plates is lower than that at the bottom, and the top portion contains oval (white) zones of the α solid solution of germanium in aluminum. The germanium content at the bottom is higher than at the top due to an increase in both the needle sizes and the needle concentration. A geometrical analysis of polished sections shows that this difference is about 5%.

Figures 1i–1l show the microstructures of Al–10 at. % Si–10 at. % Ge ingots. An ingot produced by rapid cooling of a levitated melt (Fig. 1e) has a structure similar to that of the aluminum–germanium alloy (Fig. 1i). Solidification in the centrifuge furnace at $g = 0$ causes the appearance of coarse Si–Ge crystals (Fig. 1j). The bottom portion of the ingot produced upon solidification at a centrifugal acceleration of 7*g*

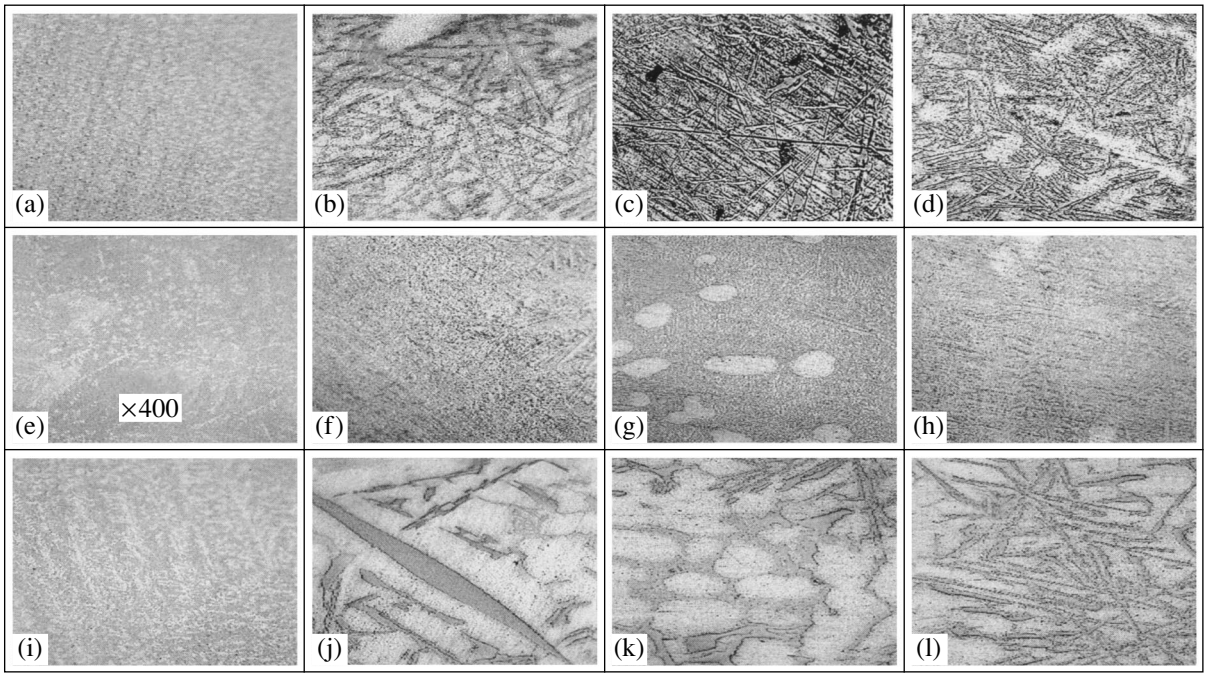

Fig. 1. Polished sections of (a–d) Al–12.7 at. % Si, (e–h) Al–29.7 at. % Ge, and (i–l) Al–10 at. % Si–10 at. % Ge alloys produced by (a, e, i) quenching at $v = 10^4$ K/s or solidification at $v = 10^{-2}$ K/s in a centrifuge (b, f, j) without rotation and (c, d, g, h, k, l) with rotation at an acceleration of 7*g*; (c, g, k) top portion of ingots (which is closer to the configuration axis) and (d, h, l) bottom portion of ingots. Magnification is ×200 except in panel (e).

(Fig. 1l) differs from its top portion (Fig. 1k) in that it has a higher concentration of Si–Ge plates.

For all alloys, the density was measured on samples produced through casting of levitated melts and solidification on a centrifuge at an acceleration of 7*g*. For the Al–Si alloy, the density was also measured on a sample that was solidified without centrifugal acceleration under conditions close to the conditions of solidification in the centrifuge furnace. Table 1 shows that the density of the Al–Si eutectic decreases by about 1% when the samples solidify at a low rate. Annealing that occurs during measurements of the temperature dependence of the Young's modulus on samples grown under centrifugation conditions does not change their densities. The densities of the Al–29.7 at. % Ge and Al–10 at. % Si–10 at. % Ge alloys produced by rapid cooling increase upon annealing by 3.8 and 0.2%, respectively. Annealing of these alloys produced on the centrifuge does not change their densities.

The Vickers hardnesses of the alloys are given in Table 2. The hardnesses of the quenched samples are seen to be equal to or higher than the hardnesses of the

Table 1. Density ρ (kg/m^3) at 20°C of alloys solidified at a cooling rate v (K/s) and a centrifugal acceleration ω (in units of gravity *g*)

v	ω	State	Alloy		
			Al–12.7 at. % Si	Al–29.7 at. % Ge	Al–10 at. % Si–10 at. % Ge
10^4	0	Quenched, aged	2.659	3.475	2.995
		tempered	2.655	3.608	3.001
10^{-2}	0	Solidified	2.660	–	–
		heated, cooled	2.632	–	–
10^{-2}	7*g*	Solidified	2.632	3.565	3.026
		heated, cooled	2.632	3.567	3.054

Note: During the measurement of the temperature dependence of the Young's modulus, the samples were heated to 550°C (Al–12.7 at. % Si), 315°C (Al–29.7 at. % Ge), or 244°C (Al–10 at. % Si–10 at. % Ge). The $E(T)$ dependences of the quenched samples were measured after natural aging at room temperature for 3 months.

Table 2. Vickers hardness (MPa) for the alloys produced at a cooling rate v (K/s) and a centrifugal acceleration ω (in units of g)

v/ω	Ingot portion	Alloy		
		Al–12.7 at. % Si	Al–29.7 at. % Ge	Al–10 at. % Si–10 at. % Ge
10^4/0	Center	450 ± 20	900 ± 20	660 ± 30
10^{-2}/7g	Top	430 ± 20	780 ± 20	660 ± 20
10^{-2}/7g	Bottom	410 ± 10	830 ± 30	660 ± 30

Note: Quenching at $v = 10^4$ K/s and ω = 0 or solidification under centrifugation at $v = 10^{-2}$ K/s and ω = 7g. The load is 5 kg.

samples solidified in the centrifuge at a low solidification rate. For the Al–Si eutectic, the hardness of the top portion of the ingot is higher than that of the bottom portion. The hardness of the Al–Ge eutectic, however, increases in the direction of the centrifugal force. The Al–10 at. % Si–10 at. % Ge exhibits no changes in the Vickers hardness along the direction of the centrifugal force.

Figure 2 shows the values of the Young's modulus for all ingots measured upon heating and cooling in the temperature ranges from room temperature to 525°C (for Al–12.7 at. % Si), 315°C (Al–29.7 at. % Ge), and 250°C (Al–10 at. % Si–10 at. % Ge).

The Young's modulus of the Al–Si sample quenched from the temperature of the levitated melt is seen to increase by 3% after heating and cooling during measurement (Fig. 2, curve *1*). A sample cut from an ingot solidified at an average cooling rate of about 10^{-2} K/s has no temperature hysteresis of the Young's modulus

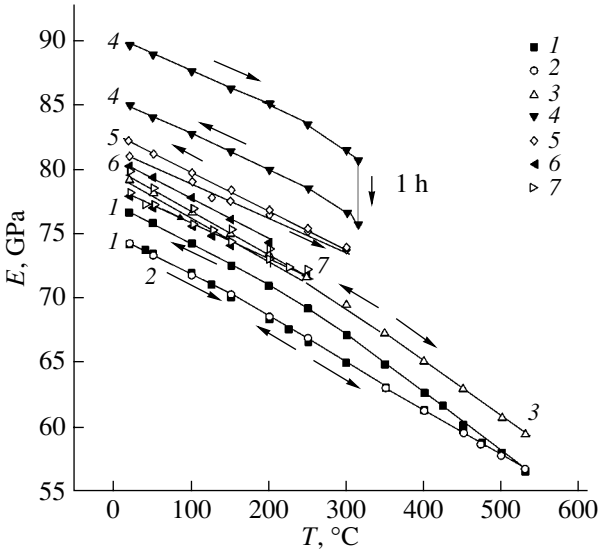

Fig. 2. Temperature dependences of the Young's modulus for (*1*–*3*) Al–12.7 at. % Si, (*4*, *5*) Al–29.7 at. % Ge, and (*6*, *7*) Al–10 at. % Si–10 at. % Ge alloys produced by (*1*, *4*, *6*) quenching at $v = 10^4$ K/s, (*2*) solidification at $v = 10^{-2}$ K/s, and (*3*, *5*, *7*) solidification at $v = 10^{-2}$ K/s in a centrifuge at an acceleration of 7g.

(Fig. 2, curve *2*). The $E(T)$ curve for a sample cut from an ingot solidified at an average cooling rate of about 10^{-2} K/s during centrifugation (Fig. 2, curve *3*) is similar to that for an ingot solidified in the absence of a centrifugal force; however, the absolute value of the Young's modulus is 7% higher.

For quenched Al–Ge samples, the Young's modulus decreases faster at temperatures above 200°C (Fig. 2, curve *4*), which is caused by a time variation in the Young's modulus. At 315°C, the modulus decreases by 7% in 1 h, and its decreased value remains unchanged upon cooling to room temperature. After this annealing, the Young's modulus remains constant in time as the temperature increases to 315°C. It should be noted that the change in the modulus, which is calculated from the measured resonance frequency of a sample, is accompanied by a 3.8% increase in density and a 1.4% decrease in the sample length. Therefore, when calculating the Young's modulus from the measured resonance frequency of a sample, we introduced a correction for the changes in ρ and Δl induced by structural transformations. A sample cut from an Al–Ge ingot solidified under centrifugation conditions has the same character of the temperature hysteresis of the Young's modulus as in the case of the alloy with silicon. The Young's modulus of a sample cut from an ingot solidified at an average cooling rate of about 10^{-2} K/s under a centrifugal acceleration of 7g increases by 1% after heating to 310°C and subsequent cooling to room temperature. To determine the cause of the irreversible changes in the modulus at about 315°C, we analyzed polished sections of the Al–Si sample before and after heating. Before measurements of the temperature dependence, the sample had a fine-grained eutectic structure with dendrites consisting of oval aluminum grains 2–4 μm in size. After heating of the sample to 315°C, these aluminum dendrites dissolve.

For Al–10 at. % Si–10 at. % Ge samples, the Young's modulus lies between the values characteristic of the Al–Si and Al–Ge samples. The $E(T)$ dependence of samples quenched at a cooling rate of about 10^4 K/s (Fig. 2, curve *6*) differs only slightly from the dependence obtained for samples solidified under centrifugation (Fig. 2, curve *7*).

The strain amplitude dependences of the decrement $\delta(\varepsilon)$ and Young's modulus $E(\varepsilon)$ of Al–12.7 at. % Si samples produced through solidification at a cooling rate of 10^{-2} K/s in the absence of a centrifugal force and at an acceleration of $7g$ are shown in Fig. 3. The absolute value of the Young's modulus of the sample solidified under centrifugation is seen to be 11% higher. The character of the amplitude dependence of E and δ for this sample changes only slightly as compared to that for the sample cut from an ingot solidified in the absence of centrifugal acceleration. The data from Fig. 3 can be used to find the amplitude of vibration stresses $\sigma = E\varepsilon$ and the inelastic vibration strain $\varepsilon_{in} \approx \varepsilon(\Delta E/E)_h$, where ΔE is the difference between E at a given total vibrational strain ε and the amplitude-independent component of the Young's modulus. The $\sigma(\varepsilon_{in})$ dependence, i.e., the nonlinear plastic microstrain of a sample in stress–strain coordinates, is shown in Fig. 4. The level of stresses required to reach a given plastic microstrain is seen to increase in the sample solidified under centrifugation.

Figure 5 shows the dependence of the load applied to a sample on the sample bending deflection measured at a constant strain rate (0.5 μm/s) for similarly shaped samples solidified under centrifugation or without centrifugation. It is seen that the level of stresses required to reach the same strain during quasi-static deformation for the sample solidified under centrifugation is higher than for the sample solidified in the absence of centrifugal acceleration.

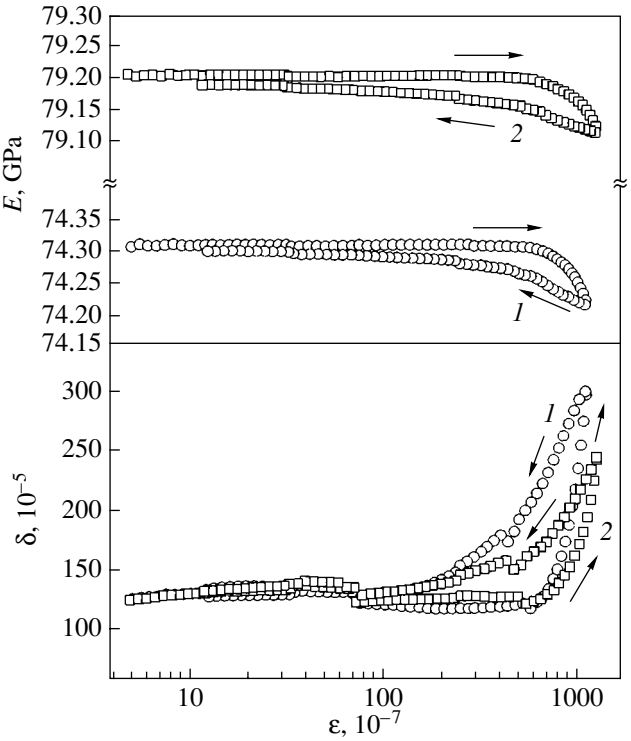

Fig. 3. Strain amplitude dependences of the Young's modulus and the decrement for an Al–12.7 at. % Si alloy produced at an average cooling rate of 10^{-2} K/s by (*1*) directional solidification and (*2*) remelting in a centrifuge at an acceleration of $7g$.

4. DISCUSSION OF THE RESULTS

The different structures of the samples shown in Fig. 1 reflect the procedures used to prepare them. For all alloys, rapid cooling of a levitated melt at an average rate of about 10^4 K/s results in the formation of a fine-grained structure. For the Al–Si alloy (Fig. 1a), the size of silicon grains in the eutectic (the β solid solution of aluminum in silicon) is less than 0.3 μm. Polished sections of the quenched Al–Ge and Al–Si–Ge alloys contain a fine eutectic and aluminum (white) dendrites (Figs. 1e, 1i).

When the alloys are solidified in the centrifuge furnace with cooling at an average rate of about 10^{-2} K/s in the absence of centrifugal acceleration, an anomalous eutectic structure forms. The size of Si–Ge needles in the ternary system is much larger than the size of silicon or germanium needles in the binary systems. Due to centrifugation, the structures that form at the bottom of an ingot (which is farther from the centrifuge axis) and those that form at the top of the ingot are different. In the Al–Si alloy, primary aluminum dendrites (bright regions) form at the bottom of the ingot. Silicon needles that enter into the eutectic Al–Si structure are large at the top of the ingot. In the Al–Ge and Al–Si–Ge alloys, on the contrary, the germanium content is higher at the bottom of an ingot and the amount of aluminum precipitates is higher at the top of the ingot.

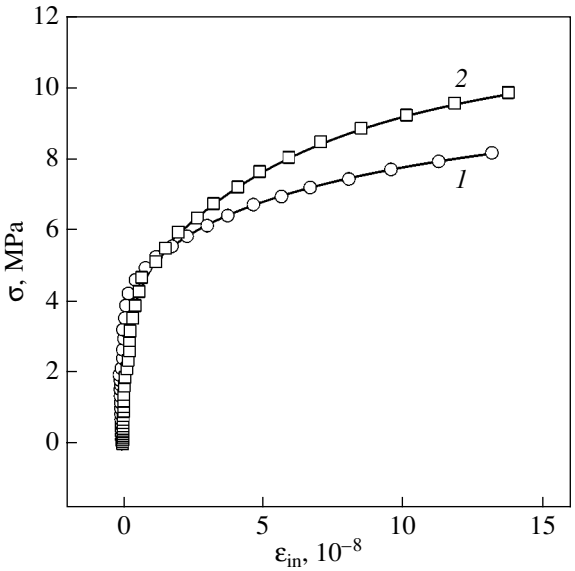

Fig. 4. Dependence of the stress on inelastic strain for samples produced (*1*) without and (*2*) under centrifugation.

The lengthwise inhomogeneity of an Al–Si ingot solidified in a centrifugal force field is likely due to the

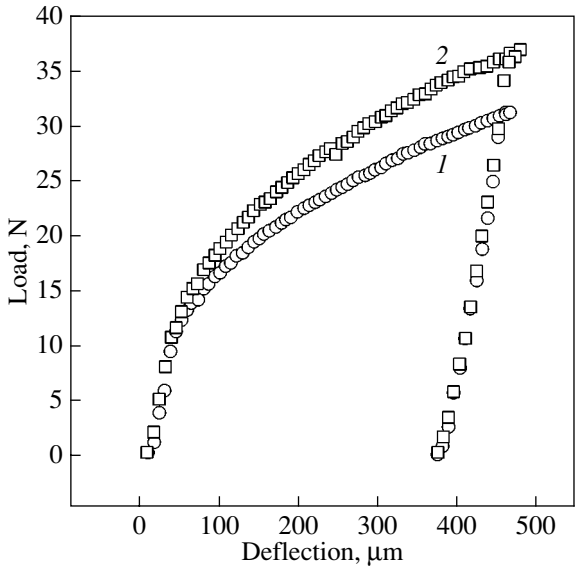

Fig. 5. Dependence of the load on the bending deflection due to three-point bending at a constant strain rate of Al–12.7 at. % Si alloy samples produced (*1*) without and (*2*) under centrifugation.

fact that the solidification centers of eutectic silicon and the silicon clusters that provide for eutectic-silicon growth during solidification have lower densities as compared to the liquid-phase density. However, solidification centers and clusters of aluminum have higher densities than the disperse phase. This results in a lower silicon concentration in the eutectic and in a rapid growth of primary aluminum crystallites at the bottom of an ingot. The authors of [4] used sedimentation analysis and revealed that, at a centrifugal acceleration of 600*g*, silumin melts were microinhomogeneous. They assumed that, at temperatures of up to 1100°C, the silumin melts contained silicon-rich groups and that the specific weight of the colonies was higher than that of the disperse medium. According to our observations, the density of silicon solidification centers that appear and grow during solidification is lower than the aluminum density. It is known [4] that, at 700°C, the silicon density is 2.30 g/cm^3 and the aluminum density is 2.40 g/cm^3. Therefore, the alloy structure is controlled by cluster structures at the solidification temperature rather than at a high temperature. Under these conditions, silicon atoms form clusters via directed covalent bonding forces.

In the case of the Al–Ge alloy, the ratio of the densities is reversed. The aluminum density in the solid state at 20°C and the liquid state at 659°C is 2.7 and 2.382 g/cm^3, respectively. For this reason, the silicon or germanium content in the eutectic changes under the action of a centrifugal force and primary aluminum crystals form at the bottom of an Al–Si ingot and at the top of an Al–Ge ingot. In the ternary system, an intermediate situation takes place; nevertheless, its structure is closer to the Al–Ge alloy structure, since, at the same silicon and germanium concentrations in the alloy (10 at. %), the difference in density between the liquid and solid phases of germanium is significantly higher than that of silicon.

The composition inhomogeneity induced by melt centrifugation is supported by hardness measurements. Table 2 shows that the hardness of the top portion of the Al–Si samples is higher than that of the bottom portion and that the reverse is true for the Al–Ge samples.

The Young's modulus of the Al–12.7 at. % Si alloy produced by rapid cooling of a levitated melt increases by 3% after heating to 500°C followed by cooling. When the temperature is repeatedly increased in this range, $E(T)$ remains unchanged. This hysteresis of the modulus can be explained by artificial aging of the sample during measurements at elevated temperatures. Aging of the alloy can cause silicon-rich zones, where directed covalent bonds can operate. The temperature dependence of the Young's modulus of the sample produced by directional solidification at an average cooling rate of about 10^{-2} K/s coincides with the forward run of the $E(T)$ dependence for the quenched sample and has no hysteresis. The Young's modulus of the same alloy solidified during centrifugation at an acceleration of 7*g* and the same average cooling rate is 7% higher and also has no hysteresis.

As follows from Fig. 3, the amplitude-dependent portions of internal friction, as well as the amplitude-dependent modulus defects, are approximately the same for the samples produced without centrifugal acceleration and at an acceleration of 7*g*. These samples differ only in terms of the Young's modulus. According to modern concepts [7, 8], the amplitude-dependent portions of the decrement and of the modulus defect are determined by the inelastic dislocation contribution to the vibration strain; this contribution increases with the dislocation density. Therefore, the higher modulus of the sample solidified under centrifugation is related to a change in the formation of the alloy structure rather than to a change in the dislocation structure. The higher stiffness of the alloy solidified under centrifugation also manifests itself in the increased level of stresses required to reach a given strain for both microplastic (Fig. 4) and macroplastic (Fig. 5) deformation of the material.

However, the differences in the elastic modulus and the micro- and macroplasticity between the samples produced in the absence and in the presence of a centrifugal force have the same order of magnitude as the changes induced by decomposition processes during aging and by recovery phenomena. Therefore, to reveal the effect of centrifugation on the mechanical properties of the alloy, additional studies need to be performed.

In the case of the Al–Ge alloy, heating to 315°C of the sample produced by rapid cooling of a levitated melt leads to a decrease in the elastic modulus. This

behavior can be explained by recovery phenomena. Micrographs of the structure of the Al–Ge sample produced by quenching followed by aging for 3 months show dendrites of the α solid solution, which formed during the decomposition of the quenched sample containing a supersaturated solid solution. Heating to 315°C results in structural homogenization due to the dissolution of a certain amount of germanium in the solid solution, which causes a decrease in the germanium content with covalent bonds and a decrease in the Young's modulus. When germanium atoms pass to the α solid solution, the density of the alloy should decrease, which is confirmed by the increased alloy density after heating (Table 1).

In the Al–Ge alloy samples produced by solidification under centrifugation at a low rate (10^{-2} K/s), the supersaturation of the α solid solution by germanium is low. Therefore, decomposition in these samples occurs upon heating to 300°C during measurements of the $E(T)$ dependence and causes the formation of zones enriched in germanium atoms that are bound by covalent bonds. This process manifests itself in an increase in the Young's modulus at room temperature after measurement of the temperature dependence. It should be noted that this increase is accompanied by a 3.6% increase in the sample density and a decrease in the sample length, which can be caused by vacancy kinetics.

For the ternary Al–Si–Ge alloy, the thermal hysteresis of the Young's modulus is similar to that detected for the Al–Si alloy. In both cases (for the Al–Ge and Al–Si–Ge alloys), the values of the Young's modulus for the samples solidified under centrifugation are lower than those for the samples produced by quenching of levitated melts, despite the fact that the samples were aged at elevated temperatures.

The higher values of the Young's modulus of the samples cut from the middle part of Al–Si ingots and the lower values of the Young's modulus of the Al–Ge samples solidified during centrifugation can be explained by changes in the silicon and germanium contents caused by centrifugation in the samples as compared to these contents in the samples solidified without centrifugation. During the solidification of the Al–Si alloy under centrifugation, the middle part of the ingot was enriched in silicon due to the displacement of the solidification centers of the α solid solution of silicon in aluminum toward the bottom portion of the ingot, with silicon sedimentation being insignificant. The Al–Ge alloy samples cut from the middle part of an ingot had a lower Ge content as compared to that in the initial state because of the sedimentation of its solidification centers and clusters.

5. CONCLUSIONS

We have established an insignificant decrease in the silicon content in the Al–12.7 at. % Si alloy, as well as an increase in the germanium content and in the amount of the germanium–silicon solid solution in the Al–29.7 at. % Ge and Al–10 at. % Si–10 at. % Ge alloys, in the direction of a $7g$ centrifugal acceleration during solidification under centrifugation. Centrifugation also increases the concentration of primary crystals of the α solid solution in the Al–Si alloy and decreases this concentration in the Al–Ge and Al–Ge–Si alloys in the direction of the $7g$ centrifugal acceleration. This finding is explained by the fact that the densities of solidification centers and crystal-forming clusters differ from the liquid-phase density during solidification. The changes in the mechanical properties of the samples solidified under centrifugation can be related to the sedimentation-induced changes in the composition of the middle part of the solidifying ingots from which the samples were cut.

The results of this work indicate that centrifugation of aluminum alloys with silicon and germanium during their solidification can be applied to modify their structures and to control their mechanical properties.

ACKNOWLEDGMENTS

The authors are grateful to R. Ramanaphan for supplying the silumin ingots.

This work was supported by the US Civil Research and Development Foundation, project no. RE2-2347-ST-02.

REFERENCES

1. *Processing by Centrifugation*, Ed. by L. L. Regel and W. R. Wilcox (Kluwer Academic/Plenum, New York, 2001).
2. J. F. Loffler, S. Bossuyt, A. Peker, and W. L. Johnson, Appl. Phys. Lett. **81**, 4159 (2002).
3. Y. Oya-Seimiya, T. Shinoda, Y. Fukui, N. Yamaguchi, T. Saitou, T. Yamada, and K. Minegishi, J. Jpn. Inst. Met. **64**, 315 (2000).
4. V. A. Izmaĭlov and A. A. Vertman, Izv. Akad. Nauk SSSR, Met. **6**, 217 (1971).
5. L. F. Mondolfo, *Aluminum Alloys: Structure and Properties* (Butterworths, London, 1979; Metallurgiya, Moscow, 1979).
6. N. N. Buĭnov and R. R. Zakharova, *Decay of Supersaturated Metallic Solid Solutions* (Metallurgiya, Moscow, 1964) [in Russian].
7. G. Gremaud and S. Kustov, Phys. Rev. B **60**, 9353 (1999).
8. S. P. Nikanorov, Solid State Phenom. **89**, 191 (2003).

Translated by K. Shakhlevich

Physics of the Solid State, Vol. 47, No. 5, 2005, pp. 920–926. Translated from Fizika Tverdogo Tela, Vol. 47, No. 5, 2005, pp. 893–898.

Thermal and Fluctuation-Induced Deformations of Chemical Bonds in Surface and Boundary Layers of Polymers

V. I. Vettegren, I. I. Novak, and V. B. Kulik

Ioffe Physicotechnical Institute, Russian Academy of Sciences, Politekhnicheskaya ul. 26, St. Petersburg, 194021 Russia

e-mail: Victor.Vettegren@mail.ioffe.ru

Abstract—The deformation of chemical bonds in polymer molecules of surface layers of samples, boundary layers between supramolecular aggregates, and boundary layers between polymers and solids in polymer composites is investigated using IR and Raman spectroscopy. It is found that the chemical bonds are elongated on a free surface and in boundary layers between supramolecular aggregates. By contrast, the chemical bonds are contracted in boundary layers between polymers and solids. The concentration and the strain of excited chemical bonds (strained to approximately a theoretical ultimate elongation) are increased on the free surface and in the boundary layers between supramolecular aggregates, whereas the concentration and the strain of excited chemical bonds in the boundary layers between polymers and solids are decreased. These effects are explained by the changes in the atomic vibrations in the surface and boundary layers. © *2005 Pleiades Publishing, Inc.*

1. INTRODUCTION

Since the late 1920s, it has been known that the surface plays a crucial role in the fracture mechanism. Ioffe *et al.* [1] established that the dissolution of a surface layer of rock salt in water leads to an increase in the strength of the salt sample by two orders of magnitude. More recently, Aleksandrov and Zhurkov [2] managed to strip a surface layer of glass and quartz fibers by etching and, thus, to increase their strength to ~20 GPa.

Earlier [1–3], the decisive role of the surface in the fracture mechanism was explained by the fact that the surface, as a rule, contains a large number of microcracks formed under external mechanical forces. However, with the advent and development of the kinetic concept of strength, it became possible to put forward another hypothesis regarding the decisive role played by the surface in the fracture mechanism. According to this hypothesis, the probability of destructive fluctuations arising in a material can increase in surface layers due to a change in the spectrum of atomic vibrations [4]. It is common knowledge that the lifetime is determined by the probability of destructive fluctuations arising in the material. Therefore, an increase in this probability should result in a change in the strength and the lifetime of solids. In the late 1970s, Zhurkov initiated studies aimed at elucidating the origin of this phenomenon.

In this paper, we summarize the results of investigations concerned with clarifying the role played by the surface in the fracture of polymer materials. For this purpose, we determined the strain of chemical bonds in the excited and ground states at the surface, in the bulk, and in boundary layers of the polymers and polymer composites. The necessary data on the strain of chemical bonds were obtained from the shift and shape of the regularity bands in the IR and Raman spectra of polymers and composites. These bands correspond to vibrations of regularly arranged segments (a few nanometers long) of polymer molecules [5].

2. CHANGES IN THE FREQUENCY AND SHAPE OF THE REGULARITY BANDS IN THE IR AND RAMAN SPECTRA OF SURFACE AND BOUNDARY LAYERS IN POLYMERS AND COMPOSITES

The IR transmission and attenuated total reflection (ATR) spectra of a 40-μm-thick polyamide 6 film are shown in Fig. 1. The IR transmission spectrum is associated primarily with the bulk of the film, whereas the ATR spectrum is attributed to a surface layer ~1 μm thick [6, 7]. It can be seen from Fig. 1 that, in the ATR spectrum of the surface layer, the main maximum of the band at a frequency of 930 cm^{-1} is shifted to the low-frequency range by ~1 cm^{-1} and its long-wavelength wing is more asymmetric. The long-wavelength wing of this band exhibits an additional maximum. In the ATR spectrum, this additional maximum is characterized by a higher intensity and a larger shift as compared to those in the IR transmission spectrum.

Figure 2 shows the IR transmission spectra of a 16-μm-thick polyamide 6 film and a sample composed of 16 films with a thickness of 1 μm each. It is seen from Fig. 2 that, in the spectrum of the composite sample, the main maximum of the band at a frequency of 930 cm^{-1} is shifted to the low-frequency range and is

1063-7834/05/4705-0920$26.00 © 2005 Pleiades Publishing, Inc.

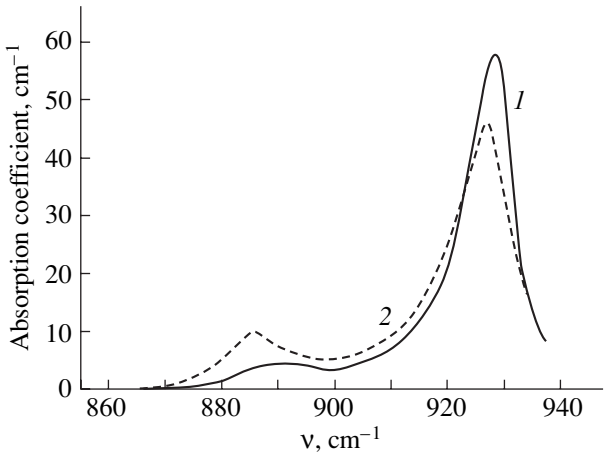

Fig. 1. (*1*) IR transmission and (*2*) attenuated total reflection spectra of a 40-μm-thick polyamide 6 film.

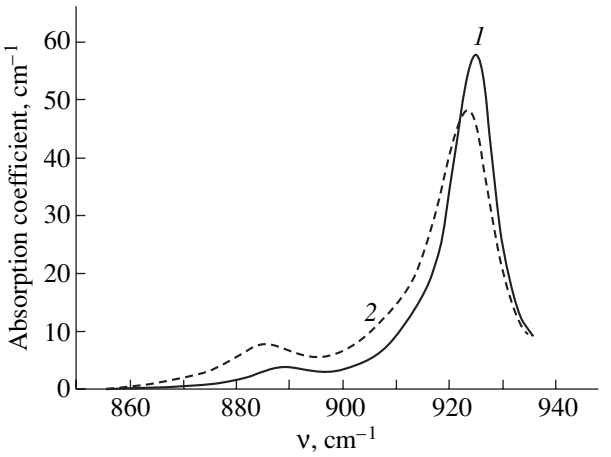

Fig. 2. (*1*) IR transmission spectra of a 16-μm-thick polyamide 6 monolithic sample and (*2*) a sample composed of 16 films with a thickness of 1 μm each.

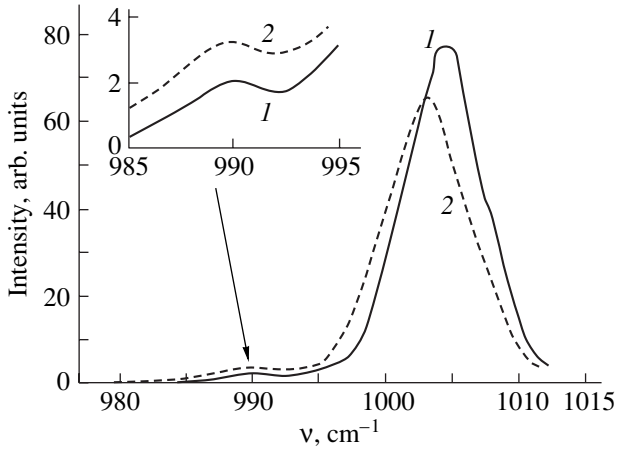

Fig. 3. Raman spectra of (*1*) a poly(styrene) block sample and (*2*) a poly(styrene) powder. The block sample is prepared from the powder.

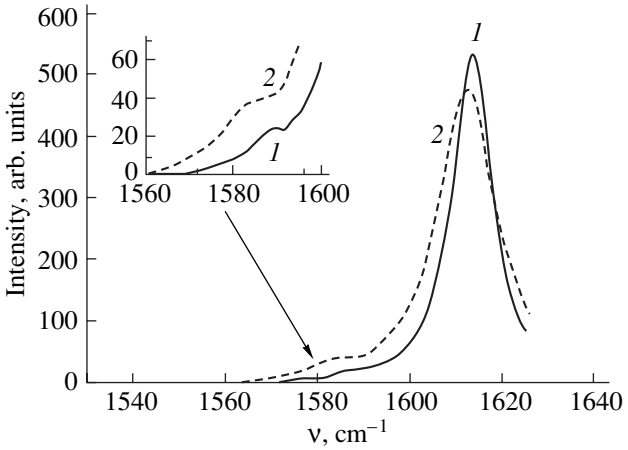

Fig. 4. Raman spectra measured for poly(ethylene terephthalate) fibers under the following conditions: (*1*) a laser beam ~3 μm in diameter passes through the center of a fiber 100 μm in diameter, and (*2*) the same laser beam only slightly touches the fiber surface.

more asymmetric. Moreover, the intensity and the shift in the frequency of the additional maximum observed in the spectrum of the composite sample are greater than those in the spectrum of the monolithic sample.

The Raman spectra of a poly(styrene) powder and a poly(styrene) block sample prepared from this powder are shown in Fig. 3. In the Raman spectrum of the powder, the main maximum of the band at a frequency of 1002 cm^{-1} is shifted to the low-frequency range by ~2 cm^{-1} and the additional maximum observed in the long-wavelength wing of this band is characterized by a higher intensity and a larger shift.

Figure 4 depicts the Raman spectra measured for poly(ethylene terephthalate) fibers under the conditions where a laser beam ~3 μm in diameter either passed through the center of a fiber 100 μm in diameter or only slightly touched the fiber surface. In the Raman spectrum of the surface layer of the fiber, the main maximum of the band at a frequency of 1614 cm^{-1} is shifted to the long-wavelength range by ~1 cm^{-1}. It can also be seen from Fig. 4 that, in the spectrum of the surface layer, the intensity and the shift in the frequency of the additional maximum observed in the long-wavelength wing of this band are greater than those in the spectrum measured in the bulk of the fiber.

Similar effects, namely, a shift in the frequency of the main maximum toward the low-frequency range, an increase in the asymmetry of the main maximum, and

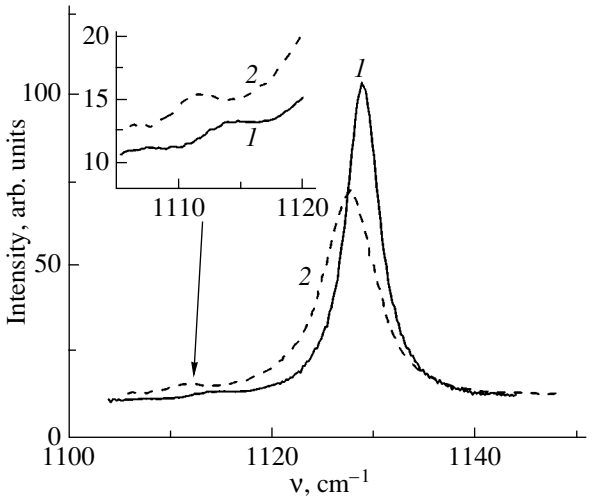

Fig. 5. Raman spectra of poly(ethylene) bulk samples containing crystallites (*1*) ~15 and (*2*) ~100 nm in length along the **c** axis.

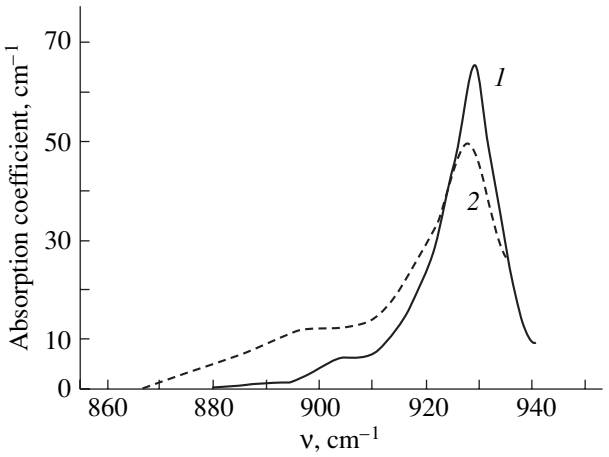

Fig. 6. Bands at 930 cm^{-1} in the IR spectra of polyamide 6 samples: (*1*) the initial sample and (*2*) the sample prepared by rapid quenching from a melt into acetone at a temperature of 178 K.

an increase in the intensity and shift of the additional maximum in the long-wavelength wing of the regularity bands in the IR and Raman spectra, were observed for a large number of polymers, including poly(ethylene), poly(propylene), poly(pyromellitimide), poly(vinyl alcohol), poly(amidobenzylimidazole), polycarbonate, etc. [6, 7].

Apart from the surface, the inner boundaries between supramolecular aggregates also have an effect on the position of the main maximum and the shape of the regularity bands, as well as on the shift and intensity of the additional maximum [8, 9]. As an illustration, let us consider the band at a frequency of 1130 cm^{-1} in the Raman spectra measured in the bulk of the poly(ethylene) sample containing crystallites whose length along the **c** axis is equal to ~15 and ~100 nm (Fig. 5). It can be seen from this figure that the frequency at the maximum of the band for the sample with crystallites ~15 nm long is approximately 1.5 cm^{-1} less than that for the sample with crystallites ~100 nm long. Moreover, the additional maximum observed in the long-wavelength wing of this band for the sample with crystallites ~15 nm long is characterized by a higher intensity and a larger shift as compared to those for the sample with crystallites ~100 nm long.

This effect is enhanced in the surface layer of the polymer. As an illustration, we consider the band at a frequency of 930 cm^{-1} in the IR spectrum of polyamide 6 (Fig. 6). It can be seen from Fig. 6 that, after rapid quenching from a melt into acetone at a temperature of 178 K (when small-sized crystallites are formed in the sample), the shift and intensity of the additional maximum in the spectrum of the surface layer increase.

Thus, it is established that the main maximum of the regularity bands in the spectra of surface and boundary layers between supramolecular aggregates is shifted to the low-frequency range. Moreover, the additional maxima observed in the long-wavelength wings of these bands are characterized by higher intensities.

By contrast, the main maximum of the regularity bands in the spectra of boundary layers in polymer composites is shifted to the high-frequency range [10]. For example, the main maximum of the regularity band at a frequency of 930 cm^{-1} in the IR spectrum of a 20-μm-thick polyamide 66/6 film on the surface of steel 45 is shifted by 1–5 cm^{-1} toward the high-frequency range (Fig. 7).

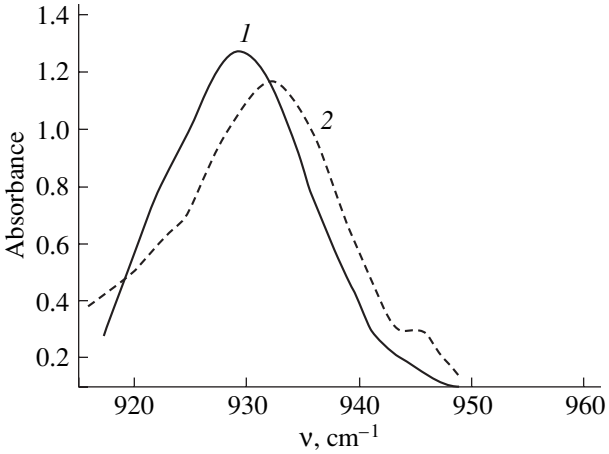

Fig. 7. IR spectra of (*1*) a polyamide 66/6 film and (*2*) a polyamide 66/6 coating prepared from a melt on the surface of steel 45.

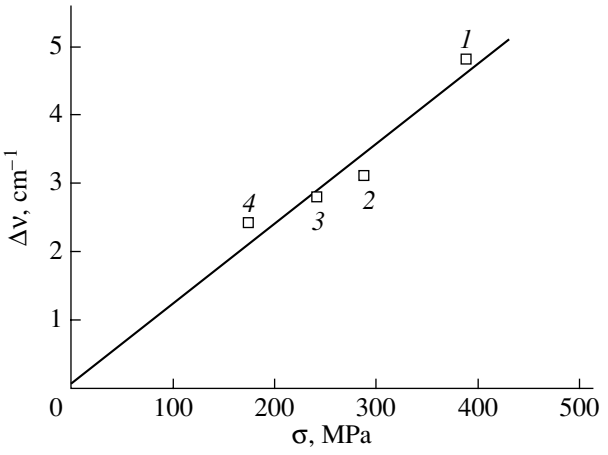

Fig. 8. Shift of the maximum of the band at 930 cm^{-1} for polyamide 66/6 coatings prepared from a melt on the surfaces of different metals as a function of the adhesion strength: (*1*) steel 45, (*2*) alloy AL-9, (*3*) bronze BrAZh9-4, and (*4*) copper.

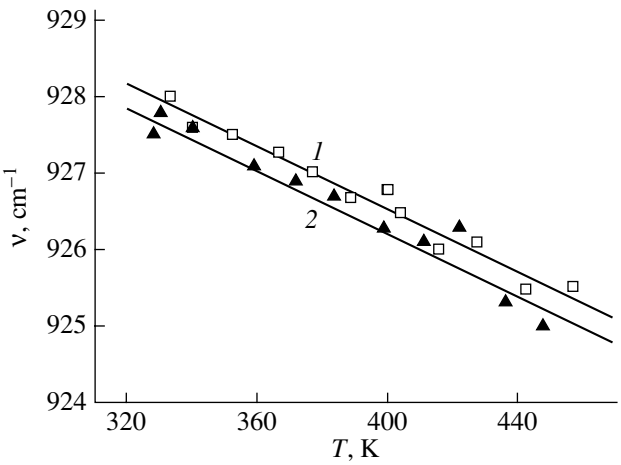

Fig. 9. Temperature dependences of the frequency at the maximum of the band at 930 cm^{-1} in the IR spectra of polyamide 6 films with thicknesses of (*1*) 50 and (*2*) 1 μm.

For convenience of the analysis of the results obtained, the shift and the increase in the asymmetry of the main maximum of the regularity bands and the change in the position and intensity of the additional maximum in the long-wavelength wing of these bands will be considered individually.

3. DEFORMATION OF CHEMICAL BONDS IN SURFACE AND BOUNDARY LAYERS OF POLYMERS AND COMPOSITES

The shift in the frequency of interatomic vibrations is associated with the deformation of the bond angles and valence bonds in polymer molecules [11]. The shift in the frequency of the *i*th interatomic vibration $\Delta\nu_i$ and the relative change ε in the length of regularly arranged segments of the polymer molecules are related by the expression

$$\Delta\nu \equiv \nu(\varepsilon) - \nu(0) = -G_i\nu(0)\varepsilon, \qquad (1)$$

where $\nu(\varepsilon)$ and $\nu(0)$ are the vibrational frequencies of the strained and unstrained segments of the polymer molecule, respectively, and G_i is the Grüneisen parameter.

For all the bands studied in this work, the Grüneisen parameter is greater than zero. Hence, the decrease in the frequency of the main maximum of the bands in the spectra of surface layers and boundary layers between supramolecular aggregates indicates that the regularly arranged segments of the polymer molecules in these layers are elongated. The asymmetry of the bands in the low-frequency range suggests that these molecular segments are strained to various degrees [12–16].

The mean strain $\langle\varepsilon\rangle$ of the molecular segments can be estimated by measuring the shift $\Delta\nu$ of the barycenter of the regularity bands. The measurements performed demonstrated that the shift of the barycenter of the regularity bands in the IR and Raman spectra of surface and boundary layers of the polymers is approximately equal to 1–5 cm^{-1}. By substituting these values into relationship (1), we found that the corresponding mean strains $\langle\varepsilon\rangle$ are approximately equal to 0.1–0.2%.

As was noted above, the main maximum of the regularity bands in the spectra of boundary layers of polymers with metals is shifted to the high-frequency range. This implies that interatomic bonds in these layers are contracted. The contraction varies from ~0.02 to 0.20% depending on the film thickness and the rate of cooling of the film prepared from the melt. Moreover, the contraction increases in proportion to the strength of the adhesive interaction (Fig. 8).

In the temperature range 200–500 K, the maxima of the regularity bands in the spectra of surface and boundary layers are equally shifted with respect to their position in the spectra measured in the bulk of the sample. Consequently, the strain of regularly arranged segments of the polymer molecules due to the effect exerted by the boundaries is independent of temperature (Fig. 9).

As the distance l to the surface (or to the interface) increases, the strain of chemical bonds decreases following the exponential law (Fig. 10):

$$\varepsilon(l) = \varepsilon_0\exp\left(-\frac{l}{l_0}\right),$$

where ε_0 is the strain at the surface (or at the interface). The strain of chemical bonds is observed at large distances up to 100 μm. Such long-range interaction cannot be associated with the difference between the interatomic interaction forces at the interface, because this effect manifests itself over distances of several nanometers.

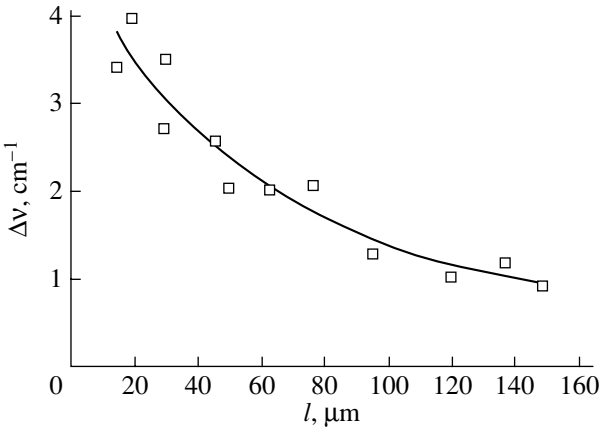

Fig. 10. Shift of the maximum of the band at 930 cm^{-1} for a polyamide 66/6 coating prepared from a melt as a function of the distance to the interface with steel 45.

4. EXCITED CHEMICAL BONDS IN SURFACE AND BOUNDARY LAYERS OF POLYMERS

In [17–21], the additional maximum revealed in the long-wavelength wing of the regularity bands was assigned to excited chemical bonds, i.e., to the molecular segments stretched to a strain ε_d that is one order of magnitude greater than the strain of the chemical bonds due to thermal expansion. The mean strain $\langle\varepsilon_d\rangle$ of excited chemical bonds can be calculated from the formula

$$\langle\varepsilon_d\rangle = -\frac{\langle\Delta\nu_d\rangle}{G},$$

where $\langle\Delta\nu_d\rangle$ is the shift in the frequency of the additional maximum. According to the calculations, the mean strain of excited chemical bonds is close to the theoretical ultimate elongation ε_*.

The relative concentration of excited chemical bonds can be determined from the relationship [17–21]

$$n_d = \frac{I_d}{I_m},$$

Strains $\langle\varepsilon_d\rangle$ (%) and concentrations c_d (%) of excited chemical bonds in the bulk and in a 1-μm-thick surface layer of polymers

Polymer	Surface layer		Bulk	
	$\langle\varepsilon_d\rangle$	c_d	$\langle\varepsilon_d\rangle$	c_d
Poly(ethylene)	6	4	4	2
Poly(propylene)	6	4	4	2
Poly(ethylene terephthalate)	6	10	3	2
Poly(caproamide)	5.5	10	2	3
Poly(pyromellitimide)	5.3	10	4	6

where I_d and I_m are the intensities of the additional and main maxima, respectively. It turned out that the relative concentration of excited chemical bonds, as a rule, amounts to several percent of the concentration of regularly arranged molecular segments in the sample [17–21].

Investigations have revealed that the excited chemical bonds are formed as a result of thermal fluctuations [17–21]. The scission of a number of such bonds initiates the development of fracture of the polymer on the molecular level [4, 16, 22, 23]. It was found that the activation energy of formation of excited chemical bonds U_{0d} is equal to the activation energy of fracture U_0 ($U_{0d} \approx U_0$) and that the rate $\dot{n}$ of formation of these bonds determines the lifetime τ of the polymer [4, 19]: $\tau \approx 1/\dot{n}$. Therefore, the results of investigations into the excited chemical bonds in surface and boundary layers between supramolecular aggregates of the polymers allow us to directly verify the validity of the hypothesis that the decisive role played by these layers in the fracture is associated with the increase in the probability of destructive fluctuations arising in the material.

As was noted above, the additional maximum in the spectra of surface layers of the polymers is characterized by a larger shift and a higher intensity as compared to those in the spectra measured in the bulk of the polymer. This suggests that, in surface layers of the polymer, the elongation of excited chemical bonds is greater and their concentration is higher than those in the bulk of the polymer (see table). Therefore, the decisive role of the surface in the polymer fracture stems from the fact that the excited chemical bonds are formed primarily at the surface.

The rate of accumulation $\dot{n}$ of excited chemical bonds, their strain ε_d, the temperature T, and the time t elapsed after changing the temperature are related by the empirical expressions [18–21]

$$\dot{n} = n_0\exp\left(-\frac{U_{0d}}{k_B T}\right),$$

$$\frac{\varepsilon_d}{\varepsilon_*} = \frac{k_B T}{U_{0d}}\ln\frac{t}{\tau_0}.$$

Here, U_{0d} is the activation energy of excitation of the chemical bonds (it is equal to the activation energy of fracture U_0 : $U_{0d} = U_0$), $\tau_0 \approx 10^{-13}$ s, k_B is the Boltzmann constant, n_0 is an empirical constant, and $\varepsilon_* \approx 0.1$ is the ultimate elongation of the chemical bonds.

It follows from the above expressions that the increase in the concentration and in the strain of excited chemical bonds in surface layers of the polymer is caused by the decrease in the activation energy U_{0d} of the formation of these bonds. Since the approximate equality $U_{0d} \approx U_0$ is satisfied, the decisive role of the surface in the polymer fracture is associated with the

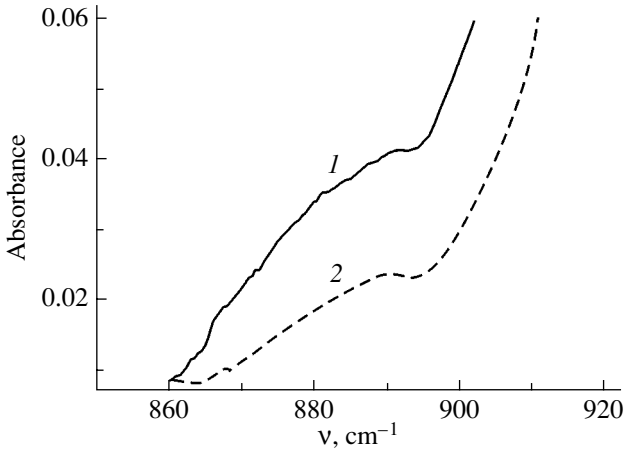

Fig. 11. Additional maxima in the long-wavelength wing of the band at 930 cm^{-1} in the IR spectra of the (*1*) dried polyamide 6 film and (*2*) polyamide 6 film wetted with water.

decrease in the activation energy of fluctuations responsible for the formation of excited chemical bonds.

It was of interest to elucidate how surfactants affect the excited segments of polymer molecules. It is known that water serves as a surface-active agent for hydrophilic polymers. Figure 11 shows the additional maxima in the long-wavelength wing of the band at a frequency of 930 cm^{-1} in the IR spectra of the dried polyamide 6 film and the polyamide 6 film wetted with water. It can be seen from this figure that moisture brings about a decrease in the shift and intensity of the additional maximum. The same effects are observed for other polymers in the presence of surface-active agents. In all cases, the presence of water and other surface-active agents results in a decrease in the concentration and strain of excited chemical bonds in surface layers of the polymers. This finding counts in favor of the assumption that surface-active agents decrease the activation energy of formation of excited chemical bonds.

5. MECHANISM OF THE INFLUENCE OF THE SURFACE AND INTERFACES ON THE STRAIN OF CHEMICAL BONDS

As is known, the spectrum of atomic vibrations changes at the surface and in boundary layers of solids; more precisely, there arise surface vibrations in addition to bulk vibrations [24]. These changes in the spectrum of atomic vibrations manifest themselves at distances as long as several hundreds of micrometers from the interfaces and can lead to variations in both the thermal expansion of chemical bonds and the probability of formation of excited chemical bonds. It seems likely that the decisive role played by the surface in the fracture of polymers is associated primarily with the transformation of the spectra of atomic vibrations.

6. CONCLUSIONS

Thus, the results obtained in this study demonstrated that chemical bonds in polymers are elongated on a free surface and in boundary layers between supramolecular aggregates. Moreover, these layers are characterized by an increased concentration of excited chemical bonds with large strains induced by fluctuations.

It was revealed that chemical bonds are contracted in boundary layers of polymer composites.

These effects were explained by the changes in the spectrum of atomic vibrations in the surface and boundary layers of polymers and polymer composites.

ACKNOWLEDGMENTS

This work was performed within the framework of the Russian federal program “Integration 2002,” project no. B0012.

REFERENCES

1. A. F. Ioffe, N. V. Kirpicheva, and M. A. Levitskaya, Zh. Russ. Fiz.–Khim. O-va **56**, 489 (1924).
2. A. P. Aleksandrov and S. N. Zhurkov, *Phenomenon of Brittle Fracture* (GTTI, Leningrad, 1993) [in Russian].
3. A. A. Griffith, Philos. Trans. R. Soc. London, Ser. A **227**, 763 (1920).
4. V. A. Petrov, A. Ya. Bashkarev, and V. I. Vettegren, *Physical Principles of Lifetime Prediction for Structural Materials* (Politekhnika, St. Petersburg, 1993) [in Russian].
5. G. Zerbi, F. Ciampelli, and V. Zamboni, J. Polym. Sci., Part C **7**, 141 (1964).
6. V. I. Vettegren and A. E. Tshmel, Eur. Polym. J. **12** (12), 853 (1976).
7. A. E. Tshmel, V. I. Vettegren, and V. M. Zolotarev, J. Macromol. Sci., Phys. B **21** (2), 243 (1982).
8. V. I. Vettegren, L. S. Titenkov, and S. V. Bronnikov, J. Therm. Anal. **38**, 1031 (1992).
9. V. I. Vettegren, V. A. Marikhin, V. B. Kulik, and L. S. Titenkov, Fiz. Tverd. Tela (St. Petersburg) **44** (12), 2234 (2002) [Phys. Solid State **44**, 2341 (2002)].
10. V. I. Vettegren, A. Ya. Bashkarev, and A. A. Lebedev, Mekh. Polim., No. 6, 978 (1990).
11. A. I. Gubanov and V. A. Kosobukin, Mekh. Polim., No. 4, 579 (1971).
12. S. N. Zhurkov, V. I. Vettegren, V. E. Korsukov, and I. I. Novak, Fiz. Tverd. Tela (Leningrad) **11** (2), 290 (1969) [Sov. Phys. Solid State **11**, 233 (1969)].
13. V. I. Vettegren and I. I. Novak, Fiz. Tverd. Tela (Leningrad) **15** (5), 1417 (1973) [Sov. Phys. Solid State **15**, 957 (1973)].
14. V. I. Vettegren and I. I. Novak, J. Polym. Sci. **11** (11), 2135 (1973).
15. V. I. Vettegren and K. Yu. Fridlyand, Opt. Spektrosk. **38**, 521 (1975) [Opt. Spectrosc. **38**, 294 (1975)].

16. S. N. Zhurkov, V. I. Vettegren, I. I. Novak, and V. E. Korsukov, in *Proceedings of the Second International Conference on Fracture*, Ed. by E. E. Pratt (Chapman and Hall, London, 1969).

17. V. I. Vettegren and A. A. Kusov, Fiz. Tverd. Tela (Leningrad) **24** (6), 1598 (1982) [Sov. Phys. Solid State **24**, 914 (1982)].

18. V. I. Vettegren and R. R. Abdul'manov, Fiz. Tverd. Tela (Leningrad) **26** (11), 3266 (1984) [Sov. Phys. Solid State **26**, 1964 (1984)].

19. V. I. Vettegren, Fiz. Tverd. Tela (Leningrad) **28** (11), 3417 (1986) [Sov. Phys. Solid State **28**, 1922 (1986)].

20. V. I. Vettegren', A. D. Gabaraeva, and N. L. Zaalishvili, Vysokomol. Soedin., Ser. A **43** (6), 988 (2001).

21. S. V. Bronnilov, V. I. Vettegren, and S. Y. Frenkel, Adv. Polym. Sci. **125**, 103 (1990).

22. V. R. Regel, A. I. Slutsker, and É. E. Tomashevskiĭ, Usp. Fiz. Nauk **106**, 2 (1972) [Sov. Phys. Usp. **15**, 2 (1972)].

23. V. R. Regel, A. I. Slutsker, and É. E. Tomashevskiĭ, *Kinetic Nature of the Strength of Solids* (Nauka, Moscow, 1974) [in Russian].

24. B. M. Agranovich, Usp. Fiz. Nauk **115** (2), 199 (1975) [Sov. Phys. Usp. **18**, 99 (1975)].

Translated by O. Borovik-Romanova

Physics of the Solid State, Vol. 47, No. 5, 2005, pp. 927–933. Translated from Fizika Tverdogo Tela, Vol. 47, No. 5, 2005, pp. 899–905.

Middle Macroradicals and Their Influence on the Strength of Oriented Polymers

É. E. Tomashevskiĭ and N. G. Kvachadze

Ioffe Physicotechnical Institute, Russian Academy of Sciences, Politekhnicheskaya ul. 26, St. Petersburg, 194021 Russia

e-mail: engel.tomashevskii@mail.ioffe.ru

Abstract—The macroradicals formed through the detachment of hydrogen atoms in amorphous–crystalline polymers are studied using electron–nuclear double resonance (ENDOR) spectroscopy. The ^{1}H ENDOR spectra are analyzed, and the hyperfine interaction constants of the nearest neighbor and remote protons are measured. The conformational structure of radicals in poly(ethylene) (PE), poly(propylene) (PP), and poly(caproamide) (PCA) is determined. The ENDOR and EPR spectra of fibers subjected to tensile loading are recorded. It is revealed that torsional strain arises in the radicals with a nonplanar structure. The results of mechanical testing of irradiated oriented polymers demonstrate that the weakening of β bonds in the radicals has an effect on the macroscopic strength. © *2005 Pleiades Publishing, Inc.*

1. INTRODUCTION

The kinetics of mechanical fracture of polymers is substantially affected by middle macroradicals. Under mechanical actions, the scission of macromolecules in polymer materials leads to the formation of secondary macroradicals with a free valence in the middle of the chain. The formation of these radicals with a low activation energy of degradation (~30 kcal/mol) can promote the molecular degradation, endow this reaction with a chainlike nature, and give rise to submicroscopic discontinuities [1, 2].

In order to elucidate how the weakening of bonds in macroradicals affects the strength of polymers, oriented fibers with middle radicals produced at rather high concentrations under irradiation were experimentally studied at the laboratory headed by Academician S.N. Zhurkov (see, for example, [3–5]). The results obtained revealed the necessity of thoroughly investigating the conformational structure and the stressed state of macroradicals in polymers with different initial structures. For this purpose, we used electron–nuclear double resonance (ENDOR) spectroscopy with a high resolution. We developed an appropriate technique [6] and recorded and then analyzed the ENDOR spectra of irradiated samples of synthetic amorphous–crystalline polymers [7–13] and natural silk fibers [14].

2. ENDOR SPECTRA

The ENDOR spectra were measured on a laboratory ENDOR spectrometer operating in the *Q* band [6] in the radio frequency range 45–120 MHz at fixed tuning to a particular component of the hyperfine structure of the EPR spectrum at a saturating input power in the cavity. The equipment used made it possible to accomplish mechanical loading of oriented samples in the spectrometer cavity. Middle macroradicals were produced through the detachment of hydrogen atoms under exposure to x-ray irradiation. The irradiation doses did not exceed 20–50 kJ/kg.

High-density poly(ethylene) (PE), poly(propylene) (PP), and poly(caproamide) (PCA) were chosen as the objects of our investigation. Poly(ethylene) and poly(caproamide) macromolecules have a planar *trans* zigzag structure, whereas poly(propylene) macromolecules are characterized by a 3_1 helical structure. The detachment of hydrogen atoms in PE, PP, and PCA macromolecules leads to the formation of the following radicals [15, 16]:

$$-CH_2\dot{C}HCH_2-,\ -CH_2\dot{C}(CH_3)CH_2-,\ -CONH\dot{C}HCH_2-.$$

The ^{1}H ENDOR spectra of these middle radicals in oriented samples placed in a transverse magnetic field are shown in Fig. 1. The spectra exhibit a number of absorption bands shifted from free proton magnetic resonance (ν_0 = 54 MHz). These absorption bands are associated with the protons that occupy different positions with respect to the unpaired electron of the radical. The best resolution is observed for the ENDOR spectra recorded under the conditions where the *L* axis of the orientation of the sample is aligned with the magnetic field *H* of the spectrometer. Figures 2 and 3 depict fragments of the ENDOR spectra of the nearest neighbor (α, β) and remote (γ, δ) protons in middle radicals of the PE and PCA samples. A good resolution of the ENDOR spectra allowed us to determine the isotropic (*A*, *a*) and anisotropic (*B*) hyperfine interaction constants. The hyperfine interaction constants measured at $T \sim 100$ K are given in the table.

1063-7834/05/4705-0927$26.00 © 2005 Pleiades Publishing, Inc.

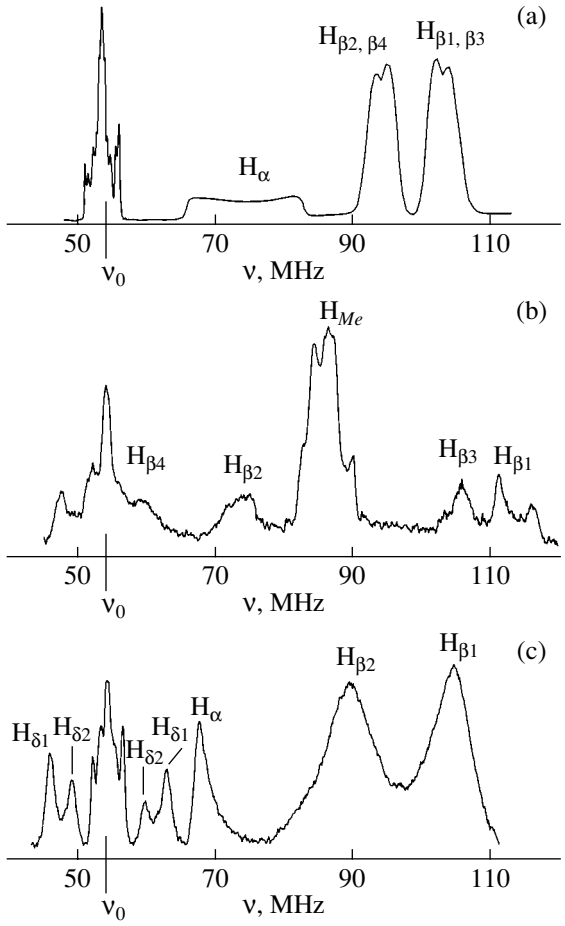

Fig. 1. ENDOR spectra of middle macroradicals in irradiated samples of (a) the uniaxially oriented poly(ethylene), (b) the uniaxially oriented poly(propylene), and (c) the biaxially oriented poly(caproamide). Measurement conditions: $L \perp H$, T = 170 K.

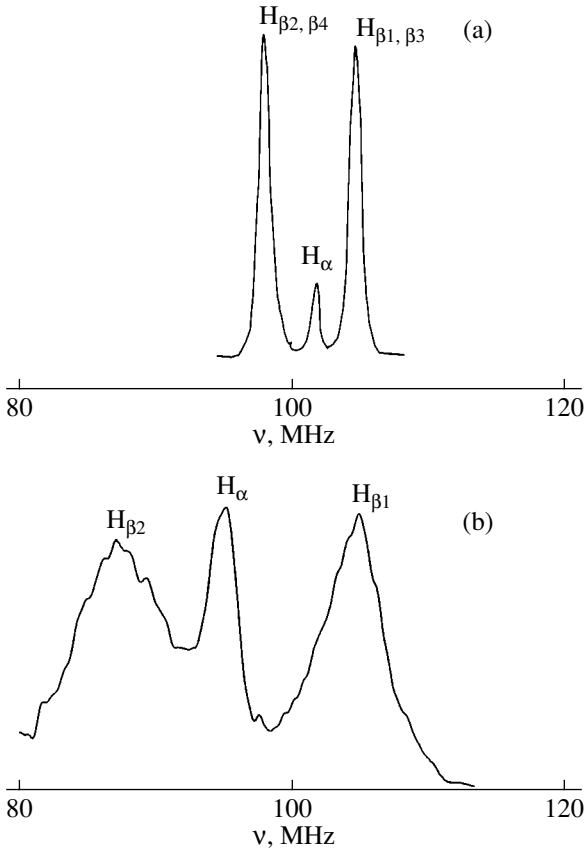

Fig. 2. ENDOR spectra of the nearest neighbor protons in radicals of (a) PE and (b) PCA samples. Measurement conditions: $L \parallel H$, T = 170 K.

3. STEREOCONFIGURATION OF MACRORADICALS

3.1. Orientation of the Radicals

The angular position of the $-\dot{C}_\alpha-$ radical center with respect to the axis of the orientation stretching was determined from the ENDOR spectra of α protons in the PE and PCA samples and from the ENDOR spectra of protons of the α-methyl groups in the PP sample. The orientation of the $-\dot{C}_\alpha H_\alpha-$ center in the PE and PCA samples is specified by the angle α_L between the stretching axis L of the polymer and the principal axis z of the anisotropic hyperfine interaction tensor of the α proton. The z axis is perpendicular to the C_α–H_α bond (the x axis) and to the 2p orbital of the unpaired electron (the y axis). Analysis of the experimental data demonstrates that, in the PE sample, radicals are well oriented along the stretching axis of the polymer and the angle α_L is small. In the PCA sample, the z axis deviates significantly from the L axis and the angle α_L can be as large as 12°–17°.

For the PP sample, the orientation of radicals can be judged from the angle $\alpha_L(Me)$ between the principal axis of the anisotropic hyperfine interaction tensor of the rotating methyl group, which is located parallel to the C_α–C_{Me} line, and the stretching axis of the polymer. The angle $\alpha_L(Me)$ = 67°–70° determined from the ENDOR spectrum of radicals in the PP crystallite is 7°–10° larger than the angle corresponding to the ideal orientation of macroradicals in the PP helical structure.

3.2. Conformation of the Radicals

The conformational structure of the radicals was evaluated from the MacConnell–Heller equation [18] for hyperfine splittings of the lines associated with the β protons. This equation is represented in the form of the dependence of the hyperfine interaction constant on the angle φ of internal rotation about the C_α–C_β bond (characterizing the deviation from the ideal *trans* conformation); that is,

$$a_{\beta 1,\beta 2} = A_\beta \cos^2(32^\circ \pm \varphi).$$

The thermal dynamics and the possibility that other types of angle deformation affected the hyperfine interaction were disregarded. The angles of internal rotation for the radicals under investigation are listed in the table. Comparison of the conformations of the middle radicals with the conformations of the "parent" macromolecules allows us to make the following inferences.

The conformation of the PE middle radical differs insignificantly from the ideal *trans* conformation, and the angles of internal rotation about the C_α–C_β bond are only 4° greater than those in the ideal conformation.

The conformation of the PCA middle radical differs substantially from the *trans* zigzag conformation. The angle of internal rotation about the C_α–C_β bond is equal to 10°. The structural feature of the PCA radical is that the protons of the methylene group located to the left of the carbonyl group of the radical (see table) are magnetically nonequivalent. The angle of internal rotation about the $C_\gamma(O)$–C_δ bond is approximately equal to the angle of internal rotation about the C_α–C_β bond.

The most significant conformational changes are observed for radicals of isotactic poly(propylene). The angles of internal rotation about the –C_α–C_β bonds in these radicals differ by 20° from the angles of internal rotation in the PP helical macromolecules involving *trans* ($\varphi_T = 0°$) and *gauche* ($\varphi_\Gamma = 120°$) segments [19]. Moreover, it was revealed that irradiated poly(propylene) contains radicals characterized by the hyperfine interaction constants corresponding to a conformation in which both β-methylene groups adopt a *gauche* conformation. These radicals can be formed in irregular regions of the polymer owing to the fragments of macromolecules whose configuration differs from the 3_1 helical structure.

The conformational changes in the carbon skeleton of the macroradicals originate from the change in the local geometry due to the detachment of the hydrogen atom. The detachment of the hydrogen atom and the formation of a middle radical lead to the formation of a planar trigonal structure. As a result, the $C\diagup^{C}\diagdown C$ bond angle increases (from 112° to 120°) and the H_α hydrogen atom or the CH_3 side group is displaced from the initial position to the plane of the $C_\beta\dot{C}_\alpha C_\beta$ radical center. In our opinion, the conformational changes that accompany the formation of radicals in the PE and PCA samples are primarily caused by the increase in the bond angle. This increase should result in bending of the carbon backbone of the polymer chain. In a solid polymer, such bending is impossible. Therefore, the emergence of a more easily induced torsional strain in the macroradical can be treated as a compensation for this hypothetical bending. In radicals of isotactic poly(propylene), the conformational changes are governed by both the increase in the bond angle and the displacement of the α-methylene group. In these radicals, the conformational angles change significantly and there are grounds to believe that the radical center undergoes an out-of-plane deformation.

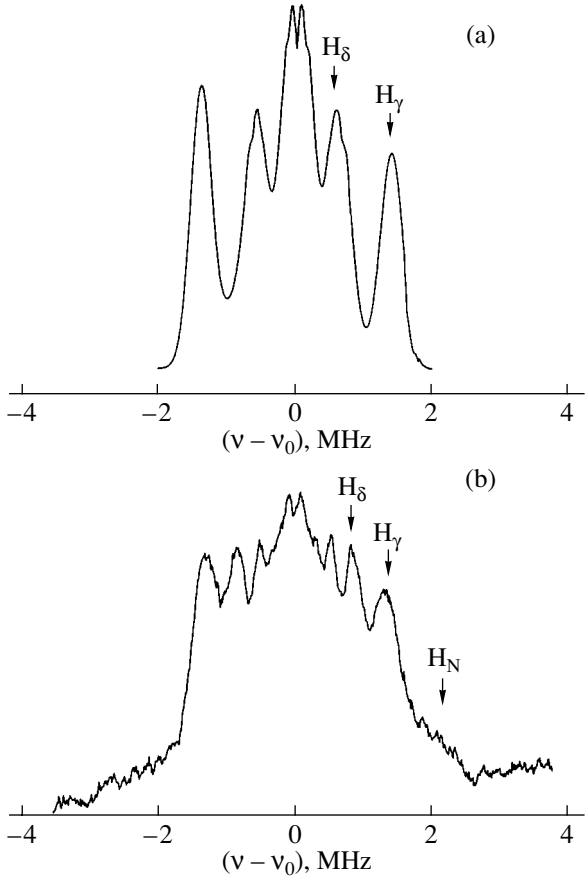

Fig. 3. ENDOR spectra of the remote protons in radicals of (a) PE and (b) PCA samples for $L \parallel H$.

The structure of the polyamide macroradical deviates from the ideal *trans* configuration both on the hydrocarbon side of the C_α atom and in the fragment located to the left of the amide group. In our opinion, the deviation of the fragment located to the left of the amide group from a planar structure characterizes the conformational structure of the PCA macromolecule itself. The angle φ_δ of rotation about the $C_\gamma(O)$–C_δ bond should correspond to the angle $\varphi_N = -\varphi_\delta$ of rotation about the N–C_α bond on the other side of the amide group. As a consequence, the plane of the amide group turns out to be rotated with respect to the plane of the methylene groups of the polyamide chain. The formation of the middle radical is attended by the displacement of the rotation axis from the N_β–C_α bond to the C_α–C_β bond:

$$\text{–CH}_2\text{CH}_2\text{CH}_2\text{CH}_2\text{CH}_2\text{–}\overset{\curvearrowright}{\text{CONH}}\text{–CH}_2\text{CH}_2\text{CH}_2\text{CH}_2\text{CH}_2\text{–}$$

$$\downarrow$$

$$\text{–CH}_2\text{CH}_2\text{CH}_2\text{CH}_2\text{CH}_2\text{–}\overset{\curvearrowright}{\text{CONHC}\dot{\text{H}}}\text{–CH}_2\text{CH}_2\text{CH}_2\text{CH}_2\text{–}.$$

Hyperfine interaction constants for macroradicals in PE [8, 9], PP [12], and PCA [11] samples at a temperature of 100 K

Atom in radical	Hyperfine interaction constant, MHz	Conformational angle
	$-CH_{\delta 3}H_{\delta 4}-CH_{\gamma 3}H_{\gamma 4}-CH_{\beta 3}H_{\beta 4}-\dot{C}H_{\alpha}-CH_{\beta 1}H_{\beta 2}-CH_{\gamma 1}H_{\gamma 2}-CH_{\delta 1}CH_{\delta 2}-$	
H_{α}	$A_{\alpha} = -60$	
	$B_{\alpha}(x, y, z) = +30, +6, -36$	
$H_{\beta 1}$, $H_{\beta 3}$	$a_{\beta 1} = a_{\beta 3} = 103.3$	$\varphi_1 = \varphi_2 = 4°$
$H_{\beta 2}$, $H_{\beta 4}$	$a_{\beta 2} = a_{\beta 4} = 84.7$	
$H_{\gamma 1, 2, 3, 4}$	$a_{\gamma} = -1.9$	
	$B_{\gamma}(x, y, z) = +6.4, -3.2, -3.2$	
$H_{\delta 1, 2, 3, 4}$	$a_{\delta} = 0$	
	$B_{\delta}(x, y, z) = +1.8, -0.9, -0.9$	
	$-CH_{\beta 1}H_{\beta 2}-\dot{C}(CH_3)-CH_{\beta 3}H_{\beta 4}-$	
$H_{Me\,\alpha}$	$a_{H}(Me) = 59.6, 62.4$	
	$B_{Me}(x, y, z) = +7, -3.5, -3.5$	
$H_{\beta 1}(T)$	$a_{\beta 1}(T) = 118.6$	$\varphi_T = 22°$
$H_{\beta 2}(T)$	$a_{\beta 1}(T) = 41$	
$H_{\beta 3}(\Gamma)$	$a_{\beta 3}(\Gamma) = 106$	$\varphi_{\Gamma} = 144°$
$H_{\beta 4}(\Gamma)$	$a_{\beta 4}(\Gamma) = 14.5$	
	$-CH_{\delta 1}H_{\delta 2}-CO-NH_N-\dot{C}H_{\alpha}-CH_{\beta 1}H_{\beta 2}-CH_{\gamma 1}H_{\gamma 2}-$	
H_{α}	$A_{\alpha} = -52.5$	
	$B_{\alpha}(x, y, z) = +28.5, +3.8, -32.3$	
$H_{\beta 1}$, $H_{\beta 2}$	$a_{\beta 1} = 101$	$\varphi_{\beta} = 11°$
	$a_{\beta 2} = 0.64$	
$H_{\delta 1}$, $H_{\delta 2}$	$a_{\delta 1} = -17.6$	$\varphi_{\delta} = 10°$
	$a_{\delta 2} = -10.8$	
$H_{\gamma 1, 2}$	$A_{\gamma} = -1.9$	
	$B_{\gamma}(x, y, z) = +6.2, -3.1, -3.1$	
H_N	$A^{*}_{HN} = -5.4$	
	$B^{*}_{HN}(x, y, z) = +8.6, -4.3, -4.3$	

* The hyperfine interaction constants are estimated from the data obtained in [17].

4. DEFORMATIONS OF MACRORADICALS

The stereoconfiguration of macroradicals is responsible to some extent for the specific features of the stressed state in loaded polymers. The mechanical deformations of radicals can be estimated from the change in the hyperfine splittings in the EPR and ENDOR spectra. It can be expected that longitudinal loading of the macroradicals should primarily lead to a change in the constants of the isotropic hyperfine interaction with protons of the β-methylene groups; that is,

$$a_{\beta 1, \beta 2} = A_{\beta}(\Delta r, \Delta\alpha)\cos^2[\Theta_{1, 2}(\Delta\varphi)].$$

This change is associated both with the strain of the valence bonds Δr and the bond angles $\Delta\alpha$ in the $C_{\beta}\dot{C}_{\alpha}C_{\beta}$ radical center and with the torsional strain $\Delta\varphi$.

In our earlier work [20], we investigated how the uniaxial elastic tension affects the EPR spectrum of $-CH_2\dot{C}HCH_2-$ middle radicals in high-strength poly(ethylene) monofilaments. The monofilaments were prepared by molding of a high-molecular polymer from a dilute solution, followed by stretching to a draw ratio of 150. The monofilaments possessed a tensile strength as high as 5 GPa and an elastic modulus of approximately 220 GPa. The monofilaments irradiated at a temperature of 77 K were loaded directly in the cavity of the EPR spectrometer at a low temperature. It was established that, under stresses higher than 1 GPa, the tension leads to a decrease in the extent of the EPR spectrum due to the weakening of the hyperfine interaction with protons of the β-methylene groups in the radical. The relative decrease in the mean constant of the

isotropic hyperfine interaction with the β protons is small:

$$(\Delta a_\beta/a_\beta)(1/\Delta\sigma) = -5 \times 10^{-3}\ \text{GPa}.$$

The strain of radicals in polymers with a normal strength was estimated using ENDOR spectroscopy. Since the sensitivity of the ENDOR method is lower than that of the EPR method, we could not repeat the experiments with high-strength poly(ethylene) monofilaments. The experiments were performed with oriented samples of poly(caproamide) and poly(propylene). The irradiated samples were loaded in the cavity of the ENDOR spectrometer at room temperature. Thereafter, the cavity with the sample was cooled to a temperature of –100°C and the ENDOR spectrum of the loaded polymer was recorded.

A comparison of the ENDOR spectra of the unstressed and stressed PCA samples showed that the loading results in a decrease in the separation between the ENDOR lines attributed to protons of two methylene groups, namely, the protons of the β-methylene group located in the vicinity of the radical center at the C_α atom and the protons of the δ-methylene group located to the left of the carbonyl group of the radical (Fig. 4). The decrease in the separation between the lines is caused by the decrease in the conformational angles φ_β and φ_δ. The magnitudes of the reversible elastic effect for the β and δ protons were almost identical; that is,

$$\Delta\varphi_\beta/\Delta\sigma = \Delta\varphi_\delta/\Delta\sigma = -2°/\text{GPa}.$$

The results obtained indicate that, under longitudinal loading of poly(caproamide) with an α crystalline structure, the macroradicals and polyamide chains undergo a torsional deformation that leads to their extension.

The observed increase in the intensity of the resonance absorption in the range between the pairs of the lines is associated with the change in the radical conformer distribution and with the formation of more extended macroradical fragments.

Analysis of the ENDOR spectra of macroradicals in the stressed and unstressed PP samples revealed the following features. The positions of the ENDOR lines corresponding to the β protons in the *trans* segment of the macroradical remain nearly unchanged. However, the high-frequency ENDOR line of the $H_{\beta 3}$ β proton located in the *gauche* fragment of the radical is considerably shifted toward the low-frequency range. This shift can be interpreted as a change in the conformational angle φ_Γ. The relative change in this angle was determined to be $\Delta\varphi_\Gamma/\Delta\sigma = -3.5°/\text{GPa}$.

Furthermore, the high-frequency wing of the ENDOR band attributed to the α-methyl group is insignificantly shifted toward the center of the band. This shift is probably caused by the decrease in the slope angle α_L of the C_α–Me_α line (by approximately 1°) with respect to the orientation axis *L* of the polymer under tensile stress.

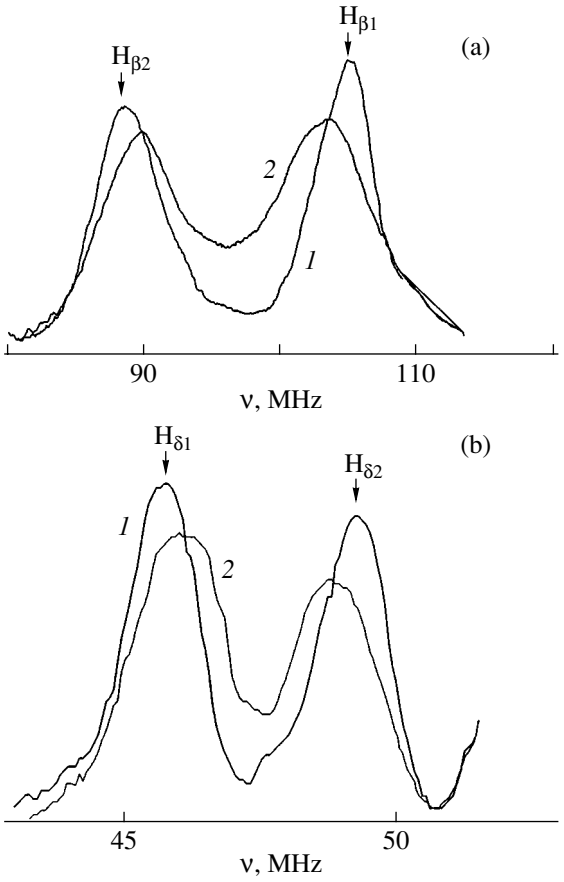

Fig. 4. Effect of uniaxial loading of PCA fibers on the ^1H ENDOR spectra of (a) β-methylene groups and (b) δ-methylene groups. σ = (*1*) 0 and (*2*) 400 MPa.

5. EFFECT OF MACRORADICALS ON THE STRENGTH OF ORIENTED POLYMERS

In order to investigate the effect of macroradicals on the strength properties of the oriented polymers, we carried out mechanical testing of irradiated fibers (filaments) at a temperature of 77 K. Irradiation performed at the same temperature made it possible to produce radicals at high concentrations (up to 10^{20} cm^{-3}). The mechanical testing was carried out either immediately after irradiation or after bleaching of the samples in visible light in order to neutralize charged radiolysis products. In this case, the observed difference between the strengths of the bleached and unbleached poly(ethylene) fibers [3] was explained by the scission of weak one-electron bonds in macroions under loading of the polymer.

This inference was qualitatively confirmed by the experiments in which the luminescence was recorded under tension of the irradiated samples to breaking. The appearance of the luminescence due to the recombina-

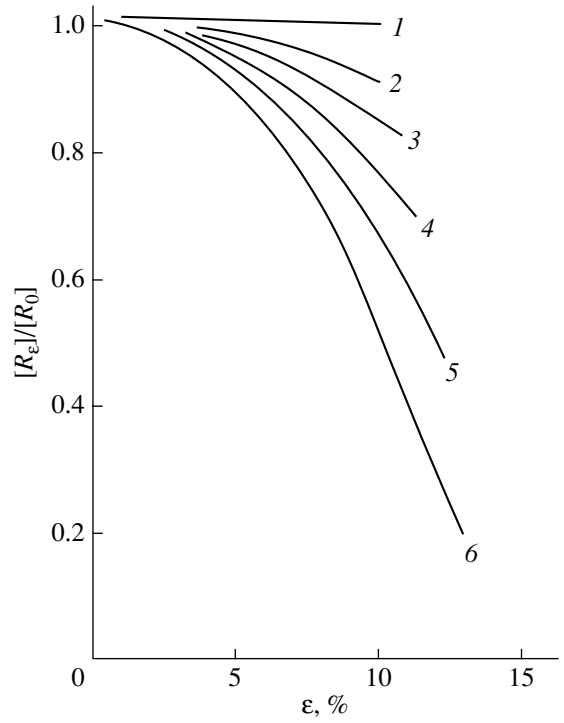

Fig. 5. Dependences of the relative concentration of middle radicals in irradiated poly(ethylene) fibers on the strain at temperatures of (*1*) –100, (*2*) –50, (*3*) –25, (*4*) –5, (*5*) 10, and (*6*) 20°C.

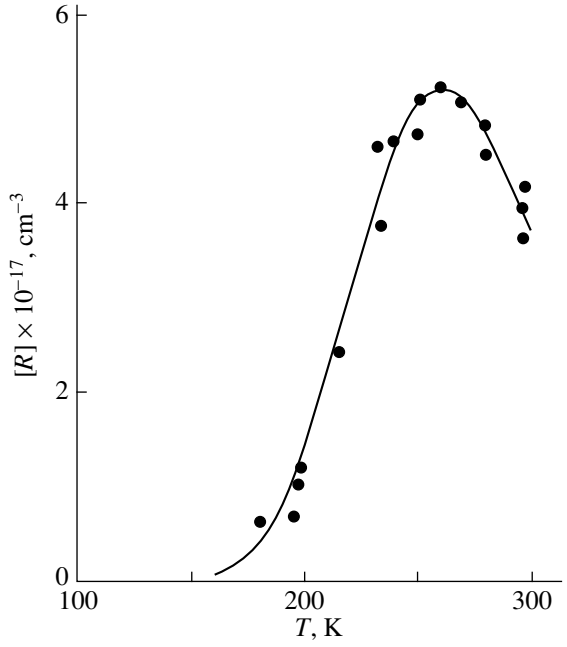

Fig. 6. Temperature dependence of the concentration of free mechanical radicals in broken fibers of unirradiated poly(caproamide).

tion of charged radiolysis products upon mechanical excitation at 77 K suggests that these products are highly sensitive to mechanical loadings.

Testing of the PE and PP bleached irradiated fibers made it possible to establish that their strength σ at 77 K and the radical concentration $[R]$ are related by the expression

$$\sigma = \sigma_0(1 - b[R]).$$

The factors b for poly(ethylene) and poly(propylene) are equal to 1.2×10^{-21} and 6×10^{-21} cm^{-3}, respectively. Although partial destruction of the polymers under low-temperature irradiation cannot be completely ruled out, the above factors b can be considered a measure of the decrease in strength due to the weakening of the β skeletal bonds in the radicals. The scission of the β bond in the middle radical occurs more readily when the 2p orbital of the unpaired electron overlaps with the sp^3 orbital of the C_β–C_γ bond. This is required to form the π component of the double bond. The overlapping of these orbitals is ensured only in nonplanar radicals with *gauche* conformations. This circumstance explains the difference between the factors b for poly(ethylene) and poly(propylene). In poly(propylene), all radicals have a helical structure. In poly(ethylene), the fraction of nonplanar fragments in noncrystalline regions is less than 30%.

Mechanical fracture of the macroradicals becomes possible when they are located in overstressed regions of the polymer. The scission of the radical

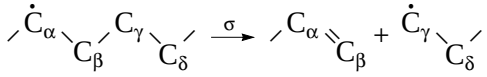

leads to the formation of a terminal free radical and the group with a double bond. An attempt was made to evaluate this reaction by the EPR method. For this purpose, irradiated poly(ethylene) filaments were loaded in the cavity of the EPR spectrometer at low temperatures ($T < 140$ K) at which the $\dot{C}H_2$–CH_2– active terminal radicals could be stabilized. However, we failed to reveal the transformation of middle radicals into terminal radicals from the change in the hyperfine structure of the EPR spectra. This is explained by the small number of broken bonds.

In the range of low temperatures at which the terminal radicals are not stabilized, the dissociation of the middle macroradicals can manifest itself in an implicit form, thus initiating the migration of a free valence and the subsequent recombination of the radicals. The experimental results demonstrate that mechanical loading stimulates the radical decay at temperatures above 170 K (Fig. 5). This makes an additional contribution to the decrease in the strength of the irradiated poly(ethylene) fibers. Therefore, the increase in the dissociation rate of radicals at moderately low temperatures contributes to the radical decay under deformation of the polymer [21].

It is worth noting that an increase in the rate of dissociation of the middle radicals is observed in the temperature range where the scission of bonds in unirradiated polymers acquires specific features of a quasihomogeneous multicenter process. Figure 6 shows the temperature dependence of the concentration of free "mechanical" radicals in broken fibers of unirradiated poly(caproamide). At a temperature of 77 K, the concentration of radicals formed under tension to breaking is relatively low and does not exceed 10^{15} cm^{-3}. At moderately low temperatures, the number of mechanical radicals increases and the maximum radical concentration $[R]$ in poly(caproamide) reaches 5×10^{17} cm^{-3}. We believe that the temperature dependence of the number of scissions along the β bonds in the macroradicals is qualitatively similar to the temperature dependence of the number of scissions along the C–C bonds in macromolecules.

The problem regarding the kinetics of degradation of stressed middle radicals calls for special theoretical treatment. The ultimate strength of the β bond was approximately estimated by Gubanov [22]. In recent years, there have appeared a number of theoretical papers in which the degradation of molecules [23] and radicals [24] has been simulated using quantum-chemical methods. It seems likely that *ab initio* methods are the most powerful tools for calculating the stressed state and the ultimate strength of middle radicals.

REFERENCES

1. S. N. Zhurkov, V. A. Zakrevskiĭ, V. E. Korsukov, and V. S. Kuksenko, Fiz. Tverd. Tela (Leningrad) **13** (7), 2004 (1971) [Sov. Phys. Solid State **13**, 1680 (1971)].
2. V. R. Regel, A. I. Slutsker, and É. E. Tomashevskiĭ, *Kinetic Nature of the Strength of Solids* (Nauka, Moscow, 1974) [in Russian].
3. B. B. Narzullaev and É. E. Tomashevskiĭ, Vysokomol. Soedin., Ser. B **23** (10), 784 (1981).
4. B. B. Narzullaev, N. G. Kvachadze, A. I. Slutsker, and É. E. Tomashevskiĭ, Fiz. Tverd. Tela (Leningrad) **23** (2), 429 (1981) [Sov. Phys. Solid State **23**, 242 (1981)].
5. B. B. Narzullaev, Candidate's Dissertation (Ioffe Physicotechnical Inst., USSR Academy of Sciences, 1983).
6. É. E. Tomashevskiĭ and N. G. Kvachadze, Prib. Tekh. Éksp., No. 6, 112 (1988).
7. N. G. Kvachadze and É. E. Tomashevskiĭ, Fiz. Tverd. Tela (Leningrad) **30** (6), 1859 (1988) [Sov. Phys. Solid State **30**, 1071 (1988)].
8. É. E. Tomashevskiĭ and N. G. Kvachadze, Vysokomol. Soedin., Ser. B **37** (10), 1788 (1995).
9. N. G. Kvachadze and É. E. Tomashevskiĭ, Fiz. Tverd. Tela (St. Petersburg) **36** (5), 1526 (1994) [Phys. Solid State **36**, 835 (1994)].
10. N. G. Kvachadze and É. E. Tomashevskiĭ, Vysokomol. Soedin., Ser. B **36** (3), 1959 (1994).
11. N. G. Kvachadze, I. A. Gorshkova, and É. E. Tomashevskiĭ, Vysokomol. Soedin., Ser. B **38** (8), 1314 (1996).
12. É. E. Tomashevskiĭ and N. G. Kvachadze, Vysokomol. Soedin., Ser. A **43** (7), 1194 (2001).
13. N. G. Kvachadze, Candidate's Dissertation (Ioffe Physicotechnical Inst., Russian Academy of Sciences, 1998).
14. N. G. Kvachadze and É. E. Tomashevskiĭ, Vysokomol. Soedin., Ser. B **45** (10), 1782 (2003).
15. P. Yu. Butyagin, A. M. Dubinskaya, and V. A. Radtsig, Usp. Khim. **38** (4), 593 (1969).
16. V. K. Milinchuk, S. Ya. Klinshpont, and S. Ya. Pshezhetskiĭ, *Macroradicals* (Khimiya, Moscow, 1980) [in Russian].
17. V. P. Chako, C. F. McDowell, and B. C. Singh, J. Chem. Phys. **79** (9), 5298 (1980).
18. C. Heller and H. H. MacConnell, J. Chem. Phys. **32**, 1535 (1960).
19. G. Natta and P. Corradini, Nuovo Cimento Suppl. **15** (1), 40 (1960).
20. N. G. Kvachadze, A. V. Savitskiĭ, and É. E. Tomashevskiĭ, Fiz. Tverd. Tela (Leningrad) **26** (1), 282 (1984) [Sov. Phys. Solid State **26**, 168 (1984)].
21. J. Becht and H. Fischer, Angew. Makromol. Chem. **18** (1), 81 (1971).
22. A. I. Gubanov, Fiz. Tverd. Tela (Leningrad) **23** (12), 3684 (1981) [Sov. Phys. Solid State **23**, 2142 (1981)].
23. J. C. L. Hageman, G. A. de Wijs, R. A. de Groot, and R. J. Meier, Macromolecules **33** (24), 9098 (2000).
24. B. É. Krisyuk, Vysokomol. Soedin., Ser. A **44** (10), 1805 (2002).

Translated by O. Borovik-Romanova

Physics of the Solid State, Vol. 47, No. 5, 2005, pp. 934–941. From Fizika Tverdogo Tela, Vol. 47, No. 5, 2005, pp. 906–913.

The Role of Chain Length and Conformation in Stress-Transmission and Fracture of Thermoplastic Polymers[1]

Hans-Henning Kausch-Blecken von Schmeling

Institute of Materials, Swiss Federal Institute of Technology Lausanne (EPFL), Lausanne, CH-1015 Switzerland
e-mail: hans-henning.kausch@epfl.ch

Abstract—In this paper, a review of the molecular aspects of fracture is given, a subject that was pioneered by S.N. Zhurkov and his colleagues. Particular attention will be paid to the mechanisms of stress transfer onto straight chain segments, the role of chain interpenetration in establishing interfacial strength during crack healing, to the concept of taut tie molecules, to stress distribution in UHMWPE fibers, and to the possible role of chain ruptures in the deformation process of fibres. Using Raman microscopy, it is observed that some chains are exposed to stresses of up to 10 GPa, which is close to their estimated strength. From these experiments, a mechanical model of the organization of almost fully oriented UHMWPE fibers is developed accounting also for the presence of numerous and dispersed defects. The principal deformation mechanisms are chain slippage, crystal plasticity, and intra- and intermicrofibrillar slippage. *© 2005 Pleiades Publishing, Inc.*

1. INTRODUCTION

The great length, large anisotropy, and high segmental flexibility of macromolecules give rise to the complex structural organization and the unique properties of polymer materials. The weak lateral coherence of strong chain segments offers an enormous potential for processing at comparatively low temperatures, and it is an essential condition for polymer ductility, rubber elasticity, and viscoelastic behavior. In this paper, we discuss amorphous and semicrystalline thermoplastics. Their mechanical properties depend on the intensity of the van der Waals attraction between molecular segments, the density of entanglements, and on long-range stress transmission by extended chain segments. These characteristics are responsible for the strong effect of time and temperature of macroscopic performance.

The emerging macromolecular science (since the early twenties [1]) rapidly identified the important role of length and conformation of chain molecules in solution [1], in the rubbery state [2], and in solids [3]. From the many and important discoveries and concepts made over the subsequent three decades, we may cite the new methods of synthesis controlling the stereoregularity of chains (Ziegler, Natta); the decisive theoretical work on chain conformation and statistical thermodynamics (e.g., W. Kuhn, H. Kuhn, Flory, Volkenstein, Rouse); the surprising discovery of the chain-folded lamellar structure of semicrystalline polymers (Fischer, Keller, Till); and the better understanding of (ultimate) mechanical properties, such as the formation and microstructure of crazes (Kambour, Hsiao, Sauer), of the nature of elementary deformation mechanisms (Eyring, Wolf, Schmieder, Heijboer), and of the essential parameters of time-dependent polymer fracture (Tobolsky, Zhurkov, Bueche). These so exiting origins and growth of polymer science have been competently reviewed by Morawetz [4].

In fracture through crack propagation of a solid polymer, chains must be disengaged from each other across the fracture plane. In thermoplastic solids, where chains cohere through van der Waals forces, this involves several terms, which all depend on the stress transfer through and the breaking of secondary bonds. The relative contributions of the different mechanisms are well reflected by the fracture energy G_{Ic} plotted in Fig. 1 as a function of chain length (molecular weight).

Using an unoriented amorphous thermoplastic as an example, such as polymethyl methacrylate (PMMA), it is seen that the separation of very small molecules (low M_W material) only requires work against the intermolecular attraction, since G_{Ic} is equivalent to two times the surface tension parameter γ. In the following region, G_{Ic} shows a moderate and linear increase with M_W, which indicates that the pullout of chains from a rather restricted fracture surface zone contributes to the dissipation of energy. Once the chains are long enough to form entanglements, energy dissipation (by plastic defromation and/or crazing) is spread out into a larger volume element leading to a strong increase of G_{Ic}. Understandably, in a solid, where cohesion occurs more or less exclusively through the lateral van der Waals interaction between chain segments, the fracture energy levels off for very long chains. For PMMA, a terminal value of G_{Ic} of about 300 J m^{-2} has been determined, which is several orders of magnitude smaller

[1] This article was submitted by the author in English.

1063-7834/05/4705-0934$26.00 © 2005 Pleiades Publishing, Inc.

than the fracture energy of a monocrystal, where primary bonds are loaded and broken [5]. (It should be noted that, in that case, most of the fracture energy is a loss of elastic energy when the highly loaded chains are discharged and the chemical surface energy of breaking primary bonds (chain scission) is rather small as compared to the elastic term; for most polymers, it is of the order of 0.4 to 3.0 Jm^{-2} [5].) It may be mentioned that a rather weak dependence of chain length is also obtained for the elastic and anelastic properties of glassy polymers, which are cohesive in nature.

A much stronger effect of chain length is found, however, under experimental conditions, which permit the (partial) unfolding of the coiled chains: in solution, in highly oriented polymers, and/or with properties involving larger strains or time to failure. Under such conditions, notable axial stresses can be transferred onto the chain backbone, thereby greatly improving the overall load bearing capability. In the pioneering work done at the Ioffe Physical Technical Institute in the then Leningrad, Zhurkov and his colleagues tackled this problem, namely, to identify molecular deformation and/or damage mechanisms in order to understand the kinetics of polymer breakdown. In referring to their work, we discuss in this paper the micromechanics of stressed samples due to the action of (and the competition between) different mechanisms: conformational changes, segmental slip, disentanglement, chain stretching and scission, and void and/or microcrack formation. The strongly time- and temperature-dependent dynamics of these mechanisms determine the modes of deformation and fracture (through, e.g., crazing, shear yielding, creep, and/or crack propagation). For this purpose, we will study two quite different systems: the fracture (and crack healing) behavior of amorphous polymers (PMMA, SAN) and the ultimate properties of highly oriented ultra high molecular weight polyethylene (UHMWPE).

2. EARLY STUDIES AT THE IOFFE PHYSICAL TECHNICAL INSTITUTE

In order to elucidate the molecular origins of polymer fracture, Zhurkov and his colleagues used, and in part developed, a variety of experimental and theoretical techniques. Their fruitful activity has given rise to several hundreds of original publications (initially mostly in Russian). Much of this work has been reviewed in two relevant monographs: Fracture Micromechanics by Kuksenko and Tamuzs [6] and Polymer Fracture by Kausch [5].

The author of this paper first became acquainted with the Leningrad investigations in Zhurkov's presentation at ICF1 in Sendai in 1965 [7], where he reported that the time to failure τ of a sample under tensile stress

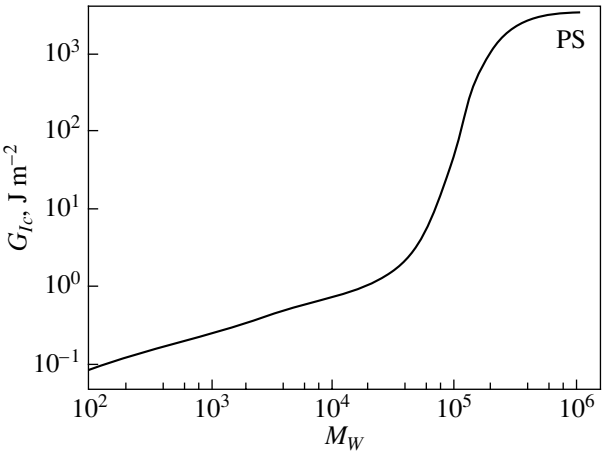

Fig. 1. Energy release rate G_{Ic} as a function of chain length (M_W) for poly(methyl methacrylate) (PMMA).

σ could be well described by one general kinetic equation valid for quite different polymers:

$$\tau = \tau_0 \exp\left(\frac{U_0 - V\sigma}{kT}\right), \quad (1)$$

where k is the Boltzmann constant and τ_0, U_0, and V are constants determining the strength characteristics of a polymer. From his experiments, he determined that the activation energy U_0 of mechanical fracture compared well with the activation energy for thermal destruction. The preexponential term τ_0 was roughly the same for all polymers studied and of the order of 10^{-12} to 10^{-13} s. Similar relationships between stress and mechanical properties had been proposed independently by Tobolsky and Eyring (creep rate) and Bueche (lifetime) [5].

In order to learn more about the micromechanics of a stressed system formed of weakly cohering strong chain backbones, the Zhurkov team followed a remarkably broad approach using techniques that were applied for the first time to such systems.

Axial forces transmitted to an extended elastic tie-chain segment stressed between two crystalline lamella were calculated [8].[2]

Stress effects on chain segments were theoretically analyzed and experimentally determined quantitatively from the shift and deformation of infrared (IR) bands of characteristic skeleton vibrations with applied load [9].

Scission of chains was traced through the accumulation of free radicals by the electron spin resonance technique (ESR) [10]. Thus, for the first time, direct evidence was presented on stress-induced homolytic chain scission during the loading of polyamide 6 (PA6) and natural silk. In ruptured specimens, the concentration

[2] Studies [8] to [13] are among the first publications on these particular subjects available in English; they are not meant to provide comprehensive coverage of the activities of the Zhurkov laboratory.

of free radicals amounted to about 5×10^{18} cm^{-3} (which in this case is about twice the number of broken chains). In view of the small loads transmitted to the axes of statistically coiled chains, most of the above ESR and IR experiments were performed with oriented films or fibers.

Following chain scission, new, oxygen-containing groups were formed and could be determined quantitatively by the IR technique [11].

Microcracks appearing in stressed samples were studied by small angle x-ray scattering [12].

Strong synergisms and similarities were detected between the kinetics of mechanical and electrical breakdown [13].

These intriguing experiments stimulated research in this area in other parts of the world, with ESR and IR investigations notably done in Salt Lake City [14] and Darmstadt [15]. They gave undisputed proof that during straining and fracture chain segments were loaded up to scission. A quantitative analysis showed that the number of highly stressed segments was small, increasing with the degree of molecular orientation. Even in highly oriented fibers, no more than between 3 and 5% of all segments were overstressed [5, 6]. In the following, we will indicate the molecular and experimental parameters favoring the stress transfer onto (extended) chain segments and discuss more recent techniques: the crack healing approach, the compatibilization using block copolymers, and bond stress analysis by Raman microscopy, techniques employed to obtain direct information on the role of chain backbones in the fracture of polymers.

3. STRESS TRANSFER ONTO EXTENDED CHAIN SEGMENTS

All axial chain stresses derive from the relative displacement of chain segments with respect to their surroundings. It is useful to distinguish between static and dynamic stress transfer. The axial stress ψ_i resulting from the static displacement of a straight, elastic linear chain segment against a sinusoidal interaction potential (modeling the repulsive forces a monomer unit encounters within a PE crystal) was first calculated by Chevychelov [8]; Kausch and Langbein [16] later extended these calculations to interaction potentials in the presence of hydrogen bonds (as in the lamellae of PA6). In both approaches, the maximum chain tension is proportional to the product of potential depth and chain elasticity. The forces thus obtained amounted to 1.4 nN (PE) and 4nN (PA6), respectively [5, 8, 16].

In the dynamic case, a stress ψ_i is transferred onto a straight segment of finite length L_i by friction

$$\psi_i = \zeta_0 \dot{\delta}_0 L_i, \quad (2)$$

where ζ_0 is the monomeric friction coefficient and $\dot{\delta}_0$ is the rate of segment displacement (e.g., during chain pullout). Stresses will obviously be the higher, the more regular and longer a segment is (absence of kinks or other irregularities capable of relaxing axial stresses by simple change of conformation) and the closer such an extended stiff segment is oriented into the principal stress direction. Small rates of loading and high temperatures, as well as all modes of ultra- or intersegmental relaxation, will decrease the attainable level of axial stresses and for that matter contribute to the toughness of a specimen (see [17] for an extended discussion of the effect of molecular mobility on toughness). A comprehensive molecular analysis of the static and dynamic loading of chains at interfaces and of their influence on the mode of failure has recently been given by Creton *et al.* [18].

Stress distribution on isotropic semicrystalline polymers is dominated by the large stiffness differences between amorphous and crystalline regions. The presence, phase structure, quality, and organization of the crystalline lamellae strongly influence all mechanical properties [19, 20]. Within the context of this paper, particular attention must be paid to tie molecules. Anchored in adjacent lamellae, the tie molecules (and/or crystalline bridges) are capable of efficient stress transfer, which is absolutely essential to attain high levels of stiffness and strength. Tie molecules bear high load, and they are the first to be overstressed and broken. Evidently, the direct study of stress effects on chain segments is best performed on highly oriented (film or fiber) specimens as this has been done so successfully at the Ioffe Institute [7–13, 21–27].

4. STRESS TRANSFER IN AMORPHOUS POLYMERS

4.1. Crack Healing

The stress transmission by chain backbones in amorphous polymers can be most conveniently studied using the crack healing approach. Conceived and developed by Jud *et al.* [28], Wool and Connor [29], Brown [30], and Kramer *et al.* [18], this approach consists in the determination of the gradual buildup of interfacial strength through chain interdiffusion between two flat surfaces of identical (or compatible) amorphous polymers brought into contact at a temperature above the glass transition T_g. The term crack healing was chosen to differentiate this slow and time-dependent approach from welding of semicrystalline thermoplastics, which involves the fusion and often rapid reformation of crystal lamellae. (The physical particularities of the welding technique, especially the advantages of nonisothermal welding, have been extensively investigated by Manson's laboratory in Lausanne; see [31, 32] for more references.) To determine the strength restored to healed or welded surfaces, appropriate fracture mechanics specimens were used and the fracture toughness K_{Ic} or fracture energy G_{Ic} were taken as a measure of interfacial strength.

The experiments with (compatible) amorphous polymers [5, 18, 28–30] confirmed that the sequence of physical events in strength buildup is the following: establishment of (partial) mechanical contact between surfaces, surface reorganization, full contact, interpenetration of segments across the interface at a rate determined by the compatibility of the interdiffusing species, chain mobility and mechanical constraints, further interpenetration of whole chains, and successive formation of entanglements at rather long times; the former interface will have disappeared completely.

Using the reptation model of de Gennes [33], Kausch *et al.* [28, 34] and Wool [29, 35] have proposed kinetic models of strength buildup in crack healing based on the formation of new entanglements. Due to the statistical nature of the process of chain diffusion by reptation, there will be a large local variation of the number of diffusing chain ends and of the curvilinear depth Δu of their interpenetration. This means that even at small values of $(\langle \Delta u^2 \rangle)^{1/2}$ there are some chains that have penetrated much further than the minimum distance $\Delta u_{\min}$ necessary to form an entanglement. During the crack healing process $n(t_h)$, new entanglements per unit surface area are formed in the interfacial region near the former crack surfaces. Unless the healing is absolutely complete, $n(t_h)$ will be smaller than n_e, the corresponding concentration of entanglements in the virgin material. The wriggling and translational motions of the chain segments within their confinement, the so-called tube, give rise to an average curvilinear displacement Δu of the chain ends, which is described by the Einstein relation

$$\langle \Delta u^2 \rangle = 2 D_t t_t. \quad (3)$$

Following the argumentation of the above authors that the fracture energy $G_c(t)$ of the healed interface is proportional to the number of entanglements formed, a relation between the stress intensity factor K_c measured after healing and the healing time t_h is obtained:

$$K_{c,\,\mathrm{rel}} = \frac{K_c}{K_{I_0}} = \left(\frac{G_c}{G_{c_0}}\right)^{1/2} = \left(\frac{n(t_h)}{n(\tau_0)}\right)^{1/2} = \left(\frac{t_h}{\tau_0}\right)^{1/4}, \quad (4)$$

where K_{10} and G_{c0} refer to the virgin material and τ_0 is the time necessary for complete healing. It is this equation that has explained for the first time and in a straightforward manner the $t^{1/4}$ dependence of the increase of the stress-intensity factor with healing time as observed in amorphous PMMA and SAN [28, 29].

Despite the quite satisfactory explanation of the time dependence of crack healing, it should be noted that the assumptions made in deriving the above model have led to the elimination of D_t from the final formula. Thus the above model does not account for a number of parameters which have been shown to influence the strength buildup in a healing interface, such as the absolute values of D_t or of the critical distance of interpenetration at complete healing, the nature of the diffusion mechanism (by reptation of the chain ends or by displacement of hairpin segments?), and the absolute number of involved connector chains or the number of connections per chain.

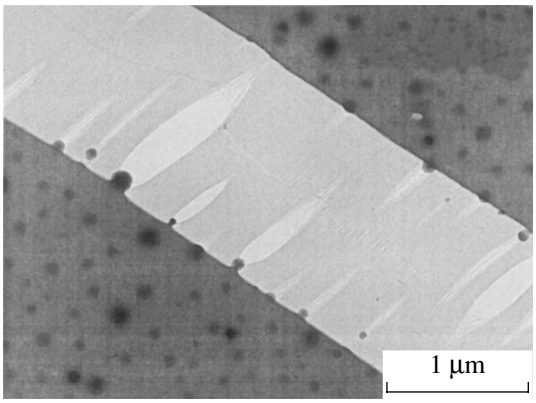

Fig. 2. Craze in a thin film of an incompatible blend (10% PSF particles in a PS matrix) deformed at room temperature (after [34]).

Such information was obtained by Creton *et al.* in their elegant interdiffusion experiments using the compatibilization between two incompatible polymers through appropriate choice of the block copolymers (reviewed in [18, 30]). The principle of this technique and some results are presented in the following section.

4.2. Use of Block Copolymers to Count Molecular Connectors

The principle of using block copolymers as compatibilizing agents is straightforward. Two incompatible polymers *A* and *B* will generally form a clearly phase-separated system. Figure 2 shows as an example a thin film of a blend of 10% polysulfone (PSF) particles dispersed in a (incompatible) polystyrene (PS) matrix. The interfaces between the two components are sharp and well defined. When such a film is deformed, large crazes open up in the matrix.

The interior of the craze is characterized by a larger number of defects: local ruptures of craze fibrils which originate without exception at the surface of the PSF particles betraying the rather weak van der Waals attraction between the incompatible polymer pair PS–PSF. Such a PS–PSF blend can be compatibilized by adding a (PPO–PSF) triblock copolymer to it. The blocks will interdiffuse into the phases with which they are compatible: the two PPO end blocks into the PS matrix, and the central PSF clock into the PSF particles. From this interdiffusion result two strong covalent bonds per molecule that penetrate the interface. Assuming the force transmitted by each bond to be f_0 and their

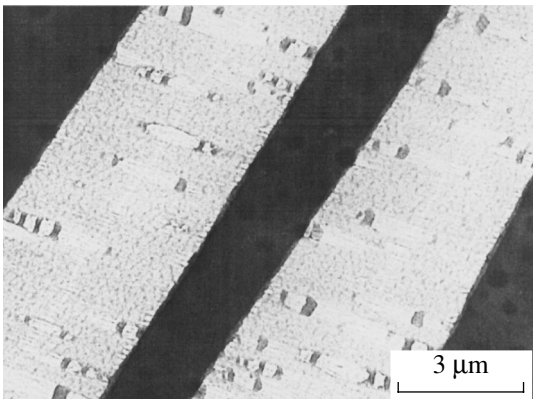

Fig. 3. Craze in a compatibilized blend (11% free PSF particles in a PS matrix, PPO–PSF triblock copolymer as compatibilizer) (after [34]).

surface density to be Σ, the following interfacial strength σ is obtained:

$$\sigma = f_0\Sigma. \quad (5)$$

As evidenced by Fig. 3, the interfacial strength σ can be higher than the crazing strength of the PSF particles such that the latter break up when the matrix craze is formed or extended.

The essential parameters controlling the interfacial strength of a compatibilized blend are evidently the number of covalent ties at the particle surface and the strength with which a block is anchored in its respective phase (which depends on block length). In their early quantitative experiments on the buildup of interfacial strength through clock copolymers, Brown *et al.* [18, 19] create a strong interfacial bond between two flat slabs of PMMA and PPO, respectively, by interdiffusing an interlayer of a PMMA–PS diblock copolymer. Each diblock thus provides a covalent bond between the slabs. These experiments have made it possible for the first time to virtually count the number N_{di} of primary bonds joining the two slabs. Using marked molecules, the authors of [18, 30] have also proven the fact that the PMMA section of the diblock interdiffuses only into the PMMA slab and the PS section only into the PPO. This way, they are assured that the number of main chain crossings at the interface must be equal to the number N_{di} of diblock chains available at the interface. For a given thickness of the diblock interlayer, e.g., 25 nm, the number N_{di} obviously decreases with the M_W of the diblocks. As it turns out, the fracture energy of the interdiffused slabs reaches saturation values for the 282*k*[3] and 355*k* material with N_{di} values of 22 and 17.5×10^{16} m^{-2}. The latter crossing densities are only 15 and 12%, respectively, of the maximum crossing density theoretically permitted by the chain cross section. With the largest molecular weight, the crossing density even drops to 5%. This is evidently equivalent to saying that one needs only relatively few, well-anchored chains crossing a given interface in order to achieve full mechanical interfacial strength. This result is in line with the earlier conclusions based on ESR and IR experiments [5, 9–11]. It also confirms the observation that the presence of some 5 to 10% of high molecular weight material has a beneficial effect on the long term and fatigue strengths of thermoplastics (see [5] for references).

5. ULTRA HIGH MOLECULAR WEIGHT POLYETHYLENE (UHMWPE) FIBERS

5.1. Modelization of Microstructure

In the previous section, we indicated that the stiffness and strength of linear molecules can be utilized maximally if all soft and misaligned segments are eliminated. A perfectly organized and strong (but also quite brittle) system would be an all-trans monocrystal, such as poly(diacetylene), which has a strength σ_b of up to 1.5 GPa. Highly oriented (semicrystalline) fibers generally retain some noncrystalline material, which is at the origin of the important flexibility without reducing fiber strength (σ_b of UHMWPE may reach up to 7 GPa). In our experiments, we used SK60 fibers,[4] which consist of 117000 macrofibrils each having a diameter of 0.2 to 2 μm [36]. They are highly ordered but not monocrystalline. From measurements of fiber crystallinity and density, it can be concluded that there is a fraction of about 25% noncrystalline material. This fraction comprises highly extended but noncrystalline segments (having a density of 0.90 g/ml), rare entanglements (about 2.5 per molecule) and folds. The NMR-amorphous phase accounts for less than 5% of the material; the absence of an amorphous x-ray halo indicates an even smaller fraction. The above data show that the amorphous component cannot be expected to form a coherent phase; more likely, it comprises all the less ordered segments, tie molecules, conformational irregularities (out of register, twists, rare entanglements), and defects in the crystalline phases and at the boundaries and interfaces of microfibrils. From these findings, a two-dimensional model of the studied SK60 fibers is proposed (Fig. 4). Basically, this model is valid for most highly oriented fibres, although it should be noted that the detailed morphology depends on the starting material (chain length and linearity, degree of entanglement, crystalline morphology) and on the applied processing technique (solid state or melt extrusion, gel spinning, hot drawing) [22, 25, 37, 38].

The regions *A* and *B* represent fully chain-extended crystalline regions (having an elastic modulus of 290 GPa). Phase *C* describes the fraction of about 25% of slightly disordered noncrystalline chain segments (most of which are well extended). It is reasonable to

[3] 282*k* designates a sample with molecular weight M_W = 282 kg/mol.

[4] Dyneema®, DSM.

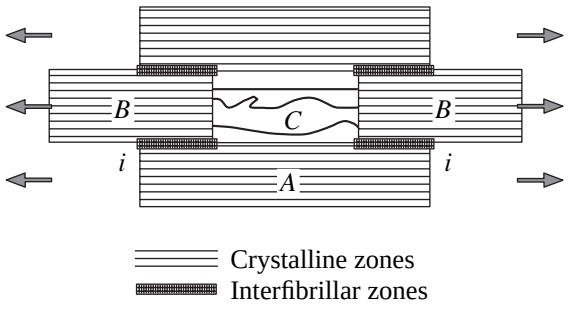

Fig. 4. Two-dimensional mechanical model of a macrofibril of UHMWPE showing the essential structural elements: crystalline regions, intermicrofibrillar zones, and noncrystalline regions containing more or less taut tie molecules (the possible slight misalignments, distortions, and variations in the width of microfibrils are not shown; see text for the size of the crystalline regions) (after [36]).

assume that this phase contains intramicrofibrillar tie molecules of various degrees of toughness. The tie molecules are capable of transmitting important axial stresses (the pullout stress of a tie molecule from a defect-free orthorhombic crystal amounts to 7.5 GPa [16]). Stresses between the crystalline blocks *B* are also transferred by shear through the interfaces *i* and region *A*. Concerning the size of the crystals in UHMWPE fibers, the lateral dimensions were found to decrease with draw ratio to a value of about 13 to 15 nm [27, 36]. The crystalline lengths in the chain direction, however, seem to depend strongly on the fiber type; values of 5 to 71 nm have been reported, which agree quite well with the distribution of straight chain lengths determined by Marikhin *et al.* by longitudinal acoustic mode spectroscopy (LAM) [26], 7 to 60 nm.

5.2. Molecular Stress Analysis

The subject of molecular stress analysis is highly intriguing. More than 40 years ago, Zhurkov, Vettegren, *et al.* [9] started to analyze the stress-induced deformation of IR absorption bands and to interpret the obtained results within the framework of the kinetic theory of fracture. Much of their work has been reviewed in the cited books [5, 6] and more recently in [23, 24]. Evidently, it is important to realize that IR techniques (even Raman microscopy) always scan a volume area, which contains much more than a million stressed bonds. The observed bonds may be stressed quite differently (this has been recognized in the subsequent stress analysis by fitting a deformed band by some 20 Lorentzian peaks). Secondly, it must be understood that (at room temperature) mechanical stress and thermal vibrations contribute to the final fracture of such an overstressed region; as outlined by all these authors in their discussion of the physical nature of the activation parameters in kinetic equation (1), the thermal and mechanical energy of bond rupture can substitute for one another. Thirdly, the reader is reminded that the existence and breakage of overstressed regions (in the following, simply called bonds or segments) is in itself not yet proof that the strength of oriented polymers is controlled by the scission kinetics of primary bonds.

Molecular stresses were determined by Raman microscopy using the stress-induced shift of the position and form of Raman bands assigned to C–C stretching vibrations [9, 36, 39]. In polyethylene, the bands at 1060 and 1130 cm^{-1} exhibit the greatest peak shift upon mechanical deformation. In our investigations, we used the symmetric stretching band at 1130 cm^{-1}, for which we determined a peak shift value of –5.73 cm^{-1} GPa [36]. Using this shift factor, the wavenumber axis of a deformed band can be converted into a stress axis

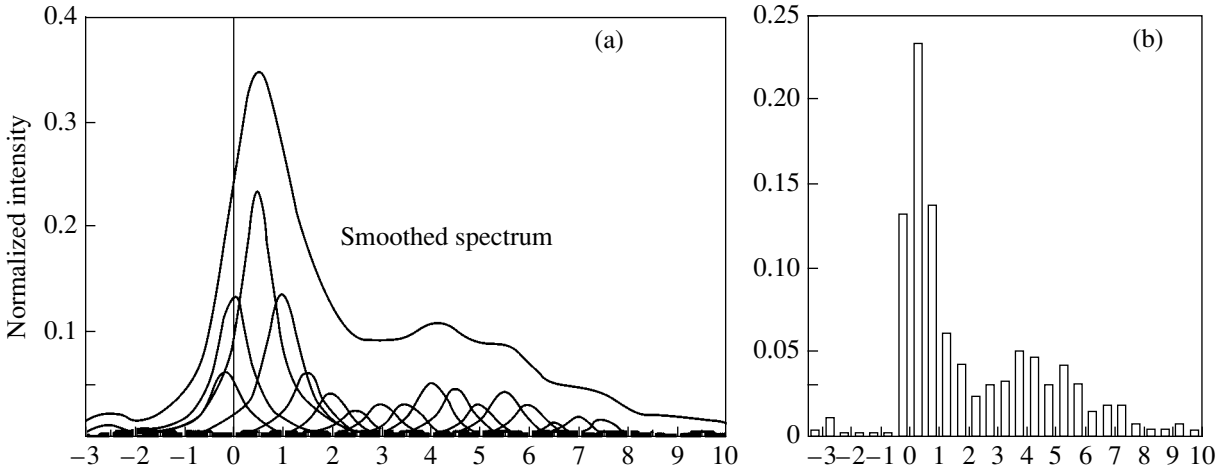

Fig. 5. Stress analysis of a single filament containing some 150 macrofibrils loaded to a uniaxial stress of 2 GPa. Using a peak shift value of –5.73 cm^{-1}/GPa the wavenumber axis is converted into (a) a stress axis and subsequently deconvoluted into (b) a stress histogram by curve fitting with some 20 Lorentzian peaks (after [36]); the histogram has a clearly bimodal structure.

(Fig. 5a). The subsequent transformation into normalized stress intensities is generally achieved by fitting the deformed Raman band by a number of (two or three) Lorentzian peaks [37]. In our approach, we used about 20 Lorentzian peaks that have a width corresponding to the width of the peak of an undeformed sample and are separated from one another on the converted wavenumber axis by 0.5 GPa (Fig. 5b).

In the above spectrum, most segments are loaded to between 0 and 1 GPa, about one-fourth of the population to between 1.5 and 4.0 GPa, and 2.5% to stresses between 5 and 10 GPa. Berger *et al.* have investigated the changes in local stress distribution occurring in the three loading modes: creep, stress relaxation, and loading at constant strain rate [36]. Their results are summarized in the following.

For creep loading, the number of weakly (0–1 GPa) and highly loaded segments (4.5–10.0) increases at the expense of segments loaded with moderate overstress (1.5–4.0 GPa), which reinforces the bimodal character of the distribution shown in Fig. 5. This observation can be explained on the basis of the structure model in Fig. 4. The increase in highly stressed bonds is assigned to an increase in the number of taut intramicrofibrillar tie molecules during elongation of the fiber (due to the separation of phases *B*) or of taut intermicrofibrillar ties (following intermicrofibrillar slip). The decrease of moderately overstressed bonds in these fibers is apparently due to the limitation of elastic strain in region *A*, to slip at the interfaces *i*, or to crystal plasticity. The latter mechanisms would also explain the large and instantaneous variation of creep rates observed by Myasnikova *et al.* [40, 41].

During stress relaxation, a decrease in the number of moderately and highly overstressed chains is observed, while the fraction of less highly loaded material increases. The strong loss in the 5–8 GPa group is ascribed to tie-chain pullout, and the decrease in moderately overstressed chains, to crystal plastic deformation. Both mechanisms are compatible with the observation that even in the stress relaxation mode a large group of crystals remain subjected to a critical strain of about 0.4% [36].

In a tensile test, most of the material is never loaded to more than about 1 GPa. Evidently, the number of moderately and highly loaded chain segments increases when the applied stress is increased. It should be noted that beyond an external stress of 1 GPa the combined number of segments stressed at 0.5 and 1.0 GPa remains relatively constant and accounts for the low stress peak found by other researchers [42].

The possible influence of chain scission were investigated by Wang *et al.* [43]. Using a nitroxide spin trap interdiffused into an SK60 fiber, they determined that, during creep at half the breaking stress, 0.2 chain scission events per centimeter of molecular length occurred. This means that only 1 out of 550 molecules was broken in the experiment. The analysis is the same as that given by Kausch [5] for the ESR investigations of polyamide fibers, namely, that chain scission is the *consequence* of stress-induced deformation, but not its cause.

6. FINAL REMARKS

The molecular aspects of fracture have been reviewed in light of the seminal work of Zhurkov and his colleagues. Although stress transmission in thermoplastic polymers occurs exclusively by secondary bonds (even entanglements are loaded in this way), chain length, conformation, and strength are important parameters. The highest values of sample strength are obtained with highly oriented systems. Polydiacetylene monocrystals composed of perfectly oriented, *strongly interacting* chains have a high strength, but they are also brittle because they are too defect sensitive. For technically required toughness, it is desirable that, at a very high stress level, local modes of *plastic* deformation are activated, such as chain straightening by elimination of gauche bonds and chain slippage. Both mechanisms can only be active if there is a certain distribution of chain conformations and of local chain stresses. Using Raman microscopy, we have demonstrated that, in highly oriented UHMWPE fibers, some regions are exposed to stresses of up to 10 GPa, which is close to the estimated chain strength. Based on the concept of taut tie-molecules, a model of the organization of almost fully oriented UHMWPE fibers has been developed accounting for the numerous and dispersed defects, which are present even in a 99% oriented fiber. Deformation of such fibers occurs by elastic stretching and aligning and straightening of backbones, crystal plasticity, and intra- and intermicrofibrillar slippage. To reduce the effect of the latter on the creep properties of the fibers, cross-linking of the molecules and/or incorporation of side groups are appropriate means of modification.

The author wishes to thank his colleagues from the Ioffe Institute for a fruitful and pleasant exchange of arguments, manuscripts, and visits for more than 30 years now.

REFERENCES

1. H. Staudinger, Ber. Dtsch. Chem. Ges. **57**, 1203 (1924).
2. W. Kuhn, Kolloid-Z. **68**, 2 (1934).
3. P. Flory, *Principles of Polymer Chemistry* (Cornell Univ. Press, Ithaca, 1953).
4. H. Morawetz, *Polymers, The Origins and Growth of a Science* (Wiley, New York, 1985).
5. H. H. Kausch, *Polymer Fracture*, 2nd ed. (Springer, Heidelberg, 1987; Mir, Moscow, 1981).
6. V. S. Kuksenko and V. P. Tamuzs, *Fracture Micromechanics of Polymer Materials* (Martinus Nijhof, Hague, 1981).
7. S. N. Zhurkov, Int. J. Fract. Mech. **1**, 311 (1965).
8. A. D. Chevychelov, Polym. Sci. USSR **8**, 49 (1966).

9. S. N. Zhurkov, V. I. Vettegren, I. I. Novak, and K. N. Kashintseva, Dokl. Akad. Nauk SSSR **176**, 623 (1967).
10. V. A. Zakrevskii, E. E. Tomashevskii, and V. V. Baptizmanskii, Sov. Phys. Solid State **9**, 1118 (1967).
11. S. N. Zhurkov and V. E. Korsukov, J. Polym. Sci., Polym. Phys. Ed. **12**, 385 (1974).
12. S. N. Zhurkov, V. A. Zakrevskii, V. E. Korsukov, and V. S. Kuksenko, Sov. Phys. Solid State **13**, 1680 (1972).
13. V. R. Regel and A. I. Slutsker, Trans. St. Petersburg Acad. Sci. Strength Probl. **1**, 226 (1997).
14. D. K. Roylance, PhD Dissertation (Univ. of Utah, 1968).
15. J. Becht and H. Fischer, Kolloid. Z. Z. Polym. **229**, 167 (1969).
16. H. H. Kausch and D. Langbein, J. Polym. Sci., Polym. Phys. Ed. **11**, 1201 (1973).
17. *Molecular Mobility and Toughness of Polymers*, Ed. by H. H. Kausch, Adv. Polym. Sci. (in press).
18. C. Creton, E. J. Kramer, H. R. Brown, and C.-Y. Hui, Adv. Polym. Sci. **156**, 53 (2002).
19. D. T. Grubb, in *Materials Science and Technology: A Comprehensive Treatment*, Ed. by R. W. Cahn, P. Haasen, and E. J. Kramer, Vol. 12: *Structure and Properties of Polymers*, Ed. by E. L. Thomas (VCH, Weinheim, 1993), Chap. 7.
20. H. H. Kausch, R. Gensler, C. Grein, C. J. G. Plummer, and P. Scaramuzzino, J. Macromol. Sci. B **38**, 803 (1999).
21. K. J. Friedland, V. A. Marikhin, L. P. Myasnikova, and V. I. Vettegren, J. Polym. Sci., Polym. Symp. **58**, 185 (1977).
22. V. A. Marikhin, Acta Polym. **30**, 507 (1979).
23. S. V. Bronnikov, V. I. Vettegren, and S. Y. Frenkel, Adv. Polym. Sci. **125**, 103 (1996).
24. V. I. Vettegren, A. D. Gabaraeva, and N. L. Zaalishvili, Polym. Sci., Ser. A **43**, 608 (2001).
25. L. P. Myasnikova, V. A. Marikhin, E. M. Ivan'kova, and P. N. Yakushev, J. Macromol. Sci., Phys. B **40**, 473 (2001).
26. V. A. Marikhin, L. P. Myasnikova, E. S. Tsobkallo, and V. V. Vasilieva, J. Macromol. Sci., Phys. B **42**, 939 (2003).
27. P. M. Pakhomov, S. Khizhnyak, H. Reuter, V. Galitsyn, and A. Tshmel, Polymer **44**, 4651 (2003).
28. K. Jud, H. H. Kausch, and G. J. Williams, J. Mater. Sci. **16**, 204 (1981).
29. R. P. Wool and K. Connor, Appl. Phys. **52**, 5194 (1981).
30. H. R. Brown, Annu. Rev. Mater. Sci. **21**, 463 (1991).
31. J.-E. Zanetto, C. J. G. Plummer, P.-E. Bourban, J.-A. E. Månson, and J. Hilborn, Polymer **39**, 5939 (1998).
32. H. H. Kausch, P.-E. Bourban, J.-A. Manson, and C. J. G. Plummer, in *PPS 18* (Guimaraes, Portugal, 2002).
33. P. G. de Gennes, *Scaling Concepts in the Physics of Polymers* (Cornell Univ. Press, Ithaca, New York, 1979; Mir, Moscow, 1982).
34. H. H. Kausch, J. Hilborn, and C. J. G. Plummer, in *Proceedings of First International Congress on Adhesion Science and Technology, Mittal-Festschrift*, Ed. by W. J. van Ooij and H. R. Anderson, Jr. (VSP, Utrecht, the Netherlands, 1998).
35. R. P. Wool, *Polymer Interfaces: Structure and Strength* (Hanser, Munich, 1995).
36. L. Berger and H. H. Kausch, Polymer **44**, 5877 (2003).
37. R. S. Porter and L. H. Wang, J. Macromol. Sci. Rev. Macromol. Chem. Phys. C **35**, 63 (1995).
38. G. K. Elyashevich, E. A. Karpov, O. V. Kudasheva, and Eyu Rosova, Mech. Time-Depend. Mater. **3**, 319 (1999).
39. R. J. Young, in *Polymer Spectroscopy*, Ed. by A. H. Fawcett (Wiley, Chichester, 1996).
40. L. P. Myasnikova, V. A. Marikhin, E. M. Ivan'kova, and P. N. Yakushev, J. Macromol. Sci., Phys. B **38**, 859 (1999).
41. V. I. Vettegren, V. A. Marikhin, L. P. Myasnikova, E. M. Ivan'kova, and P. N. Yakushev, Tech. Phys. Lett. **29**, 848 (2003).
42. J. A. H. M. Moonen, W. A. C. Roovers, R. J. Meier, and B. J. Kip, J. Polym. Sci., Polym. Phys. Ed. **30**, 361 (1992).
43. D. Wang, A. A. K. Klaassen, G. E. Janssen, E. de Boer, and R. J. Meier, Polymer **36**, 4193 (1995).

Physics of the Solid State, Vol. 47, No. 5, 2005, pp. 942–948. Translated from Fizika Tverdogo Tela, Vol. 47, No. 5, 2005, pp. 914–919.

Molecular Dynamics and Strengthening of Liquid-Crystal Polymers

E. A. Egorov and V. V. Zhizhenkov

Ioffe Physicotechnical Institute, Russian Academy of Sciences, Politekhnicheskaya ul. 26, St. Petersburg, 194021 Russia

e-mail: evg.egorov@mail.ioffe.ru

Abstract—The role of large-scale molecular motion in the self-organization and strengthening of liquid-crystal polymer fibers is discussed. It is shown that, at high temperatures, these objects are oriented liquid-crystal melts in which macromolecules remain extended but execute high-frequency conformational motions without leaving the tube approximately 20 Å in diameter. This large-scale motion is referred to as quasi-segmental motion. During annealing, the chains involved in quasi-segmental motion can accomplish longitudinal displacements (reptate) over considerable distances. It is this reptation that favors spontaneous self-organization and, consequently, strengthening of liquid-crystal polymer fibers upon heat treatment. The role played by the quasi-segmental motion of rigid macromolecules in the strengthening of polymers of different types is compared with the role played by the segmental motion of flexible chains in this process. © *2005 Pleiades Publishing, Inc.*

1. As a rule, polymers are strengthened by forming a polymer structure that provides a more uniform distribution of an external load over macromolecules. Orientation stretching is the most efficient method for strengthening flexible-chain polymer fibers. This method involves stretching of polymer fibers under external loads at elevated temperatures that are higher than the glass transition point [1]. The parallel alignment of chains obtained after the orientation stretching is fixed upon cooling due to the glass transition and crystallization. From analyzing the orientation stretching, it can be inferred that the internal ordering is not ensured by the tensile force itself, which, however, determines the energetically favorable, preferred direction in the system. In turn, the alignment of chains along this direction is provided by the thermal large-scale segmental motion of flexible macromolecules. In a polymer, chains are entangled and their disentanglement requires that the macromolecular segments move in directions not aligned with the direction of the external force [2]. For an efficient strengthening of flexible-chain polymers, it is necessary to attain an optimum ratio of the stretching rate to the rate of rapid segmental motion. In this case, an important role is played by the "mechanical vitrification" effect revealed by Zhurkov and Egorov [3]. This effect manifests itself in a retardation of the segmental motion in the field of an external tensile force. The inclusion of the mechanical vitrification effect makes it possible to establish a quantitative relationship between the draw ratio and the rate of stretching of crystallizable flexible-chain polymer fibers [4]. The segmental motion of flexible macromolecules has been widely investigated theoretically and experimentally [5].

2. Rigid-chain liquid-crystal polymers have been extensively studied over the last twenty years [6]. The large-scale motion of macromolecules in these polymers also plays an important role in structural rearrangements and strengthening. However, in this case, the motion of rigid liquid-crystal chains (especially those containing no flexible fragments, i.e., spacers) differs significantly from the conformational segmental motion of flexible macromolecules. Liquid-crystal polymer fibers can be easily prepared in an oriented state with an orientation factor of 0.9 [7]. After special heat treatment (annealing) of these "initial" fibers, their tensile strength can increase by several factors [8]. Annealing is prolonged (for several hours) heating of fibers with a stepwise increase in temperature. The main, final annealing stage is accomplished at the thermotropic phase transition temperature of the initial fiber, i.e., at the temperature of the phase transition to the liquid-crystal melt.

The highly oriented liquid-crystal melt is a specific state of the material. In this state, macromolecules remain extended (do not tend to coil up, as is the case with flexible chains) and mutually oriented, the orientation factor virtually does not decrease, and fragments of neighboring macromolecules gain the capacity to move with respect to each other. Oriented fibers in the liquid-crystal melt retain their shape but have zero strength; i.e., they flow under the smallest load (for example, under gravity). It cannot be doubted that the spontaneous strengthening of liquid-crystal polymers upon annealing is also substantially affected by the molecular mobility. However, up to now, the characteristic features of large-scale molecular motion in this specific case have not been adequately studied. The liquid-crys-

1063-7834/05/4705-0942$26.00 © 2005 Pleiades Publishing, Inc.

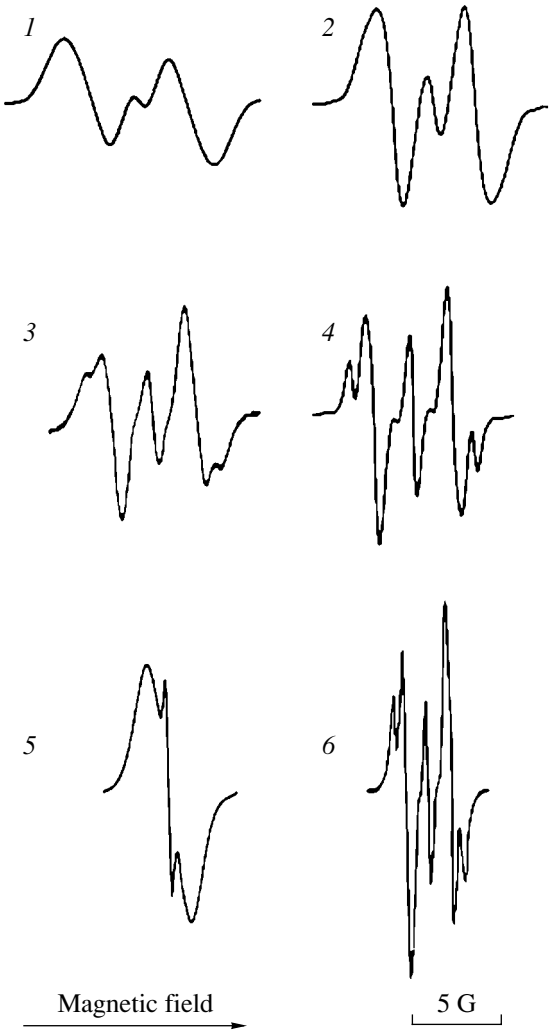

Fig. 1. NMR spectra (the first derivatives of the absorption signal with respect to the magnetic field) of Vectra fibers at temperatures T = (*1*) 20, (*2*) 150, (*3*) 250, and (*4–6*) 280°C and for orientation angles θ with respect to the magnetic field. θ = (*1–4*) 0°, (*5*) 54.7° (magic angle [15]), and (*6*) 90°.

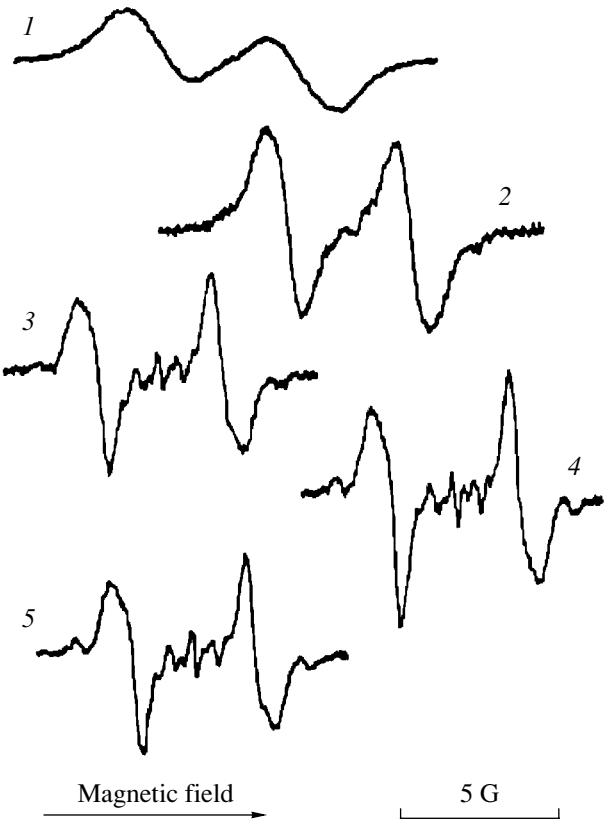

Fig. 2. NMR spectra (the first derivatives of the absorption signal with respect to the magnetic field) of Ultrax fibers (θ = 0°) at temperatures T = (*1*) 20, (*2*) 210, (*3*) 235, (*4*) 250, and (*5*) 275°C.

tal melt exhibits properties of both a solid and a liquid and retains a high structural and dynamic anisotropy.

In low-molecular thermotropic liquid crystals, the phase transition from a solid state to a liquid-crystal melt occurs in a very narrow temperature range; i.e., it is a first-order phase transition [9]. In liquid-crystal polymers, the melting proceeds over a wide temperature range due to a complex sequence of phase and relaxation transitions that are characteristic of high-molecular compounds in the course of heating [10]. It was revealed that, unlike flexible chains, chains in a liquid-crystal polymer melt remain extended and mutually oriented but can move with respect to each other. This motion leads not to a chaotic arrangement but, contrastingly, to an increase in the degree of ordering and, as a consequence, to an increase in the tensile strength.

3. Over the last several years, we have performed systematic investigations into the large-scale motion of rigid macromolecules in the liquid-crystal state. In this paper, we describe one of the stages of these investigations. It was shown that broad-line ^{1}H NMR spectroscopy is an efficient tool for studying the large-scale motion of rigid macromolecules in the liquid-crystal state [11–14]. Upon transition of a polymer to the state of a liquid-crystal melt, the NMR spectra remain broad (as is the case with the NMR spectra of solids), but there arise a number of components located symmetrically with respect to the center. As is known, the NMR spectrum of a melt of flexible-chain polymers (or other non-liquid-crystal materials) is a narrow singlet [15]. The broad NMR spectrum exhibits a fine structure in the range from temperatures of the solid state to temperatures of the transition to the liquid-crystal melt. Figures 1 and 2 show typical examples of the evolution of the NMR spectra for highly oriented fibers of two fully aromatic thermotropic liquid-crystal copolyesters with an increase in the temperature. In these polymers (Vectra A950, Hoechst–Celanese; Ultrax 4002, BASF), the chains do not contain flexible spacers and the resonant nuclei (protons) are involved only in mesogenic

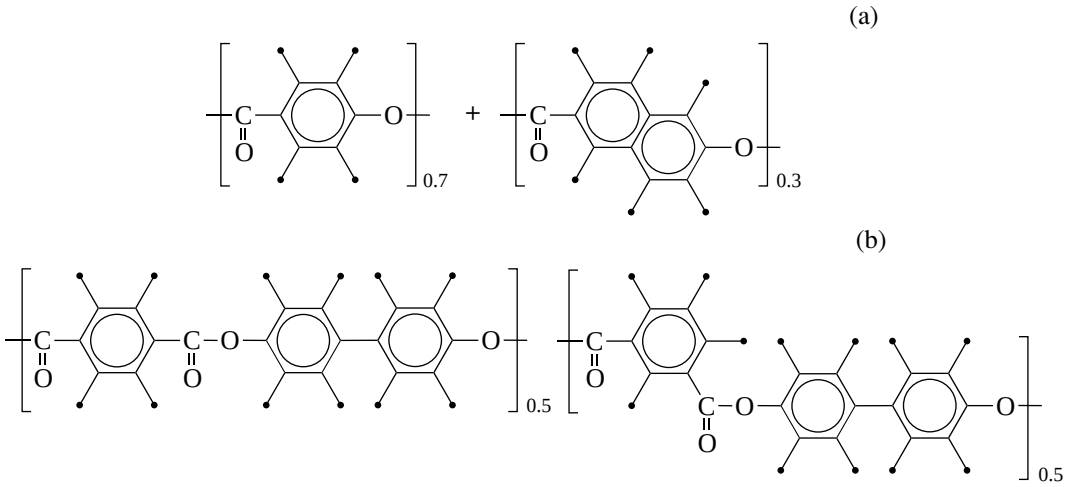

Fig. 3. Chemical formulas of (a) Vectra A950 and (b) Ultrax 4002 copolyesters. Points indicate hydrogen atoms.

groups. The chemical formulas of these compounds are presented in Figs. 3a and 3b, respectively.

Moreover, the NMR spectra shown in Fig. 1 illustrate the manifestation of the anisotropy of the liquid-crystal melt at different angles θ between the fiber axis and the magnetic field at a temperature of 280°C.

The NMR spectra of other liquid-crystal polymers are described in [13]. The Vectra copolyester proved to be most appropriate for detailed investigation of the chain motion. The choice of this copolyester was made for the reasons discussed in our previous work [14]. The considerable interest expressed in the Ultrax fibers stems from the fact that their NMR spectra exhibit an ultrafine structure (Fig. 2). This structure permits one to judge not only the specific features in the motion of an individual metaphenylene ring of the macromolecule in the melt but also the capabilities of the method used. The NMR spectra shown in Figs. 1 and 2 were recorded in the form of the first derivative of the NMR absorption signal with respect to the magnetic field [15]. This makes it possible to reveal the fine structure in a more explicit form.

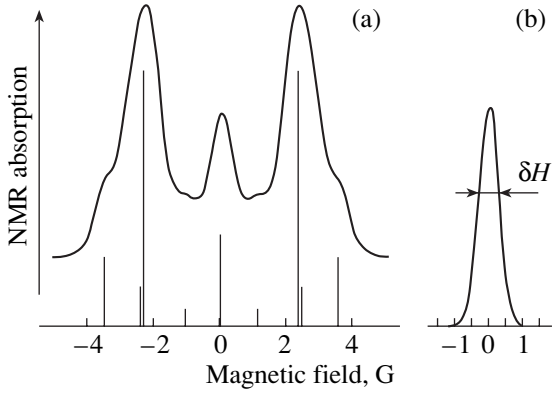

Fig. 4. (a) NMR absorption spectrum of Vectra fibers (the original spectrum corresponds to spectrum *4* in Fig. 1) at temperature $T = 280°C$ and for orientation angle $\theta = 0°$. Vertical lines indicate the calculated components of the spectrum. (b) Individual NMR component broadened in accordance with the Gaussian distribution law due to the residual intermolecular magnetic interaction is shown on an enlarged scale.

The data on the macromolecular motion in the liquid-crystal melt were obtained from the analysis of the spectral line shape rather than from traditional calculations of the second moments [7], because, in the latter case, unique information associated with the multicomponent structure of the spectrum would be lost. The vector magnetic dipole–dipole interaction of protons weakens rather rapidly as the distance increases. The spectra of isolated single protons and groups consisting of two and three protons in the absence of interaction between the groups should involve one, two, and seven lines, respectively [15]. In a solid polymer, the interaction between the groups is relatively strong and leads to smearing of the fine structure in the spectra. Upon transition to the melt, chain fragments rapidly move with respect to each other. As a consequence, the contribution from the interaction between the groups drastically decreases and the interaction of protons inside the groups becomes dominant and determines the shape of the spectrum. The appearance of the fine structure indicates that the polymer undergoes a transition to the liquid-crystal melt. The NMR spectrum of the oriented liquid-crystal melt can be likened to a spectrum of the hypothetical oriented solid polymer in which the intermolecular magnetic interaction of protons is absent and all oriented chains are bent only slightly. This bending should simulate a time-average insignificant deviation

of the fragments from the orientation axis due to the conformational motion of the macromolecules.

The separations between components in the spectrum and their intensities can be exactly calculated for specified distances between protons in the group (the data are taken from the literature) and for time-average orientations of the internuclear vectors with respect to the magnetic field of the spectrometer [16, 17]. The time-average orientations are determined by the angular amplitude φ_0 of vibrations of the chain fragments with respect to the fiber axis, i.e., by the high-frequency conformational motions of the chain. In order to simplify the calculations, we analyzed the spectra of fibers aligned along the magnetic field of the spectrometer ($\theta = 0°$). Figure 4a depicts the NMR absorption spectrum of the initial (unannealed) Vectra fibers at T = 280°C and $\theta = 0°$. This spectrum corresponds to spectrum *4* in Fig. 1, which was recorded in the form of the first derivative of the absorption signal with respect to the magnetic field. At a temperature of 280°C, the polymer completely transforms into the liquid-crystal melt. All nine spectral components (two components attributed to the pairs of protons in the phenylene rings and seven components assigned to the triads in the naphthalene rings) turned out to be well resolved. These components in Fig. 4a are indicated by vertical segments. The height of the vertical segment is proportional to the intensity of the spectral component. The NMR absorption spectrum can be represented as the sum of individual lines, each broadened in accordance with the Gaussian distribution law due to the residual intermolecular magnetic interaction. Figure 4b shows one (any) of the above spectral components on an enlarged scale. The width δH of the spectral component is determined by the residual (not averaged) interchain magnetic interaction (i.e., it accounts for the rate at which the chain fragments move with respect to each other in the oriented melt), and the position of the center of this component corresponds to the position of the line in Fig. 4a. The theoretical spectrum can be fitted to the experimental spectrum fairly well by using the iterative method (by varying the angular amplitude φ_0). Then, the angular amplitude φ_0 of fast vibrations of the chain fragments with respect to the orientation axis can be determined from analyzing the positions of the spectral components and their intensity ratios. These vibrations occur in the planes passing through the orientation axis of the fiber. Such chaotic high-frequency relaxation vibrations are accompanied by rotational motions of the chain fragments. This is confirmed by the spectra recorded for different orientations of fibers with respect to the magnetic field of the spectrometer [12, 13]. As a result, the chain moves like a snake in a tube. According to the estimates, the angular amplitude φ_0 does not exceed 30° (the value of φ_0 for the naphthalene fragments is slightly less than that for the phenylene fragments). The time-average degree of extension of the chains in the melt (the ratio of the end-to-end distance to the contour length) is equal to the average of $\cos\varphi$ and turns out to be greater than 0.9. This indicates a high degree of orientation of the macromolecules in the melt. The fact that, during their motion, the chain fragments cannot deviate from the orientation axis by more than 30° is associated with the spatial constraints imposed on the conformational motion of the chains: this motion can be simulated as a process occurring within a virtual nanotube (approximately 20 Å in diameter) oriented along the fiber axis (Fig. 5) [14]. The constrained conformational motion of chains is referred to as quasi-segmental motion [12, 13]. The spatial constraints in directions perpendicular to the orientation axis reflect the liquid-crystal nature of the melt: a preferred direction along which self-organization processes can proceed in the system arises without an external action.

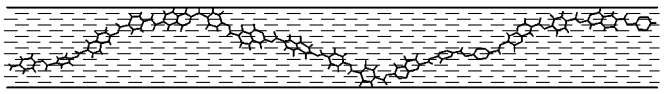

Fig. 5. Model of the quasi-segmental motion of a macromolecule.

4. Quasi-segmental motion leads to averaging of the intermolecular magnetic interaction of protons. This implies that the chain conformation changes continuously and rapidly (with a characteristic time of no longer than 10^{-5} s) [15]. Therefore, by analogy with flexible-chain polymers, it is expedient to consider the probability that the macromolecules as a whole can execute a slow diffusion motion (reptation) along the orientation axis of the fiber. According to the reptation models based on the concepts developed by Edwards and de Gennes (see, for example, [2, 5, 18, 19]), flexible chains in true melts reptate along wide spatially bent tubes formed by cross links, knots, and other steric long-lived obstacles. Owing to the segmental motion of a flexible chain in a tube, there can stochastically arise local "excess lengths" (local density increments), which then move along the axis of the bent tube according to the statistical laws. It is believed that these elementary events provide mass transfer; i.e., there occurs diffusion of the center of gravity of the chain along the tube (like the motion of a Brownian particle).

We took into account the specific features of our model: (i) the tube is rather narrow, and (ii) the diffusion and reptation motions of chains occur along the same straight line. The quasi-segmental motion of a chain can also bring about the formation of moving regions with an increased density. Consequently, the mechanism responsible for the diffusion of an extended, continuously bending chain along the tube should not differ radically from that described in [2, 18, 19]. Let us consider an individual "particular" chain similar to that depicted in Fig. 5. According to de Gennes [2], the real chain can be replaced by a model chain consisting of $N + 1$ bound balls of radius a. The

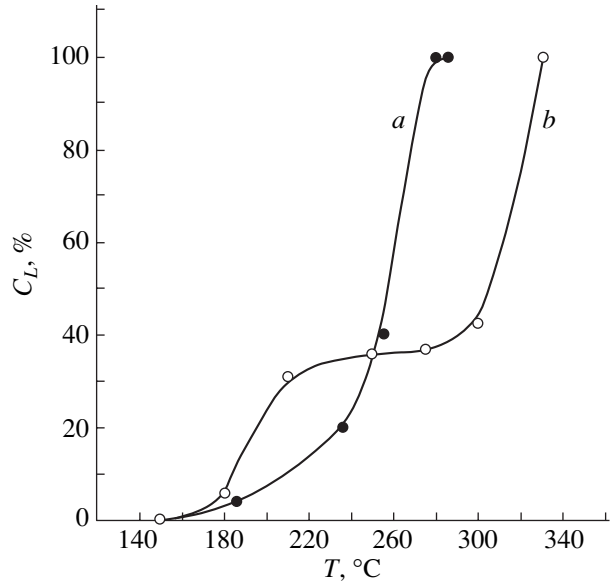

Fig. 6. "Defreezing" of the quasi-segmental motion of the (*a*) initial and (*b*) heat-treated Vectra fibers.

lengths of all N chain units (the distances between the balls) are assumed to be identical. The diffusion of this chain, irrespective of the tube shape, can be described by formula (8.11) taken from [2]:

$$\langle x^2 \rangle = (kT/3\pi\eta aN)t, \qquad (1)$$

where $\langle x^2 \rangle$ is the mean-square displacement of the center of gravity of the particular chain for a time t, k is the Boltzmann constant, T is the absolute temperature, and η is the effective viscosity of the medium in which this chain executes motion.

If each chain were to move in its own tube, the density of the material would be one order of magnitude lower than the real density (this circumstance has often been disregarded in theoretical models). Therefore, the tube walls are permeable to neighbors. Let us assume that, apart from the particular chain, units of the moving neighboring chains can also penetrate into the tube. It is these units that form the medium. The rate of high-frequency motion of the chain units is considerably higher than that of the chain as a whole. The interaction of fragments of the medium with the chain is a short-range interaction that weakens rapidly along the chain. Hence, as a first approximation, we can ignore the chain structure of the medium. Then, from the standpoint of the resistance to reptation motion of the particular chain, the medium can be treated as a low-molecular liquid. Next, it is necessary to estimate the viscosity η of this liquid.

Probable displacements of the model chain for different times

t, s	X, Å
10^{-4}	0.6
1	62
60	480
3600	3700
18000	8300

According to the theory of nuclear magnetic resonance, the absorption line of a liquid is very narrow. The linewidth δH is proportional to the ratio of the viscosity η to the temperature T [20]. It is assumed that this relationship holds for individual spectral components (Fig. 4b) whose width is equal to 0.6 G. The viscosity of the medium can be approximately estimated from the experimental dependence $\delta H = f(\eta/T)$ obtained in [20] (see also [15, Fig. 32). As follows from this dependence, the linewidth $\delta H = 0.6$ G corresponds to the ratio $\eta/T = 4.3$. The temperature of the liquid-crystal melt is equal to 553 K. Therefore, the viscosity is estimated as $\eta = 2400$ P. This estimate of the viscosity η is quite reasonable for the medium. The parameters used in the calculation according to formula (1) are chosen as follows. The ball radius is taken to be $a = 3$ Å (this value is close to the mean size of the naphthalene and phenylene rings). Since the molecular mass of the Vectra polymer is approximately equal to 20000, the mass of the medium-sized monomer unit is 135, and one monomer unit contains two balls, we set $N = 300$. As a result, we have

$$\langle x^2 \rangle = 3.8 \times 10^3 t \ [\text{Å}^2]. \qquad (2)$$

The quantity $X = (\langle x^2 \rangle)^{1/2}$ has often been considered a measure of the mean displacement [2]. However, it must be kept in mind that this quantity has a more precise meaning: in the case of the normal (Gaussian) distribution, the chain can be displaced for a time t_i over a distance X_i or greater with a probability of 0.3174. The probable displacements of the model chain due to the thermal quasi-segmental motion in an oriented liquid-crystal melt for different times were calculated according to relationship (2). The results of these calculations are given in the table. The data presented in the last row of the table correspond to a time of 5 h, which is the mean time of heat treatment of the initial Vectra fibers at high temperatures.

As can be seen from the table, the reptation rates turned out to be rather high on the molecular scale. Upon heat treatment of the initial fibers, the order is fixed due to the formation of three-dimensional crystals in which rapid quasi-segmental motion of chains is absent. According to Antipov *et al.* [21], the degree of crystallinity in the Vectra fibers subjected to annealing increases from ~5 to 30%. It is evident that, in an oriented liquid-crystal melt, the walks of chains in one direction favor their mutual adjustment. The long time required for efficient heat treatment at rather high reptation rates of macromolecules can be explained as fol-

lows. For a stable crystallite to be formed at a high temperature, the sufficiently large number of macromolecular fragments in the appropriate mutual arrangement must meet simultaneously (the probability of this meeting can be estimated). The formation of crystallites should lead to a decrease in the reptational mobility of chains in the system. This is confirmed in the experiments.

5. Let us now introduce the parameter C_L equal to the fraction of microregions in the liquid-crystal melt at a specified temperature. It can be seen from Fig. 1 (from the appearance of the ultrafine structure in the spectrum) that the quasi-segmental motion is gradually "defrozen" as the temperature increases. At 150°C (Fig. 1, spectrum *2*), the quasi-segmental motion is frozen over the entire volume ($C_L = 0$). At 280°C (Fig. 1, spectrum *4*), the melting is completed: $C_L = 100\%$. The spectrum measured at intermediate temperatures can be represented as the sum of the aforementioned two spectra (Fig. 1, spectra *2* and *4*) taken with the corresponding weights; as a result, we can determine the dependence $C_L(T)$ [22]. The dependence of the parameter C_L on the temperature (up to 280°C) for the initial fibers (not strengthened by heat treatment) is shown by curve *a* in Fig. 6. Heating of these fibers to higher temperatures (300°C and higher) leads to disorientation of the liquid-crystal domains, even though each domain retains the liquid-crystal order [22]. This overheating leads to a sharp decrease in the strength. The dependence of the parameter C_L for the fibers heat treated under the conditions providing the maximum strengthening is depicted by curve *b* in Fig. 6. In this case, the parameter C_L also increases beginning from a temperature of 150°C but does not exceed 35% up to the maximum annealing temperature (280°C). Solid regions occupy 65% of the volume, and, as was noted above, the degree of crystallinity of the sample is no higher than 30% [21]. Consequently, as the degree of crystallinity increases in the course of annealing, the quasi-segmental mobility decreases not only in crystals but also in a considerable number of noncrystalline microregions. This should result in a retardation of the reptation motions of the chains and, hence, in suppression of the self-organization and strengthening of the fibers. The effect under consideration is qualitatively similar to the effect of the mechanical vitrification on the strengthening of flexible-chain polymers during orientation stretching [4]. Owing to the spontaneous processes occurring in the course of annealing, the strength of oriented Vectra fibers can increase from 1.3 to 2.8 GPa. An increase in the temperature above the annealing temperature (280°C) leads to a further defreezing of the macromolecular motion (Fig. 6, curve *b*), and the parameter C_L at 330°C reaches 100%. The strengthened sample (like the initial sample at 280°C) completely transforms into the nematic liquid-crystal melt [21] retaining a high degree of orientation ordering. Seemingly, it can be expected that the self-organization and strengthening processes will continue to occur. However, the fibers cannot be held under these conditions for a long time to additionally increase their strength because of the onset of thermal destruction and disorientation of domains. Upon short-term holding of the annealed sample at 330°C, it does not undergo noticeable irreversible transformations. It is interesting to note that the homogeneous nematic melt retains "memory" about its own thermal prehistory. The nature of this memory was discussed in our recent paper [22].

In conclusion, it should be noted that, despite the substantial differences between the quasi-segmental motion of rigid chains and the true segmental motion of flexible chains, the large-scale conformational motion plays an identical role in the strengthening of polymers of these classes. The fundamental difference lies in the fact that, during strengthening, the preferred direction of structural transformations in flexible-chain polymers is determined by external forces, whereas the preferred direction of transformations in liquid-crystal polymers is governed by an internal factor, i.e., by the interaction of mesogenic groups [6].

ACKNOWLEDGMENTS

This work was supported by the Russian Foundation for Basic Research, project no. 03-03-32589.

REFERENCES

1. V. A. Marikhin and L. P. Myasnikova, *Supramolecular Structure of Polymers* (Khimiya, Leningrad, 1977) [in Russian].
2. P. de Gennes, *Scaling Concepts in Polymer Physics* (Cornell Univ. Press, Ithaca, 1979; Mir, Moscow, 1982).
3. S. N. Zhurkov and E. A. Egorov, Dokl. Akad. Nauk SSSR **152** (5), 1155 (1963).
4. E. A. Egorov and V. V. Zhizhenkov, Vysokomol. Soedin., Ser. A **31** (2), 398 (1989).
5. Yu. Ya. Gotlib, A. A. Darinskiĭ, and Yu. E. Svetlov, *Physical Kinetics of Macromolecules* (Khimiya, Leningrad, 1986) [in Russian].
6. *Liquid-Crystal Polymers*, Ed. by N. A. Platé (Khimiya, Moscow, 1988; Plenum, New York, 1993).
7. R. A. Allen and I. M. Ward, Polymer **32** (2), 202 (1991).
8. A. V. Savitskiĭ, A. Yu. Bilibin, and I. A. Gorshkova, Vysokomol. Soedin., Ser. A **34** (8), 143 (1992).
9. *Physical Encyclopedic Dictionary* (Sovetskaya Éntsiklopediya, Moscow, 1962), Vol. 2, p. 14 [in Russian].
10. N. A. Platé, V. G. Kulichikhin, and E. M. Antipov, Vysokomol. Soedin., Ser. A **35** (11), 1943 (1993).
11. E. A. Egorov, A. V. Savitski, V. V. Zhizhenkov, and I. A. Gorshkova, Fiz. Tverd. Tela (St. Petersburg) **41** (5), 859 (1999) [Phys. Solid State **41**, 777 (1999)].
12. E. A. Egorov, V. V. Zhizhenkov, I. A. Gorshkova, and A. V. Savitsky, Polymer **40** (13), 3891 (1999).

13. E. A. Egorov and V. V. Zhizhenkov, Vysokomol. Soedin., Ser. A **44** (7), 1119 (2002).
14. E. A. Egorov and V. V. Zhizhenkov, Vysokomol. Soedin., Ser. B **46** (11), 1965 (2004).
15. E. R. Andrew, *Nuclear Magnetic Resonance* (Cambridge Univ. Press, London, 1955; Inostrannaya Literatura, Moscow, 1957).
16. G. E. Pake, J. Chem. Phys. **16** (4), 327 (1948).
17. E. R. Andrew and R. Bersohn, J. Chem. Phys. **18** (2), 159 (1950).
18. M. Doi and S. F. Edwards, *The Theory of Polymer Dynamics* (Clarendon, Oxford, 1986; Mir, Moscow, 1998).
19. A. I. Maklakov, V. D. Skirda, and N. F. Fatkullin, *Self-Diffusion in Solutions and Melts of Polymers* (Kazan. Gos. Univ., Kazan, 1987) [in Russian].
20. N. Blombergen, E. M. Purcell, and R. V. Pound, Phys. Rev. **73**, 679 (1948).
21. E. M. Antipov, S. D. Artamonova, I. A. Volegova, and Yu. K. Godovskiĭ, Vysokomol. Soedin., Ser. A **37** (5), 800 (1995).
22. E. A. Egorov, V. V. Zhizhenkov, I. A. Gorshkova, and A. V. Savitskii, Vysokomol. Soedin., Ser. A **46** (8), 1312 (2004).

Translated by O. Borovik-Romanova

Physics of the Solid State, Vol. 47, No. 5, 2005, pp. 949–953. Translated from Fizika Tverdogo Tela, Vol. 47, No. 5, 2005, pp. 920–923.

Structural Heterogeneity and Jumplike Deformation of Polymers on the Mesoscopic Level

N. N. Peschanskaya*, P. N. Yakushev*, V. A. Bershteĭn*, M. Keating, and T. Krizan****

** Ioffe Physicotechnical Institute, Russian Academy of Sciences, Politekhnicheskaya ul. 26, St. Petersburg, 194021 Russia*

*** E.I. Du Pont de Nemours & Company, Experimental Station, Wilmington, Delaware, 19880-323 USA*

e-mail: yak@pav.ioffe.ru

Abstract—This paper reports on the results of research into the jumplike deformation of two polymers based on poly(oxymethylene) (POM) with structural aggregates (spherulites) of different micrometer-scale sizes at a temperature of 290 K, as well as of polyimide (PI) and a PI + graphite composite at temperatures of 290 and 690 K. The creep rate under compression is measured with a laser interferometer in 0.3-μm deformation increments. It is found that, in the course of deformation on the micrometer scale, the creep rate varies nonmonotonically. Periodic variations of the creep rate correspond to a jumplike (stepwise) behavior of the creep. It is shown that the mean jumps in the microdeformation correspond to the mean sizes of poly(oxymethylene) grains and graphite particles in polyimide. The results obtained are in agreement with previously drawn conclusions: the deformation jumps are determined by the scale of ordered microaggregates typical of the structure under investigation. © *2005 Pleiades Publishing, Inc.*

1. INTRODUCTION

Numerous experiments with amorphous and amorphous–crystalline polymers [1–12] have demonstrated that jumplike deformation on the micrometer (mesoscopic) level can be associated with the alternation of strong and weak interactions between molecular structural units in polymers. The results obtained do not contradict the concept that jumps, i.e., cooperative microdisplacements, are determined by the sizes of ordered aggregates in real inhomogeneous media [6–12]. It is well known that structural inhomogeneities of polymers, as a rule, have no sharp boundaries and that the degree of their ordering is not very high even in crystallizing polymers [13–15]. Consequently, the sizes of structural units are difficult to determine accurately. The sizes of globules and microfibrils are estimated at several micrometers, whereas the sizes of fibrils, macrofibrils, and spherulites are estimated at several micrometers and several tens or even several hundreds of micrometers. In recent years, the formation of ordered microregions in amorphous media has been explained in terms of synergetics [16]. In synergetics, a structure is determined by the coherent behavior of a large number of particles due to their self-organization in response to fluctuations. Creep can be considered as a process of self-organization of the structure. Therefore, one should take into account that jumps in the microdeformation can be determined not only by stable structural units but also by those formed in the course of deformation. In our previous works [5–12], we studied the nature of the jumps in deformation by using estimates available in the literature for the sizes of globules and fibrils, as well as by modifying the structure under preliminary deformation [5, 6, 10] and using plasticization [9], magnetic fields [11, 12], and chemical joining [6] to exert an effect on the intermolecular interaction.

In this work, the objects of investigation involve controlled structural inhomogeneities of micrometer-scale sizes. This makes it possible to compare directly the sizes of inhomogeneities with the jumps in the deformation and to draw more convincing conclusions.

2. MATERIALS AND EXPERIMENTAL TECHNIQUE

In order to verify the inference made previously that jumps in the deformation depend on the sizes of the structural inhomogeneities, we used specimens of the following amorphous–crystalline polymers: poly(oxymethylene) (POM5), a copolymer of oxymethylene with oxyethylene (POM3), pure polyimide (PI), and polyimide with a filler in the form of graphite particles. The specimens were purchased from Du Pont de Nemours & Company (USA). The analysis of the polarizing microscope images of POM5 and POM3 revealed that POM5 predominantly contains small-sized grains (spherulites) 1–5 μm in diameter, whereas POM3 consists of small-sized and larger sized grains (from approximately 1 to 25 μm). The particles of the graphite filler in polyimide were several micrometers in size.

Poly(oxymethylene) was tested at a temperature of 290 K, and polyimide was examined at temperatures of 290 and 600 K. Testing was performed using cylindri-

1063-7834/05/4705-0949$26.00 © 2005 Pleiades Publishing, Inc.

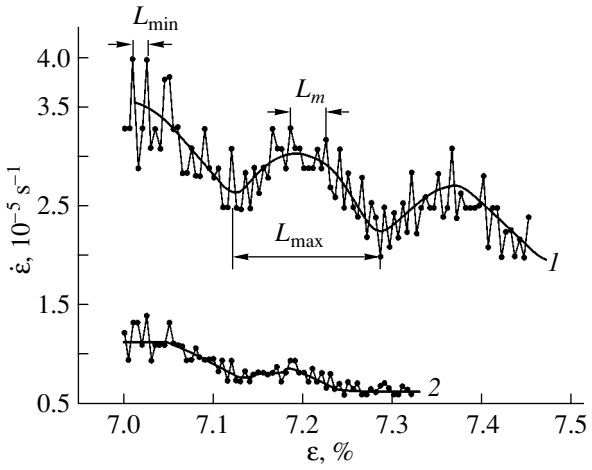

Fig. 1. Variations of the creep rate $\dot{\varepsilon}$ in narrow ranges of creep strains ε in the course of creep of poly(oxymethylene): (*1*) POM3 and (*2*) POM5. Points are obtained in 0.3-μm deformation increments. T = 290 K, σ = 70 MPa.

cal specimens 6 mm in height and 3 mm in diameter. The creep under compression was recorded on a laser interferometer [1–12] in the form of a sequence of beats. Each beat corresponds to a deformation increment of 0.3 μm, and the frequency of interferometer beats is proportional to the creep rate. In order to avoid considerable distortions of the initial structure, the creep rate was measured at the initial stage of the creep. In narrow ranges of creep strains (tenths of a percent), the creep rates were calculated in 0.3-μm deformation (0.005% strain) increments according to the formula $\dot{\varepsilon} = \lambda\nu/2l_0$, where $\lambda = 0.63$ μm is the lasing wavelength, ν is the frequency of beats in the interferogram, and l_0 is the length of the specimen. The deformation jump L was determined as the deformational period of creep rate variations in the dependence of the creep rate $\dot{\varepsilon}$ on the creep rate ε.

3. RESULTS AND DISCUSSION

Let us list the available data on the nature of deformation, which are used in the discussion of the results.

The evolution of deformation with time under constant mean stresses is accompanied by molecular rearrangement, which, in turn, leads to continuous variations in the shape and size of the structural units and the specimen. Nonchemical intermolecular (van der Waals, polar, hydrogen-type) interactions between atomic groups of polymer molecules are surmounted in shear events on the molecular level [4, 7]. The experimental results obtained earlier in [5–8] suggest that a significant role in the deformation is played by slightly ordered boundaries between structural units along which there predominantly occur shear displacements. Compression of isotropic polymers most closely corresponds to the deformation and, particularly, to micrometer-scale jumps, because the compression is not attended by tensile stresses responsible for the development of cracks and fracture [7].

As was shown in [5–7, 10], there exist different levels of deformation jumps. Larger jumps arise from smaller jumps, much as large-sized structural aggregates are formed from smaller aggregates. In those works, the compatibility of the scale of deformation jumps with the sizes of structural inhomogeneities was determined primarily from indirect results. In the present work, we used objects with structural aggregates of known micrometer sizes that specify the discreteness in the structure.

Now, we compare the scales of deformation jumps with the sizes of spherulites in two polymers based on poly(oxymethylene). Figure 1 shows typical dependences of the creep rate on the creep strain. It can be seen from these dependences that the creep rate on the micrometer scale varies nonmonotonically with different periods with respect to the creep strain. Each point in the plot corresponds to a deformation increment of 0.3 μm, and the period of creep rate variation is the deformation jump L. As can be seen from Fig. 1, simple small-scale periodic variations are combined into more complex variations with larger periods. Similar constructions were made for different creep strains reached by the specimens in the course of creep. In the entire set of jumps, we separate the smallest (for this procedure) jumps L_{min}, the moderate jumps L_m consisting of simple small jumps, and the most complex jumps L_{max} composed of the smallest and moderate jumps. The table presents jumps L for several macrostrains ε. The smallest jumps L_{min} are determined as the mean of the seven creep rate periods, whereas the larger jumps L_m and L_{max} correspond to single jumps (i.e., to periods of single creep rate variations) in narrow ranges of creep strains ε. It follows from the table that the smallest jumps for both materials are approximately equal to each other and that the moderate and largest jumps (L_m and L_{max}) for the large-grained POM3, on the average, are greater than those for POM5.

Deformation jumps of approximately 1–5 μm correspond to typical grain sizes in both polymers. The appearance of larger jumps (6–25 μm) in the POM3 copolymer corresponds to a larger number of grains of the same scale in this polymer. It also follows from the table that large jumps L_m and L_{max} exhibit a tendency toward an increase as the creep strain ε increases. Most likely, the changes in the jumps can be caused by the fact that the creep deformation occurs through shears initially along the boundaries of small-sized grains and then with the participation of larger sized aggregates. It is also quite possible that, owing to the self-organization of the structure, the creep is accompanied by orientation and transformation of the structure on the mesoscopic level and, for relatively large strains, the jumps will correspond to the sizes of new ordered aggregates rather than to those of the initial grains. In this work, the

Jumps in the deformation on the mesoscopic level for poly(oxymethylene) in different ranges of creep strains ε at a temperature of 300 K and for polyimide with graphite at 600 K

POM5 (fine-grained; spherulite size, 1–5 μm)				POM3 (coarse-grained; spherulite size, 1–25 μm)			
ε, %	L_{min}, μm	L_m, μm	L_{max}, μm	ε, %	L_{min}, μm	L_m, μm	L_{max}, μm
2	0.77	1.5	3.3	2.5	1.0	1.8	3.9
		1.5	3.9			2.1	4.8
							6.6
5.6	0.82	2.7	3.9	4.2	0.85	3.3	12
		2.7	3.9			3.9	5.7
		2.1				3	6.0
		1.8				4.8	
7.0	1.0	1.8	4.8	8.5	1.0	3.6	7.8
		1.8	5.7			4.5	11.1
		2.7	5.7			4.5	10.8
		2.7					
12	0.93	1.5	5.7	10.5	1.23	4.5	15.6
		1.8	4.8			4.5	9.6
		1.8	4.3			3.6	25.5
		3.6	5.7			4.8	7.2
						4.8	8.4

Polyimide with graphite	
Graphite grain size, μm	Jump L, μm
3–4	~4

jumps were compared with the initial structural units. For this reason, we investigated the deformations resulting in insignificant distortions of the initial structure (2–12%).

Let us consider the kinetics of creep on the mesoscopic level for polyimide. Figures 2 and 3 show the periodic variations of the creep rate as a function of the creep strain for polyimide with graphite at temperatures of 600 and 290 K. This composite can be conventionally considered to be a model material in which crystal particles (graphite) of approximately the same size with sharp boundaries are regularly distributed throughout the volume. This polymer exhibits both a more dense packing of molecular segments (clusters, domains, crystallites) and a less dense (amorphous) packing. Since the shears in the course of deformation take place predominantly in polymer layers with a low density along the boundary of denser inhomogeneities, it is assumed that the deformation jumps are determined by the size of these inhomogeneities. It turned out that, at a temperature of 600 K (Fig. 2), the periodic variations of the creep rate have a larger amplitude (large sharpness of the deformation jumps) and approximately the same period (~4 μm), which corresponds to the mean size of graphite particles.

Under conditions of deformation at a temperature of 290 K (Fig. 3a), the creep rate is characterized by less sharp periodic variations with different periods and, hence, different jumps (from 0.6 to 2 μm), which, in some cases, are combined into more complex jumps (~4–5 μm); i.e., the type of periodic variation of the creep rate at a low temperature differs significantly

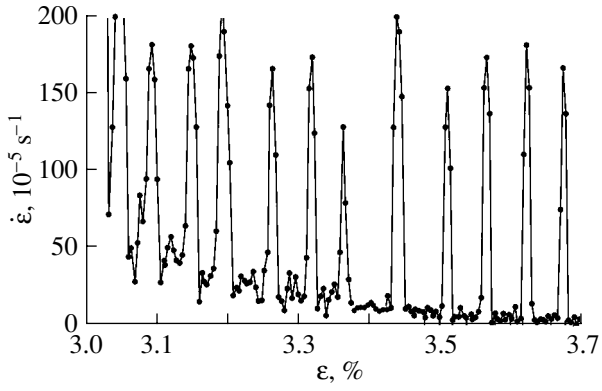

Fig. 2. The same as in Fig. 1 but for polyimide with graphite. T = 600 K, σ = 20 MPa. The creep rate varies with approximately the same period (L = 4 μm), which corresponds to the mean size of graphite particles (see table).

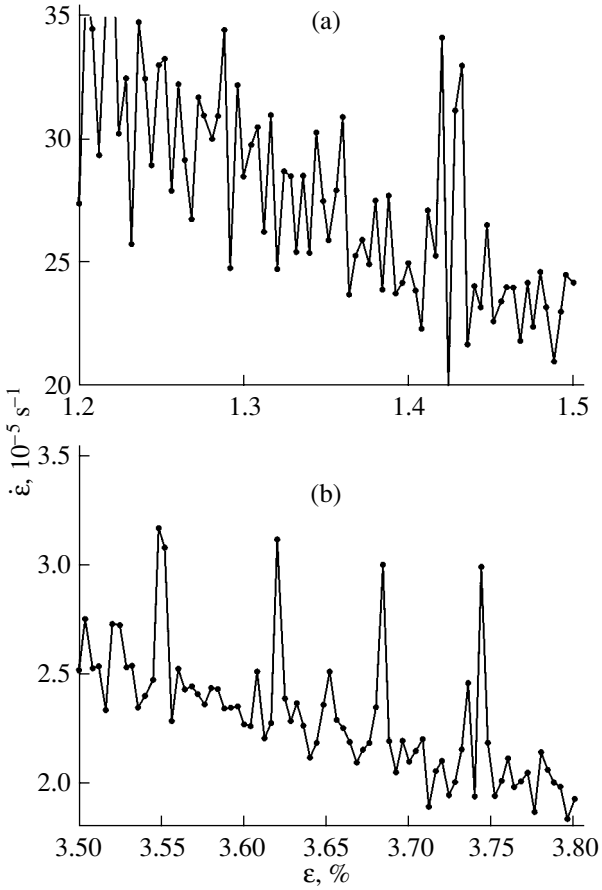

Fig. 3. The same as in Fig. 1 but for polyimide with graphite. T = 290 K, σ = 90 MPa. Illustration of the influence of the creep strain on the variability of the creep rate. Panels (a) and (b) correspond to different ranges of creep strains ε.

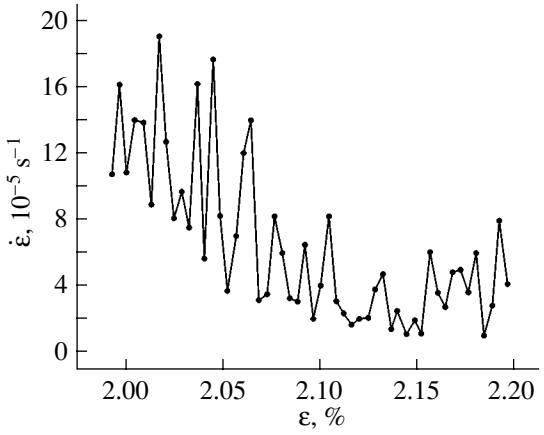

Fig. 4. The same as in Fig. 1 but for pure polyimide. T = 600 K, σ = 20 MPa.

from that observed at a higher temperature of 600 K. As the creep strain increases, the periodic variations of the creep rate become more regular (Fig. 3b) and, in terms of the regularity of the large amplitudes, more closely resemble the periodic variations presented in Fig. 2. Comparison of Figs. 2 and 3 shows that ordered regions in the polymer itself are most stable under small strains and at a relatively low temperature; consequently, these strains at 290 K make a contribution to the size distribution of jumps (Fig. 3a). At a high temperature (600 K), the packing becomes less dense and more uniform due to an increase in the mobility of molecules. In this case, the deformation jumps are caused, for the most part, by the presence of solid graphite particles that "flowed around" polymer layers and bring about stepwise creep. Since graphite particles of approximately equal diameter have sharp boundaries, the jumps are clearly pronounced (Fig. 2). The large amplitudes of the periodic variations of the creep rate can be caused by the overcoming of barriers to adhesive interactions between the polymer and graphite, which play the role of stoppers and periodically sharply decrease the rate of shear. It is quite probable that the increase in the creep strain (Fig. 3b), by analogy with heating, disturbs the packing in ordered regions of the polymer. Consequently, the influence of graphite at 290 K becomes more explicit, which leads to sharp periodic variations of the creep rate at this temperature (Fig. 3b).

The dependence of the creep rate on the creep strain at a temperature of 600 K for polyimide free of filler is depicted in Fig. 4. Comparison of Figs. 2 and 4 shows that the periods and amplitudes of creep rate variations for pure polyimide (Fig. 4) do not exhibit a definiteness that is specific to the composite (Fig. 2) and are considerably smaller than those presented in Fig. 2. The variability and smaller sharpness of the deformation jumps for polyimide free of graphite are associated with the complex structure of the polymer and suggest that the polymer involves microregions (0.6–1.0 μm) that are bound to the boundary layers more weakly than graphite is bound to the polymer.

4. CONCLUSIONS

Thus, the experiments with model polymer materials confirm the statement that the deformation jumps are determined by the sizes of structural inhomogeneities. In this case, the inference can be drawn that the study of the deformation kinetics on the mesoscopic level makes it possible to estimate the sizes of ordered microaggregates typical of the structure under investigation. In the controversy over the structure of amorphous materials, the jumplike deformation is an additional argument in support of the structural heterogeneity.

REFERENCES

1. N. N. Peschanskaya and P. N. Yakushev, Fiz. Tverd. Tela (Leningrad) **30** (7), 2196 (1988) [Sov. Phys. Solid State **30**, 1264 (1988)].

2. N. N. Peschanskaya, Vysokomol. Soedin., Ser. A **31** (6), 1182 (1989).
3. N. N. Peschanskaya, Fiz. Tverd. Tela (St. Petersburg) **35** (11), 3019 (1993) [Phys. Solid State **35**, 1484 (1993)].
4. N. N. Peschanskaya, P. N. Yakushev, A. B. Sinani, and V. A. Bershtein, Thermochim. Acta **238**, 429 (1994).
5. N. N. Peschanskaya, L. P. Myasnikova, and A. B. Sinani, Fiz. Tverd. Tela (Leningrad) **33** (10), 2948 (1991) [Sov. Phys. Solid State **33**, 1665 (1991)].
6. N. N. Peschanskaya, P. N. Yakushev, L. P. Myasnikova, V. A. Marikhin, A. B. Sinani, and M. Yakobs, Fiz. Tverd. Tela (St. Petersburg) **38** (8), 2582 (1996) [Phys. Solid State **38**, 1416 (1996)].
7. N. N. Peschanskaya, Doctoral Dissertation (Ioffe Physicotechnical Inst., Russian Academy of Sciences, St. Petersburg, 1999).
8. N. N. Peschanskaya, J. Hristova, and P. N. Yakushev, Polymer **42**, 7102 (2001).
9. N. N. Peschanskaya, Fiz. Tverd. Tela (St. Petersburg) **43** (8), 1418 (2001) [Phys. Solid State **43**, 1478 (2001)].
10. N. N. Peschanskaya, P. N. Yakushev, V. M. Egorov, V. A. Bershteĭn, and L. Bokobza, Fiz. Tverd. Tela (St. Petersburg) **44** (9), 1609 (2002) [Phys. Solid State **44**, 1684 (2002)].
11. N. N. Peschanskaya, V. Yu. Surovova, and P. N. Yakushev, Fiz. Tverd. Tela (St. Petersburg) **34** (7), 2111 (1992) [Sov. Phys. Solid State **34**, 1127 (1992)].
12. N. N. Peschanskaya and P. N. Yakushev, Fiz. Tverd. Tela (St. Petersburg) **39** (9), 1690 (1997) [Phys. Solid State **39**, 1509 (1997)].
13. Yu. S. Lipatov, *Colloidal Chemistry of Polymers* (Naukova Dumka, Kiev, 1984) [in Russian].
14. P. H. Geil, J. Macromol. Sci. Phys. **11** (8), 1461 (1977).
15. G. M. Bartenev and A. G. Barteneva, *Relaxation Properties of Polymers* (Khimiya, Moscow, 1992) [in Russian].
16. I. Prigogine, *From Being to Becoming: Time and Complexity in the Physical Sciences* (Freeman, San Francisco, 1980; Nauka, Moscow, 1985).

Translated by O. Moskalev

Physics of the Solid State, Vol. 47, No. 5, 2005, pp. 954–960. Translated from Fizika Tverdogo Tela, Vol. 47, No. 5, 2005, pp. 924–930.

Experimental Studies of the Mechanical and Thermal Stability of a Polymer–Substrate Interface

O. F. Pozdnyakov, A. O. Pozdnyakov, and V. R. Regel

Ioffe Physicotechnical Institute, Russian Academy of Sciences, Politekhnicheskaya ul. 26, St. Petersburg, 194021 Russia

e-mail: of.pozd@mail.ioffe.ru

Abstract—The use of mass spectrometry to study the mechanisms of formation and fracture of polymer adhesive joints is considered. The factors affecting the joint strengths are analyzed, and the possible development of mass spectrometry for destruction processes in solids is discussed. *© 2005 Pleiades Publishing, Inc.*

1. INTRODUCTION

In the 1960s–1970s, mechanical-load mass spectrometry (MLMS) was developed in Zhurkov's laboratory at the Ioffe Physicotechnical Institute. The first work in this field was published in the journal *Physics of the Solid State* in 1962 [1]. This method was used to discover and study fracture emission (FE). This phenomenon was first detected in polymers and then in various solids differing in nature and structure, including composite materials. At present, this method is widely applied in laboratories in the United States, Germany, and Great Britain [2–5] for studying the nature of the strength of solids. The modern concept of the FE phenomenon can be reduced to the following. When a solid is deformed, defects and submicrocracks nucleate and grow in it. Further crack growth results in macroscopic fracture of the material. When cracks grow, the material or, more specifically, crack tip and edges become a source of low-molecular volatile products. The detected volatile products are usually attributed to two main types: products caused by bond rupture in solids and impurities that are present in any material. Information on the composition and emission kinetics of the products of mechanical fracture allows one to gain a deeper understanding of the nature of fracture at the atomic–molecular level and to make recommendations for engineers for the design of new materials. MLMS data are unique and give specific information on the development of deformation and fracture processes in solids, and MLMS is an important method in the field of the physics of strength and plasticity. Some MLMS results have been described earlier for both organic [6–9] and inorganic [10] solids. In this work, we use mass spectrometry to study polymer adhesion.

Recent articles dealing with the problem of polymer adhesion demonstrate that this problem is of great interest for researchers in various fields of science and engineering. This interest pertains to the mechanisms of formation and fracture of polymer–substrate interfaces and the mechanical and thermal stabilities of the corresponding transition zones. It is generally accepted that the processes that are important for the mechanical strength of heterogeneous materials, polymer coatings, and adhesive and adhesive-free joints of solids develop mainly near an interface. For a long time, experimental studies were based on two alternative concepts of adhesion, namely, Bickerman's model of weak defect boundary layers [11] and the concept of chemical bonds at the interface playing a leading role [12]. In practice, the situation is much more complex: the fine structure of the transition zone and the conditions of its formation and evolution during operation become significant. The accumulated experimental data indicate that neglecting the complex relation between processes in favor of studying their individual aspects does not meet with much success in solving the problem. To study the processes in terms of their interrelations, it is necessary to use a wide variety of direct physical methods.

Over the past decade, interest in studying interaction at the polymer–substrate interface has increased due to the prospects for applying nanocomposite materials. The use of nanoparticles of metals, oxides, salts, fullerenes, and carbon nanotubes as polymer fillers opened up new opportunities for controlling the mechanical, thermal, optical, magnetic, and barrier properties of nanostructured composites [13].

Usually, two techniques for the formation of an interface are used: the deposition of atoms or molecules on a polymer surface (e.g., the deposition of metallic contacts on a polymer base) or the deposition of polymer molecules (a polymer coating) onto the surface of a substrate. These techniques are different because of the substantial difference in the initial conditions and initial states of interacting components of a contacting pair of materials. Hereafter, we will only consider the second technique for the formation of an interface.

To study the structure of the interface, we need information on the parameters of the transition zone and on the changes in the properties of polymer mole-

1063-7834/05/4705-0954$26.00 © 2005 Pleiades Publishing, Inc.

cules in this zone (a decrease in the thermal stability of a polymer near the interface, the type of interphase interaction involved, and the mechanism of formation of weak boundary layers). It should be noted that mass spectrometers, in particular time-of-flight mass spectrometers (TOFMS) and, especially, the latest modification (mass reflectrons [14]), have been found to be a convenient tool for solving this problem. The high sensitivity and speed of response in combination with the possibility of recording a panoramic mass spectrum (at a high resolution) make it possible to examine the nature of volatile products emitted by a solid under the action of external factors and investigate the kinetics of their formation. The design of a TOFMS ensures a high degree of compatibility with other methods of analysis that are informative, e.g., for studying thin and ultrathin polymer films on a substrate. Above all, these methods include thermo-, photo-, and electron-stimulated desorption.

Additional experimental data on the interface at the atomic–molecular level can be obtained using a combination of two methods, in particular, mass spectrometry and electron spectroscopy for chemical analysis (ESCA). Our studies are distinguished by the application of the TOFMS and ESCA methods in combination with multifunctional mechanic devices that allow *in situ* manipulation of samples in the vacuum chamber of a combined TOFMS + ESCA apparatus.

2. METHODS FOR STUDYING THE RELATION BETWEEN THE STRENGTH OF AN ADHESIVE JOINT AND THE CONDITIONS OF ITS FORMATION

A schematic diagram for our *in situ* experiments is shown in Fig. 1. It is advisable to supplement studies of adhesion at the molecular level with measurements of its strength characteristics [15]. We believe that this trend is the most promising. In our experiments (Fig. 1), the analysis of the mechanical stability includes the following stages.

(1) The formation of an adhesive joint under various conditions; an analysis of the dependences of the joint strength on the preliminary adsorption of various molecules onto the substrate, on the initial state of the substrate and polymer surfaces, and on other factors (the duration, temperature, and force of compression).

(2) Measurement of the strength of the joint during its fracture and detection of the volatile products released.

(3) Determination of the amount of polymer transferred to the substrate during fracture; for this purpose, the subsequent thermal desorption of the polymer (mass spectrometry) is used.

(4) Determination of the coverage of the substrate surface by transferred polymer molecules (with ESCA).

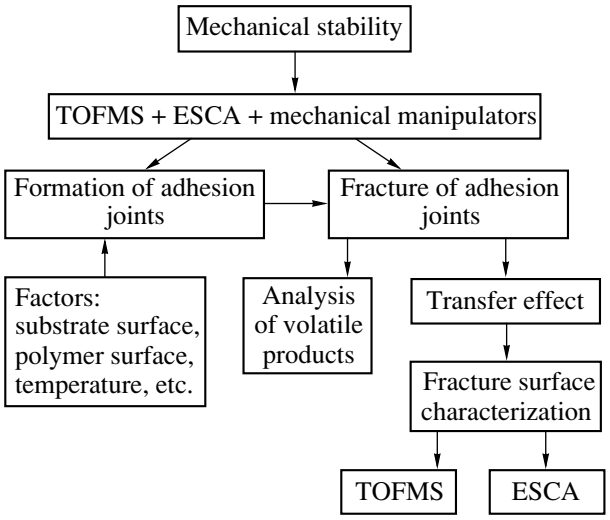

Fig. 1. Functional scheme for combined experiments in a TOFMS + ESCA apparatus.

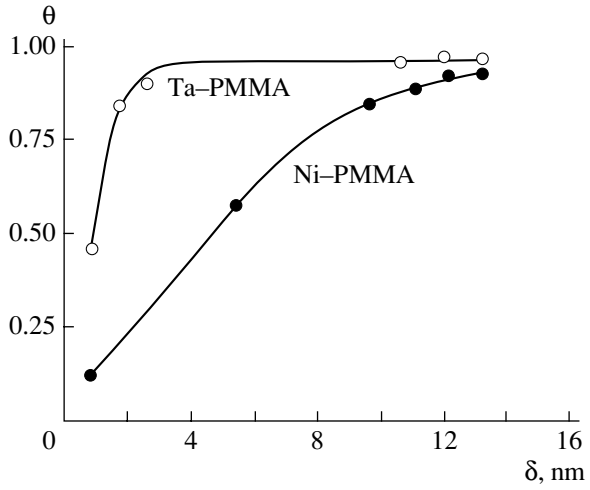

Fig. 2. Dependence of the coverage θ of tantalum and nickel substrates by polymethyl methacrylate (PMMA) molecules on the thickness δ of the transferred layer.

In our studies, prominence is given to the transfer of a polymer to the substrate. This transfer is usually observed after the contact (i.e., the adhesive joint) between two materials has been broken. The transfer effect qualitatively and quantitatively characterizes the polymer–substrate joint. It should be noted that the formation of a single contact adequately represents the compression method of producing a polymer–substrate joint used in practice. Moreover, material transfer during a single contact with a substrate can be considered an elementary act of wear (e.g., during friction). Studying the polymer transfer to a substrate during fracture of a joint makes it possible to probe the interface structure in order to relate it to the properties of the surface and

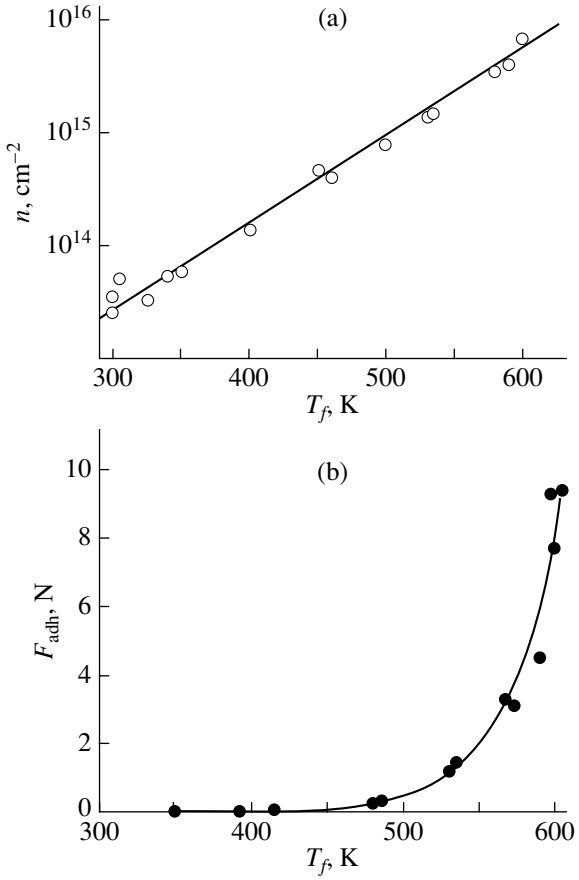

Fig. 3. Dependences of (a) the amount of transferred PTFE (the number of monomeric units) and (b) the mode-I force for PTFE–grade-20 steel on the temperature of formation T_f of the PTFE–grade-20 steel contact.

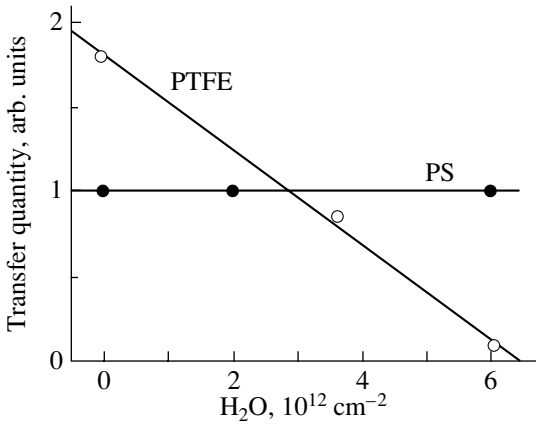

Fig. 4. Effect exerted on the transfer of PTFE and polystyrene (PS) by preliminary adsorption of H_2O molecules on an unoxidized tantalum ribbon.

near-surface layers of the polymer. The application of a vacuum adhesion meter to measure the adhesion force gives additional information on the relation between the adhesion strength and the interface parameters. Let us give some examples.

The combined use of TOFMS and ESCA in experiments on the formation and fracture of an adhesive joint allows us to determine the coverage θ of the metal surface by transferred macromolecules and its character. From the amount of transferred polymer and the coverage determined in one experiment, we can construct the dependence of θ on the thickness of the transferred layer δ (Fig. 2). The layer thickness corresponding to the onset of saturation of the θ(δ) curve gives an estimate of the distance between the surface of the substrate and a crack in the broken adhesive joint. For the polytetrafluoroethylene (PTFE)–grade-20 steel pair, Fig. 3 shows the dependences of the amount of transferred polymer n (the number of monomeric units) and the mode-I force (adhesion force) F_{adh} on the temperature T_f of formation of the adhesive joint. In [16], the dependences of the amount of transferred polymer on the duration of joint formation, on the compression force, and on the duration of preliminary ultraviolet irradiation were obtained for other polymer–metal adhesion pairs.

Figure 4 shows the results of direct studies of the effect of preliminary adsorption of H_2O molecules on a substrate (or, conversely, of thermal desorption from it) on the polymer transfer. It can be seen that the dependences of the amount of transferred molecules and, hence, of the adhesion strength on the coverage of the surface of an unoxidized tantalum ribbon by H_2O molecules deposited in ultrahigh vacuum are qualitatively different in PTFE and polystyrene (PS). In what follows, we also consider a specific situation where water adsorbed on an interface causes the hydrolysis of boundary macromolecules (in particular, the hydrolysis of the copolymer of ethylene with vinyl acetate, which is prone to hydrolytic cleavage of chemical bonds in a chain).

To illustrate the feasibility of our approach for studying the mechanochemical transformations that occur in a polymer during the fracture of an adhesive joint, we present the results of studying the mode-I fracture of a metal–polymer–metal adhesive joint followed by heating of the metallic parts (Fig. 5). The dependences of the release rate of a monomer dn/dt during fracture of an adhesive joint (Fig. 5, curve *a*) and during subsequent heating (curve *b*) can be used to determine the quantitative relations (important in understanding the mechanism of fracture) between the content of the volatile products of the mechanical destruction of macromolecules in a crack growth zone (the number of monomer molecules) and the intensity of bond rupture (the number of free macroradicals that form, which is proportional to the amount of monomer released upon heating).

Apart from the examples of *in situ* analysis given above, we also examined separately prepared objects of practical importance. Below, a number of characteristic

variants of such studies are given in items A (spallation experiments), B (model sample, a so-called optical contact), and C (fracture of a carbon–carbon composite).

(A) It was found advantageous to use the technique of peeling a polymer away from a substrate in combination with MLMS. A widely applied technique of measuring adhesion is known to be based on exfoliation. An examination of an adhesive joint of fluoroplastic with an aluminum foil showed that H_2O molecules are intensely released during exfoliation. The total amount of released water per joint area was found to be close to one monolayer (i.e., 5×10^{14} cm^{-2}). This result indicates that H_2O molecules are actively involved in the formation of a joint of fluoroplastic with the aluminum surface. It was surprising to find this amount of water molecules located on the fracture surface.

Another practically important example is related to the development of microfluid, microchannel, electrophoresis analytical systems (biochips) that consist of an elastic polydimethylsiloxane (PDMS) replica with channels and a glass plate with electrodes. Owing to the intermolecular forces acting at the PDMS–glass interface, such a chip has a satisfactory mechanical strength. However, the interface can cause segregation of low-molecular oligomers retained after the formation of PDMS, which substantially worsens the operation of the biochip. The results obtained by peeling a PDMS replica off a glass substrate in a TOFMS chamber (Fig. 6) and simultaneously analyzing the nature of the volatile products and the kinetics of their release made it possible to control and optimize the production process and improve the quality of the adhesive joint in the chips.

(B) Investigation of model objects is important for solving the structure–property problem. Producing a direct adhesive-free joint of two mirror solid surfaces of glasses and crystals (a so-called optical contact) is important from both a scientific and a practical standpoint [17]. This technology for joining materials is now finding wide use in optics and semiconductor electronics (e.g., for the production of complex high-accuracy lenses or for direct joining of silicon wafers [18, 19]). What are the forces that ensure the strength of such durable gas-proof "separable" joints? We could answer this question by studying pairs of cylindrical samples of inorganic glasses of different grades. We found that only water molecules are released during fracture (in an amount of from 10^{13} to 10^{15} molecules per square centimeter of the geometrical contact area depending on the glass grade). The amount of released water varies linearly with the optical-contact strength σ (Fig. 7). Thus, the rather high strength of the optical contact is controlled by the amount of water molecules adsorbed at the contact surfaces (or by the corresponding number of hydrogen bonds).

(C) To solve the problems concerning the strength and reliability of structures made of fibrous composites, it is important to have information on the processes of distributed fracture of fibers. Carbon–carbon fibrous composites (consisting of a carbon matrix with graphite fibers prepared from polyacrylonitrile) were deformed to failure by transverse three-point bending. In the early stages of deformation during bending, we detected multiple explosive gas release (Fig. 8). The volatile

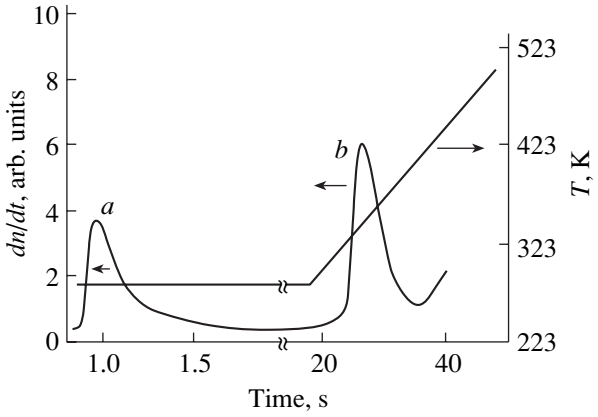

Fig. 5. Monomer formation (*a*) during fracture of an adhesive joint at room temperature and (*b*) upon subsequent heating of the resultant free mechanical macroscopic radicals.

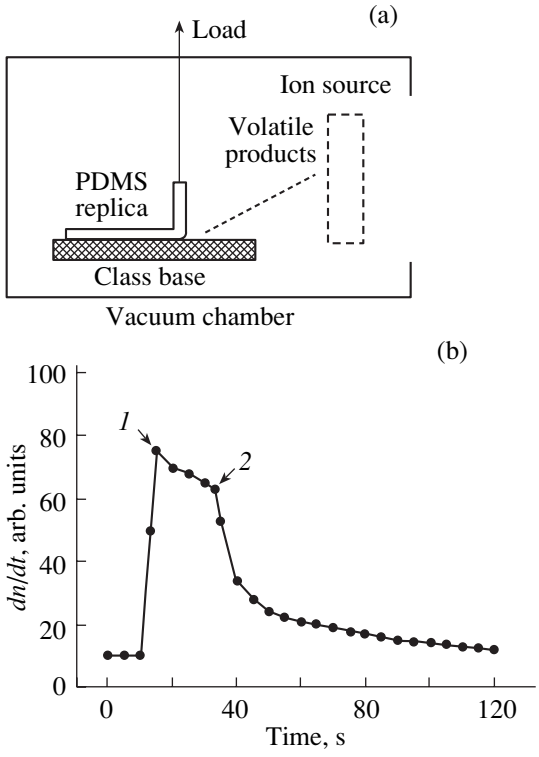

Fig. 6. (a) Schematic diagram for the experiment and (b) the release rate of one of the PDMS oligomers (*1*) when the replica is partly peeled off from a glass base and (*2*) during recovery of the contact in vacuum. The peeling rate is 1 cm s^{-1}.

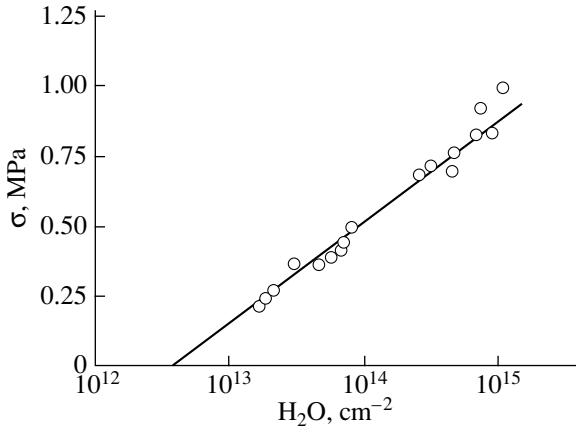

Fig. 7. Dependence of the optical-contact strength on the amount of released water molecules for glasses of various grades.

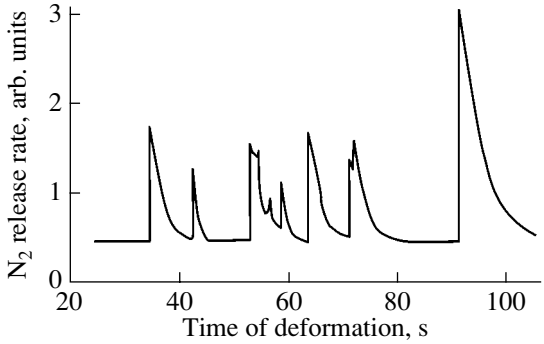

Fig. 8. Explosive N_2 release upon bending of a coal-plastic bar (see text).

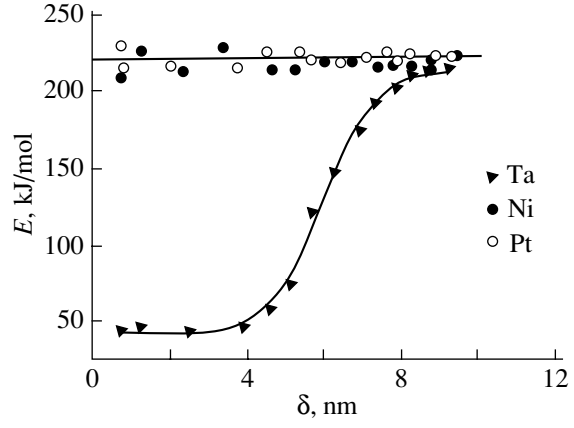

Fig. 9. Activation energy for thermal destruction of submicron-thick PMMA films on tantalum, nickel, and platinum as a function of film thickness.

products mainly consist of N_2 molecules (60–90% depending on the graphite-fiber grade), as well as of CO_2 and H_2O. The results of experiments on the fracture of individual graphite fibers allowed us to unambiguously attribute N_2 molecules released from the composite to the fracture of the fibers. Heat treatment of these fibers in a TOFMS chamber showed that N_2 molecules began to release at temperatures higher than those used in the carbonization–graphitization stage, i.e., above 2000°C. This means that nitrogen enters into the chemical structure of these carbon fibers. We also found a correlation between the amount of nitrogen released and the elastic modulus of the fibers: the higher the modulus, the lower the amount of nitrogen released during the fracture of the fibers. The formation of CO_2 and H_2O is related to the loss of the adhesive bond between the fibers and matrix. Thus, fracture-emission control gives important information on the behavior of heterogeneous systems under loading and is a direct method for studying their cracking resistance. This method is of particular importance for studying materials such as carbon–carbon composites, since they cannot be examined by other methods.

3. STUDYING THE PROPERTIES OF INTERFACES BY ANALYZING A THIN LAYER OF MACROMOLECULES ADSORBED ON A SUBSTRATE

It has been shown experimentally that a thin (less than 100-nm-thick) layer of macromolecules on the surface of a substrate is an adequate model for an interface and, therefore, can be used to model the transition zone in a polymer. Thin polymer layers can be applied on a substrate from a solution or by bringing a polymer into contact with a substrate in vacuum or another medium to realize the transfer effect. The latter technique allows preliminary cleaning of the substrate surface in vacuum by using thermal desorption and/or adsorption of certain molecules, e.g., H_2O. By measuring the parameters of thermal destruction of ultrathin polymer films on various substrates [in particular, the activation energy E as a function of the film thickness $E(\delta)$], we can reveal quantitative changes in the thermal stability of near-interface macromolecules and the character of their interaction with the substrate. The thickness of the modified polymer layer can also be determined from $E(\delta)$. The measurement of the thermal stability of near-interface macromolecules is simultaneously a test for the presence of chemical interaction between the macromolecules and the substrate. A decrease in the activation energy indicates a catalytic effect of the substrate surface (e.g., the appearance of a complex with charge transfer from the functional groups of a macromolecule to the surface atoms of the substrate), which results in significant weakening of the interatomic bonds inside a polymer chain. Figure 9 shows typical $E(\delta)$ curves for various polymer–substrate pairs. Different substrates can be either catalytic (Ta) or inert (Pt, Ni) with respect to the polymer under study. The character of the $E(\delta)$ dependence also indicates the intensity of catalysis and the catalytic "capac-

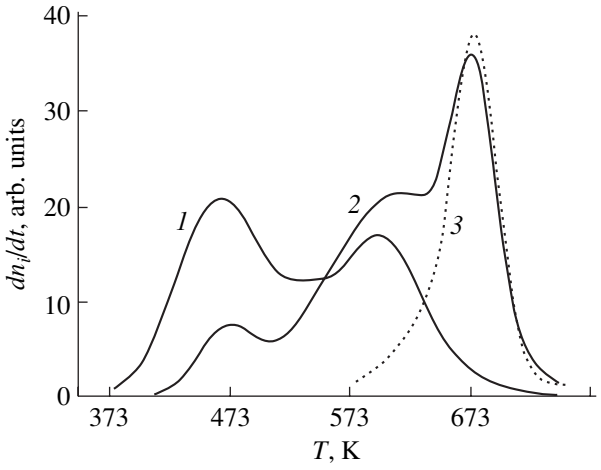

Fig. 10. Temperature dependences of the kinetics of (*1*) water desorption from an aluminum substrate, (*2*) desorption of the products of hydrolysis of a copolymer applied onto the initial substrate, and (*3*) destruction of the copolymer on a dry substrate.

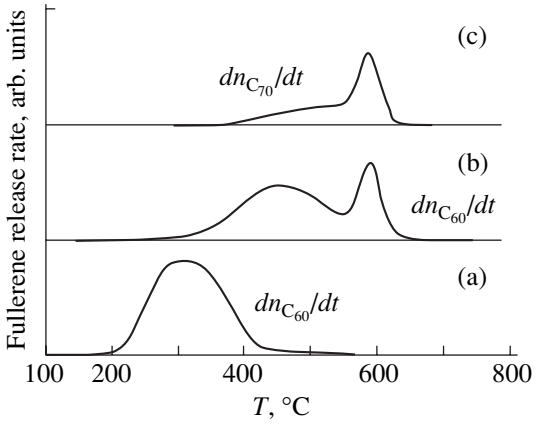

Fig. 11. Kinetics of the thermal desorption of (a) C_{60} from the surface of a polyimide coating, (b) C_{60} from a polyimide–C_{60} coating, and (c) C_{70} from a polyimide–C_{70} coating. The concentration of fullerene molecules in the coatings is $\sim 10^{19}$ cm^{-3}.

ity" of a substrate surface. This dependence can serve as a criterion for predicting the aging of a polymer at its interface with a substrate while in use.

The most typical mechanism of polymer aging at the interface, which is also simultaneously the mechanism of defect formation in a near-interface zone, is the hydrolysis of macromolecules by water, which is inevitably present at the interface. The hydrolysis negatively affects the life of adhesive joints and, of course, should be taken into account in developing new composite polymer systems. Figure 10 shows data on the kinetics of the thermal desorption of water and the hydrolytic destruction of submicron films of the copolymer of ethylene with vinyl acetate when the films are applied on initial (i.e., "wet") or preliminarily heated ("dry") substrates. It is seen that the hydrolysis of the copolymer (the hydrolysis product is acetic acid) and water desorption occur over the same temperature range. Independent comparative water-resistance tests of the coatings deposited onto wet and dry aluminum substrates unambiguously indicate that the latter coatings are more advantageous. The dry method of coating application provides higher and more stable adhesion. Similar results were obtained for substrates made from other metals.

4. POLYMER–FULLERENE COMPOSITE SYSTEMS

Researchers hope that the development of methods for introducing molecular fillers—e.g., the new allotropic form of carbon, fullerenes (for instance, C_{60} or C_{70})—in a polymer matrix will create new unique properties in these composites as compared to pure polymer matrices. Understanding the properties of these composite systems is limited by insufficient information on the structural states and temperature-induced transformations of fullerene molecules in polymers. It is known that, even in low-molecular organic materials, the solubility of a fullerene is often lower than a fraction of one percent. The main obstacle to experimental studies of polymer–fullerene systems is the insufficient sensitivity of traditional structural methods and the complexity involved in interpreting data obtained by them. Owing to the high sensitivity of thermal-desorption mass spectrometry to molecular flow in a gas phase, we could obtain detailed information on the state of a fullerene in a polymer–fullerene system even at very low fullerene concentrations (Fig. 11). We found that the character of the interaction of macromolecules with a fullerene and its structural state in the matrix manifest themselves in the thermal-desorption dependences of fullerene molecules and in the products of degradation of the polymer matrices.

The data obtained are valuable for choosing the conditions of formation of polymer–fullerene compositions intended for various purposes, e.g., for tribological, optical, and medical purposes [20–22]. We have shown that thermal-desorption mass spectrometry makes it possible to quantitatively study the diffusion of fullerene molecules and the dissolution of fullerene clusters in polymer matrices [23]. We believe that experimental studies in this field can be improved if the methods of fracture emission and thermal desorption discussed above are jointly applied to investigate polymer–fullerene systems. A practically important trend can be the use of these composite systems to study the nature and kinetics of formation of the products of thermomechanical reactions that occur directly in dry-friction units operating in high vacuum and/or in a given gas atmosphere.

In closing, we note that MLMS is promising for further studies of destruction processes occurring in various solids.

ACKNOWLEDGMENTS

This work was supported in part by the Division of Physical Sciences of the Russian Academy of Sciences (program "New Materials and Structures").

REFERENCES

1. V. R. Regel, T. M. Muinov, and O. F. Pozdnyakov, Fiz. Tverd. Tela (Leningrad) **4** (9), 2468 (1962) [Sov. Phys. Solid State **4**, 1809 (1962)].
2. W. E. Baumgartner, J. A. Hammond, G. E. Myers, and W. C. Stapleton, Polym. Prepr. (Am. Chem. Soc. Div. Polym. Chem.) **14** (1), 448 (1973).
3. M. A. Grayson, C. J. Wolf, R. L. Levy, and D. B. Miller, J. Polym. Sci., Polym. Phys. Ed. **14**, 1601 (1976).
4. J. T. Dickinson and L. C. Jensen, J. Mater. Res. **6** (1), 112 (1991).
5. G. P. Fox and J. Soria-Ruiz, Proc. R. Soc. London, Ser. A **317**, 79 (1970).
6. V. R. Regel, T. M. Muinov, and O. F. Pozdnyakov, in *Proceedings of Conference on Physical Basis of Yield and Fracture* (Oxford, 1966), p. 194.
7. O. F. Pozdnyakov and V. R. Regel, Fiz. Tverd. Tela (Leningrad) **10** (12), 3664 (1968) [Sov. Phys. Solid State **10**, 2905 (1968)].
8. V. R. Regel, O. F. Pozdnyakov, V. A. Mal'chevskiĭ, and M. G. Fal'kovskiĭ, Vysokomol. Soedin., Ser. A **13**, 2078 (1971).
9. B. Ya. Byl'skiĭ, O. F. Pozdnyakov, V. R. Regel, and B. P. Redkov, Mekh. Polim. **5**, 835 (1973).
10. V. V. Boldyrev, V. R. Regel, O. F. Pozdnyakov, F. Kh. Urakaev, and B. Ya. Byl'skiĭ, Dokl. Akad. Nauk SSSR **221** (3), 634 (1975).
11. J. J. Bikerman, *The Science of Adhesive Joints*, 2nd ed. (Academic, New York, 1968).
12. A. A. Berlin and V. E. Basin, *Fundamentals of Polymer Adhesion* (Khimiya, Moscow, 1974) [in Russian].
13. *Handbook of Nanoscience, Engineering, and Technology*, Ed. by W. A. Goddard, D. W. Brenner, S. E. Lyshevski, and G. J. Iafrate (CRC, London, 2003).
14. B. A. Mamyrin, V. I. Karataev, and D. V. Shmikk, Zh. Éksp. Teor. Fiz. **64** (1), 82 (1973) [Sov. Phys. JETP **37**, 45 (1973)].
15. B. Petica and D. Tabor, Surf. Sci. **89**, 191 (1979).
16. O. F. Pozdnyakov and B. P. Redkov, in *Mechanisms of Vulnerability to Damage and Strength of Heterogeneous Materials* (RTP LIYaF, 1985), p. 40 [in Russian].
17. P. M. Elkhin, Yu. V. Lisitsyn, O. F. Pozdnyakov, and V. S. Yudin, Fiz. Khim. Stekla **5**, 611 (1986).
18. V. B. Voronkov, I. V. Grekhov, and V. A. Kozlov, Fiz. Tekh. Poluprovodn. (Leningrad) **25** (2), 208 (1991) [Sov. Phys. Semicond. **25**, 125 (1991)].
19. R. Stengl, T. Tan, and U. Gosele, J. Appl. Phys. **28** (10), 1735 (1989).
20. A. O. Pozdnyakov, V. V. Kudryavtsev, and K. Friedrich, Wear **254**, 501 (2003).
21. N. Kamanina, L. Kaporskii, A. O. Pozdnyakov, and B. Kotov, SPIE J., No. 3939, 228 (2002).
22. A. O. Pozdnyakov, E. Yu. Melenevskaya, O. V. Ratnikova, and B. M. Ginzburg, Zh. Prikl. Khim. (St. Petersburg) **76** (12), 2015 (2003).
23. A. O. Pozdnyakov, B. M. Ginzburg, T. A. Maricheva, V. V. Kudryavtsev, and O. F. Pozdnyakov, Fiz. Tverd. Tela (St. Petersburg) **46** (7), 1328 (2004) [Phys. Solid State **46**, 1371 (2004)].

Translated by K. Shakhlevich

Physics of the Solid State, Vol. 47, No. 5, 2005, pp. 961–967. Translated from Fizika Tverdogo Tela, Vol. 47, No. 5, 2005, pp. 931–936.

Electrical Breakdown of Thin Polymer Films

V. A. Zakrevskiĭ* and N. T. Sudar'**

**Ioffe Physicotechnical Institute, Russian Academy of Sciences, Politekhnicheskaya ul. 26, St. Petersburg, 194021 Russia*

e-mail: V.Zakrevsky@mail.ioffe.ru

***St. Petersburg State Polytechnic University, Politekhnicheskaya ul. 25, St. Petersburg, 195251 Russia*

Abstract—Data are presented on the dielectric strength of thin polymer films. The conclusion is drawn that the electron avalanche concept is inapplicable to the breakdown of thin films. It is proposed to consider electrical breakdown as a consequence of an abrupt local field enhancement induced by evolution of the space charge injected into the polymer from electrodes. It is shown that the lifetime of polymer films depends exponentially on electric field strength. © *2005 Pleiades Publishing, Inc.*

Organic compounds, including polymers, are widely employed in technology as materials for the fabrication of dielectric or transport layers. Thin (~100-nm-thick) films of these materials used in modern devices are acted upon by strong electric fields (~10^6 V/cm). This accounts for the present interest in the electrical strength and operating capacity of thin polymer films in strong electric fields.

Investigation of the electric strength of thin polymer films was started by a study of the pulsed strength of 30- to 300-nm-thick polystyrene (PS) films [1]. It was established that the breakdown field F_b is about 5×10^6 V/cm. Further studies have dealt with the breakdown of thin (d = 40- to 780-nm-thick) films of diverse polymers, such as polyethylene (PE), polypropylene, polytetrafluoroethylene, polyimide (PI), derivatives of polyphenylene vinylene, and polyoctamethyl trisiloxane [2–10]. The properties of polyvinyl carbazole and polyimide (d = 200–400 nm) were investigated in ac electric fields [11, 12]. The measurements reported in [2–12] were conducted primarily at room temperature in a constant voltage-rise-rate mode. The data obtained indicate that thin films of polymers of various types break down in fields of (2–6) MV/cm. This value virtually coincide with the fields in which thicker polymer films suffer breakdown under suppression of partial discharges (PDs) [13–15].

It has also been established that the breakdown field strength F_b grows as the voltage rise rate increases [2, 3, 6, 10]. The observed effect of the voltage rise rate on F_b appears to be significant, because, in accordance with [13, 15], it should be considered an indication that electrical breakdown of thin polymer films actually occurs through a buildup of damage (changes) culminating in the breakdown itself. The rate of this process depends exponentially on the electric field strength. This conclusion is in accord with the exponential dependence of the electric lifetime on the average field strength $F = U/d$ (where U is the voltage applied across the film) observed in [10]. The electric lifetime τ is defined as the lifetime of a polymer specimen placed in an electric field, i.e., the period of time from the application of a constant voltage to breakdown of the specimen. The quantity inverse to the lifetime, $1/\tau$, characterizes the rate of the process preceding the breakdown. The last stage of electrical breakdown of a polymer, i.e., the breakdown proper, develops in a time of 10^{-8}–10^{-7} s [2, 3].

In conclusion to this brief review of the relevant literature, let us consider two recently reported important findings. It has been established that the breakdown field depends on the electrode material; more specifically, the value of F_b grows as the cathode work function increases [3, 10]. This fact indicates that injection processes play an essential role in the destruction of polymers in an electric field. Finally, it should be noted that the polypropylene films discussed in [4] were studied in a high vacuum, i.e., in conditions precluding the onset of gas discharge. The fact that the electric strength of films in this case does not exceed the strength of polymer films tested in air implies the absence of discharge phenomena in experiments on thin films conducted in atmospheric air. This conclusion does not come as a surprise, because, as is well known, gas gaps less than 1 μm wide do not break down in fields of ~1 MV/cm [16]. Therefore, when studying the electrical strength of thin ($d < 1$ μm) films, the effect of gas discharge on the films can be disregarded even when no special measures are taken for the suppression of PDs.

The above data should be taken into account when developing the theory of breakdown of thin polymer films. The corresponding mechanism was discussed in [6–8] using the concept proposed by Kao [17] on the destruction of polymers in an electric field. The mechanism put forward in [17] involves electric field–

1063-7834/05/4705-0961$26.00 © 2005 Pleiades Publishing, Inc.

induced rupture of macromolecules, which rests on the assumption that hot electrons capable of initiating chemical-bond rupture are formed. This multistage process includes electron injection from the cathode into the polymer; capture of the injected electrons by traps, which is accompanied by a release of energy in each event approximately equal to the trap depth; transfer of this energy to another electron, i.e., the formation of hot electrons; interaction of these electrons with macromolecules; breakup of macromolecules into free radicals; capture of electrons that have lost their energy by traps; etc. [17].

Unfortunately, the discussion in [17] was not supported by any quantitative data on the rates of individual stages in this chain energy-transfer reaction (not on the rate of the process as a whole). Kao [17] also did not analyze the probability of transfer of all the energy released in an electron capture by a trap to another electron, did not estimate the probability of partitioning of this energy over the vibrational degrees of freedom of macromolecules without energy transfer to an electron, did not consider the mechanism of energy transfer to an electron and the dependence of the energy transfer probability on the distance between the trap and the electron, and did not discuss the probability of bond rupture in interaction with comparatively low-energy electrons or the possibility of chain energy-transfer reactions in polymers. Chain reactions in polymers operate by free-radical mechanisms.

It is believed that the electron mean free path increases in regions with reduced density, which form as a result of macromolecule destruction [7, 17]. Therefore, conditions conducive to impact ionization of molecules are produced, which, in turn, gives rise to a strong rise in current. The heat liberated in the process initiates destruction of the polymer and the formation of a breakdown channel. The density can decrease noticeably only as a result of mass transport (displacement of macromolecules). This problem was not considered in the publications cited above, thus leaving open the question regarding the extent to which the lowering of density through the displacement of molecules is probable in solid polymers.

There are also other points to which one should pay attention. First, the formation of a loosened region with a reduced density (a void in the limiting case) near an electrode brings about an increase in the barrier height by an amount determined by the position of the conduction level of the material adjacent to the cathode and, hence, a lowering of the injection intensity. Second, a large (avalanche-like) current amplification in thin films through impact ionization of macromolecules will not occur for the same reason for which breakdown of narrow gas gaps is made difficult. For a film thickness $d = 100$ nm, a voltage of ~10 V is high enough to produce a field ~1 MV/cm. Therefore, the multistage electron multiplication (current enhancement) is obviously not realized in these conditions, because the molecule ionization energy is comparable to 10 eV. Finally, one should not overlook the fact that a region with a reduced density requires a certain time to form. Hence, current amplification should also require a certain time. No such gradual current amplification is, however, observed experimentally. As the voltage across a PE [7] or PI [8] film increases at a constant rate, the rate of current growth decreases with time, with a catastrophic current increase (breakdown) occurring in a time $\sim 10^{-8}$–10^{-7} s [2, 3, 18].

Thus, one has to admit that the breakdown mechanism operating in thin polymer films remains unclear. This stimulated our present study. It would be instructive, however, to dwell preliminarily on a few findings that, together with the above literature data, will form a basis for constructing our concept of electrical breakdown of polymers.

A current passing through a polymer dielectric is filamentary [6–8]. The injection current flows over filamentary channels of a small cross section. This situation is characteristic not only of polymers but also of crystalline dielectrics [19]. In these regions, conducting breakdown channels form. The heat liberated in breakdown carbonizes the channel walls [20]. The breakdown channels are ~10 μm in diameter [6]. Hence, the value 10^{-6} cm^2 may be considered an upper limit to the cross-sectional area of the thin filamentary channels over which current flows in polymer films.

One of the reasons for the formation of such channels is the nonuniformity of the electrode surface (the presence of bumps), which gives rise to field enhancement.

Several studies have dealt with evaluating nonuniform electric fields in various two-electrode systems. The field amplification q in a needle–plane-electrode system can be very high (as compared to the average field) and depends strongly on the actual shape of the needle [21, 22].

The problem of the strength of local fields in a system of plane electrodes with bumps on their surface holds more interest. The field amplification $q = F_{loc}/F$ at the top of a bump is usually accepted to be approximately equal to the ratio h/r, where h is the height of the bump and r is its radius. For a cylindrical bump terminating with a hemisphere, a more rigorous expression was obtained: $q = 1.2(h/r + 2.15)^{0.9}$ [23]. Earlier, it was assumed that $q = h/r + 2$ in these conditions [24]. The combined effect of closely situated bumps on the local field can be taken into account using the relation $q_1 = q[1 - \exp(-2.32s/h)]$, where s is the distance between bumps [23].

The nonuniform field produced between plane-parallel electrodes with semiellipsoidal bumps on one of them was treated in [24, 25]. The field on the ellipsoid

axis as a function of distance from the bump top was found to be [24]

$$q(\Delta x) = \frac{\beta}{1 + 2\dfrac{\Delta x}{r}}\frac{h}{r} + 1, \quad (1)$$

where Δx is the distance from the top of the bump. For $\Delta x = 0$, i.e., at the bump top, we have $q = 1 + \beta h/r$. Here, $\beta = [\operatorname{arctanh}(c/h) - c/h]^{-1}$, where c is half of the distance between the foci of the ellipse, so $r = (h^2 - c^2)/h$. If h/r is not very large, we have $\beta \approx 1$ and $q \approx 1 + h/r$.

Note that the field amplification increases with decreasing electrode gap. Generally speaking, this factor should be taken into account when studying the properties of thin films. However, calculations showed that, for $d/h = 2$ (where d is the gap between plane electrodes), the increase in the field amplification does not exceed 10% as compared to the case of $d/h \gg 1$ [26].

Thus, the local field strength can exceed the average field by a few times. Because the average breakdown field, as already mentioned, is (2–6) MV/cm, the field in the microscopic regions where processes that prepare breakdown of a polymer dielectric occur is approximately 10 MV/cm immediately after the application of voltage. In such strong fields, intense carrier injection from electrodes into the dielectric takes place. Because carriers are captured by deep traps, space charge (SC) builds up in the polymer dielectric. The SC formation lowers the electric field strength near the electrodes and thereby strongly decreases the injection current. The low leakage current in strong fields caused by SC-limited carrier injection is a property that distinguishes polymer dielectrics from the polymer materials with good transport characteristics that are used in micro- and optoelectronics (for instance, for the fabrication of LEDs). Such polymers exhibit semiconductor properties in strong fields that cause carrier injection from electrodes (the intrinsic carrier concentration is very low). The low currents observed in fairly strong fields in such polymers as PE, PP, PS, and PETP employed as insulators are due to the high deep-trap concentration and SC formation.

From the data summarized above, it can be concluded that discussion of the possible mechanism of breakdown in thin polymer films should take into account the following points: (i) the field present in a dielectric is the sum of the external field determined by the voltage applied across the specimen and the SC field; (ii) breakdown is a local process that occurs in the region of electric field amplification; (iii) current amplification initiating local destruction of a polymer is a consequence of SC evolution, which gives rise to a local electric field enhancement; and (iv) the intense surge in the current causing a breakdown channel in the polymer film is the last stage of the electric field–induced destruction of a polymer. The preparatory stage may take a fairly long time. The rate of buildup of changes in a polymer that culminate in an actual breakdown can be characterized by a quantity inverse to the lifetime of a polymer specimen.

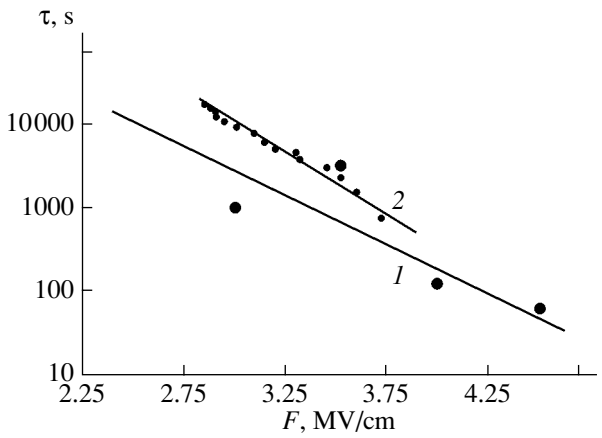

Fig. 1. Electrical lifetime of polymer films plotted vs. electric field strength for (*1*) a PS film and (*2*) a PI film.

Figure 1 shows (in semilogarithmic coordinates) the $\tau(F)$ dependence obtained by us earlier [11] for a PS film (curve *1*) and an analogous dependence (curve *2*) for a PI film constructed using data from [9]. We readily see that $\tau \sim \exp(-\alpha F)$ for both polymers.

As already mentioned, the time taken for the formation of a breakdown channel is 10^{-8}–10^{-7} s. It is believed that destruction of a polymer (the formation of a hollow channel with conducting walls as a result of polymer evaporation and the formation of soot) is the outcome of Joule heat liberation and heating of the material to high temperatures by an intense surge in current. Polymer carbonization (soot formation) occurs at a temperature of 1800 K [27]. At this temperature, two-thirds of all chemical bonds with an energy of ~2 eV each are ruptured within a given volume in a time of 5×10^{-8} s (assuming this time to be the duration of breakdown development). In order to heat a polymer to this temperature in adiabatic conditions, i.e., in the absence of interaction with the ambient medium, an energy of about 3 kJ/cm^3 has to be expended (accepting 2 J/g K as the polymer specific heat), which corresponds to a specific heat power dissipation during the breakdown of 6×10^4 MW/cm^3. For a field of 10 MV/cm, this heat corresponds to a current density of 6 kA/cm^2. Even such current densities are apparently not high enough to ensure fast polymer destruction, because in real conditions, even for a period of time of ~10^{-8} s, one would have to take into account heat dissipation from a current-heated channel. This conclusion is directly suggested by the observation of the so-called nondestructive breakdown (NDB) of polymers, i.e., consecutive bursts of current, in a sphere–plane system with an increase in voltage under current-limiting conditions [28]. The current pulse length was a few tens of nanoseconds, and the current density was estimated as

3 kA/cm^2 [28]. PETP and PS films sustained tens of current pulses of the above density without destruction.

Let us estimate the current densities needed to destroy a breakdown channel assuming that the specific heat power P released in it is given by the relation $P = jF$ and is independent of time. We consider a disk-shaped film of radius R and thickness d with an axial current-conducting channel of radius δ (we take $\delta = 5$ μm). We also assume that heat dissipates out of the film by free convective heat exchange with the ambient medium (with the corresponding coefficient $\alpha_T \approx 3$ W/s m^2 [29]).

To estimate the channel temperature with due account of heat dissipation into the ambient medium, we use the solution to the classical heat conduction equation, i.e., the problem of the temperature distribution field for a finite cylinder with an inner steady-state source of heat [30]. For the specific conditions of our model, this solution can be cast as

$$T(r, z, t) = T_0 + \frac{4d^2P\delta}{\lambda R}\sum_{m=1}^{\infty} c_m\varphi_m(z)$$
$$\times\left[\sin p_m - \frac{\mathrm{Bi}}{p_m}(\cos p_m - 1)\right]$$
$$\times\sum_{n=1}^{\infty} c_n\frac{J_1\left(\mu_n\frac{\delta}{R}\right)J_0\left(\mu_n\frac{r}{R}\right)}{\mu_n J_0^2\left(\mu_n\frac{\delta}{R}\right)} \qquad (2)$$
$$\times\frac{\left\{1 - \exp\left[-\left(p_m^2\frac{R^2}{d^2} + \mu_n^2\right)\frac{a_T}{R^2}t\right]\right\}}{\left(p_m^2\frac{R^2}{d^2} + \mu_n^2\right)},$$

where T_0 is the temperature of the specimen, which is initially equal to that of the ambient medium ($T(r, z, 0) = T_0$); λ and α_T are the coefficients of thermal conductivity and thermal diffusivity of a polymer dielectric, respectively; and p_m and μ_n are positive roots of the transcendental equations

$$\cot(p_m) = \frac{p_m^2 - \mathrm{Bi}^2}{2p_m\mathrm{Bi}} \quad \text{and} \quad \frac{J_0(\mu_n)}{J_1(\mu_n)} = \frac{\mu_n}{\mathrm{Bi}_r};$$

$$\mathrm{Bi}_r = \frac{\alpha_T R}{\lambda}, \quad \mathrm{Bi} = \frac{\alpha_T d}{\lambda},$$

$$c_m = \left[(p_m^2 + \mathrm{Bi}^2)\left(1 + \frac{\mathrm{Bi}}{p_m^2 + \mathrm{Bi}^2}\right) + \mathrm{Bi}\right]^{-1},$$

$$c_n = \frac{\mu_n^2}{\mu_n^2 + \mathrm{Bi}_r},$$

$$\varphi_m(z) = p_m\cos\left(p_m\frac{z}{d}\right) + \mathrm{Bi}\sin\left(p_m\frac{z}{d}\right).$$

Note that fast and intense processes should be described by the hyperbolic equation of heat conduction (rather than by the classical equation) [31], which takes into account the finite rate of heat propagation. However, formidable mathematical difficulties arise in its solution. We believe that Eq. (2) can be used to estimate the channel temperature, but the computations should be conducted in step-by-step manner by dividing the heating time into a number of intervals. Within each interval of time, one has to solve Eq. (2) with a prescribed initial channel temperature T_0, which is obtained by the channel temperature calculation in the preceding step, and limit the specimen size to the region of effective radius R into which the heat has propagated by the given instant of time t. In the first time interval ($t = 0$), we assumed that $R = \delta$ and $T_0 = 293$ K. The time step was chosen equal to 1 ns. Accepting the heat propagation velocity to be equal to the sonic velocity in a polymer (~1500 m/s), we obtain that the effective radius of the specimen should increase by 1.5 μm in 1 ns.

Figure 2 illustrates the channel-heating computations performed for 6-, 3-, and 1-μm-thick films (curves *1*, *2*, *3*, respectively) for a specific heat power release of 10^5 MW/cm^3. We see that films less than 3 μm in thickness do not heat to high temperatures in ~100 ns for the given power of heat liberation. Figure 3 presents data on the channel temperature in 10-, 1-, and 0.1-μm-thick films (curves *1*, *2*, *3*, respectively) heated for 80 ns by sources with different heat power outputs. We readily see that, in films of submicron thickness, a channel can be heated to a noticeable level in the given time only at heat release power levels in excess of 10^8 MW/cm^3.

Estimates showed that destruction of a polymer film (the formation of a breakdown channel) is caused by a very short, extremely high-density current surge (~10 MA/cm^2). Such currents are comparable to the limiting current densities of field emitters operating in vacuum in fields of 10 MV/cm [32]. High-density injection currents in metal–polymer–metal structures can obviously appear only when the fields near metallic electrodes approach this level. One can reasonably assume that the creation of strong local fields in a pre-breakdown state ensues from a fairly long SC rearrangement in polymers and the formation and intergrowth of filamentary channels with a high SC density. Thus, the mechanism of electrical breakdown in polymer films (the development of the process preceding the formation of a conducting channel and the polymer breakdown proper initiated by a surge of high-density current) can be qualitatively conceived as follows.

We assume for definiteness that the conditions for injection of electrons into a polymer are more favorable than those for holes from the anode, for instance,

because the barrier through which electrons tunnel from the metal into the polymer is lower than that through which electrons tunnel into the metal. Upon applying voltage, electron injection into the polymer will set in. Tunneling takes place not from all of the cathode surface but rather from microscopic tips on its surface, at which the electric field strength is in excess of its average value. The electrons are captured by traps. The negative SC (NSC) thus formed lowers the field at the cathode tips, and the injection current drops fairly rapidly, in a time of 10^{-6}–10^{-5} s [33]. For an NSC density of ~10^{13} cm^{-2}, the NSC field will be comparable to the cathode field (in the absence of NSC), with the result that the injection current will become very low.

As the NSC propagates toward the anode, the field at the anode will grow. The rate of this process depends on the rate of electron release from the traps and on the injection current density.

Let us estimate the possible field amplification at the anode as the NSC approaches it. We assume the NSC density to be

$$n(x) = \begin{cases} n, & 0 \le x \le x_b \\ 0, & x \ge x_b, \end{cases} \quad (3)$$

where x_b is the boundary reached by the NSC (the filament boundary). We use the simplest model of a plane capacitor (which is applicable to thin films), in which the electrode separation d is equal to the film thickness. Solving the Poisson equation for the field $F(x)$ and charge $n(x)$ and recalling that $\int_0^d F(x)dx = U$, we finally find that the field strength at the anode $F(d)$ is related to the penetration depth x_b as

$$F(d) = F + \frac{en}{2\varepsilon\varepsilon_0}\frac{x_b^2}{d}, \quad (4)$$

where $\varepsilon_0 = 8.85 \times 10^{-12}$ F/m and ε is the permittivity of the polymer.

Figure 4 shows the relative field strength enhancement at the anode $\Delta F/F = [F(d) - F]/F$ as a function of the NSC penetration depth. The estimates were done for $n = 10^{18}$ cm^{-3}, $\varepsilon = 2.5$, and $d = 0.1$ μm. A noticeable increase in the field strength (by more than 10%) is observed to occur when $x_b \approx 40$ nm. Note that, as the field at the electrode increases by 10%, the injection current (as follows from estimates made using the Fowler–Nordheim relation for real barriers) increases by about 10 times for a barrier height of 2.0–2.5 eV.

As a result of the NSC penetrating toward the anode, the field at the latter will reach the level at which hole injection into the polymer sets in. A cloud of positive space charge (PSC) forms and starts to move toward the cathode, thereby enhancing the field at this electrode, which, in turn, will bring about an enhancement of electron injection intensity, and so on. Thus, there appears a positive feedback, which is a necessary condition for abrupt growth of the current resulting in polymer breakdown. Because injection (tunneling) currents depend exponentially on the field at the electrode–polymer interface, even a slight increase in the field at the cathode will entail a substantial increase in the injection current density. It is this factor that, in the presence of the above positive feedback, accounts for the experimentally observed sharp increase in the current giving rise to polymer breakdown. Electron–hole recombination favors acceleration of the breakdown both as a

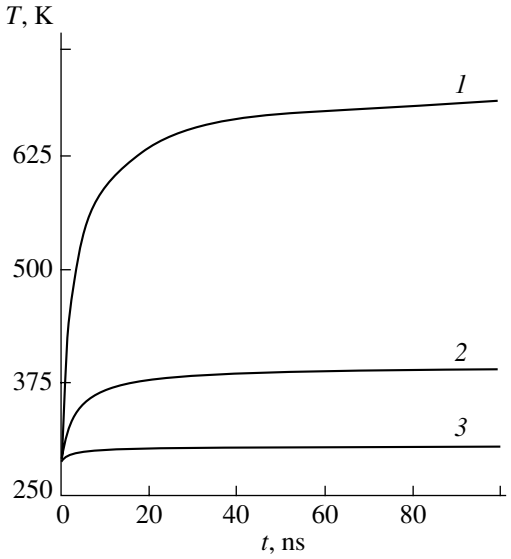

Fig. 2. Temperature of a conducting channel as a function of heating time for films with various thicknesses: (*1*) 6, (*2*) 3, and (*3*) 1 μm. $P = 10^5$ MW/cm^3.

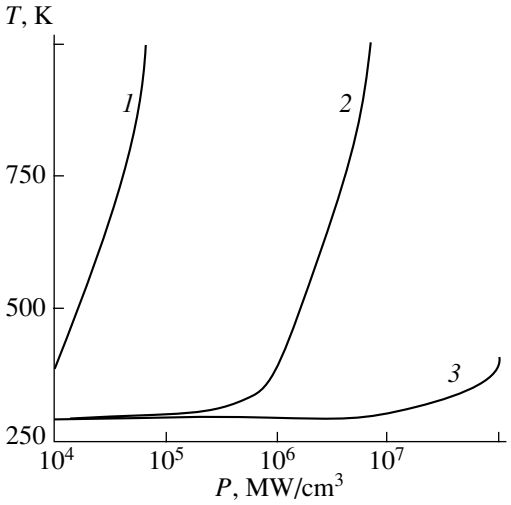

Fig. 3. Temperature of the conducting channel as a function of specific heat power release for films with various thicknesses: (*1*) 10, (*2*) 1, and (*3*) 0.1 μm. The heating time is 80 ns.

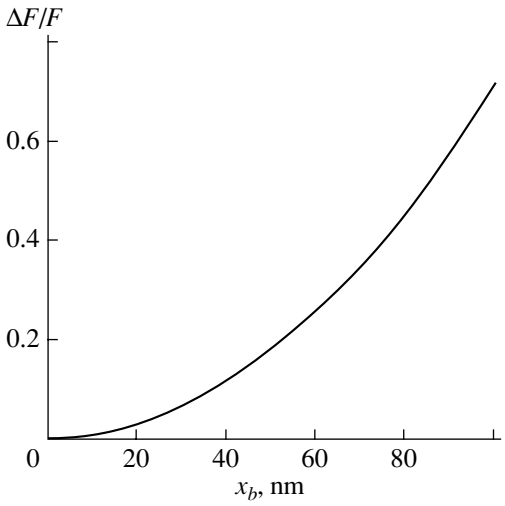

Fig. 4. Relative field amplification plotted vs. NSC penetration depth.

result of SC compensation and due to the energy release.

In our opinion, the lifetime of a polymer film in an electric field is determined by the longest stage in the above process, namely, the SC rearrangement. Therefore, we have $\tau \approx Q/j$. Here, Q is the transported charge ($Q \sim 1$ μC) and j is the SC-limited current in a material with traps, $j \approx \varepsilon\mu\Theta U^2/d^3$ [19], where μ is the carrier mobility, $\Theta = n_0/n_t$, n_0 is the free carrier concentration, and n_t is the concentration of carriers captured by traps. We can write $\Theta = q\exp(E_t/kT)$, where E_t is the trap depth, q is a dimensionless coefficient dependent on the trap concentration, k is the Boltzmann constant, and T is the temperature. In an electric field, the neutral-trap depth decreases by an amount $\Delta E = aeF$, where e is the electronic charge and a is the trap width (for an electric field $F = 5$ MV/cm and $a = 0.5$ nm, we have $\Delta E = 0.25$ eV). Hence, the lifetime τ depends exponentially on temperature and electric field strength; i.e.,

$$\tau \sim \exp[(E_t - aeF)/kT]. \quad (5)$$

As already mentioned, the $\tau(F)$ relations were studied in [6, 10] for PE and PS. Those studies yielded $\tau \sim \exp(-\alpha F)$. Assuming that $\alpha = a/kT$, we estimated a to be 0.9 and 0.7 nm for PE and PS, respectively. These figures appear physically reasonable.

Thus, the proposed mechanism of electric field–induced breakdown of thin polymer films is based on the following main points. (1) Considerations based on the concept of avalanche current amplification through ionization processes are inapplicable to thin films, because the voltage applied across a film is comparable to the ionization potential of molecules. (2) SC evolution causes local field enhancement in small volumes of the polymer, which brings about its breakdown. (3) The necessary condition for breakdown phenomena to develop (the presence of a positive feedback) is met as a result of a strong dependence of the bipolar injection intensity on electric field.

The above concepts concerning electrical polymer breakdown can be further developed and refined, in particular, by taking into account the trap distribution in energy in describing carrier transport in these materials and by quantitatively describing all stages of this process with due account of charge recombination and macromolecule ionization in strong electric fields.

REFERENCES

1. K. W. Plessner, Proc. Phys. Soc. **60** (3), 243 (1948).
2. P. P. Budenstein, P. J. Hayes, J. L. Smith, and W. B. Smith, J. Vac. Sci. Technol. **6** (2), 289 (1969).
3. V. Ya. Aĭvazov, B. O. Bertush, and V. G. Kobka, Élektron. Tekh., Ser. 4: Mikroélektron., No. 1, 94 (1971).
4. C. A. Hogarth and T. Iqbal, Thin Solid Films **51** (3), L45 (1978).
5. K. Kitagawa, G. Sawa, and M. Ieda, Jpn. J. Appl. Phys. **19**, 2 (1980).
6. D. Lin and K. C. Kao, J. Appl. Phys. **69** (4), 2489 (1991).
7. N. R. Tu and K. C. Kao, J. Appl. Phys. **85** (10), 7267 (1999).
8. D. Linfu and K. C. Kao, J. Appl. Phys. **85** (2), 1089 (1999).
9. V. I. Arkhipov, E. V. Emelianova, Y. H. Tak, and H. Bässler, J. Appl. Phys. **84** (2), 848 (1998).
10. V. A. Zakrevskiĭ, O. F. Pozdnyakov, and N. T. Sudar', Materialovedenie, No. 7, 2 (2001).
11. K. Miyairi, Jpn. J. Appl. Phys., Part 1 **42** (8), 5153 (2003).
12. K. Miyairi, Jpn. J. Appl. Phys., Part 1 **40** (3A), 1297 (2001).
13. V. A. Zakrevskiĭ and N. T. Sudar', Zh. Tekh. Fiz. **66** (4), 105 (1996) [Tech. Phys. **41**, 352 (1996)].
14. V. B. Berezhanskiĭ, V. V. Gorodov, V. A. Zakrevskiĭ, and V. I. Rud', Élektrotekhnika, No. 7, 27 (1990).
15. S. V. Zhukov, V. A. Zakrevskiĭ, S. P. Kabin, and N. T. Sudar', Izv. Vyssh. Uchebn. Zaved., Fiz. **31** (4), 86 (1988).
16. G. I. Skanavi, *Physics of Dielectrics (Strong-Field Region)* (Fizmatgiz, Moscow, 1958) [in Russian].
17. K. C. Kao, J. Appl. Phys. **55** (3), 752 (1984).
18. M. Nikita, I. Kanno, G. Sawa, and M. Ieda, Jpn. J. Appl. Phys. **24** (8), 984 (1985).
19. K. Kao and W. Hwang, *Electrical Transport in Solids* (Pergamon, Oxford, 1981; Mir, Moscow, 1984), Parts 1, 2.
20. Y. Segui, Bai Ai, and H. Carchano, J. Appl. Phys. **47** (1), 140 (1976).
21. R. W. Hare and R. M. Hill, J. Phys. D: Appl. Phys. **24** (3), 398 (1991).
22. L. M. Baskin, G. G. Vladimirov, and V. N. Shrednik, Poverkhnost, No. 7, 67 (1999).
23. S. H. Jo, Y. Tu, Z. P. Huang, D. L. Carnahan, D. Z. Wang, and Z. F. Ren, Appl. Phys. Lett. **82** (20), 352 (2003).
24. I. N. Slivkov, *Processes at High Voltage in Vacuum* (Énergoatomizdat, Moscow, 1986) [in Russian].

25. D. L. Jaeger and J. J. Hren, J. Appl. Phys. **93** (1), 691 (2003).

26. V. A. Nevrovskiĭ and V. N. Yaroslavskiĭ, Zh. Tekh. Fiz. **52** (2), 278 (1982) [Sov. Phys. Tech. Phys. **27**, 180 (1982)].

27. *New Materials*, Ed. by Yu. S. Karabaev (Mosk. Inst. Stali Splavov, Moscow, 2002) [in Russian].

28. N. Riehl, H. Baessler, S. Hunklinger, W. Spannring, and G. Vaubel, Z. Angew. Phys. **27** (7), 261 (1969).

29. O. G. Martynenko and Yu. A. Sokovishin, *Free-Convective Heat Exchange: Handbook* (Nauka i Tekhnika, Minsk, 1982) [in Russian].

30. É. I. Ermolina, A. A. Stupachenko, E. V. Kharitonov, and V. N. Cherkasov, Élektron. Tekh., Ser. 5: Radiodet. Radiokomp., No. 3(34), 3 (1979).

31. A. V. Lykov, *Theory of Heat Conductivity* (Vysshaya Shkola, Moscow, 1967) [in Russian].

32. A. Modinos, *Field, Thermionic, and Secondary Electron Emission Spectroscopy* (Plenum, New York, 1984; Nauka, Moscow, 1990).

33. V. A. Zakrevskiĭ and N. T. Sudar', Fiz. Tverd. Tela (St. Petersburg) **40** (6), 1167 (1998) [Phys. Solid State **40**, 1066 (1998)].

Translated by G. Skrebtsov

Physics of the Solid State, Vol. 47, No. 5, 2005, pp. 968–974. Translated from Fizika Tverdogo Tela, Vol. 47, No. 5, 2005, pp. 937–943.

Influence of the Supramolecular Structure on the Activation Energy of Steady-State Creep in an Oriented Ultra-High-Molecular Weight Poly(ethylene)

V. I. Vettegren, E. M. Ivan'kova, M. A. Kryuchkov, V. A. Marikhin, L. P. Myasnikova, and P. N. Yakushev

Ioffe Physicotechnical Institute, Russian Academy of Sciences, Politekhnicheskaya ul. 26, St. Petersburg, 194021 Russia
e-mail: Liuba.Myasnikova@mail.ioffe.ru

Abstract—The stepwise change in the rate of steady-state creep of gel-crystallized and melt-pressed oriented ultra-high-molecular weight poly(ethylene) (UHMWPE) samples is studied using a precision Doppler meter at room temperature. The creep activation energies are calculated from the creep rates, and the distributions of activation barriers are determined. It is established that the distributions of activation barriers are characterized by three maxima whose positions, intensities, and half-widths depend on the supramolecular structure of the samples. These maxima are assigned to the activation barriers that are overcome in the course of shears of microfibrils inside the macrofibrils and between them in the bulk of the samples and on their surface. © *2005 Pleiades Publishing, Inc.*

1. INTRODUCTION

Creep is a gradual deformation of a material in response to a constant force. This phenomenon is especially pronounced in polymer materials and considerably restricts their field of application. The creep of a material subjected to stresses over a wide range occurs through three characteristic stages: at the first stage, the creep rate decreases; at the second stage, the creep rate remains nearly constant (steady-state creep); and at the third stage, the creep rate rapidly increases to the extent of rupturing the sample.

The processes occurring at the stage of steady-state creep have been investigated most intensively. This can be explained by the fact that the steady-state creep stage lasts over the longest period of time as compared to the other creep stages; moreover, the steady-state creep phenomenon has been used for predicting the initial instant of fracture of a material. Numerous attempts to elucidate the mechanism of creep of a material, to predict the evolution of deformation with time, and to devise appropriate methods for increasing the creep resistance have been widely covered in the literature [1–11].

According to Eyring [1], steady-state creep is treated as a Newtonian flow and can be described by the Arrhenius equation

$$\dot{\varepsilon} = \dot{\varepsilon}_0\left(-\frac{Q_0 - \alpha\sigma}{k_B T}\right), \quad (1)$$

where $\dot{\varepsilon}$ is the creep rate, $\dot{\varepsilon}_0 \approx 10^{-13}$ is the preexponential factor, σ is the applied stress, Q_0 is the activation energy for steady-state creep at $\sigma \longrightarrow 0$, α is the activation volume for steady-state creep, k_B is the Boltzmann constant, and T is the absolute temperature.

Zhurkov and colleagues (see monographs [2, 3]) developed the kinetic concept of strength of solids and paid special attention to the fact that the creep exhibits a thermal fluctuation nature and that the activation energy for fracture coincides with the activation energy for steady-state creep. The elementary events of fracture were treated as "irreversible" ruptures of interatomic bonds, whereas the elementary events of deformation were considered as atomic and molecular rearrangements due to the "reversible" ruptures of interatomic bonds. The above coincidence stems from the fact that the activation energy for these processes, $Q = Q_0 - \alpha\sigma$, corresponds to the energy of generation of excited atomic states whose relaxation occurs with the formation of fracture nuclei or deformation zones.

The activation parameters of creep (Q_0, α) can be calculated from phenomenological data. This calculation is correct provided the structure of the material and the activation barrier to creep remain unchanged in the course of measurements. It is generally believed that, in the case of steady-state creep, these conditions are satisfied *a priori*.

However, the assumption that the activation parameters in the course of creep remain constant contradicts the lability of different structural units involved in a complex hierarchical supramolecular structure of polymers. In actual fact, the activation parameters remain approximately constant only within limited ranges of strains, loads, and temperatures.

1063-7834/05/4705-0968$26.00 © 2005 Pleiades Publishing, Inc.

In particular, Govaert and colleagues [4, 5] investigated the behavior of loaded gel-crystallized oriented ultra-high-molecular weight poly(ethylene) (UHMWPE) fibers and found that the creep activation energy Q_0 is equal to 118 kJ/mol under loads in the range from 200 to 1500 MPa and at temperatures in the range from 30 to 90°C.

Ward and Wilding [6, 7] studied melt-extruded oriented poly(ethylene) fibers and revealed a kink in the dependence of the rate of steady-state creep on the applied load. On this basis, it was assumed that there occur two competitive processes characterized by different thermal activation volumes α, which are equal to 50 and 10 nm^3. The former process dominates at small loads, whereas the latter process prevails at large loads. The former process was interpreted as a deformation of the network of cross-linked molecules, and the latter process was treated as an intracrystallite shear.

The same conclusion regarding the occurrence of two competitive thermally activated processes was drawn by Penning [8], who studied the creep in gel-crystallized highly oriented UHMWPE fibers. However, the activation volumes calculated for these processes appeared to be considerably smaller (α = 3 and 1.5 nm^3, respectively) than those obtained in the preceding case. This indicates that the deformation processes occurring in oriented fibers prepared from a solution are more localized than those observed in fibers produced from a melt. The process characterized by an activation volume of 3 nm^3 was interpreted as a deformation of incompletely stretched chain segments between cross links, whereas the process with an activation volume of 1.5 nm^3 was treated as an intracrystallite shear.

Peschanskaya and colleagues [9–11] investigated the creep of amorphous polymers under uniaxial compression with the use of a precision Doppler meter of creep rates and made the inference that the activation parameters are not constant and depend on the specific features of the supramolecular structure of these materials. It was revealed that the activation parameters (activation energy, activation volume) during creep vary significantly. In the authors' opinion [9–11], it is incorrect to characterize a particular polymer by a constant creep activation energy (or by a constant creep activation volume) without regard for the creep stage and the temperature.

It is known [12, 13] that oriented polymers possess a pronounced structural heterogeneity: the structure of these materials contains macrofibrils arranged parallel to each other and composed of microfibrils in which ordered crystalline regions regularly alternate with less ordered amorphous regions. In our opinion, elementary events of creep that occur inside different structural aggregates should be described by the characteristic values of the creep activation parameters (Q_0, α). To put it differently, the creep process should be controlled not by one set of Q_0 and α but by several sets of such parameters and each set should correspond to a particular type of structural aggregate.

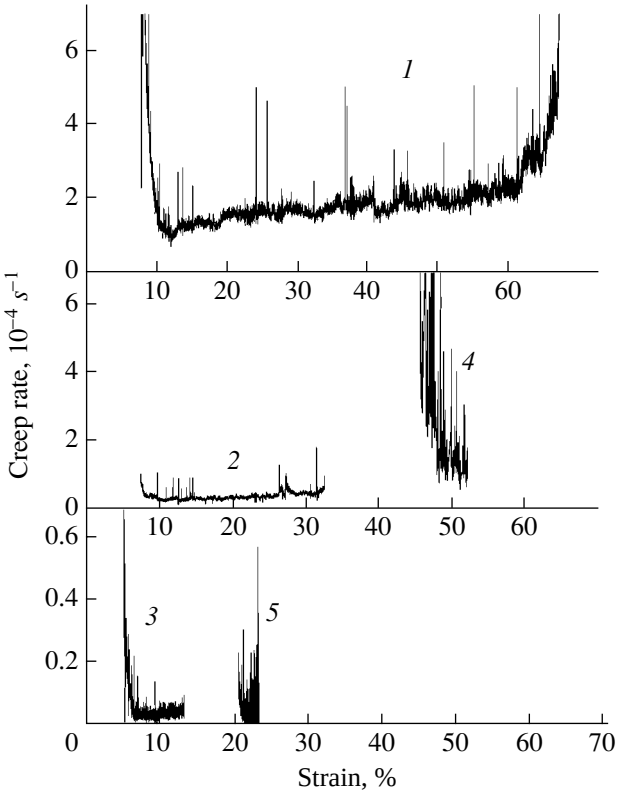

Fig. 1. Dependences of the logarithm of the creep rate $\ln\dot{\varepsilon}_0$ on the creep strain ε for (*1–3*) gel-crystallized and (*4*, *5*) melt-pressed UHMWPE films with draw ratios λ = (*1*) 24, (*2*) 64, (*3*) 120, (*4*) 4.5, and (*5*) 7.

In earlier studies [14, 15], we revealed a stepwise change in the rate of steady-state creep of oriented UHMWPE fibers and films with the use of a precision Doppler meter of creep rates. This finding was explained by the displacements of fibrillar aggregates with respect to each other according to the slip–stick mechanism. It was assumed that the total deformation predominantly occurs through shears of microfibrils and macrofibrils. In order to prove the occurrence of a slip of microfibrils and macrofibrils, we investigated the creep of oriented UHMWPE samples with different degrees of connectivity of fibrillar structural units [14, 15]. It was established that the presence of fibrils of different types in the structure is responsible for the stepwise change in the rate of steady-state creep [14, 15].

In a more recent work [16], the data on the stepwise change in the creep rate were used to calculate the distribution of activation barriers that are overcome during elementary events of steady-state creep. It turned out that not one but three activation barriers $Q = Q_0 - \alpha\sigma$ are overcome in the course of creep of highly oriented UHMWPE samples. In [16], we determined the most

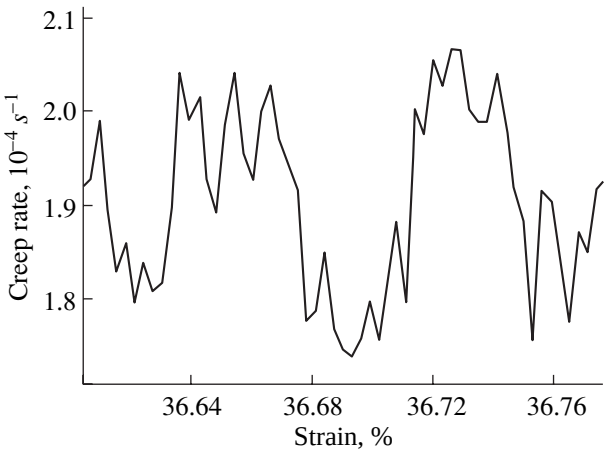

Fig. 2. Fragment of the dependence of the logarithm of the creep rate $\ln\dot{\varepsilon}_0$ on the creep strain ε for the gel-crystallized UHMWPE film with a draw ratio of 24.

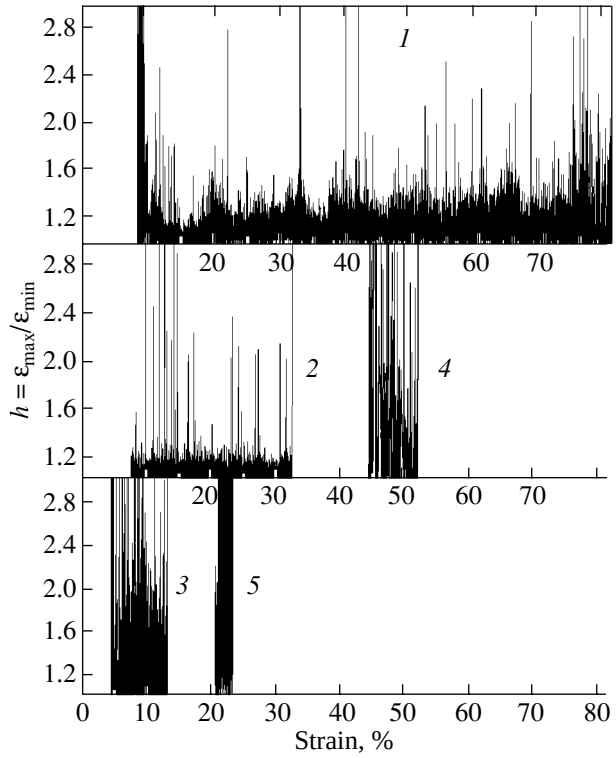

Fig. 3. Dependences of the nonuniformity parameter of the extension rate h ($h = \dot{\varepsilon}_{max}/\dot{\varepsilon}_{min}$) on the strain ε for (*1–3*) gel-crystallized and (*4, 5*) melt-pressed UHMWPE films with draw ratios λ = (*1*) 24, (*2*) 64, (*3*) 120, (*4*) 4.5, and (*5*) 7.

probable heights of activation barriers, the activation barrier distributions, and the relative concentration of stoppers with these barriers in the studied sample.

This study is a continuation of the investigation performed in [16]. In the present work, we thoroughly studied the distribution of activation barriers to creep in gel-crystallized and melt-pressed UHMWPE samples and assigned these barriers to particular types of supramolecular aggregates.

2. SAMPLE PREPARATION AND EXPERIMENTAL TECHNIQUE

For our experiments, films were prepared by two methods. According to the first method, a 1.5% UHMWPE (Stamylan, M_w = 2.6 kJ/mol) solution in decalin at a temperature of 170°C was poured into a tray cooled to room temperature. Upon cooling, the solution transformed into a gel. Then, the gel was dried. According to the second method, films were prepared by pressing from a melt at a temperature of 170°C.

The films thus prepared were cut into narrow strips. The strips were subjected to orientation multistage zone stretching on an "iron" [12] in order to obtain strip samples with different degrees of stretching (draw ratios). During orientation stretching, the temperature varied from 110 to 135°C and the stretching rate was 10 cm/min.

The steady-state creep of the sample subjected to a constant force was examined using a precision Doppler meter of creep rates at room temperature. The creep activation energy $Q = Q_0 - \alpha\sigma$ was calculated from the relationship [1, 2]

$$Q = k_B T \ln\frac{\dot{\varepsilon}_0}{\dot{\varepsilon}}. \quad (2)$$

In order to compare the results obtained, the load was chosen equal to half the ultimate tensile stress for each sample under investigation.

3. SPREAD OF CREEP RATES

Figure 1 presents the so-called Sherby–Dorn plots, i.e., the dependences of the logarithm of the creep rate $\ln\dot{\varepsilon}_0$ on the creep strain ε for the UHMWPE films under investigation. To the inexperienced reader, such dependences may seem to be usual "noisy" curves. Such a mistaken impression arises from the graphical representation of the very large amount of data obtained over the entire range of creep strains in the case when the creep rate is recorded in 0.001% strain increments. Examination of the small portion of the creep curve (Fig. 2) strongly suggests that the observed "outliers" in the creep rate cannot be treated as noise and that the deformation actually occurs in a stepwise manner.

Analysis of the data presented in Figs. 1 and 2 demonstrates that, in all the studied samples, the creep is a very irregular process: the rate at which the deformation proceeds increases and decreases in alternate fashion. It should be noted that the spread of strain rates depends on both the degree of orientation stretching (Fig. 1, curves *1–3*) and the supramolecular structure of the samples (Fig. 1; curves *1, 4* or *1, 5*). This is espe-

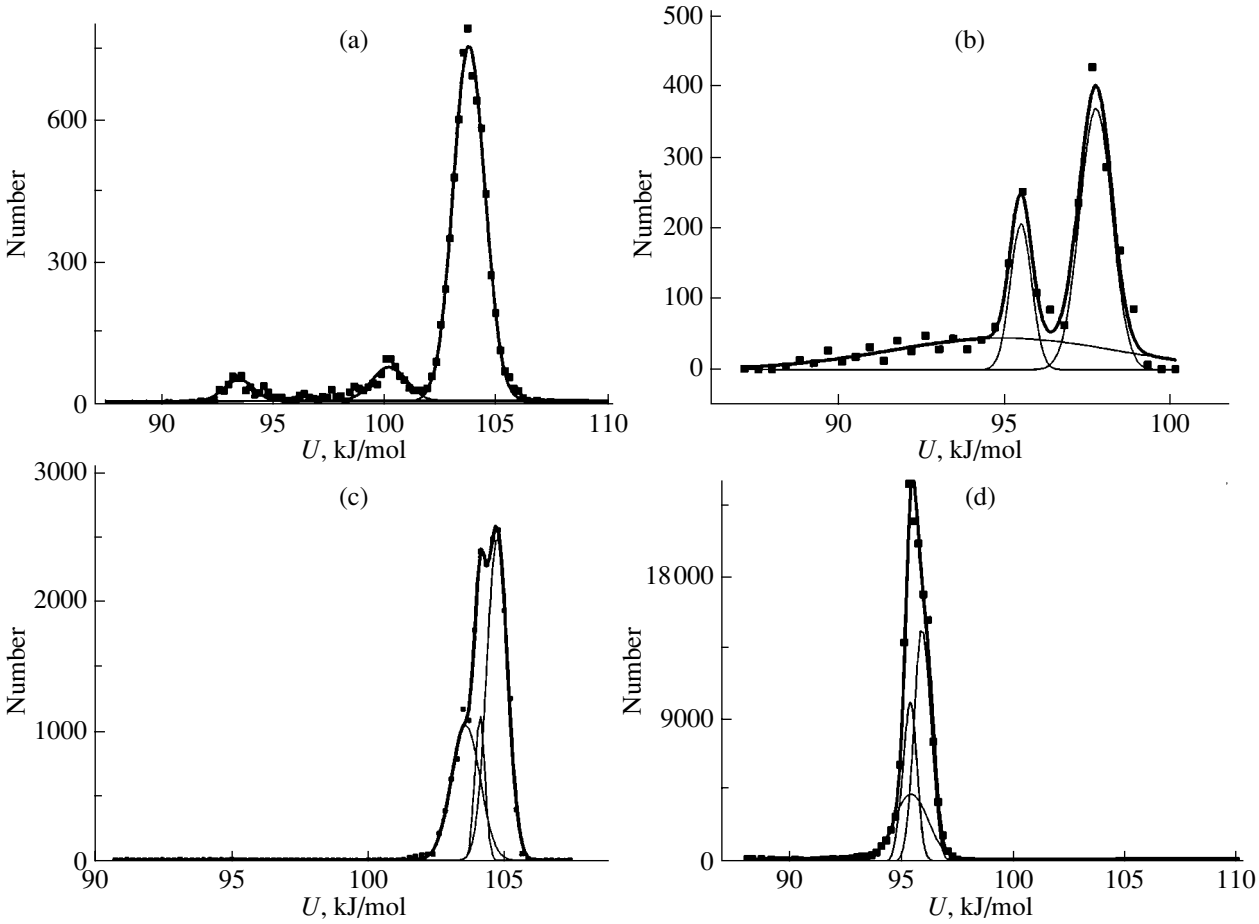

Fig. 4. Distributions of the activation energies for steady-state creep of (a, c, d) gel-crystallized and (b) melt-pressed UHMWPE films with draw ratios λ = (a) 120, (b) 4, (c) 64, and (d) 24.2.

cially pronounced in the dependences of the nonuniformity parameter of the extension rate $h = \dot{\varepsilon}_{max}/\dot{\varepsilon}_{min}$ on the strain (Fig. 3). The maximum strain rate $\dot{\varepsilon}_{max}$ in a jump for the sample with a draw ratio of 24 is higher than the minimum strain rate $\dot{\varepsilon}_{min}$ by a factor of 1.3–1.4. In some cases, the jumps are rather large. For the samples with a draw ratio λ = 64, the maximum and minimum strain rates in a jump differ by a factor of 1.2, but large jumps (in which the maximum strain rate is higher than the minimum strain rate by a factor of 2.2) are observed more frequently than those for the sample with a draw ratio of 24. For ultimately oriented films, the maximum strain rate in the majority of jumps exceeds the minimum strain rate by a factor of 2.4 and, sometimes, by a factor of 3.

4. DISTRIBUTION OF CREEP ACTIVATION ENERGIES

According to relationship (2), the observed spread in the strain rates implies that the creep activation energy $Q = Q_0 - \alpha\sigma$ varies insignificantly with respect to a mean value. To put it differently, there is a small spread of creep activation energies about a mean value. For example, the creep activation energy for the gel-crystallized sample with a draw ratio of 120 is equal to 103 ± 7 kJ/mol; i.e., the spread of activation barrier heights does not exceed 7% of the mean value. For the other UHMWPE samples, the spread of activation barrier heights also does not exceed 7%. However, even within the limits of such a small spread, not all activation energies are equally probable because the activation barrier distribution function exhibits pronounced maxima (Fig. 4). These maxima correspond to the most probable heights of activation barriers.

As can be seen from Fig. 4, the distribution of the activation energies for steady-state creep of the UHMWPE films depends on both the degree of orientation stretching (draw ratio) and the technique used for preparing an unoriented sample (from a melt or from a solution), i.e., on the supramolecular structure of the polymer.

These findings do not cast any doubt on the previous results used to make the inference that the activation energy of oriented polymers is independent of the

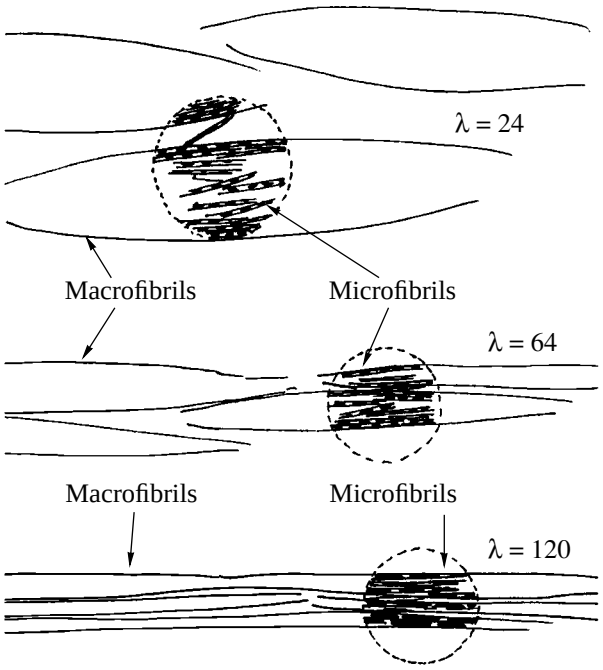

Fig. 5. Structure of an oriented polymer with different draw ratios.

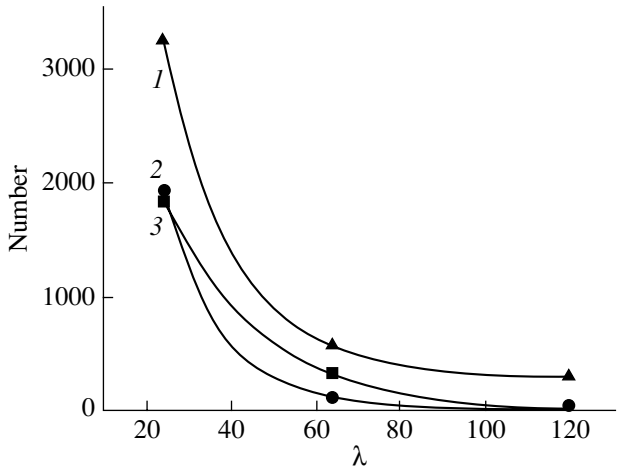

Fig. 6. Dependences of the number of activation barriers (stoppers) corresponding to shears of microfibrils in (*1*) the bulk of macrofibrils, (*2*) the interfibrillar region, and (*3*) the surface layer on the draw ratio for gel-crystallized UHMWPE films.

supramolecular structure. Actually, the spread of activation energies (approximately 7% of the mean value) for which the energy distribution depends on the structure does not exceed the experimental error of traditional measurements (as a rule, this error is approximately equal to 10%).

For the gel-crystallized UHMWPE sample stretched by a factor of 120, the distribution of the activation barrier heights exhibits three narrow maxima whose shape can be described by a Gaussian function (Fig. 4a).

For the sample prepared by pressing from a melt at 170°C and then stretched by a factor of 4.5, the distribution of the activation barrier heights is a superposition of two narrow maxima and one broad maximum (Fig. 4b). The shape of these maxima can also be described by a Gaussian function.

The distribution of the activation energies for steady-state creep of the other samples exhibits one maximum of complex shape. This maximum can be decomposed into three components (Figs. 4c, 4d) whose shape is also described by a Gaussian function.

Thus, the precision measurements of the creep rate for oriented UHMWPE samples demonstrated that the activation energies for steady-state creep are characterized by three most probable values.

5. ASSIGNMENT OF THE MOST PROBABLE ACTIVATION ENERGIES TO SPECIFIC TYPES OF SUPRAMOLECULAR AGGREGATES

Since the previously revealed stepwise behavior of the steady-state creep can be explained by the slip–stick microshears of microfibrils and macrofibrils with respect to each other, it is reasonable to assume that the three most probable activation barriers are associated with the different microshear strengths of fibrillar structural units.

The structure of an oriented polymer with different draw ratios is schematically drawn in Fig. 5. This structure consists of macrofibrils that, in turn, are composed of aggregates of microfibrils formed upon recrystallization inside the blocks of initial supramolecular aggregates (spherulites or stacks of lamellas). Regions between the macrofibrils are filled with loose microfibrils [12, 13]. The macrofibrils themselves are located both in the bulk and on the surface of the sample. Microshears under external loading proceed through the slip (or destruction) of microfibrils.

The resistance to slip of microfibrils on the surface of the macrofibrils differs from that in the bulk of the macrofibrils. This can be explained by the fact that the microfibrils inside a macrofibril are surrounded by neighbors on all sides, whereas the microfibrils on the macrofibril surface are surrounded by neighbors only on the inside. Moreover, the slip of microfibrils depends on the location of the macrofibrils in the sample: the slip of microfibrils on the surface of the sample occurs more readily than that in the bulk of the sample.

Therefore, the peaks in the distributions of the creep activation energies can be reasonably assigned to the following activation processes: the peak at the maximum energy can be attributed to the displacement of the microfibrils inside the macrofibrils, the peak at the lower energy can be associated with the microshears of

the microfibrils in the interfibrillar region, and the peak at the lowest energy can be assigned to the shear of the microfibrils inside the interfibrillar region in the surface layers of the polymer.

The area under the peak is proportional to the number of stoppers hindering microshears, and the half-width of the peak characterizes the spread of activation energies of these stoppers about a mean value.

6. INFLUENCE OF THE SUPRAMOLECULAR STRUCTURE ON THE POSITION, INTENSITY, AND HALF-WIDTH OF ENERGY PEAKS

As was noted above, the position, the half-width, and the integrated intensity of the energy peaks depend on the specific features of the technique used for preparing the sample (Figs. 6–8). Consequently, these features have an effect not only on the number of stoppers but also on the height and dispersion of the activation barriers.

In particular, an increase in the draw ratio leads to an exponential decrease in the number of all stoppers (Fig. 6). For the UHMWPE film with a draw ratio of 120, the barriers are destroyed to the greatest extent (by a factor of ≈75) in the surface layer, to a smaller extent (by a factor of ≈49) in the interfibrillar region, and to the smallest extent (by a factor of ≈10) in the bulk of the macrofibrils.

The energy of activation barriers varies nonmonotonically with an increase in the draw ratio; more precisely, the height of the activation barriers initially increases and then decreases (Fig. 7).

As is known [12, 13], the orientation stretching leads to a narrowing of the macrofibrils, their elongation, and a transformation from spindle-shaped macrofibrils in samples with a small draw ratio into band-shaped macrofibrils in samples with a large draw ratio. This is accompanied by an increase in the fibril packing density under transverse compressive stresses and, accordingly, by an increase in the resistance to slip of fibrils with respect to each other. As a consequence, the height of the activation barriers increases. However, apart from the increase in the fibril packing density, the orientation stretching leads to the scission of a number of poly(ethylene) molecules and, hence, to a decrease in the strength of the oriented polymer [12, 13]. This can be judged, for example, from the deviation of the dependence of the tensile strength on the draw ratio from a straight line (this dependence flattens out at draw ratios of more than 70, and, in some cases, the tensile strength decreases with an increase in the draw ratio). Furthermore, there arise kink bands (large-scale rotational defects) in stretched samples. The formation of kink bands is attended by the separation of the sample into layers and its loosening. As a result, the activation barrier height decreases.

The half-width of the peaks characterizes the spread of activation barrier heights about a mean value. As can

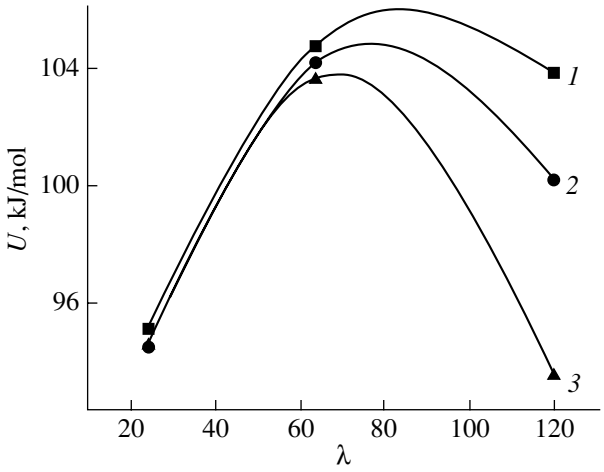

Fig. 7. Dependences of the energy of activation barriers corresponding to shears of microfibrils in (*1*) the bulk of macrofibrils, (*2*) the interfibrillar region, and (*3*) the surface layer on the draw ratio for gel-crystallized UHMWPE films.

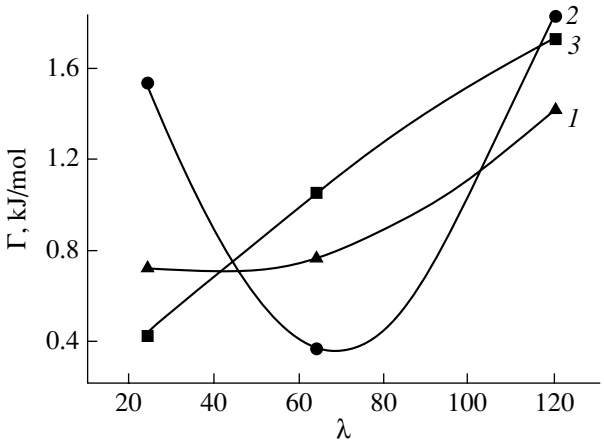

Fig. 8. Dependences of the root-mean-square deviations of the activation barriers corresponding to shears of microfibrils in (*1*) the bulk of macrofibrils, (*2*) the interfibrillar region, and (*3*) the surface layer on the draw ratio for gel-crystallized UHMWPE films.

be seen from Fig. 8, the spread of activation barrier heights that correspond to the shears of microfibrils on the sample surface and in the bulk of the macrofibrils increases monotonically with an increase in the draw ratio. At the same time, the spread of activation barrier heights that are associated with the shears of microfibrils in regions between the macrofibrils decreases upon stretching to a draw ratio $\lambda \approx 70$ and increases with a further increase in the draw ratio.

It is known that, with an increase in the degree of stretching, the supramolecular structure becomes more ordered in regions between the macrofibrils in the bulk of the sample. This is accompanied by a decrease in the spread of activation barrier heights. However, further

stretching initiates fracture of the UHMWPE structure on the molecular level [13]. Therefore, the spread of activation barrier heights increases.

7. CONCLUSIONS

Thus, the above analysis of the results obtained using a precision Doppler meter of plastic strain rates allowed us to draw the conclusion that the steady-state creep of oriented UHMWPE films is governed by the overcoming of three activation barriers. The energy required to provide slip of microfibrils with respect to each other through the slip–stick mechanism depends on their location (in the bulk of macrofibrils, in the interfibrillar region, or in the surface layer of the sample).

ACKNOWLEDGMENTS

This work was supported by the Russian Foundation for Basic Research, project nos. 03-05-64831 and 04-03-33176a. E.M. Ivan'kova acknowledges the support of the Russian Science Foundation.

REFERENCES

1. Y. Eyring, J. Chem. Phys. **4**, 283 (1936).
2. V. R. Regel, A. I. Slutsker, and É. E. Tomashevskiĭ, *Kinetic Nature of the Strength of Solids* (Nauka, Moscow, 1974) [in Russian].
3. V. A. Petrov, A. Ya. Bashkarev, and V. I. Vettegren, *Physical Principles of Lifetime Prediction for Structural Materials* (Politekhnika, St. Petersburg, 1993) [in Russian].
4. L. E. Govaert, PhD Thesis (Technische Univ., Eindhoven, Netherlands, 1990).
5. P. J. R. Leblans, C. W. M. Bastiaansen, and L. E. Govaert, J. Polym. Sci., Polym. Phys. Ed. **27**, 1009 (1989).
6. I. M. Ward and M. A. Wilding, J. Polym. Sci., Polym. Phys. Ed. **22**, 561 (1984).
7. I. M. Ward, Prog. Colloid Polym. Sci. **92**, 103 (1993).
8. J. P. Penning, PhD Thesis (Technische Univ., Groningen, Netherlands, 1994).
9. N. N. Peschanskaya, V. A. Bershteĭn, and V. A. Stepanov, Fiz. Tverd. Tela (Leningrad) **20**, 3371 (1978) [Sov. Phys. Solid State **20**, 1945 (1978)].
10. N. N. Peschanskaya, P. N. Yakushev, A. B. Sinani, and V. A. Bershtein, Thermochim. Acta **238**, 429 (1994).
11. N. N. Peschanskaya, Doctoral Dissertation (Ioffe Physicotechnical Inst., Russian Academy of Sciences, St. Petersburg, 1999).
12. V. A. Marikhin and L. P. Myasnikova, *Supramolecular Structure of Polymers* (Khimiya, Leningrad, 1977) [in Russian].
13. V. A. Marikhin and L. P. Myasnikova, in *Oriented Polymer Materials*, Ed. by S. Fakirov (Huthig and Wepf Zug, Heidelberg, Germany, 1996), p. 38.
14. P. N. Yakushev, N. N. Peschanskaya, V. A. Marikhin, L. P. Myasnikova, and M. J. N. Jacobs, Polym. Eng. Sci. **37**, 1286 (1997).
15. E. M. Ivan'kova, V. A. Marikhin, L. P. Myasnikova, N. N. Peschanskaya, and P. N. Yakushev, Fiz. Tverd. Tela (St. Petersburg) **41**, 1788 (1999) [Phys. Solid State **41**, 1641 (1999)].
16. V. I. Vettegren, V. A. Marikhin, L. P. Myasnikova, E. M. Ivan'kova, and P. N. Yakushev, Pis'ma Zh. Tekh. Fiz. **29** (20), 26 (2003) [Tech. Phys. Lett. **29** (10), 848 (2003)].

Translated by O. Borovik-Romanova

Physics of the Solid State, Vol. 47, No. 5, 2005, pp. 975–983. Translated from Fizika Tverdogo Tela, Vol. 47, No. 5, 2005, pp. 944–950.

Viscoelasticity of a Polymer Matrix and Fracture of Heat-Resistant Fiber Composites

V. E. Yudin* and A. M. Leksowskij**

** Institute of Macromolecular Compounds, Russian Academy of Sciences, Bol'shoĭ pr. 31, St. Petersburg, 199004 Russia*

e-mail: yundin@hg.macro.ru

*** Ioffe Physicotechnical Institute, Russian Academy of Sciences, Politekhnicheskaya ul. 26, St. Petersburg, 194021 Russia*

e-mail: albert.leksowskij@pop.ioffe.rssi.ru

Abstract—This paper reports on the results of investigations into the general regularities of deformation and fracture of fiber composite materials based on new heat-resistant polymer binders. Fiber composites based on these binders can find wide application in various fields of engineering. It is established that an increase in the loss modulus of the polymer matrix decreases the probability of formation of a brittle crack in the matrix at the fiber break and increases the time interval between breakages of adjacent fibers. This leads to retardation of the correlated breakage of the fibers in fiber composite materials under loading, i.e., to an increase in their strength and fracture toughness. The inference is made that the matrix of high-strength heat-resistant fiber composites with a high fracture toughness should possess not only a high elasticity (this has long been known) but also good dissipative properties over the entire temperature range of operation. © *2005 Pleiades Publishing, Inc.*

1. INTRODUCTION

Fiber composites based on high-strength fibers and polymer matrices are widely used in various fields of engineering. In this respect, extension of the temperature range in which they operate is an important problem. Polymer fiber composites that can operate for a long time not only under standard conditions but also at temperatures above 200°C are of special interest for the design of units and parts of the so-called high-speed transport [1]. It is evident that an increase in the heat resistance of polymer matrices is of primary importance, because the heat resistance of reinforcing fillers (organic and, especially, carbon fibers) in fiber composites is many times higher than the heat resistance of traditional polymer matrices (epoxy, polyester, other binders). Therefore, the replacement of traditional binders by materials having a higher resistance without changing the most significant mechanical characteristics of fiber composites (such as the strength and the interlaminar fracture toughness) over the entire temperature range of their operation is a very important aspect of the study of polymer fiber composites.

The physical approach to the study of the fracture of polymer fiber composites, as in the case of the fracture of polymers [2], involves analysis of the processes proceeding in a solid under loading up to complete fracture of the material. Under loading of fiber composites with brittle fibers and viscoelastic matrices, which are the objects of our investigation, the fracture of individual fibers can occur even at the early deformation stages due to the large spread of their strengths. Depending on the ratio between the elastic and plastic parameters of the components, their volume fraction, and the uniformity of packing, the breakage of individual fibers either can be localized without complete fracture of the material or can initiate its complete fracture. The significant contribution to solving the problems associated with the fracture mechanics and micromechanics of fiber composites, the development of the statistical cumulative damage theory, and the study of the adhesion strength at the fiber–matrix interface and the influence of polymer matrices on the strength properties of the composites has been made by a number of well-known Russian and foreign researchers [3–8]. The physical concepts according to which the fracture of fiber composites is treated as a statistical process of damage accumulation in a material were proposed by Rosen and Zweben [3–5] and then developed by Tamuzh [6]. However, it turned out that these concepts do not allow one to reliably predict the strength characteristics of fiber composites based on new heat-resistant binders. In these models, the role of the polymer matrix in the fracture is limited only to the elastic redistribution of stresses in polymer fibers. Consequently, it has been impossible to adequately describe the transition from isolated microdamages of fibers to macrofracture of the fiber composite as a whole. Experimental investigations [9–11] have revealed that a difference between the moduli of components and good adhesion of the matrix to fibers under their combined deformation necessarily lead not only to the breakage of fibers but also, what is no less important, to an explosive initiation of microcracks in matrix regions between fibers. However, until

1063-7834/05/4705-0975$26.00 © 2005 Pleiades Publishing, Inc.

Table 1. Experimental tensile strengths of fiber composites and tensile strengths calculated in the framework of the Rosen theory [3]

Fiber	l_c, mm	σ_c, MPa	
		calculation [3]	experiment
SVM	1.2	4650	4350 ± 150
Terlon	1.1	2640	3050 ± 50
Aramid T	0.24	1143	950 ± 45
Aramid VM	0.6	2086	1820 ± 65
ÉLUR	0.33	2580	1850 ± 110

recently, this circumstance had not been taken into account in fracture models.

Shami [12] and Cooper [13] were the first to consider the energy-absorbing capability of a polymer matrix with relation to the possible formation of microcracks at fiber breaks. These authors quite reasonably noted that the retardation of the propagation of a brittle crack to an adjacent fiber by the matrix should not have any serious consequences regarding the fracture of the composite as a whole. However, they did not explain the mechanism of this retardation [for example, in terms of dissipative (viscoelastic) characteristics of the polymer matrix, such as the modulus or tangent of mechanical losses]. The establishment of a correlation between the formation of cracks in the polymer matrix and its viscoelastic behavior would make it possible to thoroughly analyze how the mechanical properties of fiber composites are affected by the molecular, topological, and supramolecular structures of the polymer matrix, whose heat resistance is ultimately determined by these structures [14].

Therefore, the design of new heat-resistant binders necessitates not only the development of physical concepts regarding the mechanism of fracture of fiber composites but also the determination of the conditions responsible for the viscoelastic behavior of the polymer with rigid fibers. This opens up possibilities for increasing the heat resistance, strength, and fracture toughness of fiber composites through improving the molecular and supramolecular structures of polymer matrices.

2. RESULTS AND DISCUSSION

The main features of the fracture of fiber composites are associated with the large spread of fiber strengths [15]. Owing to this spread, the first breakages of fibers in the material occur well before the fracture of the specimen as a whole [6]. An increase in the applied load leads to an increase in the number of breaks in the specimen and, hence, to an additional overstress experienced by unbroken fibers. The minimum length l_c of the fiber fragment in the composite can be estimated from the semiempirical relationship proposed by Asloun *et al.* [16]; that is,

$$\frac{l_c}{d} = 4.7\sqrt{\frac{E_f}{E_m}}, \quad (1)$$

where d is the monofilament diameter, and E_f and E_m are the elastic moduli of the fiber and matrix, respectively.

The major factor responsible for the probabilistic development of fracture in a real fiber composite is the spread of fiber strengths. The distribution of fibers over the strength σ is most frequently described by the Weibull function [15]

$$F(\sigma) = 1 - \exp\left[-\frac{l}{l_0}\left(\frac{\sigma}{\sigma_0}\right)^{\beta}\right], \quad (2)$$

where l is the fiber length; σ is the fiber strength; and β, σ_0, and l_0 are the parameters of the distribution.

The statistical spread of fiber strengths and the notion of an ineffective fiber length $\delta \approx l_c/2$ in fiber composites underlay the Rosen model [13], which is one of the first models of fracture of fiber composites. The strengths σ_c of fiber composites based on the aramid, polyimide, and carbon fibers were calculated in terms of the Rosen theory. The results of these calculations are given in Table 1. In order to compare the estimated strength of fiber composites with the experimen-

Table 2. Experimental strengths σ_c of microplastics based on carbon fibers and an ÉDT-10 binder and the strengths calculated in the framework of the Rosen [3], Zweben [4], and Tamuzh [6] models

Fiber	β	σ_c, MPa			
		experiment	calculation [3]	calculation [4]	calculation [6]
ÉLUR	4	2200 ± 170	3460	1110	2740
UKN-10	4	3140 ± 150	4570	1060	3410
UKN-32-10	8	3520 ± 230	3630	1600	3020
Magnomit JM6	10	4920 ± 180	5150	2700	4310
Torayca T800	12	5540 ± 140	5740	3340	4830

tal data presented in Tables 1 and 2, the volume fraction of fibers is taken to be $V_f = 1$.

Analysis of the data presented in Table 1 demonstrates that the calculated and experimental strengths of fiber composites based on organic fibers are in quite satisfactory agreement. The experimental strength of fiber composites based on carbon fibers is less than the calculated value. In fiber composites based on organic fibers, the microdelamination of a monofilament at the break prevents propagation of a brittle crack in the matrix and, thus, provides a means for more reliably determining the composite strength in the framework of the Rosen statistical model of fracture [3]. It seems likely that, for carbon fibers, the local overstress has a profound effect on fibers adjacent to the broken fiber. This effect should be included in the calculation of the composite strength, as is the case in the Zweben [4] or combined Rosen–Zweben [5] models. The more recent Tamuzh model [6] takes into account that the stress concentration factor for the fiber nearest to the broken fiber gradually increases with an increase in the size of the defect and, thus, allows for the possibility of forming disk-shaped defects composed of more than two adjacent broken fibers.

According to the models proposed in [4–6], we calculated the strengths of fiber composites prepared from different carbon fibers and compared the calculated and experimental data. The calculations were carried out using experimental data on the statistical parameters of the strength of carbon fibers, the critical length, and the elastic modulus of an EDT-10 epoxy binder. The results of the calculations performed within different models and the experimental data are presented in Table 2.

A comparison of the data obtained shows (Table 2) that the experimental strengths and the results of the calculations within the Rosen model (the upper estimate of the strength) are in good agreement only for fibers characterized by the exponent $\beta \geq 8$, i.e., for fibers with a narrow strength distribution and a homogeneous structure. For fibers with a broad strength distribution, the experimental data are in disagreement with the results of the calculations for all the models. However, the strengths calculated in terms of the Tamuzh model, which accounts for the formation of breaks (cracks) with the participation of more than two adjacent fibers, are closer to the experimental values than those calculated within the Zweben model.

As follows from relationship (1), the scale effect of the fiber strength (i.e., a decrease in the minimum length l_c) should be enhanced with an increase in the elastic modulus E_m of the matrix. Hence, as the temperature increases, retention (increase) of the strength of fiber composites requires retention (increase) of the high moduli E_m.

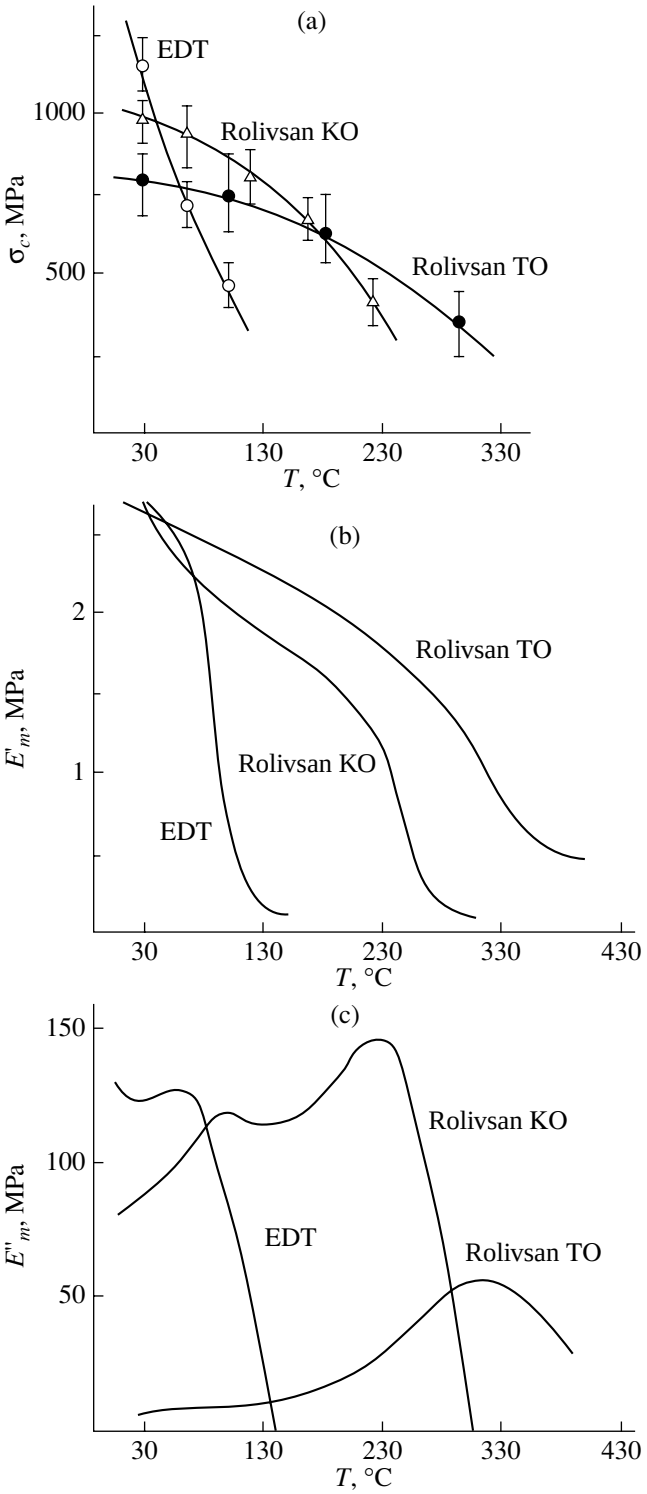

Fig. 1. Temperature dependences of (a) the strength for carbon plastics, (b) the elastic modulus, and (c) the mechanical loss modulus for the ÉDT-10, Rolivsan KO, and Rolivsan TO binders.

The changeover to the more heat-resistant binders Rolivsan TO (thermal curing) and Rolivsan KO (catalytic curing) [17] with higher densities of the network of chemical bonds ($n_c = 7 \times 10^{-3}$ and 2×10^{-3} mol/cm^3, respectively) as compared to the ÉDT-10 epoxy binder ($n_c = 10^{-3}$ mol/cm^3) indicates (Fig. 1) that the elastic properties of the matrix have an ambiguous effect on

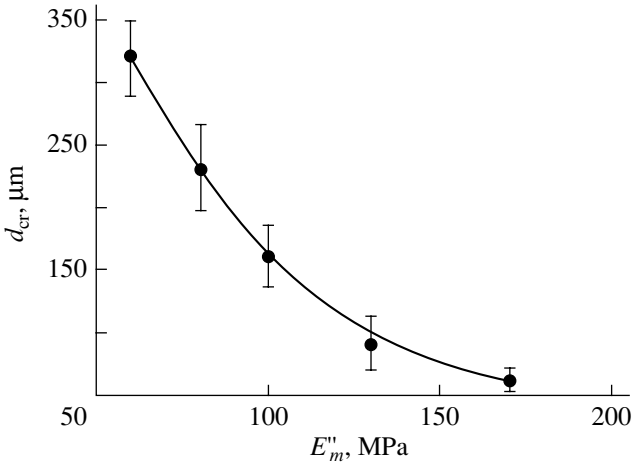

Fig. 2. Dependence of the crack diameter d_{cr} in the matrix of a model composite on the maximum modulus of mechanical losses E''_m of the Rolivsan binder used as the matrix.

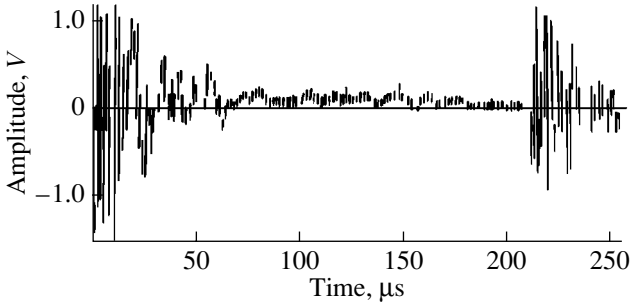

Fig. 3. Examples of acoustic emission signals from breaks of carbon fibers.

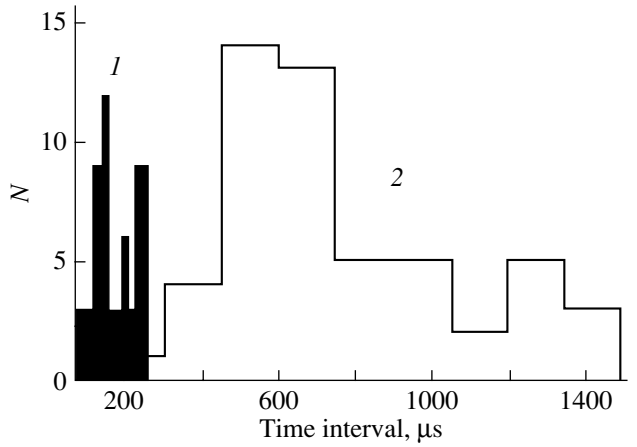

Fig. 4. Histograms of the distribution N of time intervals between acoustic emission signals for the carbon plastics based on (*1*) PEI-N and (*2*) PEI binders.

the strength of fiber composites. On the one hand, the temperature dependences of the strength σ_c (Fig. 1a) for carbon plastics based on the aforementioned binders and ELUR fibers with approximately identical volume fractions $V_f \approx 0.6$ exhibit a similar behavior. This suggests a close correlation between the strength σ_c of the composites and the dynamic elastic modulus E'_m of the matrix (Fig. 1b), especially in the range of high temperatures. On the other hand, for different matrices characterized by an insignificant difference between the elastic moduli (3%), the mean tensile strengths of the fiber composites on their base at room temperature (20–30°C) differ significantly (by 40%).

Therefore, the analysis of the strength properties of fiber composites should include not only the elastic parameters but also the dissipative characteristics of binders, for example, the dynamic modulus E''_m of mechanical losses (Fig. 1c), especially because the maximum strength of carbon plastics based on the ÉDT-10 binder at room temperature is determined by the combined high elasticity and good dissipative properties of this binder.

For a model composite, it was demonstrated that, upon fracture of a monofilament in a binder block, the microcrack formed in the bulk at the fiber break has a minimum size in the region with maximum mechanical losses of the binder, for example, in the region of the α transition. The crack size in the matrix depends on the mechanical loss modulus of the binder (Fig. 2) and decreases with an increase in the maximum loss modulus. The consequences of the brittle fracture of the matrix in the case of highly filled composites are evident. If the energy released upon fracture of the fiber does not dissipate in the matrix or along the fiber–matrix interface, this necessarily leads to impact stressing of the adjacent fiber and to an increase in the probability of its fracture.

Let us now analyze in more detail the mechanism of fiber fracture in a matrix under loading of a fiber composite. For this purpose, we performed acoustic emission investigations of fiber composites based on ELUR carbon ribbons and matrices with different dissipative properties: the polyetherimide (PEI) thermoplastic matrix and the chemically cross-linked matrix (oligoetherimides with norbornene terminal groups, PEI-N). The latter matrix at room temperature is considerably more brittle than the former matrix. The frequency and energy characteristics of the acoustic emission signals for the fiber composites based on the PEI and PEI-N matrices were compared with the corresponding characteristics of the model composite containing one carbon monofilament in the polymer matrix. This comparison showed that the signals from the fiber composites under investigations are primarily caused by the fiber breakage.

It turned out that the most interesting and somewhat unexpected data are provided by the distribution of

arrival times of the signals from fiber breaks [18]. As a rule, it is assumed that the redistribution of stresses to adjacent fibers obeys the laws of elasticity. Therefore, the distribution of acoustic emission signals from fiber breaks should exhibit a maximum at several microseconds. This corresponds to the time of propagation of a stress wave through the region between fibers.

A typical example of two acoustic emission signals from breaks of carbon fibers is given in Fig. 3. The distributions of time intervals between similar signals for a large number of events are depicted in Fig. 4. We can argue that the maximum of the distribution is located not in the time range of elastic interactions (1–3 μs) but at approximately 10^2 or 10^3 μs (depending on the dissipative properties of the matrix). Thus, it was experimentally demonstrated in real time on a microsecond scale that the dissipative properties of the matrix are responsible both for the retardation of the stress redistribution and for the decrease in the rate of accumulation of fiber breaks. Therefore, in order to ensure a higher strength of fibers for the smallest possible length, the polymer binder must possess both a high elasticity and good dissipative properties.

It follows from practice that it is insufficient to characterize the mechanical behavior of fiber composites only by the strength along the reinforcement direction. The real composite is a system of molded plates or a multilayer wound product. In this case, the strength characteristics of interlaminar fracture can prove to be decisive for the behavior of the multilayer composite under deformation. It is particularly important to determine the interlaminar fracture toughness G_{IC} of fiber composites, because these materials can be used in real constructions in which the composite is not only under tension in the direction of reinforcement with fibers but also under bending and shear. One of the most efficient tools for determining the interlaminar fracture toughness G_{IC} is the double cantilever beam method based on calculating the specific fracture work within the linear beam approach [19].

Delamination is the most dangerous type of fracture in constructions that are made up of fiber composite laminates based on chemically cross-linked heat-resistant binders with poor dissipative properties. Since cracks propagate between layers of reinforced fabrics in regions enriched with a binder, the major portion of the energy is expended in destroying the matrix. Therefore, the interlaminar fracture is primarily determined by the state of binders in fiber composites. Apart from the plastic deformation and microcracking of the matrix, the initiation of macrocrack propagation is preceded by irreversible transformations in the region of the process due to the fracture of fibers through the shear mechanism and the fracture of fiber–matrix interfaces. These elementary fracture events are efficient channels for dissipation of the stored elastic energy. The larger the volume of the material covered by microfractures at the crack tip, i.e., the larger the so-called fracture zone, the greater the cracking-resistance parameter G_{IC} of the fiber composite. All the aforementioned elementary events of fracture induce acoustic emission signals during fracture of fiber composites.

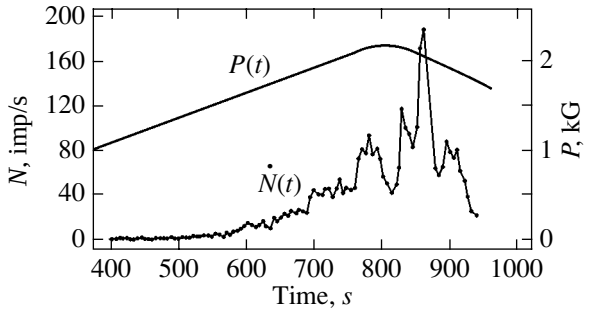

Fig. 5. Acoustic emission signal intensity under loading of the carbon plastic based on the PEI binder according to the double cantilever beam method.

Experiments demonstrated that the acoustic emission method provides a means for revealing regularities in the development of the fracture zone at the tip of an interlaminar crack that lead to crack initiation in fiber composites. Unidirectional fiber composites based on thermoreactive (Rolivsan TO, ÉDT-10) and thermoplastic (PEI) binders were studied by the acoustic emission method. The ELUR carbon ribbons served as reinforcing components. In order to determine the interlaminar fracture parameter G_{IC}, acoustic emission signals were simultaneously recorded using an acoustic emission detector (resonant frequency, 450 kHz) located at a distance of 20 mm from the crack tip.

According to the acoustic emission data, the processes occurring at the interlaminar crack tip begin well before the crack initiation. These processes are responsible for the cracking resistance of the material. The number of acoustic emission signals accumulated prior to the macrocrack initiation in the chemically cross-linked matrix is almost one order of magnitude smaller than that in the thermoplastic matrix of the fiber composite. A typical variation in the acoustic emission intensity (the number N of signals per unit time) with an increase in the load P applied to the unidirectional fiber composite specimen with an interlaminar crack is shown in Fig. 5.

Earlier [20], we performed calculations with due regard for the power relationship of the number N of acoustic emission signals on the interlaminar fracture toughness G_{IC} [21]

$$N \sim (G_{IC}E)^{n/2}, \quad (3)$$

where E is the Young's modulus in the reinforcement direction. The results obtained in these calculations demonstrated that, before the critical load (the load initiating the growth of a macrocrack) is reached, the fracture zone in the PEI thermoplastic with an interlaminar fracture toughness $G_{IC} = 1000$ J/m^2 covers five layers of

ITA

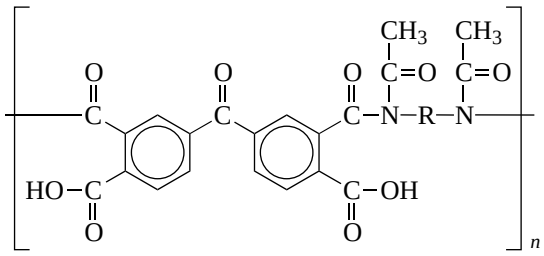

IPO

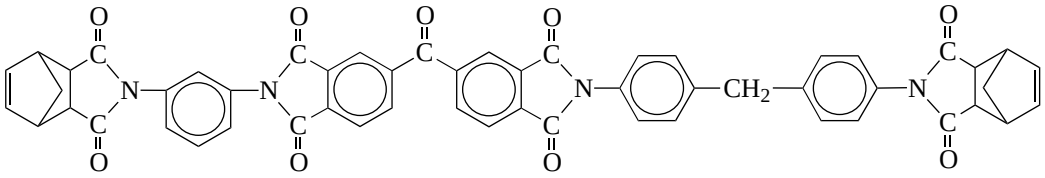

PEI

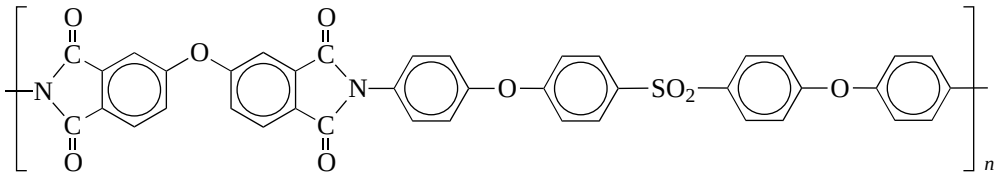

Fig. 6. Chemical structures of polyimide binders: ITA is the polyimide based on tetraacetyl diamine derivatives, IPO is the polyimide based on polymerizing oligomers, and PEI is polyetherimide.

carbon ribbons on each side of the crack plane, i.e., ten binder layers. The number of fractured layers decreases to six for the carbon plastic based on the epoxy resin with an interlaminar fracture toughness G_{IC} = 350 J/m^2 and to two for the carbon plastic based on the brittle Rolivsan TO binder with an interlaminar fracture toughness G_{IC} = 80 J/m^2. Most likely, the above regularity implies that, by the time of crack initiation, the composite with a plastic matrix has managed to accumulate a sufficient number of damages in the form of fiber breaks. It is this circumstance that ultimately determines the large cracking-resistance parameter G_{IC}.

Owing to their high heat resistance, polyimides are promising compounds for use in preparing structural fiber composites, in particular, carbon plastics. The possibility of preparing fiber composites was analyzed using different polyimide matrices (Fig. 6), such as thermoreactive polyimide based on tetraacetyl diamine derivatives (ITA) [22], polyimide based on polymerizing oligomers (IPO) [23], and polyetherimide (PEI) [24].

The thermal and mechanical characteristics of carbon plastics based on the ELUR fibers and the polyimide matrices are presented in Table 3. The volume fraction V_f of fibers in these carbon plastics depends primarily on the initial viscosity of the binders. Since the viscosity of prepolymer–oligomer melts is relatively low, the values of V_f for the ITA and IPO thermoreactive binders are equal to 58 and 60%, respectively. The volume fraction V_f of fibers in the thermoplastic binders is considerably smaller due to the high viscosity of melts and does not exceed 50–53%.

According to the volume fraction of fibers, the carbon plastics based on the ITA and IPO thermoreactive binders possess a higher bending strength σ_b. By contrast, the interlaminar cracking resistance G_{IC} for the PEI thermoplastic binder is approximately two or four times higher than that for the thermoreactive binders. The heat resistance estimated from the glass transition temperature T_g of plastics depends on the chemical structure of the binder and on the degree of its cross linking and, correspondingly, is maximum for the ITA and IPO highly cross-linked thermoreactive binders.

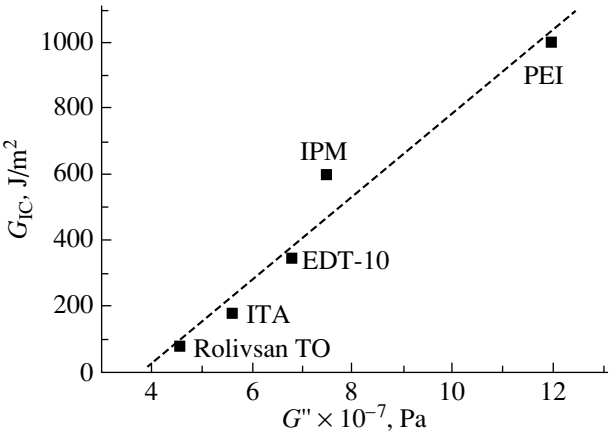

Fig. 7. Dependence of the fracture toughness on the loss modulus for carbon plastics based on different polymer binders at room temperature.

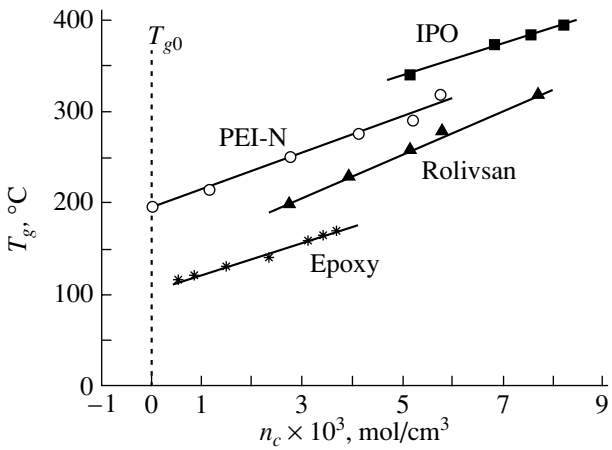

Fig. 8. Dependences of the glass transition temperature on the density of the network of chemical bonds for thermoreactive polymer binders.

An increase in the density of the network of chemical bonds, as a rule, leads to deterioration of both the dissipative properties of the polymer matrix and its ability to resist brittle fracture [14, 25]. Indeed, a comparison of the interlaminar cracking resistances G_{IC} and the shear loss moduli G'' of carbon plastics based on different polymer binders at room temperature (Fig. 7) shows that the former quantity depends almost linearly on the latter quantity. This suggests that the dissipative properties of the polymer matrix have a significant effect on the interlaminar fracture toughness of composites.

An increase in the glass transition temperature and, hence, the heat resistance of the polymer matrix due to the increase in the density of the network of chemical bonds n_c (Fig. 8) can result in a decrease in the strength and the interlaminar fracture toughness of fiber composites, especially at room temperature. It can be seen from Fig. 8 that, compared to the epoxy and Rolivsan binders, the thermoreactive polyimide binders offer significant potentialities for increasing the heat resistance without increasing the density of the network of chemical bonds n_c. This is probably associated with both the stronger intermolecular interactions in the polyimide binders and the higher glass transition temperatures T_{g0} of the initial (non-cross-linked) polyimides. The glass transition temperature T_{g0} of chemically cross-linked polymers can be represented by the standard relationship [25]

$$T_g = T_{g0} + Kn_c, \quad (4)$$

where K is an empirical constant. As follows from this relationship, polyimide-based fiber composites with a higher heat resistance can be prepared at lower densities of the network of chemical bonds n_c. In turn, this does not lead to a strong embrittlement of the polymer matrix or to a decrease in the interlaminar fracture toughness G_{IC}.

However, the design of new heat-resistant binders for fiber composites with glass transition temperatures $T_g > 200$°C on the basis of thermoreactive polyimides or thermoplastic polyimides (these materials are more promising from the standpoint of high interlaminar fracture toughnesses G_{IC}) is complicated by rheological problems [26]. In particular, the changeover to thermoplastic polyimides, which possess higher interlaminar fracture toughnesses G_{IC} in composites (Table 3), requires the introduction of flexible hinge units into the chemical chain in order to improve their processability (low melt viscosity) as matrices of composites. In this respect, much attention has been recently focused both on aromatic polyetherimides capable of processing into matrices of composites through the melt and on "structured" polyimides [27–29]. Structured polyetherimides are considered to mean polyimides with pronounced morphological features of the crystallite type [28, 29] or semi-interpenetrating polymer networks with a possible phase separation [30, 31]. At present, extensive research has been performed in this direction. There is reason to hope that the results obtained will enable one to find a way out of the impasse inherent in traditional thermoplastic or thermoreactive polymer binders.

Table 3. Thermal and mechanical characteristics of carbon plastics based on ELUR fibers and polyimide matrices

Polyimide matrix	V_f, %	σ_b, MPa	T_g, °C	G_{IC}, J/m^2
ITA	58	1270	370	230
IPO	60	1320	350	170
PEI	48	1050	230	1100

Note: ITA is the polyimide based on tetraacetyl diamine derivatives, IPO is the polyimide based on polymerizing oligomers, and PEI is polyetherimide.

These materials with an amorphous polymer structure do not permit one to solve the problem regarding the simultaneous increase in the heat resistance, the strength, and the interlaminar fracture toughness of fiber composites.

3. CONCLUSIONS

Thus, it was established that an increase in the loss modulus of a polymer matrix decreases the probability of forming a brittle crack in the matrix at the fiber break and increases the time interval between breakages of adjacent fibers. This leads to retardation of the correlated breakage of fibers in fiber composites under loading, i.e., to an increase in their strength and fracture toughness. The conclusion was drawn that the matrix of high-strength heat-resistant fiber composites with a high fracture toughness should possess not only a high elasticity (this has been long known) but also good dissipative properties over the entire temperature range of operation. It seems likely that the most promising way to design new heat-resistant composites with large values of the strength and interlaminar fracture toughness is to develop not amorphous chemically cross-linked polyimide matrices but structured polyimides (for example, partially crystalline polyimides) or matrices with a structure similar to semi-interpenetrating polymer networks.

ACKNOWLEDGMENTS

We would like to thank A.P. Tishkin (Laboratory of Physics of Composite Strength, Ioffe Physicotechnical Institute, Russian Academy of Sciences) and G.N. Gubanova (Laboratory of Mechanics of Polymer Materials, Institute of Macromolecular Compounds, Russian Academy of Sciences) for their assistance in performing the acoustic emission measurements, V.V. Kudryavtsev and the staff of his laboratory (Institute of Macromolecular Compounds, Russian Academy of Sciences) for synthesizing the polyimides, and B.A. Zaĭtsev and the staff of his laboratory (Institute of Macromolecular Compounds, Russian Academy of Sciences) for synthesizing the model Rolivsans.

This work was supported by the Russian Foundation for Basic Research, project no. 04-03-32470.

REFERENCES

1. P. M. Hergenrother, High Perform. Polym. **15** (1), 3 (2003).
2. H. H. Kausch, *Polymer Fracture*, 2nd ed. (Springer, Heidelberg, 1987; Mir, Moscow, 1981).
3. B. W. Rosen, AIAA J. **2** (11), 1985 (1964).
4. C. Zweben, AIAA J. **12** (12), 2325 (1968).
5. C. Zweben and B. Rosen, J. Mech. Phys. Solids **18** (3), 189 (1970).
6. *Fracture of Constructions from Composite Materials*, Ed. by V. P. Tamuzh (Zinatne, Riga, 1986) [in Russian].
7. A. Argon, in *Composite Materials*, Ed. by L. Broutman and R. Crock (Academic, New York, 1974; Mir, Moscow, 1978), Vol. 5.
8. A. A. Berlin, S. A. Vol'fson, V. G. Oshmyan, and N. S. Enikolopov, *Principles of Design of Polymer Composite Materials* (Khimiya, Moscow, 1990) [in Russian].
9. A. M. Leksovskiĭ, in *Kinetics of Deformation and Fracture of Composite Materials*, Ed. by A. M. Leksovskiĭ (Fiz.–Tekh. Inst. Akad. Nauk SSSR, Leningrad, 1984), p. 112 [in Russian].
10. A. M. Leksovskiĭ, A. Abdumanonov, R. M. Akhunov, G. Kh. Narzullaev, and A. P. Tishkin, Mekh. Kompoz. Mater., No. 6, 1004 (1984).
11. V. E. Yudin, A. M. Leksovskiĭ, G. Kh. Narzullaev, B. A. Zaĭtsev, L. N. Korzhavin, and S. Ya. Frenkel', Mekh. Kompoz. Mater., No. 6, 1021 (1986).
12. K. Shami, in *Composite Materials*, Ed. by L. Broutman and R. Crock (Academic, New York, 1974; Mir, Moscow, 1978), Vol. 6.
13. G. A. Cooper, in *Composite Materials*, Ed. by L. Broutman and R. Crock (Academic, New York, 1974; Mir, Moscow, 1978), Vol. 5.
14. V. I. Irzhak, B. A. Rozenberg, and N. S. Enikolopov, *Cross-Linked Polymers* (Khimiya, Moscow, 1979) [in Russian].
15. V. A. Weibull, J. Appl. Mech. **18** (3), 293 (1951).
16. El. M. Asloun, M. Nardin, and J. Schilz, J. Mater. Sci. **24**, 1835 (1989).
17. B. A. Zaĭtsev, G. I. Khramova, T. S. Tsygankova, R. F. Kiseleva, L. A. Laĭus, M. I. Bessonov, M. F. Lebedeva, and S. K. Zakharov, Mekh. Kompoz. Mater., No. 5, 775 (1982).
18. A. P. Tishkin, G. N. Gubanova, A. M. Leksovskii, and V. E. Yudin, J. Mater. Sci. **29**, 632 (1994).
19. *Interlaminar Response of Composite Materials*, Ed. by N. J. Pagano (Elsevier, Amsterdam, 1989; Mir, Moscow, 1993).
20. G. N. Gubanova, A. P. Tishkin, A. M. Leksovskiĭ, V. E. Yudin, V. M. Svetlichnyĭ, B. A. Zaĭtsev, and V. V. Kudryavtsev, Mekh. Kompoz. Mater., No. 6, 792 (1995).
21. H. L. Danegan and D. Harris, Eng. Fract. Mech. **1** (1), 105 (1968).
22. V. Ya. Goykhman, V. M. Svetlichnyi, V. V. Kudriavtsev, N. G. Antonov, Yu. N. Panov, A. V. Gribanov, and V. E. Yudin, Polym. Eng. Sci. **37** (8), 1381 (1997).
23. V. N. Artem'eva, Yu. G. Baklagina, V. V. Kudryavtsev, N. V. Kukarkina, N. S. Nesterova, Yu. N. Panov, P. I. Chupans, and V. E. Yudin, Zh. Prikl. Khim. (St. Petersburg) **66** (8), 1826 (1993).
24. V. M. Svetlichnyi, T. I. Zhukova, V. V. Kudriavtsev, V. E. Yudin, G. N. Gubanova, and A. M. Leksovskii, Polym. Eng. Sci. **35** (16), 1321 (1995).
25. L. E. Nielsen, *Mechanical Properties of Polymers and Composites* (Marcel Dekker, New York, 1974; Khimiya, Moscow, 1978).
26. V. E. Yudin, A. G. Kalbin, T. K. Meleshko, A. I. Grigor'ev, G. N. Gubanova, N. N. Bogorad, Yu. N. Panov, O. F. Pozdnyakov, B. P. Redkov, A. O. Pozdnyakov, and V. V. Kudryavtsev, Zh. Prikl. Khim. (St. Petersburg) **74** (7), 1151 (2001).

27. V. M. Svetlichnyĭ, L. A. Myagkova, V. V. Nesterov, N. G. Bel'nikevich, I. V. Gofman, G. N. Gubanova, V. E. Yudin, T. A. Kostereva, Yu. N. Panov, A. I. Grigor'ev, T. E. Sukhanova, and V. V. Kudryavtsev, Vysokomol. Soedin., Ser. A **44** (3), 373 (2002).
28. V. E. Yudin, V. M. Svetlichnyĭ, G. N. Gubanova, A. I. Grigor'ev, T. E. Sukhanova, I. V. Gofman, A. L. Didenko, E. N. Popova, R. N. Fedorova, and V. V. Kudryavtsev, Vysokomol. Soedin., Ser. A **44** (2), 257 (2002).
29. V. E. Yudin, V. M. Svetlichnyi, G. N. Gubanova, A. L. Didenki, T. E. Sukhanova, V. V. Kudriavtsev, S. Ratner, and G. Marom, J. Appl. Polym. Sci. **83**, 2873 (2002).
30. V. M. Svetlichnyĭ, L. A. Myagkova, V. E. Yudin, G. N. Gubanova, A. V. Gribanov, Yu. N. Panov, M. É. Vylegzhanina, T. E. Sukhanova, Yu. N. Sazanov, G. N. Fedorova, and V. V. Kudryavtsev, Vysokomol. Soedin., Ser. A **42** (2), 201 (2000).
31. G. N. Gubanova, V. N. Artem'eva, V. E. Yudin, T. A. Maricheva, D. G. Tochil'nikov, B. M. Ginzburg, and V. V. Kudryavtsev, Mekh. Kompoz. Mater., No. 38, 539 (2002).

Translated by O. Borovik-Romanova

Physics of the Solid State, Vol. 47, No. 5, 2005, pp. 984–988. Translated from Fizika Tverdogo Tela, Vol. 47, No. 5, 2005, pp. 951–954.

Kinetic Concept of Strength in Calculations of Elastomeric Parts

S. O. Lazarev and Yu. K. Mikhaĭlov

St. Petersburg State Polytechnical University, Politekhnicheskaya ul. 29, St. Petersburg, 195251 Russia

e-mail: Lazarev@mech.hop.stu.neva.ru

Abstract—The specific features of the kinetic concept as applied to the prediction of the lifetime of rubber parts are considered. The theoretical and experimental data on the lifetime of rubbers under uniaxial tension, combined stresses, dynamic loading with a dominant tension, and dynamic loading in the presence of a static component are analyzed consistently. Attention is drawn to the fact that standard methods can also be used to determine the strength characteristics of rubbers. It is emphasized that the methods and programs described in this paper are developed for applied purposes. © *2005 Pleiades Publishing, Inc.*

1. INTRODUCTION

Elastomeric (rubber) parts fulfill a very important function in many assemblies. For example, the required lifetime of seals in hydraulic systems for space vehicles, such as the "Mir" space station, is 15 years. Another example is provided by gaskets that are designed to operate in underwater pipelines over many years, because leaks in these gaskets can lead to environmental disasters. In the design of such parts, industry imposes heavy demands on the reliability of prediction of their lifetime. The methods based on the kinetic concept described by the Zhurkov formula have been extensively developed over the last twenty years. The results of the lifetime prediction for elastomeric parts have been reliably confirmed in practice.

In this paper, we consider the specific features of the kinetic concept as applied to the prediction of the lifetime of elastomers (the fundamental aspects of this problem were described in the monograph by Petrov *et al.* [1]).

2. LIFETIME OF ELASTOMERS UNDER UNIAXIAL TENSION

According to experimental data, the lifetime of elastomers does not obey the Zhurkov formula with constant parameters and can be adequately described by the power expression

$$\tau = C\sigma^{-b}\exp\frac{U_0}{RT}. \qquad (1)$$

However, it has been demonstrated that the coefficients involved in expression (1) are related to the Zhurkov constants. Hence, the parameters in expression (1) are treated as the activation energy U_0, the static strength exponent b (related to the structural coefficient γ), and the preexponential factor C.

Expression (1) makes it possible to interpolate satisfactorily the available data for rubbers in a high-elasticity state, i.e., in the range from the glass transition temperature to the thermal destruction temperature. An elastomer is treated as a network of long macromolecules in which regions between two neighboring cross-linked sites contain freely joined segments of length L. The stretching of segments is characterized by the draw ratio λ_{rel} [1]. It is assumed that the deformation exhibits an entropy behavior. The draw ratio, the true stress σ, and the elastic modulus E are related by the expression $\lambda_{rel} = \ln(\sigma/E)$. Replacement of the strain by the draw ratio in the relationship for the activation energy U leads to the following expression for the expected waiting time to fracture:

$$\tau = \tau_0(\sigma/E)^{-b}\exp\frac{U_0}{RT}, \quad b = \gamma E/RT. \qquad (2)$$

For a quantitative comparison of the parameters involved in expressions (1) and (2), we performed special experiments. The same elastomers were tested at temperatures below and above the glass transition point. Analysis of the dependences $\tau(\sigma, T)$ revealed that, at low temperatures, the experimental points in the $\sigma - \log\tau$ and $1/T - \log\tau$ coordinates fall on straight lines that form typical Zhurkov fans converging at a pole. This indicates that, at low temperatures, the lifetime of elastomers in the vitreous state is adequately described by the Zhurkov formula with constant coefficients. However, at high temperatures, the experimental points corresponding to the lifetimes fall on straight lines in the $\log\sigma - \log\tau$ coordinates (Fig. 1). Therefore, expression (2) is also applicable at high

1063-7834/05/4705-0984$26.00

temperatures. By this means, a satisfactory agreement was obtained for all the quantities entering into expressions (1) and (2).

Thus, the difference between the functional dependences $\tau(\sigma)$ described by the Zhurkov formula and the power expression (1) is explained by the difference between the equations of states of elastomers in the vitreous and high-elasticity states. This leads to different relationships between the strain and the stress.

3. COMBINED STRESS

It is universally accepted that, under a combined stress, the basic relationship used for predicting the lifetime should retain the proportionality $\tau \sim \tau_0 \exp\frac{U(\sigma_{ij})}{RT}$.

The Zhurkov equation was derived for uniaxial tension. The stress in this equation was treated as a scalar. Physically, the activation energy U for breaking of stretched interatomic bonds as a scalar should depend on the invariant components of the stress tensor.

Analysis of the results of experimental investigations into the fracture under biaxial tension or torsion did not provide additional information: cracks developed under the first principal tensile stresses σ_1 and propagated perpendicular to the direction of their action. The prediction of the lifetime in these cases requires only correct determination of the tensile stress σ_1.

Measurements of the long-term strength of cylindrical specimens under compression provided the most comprehensive data [2]. Under specific conditions, the fracture occurs from the surface into the bulk of the specimen (Fig. 2a), i.e., in the absence of tensile stresses. In this case, the most complicated problem is associated with the experimental implementation of uniaxial compression required to eliminate the end effects (by using special clamps; profiling, polishing, and greasing of the surfaces). Under compression of cylindrical specimens of hard elastomers with an ultimate elongation of as large as 200%, cracks always propagate from the surface into the bulk of the specimen.

A compressed cylinder with lubricated ends can be considered to be subjected to uniaxial compression. For this object, predictions can be made from formulas similar to that used for uniaxial tension. The tensile strains are directed along the circumferential coordinate and predetermine the fracture type. Only the circumferential component of the deviator stress tensor is positive and corresponds to the actually stretched bonds. To put it differently, the stress σ_{dev_1} should be used as the stress σ in expression (1). In the theory of linear elasticity, the deviator components $\sigma_{\mathrm{dev}_{ij}}$ and the tensile strains $\varepsilon_{\mathrm{dev}_{ij}}$ are related through the shear modulus $2G$

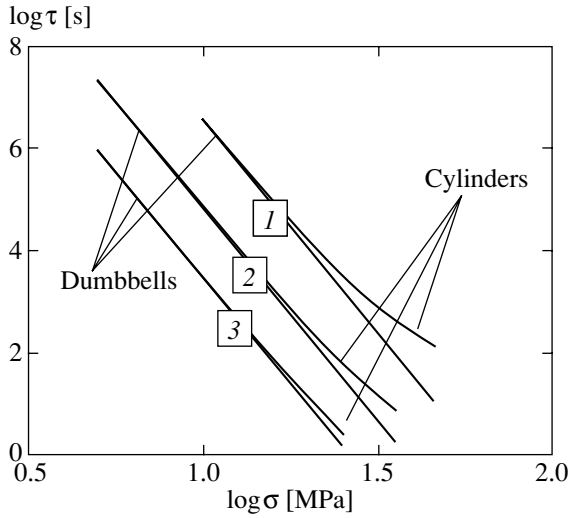

Fig. 1. Typical dependences of the lifetime of elastomers in the high-elasticity state on the true stress σ at temperatures T = (*1*) 293, (*2*) 333, and (*3*) 363 K. Straight lines correspond to the uniaxial tension of dumbbells. Curves refer to the compression of cylinders. The deference between the lifetimes of dumbbells and cylinders at identical stresses characterizes the contribution of the hydrostatic pressure to the decrease in the fracture rate.

by the expression $\sigma_{\mathrm{dev}_{ij}} = 2G\varepsilon_{\mathrm{dev}_{ij}}$. For elastomers characterized by a constant volume under deformation, the strain deviators are equal to the strains themselves. At large strains, the relationships become much more complicated. However, the calculation based on these compound relationships in combination with the finite element method is not a problem. Combining the finite element method [3] for calculating a complex stressed–strained state with the potentialities of the kinetic concept for predicting the lifetime of elastomeric parts gives an efficient tool for use in practice.

Under compression of cylindrical specimens of soft elastomers with an ultimate elongation of more than 500%, the fracture occurs from the inside of the specimen (Fig. 2b). Such cracks cannot be revealed from a change in the rigidity. Analysis was performed using the statistical accumulation of data obtained by sequentially removing and cutting the specimens. The cut specimens with initial and multiple cracks are shown in Figs. 2b and 2c.

The experimental data obtained for the cylindrical specimens are similar to those presented in Fig. 1. Here, τ is the expectation time for the appearance of the first cracks as a function of the compression load F or the final height of the cylinder in the compressed state. However, relationship (1) involves stresses. Therefore, in order to transform the dependence $\tau(F)$ into the dependence $\tau(\sigma)$, it is necessary to calculate the stressed–strained state. The problem is formulated in the framework of the finite element method [3] as fol-

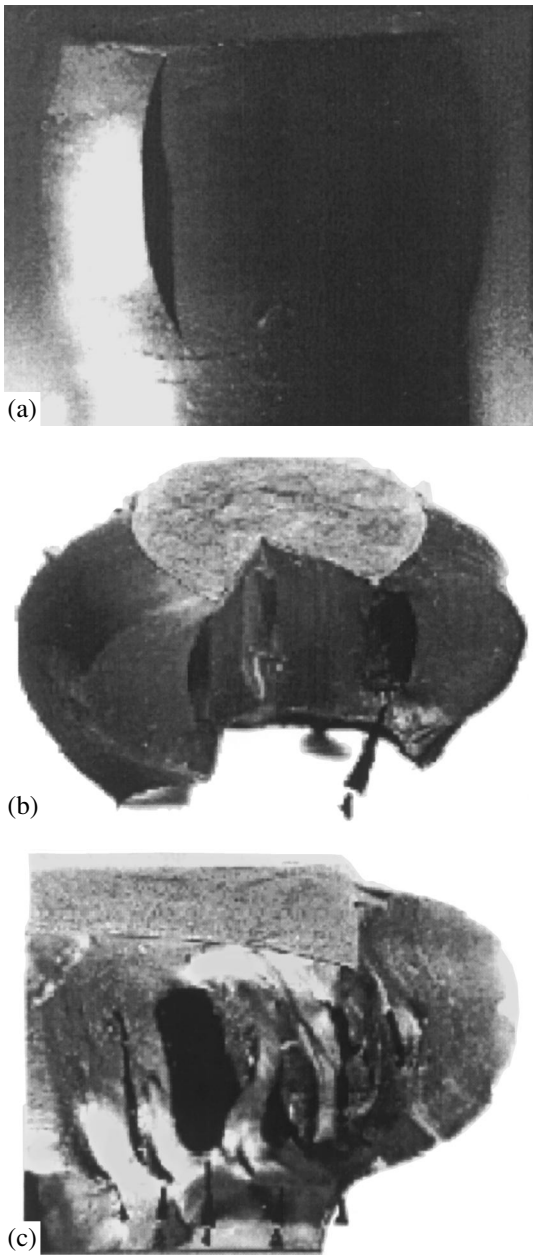

Fig. 2. Images of the cylindrical specimens fractured under compression: (a) fracture from the surface into the bulk of the hard-elastomer specimen, (b) initial (first) cracks in the soft-elastomer specimen, and (c) multiple internal cracks in the soft-elastomer specimen.

lows: the compression of the cylinder should be calculated by specifying the physicomechanical characteristics and the boundary conditions adequate for the experiment.

The contribution from the tensile stresses (including deviator stresses) to the fracture process is assumed to be constant with allowance made for the experimentally supported fact that the lifetime increases under pressure. According to [1], the pressure weakens the effect of tension in the specimen and, thus, moderates the fracture. The activation energy is represented in the form $U = U_0 + \alpha\sigma_s^2$, where the empirical coefficient α accounts for the contribution from the mean stresses or hydrostatic pressure to the change in the fracture rate. As a result, we obtain

$$\tau = C(\sigma_{\text{dev}_1})^{-b}\exp\frac{U_0 + \alpha\sigma_s^2}{RT}. \quad (3)$$

Here, the stress σ_{dev_1} corresponds to the stretched bonds. The strength characteristics U_0, b, and $\log C$ were determined from the data on the fracture of dumbbells under tension. The coefficient α can be determined by processing the data on the fracture of the dumbbells under tension and pressure (i.e., on a test machine placed in a pressure chamber). Such experiments are expensive. From the practical standpoint, the experiments on the fracture of cylindrical specimens under compression turned out to be more appropriate.

The data on the fracture of dumbbells and cylinders are compared in Fig. 1. The results of both experimental series and the strength parameters involved in the interpolation equations (1) and (3) are in reasonable agreement. For the combined stress in the $\log\sigma - \log\tau$ coordinates, the dependence ceases to be linear. This can be explained not only by the nonlinear dependences of the strain on any load parameters but also by the different contributions from the tensile stresses and hydrostatic pressure to the development and suppression of the fracture.

4. LIFETIME UNDER DYNAMIC LOADING WITH A DOMINANT TENSION

Dumbbell-like specimens subjected to bending and torsion are ideal objects for studying the lifetime under dynamic loading [4]. The necessary strain amplitude can be achieved by specifying a constant bending angle [4]. As the strain amplitude gradually decreases, the time to fracture increases from specimen to specimen. The ambient temperature in a thermal chamber is chosen and controlled in such a way as to ensure a constant temperature at the specimen surface during testing. Since the decrease in the strain amplitude leads to a decrease in self-heating, the temperature in the chamber is increased so that the temperature at the specimen surface becomes equal to the temperature at the surface of the specimen in the preceding experiment with a larger strain amplitude.

As was shown in a large number of tests, the experimental data can be interpolated using the following relationship:

$$\tau = C'\sigma_a^{-b'}\exp\frac{U_0}{R(T_{\text{amb}} + \Delta T)}, \quad (4)$$

where σ_a is the amplitude of the tensile stress, T_{amb} is the ambient temperature, ΔT is the increase in the temperature due to self-heating, C' is the frequency-dependent coefficient, and b' is the fatigue strength exponent. A comparison of the data obtained for the same elastomers shows that the activation energies U_0 in relationships (1) and (4) are equal to each other. However, as could be expected, the parameters of the fatigue strength turned out to be smaller than their static analogs: $b' < b$ and $C' < C$.

Owing to the equality of the activation energies, the lifetime under dynamic loading can be calculated from the additivity of damages with the use of relationship (4) for polyharmonic loads. In this case, the fracture criterion (the Bailey law) can be written in the form

$$\int_0^\tau \frac{dt}{\tau(\sigma(t), T(\sigma))} = 1. \quad (5)$$

For a symmetric load, the fracture occurs only in the half-cycles with tensile stresses [1]. In the compression half-cycle, the fracture occurs in other regions and directions and the fracture rate is low as compared to that in the tension half-cycles. Therefore, the integration in the above criterion is performed only over times corresponding to tensile loadings. As a result, integration in the case of a symmetric single-harmonic loading with frequency f and stress amplitude σ_a leads to the appearance of a frequency-dependent experimental coefficient n. In other words, the frequency-dependent coefficient C' in expression (4) is divided into three terms: $\log C' = \log\tau_0 + b'\log E_T - \log n$, where τ_0 is the thermal fluctuation constant ($\log\tau_0 = -12$ for the majority of elastomers), E_T is the elastic modulus extrapolated to zero temperature, and n is the coefficient of the frequency-dependent term. It should be noted that formula (5) was thoroughly verified in the experiments.

The kinetic concept as applied to the evaluation of the self-heating of elastomers [1] was also tested using dumbbell-like specimens. To date, the relationships derived have been verified thoroughly and included in the algorithms of programs based on the finite element method [2, 3] for calculating the thermal state of elastomeric parts under dynamic loading.

5. PREDICTION OF THE LIFETIME IN THE GENERAL CASE, INCLUDING DYNAMIC LOADING IN THE PRESENCE OF A STATIC COMPONENT

The operation of a number of elastomeric parts gives rise to a stressed state that is characterized by a constant or mean (with respect to time) stress σ_m and a stress amplitude σ_a. The mean stresses are governed, for example, by the weight of the supported equipment or by the preliminary treatment of the part. The stress amplitudes are determined by the vibrations or periodic processes in the system. In order to describe the combined effect of static and cyclic loadings, it is assumed that these processes make an additive contribution; i.e., the total fracture rate is the sum of the rates of fracture caused by the static and cyclic loadings. The lifetime is determined from the condition of attaining the ultimate state characterized by the accumulation of fatigue and quasi-static damages [1]. Consequently, the fracture criterion can be written as

$$\frac{\tau}{\vartheta_m(T)} + \int_0^\tau \frac{dt}{\vartheta_a(t, T)} = 1, \quad T = T_{amb} + \Delta T, \quad (6)$$

where ϑ_m and ϑ_a are the mean times to fracture under the static and symmetric cyclic loadings, respectively. Substitution of expressions (3) and (4) into relationship (6) and subsequent integration give the following expression in the logarithmic form

$$\log\tau = \log\tau_0 + b'\log E_T + \frac{[U_0 + \alpha(\sigma_s)^2]}{R(T_{amb} + \Delta T)} - \log[(\sigma_{dev_{1_m}})^{b'} + n(\sigma_{dev_{1_a}})^{b'}]. \quad (7)$$

The arguments involved in relationship (7) are as follows: the self-heating temperature; the first principal components $\sigma_{dev_{1_m}}$ and $\sigma_{dev_{1_a}}$ of the true stress deviator due to the static and amplitude dynamic loadings, respectively; and the hydrostatic pressure σ_s caused only by the static loading.

Relationship (7) contains no strength characteristics that should be determined in supplementary experiments in addition to tests with dumbbell-like specimens. The correctness of the strength characteristics and relationship (7) was checked in lifetime tests with cylindrical specimens under multiple compression [5].

By referring to domestic standards, it should be noted that the foreign analog [6] was approved only after numerous discussions at committees of the International Organization for Standardization (ISO) in 2004. Thereafter, foreign developers of the commercial programs based on the finite element method have begun to include the options of lifetime prediction in their algorithms.

Numerous examples illustrating the use of the kinetic concept (Zhurkov formula) for predicting the lifetime of different elastomeric parts can be found in [2, 3]. The authors have systematically investigated this problem over the last twenty years and collected examples confirming the validity of the proposed approach.

REFERENCES

1. V. A. Petrov, A. Ya. Bashkarev, and V. I. Vettegren, *Physical Principles of Lifetime Prediction for Structural Materials* (Politekhnika, St. Petersburg, 1993) [in Russian].
2. www.starwin.spbstu.ru, Part 4, Sect. 5, Application of Calculated and Experimental Data to the Determination of Strength Characteristics: Internal and External Fracture of Compressed Cylinders.
3. www.starwin.spbstu.ru, Part 2, Sect. 5, Application of the Finite Element Method to the Lifetime Prediction for Elastomer Products on the Basis of the Local Lifetime Distributions and Their Analysis.
4. GOST 10952-87, Rubber: Methods for Determining the Fatigue Strength under Skew-Symmetric Bending with Torsion.
5. GOST 20418-85. Rubber: Methods for Determining the Self-Heating Temperature, Residual Strain, and Fatigue Strength under Multiple Compression.
6. www.iso.org.ISO 11346:2004, Rubber, Vulcanized or Thermoplastic—Estimation of Life-Time and Maximum Temperature of Use.

Translated by O. Borovik-Romanova

Physics of the Solid State, Vol. 47, No. 5, 2005, pp. 989–993. Translated from Fizika Tverdogo Tela, Vol. 47, No. 5, 2005, pp. 955–959.

Statistical Kinetics of Rock Fracture and Forecasting of Seismic Phenomena

N. G. Tomilin, E. E. Damaskinskaya, and P. I. Pavlov

Ioffe Physicotechnical Institute, Russian Academy of Sciences, Politekhnicheskaya ul. 26, St. Petersburg, 194021 Russia

e-mail: Nikita.Tomilin@mail.ioffe.ru

Abstract—Based on kinetic concepts of the strength of solids and a related hierarchical model of rock fracture, physically justified criteria for the appearance of the fracture source stage of the process are formulated. A technique for forecasting the region, time, and energy of seismic phenomena is developed, and its algorithm is described. Examples of forecasts based on an analysis of seismic conditions on the Kamchatka Peninsula and SUBR company mines are given. © *2005 Pleiades Publishing, Inc.*

1. INTRODUCTION

Seismic phenomena detected in mechanically loaded rocks (earthquakes, rock impacts, acoustic emission signals) result from the formation of defects of different scale. This dictates solving the problem of earthquake forecasting, which consists in preliminary determination of the region, time, and energy on the basis of the physicomechanical concepts of rock fracture. This problem can already practically be solved, since techniques for determining the time, coordinates, and energy of elastic pulses have been developed methodically and technologically.

Until the mid-1950s, the fracture of solids was conventionally considered in the physics of strength to be a process that takes place when the stress or strain reach limiting values. The kinetic concept of the strength of solids opens a fundamentally new approach [1]. Based on extensive experimental data, it has been substantiated that macroscopic fracture takes place not only on reaching the ultimate strength but also at lower loads in the case of long-term exposure. The greater part of the lifetime of a loaded solid corresponds to the development of damage accumulation. The thermal-fluctuation mechanism of rock fracture was confirmed in [2]. An important consequence of the kinetic concepts of strength is the stochastic dynamics of fracture, which is controlled by the statistics of thermal fluctuations [3]. Furthermore, the randomness of the process is caused by statistical scattering of local values of the physicomechanical properties of heterogeneous materials.

Beginning from the study reported in [4], which laid the foundation for the concept of rocks as a discrete multilevel medium, the corresponding properties of a material and the processes that occur during its deformation have been actively studied. The similarity over a wide range of scales of rock structures and processes that occur under mechanical loading has been convincingly confirmed [5]. The most general similarity principle follows from empirical dependences of process parameters on the energy released during fracture [6], which makes it possible to consider this energy as a universal scale for determining the degree of fracture.

Kinetic approaches to the strength of solids and experimental studies of the features of cracking have made it possible to formulate a hierarchical model of rock fracture [7], whose basic principles are as follows. The structural inhomogeneity of a material results in a nonuniform distribution of an applied external load. This results in the formation of elements whose probability of fracture is higher than that averaged over the entire body due to a decreased thermal-activation barrier. Cracks that are initiated during fracture of such randomly distributed elements are stabilized at heterogeneity boundaries. Thus, the first stage of the process is the accumulation of noninteracting cracks, whose size is defined by a hierarchical level j of structural inhomogeneity. During the accumulation of defects, the defect concentration in a certain region randomly exceeds that averaged over the entire body. As a crack locally reaches a threshold concentration in this region (referred to as the fracture source), cracks begin to interact, which in turn enhances further defect formation. Over the course of time, the source region loses stability and a defect of the $(j + 1)$th level arises, which corresponds to the next heterogeneity size. If a material features a block size hierarchy inherent to rocks, the model implies this evolution of fracture at all existing hierarchical levels.

The sequence of defects that form during loading can be represented as a flow of discrete events each of which is specified by time and space coordinates and the size of the corresponding defect. This flow can be related to an experimentally measured seismic or acoustic-emission (AE) sequence, in which the defect size is correlated with the signal energy parameters [8]. Reformulating the two-stage model in terms of the sta-

1063-7834/05/4705-0989$26.00 © 2005 Pleiades Publishing, Inc.

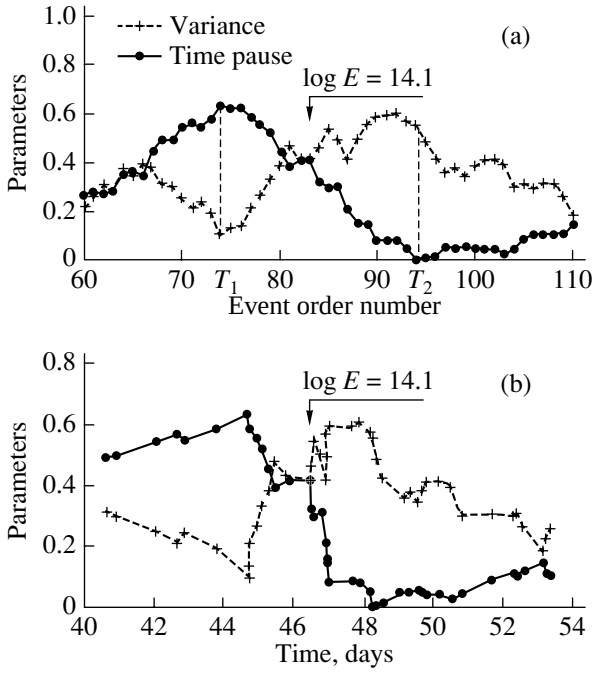

Fig. 1. Variations in the average time pause and time pause variance in the region of an earthquake with log$E$ = 14.1 (1972): (a) dependence on the sample order number and (b) the time sweep.

tistics of a discrete event flow, the first stage can be considered to satisfy the conditions of a quasi-stationary Poisson process, and violation of these conditions is a criterion for the formation of a fracture source.

Based on the results of laboratory studies of acoustic emission during rock fracture [9], the average values of time pauses Δt between chronologically sequential events and their variances $V_{\Delta t}$ as calculated for samples with a fixed number of events are taken as parameters characterizing the spatiotemporal features of fracture. At the first stage (uncorrelated formation of defects), up to the instant of time T_1 (Fig. 1a), the event flow is a Poisson process. As the concentration of defects in the region under consideration reaches a threshold value, proper conditions arise for their interaction and further stimulated nucleation, which violates the Poisson process conditions. This stage results in an increase in the parameter $V_{\Delta t}$ and a decrease in Δt. The formation of a defect corresponding to the next level in the heterogeneity hierarchy due to a loss of source stability does not necessarily complete the second unsteady stage. Relaxation of the source region (at the instant T_2) results in reverse tendencies, i.e., in an increase in Δt and a decrease in $V_{\Delta t}$ (Fig. 1a).

In general, fracture takes place simultaneously at various scale levels [7] and sequentially alternating stages occur at each of these levels. Therefore, these stages can be detected if the following two conditions are satisfied. First, the sample to be analyzed should include only events from the spatial region where a fracture source develops and, second, the energy associated with these events should correspond to a certain level (rank) in the hierarchy of the processes. In practice, these conditions are satisfied by performing double, space–energy selection of the event flow, where the criterion is the determination of trends in the characteristic variations in the statistical parameters described above. Under identical loading conditions, the following correlations were experimentally determined between the source evolution time T, the size R of the region where a source develops, and the elastic energy E that is released as the source loses stability:

$$\log T = a \log E + b, \quad (1)$$

$$\log R = c \log E + d, \quad (2)$$

where a, b, c, and d are constants.

The forecasting criteria involve only universal statistical parameters rather than physicomechanical parameters of the materials, which cannot always be determined in practice. Certainly, the difference between the physicomechanical properties of materials (including rocks) has an effect on the fracture features, including the slopes a and c in relations (1) and (2). However, according to experimental data [9], this difference does not violate the universality of the detected statistical dependences of the process.

The statistical criteria of the formation of a fracture source proposed within the hierarchical model allow one to localize the spatial region where a fracture source develops, determine the time of the transition of this region to an unstable state, and estimate the possible energy released in this region. Thus, the basic possibility arises of forecasting the region, time, and energy of a developing seismic process irrespective of its scale.

According to the concepts of conventional physical, rock fracture is a stochastic process. Therefore, any estimates or forecasts of this process can only be probabilistic and are made at various confidence levels (strategies). Currently, the efficiency EF of forecasting is estimated using conventional methods, which makes it possible to compare various forecasting methods and strategies. To this end, we used the expression for EF in the form of the ratio of the density of predicted events during the announcements of alarms to their average density over the time of observation:

$$\mathrm{EF} = (N_{\mathrm{pr}}/N_{\mathrm{tot}})/(T_{\mathrm{all}}/T_{\mathrm{tot}}), \quad (3)$$

where N_{pr} is the number of predicted events, N_{tot} is the total number of phenomena over the observation time, T_{all} is the total time of warning alarms, and T_{tot} is the total observation time. The parameter EF characterizes the relation between the reliability and accuracy of forecasts. We note that, even in the case where EF = const, this relation (i.e., the forecast strategy) can be varied by varying the alarm level. The strategy is chosen, taking into account the problems posed, at the

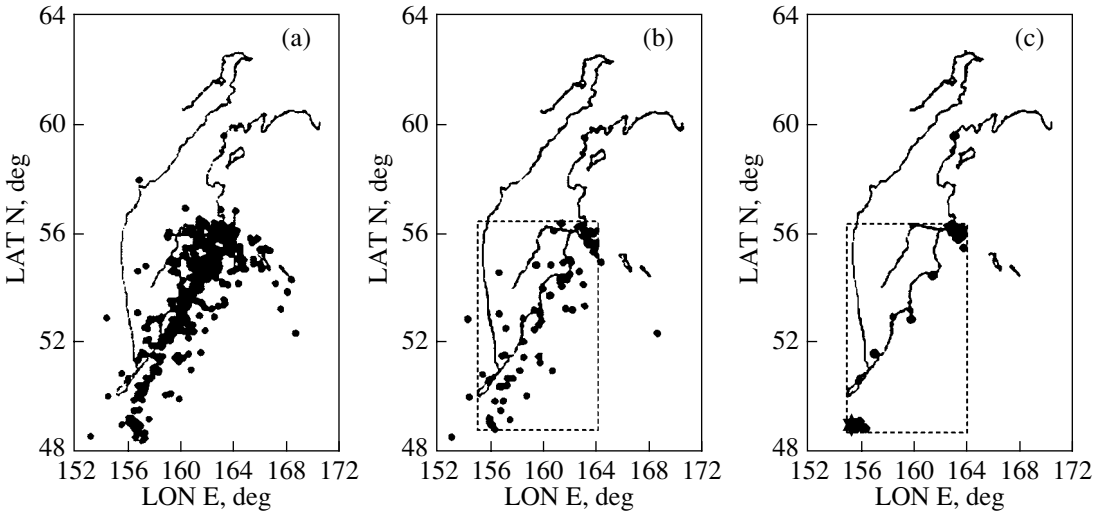

Fig. 2. Maps of earthquake epicenters in the Kamchatka Peninsula for the seismic event on August 4, 1972 with the parameter $\log E = 14.1$ in various time periods: (a) all events over June 8, 1972–October 26, 1972, (b) events with $\log E \geq 9.1$ over June 8, 1972–August 4, 1972, and (c) events with $\log E \geq 9.1$ over July 17, 1972–August 4, 1972.

stage of a retrospective analysis of the seismic conditions.

2. RETROSPECTIVE FORECASTING OF KAMCHATKA EARTHQUAKES

A database of seismic conditions in the Kamchatka region (Fig. 2) containing the following parameters for more than 50 000 earthquakes was analyzed: the time period of an earthquake (in the range 1962–2001), three coordinates, and energy (in the range 10^4–10^{16} J). The basic possibility of forecasting earthquakes in the region under study according to the algorithm described above was tested for events with $\log E \geq 14$. In this paper, we consider the features of the source formation for the event on August 4, 1972 with $\log E = 14.1$. Figure 2a shows all the seismic events detected over the period from June 8, 1972 to October 16, 1972. By varying the energy range of events using the method of successive approximations (Fig. 2b), characteristic fluctuations in statistical parameters indicating the formation of a strong earthquake source were revealed (Fig. 1).

Figure 1b shows the time dependences of the statistical parameters Δt and $V_{\Delta t}$ plotted for events with $\log E \geq 9.1$. We can see that there is a pause in the decrease in the average time and that an increase in their variance occurs simultaneously more than a day before the event under consideration. The events that occur at the unsteady stage of fracture evolution and directly determine the trends form a linear spatial structure (Fig. 2c) corresponding to a fracture arising in the Earth's crust. This allows us to assume that the mechanism of the final stage is the stick–slip process. The source regions of 36 earthquakes with $\log E \geq 14$ were analyzed in a similar way; precursors were detected in 29 cases. This 80% probability allows us to conclude that it is possible to forecast earthquakes by using the technique under consideration.

3. LONG-TERM FORECASTING OF ROCK IMPACTS FOR SUBR COMPANY MINES

Bauxite deposits in the North Urals are considered to be among the most dangerous in Russia in terms of manifestations of rock pressure. The general characteristics of seismic conditions and of the system of their measurement can be found in [10, 11].

Long-term forecasting of rock impacts have been carried out by the seismological service of the mine since 1986 within mine fields with characteristic sizes of $3 \times 3 \times 1$ km. The lower limit of the dynamic range of rock impact energies that were detected by the Severouralsk seismic station is 10 J. A reliable value for the entire seismicity field is 10^2 J. A retrospective analysis showed that the lower energy threshold of forecasted impacts exceeds the lower reliable limit of detection by four orders of magnitude. The efficiency of the rock impact forecasts is shown in Tables 1 and 2. Over the observation period, 57 rock impacts with energy E were detected in the monitored regions. The forecasting results are as follows (column C in Table 1): Y means a true forecast, N is a target loss, and R is a retrospective forecast, i.e., the case when a target loss was due to subjective reasons independent of the potential of the technique itself. Table 1 lists data on the size of a spatial region where a set alarm is localized (site forecast), the predicted energy E_{pr}, the predicted elapsed time T_{pr} (days) from the announcement of an alarm to an expected seismic event (time forecast), and the factual alarm duration T.

Table 1. Forecast parameters for rock impacts in SUBR company mines (1988–1990)

Date	*C*	$\Delta X \times \Delta Y \times \Delta Z$, m	E_{pr}, J	*E*, J	T_{pr}, days	*T*, days
Mar. 25, 1988	*Y*	$200 \times 200 \times 200$	6.1	5.5	13	85
Apr. 12, 1988	*Y*	$200 \times 200 \times 200$	6.1	6.2	13	46
Sep. 15, 1988	*Y*	$300 \times 250 \times 300$	6.7	6.7	20	68
Dec. 27, 1988	*Y*	$250 \times 250 \times 250$	6.4	5.8	17	8
Mar. 1, 1989	*R*	$100 \times 200 \times 300$	6.1	6.2	13	55
Mar. 21, 1989	*Y*	$225 \times 175 \times 200$	6.3	6.4	15	14
May 14, 1989	*Y*	$400 \times 400 \times 250$	7.2	5.3	26	26
May 21, 1989	*Y*	$250 \times 250 \times 250$	6.4	6.3	16	50
May 24, 1989	*Y*	$299 \times 325 \times 375$	6.8	6.2	22	65
July 6, 1989	*R*	$50 \times 225 \times 225$	6.3	5.8	15	19
July 29, 1989	*N*			5.7		
Aug. 21, 1989	*Y*	$200 \times 200 \times 250$	6.1	6.5	13	6
Oct. 23, 1989	*R*	$200 \times 225 \times 150$	6.3	5.8	15	33
Jan. 7, 1990	*Y*	$300 \times 225 \times 300$	6.3	6.3	15	10
Jan. 13, 1990	*Y*	$200 \times 150 \times 150$	6.1	6.7	13	8
Jan. 23, 1990	*Y*			5.6		
		$300 \times 200 \times 400$	6.7		20	25
Jan. 23, 1990	*Y*			5.8		
Mar. 6, 1990	*R*	$200 \times 320 \times 395$	6.8	6.7	21	16
Apr. 23, 1990	*R*	$235 \times 175 \times 150$	6.3	6.1	10	1
Aug. 3, 1990	*R*	$200 \times 200 \times 200$	5.9	5.7	12	51
Aug. 29, 1990	*Y*	$210 \times 245 \times 245$	6.4	6.4	16	30
Aug. 31, 1990	*Y*	$185 \times 175 \times 275$	6.2	6.2	12	6
Sep. 10, 1990	*N*			6.2		
Nov. 27, 1990	*Y*	$200 \times 300 \times 175$	6.7	6.6	20	33

Note: *C* is the forecasting result: *Y* means a true forecast, *N* is a target loss, and *R* is a retrospective forecast; ΔX, ΔY, and ΔZ are the sizes of a region where a rock impact develops; E_{pr} is the predicted energy; *E* is the true rock impact energy; T_{pr} is the predicted elapsed time from an alarm announcement to the expected seismic event; and *T* is the factual alarm duration.

Table 2. Forecast efficiency for rock impacts in SUBR company mines

Year	*P*	T_{tot}, days	T_{all}, days	T_{all}/T_{tot}	EF
1986	10/11 = 0.91	2555	939	0.37	2.5
1987	4/6 = 0.67	2745	486	0.18	3.8
1988	4/4 = 1.00	2783	762	0.27	3.6
1989	5/9 = 0.56	3345	1195	0.36	1.6
1990	7/11 = 0.64	4174	946	0.23	2.8
1991	5/12 = 0.42	2315	795	0.34	1.2
1992	3/4 = 0.75	2164	344	0.16	4.7
Total	38/57 = 0.66	20081	5667	0.28	2.4

Note: *P* is the forecast probability, T_{tot} is the total observation time, T_{all} is the total time of all announced alarms, and EF is the efficiency of forecasting decisions.

The parameters characterizing the time forecast quality are listed in Table 2. When estimating the probability *P*, only the cases for which $C = Y$ were considered to be predicted events (N_{pr}). When determining the false alarm durations T_{fa}, the preventive influence of array unloadings, performed in the framework of regular procedures, on the already formed source was disregarded. The significant overestimates of the alarm duration in some cases were caused by the following. The chosen strategy implies alarm release not by the fact of the occurrence of a predicted seismic phenomenon but by the physical criteria indicating the transition of a monitored source region to the impact-safe state. This obviously increases the alarm period but allows prediction of group impacts occurring with short pauses practically in the same region. The latter factor is of paramount importance when making a decision about con-

tinuing technological processes in the immediate vicinity of a relaxing source region.

Thus, despite the severe conditions for efficiency estimates, the results discussed above demonstrate a high quality of the time forecast. We intentionally did not consider the efficiency estimates for site forecasts, since the spatial localization of the alarm in a volume with a characteristic size of 200–250 m (for events with $E = 10^6$ J) in the case where the total monitored region is several thousands of meters in size is convincing confirmation of the potential of the technique considered. The forecast accuracy for the released elastic energy (Table 2) is within its measurement accuracy.

4. CONCLUSIONS

Based on the kinetic concepts of the strength of solids and the corresponding hierarchical model of rock fracture, a technique has been developed for forecasting seismic phenomena. A universal criterion for the formation of a local fracture source has been formalized for heterogeneous materials. Experimental studies of acoustic emission during deformation of various rock samples, as well as an analysis of seismological databases of rock impacts and earthquakes, demonstrated the stability of this physical criterion with respect to variations in the physicomechanical properties of materials and in the scales of processes over the released elastic energy range 10^{12}–10^{16} J.

ACKNOWLEDGMENTS

This study was supported by the Russian Foundation for Basic Research (projects nos. 02-05-08003, 02-05-39017, 03-05-64831, 04-05-65287) and the International Science and Technology Center (project no. 1745).

REFERENCES

1. S. N. Zhurkov, Vestn. Akad. Nauk SSSR, No. 3, 42 (1968).
2. I. S. Tomashevskaya and Ya. N. Khamidulin, Izv. Akad. Nauk SSSR, Fiz. Zemli, No. 5, 12 (1972).
3. V. A. Petrov and A. N. Orlov, Int. J. Fract. **11** (5), 881 (1975).
4. M. A. Sadovskiĭ, T. V. Golubeva, V. F. Pisarenko, and M. G. Shirman, Izv. Akad. Nauk SSSR, Fiz. Zemli, No. 2, 3 (1984).
5. M. A. Sadovskiĭ, L. G. Bolkhovitinov, and V. F. Pisarenko, *Deformation of Geophysical Environment and Seismic Process* (Nauka, Moscow, 1987) [in Russian].
6. B. Gutenberg and C. Richter, *Seismicity of the Earth and Associated Phenomena* (Princeton Univ. Press, Princeton, 1954).
7. N. G. Tomilin and V. S. Kuksenko, *Hierarchic Model of a Rock Destruction. Earth Sciences: Physics and Mechanics of Geomaterials* (Vuzovskaya Kniga, Moscow, 2002), p. 116 [in Russian].
8. V. S. Kuksenko, S. A. Stanchits, and N. G. Tomilin, Mekh. Kompoz. Mater., No. 3, 536 (1983).
9. V. Kuksenko, N. Tomilin, E. Damaskinskaya, and D. Lockner, Pure Appl. Geophys. **116** (2), 253 (1996).
10. K. A. Voinov, A. S. Krakov, V. S. Lomakin, and N. I. Khalevin, Izv. Akad. Nauk SSSR, Fiz. Zemli, No. 10, 98 (1987).
11. K. A. Voinov, A. S. Krakov, N. G. Tomilin, and D. I. Frolov, FTPRPI, No. 1, 22 (1987).

Translated by A. Kazantsev